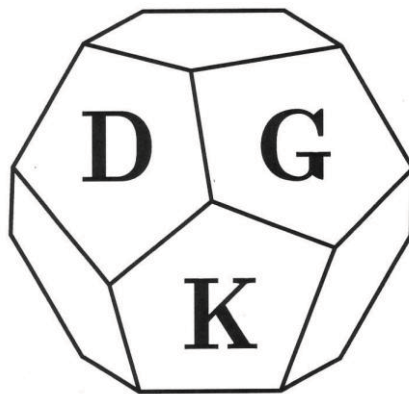


Deutsche Gesellschaft für Kristallographie

20. Jahrestagung

12. bis 15. März 2012

München



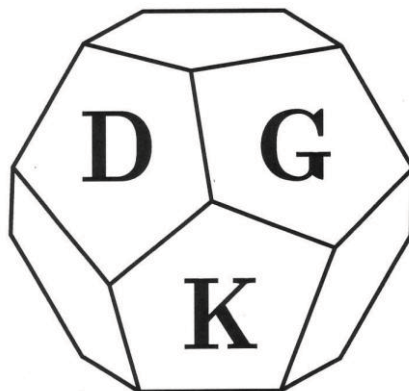
Referate
Oldenbourg Verlag – München

Deutsche Gesellschaft für Kristallographie

20. Jahrestagung

12. bis 15. März 2012

München



Referate
Oldenbourg Verlag – München

Table of Contents

Laue Talks and Lecture Laue Prize 2011.....	3
Plenary Talks	5
Talks	
Frontiers in Crystallographic Techniques and Instrumentation I.....	8
Crystallography in Engineering and Technology	10
Biocrystallography and Medicine	13
Electron Microscopy & Diffraction	15
Frontiers in Structural Analyses - Electron Density and other Precision Studies	17
Hot New Biomolecular Structures	20
Pressure-, Field-, & Temperature-Induced Processes I.....	22
Spectroscopy	24
Structure of Biological Macromolecular Complexes.....	27
Pressure-, Field-, & Temperature-Induced Processes II	29
Aperiodic Crystals	31
Theory & Simulation	34
Structure & Function: Biomaterials I.....	36
Structural Chemistry & Mineralogy	37
Frontiers of Structural Biology Methods	40
Structure & Function: Biomaterials II	41
Structure & Function: New and Smart Materials.....	44
Frontiers in Crystallographic Techniques and Instrumentation II	47
Poster	
Frontiers in Crystallographic Techniques and Instrumentation	50
Crystallography in Engineering and Technology	55
Biocrystallography and Medicine	63
Frontiers in Structural Analyses - Electron Density and other Precision Studies	65
Hot New Biomolecular Structures	67
Pressure-, Field-, & Temperature-Induced Processes	70
Spectroscopy	77
Structure of Biological Macromolecular Complexes.....	81
Aperiodic Crystals	83
Theory & Simulation	85
Structure & Function: Biomaterials	89
Structural Chemistry & Mineralogy	91
Frontiers of Structural Biology Methods	113
Structure & Function: New and Smart Materials.....	115
Preparative methods for crystalline materials	119
Index	125

LT-01

Disputed Discovery: The Beginnings of X-Ray Diffraction in crystals in 1912 and its Repercussions

M. Eckert¹

¹*Deutsches Museum, Forschungsinstitut, München, Germany*

The discovery of X-ray diffraction is reviewed from the perspective of the contemporary knowledge in 1912 about the nature of X-rays. Laue's inspiration that led to the experiments by Friedrich and Knipping in Sommerfeld's institute was based on erroneous expectations. The ensuing discoveries of the Braggs clarified the phenomenon (although they, too, emerged from dubious assumptions about the nature of X-rays). The early misapprehensions had no impact on the Nobel Prizes to Laue in 1914 and the Braggs in 1915; but when the prizes were finally awarded after the war, the circumstances of 'Laue's discovery' gave rise to repercussions. Many years later, they resulted in a dispute about the 'myths of origins' of the community of crystallographers.

LT-02

Development of diffraction-based crystallography, from Laue to the present day

D. Schwarzenbach¹

¹*École Polytechnique Fédérale, IPSB, Le Cubotron, Lausanne, Switzerland*

The first X-ray diffraction experiment of Friedrich, Knipping and Laue in 1912 marks the birth of modern crystallography. W.H. and W.L. Bragg exploited this discovery to determine crystal structure at atomic resolution, thus propelling the mathematical branch of mineralogy to global importance. Knowledge of the geometrical structure of matter had revolutionary consequences for all branches of the natural sciences, physics, chemistry, biology, earth sciences and material science. It is hardly possible for a single person to trace and appropriately value these developments, and the author will present his limited, subjective view and recollections. Tables of space groups and the theoretical foundations of structure determination still used in modern data reduction programs were available by 1920. The basic theories for the solution of the phase problem and structure refinement were available in the early 1950s. The success of crystallography as an indispensable analytical tool was then due to the development of diffraction equipment and the advent of computers. The construction of fast area detectors and novel radiation sources, synchrotrons, XFELs, neutron spallation sources and electron microscopes assure for crystallography a place at the cutting edge of modern science.

LT-03

X-ray optics, from Röntgen to Laue, Ewald, Compton, Borrmann and synchrotron radiation.

A. Authier¹

¹*Université P. et M. Curie, IMPMC, Paris, France*

The first attempts at measuring the optical properties of X-rays such as refraction, reflection and diffraction were unsuccessful. Ewald's theory of the propagation of an optical field in a triply periodic medium was at the origin of Laue's intuition and of the discovery of X-ray diffraction. The extension of Ewald's theory to X-rays led to the notions of reciprocal lattice and wavefields. Total reflection, deviation from Bragg's law, Pendellösung, anomalous absorption, standing waves, Borrmann fan, double refraction, X-ray interferometry, imaging of defects are due to the specific properties of these wavefields, which are explained by the dynamical theory of diffraction. They are made use of in all the optical devices for synchrotron radiation.

LT-04

From multigrain crystallography to 3D movies of polycrystalline materials

H. F. Poulsen¹

¹*Technical University of Denmark, Department of Physics, Lyngby, Denmark*

Conventionally crystallography is performed on two extremes of sample

constitution: a single crystal or a mono-dispersed powder. However, many samples are available only as a heterogeneous assembly of a limited number of crystals. Within the last decade methods have been demonstrated for multi-grain crystallography, where hundreds of grains are simultaneously illuminated and subject to individual analysis [1]. First results in the fields of chemistry and structural biology are summarized. For use in materials science the methods have been generalized to enable the acquisition of 3D movies of the structural evolution in polycrystals. In favorable cases, the change in morphology, orientation and stress-state in ~1000 grains can be observed during typical processing steps such as annealing or plastic deformation. The spatial resolution is of order 1 micron. Examples of such work will be presented along with new techniques - based on x-ray microscopy - which aim at mapping polycrystals in 3D also at the nano-scale. Finally, the concept of TotalCrystallography is introduced: the simultaneous characterization of the 3D atomic and 3D grain-scale structure of polycrystalline specimens [1].

[1] H.O. Sørensen et al. *Z. Kristallogr.* 227, 63-78 (2012).

LT-05

„Laue's Gateway to the Nano Cosmos: The Future"

H. Dösch¹

¹*DESY, Hamburg, Germany*

With a revolutionary experiment in 1912, Max von Laue and his collaborators entered a new world which has remained invisible and sealed to mankind: the world of crystals, atoms and molecules. The Laue diffraction experiment opened the gateway to the nano space and to a heroic century of materials-driven innovations. None of our current technologies would have been possible without this bold exploration of the molecular structure of matter. Hundred years later, mankind is opening another gateway to explore the invisible world of molecules: the real-time observation of how molecules and atoms move, how chemical bonds form and break and how a biochemical or a catalytic reaction evolves. For this scientists have devised a new tool which combines the power of x-rays and lasers and the analytical potential of microscopes and high-speed cameras: free electron lasers. I will guide the audience through a fascinating nano world enlightened by x-rays and into a new world of nano movies enabled by x-ray lasers. A fascinating story written by many authors and dedicated to Max von Laue

LT-06

Laue's legacy to biology: the impact of X-ray diffraction on our understanding of living systems

E.N. Baker¹

¹*University of Auckland, School of Biological Sciences, Auckland, New Zealand*

The discovery of X-ray diffraction by crystals, by Laue, Knipping and Friedrich in 1912, was part of a spectacular flowering of physics, much of it taking place in Germany. The full impact of this discovery came later, first in chemistry and then in biology. In this lecture I will trace the development of X-ray crystallography as a structure determination technique, from Bragg's crucial insight into Laue's discovery, through the work of J. D. Bernal, Dorothy Hodgkin, Max Perutz and others to the spectacular birth of molecular biology with the Nobel Prize awards of 1962. This brought Nobel Prizes to Crick, Watson and Wilkins for the structure of DNA, and to Kendrew and Perutz for the first protein structures. It also announced the arrival of macromolecular crystallography on the world stage. Today more than 80,000 protein structures can be found in the Protein Data Bank. Advances in molecular biology, in computing and in the availability of synchrotron sources have transformed the field, allowing ever more complex systems to be defined in atomic detail and with increasing speed and accuracy. We can now visualize the architecture of viruses, see how huge biological machines such as the ribosome work, and follow the way in which large transcriptional complexes copy and synthesize nucleic acids. At the same time, crystallography remains a powerful tool for the discovery of new chemistry in biology, and for applications in protein engineering and drug discovery. The pioneers of the field might not recognize it today, but it was their vision that made it possible.

LT-07

Beauty and Fitness for Purpose: Architecture of proteins, the Building Blocks of life

R. Huber^{1,2,3}

¹*Max-Planck-Institut für Biochemie, Martinsried, Germany*

²*Universität Duisburg-Essen, Zentrum für Medizinische Biotechnologie, Essen, Germany*

³*Cardiff University, School of Biosciences, Cardiff, Germany*

Atomic views of protein structures are determined with increasing pace in the last twenty years by a rapid development of methods and instrumentation of protein crystallography, electron microscopy, and nuclear magnetic resonance, allowing the determination of very large and complex protein structures. These structures document the beauty and unlimited versatility of the proteins' architecture, but reveal also unexpected relationships, allowing views on biological evolution far back in time. The structures are a basis for understanding the proteins' binding specificities and catalytic properties (chemistry), their spectral and electron transfer properties (physics), and their roles in physiological systems (biology and medicine). They allow design and development of specific ligands of target proteins opening novel strategies for therapeutic intervention and development of new medicaments and for plant protection.

P-01

Coupling of charge orbital and magnetic order in transition-metal oxidesM. Braden¹¹*II. Physikalisches Institut, Köln, Germany*

The coupling of electronic and magnetic degrees of freedom in transition-metal oxides leads to novel phases with combined order. The stripe phases in the superconducting cuprates form the most famous example of such ordering and yield continuing controversy concerning their role in the superconducting pairing. In manganites, however, there is no doubt that combined charge, orbital, and magnetic order is the key element for understanding the effect of colossal magneto resistance. For particularly stable order in layered perovskites, $\text{La}_{2-x}\text{A}_x\text{MeO}_4$ (A=Sr, Ca and Me=Mn, Ni and Co), single-crystal neutron diffraction can determine the precise crystal structure, which then allows identifying the character of charge and orbital order by density-functional theory. By varying the electronic doping the ordering can become anharmonic and of short-range yielding a complex real structure. For example, in overdoped manganites we find a coupling of three incommensurate order parameters (charges, orbitals and magnetic moments) with one commensurate one resulting in a stripe-like or soliton arrangement, see Figure and [1]. Mapping the reciprocal space with area detectors combined with simulations is crucial for analysing such phases. The magnetic excitations in several complex ordered phases exhibit remarkable similarities, which yield further insight to the puzzle of high-temperature superconductivity.

[1] H. Ulbrich, D. Senff, P. Steffens, O.J. Schumann, Y. Sidis, P. Reutler, A. Revcolevschi and M. Braden, *Phys. Rev. Lett.* 106, 157201 (2011).

P-02

The Energy Landscape Concept of Matter, Bridging Crystallography and ChemistryM. Jansen¹¹*Max-Planck-Institut für Festkörperforschung, Chemie III, Stuttgart, Germany*

Atomic configurations, defined by the number of atoms involved and their positions, is in the focus of crystallography, while the traditional space of chemistry is spanned by the thermodynamic variables of state, unequivocally defining the equilibrium state of a given chemical system. Our approach to synthesis planning in inorganic solid state and materials synthesis connects these completely independent domains^[1] and is based on representing the multitude of all known and still unknown chemical compounds on an energy landscape. A rather simple scenario results if one resorts to the hypothetical conditions of $T = 0$ K, and the zero-point vibrations suppressed. Then for each imaginable configuration the energy can be calculated. The resulting continuous (hyper)surface of potential energy is directly related to the configuration space, and each minimum of the landscape is corresponding to a stable configuration, and vice versa^[2]. Admitting finite temperature and pressure, i. e. realistic conditions, all unstable configurations will decay, while the (meta)stable ones constitute locally ergodic minimum regions, corresponding to a respective macroscopic thermodynamic state. Depending on the thermodynamic boundary conditions applied, one of these minimum regions corresponds to the thermodynamically stable state of the system under consideration, while the (numerous) remaining minimum regions represent metastable ones, showing a wide spread of life times. Such physically realistic energy landscapes, exhibiting numerous ergodic regions, offer a firm foundation for dealing with virtually all aspects of chemistry, on a rational basis. Since the sufficient and necessary precondition for any chemical configuration to exist is that it belongs to a minimum region, without any exception all manifestations of chemical matter are covered, and consequently the diverse

fields of preparative chemistry are unified and can be dealt with on a comparable footing. In our approach to purposeful solid state and materials synthesis, we computationally search the respective energy landscapes for (meta)stable compounds. The wealth of the candidates predicted appears to indicate an extreme (unrealistic?) complexity of chemical matter. However, applying appropriate experimental tools has enabled to realize parts of the tree graphs of the Lithium halides and of elusive Na_3N , including almost all of its predicted polymorphs, many years after the predictions were published.^[3] Starting from such atomistic energy landscapes, we have developed an approach for calculating phase diagrams, including metastable states of matter, from first principles.^[4]

[1] M. Jansen, *Angew. Chem. Int. Ed.* 41 (2002) 3746 – 3766

[2] J. C. Schön, M. Jansen, *Angew. Chem. Int. Ed.* 35 (1996) 1286 - 1304

[3] M. Jansen, K. Doll, J. C. Schön, *Acta Cryst.* A66 (2010) 518 – 534

[4] M. Jansen, I. V. Pentin, J. C. Schön, *Angew. Chem. Int. Ed.* (2011) DOI: 10.1002/anie.20110622, early view

P-03

New Light Sources for Structural StudiesE. Weckert¹¹*DESY, Hamburg, Germany*

Structural studies using synchrotron radiation have a long tradition. Crystal structure determinations of complex macromolecules exploiting anomalous dispersion are almost standard meanwhile. Spectroscopic methods using synchrotron radiation provide information on the local atomic environment as well as on electronic properties on an atomic scale. Small angle scattering on the other hand is able to provide information on larger correlation lengths also of non-crystalline samples. Recent achievements in source as well as in X-ray optics development provides focal spot sizes below 100 nm thus enabling spatial resolved diffraction, scattering, imaging and spectroscopic investigations on this length scale. The new high brilliance, hard X-ray synchrotron radiation source PETRA III at DESY that is characterized by the worldwide smallest source size and which is just ramping up user operation represent the forefront of this development, at present. While storage ring based sources are able to probe the static and slow dynamic structure of matter free electron lasers (FELs) with photon pulse lengths in the range of 100 fs and below are also able to probe extremely fast dynamics. At these time scales identifying e.g. intermediate or excited structural states far away from equilibrium e.g. during chemical reactions will become feasible thus providing us with a better understanding of reactions of interest. At DESY FLASH, a FEL in the VUV and soft X-ray regime, is in user operation since several years enabling the investigation of fast electronic effects by spectroscopic means. The lowest achieved wavelength at FLASH in the 4 nm regime allows also for scattering and coherent light imaging experiments in the so called water window probing matter at the nm length scale. The European X-ray FEL at present under construction in Hamburg will deliver photons well above 20 keV in energy and therefore enable the investigation of the dynamic properties of matter on both atomic time and length scales. The extremely short pulses at FELs have the additional advantage that within the duration of the photon pulse effects of unavoidable radiation damage under extreme flux densities have no time to manifest themselves. This lead to ‘diffraction before destroy’ techniques that allowed e.g. for the determination of the first macromolecular structure from sub micrometre size crystals.

P-04

X-ray Free-Electron Lasers - Emerging Opportunities for Structural Biology

I. Schlichting^{1,2}

¹Max Planck Institute for Medical Research, Heidelberg, Germany

²Center of Free Electron Laser Science, Max Planck Advanced Study Group, Hamburg, Germany

X-ray free-electron lasers (XFELs) exceed the peak brilliance of conventional synchrotrons by almost 10 billion times. It has been proposed that radiation damage, which limits the high resolution imaging of soft condensed matter, can be “outrun” by using ultra-fast and extremely intense X-ray pulses that pass the sample before the onset of significant radiation damage [1]. Thus, one of the most promising scientific applications of XFELs is in sub-nanometer resolution imaging of biological objects, including cells, viruses, macromolecular assemblies, and nanocrystals. The concept of “diffraction-before-destruction” has been demonstrated recently at the Linac Coherent Light Source (LCLS) [2], the first operational hard X-ray FEL, for protein micro- and nanocrystals [3] and single mimivirus particles [4]. These experiments and recent developments and progress will be presented.

[1] R. Neutze, R. Wouts, D. van der Spoel, E. Weckert, and J. Hajdu, "Potential for biomolecular imaging with femtosecond X-ray pulses," 406, 752-757 (2000).

[2] P. Emma, "First lasing and operation of an ångstrom-wavelength free-electron laser," 6 4, 641-647 (2010).

[3] H. N. Chapman, et al., "Femtosecond X-ray protein nanocrystallography," 470, 73-77 (2011).

[4] M. M. Seibert, et al., "Single mimivirus particles intercepted and imaged with an X-ray laser," 470, 78-81 (2011).

P-05

Bio-Inspired Crystallization: Challenging Single Crystal Shape and Structure

F. Meldrum¹

¹University of Leeds, School of Chemistry, Leeds, United Kingdom

Biominerals exhibit many remarkable features which ensure that they are optimised for their function, including complex morphologies, hierarchical ordering over many length scales and superior mechanical properties. Categorized as either amorphous, polycrystalline or single crystal, nature demonstrates that it is possible to manipulate all of these classes of minerals into unusual forms using strategies which operate under ambient conditions. Of these, however, the most remarkable category is arguably the single crystals. While single crystals are generally associated with regular morphologies and geometric forms, biology demonstrates that it is quite possible to produce single crystals with complex, non-crystallographic morphologies. A further feature which sets biogenic single crystals apart from synthetic crystals is their nanocomposite structure, which derives from intimate association of organic molecules with the mineral host. Although crystallization is a traditional method for purifying crystalline materials, where the impurities are excluded from the growing lattice, biology demonstrates that it is quite possible to entrap relatively high amounts of organic additives within calcite single crystals, thereby altering their textures and mechanical properties.

This lecture will show that it is possible to take inspiration from nature to generate single crystals with complex morphologies and composite structures that challenge our ideas of single crystals. A range of organic additives have been employed to control particle morphologies and internal structures, while templating approaches were used to produce single crystals with complex 3D structures. It is demonstrated that simple precipitation of crystals within suitable templates can lead to single crystals with morphologies defined by their growth environments, provided that the crystal grows to a size

larger than the length scale of the template. In the case of calcite, this methodology could not only be used to prepare “synthetic” sea urchin spines with bicontinuous structures and curved surfaces, but it can be used to produce analogous structures with much smaller length scales. The influence of the confining environment of the template on crystallization has also been explored, and it is shown that confinement offers the possibility to select crystal polymorphs, and to define the size, shape and structure of the crystalline products. The formation of composite single crystals, and the relationship between their structure and function was also explored, using the entrapment of polymer particles within calcite single crystals as a model system. Very high levels of occlusion can be achieved, generating crystals incorporating over 20 vol% of particles, according to the particle surface chemistry and the reaction conditions. The methodology was also extended to investigate the entrapment of 20 nm anionic block copolymer micelles, which act as ‘pseudo-proteins’, within calcite single crystals. This strategy led to the production of “artificial biominerals” which had analogous texture and defect structures to biogenic calcite crystals and which are also harder than pure calcite. The micelles are specifically adsorbed on {104} faces and undergo a change in shape on incorporation within the crystal lattice. This system provides a unique model for understanding biomineral formation, giving insight into both the mechanism of occlusion of biomacromolecules within single crystals, and the relationship between the macroscopic mechanical properties of a crystal and its microscopic structure.

In combination, these results demonstrate that biomimetic strategies can be successfully applied to synthetic crystal growth and that the control over crystallisation exhibited by nature is an achievable synthetic goal.

P-06

Integrated structural analysis of DNA double-strand break repair

K.-P. Hopfner¹

¹Ludwig-Maximilians-University Munich, Gene Center and, Munich, Germany

DNA double-strand breaks (DSBs) are critical lesions that can lead to the introduction of mutations, chromosomal translocations, apoptosis and cancer. The multifunctional Mre11/Rad50/Nbs1 (MRN) complex helps to sense and repair DSBs but also initiates DSB signaling by recruiting and activating the kinase ataxia-telangiectasia mutated (ATM). The mechanism of MRN to coordinate early events at DNA double-strand breaks is poorly understood. To help understand how MRN senses and signals DSBs, we use different structural biology methods to address both the structure and conformational dynamics of complexes between Mre11 and Rad50 as well as between Mre11 and Nbs1. We determined the crystal structure of the catalytic head of *Thermotoga maritima* MRN both in the absence and presence of ATP and analyzed ATP-dependent conformational changes by crosslinking and small angle scattering. The results suggest that MRN is an ATP-controlled transient molecular clamp at DNA double-strand breaks. We also determined the structure of the complex of *S. pombe* Mre11 bound to Nbs1, which explains the hypomorphic phenotype of AT like disease and indicates that Mre11 dimers are not only critical for processing and binding of DNA but also DSB signaling. Our results clarify the architecture of the DSB sensor MRN and help understand molecular pathologies associated with MRN associated cancer predisposition diseases and neurological disorders.

Lecture Laue-Prize 2011

Crystallography and crystal chemistry in the diamond anvil cell

A. Friedrich

Institut für Geowissenschaften, Abt. Kristallographie, Goethe-Universität Frankfurt am Main, Germany

The invention of the diamond anvil cell in 1959 was a major step in crystallography moving it to a new dimension by involving pressure as an additional variable in the studies of crystal structures and their properties. However, it was only at the beginning of the 21st century that the combination of new 3rd generation synchrotron sources, new diamond anvil designs, as well as the relatively wide spread of gas-loading and laser-heating systems further enhanced crystallographic research within the diamond anvil cell to higher pressures and temperatures and to new materials with smaller crystallite sizes.

The understanding of the crystal chemistry and of structure-property relations of compounds is a pre-requisite for materials design. This understanding is facilitated enormously by the study of pressure-induced phenomena. In the first part of my contribution the possibility to obtain new insight into the nature and high-pressure stability of electronic distortions, especially of the stability of the stereochemical activity of lone electron pairs, and of crystal-field transitions will be discussed. The second part of the contribution will focus on recent synthesis approaches within a wide (p, T)-field by reaction of elements in the laser-heated diamond anvil cell and the crystal chemistry and structure-property relations of transition metal nitrides, carbides and borides. These compounds are of special interest due to their high hardness, incompressibility and high melting points. The synthesis of novel rhenium nitrides at high pressures and temperatures will serve as an example to show how the combination of micro-techniques like micro-Laue X-ray diffraction and micro-Raman spectroscopy with the power of quantum-mechanical calculations can be used for crystallographic characterization of novel high- (p, T) materials.

Financial support from the DFG within SPP1136 (Wi1232) and SPP1236 (Wi1232,Fr2491/2-1), from the DAAD and the BMBF (project 05KS7RF1), from COMPRES, Vereinigung der Freunde und Förderer der Goethe Uni and from the Goethe-University is gratefully acknowledged. Thanks are due to ALS, HASYLAB/DESY and ESRF for beamtime. I thank my colleagues and beamline scientists for their help and cooperation.

MS01-T01

New strategies and better data with PILATUS detectors

M. Müller¹

¹Dectris Ltd., Baden, Switzerland

PILATUS hybrid pixel detectors have revolutionized crystallographic data collection by combining noise-free counter properties with highest data acquisition rates. These features enable optimized data collection strategies and new experimental techniques.

PILATUS detectors are modular two-dimensional hybrid pixel array detectors, which operate in single-photon counting mode (Brönnimann *et al.*, 2006). The hybrid pixel technology offers several distinct advantages over current state-of-the-art CCD, imaging plate, or conventional CMOS detectors. The main features include: no readout noise and no dark current, a point-spread-function smaller than one pixel, wide dynamic range, high detective quantum efficiency as well as millisecond readout times and high frame rates.

The advantages of the hybrid pixel technology allow new techniques and strategies in crystallographic data acquisition. The short readout time enables shutter free data collection in continuous rotation, eliminating shutter jitter and minimizing acquisition times. High frame rates and the absence of readout noise allow for further improved data quality in fine sliced data collection (Mueller *et al.*, 2012). Furthermore, the noise-free and highly sensitive detector allows optimal balancing of dose-rate and redundancy for superior accuracy of intensity estimates at a given dose-limit. PILATUS detectors specifically developed for laboratory experiments make these advantages and new techniques, which were previously only accessible at synchrotron beamlines, now also available for laboratory instrumentation.

Results from various X-ray experiments are presented, demonstrating how to apply and exploit the advantages of hybrid pixel detectors in crystallographic data acquisition at the synchrotron and in the laboratory. Furthermore, an outlook on the EIGER detector will be given, the next evolutionary step in hybrid pixel technology and detector instrumentation.

References:

Broennimann, Ch., Eikenberry E. F., Henrich B., Horisberger R., Huelsen G., Pohl E., Schnitt B., Schulze-Briese C., Suzuka M., Tomizaki T., Toyokawa H., Wagner A. (2006). *J. Synchrotron Rad.* 13, 120-130.
 Mueller, M., Wang, M., Schulze-Briese, C., *Acta Crystallographica D*, accepted for publication

MS01-T02

SINGLE: a program to control single-crystal diffractometers for high-precision lattice parameter measurements

R. Angel¹, L. Finger²

¹Universita di Padova, Geoscienze, Padova, Italy

²Geophysical Laboratory, Washington DC, United States

Many areas of solid-state physics, chemistry, mineralogy and materials science require very precise unit-cell parameters to be determined from single-crystal samples, often under non-ambient conditions. Examples include the variations of unit-cell parameters under pressure and temperature required for the determination of the equation of state of materials and the spontaneous strain associated with structural and electronic phase transitions. Precise measurements of lattice parameters require precise determination of the angular positions of the diffracted beams from the sample crystal, which cannot be accomplished by measurement of 2theta values alone, but require examination of the rocking curve of the crystal. Many diffractometers equipped with area detectors are incapable of these motions and their omega and detector resolution is usually too low for measuring rocking curves. By contrast, traditional 4-circle diffractometers equipped with point

detectors can do so rapidly with high angular precision. The SINGLE program has been developed over the last two decades to drive a variety of commercially-produced Eulerian-cradle diffractometers equipped with point detectors. Recent developments include interfaces for the Stoe Stadi4, Siemens P4 and Huber SMC9300 controllers, allowing older diffractometers to be used with modern PCs running Windows. SINGLE specifically exploits the potential for precise measurements of unit-cell parameters through the use of peak-centring algorithms that are usually not implemented as standard utilities in the software supplied commercially with the instruments. The SINGLE software routinely allows the determination of individual unit-cell edges of good-quality single crystals to 1 part in 30,000 corresponding to a precision in unit-cell volumes of 1 part in 10,000. The software supports a wide variety of diffraction geometries so that measurements can be made from crystals held in a variety of environmental devices such as diamond-anvil pressure cells, furnaces and cryogenic coolers. Examples of recent results will be presented. Further details in *J Appl. Crystallogr.* 44:247 and atwww.rossangel.net.

MS01-T03

Utilizing synergetics: coupling μ -XRD² with μ -Raman

C. Berthold¹, M. Keuper¹, V. Presser², K.G. Nickel¹

¹Eberhard Karls University Tübingen, Faculty of Science, Applied Mineralogy, Tübingen, Germany

²Drexel University, Department of Materials Science & Engineering, Philadelphia, United States

The use of X-ray optics, microfocus X-ray sources, and large 2-dimensional detectors (XRD²) have enabled significant improvements in spatial resolution, measurement times, and information density of commonly available laboratory X-ray diffractometers. Measurement times of a few seconds and spot sizes below 100 μm are becomingstate of the art.

Nevertheless, typical restrictions of X-ray powder diffraction still apply and a sufficiently large number of randomly oriented crystals has to be present in the small volume illuminated by the microfocus beam. Only then can the measured intensities directly be used for correct phase identification, quantitative analysis, and possible texture studies. This issue is of particular concern as the spatial resolution is decreased to the actual grain size in many polycrystalline materials (10 μm range) and can only partially be overcome by sample rotation. In addition, the limited applicability of X-ray diffraction to characterize amorphous or strongly disordered materials remains.

From this it is evident that XRD alone is often insufficient to comprehensively characterize advanced functional and heterogeneous materials. To overcome these limitations, we have integrated a micro-Raman probe inside a microdiffractometer. Micro-Raman spectroscopy is a well suited complementary method and can easily be integrated in a diffractometer. This has been made possible by utilizing a compact small fiber-optical probe which allows a spatial resolution down to the μm -range, combined with the possibility to obtain an optical image of the measurement region using exchangeable microscopic optics. This way, the measurement spot can be adjusted in such a manner that XRD and Raman measurements are carried out at the same location. We will discuss the problem of the different excitation volume of both methods, which is of particular importance for heterogeneous samples.

We will demonstrate high resolution phase mappings of heterogeneous material systems as performed in a set-up, which integrates the fiber-optical measurement head of a inVia Raman microscope from RENISHAW in a BRUKER D8-Microdiffractometer. Further advantages like the identification of organic substances, amorphous phases, structurally bound water and large single crystals are also shown, representing a significant step forward in the analyses of complex samples.

MS01-T04

In-house research facility for simultaneous measurements of elastic properties and densities of single crystals at high pressures.A. Kumosov¹, D. Trots¹, T. Boffa-Balaran¹, D. Frost¹¹Universität Bayreuth, Bayerisches Geoinstitut, Bayreuth, Germany

Recent development of ultra high-pressure diamond anvil cells and exploiting highly hydrostatic pressure media allow measurements of lattice parameters by x-ray diffraction and acoustic velocities by Brillouin spectroscopy at megabar pressures. However increase of pressure range results in decrease of sample size. For in-situ measurements of samples at conditions of Earth's lower mantle one need to use non-conventional facilities (high brilliance x-ray source, such as synchrotron, rotating anode or micro-focusing tube). In addition, correct measurements of elastic properties at high pressure require the simultaneous measurements of the density and the sound velocities vs. orientation.

Here we present the combined single-crystal x-ray diffraction/Brillouin scattering system which has been recently built up at Bayerisches Geoinstitut, University of Bayreuth. Due to the combination of the Brillouin spectrometer with high intensity x-ray source, the system opens a new area for in situ studies of materials under extreme conditions. With this system, it is now possible to measure sound velocities and densities of materials simultaneously as a function of pressure. These data will lead to new pressure scales, as the current scales are still essentially based on interpolations to dynamic shock-wave data. The experimentally determined density-velocity relationships will also provide essential information for understanding seismic observations and modeling the composition and evolution of the Earth. So far such measurements were possible only at the synchrotron facilities, namely, APS and SPring-8.

Here we report the results of set of single-crystal Brillouin measurements of MgSiO₃ perovskite (end member of the main lower mantle candidate mineral) at pressures up to 31 GPa. The crystal orientation was determined in-situ using X-ray diffraction. The sample was double-side polished to 15 μm thickness with diameter of 80 μm. The sample with a ruby chip was loaded into a 200 μm Re gasket sample chamber of a 90° symmetric diamond-anvil cell with hydrostatic He pressure medium.

All nine elastic constants as a function of pressure, bulk and shear moduli for orthorhombic crystal of MgSiO₃ perovskite were determined from one non-specifically oriented single crystal. We used our x-ray diffraction data to apply constraints which help to reduce correlation. The error analysis was performed by weighting of errors for every data point and calculation of correlation matrix. Our data provide essential insight for constraining of the Earth's interior profile based on seismic observations.

MS01-T05

Progress in Laue TopographyA. Danilewsky¹, J. Wittge¹, D. Allen², J. Stopford², P. McNally², T. Baumbach³¹Kristallographie, Universität Freiburg, Freiburg, Germany²Dublin City University, The RINCE, Dublin, Ireland³Karlsruhe Institute of Technology, ANKA, ISS, Karlsruhe, Germany

X-Ray topography has been used for over half a century for the characterization of extended defects such as dislocations, slip bands, stacking faults, etc. in single crystals and devices fabricated thereupon. Classically the monochromatic Lang or Berg-Berett method is in use where the sample has to be adjusted for every single diffraction vector. This was becoming redundant with the use of the Laue or synchrotron X-ray topography [1]. The white beam produces within several minutes a Laue pattern of reflections with various diffraction vectors \mathbf{g} which are collected on X-ray sensitive films. Each reflection contains a topograph from the same sample volume and by using the simple expression $\mathbf{g} \cdot \mathbf{b} = 0$, the Burgers vector \mathbf{b} can be easily analysed. Crystals with high

dislocation densities up to 10^5 cm^{-2} can be characterised quantitatively as well as high absorbing materials because of the coherency and low divergence of the synchrotron beam.

The development of fast and high resolving indirect digital detector systems [2] allows a tremendous reduction of the exposure time for a single topograph. Integration times of less than 0.2 s allow a *real-time* and *in-situ* topography e.g. at high temperatures [3]. Fig. 1a-c shows a series of 0-22 large area transmission topographs from a Si sample which were extracted from a *real-time* movie taken at about 1000 °C. Concentric dislocation loops develop around 8 artificial defects and extend over pairs of inclined {111} planes [4].

Another application for the high speed topography is the *real-time* metrology of Si wafers with a diameter of 450 mm in approx. 4 hours [3].

A very promising new development based on the Laue topography is the 3-dimensional diffraction imaging [5]. The 3D diffraction image results from the 3-dimensional rendering of a high number of section transmission topographs across the sample with the beam collimated to 10 mm x 15 μm and a step size of 15 μm. It will be shown, that the absolute strain value around defects can be measured quantitatively with this new approach.



Fig. 1: *In-situ* X-ray diffraction imaging with CCD-system, 1s integration time: Dislocation loops in a (100) Si wafer originating from 600 - 200mN Berkovich indents at 1000 °C after (a) 55, (b) 65 and (c) 80 seconds

[1] Tuomi, T. et al., *phys. stat. sol. a* 25(19974) 93.[2] Rack, A. et al., *Nucl. Instr. Methods Phys. Res. B* 267 (2009), 1978.[3] Danilewsky, A. et al., *phys. stat. sol. A* 208(11) (2011), 2499.[4] Wittge et al., *J. Appl. Cryst.* 43 (2010), 1036.[5] Allen, D. et al., *J. Appl. Cryst.* 44 (2011), 526.

MS01-T06

Exploring Structural Properties at the Micron and Sub-micron Scale with Focused Synchrotron Radiation and Scanning Diffraction TechniquesM. Burghammer¹¹European Synchrotron Radiation Facility, Microfocus Beamline ID13, Grenoble, France

Materials can be probed with high spatial resolution at third generation synchrotron radiation sources employing focused x-rays. Methods and instrumentation related to the production of such beams in the range of less than 100 nm to several microns will be described. Their application within scanning diffraction experiments at the ESRF Microfocus Beamline ID13 will be presented using examples from different domains of material research such as bio-materials, superconductors[1], polymers[2], and structures on semiconductor surfaces. Future perspectives regarding technical challenges like the implementation of nano-beam compatible sample environments and opportunities for applications in industrial research will be discussed.

[1] Fratini et al., *Nature* 2010 **466**(7308) 841-844[2] Rosenthal et al., *Angewandte Chemie* 2011 **50**(38) 8881-8885

MS02-T01

On the validity of the Warren model of stacking faults

D. Rafaja¹, C. Krbetschek¹, D. Borisova¹, S. Martin¹, G. Schreiber¹, V. Klemm¹

¹TU Bergakademie Freiberg, Materials Science, Freiberg, Germany

In situ X-ray diffraction (XRD) analysis of the austenitic steels with low stacking fault density that show the transformation induced plasticity effect (TRIP steels) was applied to find out the validity range of the Paterson [1] and Warren [2, 3] model describing the shift of XRD lines, which is caused by the presence of stacking faults in a face centred cubic structure. As the in situ XRD experiments were carried out during the tensile deformation of the TRIP steels, the observed XRD line shift was controlled both by elastic and plastic deformation of the austenite. The contribution of the elastic deformation to the XRD line shift was described by the X-ray elastic constants (XECs), the contribution of the plastic deformation to the XRD line shift by the contrast factors of the stacking faults as usual.

Although the crystallographic anisotropy of XECs strongly correlates with the crystallographic anisotropy of the contrast factors of stacking faults for strong (and thus typically used) XRD lines, the macroscopic lattice deformation could be distinguished from the local strain fields that arose in the vicinity of the stacking faults and other microstructure defects generated by the plastic deformation of austenite. The in situ XRD experiments revealed that the Paterson and Warren model is only valid in an intermediate range of the plastic deformation. At the beginning of the plastic deformation, when the stacking faults form through the splitting of perfect dislocations into the partial dislocations, XRD recognizes mainly the lattice strain around the partial dislocations, and the classical stacking fault model yields a wrong stacking fault density. At high degrees of the plastic deformation, the stacking faults on equivalent crystallographic planes start to intersect each other; this overlap strongly modifies the crystallographic anisotropy of the contrast factors of such stacking faults, which influences the calculated stacking fault density as well. Moreover, the originally isolated stacking faults arrange continuously during the plastic deformation of austenite. Clusters of ordered stacking faults in austenite are identified by XRD as hexagonal ϵ -martensite [4].

- [1] M.S. Paterson, J. Appl. Phys. 23 (1952) 805.
- [2] B.E. Warren, E.P. Warekois, J. Appl. Phys. 24 (1953) 951.
- [3] B.E. Warren, J. Appl. Phys. 32 (1961) 2428.
- [4] S. Martin, C. Ullrich, D. Šimek, U. Martin, D. Rafaja, J. Appl. Cryst. 44 (2011) 779.

MS02-T02

Hydrothermale Synthese von CSH-Phasen (Tobermorit) mit dem Additiv Ca-Format

A. Hartmann¹, J.-C. Buhl¹, M. Khakhutov¹

¹Institut für Mineralogie, Leibniz Universität Hannover, Hannover, Germany

Im Rahmen dieser Arbeit wurden Experimente zur CSH-Phasen Synthese (Tobermorit) mit dem Additiv Ca-Format ($C_2H_2CaO_4$) durchgeführt [1]. Ca-Format Zusätzen wird bei der Zementhärtung ein beschleunigender Einfluss auf die Bildung von Tricalciumsilikat zugeschrieben [2].

Ziel der Untersuchung ist, die Wirkung von Additiven auf den Mechanismus, die Reaktionskinetik und die Morphologie der CSH-Phasenbildung im Kalk-Sand System zu beobachten. In unseren bisherigen Untersuchungen mit dem Additiv Sucrose, konnte bereits ein Verzögerungseffekt der Bildung von CSH-Phasen (Tobermorit) beobachtet werden [3].

Als Edukte für die CSH-Synthese wurden Quarzpulver und Quarzsand ausgewählt, um neben der Ca-Format Zugabe auch den Einfluss der Korngröße der Siliziumquellen auf das Kristallisationsverhalten von Tobermort zu prüfen. In Anlehnung an unsere bisherigen Experimente [4] wurden auch

unterschiedliche C/S-Verhältnisse ($C/S= 0,53$ und $C/S= 0,83$) in die Untersuchungen mit einbezogen. Das Additiv Ca-Format wurde entsprechend der molaren Verhältnisse Ca-Format/Calciumoxid (F/C) von 0.50 und 0,25 hinzugefügt. Dadurch erhöhte sich das C/S-Verhältnis entsprechend. Die Ausgangsstoffe wurden als Pulvergemenge und in Form von Presslingen einer Hydrothermalbehandlung in Stahlautoklaven unterzogen. Die Reaktionsbedingungen lagen bei einer Temperatur von 200°C und einer Reaktionszeit von 40,5 h.

Die Charakterisierung der CSH-Phasen erfolgte anhand röntgenographischer (XRD), elektronenmikroskopischer (REM und EDX) und IR-spektroskopischer (MIR) Methoden.

Die Ergebnisse zeigen unter den hier verwendeten Reaktionsbedingungen eine verzögernde Wirkung des Zusatzes von Ca-Format auf die Bildung von Tobermorit im System $CaO-SiO_2-H_2O-C_2H_2CaO_4$. Mit steigender Menge an Ca-Format ändert sich die Morphologie der CSH-Kristalle (Tobermorit) und ihre Anzahl deutlich. Abb. 1 zeigt REM-Aufnahmen der Syntheseprodukte für $C/S=0,53$ ohne Additiv (Abb. 1a) sowie unter Zusatz von Ca-Format entsprechend $F/C=0,5$ (Abb. 1b). Analog zu [3, 4] hatte die spezifische Oberfläche der Siliziumquellen (Quarzpulver und Quarzsand) wiederum einen deutlichen Einfluss auf den Reaktionsablauf. So führte auch im Falle der Synthesen mit Ca-Format eine Verwendung der Si-Quelle mit großer spezifischer Oberfläche zu ausgeprägterer CSH-Phasenbildung. Auch die Untersuchung der Presslinge zeigte, dass die Bildung von Tobermorit zwar stattfindet, daneben aber auch große Portlanditkristalle vorliegen.

- [1] Khakhutov, M.: Diplomarbeit. Institut für Mineralogie, Leibniz Universität Hannover, Hannover 2011
- [2] Dodson, V. H.: Concrete admixtures. Van Nostrand Reinhold, New York 1990
- [3] Hartmann, A., Buhl, J.-C.: Materials Research Bulletin 45 (2010), 396-402
- [4] Hartmann, A., Buhl, J.-C., van Breugel, K., Hendriks, Ch. F.: Cement and Concrete Research 37 (2007) 21-31

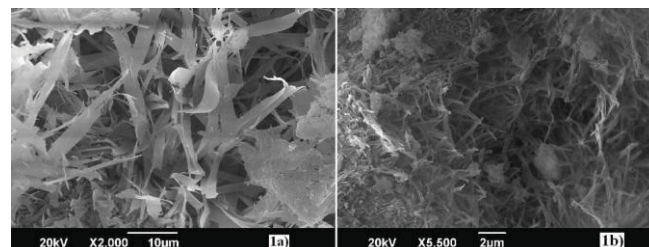


Abb. 1: REM-Aufnahmen der Syntheseprodukte; a) Synthese mit Quarzpulver, $C/S= 0,53$ ohne Additiv nach [3]; b) gleiche Bedingungen aber Ca-Formatzusatz ($F/C=0,5$).

MS02-T03

Determining glass-content of dental ceramics with high-energy synchrotron radiation

C. Hartmann¹, L. Raue¹, H. Klein¹

¹Geowissenschaftliches Zentrum Göttingen, Kristallographie, Göttingen, Germany

Most dental ceramics consist of a crystalline and an amorphous phase, e.g. vitrified feldspar ceramic. For practical use, it is important to know the physical properties like thermal expansion, Young's-Modulus and translucence which depend on both crystalline and amorphous phases and on their proportions. This study concentrates on determining the glass-content which can be done either with optical or electron microscope or by using X-ray diffraction. Since crystals in silicate-glass ceramics are small (ranging from less than 1µm up to 50µm) and the often indistinct crystal-glass border difficult to determine, quantitative X-ray

analysis seems to be the best method. In this study, a test series of calcite and silica glass spiked with 10 wt.% zincite as internal standard was made and examined by high-energy synchrotron radiation in transmission geometry ($\lambda = 0.1251 \text{ \AA}$) at DESY/HASYLAB (Hamburg). The powder diffractograms were analysed with the combined Rietveld-texture analysis program MAUD (Lutterotti et al., 1999; Lutterotti et al., 2007). In order to obtain the glass-content, two different methods have been established in the last years: recalculation of the glass-content by means of an internal standard (De la Torre et al., 2001) or direct refinement of the amorphous phase by assuming a structural model (Le Bail, 1995; Lutterotti et al., 1998). Both methods, applied on the model samples, returned good results. In a next step, the procedures are applied on dental ceramics: glassy feldspar-ceramic and La-glass infiltrated alumina-ceramic. Problems of overlapping reflections, strong texture effects, solid solution phases and differences between both methods will be discussed.

A. G. De La Torre, S. Bruque, M.A.G. Aranda (2001). Rietveld quantitative amorphous content analysis, *J. Appl. Cryst.* 34, pp. 196-202.

A. Le Bail (1995). Modelling the silica glass structure by the Rietveld method, *J. Non-Cryst. Solids* 183, pp. 39-42.

L. Lutterotti, M. Bortolotti, G. Ischia, I. Lonardelli, H.-R. Wenk (2007). Rietveld texture analysis from diffraction images, *Z. Kristallogr. Suppl.* 26, 125.

L. Lutterotti, R. Ceccato, R. Dal Maschio, E. Pagani (1998). Quantitative Analysis of Silicate Glass in Ceramic Materials by the Rietveld Method, *Mater. Sci. Forum* 278-281, pp. 87-92.

L. Lutterotti, S. Matthes and H. -R. Wenk (1999), MAUD (Material Analysis Using Diffraction): a user friendly Java program for Rietveld Texture Analysis and more, *Proceeding of the Twelfth International Conference on Textures of Materials (ICOTOM-12)*, 1, pp. 1599-1604.

MS02-T04

Neutron diffraction on ferroelectric ceramics under electric field

M. Hoelzel¹, M. Hinterstein², H. Kungl³, W. Jo⁴, H. Fuess⁴
¹Technische Universität München, FRM II, Garching, Germany
²TU Dresden, Institut für Materialwissenschaft, Dresden, Germany
³Karlsruher Institut für Technologie, Institut für Keramik im Maschinenbau, Karlsruhe, Germany
⁴TU Darmstadt, Material- und Geowissenschaften, Darmstadt, Germany

Ferroelectric ceramics were studied under electric fields by neutron diffraction. The analysis of structural changes under the influence of electric fields enables a better understanding of the poling mechanisms in technical piezoceramics. Two material systems were considered: lanthanum doped lead zirconate titanate ($\text{PbZr}_{1-x}\text{Ti}_x\text{O}_3$) with Ti/Zr ratios around the morphotropic phase boundary as well as the lead free system $\text{Bi}_{0.5}\text{Na}_{0.5}\text{TiO}_3$ - BaTiO_3 - $\text{K}_{0.5}\text{Na}_{0.5}\text{NbO}_3$ (BNT-BT-KNN).

A sample chamber which can be evacuated and filled with SF_6 gas was developed to enable the application of high electric fields for bulk samples. It is equipped with a high voltage supply for 35 kV. Depending on the sample size, electric fields up to 7 kV/mm can be applied. Two setups are available for electric field directions either vertical to the scattering plane or within the scattering plane. In the first case, the electric field vector is perpendicular to the scattering vector for all reflections. In the latter case, different orientations of the electric field vector with respect to scattering vectors of distinct lattice planes can be chosen.

Electric field induced phase transformations were observed in two compositions of the system BNT-BT-KNN at the neutron powder diffractometer SPODI (FRM II). Hence, the large field induced macroscopic strain in these materials could be attributed to a phase transformation occurring during the poling process. In both cases, the partial transition from a pure tetragonal symmetry to a rhombohedral phase was identified by the appearance of

corresponding superlattice reflections, resulting from a superstructure caused by a collective tilting of the oxygen octahedra around Ti/Zr atoms. A full pattern analysis by Rietveld refinement revealed the phase fractions and structural parameters. In lanthanum doped $\text{PbZr}_{1-x}\text{Ti}_x\text{O}_3$ samples with different Ti/Zr ratios, the structural changes under the influence of electric fields could be described in terms of anisotropic displacement parameters of the A-site cations. Different types of changes under electric field were observed for different compositions across the morphotropic phase boundary.

Moreover, lanthanum doped $\text{PbZr}_{1-x}\text{Ti}_x\text{O}_3$ with various compositions across the morphotropic phase boundary were studied at 5 K without electric field. Rietveld analysis based on monoclinic model phases revealed a smooth transition between tetragonal and rhombohedral phase regions. The analysis was based on superlattice reflections which result from a superstructure in the octahedral tilting in the Cc model phase.

The neutron diffraction studies reported in this contribution are accompanied by further structural investigations of collaborators using neutron and synchrotron diffraction as well as transmission electron microscopy.

MS02-T05

The Effect of Polyaniline and BaTiO3 on Crystal structure, Electric and Magnetic properties of Nanocrystalline Ni1-xZnxFe1.5Cr0.5O4

K. El-Sayed¹, M.B. Mohammed¹, K. El-Sayed¹, M.B. Mohammed¹
¹Ain-Shams University, Physics, Cairo, Egypt

Multiferroic composites are synthesized by a combination of magnetic and ferroelectric materials, taking into account the advantage of mutual interactions between these two phases. $\text{Ni}_{0.5}\text{Zn}_{0.5}\text{Cr}_{0.5}\text{Fe}_{1.5}\text{O}_4$ is one of the ferrite materials which has a diffuse phase transition at 305 K with a giant dielectric constant (10^6) [1]. Three nano-multiferroic systems prepared by different wet techniques were investigated in this work. Differential thermal analysis (TG/DTA), X-ray diffraction (XRD), SEM, TEM, Ft-IR, vibrating sample magnetometer (VSM), Mossbauer spectroscopy and impedance spectroscopy are used for the investigation. These study were made in order to see: 1) the role of Zn substitution on the giant dielectric properties of $\text{NiCr}_{0.5}\text{Fe}_{1.5}\text{O}_4$; 2) The effect of $\text{Ni}_{0.5}\text{Zn}_{0.5}\text{Cr}_{0.5}\text{Fe}_{1.5}\text{O}_4$ on the properties of Polyaniline polymer which is used as electromagnetic shield; 3) Finally, to see the effect of the composite formed from BaTiO_3 which is a normal ferroelectric material and $\text{Ni}_{0.5}\text{Zn}_{0.5}\text{Cr}_{0.5}\text{Fe}_{1.5}\text{O}_4$ which is magnetic on the multiferroic properties of this composite. XRD confirms that $\text{Ni}_{1-x}\text{Zn}_x\text{Cr}_{0.5}\text{Fe}_{1.5}\text{O}_4$ have cubic spinel single phase with crystallite size around 5 nm. Its magnetic properties indicated a soft magnetic behavior. The lattice parameter and saturation magnetization increase with increasing Zn content. An anomaly has been observed in lattice parameter and saturation magnetization. The variations of cation distribution are obtained by combining XRD and Mossbauer spectroscopy on basis of site preference and valences. The effects of grain and grain boundary on the electrical properties have been investigated by the Impedance spectroscopy. The effect of constituent phase variation of magneto- electric (1-x) $\text{Ni}_{0.5}\text{Zn}_{0.5}\text{Fe}_{1.5}\text{Cr}_{0.5}\text{O}_4$ -x BaTiO_3 , x=0.35, 0.5 and 0.65 nanocomposite on the B-H hysteresis behavior and the dielectric properties was examined. Also, the details of conductivity measurements of (PANI)/ $\text{Ni}_{0.5}\text{Zn}_{0.5}\text{Fe}_{1.5}\text{Cr}_{0.5}\text{O}_4$ nanocomposites were discussed. The different data obtained from the three nano- samples prepared by different techniques are going to be correlated with each other.

[1] Muhammed Tan, Yuksel Koseoglu, Furkan Alan, Erdogan Senturk, *Journal of Alloys and Compounds* 509 (2011) 9399- 9405

MS02-T06

Incommensurate magnetic ordering in BiFeO₃-PbTiO₃ composites

R. Ranjan¹, A. Senyshyn², V. Kothai¹, A. Daoud-Aladine³

¹Indian Institute of Science, Department of Materials Engineering, Bangalore, India

²Technische Universität München, Forschungsneutronenquelle Heinz Maier-Leibnitz FRM-II, Garching b. München, Germany

³Rutherford Appleton Lab, ISIS Facility, Chilton, United Kingdom

Interest in multiferroic magnetoelectric materials which not only shows coexistence of the ferroelectric and magnetic orders, but also coupling between them, such that the magnetic degree of freedom can be manipulated by an electric field and vice versa, has significantly increased in recent years as they promise attractive technological applications in several multifunctional devices like data storage, spintronics, sensor and actuator devices, etc. For practical application it is always important to have a multiferroic material showing the magnetoelectric effect at room temperature, and from this view point BiFeO₃ is one of the hotly pursued materials. BiFeO₃ exhibits a rhombohedral perovskite structure (space group R3c). BiFeO₃ is reported to exhibit a spatially modulated G-type canted antiferromagnetic structure. The modulation is in the form of a cycloidal spiral of the length of about 620 Å, with the [110] spiral direction and (110) spin rotation plane, corresponding to a modulation vector $k=(k_x, k_x, 0)$ with $k_x \approx 0.035$. This long range spiral modulation leads to cancellation of the net magnetization of the system thereby limiting the magnetoelectric effect.

It has been proposed that chemical substitutions can suppress the spiral spin structure and, thereby, release the latent magnetization of the spatially modulated G-type canted antiferromagnetic structure of BiFeO₃ [1]. As a consequence, there is an increasing trend with regard to the study of ferroic transitions in modified BiFeO₃. Of the various modifications of BiFeO₃ reported in the literature, modification by PbTiO₃, i.e. (x)PbTiO₃-(1-x)BiFeO₃, has shown formation of morphotropic phase boundary (MPB) for 0.2 < x < 0.3. Such MPB compositions are important from the point of view of high performance piezoelectric based applications.

As compared to the pure BiFeO₃, only a few reports on the magnetic characterization of the (1-x)BiFeO₃-(x)PbTiO₃ are known. One of the early investigations in this regard was reported in [2], where a decrease in the Neel temperature on increasing the fraction of PbTiO₃ content was observed. Magnetic structure analysis of a rhombohedral composition (x=0.10), using neutron powder diffraction data, led Comyn et al [3] to conclude that the most likely magnetic structure can be described as a G-type collinear antiferromagnetic ordering with the moments in the a-b plane of the hexagonal cell, whilst in Ref. [4] the commensurate G-type ordering with moments parallel to the c-axis (of the hexagonal cell) has been found for x=0.20. Bhattacharjee et al. [5] reported an abrupt change in magnetic structure from a noncollinear antiferromagnetic one to a collinear G-type antiferromagnetic as the nuclear structure of the ferroelectric phase changes from monoclinic (Cc space group) for x~0.27 to tetragonal (P4mm space group) for x~0.31 across the morphotropic phase boundary.

These studies suggest that PbTiO₃ modification influences the type of magnetic ordering found in BiFeO₃. However, since the long modulation period of the magnetic structure leads to an extremely weak splitting of magnetic reflections at low Q range, the issue of existence or suppression of the modulation in the magnetic structure can be resolved only by using time-of-flight neutron powder diffraction data. Here we report the analysis of the nuclear and magnetic structures of a series of (1-x)BiFeO₃-(x)PbTiO₃ solid solutions at room temperature using high resolution time of flight neutron powder diffraction data collected at ISIS, Rutherford Appleton Lab.

[1] N. Wang et al., Phys. Rev. B 72, 104434 (2005).

[2] S. A. Fedulov et al., Soviet. Phys. -Solid State 6, 375 (1964)

[3] T. P. Comyn et al., J. Appl. Phys. 105, 094108 (2009)

[4] R. Ranjan et al. J. Appl. Phys. 109, 063522 (2011).

[5] S. Bhattacharjee et al., Appl. Phys. Lett. 97, 262506 (2010)

MS03-T01

Structure-based reengineering of designed Armadillo repeat proteins abandoned domain swapping of N-terminal capping repeats.

P. Mittl¹

¹University Zürich, Department of Biochemistry, Zürich, Switzerland

Armadillo repeat proteins (ArmRPs) fold into right-handed super-helical molecules that possess modular architectures consisting of different numbers of structurally similar armadillo repeats. ArmRPs are frequently involved in protein transportation and signal transduction and because of the regularity of their peptide binding modes they serve as attractive templates for the design of artificial peptide recognition modules. The design of ArmRPs consisting entirely of identical internal repeats (full-consensus design) has been described (Parmeggiani et al. 2008). In order to analyze their three-dimensional structures we synthesized several full-consensus ArmRPs with different numbers of identical internal repeats (M-type repeats) and different combinations of N- (Y-type) and C-terminal (A-type) capping repeats. They all showed high thermodynamic stabilities compared to naturally occurring ArmRPs. Surprisingly the crystal structures of YM₃A and YM₄A at 2.4 Å and 2.5 Å resolution, respectively, revealed dimers with domain swapped N-terminal capping repeats. Because ArmRP dimers are unsuitable for the continuation of the design the N- and C-caps were reengineered to overcome the domain swapping. The introduction of 9 and 6 point mutations in the N- and C-caps yielded ArmRPs with Y'- and A'-prime capping repeats, respectively. The 1.8 Å resolution Y'M₃A and 2.4 Å resolution Y'M₃A' structures confirmed that the reengineering successfully eliminated domain swapping. Biophysical analysis showed that the reengineering of the N-cap further improved the thermodynamic stability. Thus, the high-resolution structure of the most stable Y'M₃A will serve as an excellent template for the design of sequence specific peptide recognition modules entirely based on armadillo repeats.

Parmeggiani, F., Pellarin, R., Larsen, A. P., Varadamsetty, G., Stumpp, M. T., Zerbe, O., Caflisch, A. & Pluckthun, A. (2008). Designed armadillo repeat proteins as general peptide-binding scaffolds: consensus design and computational optimization of the hydrophobic core. J. Mol. Biol. 376, 1282-1304.

MS03-T02

A specific binding motif enables SycD-YopD recognition

M. Schreiner¹, H. Niemann¹

¹Bielefeld University, Department of Chemistry - Biochemistry IV, Bielefeld, Germany

The type III secretion system (T3SS) is used by many Gram-negative bacteria to transport cytotoxins, so called effector proteins, into the host cell to manipulate the host for their own benefit. The effector translocation occurs via a needle-like nanomachine, the injectisome, that spans the whole bacterial membrane. The effectors enter the cell through pores within the cell membrane formed by translocator proteins. Both effectors and translocators need specific chaperones that prevent aggregation prior to secretion and keep their targets in a partially unfolded state to enable the passage through the small needle pore. T3S chaperones are divided into three subclasses: Class I chaperones interacting with effector proteins, class II chaperones interacting with translocator proteins and class III chaperones interacting with needle components. While class I chaperones have been studied

intensely and are well understood there is still poor knowledge about the versatile functionality of class II, especially concerning the chaperone substrate interaction.

SycD from *Yersinia enterocolitica* is the class II chaperone of the translocator proteins YopD and YopB, which exhibits a characteristic overall helical fold consisting of three tetratricopeptide repeats (TPR). The arrangement of the TPR results in a convex outer surface and a concave inner region forming a hydrophobic cleft. [1]

Recently a binding motif has been identified within the N-terminal region of the translocators IpaB from *Shigella spp.*[2] and PopD from *Pseudomonas spp.* [3]. Based on their results Lunelli and co-workers suggested the existence of similar binding motives within other T3S translocators. In order to verify the binding of YopD to its respective chaperone via the identified sequence we successfully co-crystallized SycD with a synthetic YopD peptide and solved the structure to a resolution of 2.5 Å. The electron density clearly revealed that the peptide binds in an elongated form into the hydrophobic cleft of SycD mainly mediated by van-der-Waals interactions involving the residues Pro58, Leu60 and Pro64 of the peptide. Thus YopD binds into the concave groove in a similar fashion like it has been previously shown for the translocator proteins IpaB [2] and PopD [3].

[1] C. R. Büttner, I. Sorg, G. R. Cornelis, D. W. Heinz, H. H. Niemann, *J. Mol. Biol.* **2008**, 375, 997-1012. [2] M. Lunelli, R. K. Lokareddy, A. Zychlinsky, M. Kolbe, *Proc. Nat. Acad. Sci.* **2009**, 106, 9661-9666. [3] V. Job, P. Mattei, D. Lemaire, I. Attrée, A. Dessen, *J. Biol. Chem.* **2010**, 285, 23224-23232.

MS03-T03

The Crystal Structure of Death Receptor 6 (DR6): A potential receptor of the amyloid precursor protein (APP)

M. Kuester¹, S. Kemmerzehl¹, S. Dahms¹, D. Roeser¹, M. Than¹
¹Leibniz Institut für Altersforschung - FLI, Protein Crystallography Group, Jena, Germany

Death receptors belong to the tumor necrosis factor receptor (TNFR) super family and are intimately involved in the signal transduction during apoptosis, stress response and cellular survival. Here we present the crystal structure of recombinantly expressed death receptor six (DR6), one family member that was recently shown to bind to the amyloid precursor protein (APP) and hence to be probably involved in the development of Alzheimer's disease. The extracellular cysteine rich region of DR6, the typical ligand binding region of all TNFRs, was refined to 2.2 Å resolution and shows that its four constituting cysteine rich domains (CRDs) are arranged in a rod-like overall structure of TNFR-typical architecture, which presents DR6-specific surface patches responsible for the exclusive recognition of its ligand(s). Comparison of APP to known, typical ligands of TNFR-family members, however, shows an unprecedented symmetry and structure suggesting that its interaction with DR6 is different from prototype TNFR ligands. Based on the structural data, the general ligand binding modes of TNFRs and molecular modeling experiments we were able to elucidate structural features of the potential DR6-APP signaling complex.

References:

[1] Nikolaev, A., McLaughlin, T., O'Leary, D. D. & Tessier-Lavigne, M. (2009). APP binds DR6 to trigger axon pruning and neuron death via distinct caspases. *Nature* 457, 981-989.
 [2] Kuester, M., Kemmerzehl, S., Dahms, S. O., Roeser, D. & Than, M. E. (2011). The Crystal Structure of Death Receptor 6 (DR6): A potential receptor of the amyloid precursor protein (APP). *J. Mol. Biol.* 409, 189-201.

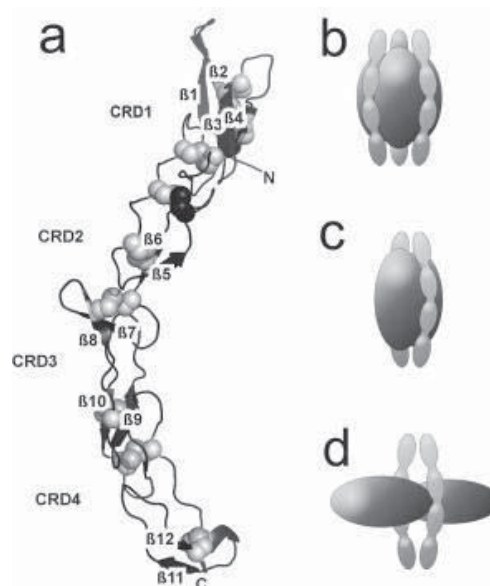


Figure Legend:

Crystal structure of death receptor six (DR6). (a) Cartoon representation of DR6 comprising four cysteine rich domains (CRDs). (b-d) Schematic representation of possible binding modes between TNFR's and their ligands illustrating the observed trimeric (b) and dimeric (c) interaction modes as well as a potential novel binding mode between APP and DR6 (d) based on the oligomerization properties differing between APP and prototypical TNFR-ligands.

MS03-T04

Characterization of Glyoxalase I/Bleomycin Resistance Proteins in *Pseudomonas aeruginosa* PA01

A. Vit¹, E. Kalawy-Fansa², S. Yu³, W. Blankenfeldt¹
¹University of Bayreuth, Biochemistry, Bayreuth, Germany
²University of Düsseldorf, Düsseldorf, Germany
³Massachusetts General Hospital, Boston, United States

Pseudomonas aeruginosa is a multiresistant pathogen that can cause infection in cystic fibrosis patients. It has complex pathophysiology and produces a large number of exoproducts, among which the phenazines are especially prominent. In *P. aeruginosa*, the blue phenazine derivative pyocyanin plays a crucial role in infection of the host. This phenazine can generate reactive oxygen species and is thought to act as respiratory pigment and as a virulence factor at the same time. Pyocyanin is secreted by *Pseudomonas aeruginosa*, but the transport and secretion mechanism are not known until now.

P. aeruginosa has to protect itself from its own phenazines because of the antibiotic action of these substances. Inspired by the fact that the phenazine biosynthesis operon of several bacteria contains a phenazine resistance factor of the glyoxalase I/bleomycin resistance protein family, we have searched the genome of *P. aeruginosa* for proteins of this fold. We show here that *P. aeruginosa* possesses 21 of these genes, most without previous functional characterization. Using protein crystallography and biophysical methods, we further demonstrate that several of these proteins indeed bind phenazines and possibly other antibiotics that contain aromatic moieties. Ultimately, these data may lead to novel anti-infective strategies.

MS03-T05

Unwinding the Differences of the Mammalian PERIOD Clock Proteins by X-ray Crystallography

I. Schmalen¹, N. Kucera^{2,3}, S. Hennig^{2,3}, H.M. Strauss^{4,5}, C. Wiczorek², E. Wolf¹

¹Max Planck Institute of Biochemistry, Structural Chronobiology/ Cell Biology, Martinsried, Germany

²Max Planck Institute of Molecular Physiology, Dortmund, Germany

³Western Australia Institute for Medical Research, Perth, Australia, Germany

⁴Novo Nordisk A/S, Måløv, Denmark, Germany

⁵Nanolytics, Potsdam, Germany

Three homologues PERIOD proteins (PER1, PER2, PER3) constitute central components of the mammalian circadian clock. Here we present the crystal structures of PAS (PER-ARNT-SIM) domain containing mPER1 and mPER3 fragments and their comparison with the previously reported mPER2 structure.

In PERIOD proteins, the two PAS domains (PAS-A and PAS-B) mediate homo- and heterodimeric mPER-mPER interactions as well as interactions with transcription factors and kinases. Our structures confirmed PER homodimers and revealed different stabilizing interfaces in the mPER1 homodimer compared to mPER3 and mPER2 homodimers. We have further verified the existence of these interfaces in solution and inside cells using biochemical and cell biological assays and quantified their contributions to homodimer stability. The structural and quantitative differences between the homodimeric interactions of the three mouse PERIOD homologues are likely to contribute to their distinct clock functions.

MS03-T06

Hexokinase flexibility causes oligomer-dependent activity

B. Küttner¹, K. Kettner², T. Kriegel², N. Sträter¹

¹Institut für Bioanalytische Chemie, Universität Leipzig, Strukturanalytik von Biopolymeren, Leipzig, Germany

²Institut für Physiologische Chemie/TU Dresden, Medizinische Fakultät Carl Gustav Carus, Dresden, Germany

Yeast hexokinases perform the classical ‘open-close’ motion as described in many biochemical text books. The current data on *Saccharomyces cerevisiae* hexokinase suffers from the use of different isoenzymes for the comparison of the open and closed enzyme forms [1,2]. Our analysis is based solely upon a single enzyme: hexokinase 1 from the yeast *Kluyveromyces lactis* (KlHxk1; 484 amino acids, 53 kDa). It shows a concentration-dependent monomer/dimer equilibrium and is also involved in glucose repression via interaction with the Zn-finger repressor protein Mig1 [3]. As known from hexokinase 2 of *S. cerevisiae* (ScHxk2) [4], KlHxk1 could be phosphorylated at Ser-15 causing dimer dissociation.

The monomer exhibits highest activity. Therefore, the enzyme activity is controlled by oligomerization.

In order to analyze oligomerization and function, we have managed to crystallize KlHxk1 in thirteen crystal forms either containing monomers or dimers. The crystallographic dimer (Fig. 1 [5]) was confirmed by small-angle X-ray scattering in solution. Binding of a natural substrate (glucose) or inhibitor (xylose) could be shown in several crystal forms.

Dimer dissociation initiated by protein phosphorylation could be traced back to the repulsion between the phosphoryl group and acidic amino acids nearby. The conformational flexibility of KlHxk1 monomers (28° closure angle) is larger than that known from baker’s yeast hexokinases (18°). Crystals of N-terminal phosphorylated KlHxk1 were examined in terms of Ser-15 modification. Additional dimer distortion parameters were analyzed to describe conformational properties of the KlHxk1 dimer and its residual enzymatic activity:

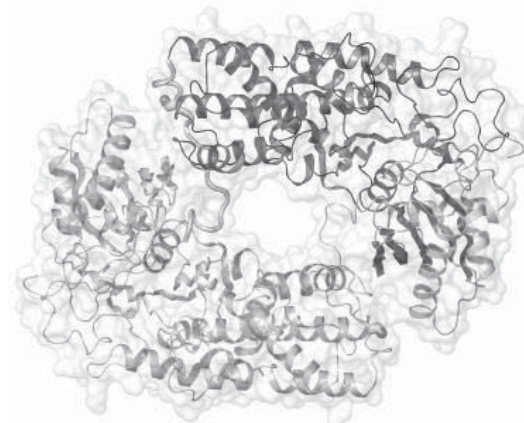
[1] Bennett, W. S. and Steitz, T. A. (1978), Proc. Natl. Acad. Sci. U. S. A. 75, 4848-4852.

[2] Kuser, P. et al. (2008), Proteins 72, 731-740.

[3] Ahuatz, D. et al. (2007), J. Biol. Chem. 282, 4485-4493.

[4] Behlke, J. et al. (1998), Biochemistry, 37, 11989-11995.

[5] Kuettner, E.B. et al. (2010), J. Biol.Chem. 285, 41019-41033.



MS04-T01

The importance of the correct intensity simulation of EBSD patterns

G. Nolze¹, A. Winkelmann²

¹Federal Institute for Materials Research and Testing (BAM), Constructive Materials, Berlin, Germany

²MPI für Mikrostrukturphysik, Halle, Germany

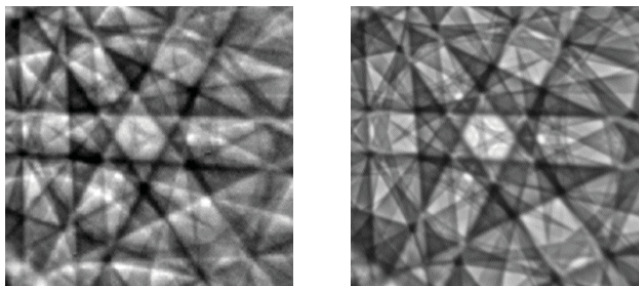
Electron backscatter diffraction (EBSD) has become a common tool for characterization of crystalline materials using scanning electron microscopy. Forming diffraction patterns from a single-crystalline volume in the scale of a few ten nanometers in diameter, this technique is preferably used for millions of single orientation measurements in high resolution, acquired in a time scale of hours. Optimum conditions enables an orientation determination in about 1ms. Using a scanning mode EBSD systems are able to display orientation maps covering complete microstructures. The local assignment of the orientations also permits the investigation of misorientations which ends in a quantitative descriptions of grain and phase boundaries, deformation state etc. Although this technique is quite successful for simple crystal structures like typical metals, for more complex phases the applied intensity prediction is unacceptable. The reason is, that all available EBSD systems use a simple kinematic approach which is based on the assumption that the intensity of a "band" is proportional to the square of the structure amplitude of the most intense reflection order. However, the bands used for indexing are actually a superimposition of all diffraction orders formed by a single lattice plane. Moreover, all other reflections are crossing this single band and influencing the integral intensity as well, so that a simple excess-intensity prediction describing the detectability is impossible.

New approaches [1] based on dynamical theory and consideration of multiple scattering and diffraction generate radial intensity distributions which match experimental patterns in a convincing quality, cf. Fig.1. These simulations are suitable to substitute the intensity prediction still implemented in EBSD systems. The extracted band intensities can be applied for an optimization of band and indexing strategies. Simulation tools will push the further automation of the nowadays still manually operated system. One can investigate before any experiment whether phases can be distinguished by EBSD or not. Comparing the ideal simulations with high-resolution diffraction patterns EBSD can be used for phase identification or point group determination. The importance of local strain measurements are still limited since required

reference patterns are not available. Using the simulations they can be practically generated in real-time for any orientation and phase.

Fig.1: Experimental (left) and simulated intensity distribution around [111] of Nickel.

[1] A. Winkelmann, C. Trager-Cowan, F. Sweeney, A.P. Day, and P. Parbrook. *Many-beam dynamical simulation of electron backscatter diffraction patterns*. *Ultramicroscopy*, 107(4-5):414-421, 2007.



MS04-T02

Accurate band profile analysis in EBSD patterns using frequency space tiling

F. Ram¹, S. Zaeferrer¹

¹Max-Planck-Institut für Eisenforschung GmbH, Microstructure Physics and Alloy Design, Düsseldorf, Germany

Electron Backscatter diffraction (EBSD) patterns possess information about an approximately 20 nm-thick layer on the surface of a crystalline specimen. An EBSD pattern consists of a set of Kikuchi bands (K-bands). The intensity profile across these bands contains information about the geometry of the diffraction set-up, the lattice parameters, and the defect density. However, the intensity content of each K-band is obscured by the intersection of the other K-bands in the pattern. As a consequence, the only way to analyze an individual K-band is to extract it from the pattern. Here we show how to decompose an EBSD pattern into its constituting K-bands using frequency space tiling. As a first step, the frequency space of a given EBSD pattern is calculated using the two-dimensional Fourier Transform. To reconstruct each K-band, its corresponding directional wedge-shaped frequency tile is extracted from the frequency space and then back-transformed. Results reveal the geometry of the K-bands in the form of hyperbolic intensity contours. These contours show discontinuities at the position of the crystallographic poles where many K-bands intersect. The asymmetric nature of the K-bands is also clearly visible in the intensity profiles. In a final step, the exact band profile is determined and used to calculate the projection center of the pattern, and the orientation of the crystal.

MS04-T03

CryoTEM in Materials Science: Studying biomimetic mineralization

N. Sommerdijk¹

¹Eindhoven University of Technology, Chemical Technology and Chemistry, Eindhoven, Netherlands

The often astonishing materials properties of crystalline biominerals are generally related to the hierarchical assembly of specifically interacting organic and inorganic components. A yet unfulfilled dream of many scientists is to synthesize new materials with similar advanced properties applying Nature's biomimetic strategies.^[1] For the design of such biomimetic hybrid materials with predetermined structure and properties it is essential to understand the factors that dictate their formation.

The *in situ* study of the development of mineral formation can make an important contribution to the understanding of the processes involved in bio(mimetic) mineralization.^[2] It is however not a trivial matter to obtain morphological and structural information of such systems in their native hydrated state. We and others recently have presented the possibility to use cryoTEM as a method to investigate the early stages of mineral formation without removing the developing particles from their aqueous environment.^[3, 4]

Using dedicated tools including a vitrification robot with attached glovebox also makes it possible to investigate mineral formation at interfaces,^[5] while cryo-electron tomography allows us to investigate template-mineral interactions in 3D.^[4,6,7] Moreover, we combine cryo-TEM imaging with more materials science oriented techniques such as cryo-STEM/EDX and low dose selected area electron diffraction to combine morphology with structural and chemical information. We will discuss the biomimetic formation of calcium phosphate using templates from both synthetic and biological origin.

[1] N.A.J.M. Sommerdijk, H. Cölfen, *MRS bulletin*, **35**, 116 (2010).

[2] A. Dey, G. de With, N.A.J.M. Sommerdijk, *Chem. Soc. Rev.* **92**, 381, (2010).

[3] B.P. Pichon, P.H. H. Bomans, P.M. Frederik N. A. J. M. Sommerdijk, *J. Am. Chem. Soc.* **130**, 4034 (2008).

[4] E.M. Pouget, P.H.H. Bomans, J.A.C.M. Goos, P.M. Frederik, G.de With, N.A.J.M. Sommerdijk, *Science*, **323**, 1455 (2009).

[5] M.R. Vos, P.H.H. Bomans, P.M. Frederik and N.A.J.M. Sommerdijk, *Ultramicroscopy (Special Issue FEMS Meeting)* **108**, 1478 (2008)

[6] A. Dey, P.H.H. Bomans, F.A. Müller, J. Will, P.M. Frederik, G. de With and N.A.J.M. Sommerdijk, *Nature Mater*, **9** 1010 (2010).

[7] F. Nudelman, K. Pieterse, A. George, P.H.H. Bomans, H. Friedrich, L. J. Brylka, P.A.J. Hilbers, G. de With N.A.J.M. Sommerdijk, *Nature Mater*, **9** 1004 (2010)

MS04-T04

Structure elucidation of germanium tin antimony tellurides by TEM and X-ray methods

T. Rosenthal¹, L. Neudert¹, S. Welzmler¹, O. Oeckler¹

¹LMU Munich, Chemistry, Munich, Germany

Bulk samples of partially ordered metastable Ge/Sb/Te (GST) phases can be obtained by quenching the rocksalt-type high-temperature phase. These materials exhibit pronounced nanostructures that can be tuned by the composition and the thermal treatment, both for strongly disordered rocksalt-type structures and for phases characterized by layer-like cation defect ordering.^[1] This results in a low lattice thermal conductivity (k_L) and remarkable thermoelectric properties ($ZT > 1.3$). Partially substituting Ge for Sn increases the disorder, since the cation sites are occupied by three different elements and additional vacancies. This might further reduce the k_L and thus increase ZT.

Temperature programmed powder X-ray diffraction on $\text{Ge}_2\text{Sn}_2\text{Sb}_2\text{Te}_7$ prove the existence of a rocksalt-type high-temperature phase as well as a trigonal phase stable at room temperature. TEM investigations on quenched bulk samples reveal small domains of layered phases embedded in a matrix consisting of a rocksalt-type phase. Thinned single crystals synthesized by chemical transport reactions exhibit a parquet-like structure intergrown with 2D extended domains consisting of the thermodynamically stable layered trigonal phase (Fig. 1). The number of layers and the cell parameters match the predictions for $39R\text{-Ge}_2\text{Sn}_2\text{Sb}_2\text{Te}_7$. Single crystal X-ray data of these crystals show a multiply twinned long-periodic structure. The strong reflections can be described by a pseudocubic cell.

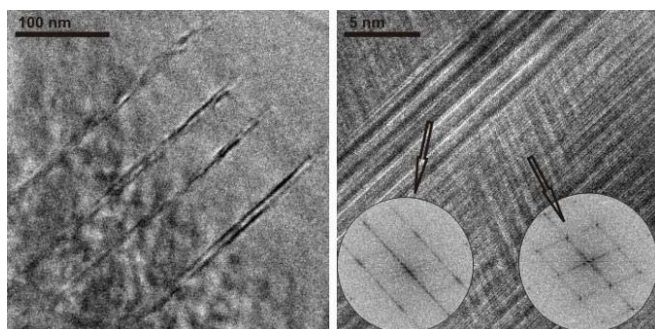


Fig. 1: HRTEM images of PIPS-thinned single crystals of $\text{Ge}_2\text{Sn}_2\text{Sb}_2\text{Te}_7$ (pseudocubic [110]) with Fourier transforms of the coexisting phases.

References:

[1] T. Rosenthal, M. N. Schneider, C. Stiewe, M. Döblinger, O. Oeckler; *Chem. Mater.* 2011, 23, 4349-4356.

MS04-T05

Oxygen precipitation in semi conductor silicon wafers studied with X-ray diffraction in an energy dispersive Laue geometry

A. Gröschel¹, J. Will¹, C. Bergmann¹, A. Magerl¹

¹Universität Erlangen, Kristallographie, Erlangen, Germany

The formation of bulk micro defects (BMD) from systematically precipitated oxygen in Czochralski silicon (Cz-Si) is the key of internal defect gettering in modern semiconductor devices. The study of the formation process therefore is of outmost interest. An useful means for that is the investigation of the Bragg diffraction of X-rays by silicon crystals. While in a perfect crystal the scattered intensity is completely coherent, there is also an incoherently scattered component in strained crystals [1]. The measurement of the dependence of the Bragg intensity on the photonic energy for samples of constant thickness reveals the period of the Pendellösung oscillations and the increase of the diffracted intensity by an incoherently scattered component which both are highly sensitive to lattice distortions as introduced by statistically distributed BMDs. The energy dispersive course of Bragg intensity can be evaluated within the framework of the statistical dynamical theory [2-5], which yields the static Debye-Waller-factor, that describes the proportion of strained crystal volume and depends on BMD size, density and shape. This enables the study of BMDs at their early states of formation.

We present a defocused Laue setup for the energy dispersive measurement of the Bragg intensity diffracted by plane parallel Si wafers utilizing a high energy X-ray tube with a tungsten target. The wafers have typical thicknesses in the order of 0.3 to 1 mm. The photonic energy ranges typically from 30 to 100keV.

In this setup Cz-Si wafers of 0.6 mm thickness have been studied after being annealed with a temperature ramp of 10K/min up to 1000°C maximum followed by optional different dwell times at 1000°C and the static Debye-Waller-factor has been deduced. For comparison the BMD sizes and densities have been determined with TEM [6]. The values found ranged from 8 to 25 nm and $1.3 \cdot 10^{13}$ to $1.8 \cdot 10^{13} \text{ cm}^{-3}$, respectively. The evaluation of the static Debye-Waller-factor with the aid of the BMD densities found in TEM and a model for the strain field of spherical BMDs [7] yields BMD sizes comparable with those found in TEM.

Further two Cz-Si wafers prepared from the same ingot have been investigated, while one was exposed to an annealing step of 40 minutes at 650°C to eliminate thermal donors the other was investigated as-grown. The comparison of the static Debye-Waller-factor of the two samples shows a reduction of strained volume through the annealing step.

In conclusion we could observe differences in the strain inventory of Si wafers with different BMD inventory with an X-ray diffraction setup utilizing a laboratory source. The evaluation of the static Debye-Waller-factor principally gives access to BMD sizes and densities.

[1] A. Authier, *Dynamical Theory of X-Ray Diffraction*, Oxford University Press, Oxford, 2001.

[2] N. Kato (1980). *Acta Cryst.* A36, 763-769

[3] N. Kato (1980). *Acta Cryst.* A36, 770-778

[4] J. P. Guigay (1989). *Acta Cryst.* A45, 241-244

[5] T. Takama & H. Harima (1994). *Acta Cryst.* A50, 239-246

[6] H. Grillenberger (2010), PhD-Thesis, Erlangen

[7] S. Iida, H. Sugiyama, Y. Sugita & H. Kawata (1988). *Jpn. J. Appl. Phys.* 27, 1081-1087

MS04-T06

In-Situ measurement of early stages of oxygen precipitation in silicon by dynamical X-ray diffraction

J. Will¹, A. Gröschel¹, C. Bergmann¹, A. Magerl¹

¹University Erlangen-Nuremberg, Chair of Crystallography and Structural Physics, Erlangen, Germany

The identification of impurities in high quality mono crystals is a major task in the field of crystal characterization. The measurement of Pendellösungs fringes [1] is a highly sensitive method for investigating the strain inventory in the crystal.

The thickness dependence of the integrated Bragg intensities for dislocation free Czochralski samples were measured at our high energy X-ray laboratory [2] with the characteristic tungsten $K_{\alpha 1}$ -line at 59.3keV. These measurements were made in focusing Laue setup with wedge shaped samples (Fig. 1) [3-4]. The wedges were used to measure different thicknesses covering a wide range corresponding to several Pendellösungs fringes with one exposure only by an average exposure time of 5min. Strain free surfaces, which otherwise would influence the signal, were assured by surface polishing and subsequently wet chemical etching.

In our experiments we measured in-situ the nucleation of oxygen in silicon at 650°C and 750°C. Fig. 2 shows the evolution of the measured 400-reflection with the annealing time at 750°C. Besides a slight elongation of the Pendellösungs fringes a clear increase of the average Bragg intensity with the sample thickness was observed. Within the framework of the statistical dynamical theory [5-7] these two effects are strongly correlated and correspond to the increasing strain inventory in the sample with annealing time. The increasing strain inventory corresponds to the clustering of oxygen in the silicon host matrix, thus early stages of the oxygen precipitation and their kinetics in silicon was observed in-situ.

Due to the strong correlation between the average Bragg intensity, the Pendellösungs distance and the static Debye-Waller factor E, it is possible to determine E with an accuracy of up to 0.1 %. Which can be interpreted with in certain models [8-10] leading to reasonable sizes and densities of the precipitates.

In conclusion we were able to observe the very first stages and the kinetics of the oxygen clustering in silicon. Moreover the data evaluation in the framework of the statistical dynamical theory gives access to quantitative data like the size and the density of the oxygen agglomerates.

[1] A. Authier, *Dynamical Theory of X-Ray Diffraction*, Oxford University Press, Oxford, 2001.

[2] M. Stockmeier, A. Magerl, *J. Appl. Cryst.*, 41 (2008) 754-760.

[3] J. Will, A. Gröschel, M. Weißer, A. Magerl, *Appl. Phys. Lett.*, 98 (2011) 041910.

[4] J. Will, A. Gröschel, C. Bergmann, A. Magerl, *Solid State Phenomena*, 178-179 (2011) 353-359.

[5] N. Kato, *Acta Cryst.*, A36 (1980) 763-769.

[6] N. Kato, *Acta Cryst.*, A36 (1980) 770-778

[7] M. Al Haddad, P. J. Becker, Acta Cryst., A48 (1992) 121-134.
 [8] P. H. Dederichs, J. Phys. F, 3 (1973) 471-496.
 [9] S. Iida, H. Sugiyama, Y. Sugita, H. Kawata, Japanese J. Appl. Physics, 27 (1988) 1081-1087.
 [10] J. R. Schneider, R. Bouchard, H. A. Graf, H. Nagasawa, Acta Cryst., A48 (1992) 804-819.

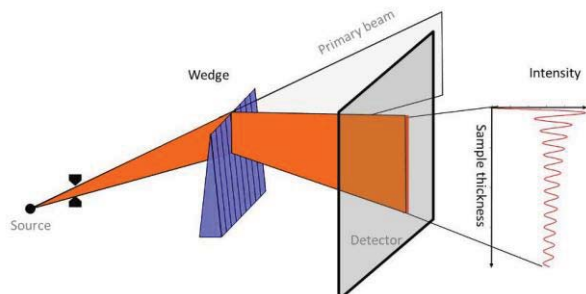


Fig. 1: Focusing Laue-geometry for a wedge-shaped crystal

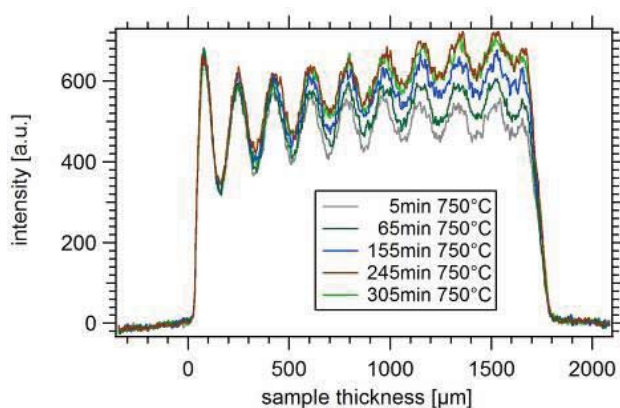


Fig. 2: Time evolution of the strain inventory in a Czochralski grown sample with the annealing time at 750°C

MS05-T01

Electron Density Contributions to Drug Development

P. Luger¹, M. Weber¹

¹Freie Universität Berlin, Chemistry, Berlin, Germany

It is one of the major challenges in drug development to understand the mutual recognition and interaction of biologically interacting systems. Following the “key-lock” principle, a potential drug molecule and the corresponding receptor pocket have to match at least sterically, but also electronic complementarity is a prerequisite. It follows that experimental electron density distributions can provide useful additional information for the analyses of these processes.

We have examined the electron densities of potential drug molecules either from high resolution low temperature X-ray diffraction experiments or from conventional low order data sets where the aspherical modelling was carried out using the Invariom formalism.[1]

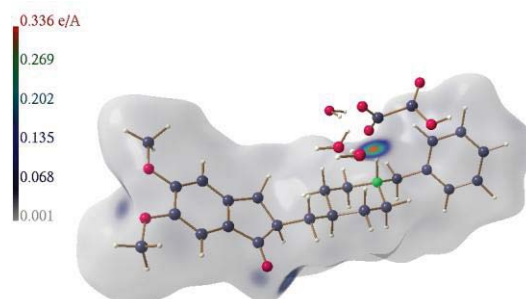
Results will be presented for:

- A potential anti cancer drug, where the electrostatic potential can serve as an indication for the selectivity.
- A group of protease inhibitor model compounds, where the source function was analyzed to provide information about substituent influences.
- The electronic complementarity of an azapeptide epoxide substrate and the SARS coronavirus main protease MPro.

• The Hirshfeld surface of the anti-Alzheimer drug donepezil [2] (Fig.1) making the electronic interactions with the acetylcholinesterase receptor pocket visible.

[1] B. Dittrich, T. Koritsanszky, P. Luger, Angew. Chem. Int. Ed., 2004, 43, 2718-2721.

[2] K. Ravikumar, B. Sridhar, D. G. Sathe, A. V. Naidu, K. D. Sawant, Acta Cryst., 2006, C62, o681 - o683.



Moliso (c) 2007 Christian B. Hübschle

Figure 1. Hirshfeld surface of donepezil

MS05-T02

A joint modelisation of X ray and neutron diffraction data : application to magnetic molecular materials

C. Lecomte¹, M. Deutsch¹, M. Souhassou¹, N. Claiser¹, J.M. Gillet², B. Gillon³

¹UMR CNRS-Université de Lorraine 7036, Laboratoire de Cristallographie, Résonance Magnétique et Modélisations, Vandoeuvre-lès-Nancy, France

²École Centrale Paris, Laboratoire. S.P.M.S., UMR CNRS 8580, Chatenay-Malabry, France

³Centre d'Etudes de Saclay, Laboratoire Léon Brillouin (CEA-CNRS, UMR 12), Gif-sur-Yvette, France

Accurate high resolution x ray diffraction data allow a fine modeling of the valence electron density thanks to the Hansen Coppens model(1) multipolar formalism. Such a formalism has been adapted to the spin density which is refined against polarized neutrons (pn) diffraction data (2) . Therefore these two experiments give rise to

$$\rho(\vec{r}) = \int \Gamma_1(\vec{x}_1; \vec{x}'_1)_{\vec{x}_1 = \vec{x}'_1, \vec{r}_1 = \vec{r}} ds_1 = \Gamma_1(\vec{r}; \vec{r}) = \rho_\uparrow(\vec{r}) + \rho_\downarrow(\vec{r})$$

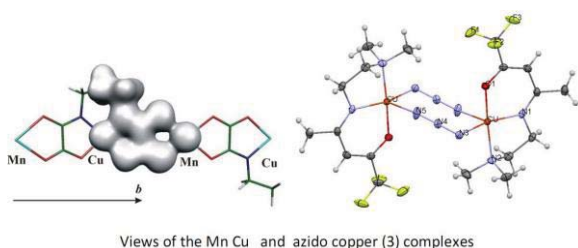
And to

$$s(\vec{r}) = \int [\delta(s - s_\uparrow) - \delta(s - s_\downarrow)] \Gamma_1(\vec{x}; \vec{x}')_{\vec{x} = \vec{x}'} ds = \rho_\uparrow(\vec{r}) - \rho_\downarrow(\vec{r})$$

Where $\Gamma_1(\vec{x}_1; \vec{x}'_1) = N \int \psi^*(\vec{x}_1, \vec{x}_2, \dots, \vec{x}_N) \psi(\vec{x}'_1, \vec{x}'_2, \dots, \vec{x}'_N) d^4 x_2 \dots d^4 x_N$ is the one electron reduced density matrix. Quantum mechanics tell us that the one electron reduced density matrix allows the calculation of the ground state properties of the system; therefore it is of utmost importance to estimate the density matrix from experiment. As shown above, its diagonal part is related to the charge and spin densities and the off diagonal terms may be obtained from Compton scattering experiments

$$J(\vec{u}, q) = \int \Gamma_1(\vec{x}_1; \vec{x}'_1 + (\vec{u}\vec{t})\vec{u}) e^{iq\vec{u}\cdot\vec{r}} d^3 r. d^3 t$$

In this talk we shall focus on the diagonal part describing our first results on the x, n, pn joint refinement applied to two paramagnetic crystals: a Mn Cu complex (3) et an azido copper dimer (4) for which the x and pn data have been respectively collected at 10K in CRM2 Nancy and LLB Saclay



We thank the Agence Nationale de la Recherche (project CEDA), CNRS and Nancy University for financial support.

- 1) N. K. Hansen & P. Coppens, *Acta Cryst.*, 1978, A34, 909
- 2) P.J. Brown, J. B.Forsyth, & R. Mason, 1980. *Phil. Trans. R. Soc. Lond.* B290, 481-4
- 3) S.Pillet, M. Souhassou, C.Lecomte, C. Mathonière - *J.A.C.S.* (2004) 126(4), 1219-1228
- 4) C. Aronica, E. Jeanneau, H. ElMoll, D. Luneau, B. Gillon, A. Goujon, A. Cousson, M. Angels Carvajal, V. Robert ; *Chem. Eur. J.*, 2007, 13, 3666

MS05-T03

Charge Density Study of alpha-Boron at 100 K.

S. Mondal¹, S. van Smaalen¹, N. Dubrovinskaia¹, G. Parakhonskiy², L. Dubrovinsky²

¹University of Bayreuth, Laboratory of Crystallography, Bayreuth, Germany

²Bayerisches Geoinstitut, University of Bayreuth, Bayreuth, Germany

Elemental boron and boron rich compounds show unusual chemical bonds, mainly due to the electron deficient nature of boron. Recently, we have provided an explanation for the unusual chemical bonding in gamma-boron, the high-pressure orthorhombic form, by a charge density study [1]. The present experimental charge density study of alpha-boron has been undertaken in order to obtain more insight into the chemical bonding in elemental boron polymorphs. Single crystals of alpha-boron have been synthesized under high pressure and temperature [2]. Single crystal X-ray diffraction data was collected at a temperature of 100 K at the beamline F1, Hasylab, Hamburg, Germany. Charge densities in alpha-boron have been obtained by the multipole refinement using the software package XD2006 [3]. The final multipole model shows excellent fit to the experimental data with $R_F = 0.017$. Electron densities have been analyzed with the aid of Bader's quantum theory of atoms in molecules (QTAIM) [4]. Charge densities in the gamma and alpha forms of boron will be compared in order to procure information on the nature of chemical bonding in elemental boron.

References:

- [1] S. Mondal, S. Van Smaalen, A. Schönleber, Y. Filinchuk, D. Chernyshov, S. I. Simak, A. S. Mikhaylushkin, I. A. Abrikosov, E. Zarechnaya, L. Dubrovinsky, N. Dubrovinskaia, *Phys. Rev Lett.*, **106**, 215502, (2011).
- [2] G. Parakhonskiy, N. Dubrovinskaia, L. Dubrovinsky, S. Mondal, S. Van Smaalen, *J. Cryst. Growth*, **321**, 162-166, (2011).
- [3] A. Volkov, P. Macchi, L. J. Farrugia, C. Gatti, P. R. Mallinson, T. Richter, T. Koritsanszky, XD2006, *A Computer Program Package for Multipole Refinement, Topological Analysis of Charge Densities and Evaluation of Intermolecular Energies from Experimental or Theoretical Structure Factors*, (2006).

[4] R. F. W. Bader, *Atoms in Molecules*, Oxford University Press, (1990).

MS05-T04

ShelXle - A cute GUI for SHELXL

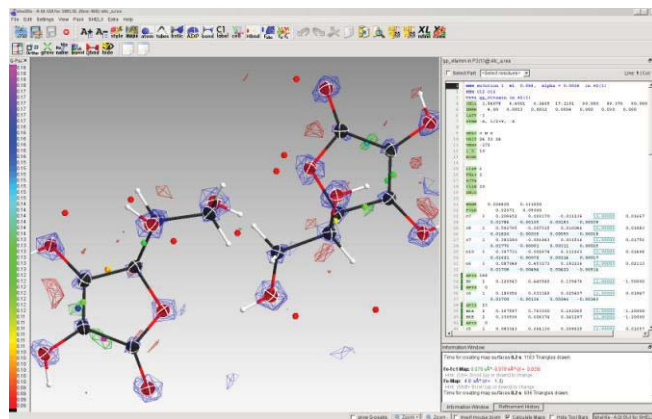
C.B. Hübschle¹, G.M. Sheldrick¹, B. Dittrich¹

¹Georg-August-Universität Göttingen, Institut für Anorganische Chemie, Göttingen, Germany

ShelXle is a graphical user interface (GUI) for SHELXL[1], the currently most widely used program for small-molecule structure refinement. It combines an editor with syntax highlighting for the SHELXL associated .ins (input) and .res (output) files with an interactive graphical display for visualization of a three dimensional structure including the electron density (F_o) and difference density ($F_o - F_c$) maps. Special features of ShelXle include intuitive atom (re-)naming, a strongly coupled editor, structure visualization in various mono and stereo modes, and a novel way of displaying disorder extending over special positions. ShelXle[2] is completely compatible with all features of SHELXL and is written entirely in C++ using the Qt4 and FFTW libraries. It is available at no cost for Windows, Linux, Mac-OS X and as source code. ShelXle can be downloaded here: <http://ewald.ac.chemie.uni-goettingen.de/shelx/>

[1] G. M. Sheldrick, *Acta Cryst.* (2008). **A64**, 112-122.

[2] C. B. Hübschle,* G. M. Sheldrick and B. Dittrich, *J. Appl. Cryst.* (2011). **44** (in press) doi:10.1107/S0021889811043202



MS05-T05

Frontiers in structural analysis of high-pressure molecular crystal structures

F. Fabbiani¹, B. Dittrich²

¹Georg-August Universität Göttingen, GZG, Abt. Kristallographie, Göttingen, Germany

²Georg-August Universität Göttingen, Institut für anorganische Chemie, Göttingen, Germany

In general, precision diffraction studies require collection of high-resolution, highly-redundant data with a low background and minimal parasitic scattering. These requirements are essentially never met when collecting high-pressure single-crystal data in a diamond-anvil cell. This is because the diamond-anvil cell physically imposes a) a restricted access to reciprocal space, b) the unavoidable presence of two large diamond single-crystals, and c) the (partially avoidable) presence of diffraction and absorption from other cell components, e.g. the gasket used to create the sample chamber.[1,2]

Through a series of case studies, we will explore various degrees of precision and demonstrate that it is nowadays possible to collect very good high-pressure data, both in the home laboratory and at the synchrotron, and obtain very high-quality crystal structures on

molecular crystals of small and larger molecules, up to *ca.* 100 non-H atoms in the asymmetric unit. We will also illustrate how high-pressure data can in some cases be amenable to charge-density analysis, by performing free refinement of multipole parameters when fixing atomic positions and anisotropic displacement parameters to values derived from an invariom refinement [4] or from values calculated independently *ab initio*. [5] Previous examples reported in the literature involved using a monopole-kappa refinement [5] or a maximum entropy method (MEM) approach. [6]

- [1] A. Katrusiak, *Acta Cryst.* (2008), **A64**, 135-148.
 [2] R. Miletich, D. R. Allan & W. F. Kuhs, *Rev. Mineral. Geochem.* (2000), **41**, 445-519.
 [3] B. Dittrich, C. B. Hübschle, J. Holstein and F. P. A. Fabbiani, *J. Appl. Cryst.* (2009), **42**, 1110-1121.
 [4] B. Dittrich, S. Pfitzenreuter and C. B. Hübschle, *Acta Cryst A* (2012), in press.
 [5] T. Yamanaka, T. Fukuda, Y. Komatsu and H. Sumiya, *J. Phys.: Condens. Matter* (2002), **14**, 10545-10551.
 [6] T. Yamanaka, T. Okada and Y. Nakamoto, *Phys. Rev. B* (2009), **80**, 094108.

MS05-T06

Structural investigation of ZnO nanoparticles by pair distribution function (PDF)

H. Chatterjee¹, K. Datta¹, R. Neder¹

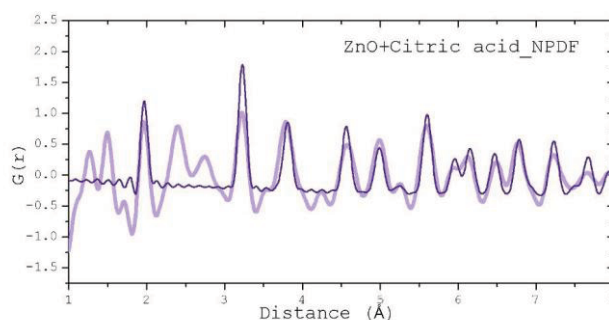
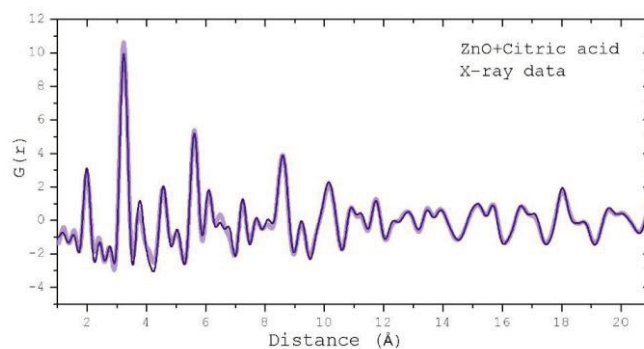
¹University of Erlangen-Nürnberg, Crystallography and Structural Physics, Erlangen, Germany

The analysis of the pair distribution function (PDF) is a powerful method to investigate the local structure of crystalline, amorphous, disordered and nanocrystalline materials [1]. Here we present a detailed structural investigation including size, shape and defects, carried out on ZnO nanoparticles of sizes between 2 to 6 nm. Nanoparticles were synthesized through a bottom up non-aqueous sol-gel process using organic compounds as a stabilizer [2], such as 1,5-Diphenyl-1,3,5-pentanetrione, Dimethyl L-tartrate and Citric acid, at ambient temperature. Both x-ray and neutron powder diffraction data were collected to extract the pair distribution function (PDF) of the system and the data were refined against a structural model consisting defects. X-ray PDF data were refined against a Wurtzite type ZnO structure which provided satisfactory match between the experimental and the calculated pattern. However the neutron PDF (Fig: 1b light shaded curve) provided additional information on the organic ligand molecules and a model consisting of only ZnO was not able to mimic the experimental data thoroughly. Figure-1 depicts an example of such results for ZnO nanoparticles stabilized by Citric acid. It is anticipated that a comprehensive study on a range of similar systems will aid in understanding the formation of these small nanoparticles and therefore tune them according to a specific application.

Figure 1: (a) X-ray PDF data for ZnO nanoparticles. Data were collected at the beamline BW5 of HASYLAB, DESY. (b) Neutron PDF of the same sample collected at NPDF beamline in Los Alamos. Light shaded pattern demonstrates the experimental data whereas the dark shaded data shows the calculated pattern obtained using DISCUS package [3].

References:

- [1] T. Egami and S. J. L. Billinge, *Underneath the Bragg peaks*, Pergamon (2003)
 [2] C. Choryet. *al.physica status solidi (c)*, 4: 3260-3269 (2005).
 [3] R. B. Neder and T. Proffen, *Diffuse Scattering and Defect Structure Simulations*, Oxford University Press (2008).



MS06-T01

Convergent evolution of Rubisco activases from green plants and red algae

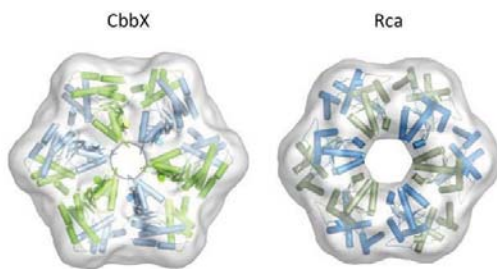
A. Bracher¹, M. Stotz¹, O. Mueller-Cajar¹, P. Wendler², S. Ciniawsky², F.U. Hartl¹, M. Hayer-Hartl¹

¹Max-Planck-Institut für Biochemie, Abt. Zelluläre Biochemie, Martinsried, Germany

²Ludwig-Maximilians-Universität, Genzentrum, München, Germany

Rubisco, the enzyme that catalyzes the fixation of atmospheric CO₂ in photosynthesis, is prone to inactivation by inhibitory sugar phosphates. Green plants and organisms containing red-type Rubisco independently evolved AAA⁺ proteins for restoring Rubisco activity, Rubisco activase (Rca) and CbbX. Here we present the structural and functional characterization of the molecular chaperones (1,2). The combination of X-ray crystallography and electron microscopy showed that both form active hexamers. However, while Rca is constitutively active, CbbX needs to be allosterically activated by ribulose-(1,5)-bisphosphate, which builds up upon Rubisco inhibition. Rca employs both its N-terminal domain and a helical insertion into the C-terminal domain for Rubisco targeting, while CbbX requires elements of the nucleotide binding domain and the central pore of the hexamer for contacting Rubisco. Mechanistically, CbbX functions by transiently pulling the carboxy-terminal peptide of the red Rubisco large subunit into the hexamer pore, resulting in the release of the inhibitory RuBP. Green-type Rubisco lacks such a C-terminal tail. How Rca remodels Rubisco for release of the inhibitor is still unclear. Our mutational data however show that loop segments exposed toward the central pore of the hexamer are required.

1. Mueller-Cajar, O., Stotz, M., Wendler, P., Hartl, F.U., Bracher, A. and Hayer-Hartl, M. (2011) Structure and function of the AAA⁺ protein CbbX, a red-type Rubisco activase. *Nature* 479, 194-199.
2. Stotz, M., Mueller-Cajar, O., Ciniawsky, S., Wendler, P., Hartl, F.U., Bracher, A. and Hayer-Hartl, M. (2011) Structure of green-type Rubisco activase from tobacco. *Nature Struct. Mol. Biol.* 18, 1366-1370.



MS06-T02

Structural insight into the activation mechanism of toxoplasma gondii nucleoside triphosphate diphosphohydrolases by disulfide reduction

U. Krug¹, M. Zebisch^{2,1}, M. Krauss¹, N. Sträter¹

¹University of Leipzig, Institute of Bioanalytical Chemistry, Center for Biotechnology and Biomedicine, Leipzig, Germany

²University of Oxford, 2Division of Structural Biology, Wellcome Trust Centre for Human Genetics, Oxford, United Kingdom

Nucleotides released as extracellular signaling molecules are hydrolyzed by nucleoside triphosphate diphosphohydrolases (NTPDase) (1, 2). These enzymes are found in mammals as well as in microbial pathogens where they are thought to modulate the host-response to an infection by hydrolysis of host ATP or where they play a role in purine salvage (3).

The intracellular parasite *Toxoplasma gondii* produces two nucleoside triphosphate diphosphohydrolases (NTPDase1 and -3). These tetrameric, cysteine-rich enzymes require activation by reductive cleavage of a hitherto unknown disulfide bond. Despite a 97% sequence identity both isozymes differ largely in their ability to hydrolyze ATP and ADP (4).

We determined crystal structures of the inactive NTPDase3 as the apo form and in complex with the product AMP. These structures showed the enzyme in an open conformation that precludes productive substrate binding and catalysis (2, 5). In mutagenesis experiments the cysteine bridge 258-268 was identified to be responsible for locking of activity. Crystal structures of constitutively active variants of NTPDase1 and -3 generated by mutation of C258-C268 showed that opening of the regulatory cysteine bridge induces a pronounced contraction of the whole tetramer. This motion is accompanied by a 12° domain rotation resulting in the correct arrangement of all active site residues (5).

Furthermore, a complex structure of activated NTPDase3 with a non-hydrolyzable ATP analog and the cofactor Mg²⁺ to a resolution of 2.85 Å indicates that catalytic differences between the NTPDases are primarily dictated by differences in positioning of the adenine base. These differences are caused by substitution of R492 and E493 in NTPDase1 by glycines in NTPDase3 (5).

References:

1. S. C. Robson, J. Sévigny, H. Zimmermann, *Purinergic Signal.*, 2, (2006) 409-430.
2. M. Zebisch & N. Sträter, *PNAS* 105, (2008), 6882-6887.
3. F. M. Sansom, S. C. Robson, E. L. Hartland, *Microbiol. Mol. Biol. Rev.*, 72, (2008), 765-81.
4. T. Asai, S. Miura, L. D. Sibley, H. Okabayashi, T. Takeuchi, *J. Biol. Chem.*, 270, (1995), 11391-11397.
5. U. Krug, M. Zebisch, M. Krauss, N. Sträter, *JBC*, in press.

MS06-T03

Identification of a novel TGF-β-binding site in the structure of the ZP-C domain of murine TGFR-3

U. Diestel¹, Y.A. Muller¹

¹Friedrich-Alexander-Universität Erlangen-Nürnberg, Biologie, Lehrstuhl für Biotechnik, Erlangen, Germany

The zona pellucida (ZP) domain is a structural element mainly found in extracellular proteins, such as the eponymous ZP proteins (ZP1-ZP4), tectorins, uromodulin, endoglin and the transforming growth factor β (TGF-β) receptor type 3 (TGFR-3) (1). TGFR-3, a member of the TGF-β superfamily involved in cell signaling and growth regulation processes, features a ZP domain in its ectodomain part (2). In order to better understand the structure and function of the TGFR-3 ZP domain within the context of TGF-β-binding, we investigated the domain structure of the murine TGFR-3 ZP domain using limited proteolysis, ligand binding studies and X-ray crystallography.

Our data indicate that the murine TGFR-3-ZP core domain retains a relatively rigid fold which is less susceptible to limited proteolysis. We identified that it is not the ZP domain with its previously delineated borders that is required for ligand-binding, but the FG-loop between the ZP core structure and the external hydrophobic patch (EHP) region.

We demonstrate that the TGFR-3-ZP(ΔC) protein lacking this loop region is incapable of ligand-binding whereas the isolated FG-loop sequence together with the EHP (~50 residues) shows binding of TGF-β with a dissociation constant in the nanomolar range.

We also crystallized the TGFR-3-ZP-C subdomain and solved its structure to a resolution of 2.9 Å. Structural insights into the ZP domain architecture were gained during the last years and revealed a subdomain arrangement into ZP-N and ZP-C (3-5). Since the FG-loop-EHP residues are not visible in our mouse TGFR-3-ZP-C crystal structure and there are no differences between mouse and rat sequence in the referred part of sequence, we spot this region in the crystal structure of rat TGFR-3-ZP-C published by Lin *et al.* All biochemical and structural data together allow us to narrow the binding site down to only a few amino acids.

1. Jovine, L., Darie, C. C., Litscher, E. S., and Wassarman, P. M. (2005) *Annual review of biochemistry* 74, 83-114
2. Bilandzic, M., and Stenvers, K. L. (2011) *Mol Cell Endocrinol* 339, 180-189
3. Han, L., Monné, M., Okumura, H., Schwend, T., Cherry, A. L., Flot, D., Matsuda, T., and Jovine, L. *Cell* 143, 404-415
4. Lin, S. J., Hu, Y., Zhu, J., Woodruff, T. K., and Jardetzky, T. S. *Proceedings of the National Academy of Sciences of the United States of America* 108, 5232-5236
5. Monne, M., Han, L., Schwend, T., Burendahl, S., and Jovine, L. (2008) *Nature* 456, 653-657

MS06-T04

Structural and functional organization of the Ska complex, a key assembly for stable kinetochore-microtubule attachments

A.A. Jeyaprakash¹, A. Santamaria², U. Jayachandran¹, G. Chan², E.A. Nigg², E. Conti¹

¹Max Planck Institute of Biochemistry, Structural cell biology, Martinsried, Germany

²Biozentrum, Growth & Development, Basel, Switzerland

Accurate chromosome segregation during cell division requires stable kinetochore-microtubule (MT) attachments to physically connect the chromosomes and the spindle microtubules. Several KT associated protein complexes work in concert to achieve stable KT-MT attachments. These include the protein-protein interaction network known as KMN (KNL1/Mis12/Ndc80) and in budding yeast the Dam1 complex [1]. Dam1 is a multi-subunit assembly that has the ability to form rings around MTs, but no orthologs of Dam1 have been identified in higher eukaryotes. The recently identified Ska complex is emerging as a key player in establishing

stable KT-MT attachments in mammalian cells. The Ska complex localizes at the outer KT and exerts its function by interacting directly with MT [2-4]. The complex is composed of three proteins: Ska1, Ska2 and Ska3/Rama1/C13orf3. We have recently determined the 3.3 Å resolution crystal structure of the core Ska complex. The structure shows a W-shaped dimer formed by the intertwined interactions of the three Ska components. The C-terminal domains of Ska1 and Ska3 protrude at each end of the homodimer, bind microtubules in vitro when connected to the central core and are essential *in vivo*. Mutations disrupting the central coiled coil or the dimerization interface result in chromosome congression failure followed by cell death. The Ska complex thus endowed with bipartite and cooperative tubulin-binding properties at the ends of a 350 Å long molecule. The symmetric structural framework of the Ska complex provides insights into how the Ska complex might complement and stabilize the Ndc80 microtubule attachments in mammals analogous to the Dam1/DASH complex in yeast.

References:

1. Santaguida, S., and Musacchio, A. (2009). The life and miracles of kinetochores. *EMBO J*28, 2511-2531.
2. Welburn, J.P., Grishchuk, E.L., Backer, C.B., Wilson-Kubalek, E.M., Yates, J.R., 3rd, and Cheeseman, I.M. (2009). The human kinetochore Ska1 complex facilitates microtubule depolymerization-coupled motility. *Dev Cell*16, 374-385.
3. Theis, M., Slabicki, M., Junqueira, M., Paszkowski-Rogacz, M., Sontheimer, J., Kittler, R., Heninger, A.K., Glatter, T., Kruusmaa, K., Poser, I., et al. (2009). Comparative profiling identifies C13orf3 as a component of the Ska complex required for mammalian cell division. *EMBO J*28, 1453-1465.
4. Gaitanos, T.N., Santamaria, A., Jeyaprakash, A.A., Wang, B., Conti, E., and Nigg, E.A. (2009). Stable kinetochore-microtubule interactions depend on the Ska complex and its new component Ska3/C13Orf3. *EMBO J*28, 1442-1452.

MS06-T05

Crystal Structure of Yeast Splicing Factor Cwc2 Reveals a Novel Architecture of a Multipartite RNA-binding Protein

J. Schmitzová¹, N. Rasche¹, O. Dybkov¹, K. Kramer¹, P. Fabrizio¹, H. Urlaub¹, R. Lührmann¹, V. Pena¹

¹Max-Planck-Institute for Biophysical Chemistry, Dept. of Cellular Biochemistry, Göttingen, Germany

Nuclear pre-mRNA splicing is an essential step of gene expression in eukaryotes, whereby non-coding introns are excised from the pre-mRNA via two consecutive transesterification reactions that are catalysed by a large dynamic molecular RNA-protein complex, the spliceosome. Initially assembled in a catalytically inactive form, the spliceosome undergoes an extensive reconfiguration of its inner RNA network that leads to the formation of the catalytic center. In active spliceosomes, yeast Cwc2 contacts important RNA elements of the catalytic center, including the U6 internal stem-loop (ISL), and other regions of U6 and the pre-mRNA intron near the 5' splice site (1).

To gain insight into how Cwc2 is capable to recognize simultaneously several distinct RNA regions and possibly juxtapose these sites, we have determined the crystal structure of the Cwc2 functional core that is sufficient for splicing and RNA binding. The X-ray crystal structure of yeast Cwc2 reveals, how a zinc-finger (ZnF), an RNA recognition motif (RRM), and a previously uncharacterized Torus domain are tightly integrated in a novel compact folding unit (2).

UV-induced crosslinking of Cwc2-U6snRNA followed by mass spectrometry allowed the identification of six RNA-contacting sites: four in or close to the RRM domain, one in the ZnF and one on a protruding connector element between Torus and RRM domains. The three distinct regions contacting RNA are connected by a contiguous and conserved positively charged surface,

suggesting an expanded interface for RNA accommodation. Mutation analysis confirmed that the identified cross-linked sites are important for RNA binding. Additionally, a single point mutation in the connector element has shown its crucial role in splicing.

In conclusion, crystal structure of yeast spliceosomal protein Cwc2 reveals a novel architecture of a multipartite RNA binding platform.

Literature

1. Nicolas Rasche, Olexandr Dybkov, Jana Schmitzová, Berktañ Akyildiz, Patrizia Fabrizio and Reinhard Lührmann. Cwc2 and its human homolog RBM22 promote an active conformation of the spliceosome catalytic center. *Embo J.*, submitted
2. Jana Schmitzová, Nicolas Rasche, Olex Dybkov, Katharina Kramer, Patrizia Fabrizio, Henning Urlaub, Reinhard Lührmann, Vladimir Pena. Crystal Structure of Cwc2 Reveals a Novel Architecture of a Multipartite RNA-binding Protein *Embo J.* submitted

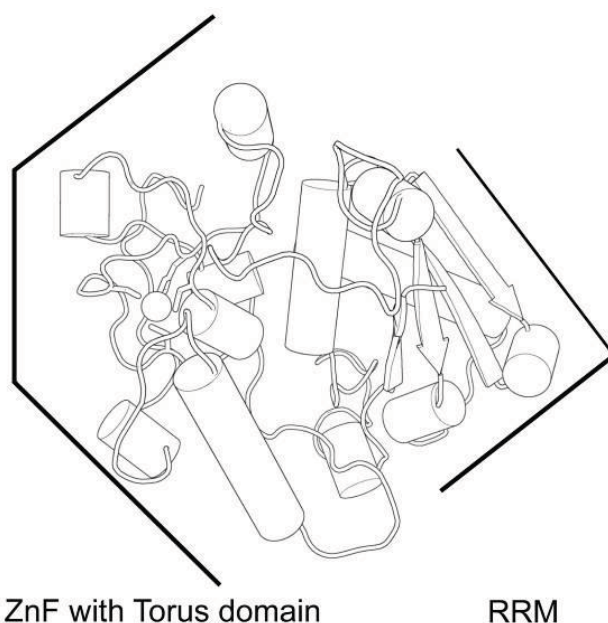


Fig. 1. Crystal structure of yeast splicing factor Cwc2 reveals, how a ZnF, an RRM, and a previously uncharacterized Torus domain are tightly integrated in a novel compact folding unit

MS06-T06

Structural and functional studies of spliceosome catalytic activation

K. Santos¹

¹Free University Berlin, Institut für Chemie und Biochemie - Biochemie, Berlin, Germany

Pre-mRNA splicing entails the excision of non-coding introns and the joining of neighboring exons via two consecutive transesterification reactions carried out by the spliceosome. For each catalytic cycle, a spliceosome assembles *de novo* on the substrate pre-mRNA by the stepwise recruitment of five small nuclear RNPs (snRNP) and numerous non-snRNP factors. The initial assembly is catalytically inactive and requires profound remodeling to become catalytically competent. The spliceosome is further remodeled between the two catalytic steps and is disassembled in an ordered fashion after splicing catalysis. Spliceosome catalytic activation depends on the Brr2 protein, a

large, unconventional DEXD/H-box ATPase/RNA helicase. Brr2 activity is regulated by Prp8, generally considered the master regulator of the spliceosome, and Snul14, an eEF2-like G-protein. Furthermore, the same machinery has been found to be required again for spliceosome disassembly. We are interested in the molecular mechanisms underlying Brr2 activity as an RNP remodeling enzyme and its regulation via Prp8 and Snul14, and will report on results from a combined structural and functional approach (1-3).

References:

1. Pena, V., Liu, S., Bujnicki, J., Lührmann, R., Wahl, M. C. (2007) Structure of a multipartite protein-protein interaction domain in splicing factor Prp8 and its link to retinitis pigmentosa. *Mol. Cell* 25, 615-624.
2. Pena, V., Rozov, A., Fabrizio, P., Lührmann, R., Wahl, M. C. (2008) Structure and function of an RNase H domain at the heart of the spliceosome. *EMBO J.* 27, 2929-2940.
3. Pena, V., Mozaffari Jovin, S., Fabrizio, P., Orłowski, J., Bujnicki, J. M., Lührmann, R., Wahl, M. C. (2009) Common design principles in the spliceosomal RNA helicase Brr2 and in the Hel308 DNA helicase. *Mol. Cell* 35, 454-466.

MS07-T01

Behaviour of alpha-boron at high pressures and temperatures

N. Dubrovinskaia¹, G. Parakhonskiy^{1,2}, E. Bykova^{1,2}, M. Hanfland³,

M. Merlini⁴, L. Dubrovinsky²

¹Universität Bayreuth, Laboratory of Crystallography, Bayreuth, Germany

²Bayerisches Geoinstitut, Bayreuth, Germany

³ESRF, Grenoble, France

⁴Università degli Studi di Milano, Milano, Italy

Boron-rich compounds are very attractive materials for research because of their unique physical properties suitable for many applications. They are widely used, for example, in thermally stable glass and ceramic. Many boron-rich solids crystallise in the icosahedral structure of alpha-rhombohedral boron, which is the simplest one among pure boron polymorphs.

In the present work we reproducibly synthesized single crystals of pure alpha-boron. The synthesis was realised at high pressures, while previously alpha-boron was produced based on ambient pressure techniques. The obtained single crystals were investigated by means of the Raman spectroscopy and single crystal X-ray diffraction at pressures up to 66 GPa and high temperatures. The effect of compression on B12 icosahedra will be discussed.

MS07-T02

Elasticity of Sm-doped Y₃Al₅O₁₂ with an independent absolute pressure scale and its calibration as a primary pressure standard

D. Trots¹, A. Kurnosov¹, S. Tkachev², K. Zhuravlev², V. Prakapenka², T. Boffa Ballaran¹, D. Frost¹

¹Universität Bayreuth, Bayerisches Geoinstitut, Bayreuth, Germany

²Advanced Photon Source, GSECARS, Chicago, United States

The absence of absolute pressure/temperature calibrants brings large uncertainties in pressure measurements, which lead to discrepancies in elasticity and high-temperature high-pressure phase boundaries of mantle minerals. The commonly used optical pressure sensors (ruby and Sm-doped Y₃Al₅O₁₂(Sm:YAG)) are secondary standards calibrated from the equations of state (EoS) of metals derived from shock-wave data (primary standard) and therefore are biased by the uncertainties on such EoS. A more precise and accurate approach is to calibrate the fluorescence shift of such material versus an absolute pressure obtained by measuring simultaneously their density and their full elastic constant tensor. Therefore we have undertaken a X-ray single-crystal diffraction and Brillouin and Raman spectroscopic study of Sm:YAG at high-pressure and room temperature and we are planning to extend such

calibration also at high temperature.

The sample of Sm:YAG was initially characterized by single crystal diffraction indicating excellent crystallinity even after double side polishing of the sample to less than 20 μm. The composition and homogeneity of the sample were checked by laser-ablation ICP-MS. At this point we must also note that pressure response in Sm:YAG is insensitive to doping amount [1].

The absolute pressure was derived from simultaneous Brillouin and X-ray diffraction measurements on double-side polished Sm:YAG in diamond anvil cell (DAC), whereas respective fluorescence shifts were measured from the same sample using Raman spectrometer. Such a combination of methods on a single sample performed simultaneously eliminates any influence of the temperature and pressure gradients in DACs and allows the implementation of this pressure marker for both X-ray and optical pressure determinations in DACs. The measurements were commenced at the Advanced Photon Source in Chicago (13-BM-D-GSECARS) whereby samples were pressurized to 21 GPa. Further extensive measurements are continued at BGI using state-of-the-art home facility for simultaneous measurements of densities and sound velocities in Earth's minerals.

Results indicate a 5% deviation from the universally employed ruby pressure scale, even at 21 GPa. This is in excellent agreement with recent results of Li et al. and Kono et al. [2,3], who performed simultaneous ultrasonic and X-ray diffraction measurements on MgO. These results will have major implications in many fields of high pressure research and, in particular, for the determination of the equivalent depth in the Earth for phenomena found in laboratory high pressure experiments. Further measurements aiming extend pressure and temperature ranges are being undertaken at BGI and envisaged in near future at APS.

We acknowledge the support of the ERC advanced grant no. 227893 "DEEP" funded through the EC 7th Framework Programme. Laser-Ablation ICP-MS experiments & Data analysis are courtesy of Dr. Andreas Audétat.

[1] Sanchez-Valle et al., *J. Appl. Phys.* 92, 4349, 2002

[2] Li et al., *Journal of Geophysical Research* 111, B11206, 2006

[3] Kono et al., *Physics of the Earth and Planetary Interiors* 183, 196, 2010

MS07-T03

Influence of crystal size and uniaxial stress on the B4 to B1 phase transition pressure in AlN and ZnO nanocrystals investigated with second harmonic generation (SHG)

L. Wiehl¹, L. Bayarjargal¹, B. Winkler¹

¹Institut für Geowissenschaften, Abt. Kristallographie, Frankfurt am Main, Germany

In the course of the miniaturization in technical applications, the size variation of physical properties of semiconductor nanocrystals comes increasingly into focus. This applies not only to electrical or optical properties but also to thermodynamic properties like phase equilibria.

A variety of materials such as ZnO, AlN, GaN, InN, CdS, CdSe, BeO, MgTe transform from the wurtzite structure (B4, P6(3)mc) to the much denser rocksalt phase (B1, Fm-3m) under high pressure. For several of these compounds, including ZnO [1], a shift of transition pressure to higher values in nanocrystals when compared to bulk crystals was reported, whereas for a 10 nm sized sample of AlN [2] an opposite shift was found. The increased transition pressure was explained by a shape effect [3] of the increased surface energy produced during the transformation along specified deformation paths [4].

The open questions in this field were our motivation for a systematic study of the effect of crystal size and axial strain on the B4 to B1 phase transition pressure in ZnO and AlN. In an earlier work the influence of deviatoric stress was shown to reduce the transition pressure of bulk ZnO from 11 to 9.3 GPa [5]. Here, we present our results on nanocrystals of ZnO (10 nm) and AlN

(100 nm, 20 nm). Pressures up to 30 GPa were generated in diamond anvil cells (DACs). We used different pressure transmitting media, namely Ne gas or KCl to achieve hydrostatic or non-hydrostatic conditions, respectively. The phase transition was detected by the vanishing of the second harmonic generation signal when going from the acentric (B4) to the centrosymmetric (B1) phase. The size of the nanocrystals was determined by powder diffraction from the width of the diffraction peaks, using a Williamson-Hall-Plot of the Scherrer formula.

Our results confirm the shift of transition pressures in nanocrystalline ZnO by 2-3 GPa to higher and in AlN by ~10 GPa to lower pressures relative to the bulk crystals in accordance with the values reported for 12 nm ZnO [1] and 10 nm AlN [2] in the hydrostatic case. The intermediate transition pressure of 100 nm sized AlN confirms this trend. For the non-hydrostatic KCl loadings transition pressures were reduced by 2-3 GPa. Financial support from the DFG (Ba 4020) is gratefully acknowledged.

- [1] J. Z. Jiang et al., *Europhys. Lett.* 50 (2000) 48-53
 [2] Z. Wang et al., *J. Phys. Chem. B* 108 (2004) 11506-11508
 [3] A. P. Alivisatos, *J. Phys. Chem.* 100 (1996) 13226-13239
 [4] R. F. Zhang et al., *Acta Materialia* 57 (2009) 2259-2265
 [5] L. Bayarjargal et al., *Appl. Phys. Lett.* 95 (2009) 061907(3p)

MS07-T04

Crystal structure of α -FeOOH under high-pressure

E. Bykova^{1,2}, K. Glazyrin¹, E. Greenberg³, T. Boffa Ballaran², V. Prakapenka⁴, M. Hanfland⁵, N. Dubrovinskaia¹, L. Dubrovinsky¹
¹Universität Bayreuth, Physikalisches Institut, Materialphysik und Technologie, Lehrstuhl für Kristallographie, Bayreuth, Germany
²University of Bayreuth, Bayerisches Geoinstitut, Bayreuth, Germany
³Tel-Aviv University, Tel-Aviv, Israel
⁴Advanced Photon Source, GSECARS, ID-13D, Argonne, United States
⁵European Synchrotron Radiation Facility, ID09A, Grenoble, France

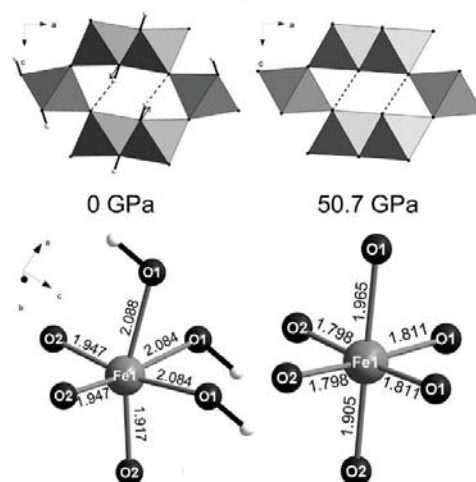
Goethite, α -FeOOH, is widely present in the Earth crust as a component of soils, sediments and ore deposits. The mineral crystallizes in an orthorhombic structure (Pnma, $a = 9.9510(5)$, $b = 3.0178(1)$, $c = 4.5979(2)$ Å [1]) and is isostructural with diaspor, AlOOH. At ambient conditions α -FeOOH structure consists of distorted FeO₃(OH)₃ octahedra linked together by sharing edges to form infinite bands. The bands are connected via shared octahedra vertices that results in infinite channels parallel to the b-axis. Investigations of the crystal structure of goethite as well as calculations of the equation of state (EoS) based on experimental data at non-ambient conditions (up to 29.4 GPa and 250 °C) have been performed by several authors (see, for example, refs. 2 and 3). At higher pressures (up to 57 GPa) the behavior of the material have been studied only theoretically using density-functional theory [4]. A phase boundary between goethite and its high-pressure polymorph, ϵ -FeOOH, hasn't been established unambiguously. While DFT predicted the transition at 6-7 GPa, Gleason et al. [3] observed a slow conversion above 5 GPa only under heating above 200 °C.

Our work presents the first in-situ single crystal X-ray diffraction (XRD) and Raman spectroscopy study of α -FeOOH in a diamond anvil cells under compression up to ~51 GPa. Single crystal XRD measurements at ambient temperature were carried out both with in-house and synchrotron facilities at ID09a beam line at ESRF. It was observed good correlation in volume-pressure dependence between data obtained with in-house and synchrotron facilities. Accuracy of the data allows us to fit 2nd-order Birch-Murnaghan EoS in both cases. Obtained values (bulk modulus and unit cell volume at ambient pressure) are in a good agreement with each other as well as with literature data.

Like diaspor, AlOOH [5], goethite structure compresses anisotropically with c-compression easier than a and b. Turning to the crystal structure it indicates that major compression occurs due to the decreasing of channel size and therefore it leads to the shortening of the hydrogen bond. During experiments no phase transitions predicted by theoretical calculations were found. But we

have observed first order phase transition at ~44 GPa characterized by sharp reduction in volume. In Raman spectra all lines disappear above 44 GPa but during decompression they again re-appear which points out on a reversible phase transition. The new phase can be described in terms of the Pnmaspace group with the following unit cell parameters: $a = 9.27(5)$, $b = 2.6420(9)$, $c = 3.975(2)$ Å (at 50.7 GPa). No significant structural changes in a compare with low-pressure phase were occurred. However after transition distortion of FeO₆H₃ octahedra was considerably reduced.

1. Yang, H., Lu, R., Downs, R.T., et al. α -FeO(OH), from single-crystal data // *Acta Crystallogr. E* (2006).62, 250-252.
 2. Nagai, T., Kagi, H., Yamanaka, T. Variation of hydrogen bonded O...O distances in goethite at high pressure // *Am. Mineral.* (2003).88, 1423-1427.
 3. Gleason, A.E., Jeanloz, R., Kunz, M. Pressure-temperature stability studies of FeOOH using X-ray diffraction // *Am. Mineral.* (2008).93, 1882-1885.
 4. Otte, K., Pentcheva, R., Schmahl, W.W., et al. Pressure-induced structural and electronic transitions in FeOOH from first principles // *Phys. Rev. B* (2009).80, 205116.
 5. Friedrich, A., Haussuehl, E., Boehler, R., et al. Single-crystal structure refinement of diaspor at 50 GPa // *Am. Mineral.* (2007).92, 1640-1644.



MS07-T05

In Situ Structural Studies At Conditions of Earth and Planetary Mantles and Cores: Techniques and Applications

L. Dubrovinsky¹, K. Glazyrin¹, T. Boffa-Ballaran¹, E. Bykova¹, N. Dubrovinskaia¹, M. Merlini², M. Hanfland³
¹Bayreuth University, BGI, Bayreuth, Germany
²Università degli Studi di Milano, Milano, Germany
³ESRF, Grenoble, France

Modern science and technology rely on the fundamental knowledge of matter that is provided by crystallographic studies. The most reliable information about crystal structures and their response to changes in pressure and temperature is obtained from single crystal diffraction experiments. Advantages in diamond anvil cell techniques (DACs) and modern X-ray sources have increased the accessible pressure range for structural research up to several dozens gigapascals. We have developed a methodology to perform single crystal X-ray diffraction experiments in double-side laser-heated DACs and demonstrate that solution of crystals structure refinements and accurate measurements of the thermal equation of state of metals, oxides, silicates from single crystal intensity data are possible in a megabar pressure range at temperatures of thousands degrees. Particular attention we paid on in situ study of geomaterials at extreme conditions.

We studied silicate perovskites (Mg_{0.88}Fe_{0.12})SiO₃, (Mg_{0.9}Fe_{0.1})(Si_{0.975}Al_{0.025})O₃, and (Mg_{0.6}Fe_{0.4})(Si_{0.655}Al_{0.35})O₃, series of magnesiowustites with different compositions, and iron carbides by means of single crystal X-ray diffraction in laser-heated diamond anvil cells, Mossbauer spectroscopy, and nuclear forward scattering at pressure up to 150 GPa and temperature above 2500 K. We will discuss effects of changes in iron electronic state on structure and properties of mantle minerals.

MS07-T06

Comparative first principles study of pressure induced phase transitions in Mn₂O₃ and MnTiO₃

C. Quiroga¹, W. Schmahl¹, R. Pentcheva¹

¹Ludwig-Maximilians-Universität, Earth and Environmental Sciences, München, Germany

Phase transitions in sesquioxides (A₂O₃) are relevant for the Earth sciences due to the relation of their high-pressure structures to mantle minerals. ABO₃ compounds, in turn, as a subgroup of the former, hold a close relationship in their crystal structures. With the discovery of post-perovskite MgSiO₃ [1,2], the dominant Earth's lower-mantle mineral, much attention has been devoted to find post-perovskite phase transitions in other ABO₃ compounds and sesquioxides at high pressures. In the case of Mn₂O₃, a direct phase transition from the ambient structure to post-perovskite has been reported experimentally above 27 GPa [3]. On the other hand, there is so far no experimental evidence for a perovskite to post-perovskite transition in titanates. However, the enhancement of octahedral distortions in MnTiO₃ perovskite may point towards affinity for such a phase transformation at higher pressures [4].

Using density functional theory calculations, including an on-site Coulomb repulsion term, we explore the relative stability of the ambient phases of α -Mn₂O₃ (Pbcn) and MnTiO₃ (ilmenite, R-3) with respect to their candidate high-pressure polymorphs. For Mn₂O₃, these include corundum (R-3c), Rh₂O₃ II-type (Pbcn) as well as orthorhombic (Pbnm) and rhombohedral (R-3c) perovskite and post-perovskite of CaIrO₃ (Cmcm), where we focus on the effect of pressure on the charge, spin and structural degrees of freedom. For MnTiO₃ we explore the LiNbO₃ (R3c) and GdFeO₃-type perovskite structures and predict a transition from perovskite to the post-perovskite phase at around 50 GPa.

Funding by DFG SPP1236 (PE883/8-1) is acknowledged.

[1] M. Murakami et al. *Science* 304, 855 (2004)

[2] A.R. Oganov and S. Ono. *Nature* 430, 445 (2004)

[3] J. Santillán et al. *Geophys. Res. Lett.* 33, L15307 (2006)

[4] Wu et al. *Geosci. Front.* 2, 107 (2010).

MS08-T01

Aluminum ordering and clustering in Al-rich synthetic phlogopite: The influence of fluorine investigated by ¹⁹F/¹H} ²⁹Si CPMAS NMR spectroscopy

M. Fechtelkord¹, R. Langner¹

¹Ruhr-Universität Bochum, Institut für Geologie, Mineralogie und Geophysik, Bochum, Germany

The influence of fluorine on cationic and anionic ordering in the mica mineral phlogopite has been investigated using ²⁹Si, ¹H, and ¹⁹F MAS as well as ¹H/¹⁹F} → ²⁹Si CPMAS NMR spectroscopies. It can be shown that the mere presence of fluorine achieves a tremendous loss of capability to incorporate aluminum into the phlogopite structure. Fluorine is usually located in Mg-rich octahedral and Si-rich tetrahedral clusters of the phlogopite structure while hydroxyl groups are located in Al-rich octahedral and tetrahedral clusters as derived from ¹H/¹⁹F} → ²⁹Si CPMAS NMR spectroscopies. The ordering effect in these two basic structural clusters can also be proven by the smaller ²⁹Si

linewidth in the two different ¹H/¹⁹F} → ²⁹Si CPMAS NMR experiments compared to the usual ²⁹Si MAS NMR experiment showing a stronger ordering of Si -environments in neighborhood to the two different anion types fluorine and hydroxyl. Contact time dependent magnetization curves show F-Si distances of about 4 Å and H-Si distances of approximately 3.4 - 3.7 Å as calculated from the heteronuclear second moment. In addition, the evidence of fluorine / hydroxyl clustering is supported by the conclusion that a ¹H/¹⁹F-²⁹Si multi-spin system is present which can be easily observed from the magnetization curves.

MS08-T02

The Automatic Tuning Matching Goniometer (ATMG) probe system -

mapping chemical questions using orientation dependent NMR experiments

O. Pecher^{1,2}, F. Haarmann¹

¹RWTH Aachen University, Institut für Anorganische Chemie (IAC), Aachen, Germany

²Max-Planck-Institut für Chemische Physik fester Stoffe, Dresden, Germany

There is still a lack of understanding of the chemical bonding in intermetallic phases limiting a knowledge based modification of properties and resulting applications of this fascinating class of materials [1]. NMR spectroscopy as a local probe may shed light on this issue [2-4]. Investigations on powder samples aligned in the magnetic field enable the exploitation of orientation dependent NMR couplings. Very characteristic NMR signals with detailed features of the line shapes or an increase of the experimental resolution result [4]. The achieved sustainable improvement of the data quality allows the deconvolution of broad and overlapping NMR signals which is not possible for samples of randomly oriented crystallites.

In this contribution we refer on the processing and usage of a special designed Automatic Tuning Matching Goniometer (ATMG) probe system for orientation dependent NMR experiments. The interplay of the automated working ATMG probe with the NMR spectrometer synchronized by the ATMG controller box is depicted in Figure 1. The probe holds the sample of aligned crystallites in a goniometer with ±1° accuracy regulated by a piezoelectric engine fixed at the bottom outside of the magnet (Fig. 1a). By analysis of forwarded (FWD) and reflected (REF) power at a certain carrier frequency the resonant circuit is automatically tuned and matched by additional piezoelectric engines of the probe triggered by the ATMG box (Fig. 1b). Transistor-Transistor Logic (TTL) signals enable the communication between the NMR spectrometer and the ATMG box concerning start and stop of tuning, matching and goniometer steps, respectively (Fig. 1c). A preamble in the pulse program for the NMR spectrometer synchronises the interplay of the hardware components to fulfill the experimental requirements (Fig. 1d). The ATMG probe system operates fulltime in wideline as well as frequency sweep NMR experiments with possible sample orientations between 0° and 360° without permanent control by an operator.

Applications of the ATMG probe system in orientation dependent NMR measurements on the intermetallic phases BaGa₂, Sr_{1-x}Ba_xGa₂ and Cu_{1-x}Al₂ will be presented [2,5,6].

[1] R. Nesper, *Angew. Chem.* **1991**, *103*, 805.

[2] F. Haarmann, K. Koch, D. Grüner, W. Schnelle, O. Pecher, R. Cardoso-Gil, H. Borrmann, H. Rosner, Yu. Grin, *Chem. Eur. J.* **2009**, *15*, 1673.

[3] F. Haarmann, K. Koch, P. Jeglič, O. Pecher, H. Rosner, Yu. Grin, *Chem. Eur. J.* **2011**, *17*, 7560.

[4] F. Haarmann. Quadrupolar NMR of Intermetallic Compounds. In R. K. Harris and R. E. Wasylshen (Eds-in-chief), *Encyclopedia of Magnetic Resonance*. John Wiley, Chichester, in press, **2011**.

[5] O. Pecher, F. Haarmann, *Z. Anorg. Allg. Chem.* **2010**, *636(11)*, 2089.

[6] F. Haarmann, M. Armbrüster, Yu. Grin, *Chem. Mater.* **2007**, *19*, 1147.

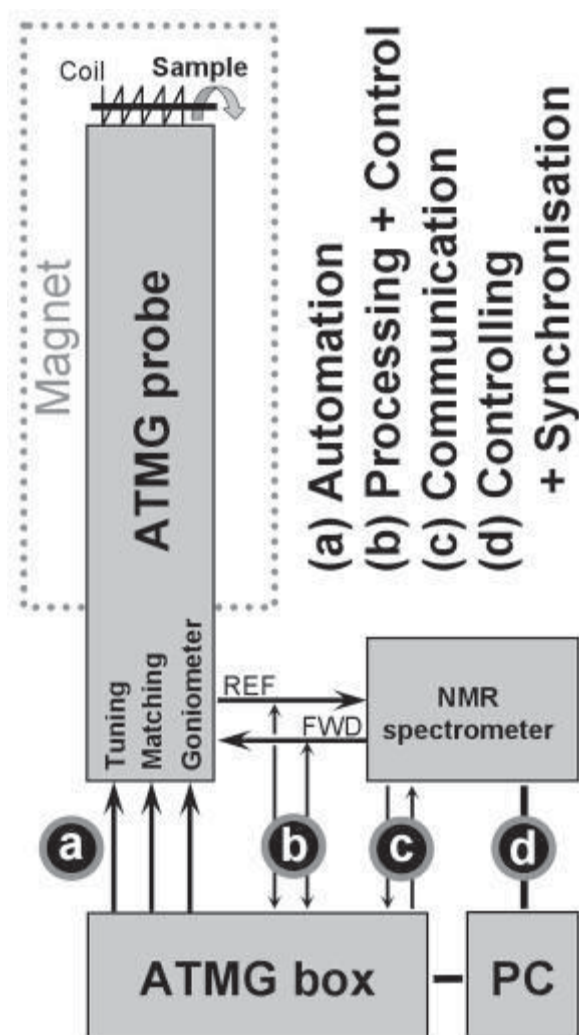


Figure 1: Interplay of the components of the Automatic Tuning Matching Goniometer (ATMG) probe system in a schematic sketch.

MS08-T03

A ^{57}Fe Mössbauer Study of Local Structure and Cation Distribution in Mullite-type $\text{Bi}_2\text{Fe}_4\text{O}_9$ - $\text{Bi}_2\text{Mn}_4\text{O}_{10}$ and $\text{Bi}_2\text{Fe}_4\text{O}_9$ - $\text{Bi}_2\text{M}_4\text{O}_9$ (M=Al, Ga) solid solutions

S.-U. Weber¹, T.M. Gesing², M. Lufaso³, H. Schneider⁴, K.-D. Becker¹

¹Technische Universität Braunschweig, Institut für Physikalische und Theoretische Chemie, Braunschweig, Germany

²Universität Bremen, Institut für Kristallographie, Bremen, Germany

³University of North Florida, Department of Chemistry, Jacksonville, FL, United States

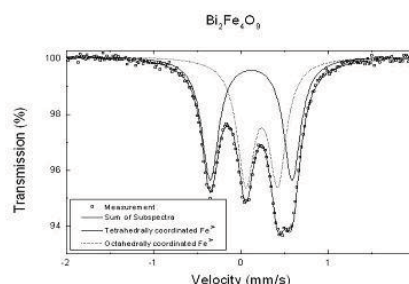
⁴Universität zu Köln, Institut für Kristallographie, Köln, Germany

In the present work, the local structure of solid solutions series of $\text{Bi}_2(\text{Fe}_x\text{M}_{1-x})_4\text{O}_9$ (designated as O9-phases) with M=Al, Ga, and Mn and of $\text{Bi}_2(\text{Fe}_x\text{Mn}_{1-x})_4\text{O}_{10}$ (designated as O10-phases) is studied by ^{57}Fe Mössbauer spectroscopy. Spectra are composed by superposition of two quadrupole doublets due to iron located on octahedrally and tetrahedrally coordinated sites (O9-phases), see Fig. 1, or on octahedrally and pyramidally coordinated sites (O10-phases), where the doublet with the smaller of the two splittings is always due to the octahedrally coordinated species. The spectra yield quantitative information on the iron occupancy of the two structural sites in the mullite-type lattices. In the Fe-Al system, the distribution of cations is found to be almost random, whereas in the

Fe-Ga system, gallium ions are found to develop a strong preference for the occupation of tetrahedral sites, thus displacing Fe cations to the octahedral sites.

The phase diagram Fe-Mn system at room temperature is characterised by three regions: a) a Fe-rich single-phase region with O9-Structure, b) a two-phase region ($0.875 \leq x_{\text{Fe}} \leq 3.125$), and c) a Mn-rich single-phase region with O10-Structure. Manganese ions reveal a strong preference for the octahedral position: in the O9-type solid solution Mn ions are found to exclusively occupy this site, whereas the tetrahedrally coordinated sites are completely filled by Fe. In the O10-phase, the Fe occupancy of the pyramidal site is about twice as large as that of the octahedral sites.

Hyperfine parameters, isomer shifts, and quadrupole splittings derived from the spectra as a function of composition, e.g., provide evidence for a strong distortion of the iron sites at low iron concentrations in the Fe-Al system. In addition to measurements at room temperature, high-temperature in-situ Mössbauer spectroscopy provides information on the temperature dependence of the cation distribution of Fe, Al, and Ga on the two inequivalent lattice sites of the O9-structure. In the two solid solutions series, cation distributions show almost no temperature dependency, yielding site exchange energies close to zero. Also, in the Fe-Mn series, the cation distribution shows no temperature dependence.



MS08-T04

Application of a nanoscope: Fayalite 3D difference electron densities from synchrotron diffraction measurements

W. Lottermoser¹, S.-U. Weber², M. Grodzicki¹, A. Kirfel³, G. Amthauer¹

¹University of Salzburg, Materials Engineering and Physics, Salzburg, Austria

²University of Technology, Physical and Theoretical Chemistry, Braunschweig, Germany

³University of Bonn, Mineralogy and Palaeontology, Bonn, Germany

Experimental and calculated structure factors from a previous, very accurate synchrotron diffraction measurement on synthetic fayalite have been converted by an inverse Fourier transformation to difference electron (deformation) densities (DED). These were processed in our revised 3D-display program giving hyperareas of DED floating in space around the iron positions M1 and M2 within the fayalite unit cell and spanning a volume of 6 and 4 Å, respectively. These comparably wide limits are due to the different site symmetries and had been proposed by earlier DFT (density functional theory) calculations. From the different hyperareas the supposed charges were integrated in space and processed to electric field gradients (efg) on M1 and M2 using a point charge model. The two efgs with respect to the crystallographic axes' system were compared with those from single crystal Mössbauer measurements (experimental efgs) published elsewhere, yielding excellent agreement within $\pm 5^\circ$ and surpassing even the DFT results. This study reports the proceeding and the conditions of success of the underlying semi-quantitative method being located between theory (DFT) and experiment (diffractometry) and promising valuable

results on many other compounds - the term “nanoscope” for the graphical representation due to its high spatial resolution may be justified.

MS08-T05

Ion Exchange and Adsorption of Schwertmannite compared to Goethite and Lepidocrocite

P.M. Kadletz¹, A.J. Götz¹, K. Otte¹, R. Pentcheva¹, W.W. Schmahl¹, S.H. Park¹, S. Peiffer², S. Paikaray², F.E. Wagner³, A. Ziegler⁴, J. Kipry⁵, C. Wiacek⁶, M. Schlömann⁵, E. Janneck⁶

¹LMU Munich, Dept. of Earth and Environmental Sciences, Munich, Germany

²University of Bayreuth, Department of Hydrology, Bayreuth, Germany

³TUM, Physik-Department E 15, Munich, Germany

⁴University of Ulm, Central Facility for Electron Microscopy, Ulm, Germany

⁵Tech. University of Freiberg, Department of Environmental Microbiology, Freiberg, Germany

⁶GEOS Ingenieurgesellschaft mbH, Halsbrücke, Germany

Schwertmannite is a poorly crystalline iron-oxyhydroxy-sulfate. It has a non-stoichiometric composition that is close to $\text{Fe}_8\text{O}_8(\text{OH})_6\text{SO}_4$ and can be used as an adsorbent for toxic metals in water [1], since there is ion exchange between the sulphate and e.g. arsenate, chromate or vanadate.

We synthesised schwertmannite by different biotic and abiotic pathways. The products show different particle morphologies and slightly varying XRD Profiles. Most importantly the “hedgehog” morphology previously attributed to bacterial cells encrusted with fibrous schwertmannite [2] has also been obtained with purely abiotic syntheses.

The quasi amorphous structure is commonly assumed to be related to akaganeite (Fig. 1, right). Our Mössbauer spectra show that Fe is entirely octahedrally coordinated Fe^{3+} . Our Rietveld refinements with the Fernandez-Martinez et al. 2010 [3] structure model gave a good fit when anisotropic crystallite size broadening was applied (Fig. 1, left).

Bigham et al. 1994 assumed, that sulfate is both adsorbed to the surface and incorporated into the tunnels of schwertmannite with changing proportions of both species [4]. We studied schwertmannite-like compounds in which the sulfate is substituted against chromate, arsenate and vanadate. The XANES spectra of heavy metal substituted schwertmannites with varying chromate and arsenate content show isosbestic points indicating that a mixture of different configurations is present (Fig. 2). Referring to chromate (Fig. 2, right), the accuracy of the data suffers from aging of the samples during the measurement. In the spectra of arsenate substituted schwertmannites the isosbestic points correlate with those of the goethite and lepidocrocite spectra, therefore similar configurations of arsenate anions are present in all three phases in varying quantity (Fig. 1, left).

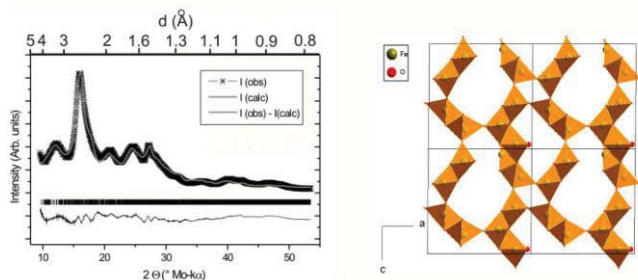


Fig. 1: Rietveld refinement of schwertmannite (left) based on the Fernandez-Martinez et al. 2010 [3] structure model (right). The lattice constants and anisotropic grain size broadening parameters were refined.

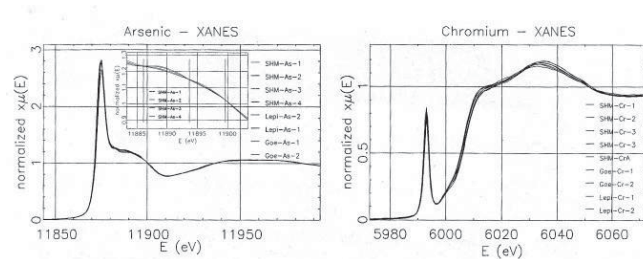


Fig. 2: As- and Cr-K-edge XANES spectra of heavy metal substituted schwertmannite samples and references that adsorbed the corresponding heavy metal (SHM=schwertmannite, Goe=goethite, Lepi=lepidocrocite). Isosbestic points of the K-edge-XANES spectra of the As-substituted schwertmannite samples are shown in the small graph on the left hand side.

References:

- [1] Peiffer S., Burghardt D., Janneck E., Pinka J., Schlömann M., Wiacek C., Seifert J., Schmahl W., Pentcheva R., Meyer J., Rolland W. (2008): Development and Optimisation of a Process to Biosynthesize reactive Iron Mineral Surfaces for Water Treatment Purposes (SURFTRAP). Mineral Surfaces - From anionic Processes to industrial Application Kick-Off-Meeting, Geotechnology Science Report, 12, 641-648.
- [2] Ferris F. G., Hallbeck, L., Kennedy, C.B., Pedersen, K. (2004): Geochemistry of acidic Rio Tinto headwaters and role of bacteria in solid phase metal partitioning. Chemical Geology, 212, 291-300.
- [3] Fernandez-Martinez A., Timon V., Roman-Ross G., Cuello G. J., Daniels J. E., Ayora C. (2010): The structure of schwertmannite, a nanocrystalline iron oxyhydroxysulfate. American Mineralogist, 95,1312-1322.
- [4] Bigham J. M., Carlson L., Murad E. (1994): Schwertmannite, a new iron oxyhydroxy-sulphate from Pyhäsalmi, Finland, and other localities. Mineralogical Magazine, 58, 641-648.

MS08-T06

Scanning coherent x-ray diffraction microscopy with spatial resolutions down to below 10 nm

C. Schroer¹, S. Hönig¹, R. Hoppe¹, J. Patommel¹, A. Schropp¹, S. Stephan¹, S. Schöder², M. Burghammer³, G. Wellenreuther⁴, G. Falkenberg⁴

¹TU Dresden, Institut für Strukturphysik, Dresden, Germany

²Synchrotron Soleil, Gif-sur-Yvette, France, France

³European Synchrotron Radiation Facility, Grenoble, France, France

⁴DESY, HASYLAB, Hamburg, Germany

Real-space x-ray imaging techniques, both in full-field and scanning mode, are limited in spatial resolution by the numerical aperture of x-ray optics. This limitation can be overcome by using coherent x-ray diffraction imaging techniques, such as scanning coherent x-ray diffraction microscopy also called ptychography

[1,2,3]. This technique gains its strength out of a combination of real-space information combined with far-field diffraction data. An object is scanned through a laterally confined beam, recording at each position of the scan a far-field diffraction pattern. From these data, numerical phasing algorithms can reconstruct the complex transmission function of the object with a spatial resolution much better than the lateral size of the illuminating beam [1,4,5].

Based on this technique we have developed and built two x-ray scanning microscopes at the synchrotron radiation sources ESRF in Grenoble, France and PETRA III at DESY in Hamburg [6] that can generate hard x-ray real-space images of optically thin objects (kinematic approximation) with spatial resolutions in the 10 nm range and below (Fig. 1). In addition to this ptychographic contrast, x-ray fluorescence yields the elemental distributions in the sample on the scale of the lateral size of the illuminating beam, i. e., with 50 to 80 nm resolution [7,8]. We discuss the potential and limitations of real space imaging in view of spatial resolution, in particular for scanning coherent x-ray diffraction imaging [9].

References:

- [1] J. M. Rodenburg and H. M. L. Faulkner, *Appl. Phys. Lett.* **85**(20), 4795 (2004).
- [2] P. Thibault, M. Dierolf, A. Menzel, O. Bunk, C. David, and F. Pfeiffer, *Science* **321**, 379 (2008).
- [3] A. Schropp, P. Boye, A. Goldschmidt, S. Hönig, R. Hoppe, J. Patommel, C. Rakete, D. Samberg, S. Stephan, S. Schöder, M. Burghammer, and C. G. Schroer, *J. Microscopy* **241**, 9 (2011).
- [4] P. Thibault, M. Dierolf, O. Bunk, A. Menzel, and F. Pfeiffer, *Ultramicroscopy* **109**, 338 (2009).
- [5] A. M. Maiden and J. M. Rodenburg, *Ultramicroscopy* **109**, 1256 (2009).
- [6] C. G. Schroer, P. Boye, J. M. Feldkamp, J. Patommel, D. Samberg, A. Schropp, A. Schwab, S. Stephan, G. Falkenberg, G. Wellenreuther, and N. Reimers, *Nucl. Instrum. Meth. A* **616**, 93 (2010).
- [7] A. Schropp, P. Boye, J. M. Feldkamp, R. Hoppe, J. Patommel, D. Samberg, S. Stephan, K. Giewekemeyer, R. N. Wilke, T. Salditt, J. Gulden, A. P. Mancuso, I. A. Vartanyants, E. Weckert, S. Schöder, M. Burghammer, and C. G. Schroer, *Appl. Phys. Lett.* **96**, 091102 (2010).
- [8] C. G. Schroer, A. Schropp, P. Boye, R. Hoppe, J. Patommel, S. Hönig, D. Samberg, S. Stephan, S. Schöder, M. Burghammer, G. Wellenreuther, and G. Falkenberg, *AIP Conference Proceedings* **1365**, 227 (2011).
- [9] A. Schropp and C. G. Schroer, *New Journal of Physics* **12**, 035016 (2010).

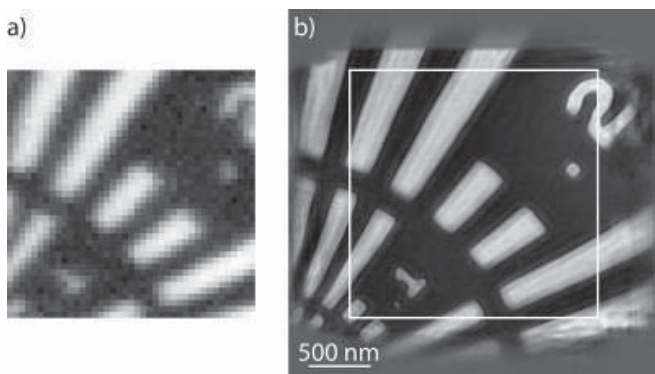


Fig 1: Scanning micrograph of a resolution test pattern recorded with the x-ray microscope at PETRA III at DESY in Hamburg. (a) Fluorescence map, showing the Ta distribution with approximately 80 nm resolution, (b) ptychographic image showing the phase shift by the test object with approximately 10 nm resolution.

MS09-T01

Inhibition of PDZ domain mediated protein-protein interactions

Y. Roske¹, J. Saupe², N. Kamdem², A. Diehl², H. Oschkinat², J. Rademann³, U. Heinemann¹

¹MDC-Berlin, Crystallography, Berlin, Germany

²FMP, Chemistry, Berlin, Germany

³University, Pharmaceutical and medicinal chemistry, Leipzig, Germany

PDZ domains are among the most common protein interaction domains. More than 450 PDZ domains in close to 200 human proteins are known and play a key role in cellular signaling e.g. Dishevelled-PDZ (Dvl-PDZ) domain and in organization of multi-protein complexes e.g. Shank-PDZ domain. PSD-95, DlgA and ZO-1 are the three founding members of the family of PDZ domain containing proteins.

Dvl proteins are intracellular scaffolds, and there is mounting evidence that the Dvl-PDZ domain is critical for Wnt signal propagation. Dvl transduces Wnt signals from the receptor Frizzled (FZ) to downstream components in canonical and noncanonical Wnt signaling pathways. Up-regulation and overexpression of Dvl proteins have been reported in many cancers, including those of breast, colon, prostate, mesothelium and lung.

An example of a protein network mainly organized by PDZ-domain interactions, is the post synaptic density (PSD) in the synapse. The central scaffolding protein of the PSD is Shank which interlinks clusters of glutamate receptors. Mutations in the Shank gene have been ascertained in neuronal disorders e.g. mental retardation, typical autism and Asperger syndrome.

Therefore we selected the Dvl3-PDZ and Shank3 PDZ domain as biologically attractive targets for the development of small molecule PDZ ligands.

MS09-T02

Structural and functional investigation of spliceosomal U5 snRNP assembly

G. Weber¹

¹FU Berlin, Strukturbiochemie, Berlin, Germany

The spliceosome is a complex RNA-protein (RNP) machine required for the removal of non-coding intervening sequences (introns) from eukaryotic precursor messenger RNAs (pre-mRNAs) and the ligation of neighboring coding regions (exons) to generate continuous open reading frames for protein biosynthesis on the ribosome. For each round of splicing, a spliceosome is assembled *de novo* on a substrate pre-mRNA by the stepwise recruitment of complex subunits, the small nuclear ribonucleoprotein particles (snRNPs), and many non-snRNP proteins. During splicing, several of the snRNPs are profoundly remodeled and require specific recycling or re-assembly to participate in additional rounds of splicing. The common core structures of snRNPs consist of a set of seven Sm proteins bound in a ring-like fashion to a uridine-rich Sm site in the small nuclear RNAs (snRNAs) of the snRNPs. Special assembly machineries guide the biogenesis of the Sm core RNPs in higher eukaryotes. In addition, each snRNP contains a number of particle-specific proteins. Presently, little is known about when, where and how the specific proteins are assembled.

Among the particle-specific proteins of the U5 snRNP, Prp8p (a ca. 280 kDa regulatory scaffold protein) and Brr2p (a ca. 250 kDa unconventional RNA helicase) are essential for spliceosome assembly and splicing catalysis. In yeast, U5 snRNP is assembled *via* a cytoplasmic precursor form, which contains Prp8p but lacks Brr2p. Instead, pre-U5 snRNP contains the Aar2 protein, which is not found in mature U5 snRNP or in the spliceosome. Thus, Aar2p exhibits hallmarks of a U5 snRNP assembly factor. We have investigated the structural basis for the mutually exclusive binding of Aar2p and Brr2 to U5 snRNP. Aar2p and Brr2p bind preferentially to different domains in the C-terminal region of Prp8p connected by a long, flexible linker. Binding of Aar2p to

Prp8p sequesters the region of Prp8p required for Brr2p association thus preventing Brr2p incorporation (Weber *et al.*, 2011). Based on our results, we propose a model, in which Aar2p acts as a U5 snRNP assembly factor that regulates the incorporation of the particle-specific Brr2p. The purpose of this regulation may be to safeguard against nonspecific RNA binding to Prp8p and/or premature activation of Brr2p activity.

References:

Weber, G., Cristao, V. F., Alves, F. L., Santos, K. F., Holton, N., Rappsilber, J., Beggs, J. D., Wahl, M. C. (2011) Mechanism for Aar2p function as a U5 snRNP assembly factor. *Genes Dev.* 25, 1601-1612.

MS09-T03

Structural studies of a bidirectional transport factor

M. Grünwald¹, D. Lazzaretti¹, F. Bono¹

¹MPI for Developmental Biology, AG BONO, Tübingen, Germany

Karyopherins are central players in nucleo-cytoplasmic transport. These large receptors (>100 kDa) are called importins if they import protein cargoes into the nucleus and exportins if they export cargoes to the cytoplasm. The directionality of the process is driven by the GTPase Ran that regulates import and export in opposite ways. Importin13 (Imp13) is an unusual b karyopherin that is able to both import and export cargoes. In the cytoplasm, Imp13 associates with different cargoes such as Mago-Y14 and Ubc9 and facilitates their import into the nucleus where RanGTP binding promotes cargo release. In the nucleus, Imp13 can form a trimeric complex with the translation initiation factor eIF1A, small enough to passively diffuse through the nuclear pore complexes, and to export it back to the cytoplasm where it plays an essential role in the initiation of translation. Here we present the 3.6 Å crystal structure of Imp13 in complex with RanGTP and eIF1A. The structure shows that the export cargo binds at the inner surface of Imp13 C-terminal arch adjacent to RanGTP. Comparison of the Imp13-RanGTP-eIF1A trimeric complex with the Imp13-Mago-Y14 and Imp13-Ubc9 import complexes shows the remarkable plasticity of Imp13, whose conformation changes from a closed ring to an open superhelix when bound to the different cargoes. The structure also shows that the overall conformation of Imp13 in the export complex is very similar to the conformation of the exportin Crm1. Finally, the structure gives interesting insights into how Imp13 can both function as an import and as an export factor.

MS09-T04

Why Is the Mollusc Chitin Synthase Such a Complex Molecular Machine?

I. Weiss¹, V. Schönitzer²

¹INM - Leibniz Institute for New Materials, Materials in Biology, Saarbrücken, Germany

²LMU – Clinical Center University of Munich, Department of Surgery, Experimental Surgery and Regenerative Medicine, München, Germany

The mollusc chitin synthase would be essentially a biological molecular machine, if it produces quasi-mechanical movements in response to specific stimuli. Molecular motors such as myosins are molecular machines by definition, which are frequently found within cells. The chitin synthase involved in mollusc shell formation is, in fact, directly linked to the cytoskeleton with such a myosin domain. However, the question remains whether and how its motor activity is related to specific stimuli in shell formation.

We achieved molecular cloning and functional expression of the mollusc myosin chitin synthase in the slime mold *Dictyostelium discoideum*, a universal model organism for cell mechanics and motor proteins.^[1-3] This allows us to study now different molecular aspects of this complex transmembrane enzyme and its various potential functions in shell formation.

Our data suggest that certain domains at the extracellular interface, which are exposed to the forming shell in the natural system, interfere with mineral surfaces in a very controlled manner. By comparing the chitin synthases of *Atrina*, *Mytilus*, *Pinctada*, and *Lottia*, one can discuss their possible functions in view of different shell structures, which are obtained in the various mineralization processes in living molluscs.

[1] I. M. Weiss, V. Schönitzer, N. Eichner, M. Sumper; FEBS Letters 2006, 580:1846-1852.

[2] V. Schönitzer, I. M. Weiss; BMC Structural Biology 2007, 7:71.

[3] V. Schönitzer, N. Eichner, H. Clausen-Schaumann, I. M. Weiss; Biochemical and Biophysical Research Communications 2011, 415:586-590.

MS09-T05

Insight into the allosteric mechanism of GntR/HutC-type bacterial repressor molecules

S. Fillenbergl¹, Y. Muller¹

¹Universität Erlangen-Nürnberg, Lehrstuhl f. Biotechnik, Erlangen, Germany

YvoA^{1,2} and DasR³ are bacterial transcriptional repressors from the GntR/HutC-family and are involved in the regulation of genes from the N-Acetylglucosamine-degrading pathway of *B.subtilis* and *S.coelicolor*, respectively. Former studies have shown that DasR also controls the uptake and metabolism of chitobiose⁴ as well as the life cycle³ of *S.coelicolor* in general.

Although several structures of “apo”-HutC family proteins have become available, in none of these structures effector-binding to the effector-binding site has been observed. Furthermore no structure of a DNA-bound HutC family member has been published by now. As a consequence, these structures provide only a limited atomic insight into the mechanism by which the binding of the effector to the C-terminal domain causes the repressor molecule to detach from its operator site on the DNA.

Here, we present the 1.95 Å crystal structure of isolated YvoA-DNA-binding domains (YvoA-DBD) in complex with a 15bp-dsDNA-fragment (Figure 1A). Furthermore we were able to crystallize the effector-binding domain of DasR (DasR-EBD) in complex with the putative effector molecule Glucosamine-6-phosphate and determine the structure at a resolution of 1.75 Å (Figure 1B). In combination with other structures (YvoA wildtype, DasR wildtype, DasR-EBD without effector and DasR-EBD in complex with sulfate) we gained insight into the repression- & induction-mechanism of GntR/HutC transcriptional regulators.

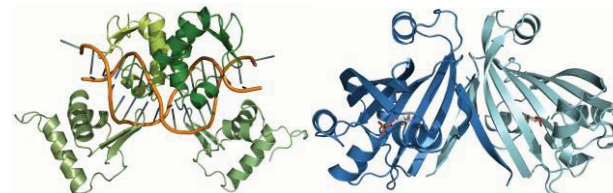


Figure 1: A) Four YvoA-DBD molecules bound to a 15bp-dsDNA-fragment. The two central DBDs show a putative in-vivo-binding state. B) Dimer of DasR-EBD with each monomer in complex with the putative effector molecule Glucosamine-6-phosphate.

References:

1. M. Resch, E. Schiltz, F. Titgemeyer, Y. A. Muller, *Nucleic Acids Res.* 38, (2010), 2485-2497.
2. R. Bertram, S. Rigali, N. Wood, A. T. Lulko, O. P. Kuipers, F. Titgemeyer, *J Bacteriol.* 193(14), (2011), 3525-3536.
3. S. Rigali, H. Nothhaft, E.E.E. Noens, M. Schlicht, S. Colson, M.

Müller, B. Joris, H. K. Koerten, D. A. Hopwood, F. Titgemeyer, G. P. van Wezel, *Mol Microbiol*, 61(5), (2006), 1237-1251
 4. S. Colson, G. P. van Wezel, M. Craig, E. E. E. Noens, H. Nothaft, M. Mommaas, F. Titgemeyer, B. Joris, S. Rigali, *Microbiology*, 154, (2011), 373-382.

MS09-T06

Structure and Mechanism of Human DNA Polymerase η

C. Biertümpfel^{1,2}, Y. Zhao², Y. Kondo³, S. Ramón-Maiques², M. Gregory², J.Y. Lee², C. Masutani³, A.R. Lehmann⁴, F. Hanaoka³, W. Yang²
¹MPI of Biochemistry, Structural Cell Biology/DNA Repair, Martinsried, Germany

²NIDDK, National Institutes of Health, Laboratory of Molecular Biology, Bethesda, MD, USA, United States

³Graduate School of Frontier Biosciences, Osaka University, Osaka, Japan, Japan

⁴University of Sussex, Genome Damage and Stability Centre, Brighton, UK, United Kingdom

The variant form of human xeroderma pigmentosum syndrome (XPV) is caused by a deficiency in DNA polymerase η (Pol η), a DNA polymerase that enables replication through ultraviolet-induced pyrimidine dimers. Here we report high-resolution crystal structures of human Pol η at four consecutive steps during DNA synthesis through cis-syn cyclobutane thymine dimers (CPDs). Pol η acts like a ‘molecular splint’ to stabilize damaged DNA in a normal B-form conformation. An enlarged active site accommodates the thymine dimer with excellent stereochemistry for two-metal ion catalysis. Two residues conserved among Pol η orthologues form specific hydrogen bonds with the lesion and the incoming nucleotide to assist translesion synthesis. On the basis of the structures, eight Pol η missense mutations causing XPV can be rationalized as undermining the molecular splint or perturbing the active-site alignment. The structures also provide an insight into the role of Pol η in replicating through D loop and DNA fragile sites.

MS10-T01

Crystal structure and magnetic ordering in the metal(III)oxyhalide CrOCl at low temperatures

A. Schönleber¹, J. Angelkort¹, J. Zhang¹, S. van Smaalen¹, R.K. Kremer², A. Senyshyn³

¹University of Bayreuth, Laboratory of Crystallography, Bayreuth, Germany

²MPI for Solid State Research, Stuttgart, Germany

³Forschungs-Neutronenquelle Heinz Maier-Leibnitz, FRM-II, Garching, Germany

The metal(III) oxyhalide *MOX* compounds with $M = \text{Ti, V, Cr}$ and $X = \text{Cl, Br}$ are isostructural with FeOCl at room temperature [1-3]. Their crystal structures are built by slabs consisting of M_2O_2 bilayers enclosed by layers of X atoms, with van der Waals type interaction between the slabs. The symmetry is orthorhombic, space group *Pmmn*. However, at low temperatures the *MOX* compounds exhibit different magnetic order [4,5]. In CrOCl one phase transition was observed towards antiferromagnetic ordering [4].

We have performed single-crystal X-ray diffraction experiments at low-temperatures at the synchrotron HASYLAB/DESY (Hamburg, Germany) to explore the nuclear structure and the development of nuclear superstructure peaks ($h, k+\frac{1}{2}, l$) below $T_N = 13.5$ K. The phase transition at T_N is associated upon cooling with a loss of symmetry from orthorhombic towards monoclinic [6]. Further on we found by magnetic susceptibility measurements evidence for a second phase transition at $T_{c2} = 27.8$ K [6].

Our low temperature powder neutron diffraction experiments at the neutron reactor FRM-II (Garching, Germany) indicate the low temperature phase below T_N as a monoclinic fourfold magnetic superstructure ($\mathbf{a} \times 4\mathbf{b} \times \mathbf{c}$) with respect to the room temperature phase, which can be described in the extended magnetic superspace

group symmetry $P2_1/m1'(0\sigma_2\sigma_3)0ss$ (monoclinic, \mathbf{a} -unique). The intermediate phase ($T_N \leq T \leq T_{c2}$) is understood as an incommensurately modulated magnetic superstructure, the extended magnetic superspace group symmetry $Pmmm1'(0\sigma_2)0s0ss$ (orthorhombic) is applied in the Rietveld refinements. The additional symmetry operator ($1', s$) in the extended symbol stands for the time inversion operator combined with an additional shift of $\frac{1}{2}$ of the modulation function to describe antiferromagnetic order [7].

[1] Schäfer & Wartenpfehl, *Z. Anorg. Allg. Chemie* **308** (1961) 282-289.

[2] Goldsztaub, *C. R. Hebd. Seances Acad. Sci.* **198** (1934) 667-669.

[3] Lind, *Acta Crystallogr.* **B26** (1970) 1058-1062.

[4] Nørlund Christensen et al., *Acta Chem. Scand. A* **28** (1975) 1171-1174.

[5] Adam & Buisson, *Phys. Stat. Sol.* **A 30** (1975) 323-329.

[6] Angelkort et al., *Phys. Rev. B* **80** (2009) 144416.

[7] Petricek et al., *Acta Crystallogr.* **A66** (2010) 649-655.

MS10-T02

Temperature dependence of cation distribution in $(\text{Co}_x\text{Mg}_{1-x})_2\text{SiO}_4$ olivines

J. Shi¹, B. Pedersen², S. Ganschow³, K.-D. Becker¹

¹Technische Universität Braunschweig, Institut für Physikalische und Theoretische Chemie, Braunschweig, Germany

²Forschungs-neutronenquelle, Heinz Maier-Leibnitz (FRMII), München, Germany

³Leibniz-Institut für Kristallzüchtung, Berlin, Germany

The olivine structure has recently drawn great attention because materials of this structure are widely used as electrodes in lithium ion batteries. Understanding the crystal structure variations in response to the external parameters, such as temperature, gas atmosphere, pressure and electrical field provides information at atomic scale with regard to reactivity, ionic transport, and stability of the materials.

In the $(\text{Co}_x\text{Mg}_{1-x})_2\text{SiO}_4$ olivines, divalent cations occupy the two non-equivalent octahedral sites, M1 and M2. Upon a change in external parameters, e.g., temperature, the re-equilibrium of cation distribution is attained through a cation site exchange reaction, $\text{Co}_{\text{M2}} + \text{Mg}_{\text{M1}} = \text{Co}_{\text{M1}} + \text{Mg}_{\text{M2}}$, which is characterized by a cation distribution coefficient, $K_D = [\text{Co}_{\text{M1}}][\text{Mg}_{\text{M2}}]/[\text{Co}_{\text{M2}}][\text{Mg}_{\text{M1}}]$. In this presentation, we report on the temperature dependence of the cation distribution obtained from in-situ neutron diffraction experiments. Neutron diffraction data on the single crystal sample with $x = 0.64$ from room temperature up to 1473 K were collected using a 1.5 Å q-resolution at FRM II. Cation distributions from structure refinements show a substantial temperature dependence and are in agreement with our optical kinetic investigations. The crystal chemistry, thermodynamics and kinetics of cation site exchange reaction will be discussed based on the combined knowledge on the cation distribution at high temperatures in olivines from neutron diffraction and from optical spectroscopy.

MS10-T03

Structure-property relationships in silicates: Elasticity of natural beryl

C.S. Pandey¹, J. Schreuer¹

¹Ruhr University Bochum, Institute for Geology Mineralogy and Geophysics, Bochum, Germany

The crystal structure of hexagonal beryl, $\text{Be}_3\text{Al}_2\text{Si}_6\text{O}_{18}$, consists of six-membered rings of SiO_4 tetrahedra parallel to (001) which are cross-linked by BeO_4 tetrahedra and AlO_6 octahedra to form a framework with open channels parallel to the c-axis. These channels consist of cavities with ~ 5.1 Å in diameter separated by ‘‘bottlenecks’’ of ~ 2.8 Å in diameter. In principle up to 1 molecule

H₂O per formula unit can be present in the cavities. In natural beryls certain amounts of Al in octahedral and Be in tetrahedral sites are usually substituted by Li⁺ and/or divalent cations. Both substitutions require the entry of alkali ions in the channels for charge compensation, which affects the arrangement of the water molecules. In respect to the main type of substitution “octahedral”, “tetrahedral” and “normal” beryls with characteristic/a ratios can be distinguished [1].

In order to detect correlations between chemical composition, crystal structure and elastic properties of beryls we determined the coefficients of thermal expansion and the elastic stiffnesses of 3 natural goshenite single crystals from Brazil between about 100 K and 1083 K employing dilatometry and resonant ultrasound spectroscopy, respectively. The crystals were further characterized by means of electron microprobe analysis, infrared spectroscopy and X-ray diffraction techniques. Our elastic constants fit well to literature values obtained on aquamarines [2,3].

The elastic anisotropy of beryl is closely related to specific structural features. Moreover, the mean elastic stiffness clearly depends on the dominant type of substitution. This behavior can be interpreted in terms of elastic S-values using the quasi-additivity rule proposed by Haussühl [4]. Within experimental error no influence of the water on the elastic properties at room temperature could be detected. However, the pronounced non-linear softening of the shear resistances c_{44} and c_{66} above room temperature might be related to the increasing thermal motion of H₂O. Our experimental volume thermal expansion agrees reasonably with the results of recent ab initio calculations [5].

[1] C. Aurisicchio, G.Fioravanti, O. Grubessi, P. F. Zanazzi, *Am. Min.* 73(1988) 826-827.

[2] S. Haussühl, *Z. Kristallogr.* 204(1993) 67-76.

[3] H. S. Yoon, R. E. Newnham, *Acta Crystallogr.* A29(1973) 507-509

[4] S. Haussühl, *Z. Kristallogr.* 205(1993) 215-234.

[5] M. Prencipe, I. Scanavino, F. Nestola, M. Merlini, B. Civalleri, M. Bruno, R. Dovesi, *Phys. Chem. Minerals* 38 (2011) 223-239.

MS10-T04

Atomic scale description of the Macroscopic Piezo-Ferroelectric properties of high performance Lead Zirconate Titanate (PZT)

M. Hinterstein¹, J. Rouquette², M. Hoelzel³, H. Kungl⁴, M. Knapp⁵, H. Ehrenberg⁵

¹Technische Universität Dresden, Institut für Werkstoffwissenschaft, Dresden, Germany

²Université Montpellier II, Institut Charles Gerhardt, Montpellier, France

³Technische Universität München, FRM II, München, Germany

⁴Karlsruher Institut für Technologie, Institut für Angewandte Materialien - Keramik im Maschinenbau, Karlsruhe, Germany

⁵Karlsruher Institut für Technologie, Institut für Angewandte Materialien - Energiespeichersysteme, Karlsruhe, Germany

Materials science can be defined as an interdisciplinary field involving the properties of matter and its applications. This scientific field investigates the relationship between the structure of materials and their macroscopic properties. In this framework their situatomic-scale structural description of the origin of the ferroelectric properties as a function of the applied electric field, corresponds to a perfect example of such a goal.

In this contribution, an appropriate set up was used to minimize the effects of preferred orientation and solvoin situ the crystal structure as a function of the applied electric field [1]. Hence, we were able to describe the microscopic origin of the macroscopic physical properties of a commercial ferroelectric material, lead zirconate titanate (PZT), which is intensively used for technological applications (sensors and actuators). Therefore, it is possible in our case to directly correlate structural and physical ferroelectric properties as a function of the electric field and thus elucidate the structural origin of such properties.

With careful analysis of different sample orientations a new poling mechanism could be identified. Especially for the investigation of fatigue this new poling mechanism plays a crucial role. We were able to correlate a degradation of this process with the reduction of macroscopic strain during fatigue.

Using state of the art detectors time resolved pump-probe experiments can be conducted for studying the microstructure under real working conditions. With the detector coupled to the periodically alternating electric field at 50 Hz time resolutions in the order of submilliseconds could be achieved for complete diffraction patterns with high statistics. All results will be discussed by means of diffraction data from the Materials Science X-ray beamline at the Swiss Light Source with the MYTHEN II detector and the high flux and high resolution neutron beamline D20 at the Institute Laue-Lauevin.

[1] M. Hinterstein, J. Rouquette, J. Haines, Ph. Papet, M. Knapp, J. Glaum, and H. Fuess, *Phys. Rev. Lett.* 107, 077602 (2011).

MS10-T05

Observation of a low-symmetry phase in Na_{0.5}Bi_{0.5}TiO₃ by high resolution X-ray diffraction and optical birefringence microscopy

S. Gorfman¹, M. Glazer², Y. Noguchi³, H. Luo⁴, P. Thomas⁵

¹University of Siegen, Department of Physics, Siegen, Germany, Germany

²University of Oxford, Department of Physics, Oxford, UK, United Kingdom

³University of Tokyo, Tokyo, Japan, Japan

⁴Shanghai Institute of Ceramics, Shanghai, China, China

⁵University of Warwick, Department of Physics, Coventry, UK, United Kingdom

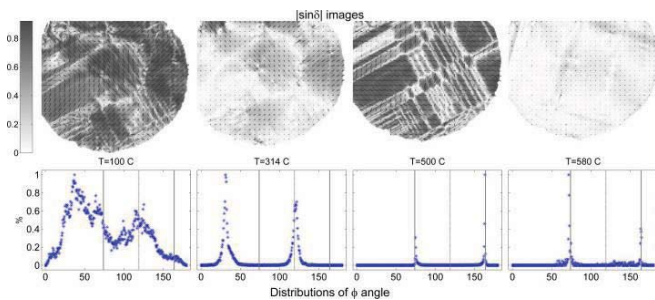
Na_{0.5}Bi_{0.5}TiO₃ (NBT) is a perovskite-based ferroelectric that is currently attracting considerable interest as a potential lead-free piezoelectric material. NBT is unusual in showing two temperature induced phase transformations (see for example [1]), phase coexistence, hierarchical domain systems, strong and anisotropic diffuse scattering, and an ability to form a morphotropic phase boundary (MPB) in solid solutions with other perovskite-based structures. This rich combination of properties means that NBT is not only a potential replacement for lead-based piezoelectric materials but also an extremely interesting model system for fundamental crystallography / physics of perovskites and can be studied on its own right. There is a significant amount of X-ray, neutron diffraction and electron microscopy already published and yet considerable disagreement remains concerning the crystal structure and nature of the NBT phases.

The aim of this work was to obtain the most precise up to date information about symmetry of a single ferroelectric domain of NBT and reinforce investigation of its temperature dependence. Determination of a true symmetry (crystal class) is mandatory as symmetry plays important role in physical properties of a single domain and a type of a ferroelectric (ferroelastic) domain patterning. To resolve the present controversies about the symmetry of NBT we have undertaken high-resolution reciprocal space mapping of selected Bragg peaks allowing observing fine Bragg peak splitting due to different twin domains [2]. The analysis of separation of X-ray beams diffracted by different ferroelastic domains suggested that the symmetry of a room temperature NBT must be monoclinic and not rhombohedral as it was commonly accepted before.

Above high-resolution X-ray diffraction studies of NBT were complemented by multi-temperature optical birefringence microscopy [3] that is also a sensitive probe of a single domain symmetry and a domain structure. The birefringence studies confirmed that the symmetry of NBT below 300 °C is lower than

rhombohedral. The most interesting result of this work is that in some case rotation of a polar direction within a monoclinic plane (as allowed in crystal of monoclinic symmetry) were directly observed. The peculiar temperature induced transformations of symmetry and domain patterns as visible by birefringence microscopy will be discussed in the talk.

- [1] Jones, G. O. & Thomas, P. A. (2002). *Acta Cryst.* B58, 168-178
 [2] Gorfman, S. & Thomas, P. A. (2010). *J. Appl. Cryst.* 43(6), 1409-1414.
 [3] Gorfman, S., Glazer A.M., Noguchi, Y., Myayayma, Luo, H., Thomas, P. J. *Appl. Cryst.* (submitted)



Selected images showing combined maps of optical anisotropy and orientation of the optical indicatrix of investigated NBT single crystal. The bottom graphs display normalized distributions (histograms) of the observed orientations of optical indicatrix (see the talk and [3] for more details).

MS10-T06

Influence of electric field on temperature-induced local phase transformations in relaxor ferroelectrics studied by polarized Raman spectroscopy

B. Maier¹, T. Steilmann¹, B. Mihailova¹, M. Gospodinov², U. Bismayer¹
¹Universität Hamburg, Department Geowissenschaften, Hamburg, Germany
²Bulgarian Academy of Sciences, Institute of Solid State Physics, Sofia, Bulgaria

Relaxor ferroelectrics great interest to the scientific community due to their outstanding dielectric, electroelastic and electrooptic properties which are related to their complex local structure comprising the formation and development of dynamic polar nanoregions (PNR) with temperature decrease. There are three important characteristic temperatures associated with PNR: (i) the Burns temperature T_B at which the PNR are formed; (ii) T^* , at which the PNR couple into larger polar clusters with slower dynamics; (iii) the freezing temperature T_f at which the PNR become static or the Curie temperature T_C at which some relaxors exhibit a phase transition to a normal ferroelectric state.

Recently, the model relaxor compounds lead scandium tantalate (PST) and Ba-doped PST have been studied by acoustic emission as a function of temperature under electric field [1]. A shift of T^* and T_C to higher temperatures with increasing electric field has been observed.

In this study we applied polarized Raman spectroscopy as a function of temperature under electric field along the cubic [100], [110], and [111] directions on PST, PST-Ba, and on lead scandium niobate (PSN) in order to study the field-induced changes of the local phase transformations in terms of Pb- and B-site cations by hard-mode analysis. We show that the field-induced shift to higher temperatures is much more pronounced if the electric field is applied along the cubic [111] direction, revealing that the preferred direction of polar shifts in PNRs is along the cubic body diagonal, which implies a rhombohedral configuration of the polar species. In addition, the field dependence of T^* as deduced from the coupling of B-site cations saturates above a certain threshold field. This underlines the importance of Pb-cations for the coupling

processes of PNRs which is revealed by hard-mode analysis of the Pb-dependent modes.

- [1] E. Dul'kin et al., *Europhys. Lett.* 94, 57002 (2011)

MS11-T01

Unravelling the Local ~8 Å Structure of Al-Cu-Co Quasicrystals by the use of Three-Dimensional Pair Distribution Function Analysis

P. Schaub^{1,2}, T. Weber², W. Steurer²
¹Paul Scherrer Institute, Laboratory for Waste Management, Villigen, Switzerland
²ETH Zürich, Laboratory of Crystallography, Zürich, Switzerland

Structural disorder is naturally present in many crystals. To date, there is still need for applicable and straightforward single-crystal methods to analyse the local structure of disordered crystals. The novel methods *three-dimensional (3D) Pair Distribution Function (PDF) analysis* and, in particular, *three-dimensional ΔPDF (3D-ΔPDF) analysis* [1, 2] are presented in this study. 3D-PDF techniques allow to investigate short- and medium-range disorder phenomena. In analogy to traditional Patterson function analysis, advantage is taken from the Fourier transformation either of the full 3D diffraction pattern of a disordered crystal (3D-PDF), or just of the isolated diffuse scattering (3D-ΔPDF), respectively. Based on 3D interatomic pair correlations, this approach is straightforward and illustrative, because 3D-PDFs can be directly linked with the real atomic crystal structure. Thus, it becomes possible to investigate far more complicated structures than is feasible with well-established powder diffraction based PDF analysis. Further, in contrast to state-of-the-art single-crystal methods used for characterisation and modelling of 3D disorder, which are based on diffuse scattering intensities in reciprocal space, the 3D-ΔPDF approach provides direct access to disorder models in real space and allows selective modelling of distinct structural features, which are, in contrast to reciprocal space, well localised in PDF space. Principles and application of the 3D-ΔPDF method are demonstrated on the analysis of the twofold (~8 Å) periodic superstructure of a decagonal Al-Cu-Co quasicrystal [2]. A structural model of disorder for this superstructure is presented. The superstructure was found to be built from columnar units, having a maximum diameter of ~14.5 Å. The lateral correlation between these columns is weak. Internally, the columns consist of a long-range ordered alternation of flat and puckered layers. The differential evolution method was used for model optimisation. The obtained model of disorder is solely based on geometrical assumptions derived from the 3D-ΔPDF, without using any constraints on chemical or physical structural properties.

- [1] Schaub Ph., Weber Th., Steurer W., *Phil Mag* 87 (18-21), p. 2871 (2007)
 [2] Schaub Ph., Weber Th., Steurer W., *J Appl Cryst* 44 (1), p. 134 (2011)

MS11-T02

Standard and non-standard settings of superspace groups

S. van Smaalen¹, H.T. Stokes², B.J. Campbell²
¹University of Bayreuth, Lehrstuhl für Kristallographie, Bayreuth, Germany
²Brigham Young University, Department of Physics and Astronomy, Provo, Utah, United States

Tables of (3+d)-dimensional superspace groups have recently been generated by us for $d = 1, 2, 3$ [1]. The table for $d = 1$ is in agreement with previous tabulations of (3+1)-dimensional superspace groups [2], but the tables for $d = 2$ and 3 contain numerous corrections to previous information. The tables are available as the online data repository SSG(3+d)D at <http://stokes.byu.edu/ssg.html> [3]. Part of SSG(3+d)D is a utility,

'findssg,' which returns the standard setting of a superspace group for any user-given superspace group, along with the transformation between the two settings.

The standard setting of a superspace group can be directly obtained by an appropriate transformation of the external-space lattice vectors (the basic-structure unit cell) and a transformation of the internal-space lattice vectors (new modulation wave vectors are linear combinations of old modulation wave vectors plus a 3D reciprocal lattice vector). Here we discuss the need for non-standard settings in some cases and the desirability of employing standard settings of superspace groups in other cases [4]. These features are illustrated by the analysis of the symmetries of a series of compounds, comparing published and standard settings and the transformations between them. A compilation is provided of standard settings of superspace groups of compounds with two- and three-dimensional modulations. The problem of settings of superspace groups is discussed for incommensurate composite crystals and for chiral superspace groups.

[1] Stokes, H.T., Campbell, B.J. & van Smaalen, S., *Acta Crystallogr. A* **67**, 45-55 (2011).

[2] van Smaalen S.: *Incommensurate Crystallography* (Oxford University Press, Oxford, 2007).

[3] Stokes, H.T., Campbell, B.J. and van Smaalen, S., SSG(3+d)D at <http://stokes.byu.edu/ssg.html>. (2011). Provo, Utah, USA: Brigham Young University.

[4] van Smaalen, S., Stokes, H.T., Campbell, B.J., in preparation (2011).

MS11-T03

CuTe - A Modulated Structure and its Electronic Origin

K. Stolze¹, A. Isaeva¹, F. Nitsche¹, T. Doert¹

¹TU Dresden, Anorganische Chemie, Dresden, Germany

CuTe, also known as the mineral Vulcanite, can be described as a strongly distorted *a*-PbO structure of corrugated copper layers alternating with linear, equidistant telluride chains along [001] (figure, left). According to theoretical considerations, these telluride chains could undergo a Peierls-like distortion resulting in alternating shorter (bonding) and longer (non- or anti-bonding) distances [1]. However, no distortion was found experimentally [2].

In the current work gold-coloured, metallic lustrous CuTe crystals were grown under solvothermal conditions from the elements in ethylenediamine at 200° C. EDX and WDX analysis confirm the composition of the crystals.

The diffraction images of the crystals show weak satellites beneath the main reflections of an orthorhombic cell. A model for the modulated structure has been developed in superspace group $Pmmm(\alpha 0\frac{1}{2})000$ with unit cell parameters $a = 3.151(1)$ Å, $b = 4.089(1)$ Å, $c = 6.950(1)$ Å and a modulation wave vector $\mathbf{q} = (\alpha 0\frac{1}{2})$ with $\alpha = 0.40(1)$ using the superspace approach [3] and the JANA2006 software package [4]. The modulation primarily influences the Te-Te distances along the Te chains. As a result, units of two or three tellurium atoms with slightly shorter distances along [100] alternate with single tellurium atoms in this direction (figure, right). The modulation of the Te position forces a distortion of the corrugated Cu layers leading to a slight deflection of the Cu atoms along [001].

Analysis of the bonding scenario in modulated CuTe by quantum chemical calculations [5] revealed that the structural distortion can be understood as a result of a competition for electrons among copper and tellurium. Electronic balance is attained via the formation of Te₂ and Te₃ units together with increased Cu-Cu interactions.

[1] S. Seong, T. A. Albright, X. Zhang, M. Kanatzidis, *J. Am. Chem. Soc.* **1994**, *116*, 7287.

[2] F. Pertlik, *Miner. Petrol.* **2001**, *71*, 14.

[3] A. Janner, T. Janssen, *Phys. Rev. B*, **1977**, *15*, 643; S. van Smaalen, *Incommensurate Crystallography*, Oxford University Press, 2007.

[4] Jana2006, The Crystallographic Computing System, V. Petricek, M. Dusek, L. Palatinus, Prag, 2011.

[5] ELK, All-electron full-potential linearised augmented-plane wave code, (<http://elk.sourceforge.net>); J.P. Perdew, Y. Wang, *Phys. Rev.* **1992**, *B 45*, 13244.

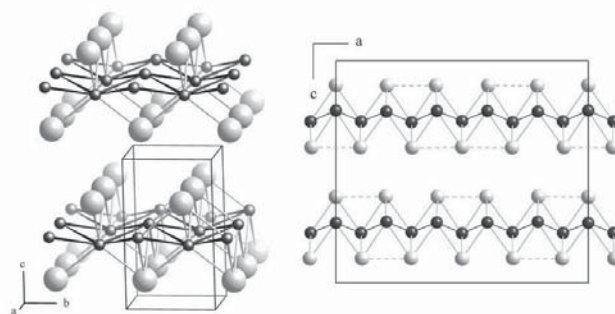


Figure Caption:

Average structure of CuTe, Cu atoms black, Te atoms grey (left); 5×2 approximant of CuTe, slightly shorter Te-Te distances along a shown in dashed lines (right).

MS11-T04

Incommensurately modulated structure of nepheline

K. Friese¹, A. Grzechnik¹, V. Petricek², A. Schönleber³, S. van Smaalen³, W. Morgenroth^{3,4}

¹University of the Basque Country, Condensed Matter Physics, Bilbao, Spain

²Academy of Science, Institute of Physics, Praha, Czech Republic

³University of Bayreuth, Laboratory of Crystallography, Bayreuth, Germany

⁴University of Frankfurt, Institute for Geoscience, Section Crystallography, Frankfurt, Germany

Nepheline, a feldspathoid and an important rock forming mineral, has been known to form an incommensurately modulated structure since satellite reflections were first observed in a sample from Finland more than 50 years ago [1]. We have now determined the incommensurately modulated structure of a nepheline of composition $K_{0.54}Na_{3.24}Ca_{0.03}Al_{3.84}Si_{4.16}O_{16}$ from Tambani, Nyasaland-Malawi [2].

The average structure of nepheline has first been described by Hahn & Buerger (space group $P6_3$, $a \approx 10$ Å, $c \approx 8.36$ Å; [3]). It is characterized by a framework of edge connected (Al,Si)O₄ tetrahedra and can be considered as a stuffed derivative of tridymite. Two different types of channels formed by six-membered rings of tetrahedra can be distinguished: the smaller, oval ones are fully occupied by Na⁺ ions, while the larger ditrigonal ones are predominantly occupied by K⁺. In the sample studied here the occupation is 0.54 K⁺ + 0.24 Na⁺ + 0.03 Ca²⁺ + 0.19v (vacancies).

We performed single crystal X-ray diffraction experiments at beamline D3 of the Hasylab/DESY ($\lambda=0.400$ Å). The data were integrated with the program EVAL15 [4] and the structure was refined with Jana2006 [5]. The (3+1)-dimensional description is based on a unit cell with $a=b=17.2889(8)$ Å, $c=8.3622(10)$ Å and $\gamma=120^\circ$. The superspace group is $X3(0,0,\gamma)$, with $X=(0,0,0; 1/3,2/3,0,2/3; 2/3,1/3,0,1/3)$ and the modulation wave vector is $q=0.2048$ c* (Superspace group No. 143.1.23.1, ref. [6]). This centered setting was chosen to avoid rational components of the q-vector. A mirror plane perpendicular to [001] had to be taken into account as additional twinning operation.

All atoms in the structure are displacively modulated with amplitudes below 0.1 Å. The modulation can be well described

taking into account harmonics of first order only. Atomic positions in the smaller channel are fully occupied by Na^+ . Cationic positions in the larger channel are occupationally modulated, yet the variation of the electron density as a function of the phase of the modulation is small and indicates that the incorporation of the different types of cations (K^+ , Na^+ , Ca^{2+}) and vacancies is realized in a highly disordered manner. The average distances in the tetrahedra indicate that the Al/Si distribution is highly ordered. A large part of the oxygen atoms of the framework is approximated by split atom positions, which are additionally affected by occupationally modulation resulting in a high degree of disorder. Occupational modulations of the cations in the larger channel and the O-atoms of the tetrahedral framework are coupled and correlations between occupational and displacive modulations exist.

[1] Sahama T. G., *Am. Mineral.* 43, 165, 1958.
 [2] Friese, K., Grzechnik, A., Petricek, V., Schönleber, A., van Smaalen, S. Morgenroth, W., *Acta Crystallogr.* B67, 18-29, 2011.
 [3] Hahn T., Buerger M. J., *Z. Anorg. Allg. Chem.* 106, 308-338, 1955.
 [4] Schreurs A. M. M., Xian X., Kroon-Batenburg L. M. J., *J. Appl. Crystallogr.* 43, 70-82, 2010.
 [5] Petricek, V., Dusek, M., Palatinus, L., JANA2006, Institute of Physics, Praha, Czech Republic, 2006.
 [6] Stokes, H. T., Campbell, B. J., van Smaalen, S., *Acta Crystallogr.* A67, 45-55, 2011.

MS11-T05

From transition kinetics to lock-in mechanisms: Manipulating incommensurately modulated structures in Rb-doped K_2ZnCl_4

K. Behrendt¹, H. Gibhardt¹, J. Leist¹, G. Eckold¹
¹Georg-August-Universität, Institut für physikalische Chemie, Göttingen, Germany

Crystals of the A_2BX_4 -family exhibit incommensurably modulated phases as well as low temperature ferroelectric phases. Close to the lock-in transition, the modulation waveform changes from sinusoidal to square-like. The structure can therefore be described as an ordered sequence of commensurate nanodomains of alternating polarization [1]. The discommensuration density decreases on cooling via the nucleation of topological defects, known as anti-stripples. This motion of domain walls and hence the transition into the ferroelectric phase is strongly influenced by lattice defects like impurities. As a consequence the thermal hysteresis is enhanced by chemical doping [2]. Moreover the transition kinetics is expected to slow down drastically by the pinning of domain walls at structural imperfections [3].

In order to study this effect systematically, a series of high-quality K_2ZnCl_4 single crystals doped with different amounts of Rb (from 0.4 % to 8 %) was grown from aqueous solution. High-resolution γ -ray diffraction was used to study the temperature-dependent variation of satellite reflections (from 1st to 5th order) characterizing the modulated structure. Complementary information about the dielectric properties, reflecting domain behaviour, was obtained by in-situ impedance spectroscopy.

It is found that at a dopant concentration of 0.4 % the transition into the commensurate phase already takes several hours. Further doping results in a pronounced temperature dependence of the transition time with a minimum value well below the actual transition temperature. In a sample with 8 % Rb transition kinetics becomes extremely sluggish and proceeds on a timescale of weeks. At room temperature the incommensurate phase remains metastable over months. An attempt has been made to extrapolate the equilibrium phase diagram which differs considerably from earlier Literature data [2]. The transition progress, however, is qualitatively comparable to that in a sample of pure, but strained Rb_2ZnCl_4 [4]. Additionally, the distortion of the modulation shape, as reflected by the intensities of higher-order satellites, varies significantly with dopant concentration.

We demonstrated that Rb-impurities are very efficient to hinder the nucleation of anti-stripples and the motion of domain walls in K_2ZnCl_4 . Those structural defects therefore affect predominantly the transition kinetics. By quenching such systems from different starting temperatures, the shape of the modulated structure and thus the domain pattern can be deliberately modified. It is particularly possible to stabilize polar nanodomains at ambient conditions.

[1] J. Leist et al, *J. Phys.: Condens. Matter* 20 (2008) 415209.
 [2] K. Hamano et al, *Ferroelectrics* 36 (1981) 343.
 [3] H. Mashiyama et al, *J Phys. Soc. Jpn.* 56 (1987) 3347.
 [4] A. Gibaud et al, *J. Phys.: Condens. Matter* 3 (1991) 4817.

MS11-T06

Phase transitional and critical phenomena in crystallographic superspace

L. Guerin¹, C. Mariette¹, P. Rabiller¹, B. Toudic¹
¹Institut de Physique de Rennes, Ille t Vilaine, Rennes, France

Much work has been in the past dedicated to the study of phase transitions in aperiodic crystals. The simplest cases concerned the structural instability leading to modulated incommensurate phase. There, the high symmetry phase is periodic, the phase transitions are usually continuous and a Landau-type approach was successfully applied to describe both the symmetry lowering and the associated critical phenomena [1].

Here, we will consider materials which are aperiodic by construction, which means that even their high symmetry phase requires a crystallographic superspace description. A prototype example is given by aperiodic host-guest composites, focussing here on n-nonadecane/urea. This compound shows a group/subgroup phase transition from a four dimensional superpace group towards a five dimensional evidenced by the appearance of satellites with a new periodicity ([2,3] and figure left). The static aspect of the pretransitional fluctuations of the order parameter is studied around the transition temperature, using high resolution X-ray diffraction technique coupled with 3D reconstructions. Quite specific observations are reported. Correlation lengths along the internal direction of the crystallographic superspace show a peculiar behaviour in temperature compare to the correlation lengths observed in the perpendicular commensurate plane. In particular, very long correlation lengths persist in the high symmetry phase, even far above the transition temperature.

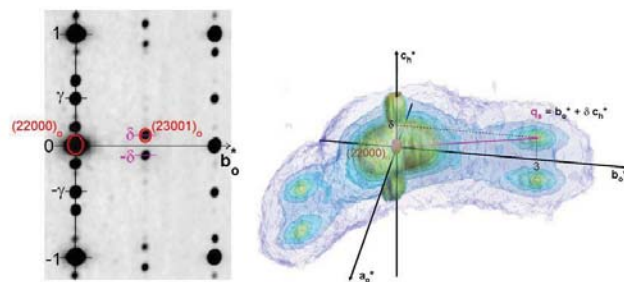


figure legend : left: 4D to 5D group/subgroup phase transition in n-nonadecane/urea [2,3]. right: Pretransitional diffuse scattering associated to the transition.

MS12-T01

The Role of Metric Parameters in the Interpretation of Order/Disorder (O/D) StructuresB. Stöger¹¹TU Wien, Institut für Chemische Technologien und Analytik, Abt. für Strukturchemie, Vienna, Austria

Order-disorder (OD) theory was conceived in the 1950ies[1] to explain unusual X-ray diffraction effects in minerals like wollastonite[2]. Since then, it has been developed into a versatile theory for the explanation of polytypism, diffuse scattering, non-crystallographic extinctions, twinning and as a means to classify structures by symmetry principles. It has been applied to all major classes of compounds from minerals to biological macromolecules[3,4].

OD theory is based on the geometric (and in consequence energetic) equivalence of pairs of adjacent layers. Besides lattice parameters and layer thickness, for each kind of layer contact up to two metric parameters are introduced. They describe the origin shift of adjacent layers projected on the layer plane. So far the role of these parameters in OD interpretation has not been closely investigated.

The parameters not only vary among different OD-structures, but are also affected by desymmetrization: Different polytypes of the same system may feature (slightly) different parameters and a complex polytype may even exhibit different parameters for the same kind of layer contact. The value of the parameters may be fixed to a discrete value for crystal-chemical reasons. If not, they are derived from lattice parameters or computed from atomic positions.

It is useful to distinguish characteristics of a family of OD structures which are independent of the metric parameters (e.g. the category, the associated point group) and those which depend on them (e.g. the subcategory, stacking possibilities, polytypes with a maximum degree of order, family structure, superposition group). These dependencies will be illustrated with real world examples.

[1] Dornberger-Schiff K. (1956). On Order-Disorder Structures (OD-Structures). *Acta Crystallogr.* 9, 593-601.

[2] Jeffery J. W. (1953). Unusual X-ray Diffraction Effects from a Crystal of Wollastonite. *Acta Crystallogr.* 6, 821-825.

[3] Rye C. A., Isupov M. N., Lebedev A. A. & Littlechild J. A. (2007). An order-disorder twin crystal of L-2-haloacid dehalogenase from *Sulfolobus tokodaii*. *Acta Crystallogr.* D63, 926-930.

[4] Pletnev S., Morozova K. S., Verkhusha V. V. & Dauter Z. (2009). Rotational order-disorder structure of fluorescent protein FP480. *Acta Crystallogr.* D65, 906-912.

MS12-T02

Optimising the Debye Scattering Equation for use with polycrystalline materialsN. Thomas¹¹Fachhochschule Koblenz, Werkstofftechnik Glas Keramik, Höhr-Grenzhausen, Germany

Although the Debye Scattering Equation (DSE) has been known since 1915, its use in connection with X-ray and neutron diffraction from conventional powders has been limited because of the heavy computational overhead.

Significant improvements in computational efficiency for crystalline systems can be obtained by treating the pairwise atomic interactions within a crystal as sums of lattice (LV) and Patterson vectors (PV). Since the frequencies of occurrence of both types of vectors are known for a crystallite of given habit and crystal structure, the interatomic distance associated with a particular combination of lattice and Patterson vector needs to be calculated just once, instead of many times, as in conventional algorithms.[1] Further efficiency-gains may be brought about by exploiting crystal symmetry, in order to ascertain which combinations of lattice and

Patterson vectors are equivalent. Moreover, a recasting of the histograms of interatomic distances as compound slit functions allows standard FFT algorithms for real functions to be used. As a consequence, the intrinsic Bragg reflection profiles arising from crystallites of dimension up to ca. 0.4 µm can now be calculated in reasonable times on a conventional PC.[2] The observed sharpness of the calculated Bragg reflections suggests that an explicit calculation for larger crystallites is unnecessary.

The flexibility of the LV-PV approach in modelling crystalline systems with planar disorder is demonstrated by reference to two clay minerals, kaolinite and montmorillonite. The capability of modelling intrinsic reflection profiles for nanocrystals is also shown.

Further progress in developing the method requires the inclusion of instrumental (diffractometer) parameters in determining the observed peak shapes. A vision is also given of the potential use of the method for structural refinements from powder diffraction data.

[1]N.W. Thomas, *Acta Crystallogr.* A66, 64-77 (2010)

[2]N.W. Thomas, *Acta Crystallogr.* A67, 491-506 (2011)

MS12-T03

Rigid bodies and symmetry modes - a great combinationM. Müller^{1,2}, B. Campbell³, R.E. Dinnebier¹¹Max Planck Institute for Solid State Research, Stuttgart, Germany²University of Trento, Department of Materials Engineering and Industrial Technologies, Trento, Germany³Brigham Young University, Department of Physics & Astronomy, Provo, United States

Symmetry modes provide an alternative way to parameterize the structural changes that occur when partial symmetry loss occurs at a phase transition. Such modes are order parameters of the irreducible representations of the parent space-group symmetry, and have recently been employed in the determination and direct refinement of displacive superstructures [1]. Compared to a traditional description based on the coordinates of individual atoms, the symmetry-mode basis has the advantage that nature tends to activate a relatively small fraction of the modes available to a given distortion, so that structural complexity is effectively reduced. The rigid-body motions encountered in molecular crystals and polyhedral inorganics can be treated strictly in terms of atomic displacements, and therefore can be described using symmetry modes. However, each because each atom in the rigid body will typically possess the same symmetry modes, which must then be tied together in an unnatural fashion to preserve the internal structure of the rigid body, this is not a very natural parameter set for a rigid body containing a large number of atoms. To address this problem, we will demonstrate the use of purely rotational symmetry modes to refine the rigid-body motions that occur in the cubic-monoclinic phase transition of $[\text{Mg}(\text{H}_2\text{O})_6]\text{RbBr}_3$ (Fig. 1) [2].

References:

[1] B.J. Campbell, J. S.O. Evans, F.Perselli, H.T.Stokes, *IUCr Computing Commission Newsletter* (2007) 8, 81-95.

[2] R.E. Dinnebier, Y. Liebold-Ribeiro, M. Jansen, *Z. Anorg. Allg. Chem.* (2008), 634, 1857-1862.

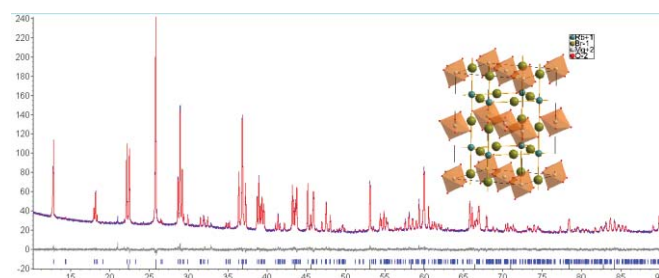


Fig. 1: Observed and calculated (using rotational symmetry modes) X-ray powder pattern of monoclinic $[\text{Mg}(\text{H}_2\text{O})_6]\text{RbBr}_3$ and the corresponding monoclinic structure with rigid Mg-O octahedra.

MS12-T04

The Bilbao Crystallographic Server: Structure utilities toolbox

E.S. Tasci¹, G. de la Flor¹, J.M. Perez-Mato¹, M.I. Aroyo¹

¹University of the Basque Country, Condensed-Matter Physics, Bilbao, Spain

The structure-utilities toolbox hosted by the Bilbao Crystallographic Server (<http://www.cryst.ehu.es>) [1] offers basic computer tools for transformations between different structure descriptions as well as more complex applications necessary for comparisons of structures or studies of their relationships.

The set of basic tools includes the programs CELLTRAN and TRANSTRU that transform unit-cell parameters with respect to a given transformation matrix. In addition, TRANSTRU validates the transformation and the resulting structure in the destination space-group setting for group-subgroup related transformations. The tool SETSTRU converts alternative settings structure descriptions to a standard setting and vice versa. The program EQUIVSTRU applies the Euclidean space-group normalizers to derive all equivalent descriptions of the same structure. The program WPASSIGN identifies the Wyckoff positions to which the occupied atomic orbits belong. For a given pair of structures, STRAIN is used to calculate the linear and finite-strain tensors as well as the degree of the lattice deformation. The structures can be visualized in an interactive 3D environment via the VISUALIZE tool.

The program COMPSTRU compares two structure descriptions of the same compound characterizing the similarity of the structure models by different quantitative descriptors (e.g. the *measure of similarity* [2]). The program is also helpful for the recognition of similar atomic arrangements of different compounds that is essential for the classification of crystal structures into iso-configurational structure types. The program STRUCTURE RELATIONS studies the relations between two phases of the same compound whose symmetries are described by group-subgroup related space groups. The crystal-structure relationship is characterized by a global distortion that, in general, can be decomposed into homogeneous strain and atomic displacement field. The program searches for a mapping between the two structures such that the global distortion accompanying the mapping is tolerably small. The program STRUCTURE RELATIONS is also an efficacious tool for the construction of family trees of homeotypic crystal structures (known also as *Baernighausen trees* [3]).

Where applicable, the structure tools hosted by the Bilbao Crystallographic Server support the CIF file format both for input and output, making it easy to exchange information between various related software packages.

[1] M. I. Aroyo, J. M. Perez-Mato, C. Capillas, E. Kroumova, S. Ivantchev, G. Madariaga, A. Kirov & H. Wondratschek. *Z. Kristallog.* **221** (2006), 15.

[2] G. Bergerhoff, M. Berndt, K. Brandenburg and T. Degen. *Acta Cryst.* **B55** (1999), 147.

[3] U. Mueller. *Z. Anorg. Allg. Chem.* **630** (2004), 1519.

MS12-T05

Ab initio simulations of lattice stability: an effect of temperature and temperature induced excitations.

I. Abrikosov¹

¹Linköping University, IFM, Linköping, Sweden

Ab initio electronic structure theory is known as a useful tool for prediction of materials properties and for their understanding. However, majority of simulations still deal with calculations of total energies at zero temperature. In this talk we show that for large number of problems it is necessary to take proper experimental conditions into account to obtain reliable theoretical results. In particular, we show that the problem of lattice stability, the energy difference between different crystal structures of a material, can be consistently described by theory and experiment if the former is done at elevated rather than at zero temperature [1]. Considering random Ni-rich Fe-Ni alloys, which undergo chemical order-disorder transition approximately 100 K below their Curie temperature, we demonstrate from ab initio calculations that deviations of the global magnetic state from ideal ferromagnetic order due to temperature induced magnetic excitations have a crucial effect on the structural transition temperature. Within our approach, we are able to reproduce quite accurately not only the experimental ordering transition temperature, but also its behavior as a function of the alloy composition [2]. Using first-principles calculations we also study the effect of magnetic disorder above the magnetic transition temperature on the structural and thermodynamic properties of CrN, a material which undergoes a structural transition from orthorhombic antiferromagnetic to cubic paramagnetic phase around room temperature. The need of a treatment of electron correlations effects beyond the local density approximation is proven. When magnetic disorder and strong electron correlations are taken into account simultaneously, pressure- and temperature-induced structural and magnetic transitions in CrN can be understood [3].

[1] Asker C., Belonoshko A. B., Mikhaylushkin A. S., Abrikosov I. A., *Phys. Rev. B*, 2008, **77**, 220102(R)

[2] M. Ekholm, H. Zapolsky, A. V. Ruban, I. Vernyhora, D. Ledue, and I. A. Abrikosov, *Phys. Rev. Lett.* **105**, (2010) 167208.

[3] B. Alling, T. Marten, and I. A. Abrikosov, *Nature Materials* **9**, (2010) 283; *Phys. Rev. B* **82**, (2010) 184430; P. Steneteg, B. Alling, I. A. Abrikosov, arXiv:1110.1331v1 [cond-mat.mtrl-sci]

MS12-T06

Arsenate adsorption at hydrous FeOOH surfaces: an *ab initio* study

K. Otte¹, W.W. Schmahl¹, R. Pentcheva¹

¹University of Munich, Crystallography, Munich, Germany

Mineral surfaces and in particular the ones of iron oxides play an important role in the cycling and retention of contaminants such as arsenic complexes. Based on density functional theory (DFT) calculations including an on-site Coulomb repulsion term, we explore the mechanism of arsenate adsorption on iron oxyhydroxide (FeOOH) surfaces. Despite their different surface geometry, goethite(101), akaganeite(100), and lepidocrocite(001) show striking similarities in their properties and reactivity. In a humid environment the FeOOH surfaces are hydrated and a reconfiguration of surface functional hydroxyl groups takes place. This facilitates adsorption of arsenic complexes on the FeOOH surfaces via ligand exchange. We consider different inner sphere adsorption modes and identify a clear preference for monodentate or mixed mono- and bidentate adsorption for all FeOOH surfaces. Funding by the BMBF programme Geotechnologies: Mineral Surfaces (Project SURFTRAP) and Elitenetzwerk Bayern is acknowledged.

MS13-T01

Organic and Inorganic Crystals in Bioinspired Hybrid Materials

N. Sommerdijk¹

¹Eindhoven University of Technology, Chemical Technology and Chemistry, Eindhoven, Netherlands

We investigate the formation of both synthetic/biological and organic/inorganic hybrid materials using molecular design as well as 2D and 3D cryogenic transmission electron microscopy and electron diffraction. First it will be demonstrated using cryoTEM how a synthetic designer surfactant forms ribbon-shaped 2D organic crystals [1] that allow the self-assembly of layer-by-layer films with DNA for application as biomedical coatings. The crystallinity is due to the incorporation of a bis-urea unit in the surfactant structure and is essential to prevent mixing of the layers. We with cryo-electron tomography demonstrate how the layered structure together with the bis-urea system provides the possibility to anchor bioactive molecules in a predefined layer of the coating [2]. *In vitro* as well as *in vivo* tests show that these coatings show biocompatibility and bioactivity comparable to conventional calcium coatings [3].

Secondly the study of organic/inorganic hybrid materials is discussed. A yet unfulfilled dream of many scientists is to synthesize new materials with similar advanced properties as those found in biominerals. [4] An absolute prerequisite for the design of such hybrid materials is to unravel the mechanisms of bio(mimetic) mineral formation. The *in situ* study of the development of mineral formation can make an important contribution to the understanding of the processes involved in biomineralization. [5] CryoTEM has been demonstrated as a method to investigate the early stages of mineral formation without removing the developing particles from their aqueous environment. [6] These investigations revealed that the formation of both calcium carbonate and calcium phosphate is preceded by an amorphous phase, which itself is formed through the assembly and aggregation of nanometer building blocks termed pre-nucleation clusters [7]. They also revealed the role of the templating surfaces and matrices in these processes. Using high resolution cryoTEM in combination with several other *in-situ* techniques we will demonstrate in detail the structure of these clusters and their role in the formation of the subsequent amorphous and crystalline phases.

[1] M.R.J. Vos, N.A.J.M. Sommerdijk, et al *J. Am. Chem. Soc.*, **127**, 16768 (2005), M.R.J. Vos, N.A.J.M. Sommerdijk, et al. *Chem Commun*, **46** 6063 (2010).

[2] M.R.J.; Vos, N.A.J.M. Sommerdijk, et al. *J. Am. Chem. Soc.* **130**, 12608-12609, (2008).

[3] J.J.J.P. van den Beucken, N.A.J.M. Sommerdijk, et al *Acta Biomater.*, **3**, 587 (2007). J.J.J.P. van den Beucken, N.A.J.M. Sommerdijk, et al. *Tissue. Eng.* **13**, 711 (2007), J.J.J.P. van den Beucken, N.A.J.M. Sommerdijk, et al *Key Eng. Mater.*, **361-363**, 605 (2008), C. Schouten, N.A.J.M. Sommerdijk et al. *J. Biomed. Mater Res A*, **92A**, 931(2010).

[4] N.A.J.M. Sommerdijk, H. Cölfen, *MRS bulletin*, **35**, 116 (2010).

[5] A. Dey, G. de With, N.A.J.M. Sommerdijk, *Chem. Soc. Rev.* **92**, 381, (2010).

[6] B.P. Pichon, N. A. J. M. Sommerdijk, et al, *J. Am. Chem. Soc.* **130**, 4034 (2008). E.M. Pouget, N.A.J.M. Sommerdijk, et al. *Science*, **323**, 1455 (2009).

[7] A. Dey, N.A.J.M. Sommerdijk et al, *Nature Mater*, **9** 1010 (2010). F. Nudelman N.A.J.M. Sommerdijk, et al. *Nature Mater*, **9** 1004 (2010)

MS13-T02

Cellulose fibril orientation in primary cell walls of Arabidopsis thaliana(L.)

F. Saxe¹, M. Rüggeberg², M. Eder¹, I. Burgert²

¹Max-Planck Institute of Colloids and Interfaces, Biomaterials, Potsdam, Germany

²ETH Zürich, Institute for Building Materials, Zürich, Switzerland

Plant cells are encased by a cell wall. Depending on the particular function (e.g. protection, support, transport, seed dispersal) the architecture of the wall is highly variable. As long as the cell is growing it is surrounded by only a thin primary cell wall which needs to be rigid and pliant at the same time to allow for cell growth while determining and maintaining the cell shape and resisting internal and external forces. For this the orientation of the stiff, partly crystalline cellulose microfibrils, which are embedded in a softer matrix of hemicelluloses and pectins, plays a key role. Although the individual cell wall composing polymers are well described, their arrangement and the orientation of the cellulose fibrils in the wall are not completely understood yet. We chose an integrative approach using small (SAXS) and wide angle X-ray scattering (WAXS) at a Synchrotron microfocus beamline (BESSY II) to characterize orientation and structure of primary cell wall microfibrils at different ages, positions and tissues in dark grown hypocotyls of Arabidopsis seedlings (Fig. 1). A broad distribution of microfibril orientations with two peaks between 15° and 20° and around 90° with respect to the longitudinal axis of the cell was found. As expected, the tip of the seedling, where cells are elongating, has more transversely oriented microfibrils than basal regions of the seedling with a gradual transition in between. The SAXS measurements of dried seedlings lacked the scattering signal of the transverse orientation, leading to the assumption that structural differences exist in different cell walls or cell wall layers. In the SAXS signal of never-dried plants, both main orientations could be observed. A structural analysis of the cell wall components from the WAXS signal revealed a low ratio of crystalline to amorphous scattering contributions. Our results add to the understanding of the structure of primary cell walls during growth and especially on how the arrangement of the stiff cellulose microfibrils determines the preferential direction of cell expansion.

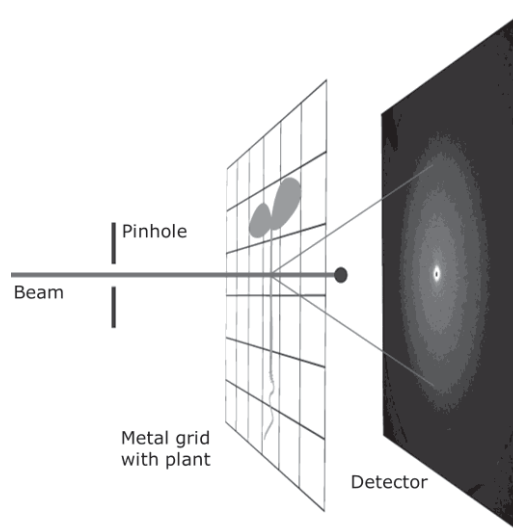


Figure 1: Setup at BESSY II. Native, wet or freeze dried four and seven day old dark grown plants were mounted on a metal grid and placed in the beam.

MS13-T03

Improved analysis of cellulose microfibril orientation distribution in hardwood by X-ray diffraction

M. Rueggeberg^{1,2}, H. Metzger², P. Fratzl², I. Burgert^{1,2}¹ETH Zürich, Institut für Baustoffe, Zürich, Switzerland²Max-Planck-Institute of Colloids and Interfaces, Biomaterials, Potsdam, Switzerland

X-ray diffraction has been frequently used for analyzing structure and orientation of the cellulose microfibrils in the plant cell wall. By using X-ray diffraction insights into the nanostructure of the cell wall can be gained while the samples remain in almost native state. However, the evaluation of diffraction data of plant cell walls is not trivial due to the small size of the cellulose crystallites, the complex geometry of the plant cells and possible superimposition of several orientation distributions. We have developed an improved and integrated way of evaluating data from WAXD and SAXS measurements of the plant cell wall which enable extracting more and reliable information on the complete orientation distribution of the cellulose microfibrils within the plant cell wall. We will present this method and will give an example of its use in recent studies on poplar wood.

MS13-T04

The effect of physiological saline and soluble matrix proteins of *Porcellio scaber* ACC deposits on calcium carbonate precipitationA. Ziegler¹, S. Hennig¹, H.-O. Fabritius², S. Hild³¹University of Ulm, Central Facility for Electron Microscopy, Ulm, Germany²Max-Planck-Institute for Iron Research GmbH, Department Microstructure Physics and Metal Forming, Düsseldorf, Germany³Johannes Kepler Universität, Institute of Polymer Science, Linz, Austria

The terrestrial isopod, *Porcellio scaber* stores cuticular calcium in sternal deposits before moulting. The deposits consist of spherules that are formed within a confined ecdysial space filled with fluid. The spherules are composed of granular particles containing mainly amorphous calcium carbonate, little amorphous calcium phosphate and an organic matrix. Using ion selective microelectrodes we measured the cationic composition and the pH of the ecdysial fluid of the sternites during mineral deposition (Ziegler, 2008). We designed a near physiological but phosphate-free saline for precipitation of calcium carbonate in the presence of soluble matrix proteins extracted from native deposits, and analysed structure, mineral phase and composition of the precipitates. Within the test solutions the total soluble fraction leads to precipitation of ACC granules. Agglomerations of ACC granules and the dried soluble fraction of the organic matrix are virtually devoid of organic phosphates. The agglomerations mimic several aspects in the architecture of native sternal deposits and were stable for at least one month. The saline alone has no effect on the crystal phase but leads to changes in calcite crystal morphology due to the effects of magnesium. BSA that was used as a control protein apparently has no effect on the mineral phase, but in the presence of Mg^{2+} , severe effects on the surface structure of calcite crystals, suggesting a combined effect of BSA and Mg^{2+} on crystal growth.

Supported by the DFG within the priority program „Principles of Biomineralisation“ SPP 1117 Zi 368/4-2.

Ziegler A. (2008). The cationic composition and pH in the moulting fluid of *Porcellio scaber* (Crustacea, Isopoda) during calcium carbonate deposit formation and resorption. J Comp Physiol B 178:67-78.

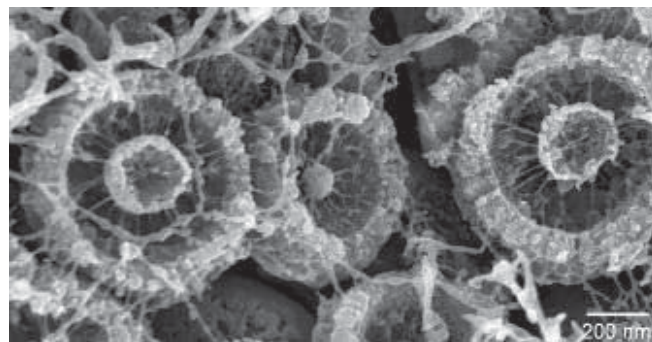


Figure 1. Spherules of amorphous $CaCO_3$ from sternal deposits of the terrestrial isopod *Porcellio scaber* contain radial and concentric organic matrix elements.

MS14-T01

Structural variability in complex uranyl phosphates and uranyl arsenates of divalent elements

E. Alekseev¹, S. Wu², W. Depmeier²¹Forschungszentrum Jülich, Institute of Energy and Climate Research (IEK-6), Jülich, Germany²Kiel University, Institut für Geowissenschaften, Kiel, Germany

Uranyl phosphates and uranyl arsenates are very well known as a large group of natural minerals and mineral-like materials. These phases also can form during the migration processes of actinide elements in nature. In view of a better understanding we are studying the formation, structures and properties of new phases in the A - UO_3 - $P_2O_5(As_2O_5)$ - (H_2O) systems (A - mono-, bi- and trivalent elements). Recently we focused on the synthesis and structural investigation of novel uranyl phosphates and arsenates with divalent elements. With different synthetic approaches (high temperature solid state reactions, hydrothermal synthesis and mild temperature flux reactions) we obtained several Mg, Ca, Sr, Ba and Pb containing phases: $Mg[(UO_2)(As_2O_7)]$ (1), $Sr[(UO_2)(As_2O_7)]$ (2), $CaBa_5[(UO_2)_8(AsO_4)_4O_8]$ (3), $Ba_4(UO_2)_2(AsO_4)_4$ (4), $Ba_4[(UO_2)_7(UO_4)(AsO_4)_2O_7]$ (5), $Ba_4[(UO_2)_2(As_2O_7)_3]$ (6), $Ba_3[(UO_2)_2(AsO_4)_2(As_2O_7)_2]$ (7), $Pb_3[(UO_2)(As_2O_7)_2]$ (8), $Na_2Ba_2[(UO_2)_3(PO_4)_4]_2(H_2O)$ (9), $BaU(PO_4)_2$ (10), $Ba[(UO_2)_3U_2(As_2PO_4)_2O_{12}]$ (11), α - and β - $Ba_2UO_2(PO_4)_2$ (12, 13).

The compounds have very rich structural chemistry with 1D, 2D and 3D structural types. Mg and Sr uranyl arsenates adopt 3D frameworks strongly related to the structures found in Li uranyl phosphates and arsenates. 3 exhibits a new type of UO_7 pentagonal bipyramid condensation with new anion topology in the whole class of uranium compounds. The structure of 4 is only based on single AsO_4 and UO_6 groups, which is quite rare for uranyl arsenates obtained from high temperature reactions. Compounds 5, 7 and 11 demonstrate new frameworks with complex topology and very unusual groups such as UO_4^{2-} anti-uranyl and mixed valences of uranium. 6 is based on 1D chains with complex composition and unprecedented topology in the class of oxo-salt compounds. The Pb uranyl arsenate (8) shows complex packing mode of the separate layers based on uranyl arsenate and lead arsenate fragments. It is possible to write the formula of this phase as $[Pb_2(As_2O_7)] [Pb(UO_2)(As_2O_7)]$. Phase 9 is based upon a complex framework with two types of channels occupied by Ba and Na separately. $BaU(PO_4)_2$ (10) is the result of U^{6+} reduction in high temperature reaction and possesses a new structure type in U^{4+} chemistry. The structures of α - and β - $Ba_2UO_2(PO_4)_2$ (12, 13) are perfect examples of structure evolution in polymorphic modifications. Very unusual uranium coordination was found in the structure of the beta modification.

This work was supported by DE 412/30-2 and DE 412/43-1 DFG projects.

MS14-T02

Boron in mullites - syntheses, properties and a structural puzzle

H. Lührs¹, R.X. Fischer¹, H. Schneider^{1,2}, J.V. Hanna³, S.P. King³¹University of Bremen, Geosciences, Bremen, Germany²University of Köln, Crystallography, Köln, Germany³University of Warwick, Physics, Warwick, United Kingdom

The crystal structure of mullite can incorporate a large variety of ions [1]. A solid-solution series between mullite and $\text{Al}_{18}\text{B}_4\text{O}_{33}$ was proposed by [2]. Griesser [3] studied the incorporation of boron into mullite based on a 1:2 substitution of Si by B and proposed that 20 mole% B_2O_3 can be incorporated into mullite. Here a series of boron doped mullites (B-mullite) was prepared based on a 1:1 isomorphous substitution of Si by B, starting from a 3:2 mullite composition ($\text{Al}_{4.5}\text{Si}_{1.5}\text{O}_{9.75}$). By means of simultaneous thermal analysis (STA), XRD, high-temperature XRD, neutron diffraction, FTIR, and ^{11}B MAS NMR the syntheses, properties, and crystal structure of B-mullite were studied.

Investigation of the in-situ phase formation of B-mullite revealed a decrease of the formation temperature for B-mullite with increasing boron. For B-mullites a significant decrease in lattice parameters b and c with increasing amount of boron was observed (Figure 1). Based on the phase composition and the development of lattice parameters it was shown that more than 10 mole% B_2O_3 can be incorporated into mullite. However, alumina impurities indicate that there is no complete solid solution between mullite and aluminum borate. Long annealing at 1400°C leads to an increase of lattice parameters b and c and decomposition of B-mullite to boron-free mullite and α -alumina.

Due to the replacement of about one third of the Si by B the thermal expansion coefficients were reduced by 7% (a-axis), 14% (b-axis), and 12% (c-axis) in comparison to boron-free mullite. The expansion of the unit-cell volume was reduced by 12%.

The presence of threefold coordinated boron was confirmed by FT-IR spectroscopy and ^{11}B MAS NMR spectroscopy. The measured values of the ^{11}B quadrupole interaction yielded $C_Q = 3.2$ MHz and $\eta_Q = 0.05$; the low η_Q value suggests that the B site possesses a near-three fold axis of rotation. First refinements based on powder neutron diffraction data indicated that boron resides in three-coordination linking the octahedral chains.

References:

- [1] H. Schneider & S. Komarneni (2005), Mullite, Wiley-VCH Verlag, Weinheim.
 [2] A. Dietzel, & H. Scholze, *Glastechn. Ber.* 28, pp.47-51 (1955).
 [3] K.J. Griesser et al. (2008), *Mineralogy and Petrology* 92(3-4) pp. 309-320 (2008).
 [4] R.X Fischer et al., *J. Eur. Ceram. Soc.* 16(2) pp. 109-113 (1996)

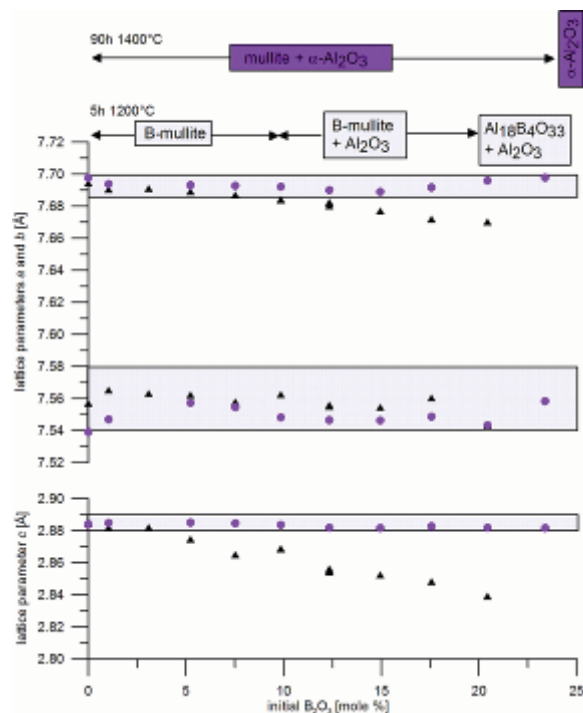


Figure. 1: Lattice parameters vs. initial boron content. Triangles: 1200°C syntheses, circles: after 90h at 1400°C , grey: variation of a , b and c observed in mullites with varying Al_2O_3 content [4]. On top of the figure the qualitative phase composition is given.

MS14-T03

Combined neutron, X-ray and DFT study of Croconic Acid

M. Gutmann¹, F. Fernandez-Alonso¹, K. Refson², M. Jura¹, M. von Zimmermann³, A. Wagner⁴¹Rutherford Appleton Laboratory, ISIS Facility, Chilton Didcot, United Kingdom²Rutherford Appleton Laboratory, CSED, Chilton Didcot, United Kingdom³Deutsches Elektronensynchrotron, HASYLAB DESY, Hamburg, Germany⁴Diamond Light Source LTD, Chilton Didcot, United Kingdom

Croconic Acid, $\text{C}_5\text{O}_5\text{H}_2$, has emerged as the first and only example of an above room-temperature single molecule organic ferroelectric [1]. Although the compound has been known for over 185 years, single crystals could be grown for the first time about 10 years ago [2]. Here, we present the results of a temperature-dependent single-crystal neutron diffraction study. This is further augmented with single crystal diffuse X-ray scattering and a comparison with phonons calculated from DFT is made. Quasielastic neutron scattering as a function of temperature shows an intriguing correlation between the proton behavior and ferroelectricity, indicating that the phenomenon is dynamic in origin.

[1] S. Horiuchi, et al., *Nature* 463, 789 (2010).[2] D. Braga, L. Maini, and F. Grepioni., *CrystEngComm* 6, 1 (2001).

MS14-T04

IONIC SUBSTITUTION IN MERIDIANITE
(MgSO₄·11H₂O): SOLID SOLUTIONS AND NOVEL
HYDRATESD. Fortes¹, F. Browning¹, I. Wood¹¹University College London, Department of Earth Sciences, London, United Kingdom

MgSO₄·11H₂O (MS11) is the most highly hydrated phase in the MgSO₄—H₂O system, having a narrow stability field in contact with aqueous solution [1]. Whilst all the other known MgSO₄ hydrates (1, 2, 2½, 3, 4, 5, 6, and 7H₂O) have isomorphous or isodimorphous analogues with alternative cation and oxyanion substituents, MS11 is hitherto unique in occurring solely in the MgSO₄—H₂O system. MS11 occurs naturally in periglacial environments on Earth as the mineral meridianite [2,3], and is thought to be abundant on Mars even at low latitudes [4,5]. The objective of our work was to examine the possibility that end-member 11-hydrates isostructural with MS11 could form with alternative cations or oxyanions, or else to determine their solubility limits in the MS11 structure.

Most of our work so far has been carried out using powder specimens prepared by quenching aqueous solutions in liquid nitrogen. The resulting solid blocks consist of one or more hydrates + water ice, which are powdered under liquid nitrogen and then analysed using X-ray powder diffraction. We have collected X-ray data from aqueous MgSO₄ specimens doped with Ni²⁺, Zn²⁺, Cu²⁺, Fe²⁺, Co²⁺ and Mn²⁺ in molar abundances from 0–100 % in 10 % increments, and from a pure aqueous solution of MgCrO₄; although we have so far only examined the end-member in this system, we intend to characterise mixed crystals with MgSO₄ in the future.

Contrary to expectation (based on the behaviour of lower hydrates) we discovered that of the seven end-member metal sulfates studied, only MgSO₄ forms an 11-hydrate. Amongst the quenched end-members, all species except one formed familiar heptahydrates (ZnSO₄, MnSO₄, FeSO₄, and CoSO₄) or pentahydrates (CuSO₄). The exception was NiSO₄, which was observed to form a new triclinic crystal that we believe to be an octahydrate. Further analysis of doped specimens with mixed cation compositions has shown that synthetic meridianite can accommodate significant quantities of foreign cations in its structure; ~ 50 mol. % Co²⁺ or Mn²⁺, 20–30 mol. % Ni²⁺ or Zn²⁺, but less than 10 mol. % of Cu²⁺ or Fe²⁺. In the NiSO₄- and ZnSO₄-doped systems we identified a new monoclinic hydrate, which exists across a wide range of dopant concentrations; this phase is also seen in the CuSO₄- and FeSO₄-doped systems, but over a more limited range, appearing to be metastable with respect to the melanterite-structured heptahydrate. The unit-cell volume of this new phase is consistent with it being an enneahydrate. We find that there is a linear relationship between the rate of change in MS11 unit-cell volume as a function of dopant concentration and the ionic radius of the dopant cation.

In contrast, we have discovered that it is possible to form end-member 11-hydrates containing alternative oxyanions. The first of these we identified was MgCrO₄·11H₂O, which is isostructural with meridianite but with a substantially inflated (and anisotropically strained) unit-cell.

References:

- [1] Int. Crit. Tables;
- [2] Peterson et al., 2007, Am. Min., 92, 1756-1759;
- [3] Genceli et al., 2009, J. Glaciol., 55, 117-122;
- [4] Fialips et al., 2004, LPSC35, #2054;
- [5] Peterson & Wang, 2006, Geology, 34, 957-960.

MS14-T05

New Methods for the Synthesis of Ternary Rare-Earth
Metal(III) Oxoarsenates(III) and (V) with a Comparison of the
Comprehensive Crystal StructuresS.J. Metzger¹, T. Schleid¹¹University of Stuttgart, Institute for Inorganic Chemistry, Stuttgart, Germany

Rare-earth metal(III) oxoarsenates(V) with the general formula $M[\text{AsO}_4]$ can be synthesized by solid-state reactions or from aqueous solution. Whereas the representatives with larger ionic radii ($M = \text{La-Nd}$) crystallize in the *monazite*-type structure (monoclinic, $P2_1/n$), the compounds with smaller M^{3+} cations ($M = \text{Sm-Lu}$) exhibit the *xenotime*-type structure (tetragonal, $I4_1/amd$). Since *Stubican* and *Roy* [1] have discovered phase transitions from *monazite*- and *xenotime*-type $M[\text{AsO}_4]$ to the *scheelite*-type structure (tetragonal, $I4_1/a$) at high pressures (8 GPa) and temperatures (600 °C) by using an uniaxial pressure device, only occasional X-ray diffraction data exist in the literature. While $\text{La}[\text{AsO}_4]$ and $\text{Ce}[\text{AsO}_4]$ showed no alteration under these conditions, treatment at more than 8 GPa with the help of a planetary ball mill lead to the phase transition into *scheelite*-type $M[\text{AsO}_4]$ for $M = \text{La}$ and Ce . Unfortunately, just microcrystalline products occur in any case. Transparent single crystals of $M[\text{AsO}_4]$ ($M = \text{La, Pr-Nd}$ and Sm) with the *scheelite*-type structure can be obtained by increasing the pressure up to 11 GPa and choosing even higher temperatures (1100 °C) in a modified *Walker*-type module in combination with a 1000 ton press.

Modifying the pressure conditions along with the temperature and the heating- and cooling rates gave access to rare-earth metal(III) oxoarsenates(III) $M[\text{AsO}_3]$ ($M = \text{La-Pr}$) with $\text{K}[\text{ClO}_3]$ -type structure. Based on this knowledge the ternary compounds $\text{La}[\text{AsO}_3]$ and $\text{Ce}[\text{AsO}_3]$ were synthesized phase pure by the reaction of the sesquioxides $M_2\text{O}_3$ and As_2O_3 [2]. Without high pressure the two sesquioxides undergo a disproportionation to the known rare-earth metal(III) oxoarsenates(V), elemental arsenic and the remaining surplus of $M_2\text{O}_3$. With an excess of As_2O_3 the systems avoid to constitute the As_2O_3 -richer triclinic $M_2\text{As}_4\text{O}_9$ phases ($M = \text{Nd}$ and Sm) [3] at 850 °C.

These different preparation methods lead to familiar and new members of the family of ternary rare-earth metal(III) oxoarsenates(III) and (V) containing a manifold of building units in the crystal structures: isolated ψ^1 -tetrahedral $[\text{AsO}_3]^{3-}$ anions in the $M[\text{AsO}_3]$ (Figure 1, right) or pyroanionic $[\text{As}_2\text{O}_5]^{4-}$ groups and *cyclo*- $[\text{As}_4\text{O}_8]^{4-}$ anions as eight-membered rings in the $M_2\text{As}_4\text{O}_9$ representatives according to $M_4[\text{As}_2\text{O}_5]_2[\text{As}_4\text{O}_8]$ (Figure 2), and isolated $[\text{AsO}_4]^{3-}$ tetrahedra in the three different oxoarsenates(V) $M[\text{AsO}_4]$ as well (Figure 1, left). In the same way the polyhedra around the trivalent cations change their size and shape from $[\text{MO}_{7+2}]^{15-}$ in $M[\text{AsO}_3]$ to $[\text{MO}_{8+1}]^{15-}$ in *monazite*-type $M[\text{AsO}_4]$ and to $[\text{MO}_8]^{13-}$ in *xenotime*- and *scheelite*-type $M[\text{AsO}_4]$ following the different connectivities between these polyhedra and the attached oxoarsenate anions. In summary the amount of shared edges and vertices between the fundamental building units coincide with the pressure and the temperature during the synthesis and is reflected by the density of the obtained ternary compound.

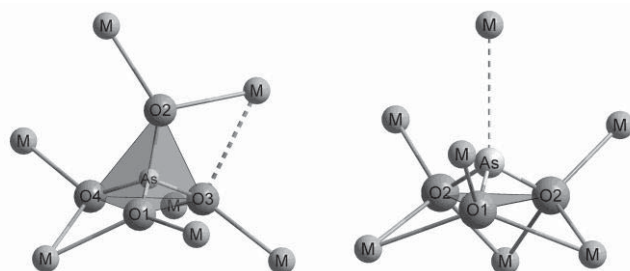


Figure 1: Isolated $[\text{AsO}_4]^{3-}$ tetrahedron in *monazite* $M[\text{AsO}_4]$ (left) and isolated ψ^1 -tetrahedral $[\text{AsO}_3]^{3-}$ anion in $M[\text{AsO}_3]$ (right).

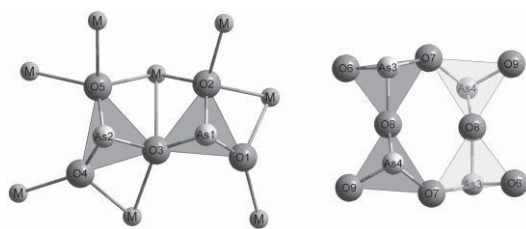


Figure 2: Pyroanionic $[\text{As}_2\text{O}_5]^{4+}$ group (left) and $\text{cyclo-}[\text{As}_4\text{O}_8]^{4-}$ anion (right) in $M_4[\text{As}_2\text{O}_5]_2[\text{As}_4\text{O}_8]$.

References:

- [1] V. S. Stubican, R. Roy, *Z. Kristallogr.* **1963**, 119, 90.
- [2] S. J. Metzger, G. Heymann, H. Huppertz, Th. Schleid, *Z. Anorg. Allg. Chem.* **2012**, 638, in press.
- [3] D.-H. Kang, Th. Schleid, *Z. Anorg. Allg. Chem.* **2006**, 632, 91.

MS14-T06

Time-resolved investigation of crystallization processes

T. Gnutzmann¹, M. Klimakow¹, K. Rademann², F. Emmerling¹
¹BAM Federal Institute for Materials Research and Testing, 1.3 Structure Analysis, Berlin, Germany

²Humboldt-Universität zu Berlin, Department of Chemistry, Berlin, Germany

The need to control and manipulate the crystallization processes and particularly the final crystal product requires thorough understanding of the underlying crystallization mechanisms and kinetics but also of the effect of a range of external influencing factors. This is especially true in case of polymorphic compounds which are chemically identical but can adapt different crystalline structures. Therefore, crystallization of polymorphic compounds can only be investigated in detail using time-resolved characterization methods. In this context, in-situ methods enable detection and identification of transient metastable polymorphs and elucidation of the mechanism of the conversion from one form into another. X-ray diffraction using synchrotron radiation allows the investigation to be performed at high time-resolution. Additionally, by employing an ultrasonic levitator as sample holder the influence of the surface of container walls on the crystallization process can be eliminated. Such setup was used to investigate the crystallization of various organic compounds. Among those, the compound ROY (5-methyl-2-[(2-nitrophenyl)amino]-3-thiophenecarbonitrile) is known for its numerous and colourful polymorphs but also for its unspecific crystallization.¹ To date, there are ten known polymorphs whereof seven crystal structures are characterized.² Crystallization of ROY often results in a mixture of more than one polymorph. Our investigations showed that the choice of the solvent has a strong influence on the resulting crystallization product. The combination of Synchrotron X-ray diffraction with optical spectroscopy enabled further insight into the crystallization mechanism (see Figure 1). The advantages of this approach are exemplarily shown for the organic polymorphic compound nifedipine, which can exist in an amorphous and at least three crystalline forms. It is believed that additional metastable polymorphs might also exist.^{3,4} The unusually fast crystallization of nifedipine, starting from an amorphous film on a surface, can be monitored by time resolved Raman micro-spectroscopy.⁵

(1) Yu, L.; Stephenson, G. A.; Mitchell, C. A.; Bunnell, C. A.; Snorek, S. V.; Bowyer, J. J.; Borchardt, T. B.; Stowell, J. G.; Byrn, S. R.J. *Am. Chem. Soc.* 2000, 122, 585-591.

(2) Singh, A.; Lee, I. S.; Myerson, A. S. *Cryst. Growth Des.*, 2009, 9, 1182-1185.

(3) Klimakow, M.; Rademann, K.; Emmerling, F. *Cryst. Growth Des.*, 2010, 10, 2693-2698.

(4) Grooff, D.; De Villiers, M. M.; Liebenberg, W. *Thermochim. Acta*, 2007, 454, 33-42.

(5) Gnutzmann, T.; Rademann, K.; Emmerling, F. *Chem. Commun.*, 2012, DOI: 10.1039/C1CC16301A

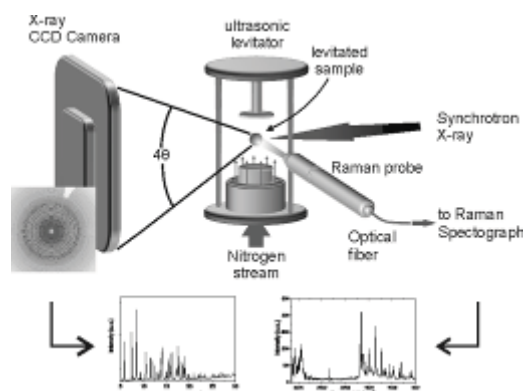


Figure 1: Setup of the XRD/Raman experiments at the $\mu\text{Spot-Beamline}$ at BESSY II

MS15-T01

EMBL@PETRA3 - An integrated Facility for Structural Biology

T.R. Schneider¹, S. Fiedler¹, G. Bourenkov¹, M. Cianci¹, M. Roesle¹, R. Meijers¹, J. Müller-Dieckmann¹, M. Wilmanns¹

¹EMBL c/o DESY, Hamburg Outstation, Hamburg, Germany

The European Molecular Biology Laboratory is constructing an integrated facility for structural biology at PETRA III, the new 3rd generation synchrotron at DESY in Hamburg. At the center of the facility are three beamlines for life science applications. The BioSAXS beamline provides excellent conditions for small angle X-ray scattering on solutions of biological macromolecules while the two crystallography beamlines (MX1 and MX2) will be optimized for long-wavelength and microfocus-based experiments, respectively.

On BioSAXS and MX2 experiments have been started during the summer of 2011 and the results are promising. On MX2, the first unknown crystal structure was solved by molecular replacement in October 2011. On MX1, first experiments will be performed in December of 2011.

The beamlines are complemented by facilities for sample preparation and characterization comprising various biophysical techniques. Most notably, the EMBL high-throughput crystallization facility (<http://www.embl-hamburg.de/facilities/htpx/>) is now situated in an extension building to the PETRA III experimental hall in close vicinity of the beamlines. A laboratory especially equipped for handling chemicals needed for derivatization of macromolecular crystals has been set up close to the beamlines as well.

Building on the existing computing services such as Auto-Rickshaw (<http://www.embl-hamburg.de/Auto-Rickshaw/>) and ATSAS on-line (<http://www.embl-hamburg.de/ExternalInfo/Research/Sax/atsas-online/>), on-site data evaluation and structure determination will be enabled by a state-of-the-art computing infrastructure.

We will present the current status of the beamlines and the complementary facilities and our plans for the future. We are very interested to discuss ideas and perspectives with future users of the new facilities.

Table: Key parameters of the new beamlines

	BioSAXS	MX1	MX2
Energy [keV]	4-20	5(4)-17	7-35
Monochromators	Si(111)	Si(111)	Si(111)
Beam size H x V [μm^2]	200 x 60	28 x 13	4 x 1
Divergence H x V [mrad ²]	0.04 x 0.01	0.2 x 0.15	<0.5 x <0.3
Demagnification H / V	1:1.4 / 1: 1.2	1:12 / 1:15	1:60 / 1:40
Intensity [ph/sec]	10 ¹³	10 ¹³	10 ¹²
Sample handling	robotic	robotic (Jul-12)	robotic (Oct-12)
Detector	PILATUS 2M	Rayonix 225HE	TBD

MS15-T02

The New D8 Structural Biology Solutions for Macromolecular Crystallography - initial results

M. Adam¹, V. Smith², M. Biadene³

¹*Bruker AXS GmbH, SC-XRD Product Manager, Karlsruhe, Germany*

²*Bruker AXS GmbH, Business Development Manager, Karlsruhe, Germany*

³*Bruker AXS GmbH, Application Laboratory, Karlsruhe, Germany*

The D8 Structural Biology Solutions for Macromolecular Crystallography were recently introduced. The systems feature revolutionary technology such as the PHOTON 100 CMOS detector coupled with an improved $\text{I}\mu\text{S}$ microfocus source which delivers 30% more intensity than earlier versions. For the most weakly diffracting small crystals the TXS microfocus rotating anode generator delivers an intensity greater than any equivalent source previously available.

This presentation will present examples of data collected on these systems and discuss how the technological innovations enabled better quality data to be collected.

MS15-T03

XDSAPP - A graphical user interface for processing diffraction data using XDS

U. Mueller¹, M. Krug^{1,2}, M.S. Weiss¹, U. Heinemann²

¹*Helmholtz-Zentrum Berlin, F-12, Macromolecular Crystallography (HZB-MX), Berlin, Germany*

²*Max-Delbrück Center for Molecular Medicine, Berlin, Germany*

Today's third generation synchrotrons allow the collection of diffraction images of protein crystals using typical exposure times of less than one second per image. Since the corresponding end stations for macromolecular crystallography (MX) are equipped with fast detector hardware, the time necessary to collect a complete diffraction data set has decreased from hours a few years ago to minutes.

In order to enable the synchrotron users to analyse all diffraction data during the data collection at the beamline, we have developed the program XDSAPP (XDS Automation and Plotting Protocols) (Krug et al., 2012), which mainly utilizes the diffraction data processing program XDS (Kabsch et al., 2010), but also other software like POINTLESS of the CCP4 software suite (CCP4, 1994), XDSSTAT (Diederichs 2006), SFCHECK (Vaguine et al, 2999) and PHENIX.XTRIAGE (Adams et al., 2010). XDSAPP is a Tcl/Tk based graphical user interface for processing diffraction data sets using XDS. It provides easy access to all XDS functionalities, automatizes the data processing and generates graphical plots of various data set statistics provided by XDS. By incorporating additional software, further information on certain features of the data set, such as for instance radiation decay during data collection or the presence of pseudo translational symmetry and/or twinning can be obtained. Intensity files suitable for CCP4, CNS and SHELX are generated.

References:

Adams, P. D., P. V. Afonine, et al. (2010). "PHENIX: a comprehensive Python-based system for macromolecular structure solution." *Acta Crystallogr D Biol Crystallogr* 66(Pt 2): 213-221.

Collaborative Computational Project, N. (1994). "The CCP4 suite:

programs for protein crystallography." *Acta Crystallogr D Biol Crystallogr* 50(Pt 5): 760-763.

Diederichs, K. (2006). "Some aspects of quantitative analysis and correction of radiation damage." *Acta Crystallogr D Biol Crystallogr* 62(Pt 1): 96-101.

Kabsch, W. (2010). "XDS." *Acta Crystallogr D Biol Crystallogr* 66(Pt 2): 125-132.

Krug, M. et al. (2012). "XDSAPP - A graphical user interface for processing diffraction data using XDS", submitted for publication

Vaguine, A. A., J. Richelle, et al. (1999). "SFCHECK: a unified set of procedures for evaluating the quality of macromolecular structure-factor data and their agreement with the atomic model." *Acta Crystallogr D Biol Crystallogr* 55(Pt 1): 191-205.

MS15-T04

Localization and orientation of heavy atom cluster compounds using automated molecular replacement.

S. Dahms¹, M. Kuester¹, M.E. Than¹

¹*Leibniz Institute for age research - Fritz Lipmann Institute, Protein crystallography, Jena, Germany*

As heavy atom clusters contain a large number of specifically arranged electron-dense scatterers, they proved especially useful for experimental phase determination of large complex structures or structures with large unit cells. Usually the exact orientation of the cluster and hence of the individual heavy atom positions proved as critical point for successful phasing.

Here we describe the application of molecular replacement (MR) for orientation and localization of different heavy atom cluster compounds. A hexa-sodium α -metatungstate cluster was applied for the first time for phasing of the structure of the death receptor 6 (DR6). Even though the cluster is bound in a multiple occupied state and is located at a special position, we were able to orient and localize the cluster at resolutions as low as 4.4 Å with MR. The phasing procedure succeeded with isomorphous as well as with anomalous differences. To verify the performance of this approach, hexagonal lysozyme crystals were soaked with tri-sodium phosphotungstate and hexa-tantalum tetradeca-bromide. Both heavy atom clusters were successfully oriented and localized with automated MR using anomalous differences. This method is a useful tool for phasing of medium and low diffracting crystals or crystals composed of large unit cells.

MS16-T01

Hydroxyapatite-Nanoceramics-Patent: EP 01824443

U. Bismayer^{1,2}, A. Klocke^{1,2}, J. Shi^{1,2,3}, S. Gierlotka^{1,2,3,4}, B. Palosz^{1,2,3,4}

¹*University of Hamburg, Mineralogy, Hamburg, Poland*

²*University Medical Center Hamburg-Eppendorf, Orthodontics, Hamburg, Poland*

³*Technical University of Braunschweig, Institute of Physical and Theoretical Chemistry, Braunschweig, Poland*

⁴*Polish Academy of Sciences, High Pressure Research Center, Warsaw, Poland*

Synthetic Hydroxyapatite ($\text{Ca}_{10}(\text{PO}_4)_6(\text{OH})_2$), ceramics are bioactive and biocompatible materials due to close similarity in composition and crystal structure with the biomineral apatite of bone and dental tissues. The mechanical strength and fracture toughness of conventionally sintered HA ceramics limits applications to powders, coatings, porous bodies and nonload-bearing implants. Nanostructured materials have mechanical properties substantially different from their coarse-grained counterparts due to the grain size effect [1]. In this study, nanosized HA powders were consolidated at high-pressure and -temperature and the resulting nanostructured hydroxyapatite ceramics was patented. The microstructure of hydroxyapatite ceramics sintered at 2.5GPa and a temperature range from 473-973K with a very short dwell time were characterized using X-ray diffractometry, scanning electron microscopy, and infrared spectroscopy, respectively. The sample

densified at 2.5GPa, 973K shows an inhomogeneous grain coarsening into micron sized structure while samples fabricated at temperature below 973K keep their nanosized structure. XRD patterns and FTIR spectra indicate an increasing crystallinity and crystalline order with increasing temperature. The results show that nanostructured hydroxyapatite ceramics with favorable biomechanical properties can be obtained at 2.5GPa and temperature below 973K [2].

- [1] Shi (2004) Thesis, University of Hamburg
 [2] 14.07.2010 Patentblatt 2010/28, EP 1 824 443 B1, PCT/EP2005/011578

MS16-T02
Crystallographic, structural and mechanical properties of shark teeth

O. Prymak¹, J. Enax², D. Raabe³, M. Epple²
¹University of Duisburg-Essen / Inorganic Chemistry, Department for X-Ray Diffraction, Essen, Germany
²University of Duisburg-Essen, Inorganic Chemistry, Essen, Germany
³Max-Planck-Institut fuer Eisenforschung, Microstructure Physics and Metal Forming, Duesseldorf, Germany

In contrast to human teeth with hydroxyapatite as inorganic matrix, shark teeth consist of fluoroapatite $Ca_{10}(PO_4)_6F_2$ with a fluoride content in the enameloid of approximately 3 wt%. Due to its ability to release fluoride ions which can prevent dental caries, fluoroapatite is an attractive biomaterial for the dental protection of teeth. Therefore, the teeth of two different sharks (shortfin mako shark: *Isurus oxyrinchus*, and tiger shark: *Galeocerdo cuvier*) were structurally and mechanically characterized.

The results of optical and electron microscopy, infrared spectroscopy and thermogravimetry are presented separately for dentin and enameloid (biological fluoroapatite) and compared with synthetic and geological fluoroapatite. It was shown that the hexagonal crystals in the enameloid are highly ordered with a special orientation (perpendicular to the outside surface and parallel in the middle). IR spectra of the shark teeth showed the characteristic bands of biological apatite (phosphate, carbonate and water). Thermogravimetry showed that dentin had a higher content of water, organic matrix and carbonate, than the enameloid.

Elemental analysis was carried out by atomic absorption spectroscopy (Ca^{2+} , Mg^{2+} , Na^+), UV spectroscopy (PO_4^{3-}) and ion-selective potentiometry (F⁻). The analysis shows, that the fluoride content in enameloid and in synthetic and geological fluoroapatites corresponds the theoretical value (3.7 wt%). In dentin, a lower concentration of fluoride was found.

The lattice parameters as obtained by Rietveld analysis using TOPAS (Bruker) were similar for all investigated samples. The enameloid of both shark species showed anisotropy in crystallite size in c-direction, resulting in narrower diffraction peaks in the (00l) direction. The substitution of hydroxide ions by smaller fluoride ions in FAP was confirmed by decreasing of a-axis (with constant c-axis). In contrast to dentin, enameloid showed sharp diffraction peaks which indicated a higher crystallinity of enameloid.

The mechanical properties were determined by nanoindentation and Vickers hardness tests. It was shown that enameloid of shark teeth was approximately six times harder than the dentin. The hardness was isotropic, i.e. it did not depend on the orientation of the cut through the tooth.

MS16-T03
Characteristics of the aragonite - calcite transition in bivalve shells

K. Kelm¹, E. Griesshaber², W.W. Schmahl², H.S. Ubhi³
¹Deutsches Zentrum für Luft- und Raumfahrt, Institut für Werkstoffwissenschaften, Köln, Germany
²Ludwig-Maximilians-Universität München, Sektion Kristallographie, München, Germany
³Oxford Instruments plc, High Wycombe, United Kingdom

Bivalves and gastropods contain both, calcite and aragonite within their shells (e.g. Checa & Rodriguez-Navarro 2005, Checa et al. 2009). The transition between these phases is neither interlinked nor gradual, it is abrupt and occurs within a spatial range of one to two microns.

We have investigated in the shell of the modern oyster *Crossostrea gigas* the transition zone between the calcite and the aragonite portion of the shell with TEM (Fig.1) and high-resolution EBSD (Fig. 2). Adult oyster shells are composed mainly of calcite. However, there are small areas within the shell where aragonite is present, shell portions where the muscles (the two adductor muscles, the Quenstedt muscles and the pedal muscles) are attached to the skeleton. Thus, the presence of aragonite at these skeletal parts is required for the overall function of the shell.

Our TEM results (Fig. 1) show gradual increase of the order in the aragonite layers, starting from well-ordered aragonite platelets (Fig. 1 left) over smaller, less well developed plates into a sparsely crystallized crystallites exhibiting frayed edges (Fig. 1, right). The rudimental order of the outmost portion of the aragonitic layer is also visible in the EBSD map, where the indexing decreases towards the calcite-aragonitic interface (Fig. 2). Our high-resolution EBSD results (Fig. 2) demonstrate the abrupt switch between fibrous calcite and the patchy appearance of aragonite within the transition zone. At some distance away from the transition zone aragonite platelets get ordered and form the well-known assemblage of aragonite plates.



Fig. 1. TEM images showing the mode of nacre platelet formation within the calcite - aragonite transition zone.

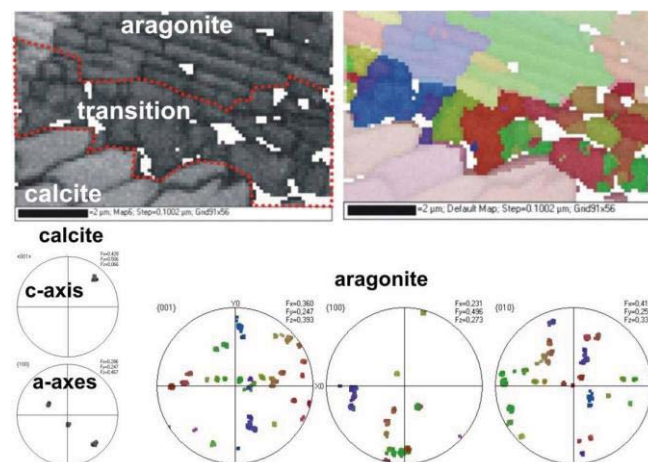


Fig. 2. EBSD results from the calcite - aragonite transition zone and adjacent calcite and aragonite shell portions.

MS16-T04

Crystallographic assembly of the coccolith elements of *Emiliania huxleyi*- an electron diffraction study

R. Hoffmann¹, A. Wochnik², S. Betzler², A. Müller², S. Matich³, E. Griesshaber¹, J. Young⁴, H. Schulz⁵, M. Kučera⁵, C. Scheu², W.W. Schmahl¹

¹LMU Munich, Earth and Environmental Sciences, Munich, Germany

²LMU Munich, Chemistry, Munich, Germany

³TUM, Walter-Schottky-Institut, Garching, Germany

⁴Natural History Museum, London, United Kingdom

⁵Eberhard Karls University, Geosciences, Tübingen, Germany

Coccolithophores are one of the most important primary producers in the recent oceans. These marine single-celled algae contribute to the global ocean biomass with roughly 15 %. Their exoskeleton composed of calcium carbonate (CaCO₃), is the major component among calcareous deep sea sediments. During the cretaceous these small algae formed rocks like the White Cliffs of Dover. Hence the coccolithophore plates, the so called coccoliths, are of high interest for several geological and mineralogical questions like paleoclimate studies and biomimetic applications.

This study concentrates on the crystallographic assembly within a single coccolith, in particular the coccolithophore species *Emiliania huxleyi*. The coccoliths of this species are assumed to consist of upper and lower shield elements and a central area element [1]. According to Young et al. [2] the coccoliths are composed of two different units: the radial R-unit with the crystallographic c-axis oriented parallel to the coccolith plane and the vertical V-unit with the c-axis perpendicular oriented to the coccolith plane. The biomineralization of *E. huxleyi* coccoliths starts with the formation of a Protococcolith ring with an alternating sequence of V- und R-units [2]. During the crystal growth the species specific morphology forms and the V-unit will be overgrown by the R-unit [2] (fig.1).

In our work we used cross-sectional transmission electron microscopy (TEM) samples to investigate the crystallographic assembly of the R-unit in detail. The samples were prepared by focused ion beam (FIB) sectioning with a Zeiss NVision40. For the TEM measurements a FEI S/TEM Titan equipped with an energy-dispersive X-ray spectrometer and a Gatan imaging filter was used. To gain information about the crystallographic orientation and assembly of the R-unit we mainly applied electron diffraction. The experiments were conducted at 80 kV and a low dose to prevent the beam sensitive CaCO₃ from beam damage and phase transformation. We did the diffraction experiments without changing the angle to see if the orientation of the upper- and lower shield elements as well as the central area element differs. So far we found three different orientations within the R-unit. The diffraction patterns indicate that the upper shield-, the lower shield- and the central area elements have different orientations (fig. 2). The c-axis of these three crystals are parallel to the coccolith plane oriented and confirm the model of Young et al. [2]. Until now the existence of an overgrown V-unit in *E. huxleyi* could not be proven. So the aim of our further studies is to detect the V-unit and investigate it in detail, what is according to its expected small size challenging.

- [1] Mann S. (2001) Oxford University Press: Oxford, U.K., 1-198.
- [2] Young J. R., Didymus J. M., Brown P. R., Prins B., Mann S. (1992) Nature, 356, 516-518.

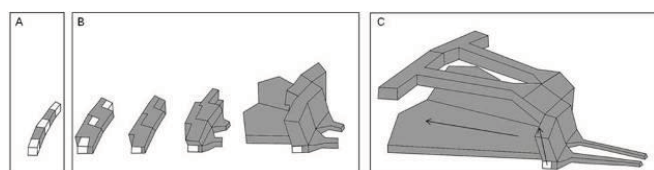


Figure 1: Biomineralization of the coccolith species *E. huxleyi*. A) In the beginning of the mineralization a protococcolithring with alternating V- (white) and R-crystals (grey) is formed. B) During

the crystal growth the species specific ultra structure will be formed. C) In the coccolith species *E. huxleyi* the V-unit will be overgrown by the R-unit. The crystallographic c-axis of the R-unit is parallel to the coccolith plane (black arrow) while the crystallographic c-axis of the V-unit is perpendicular to the coccolith plane (black arrow). Figure modified from [2].

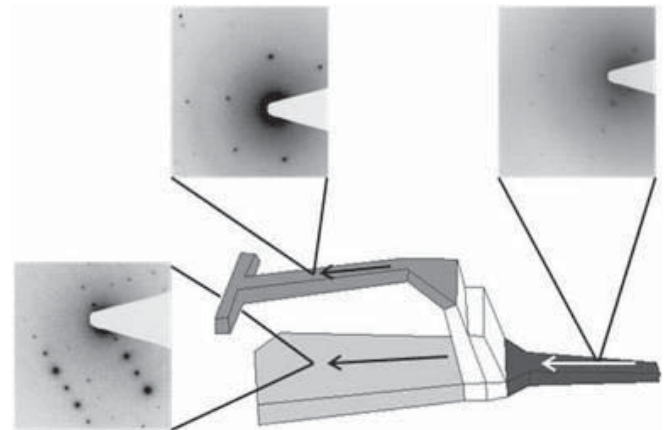


Figure 2: With electron diffraction we found three different orientations in the R-unit of *E. huxleyi*. The shown diffraction patterns were taken with the same angles ($\alpha=11.8$ and $\beta=3.5$) and magnification. The c-axis of the three orientations are parallel to the coccolith plane oriented (black arrows) and confirms the model of Young et al. [2] so far. Schematic drawing modified from [1].

MS16-T05

The nanoscale composite nature of biological materials

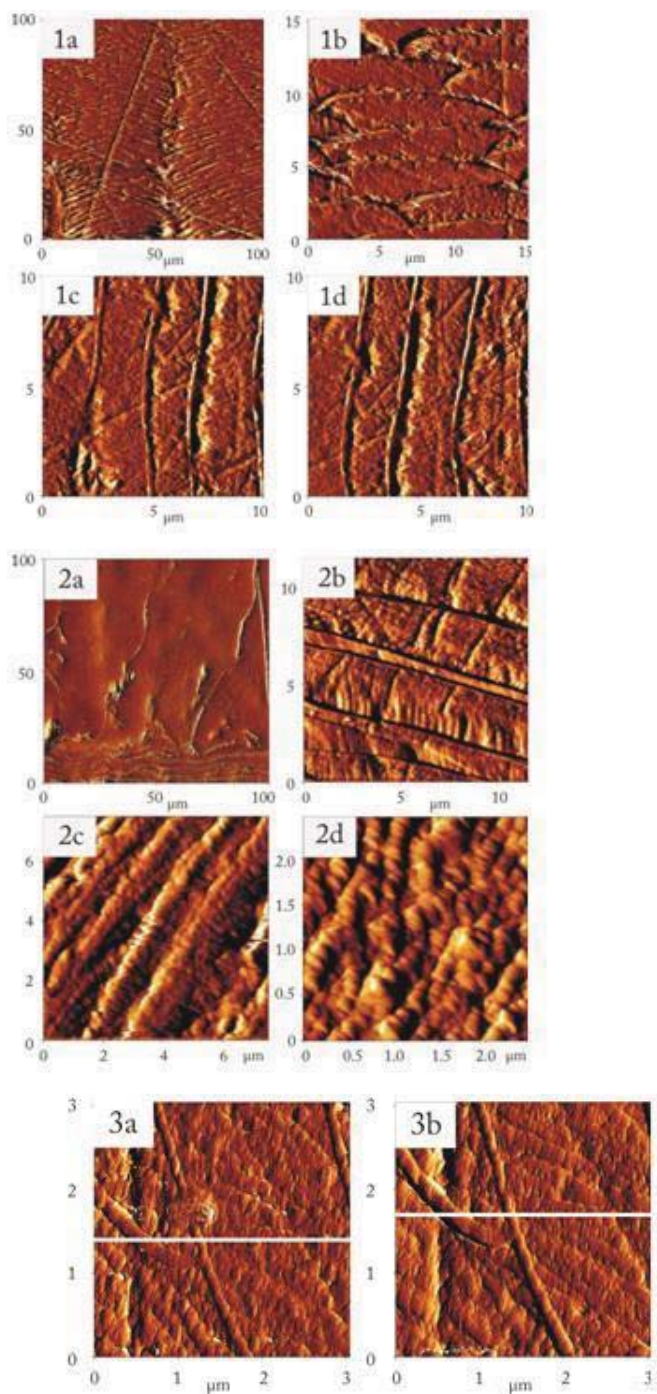
P. Alexa¹, G. Jordan¹, E. Griesshaber¹, W.W. Schmahl¹

¹LMU, Department of Geo- and Earth Sciences, Munich, Germany

In order to highlight the composite nature and nanoscale internal structure of carbonate biomaterials we performed dissolution experiments and monitored the changes with AFM. The investigated samples were skeletons of modern calcitic brachiopods, sea urchin teeth and sea urchin spines. By using different solutions in the AFM cell, both components, the organic and the inorganic component present within the skeletons could be dissolved selectively. The mineral phase was dissolved by using distilled water, the organic polymers within the skeletons were digested with the enzymes trypsin and chitinase. The resulting morphology highlighted the dissolved and the remaining undissolved components. Thus the nanoscale structure of both, the inorganic and the organic components (Figures 1 and 2) as well as their dissolution behavior and distribution pattern in the skeleton (Figure 3) could be resolved in-situ.

Figures 1 and 2. Arrays of brachiopod fibres in the shell of the modern brachiopod *Magellania venosa*. The fibres are lined by organic sheaths (e.g. Figs. 1c, 1d, 2b) and have an internal granular nanostructure (Figs. 2b, 2c, 2d).

Figure 3. Dissolution of brachiopod calcite for 1 hour by distilled water. Figs. 3a and 3b show in AFM images brachiopod fibre structures before and after water was used to leach the calcite component. Fig. 3c shows the height of the sample at the position of the white line in Figs. 3a and 3b before (red graph in 3c) and after (black graph in 3c) the dissolution experiment. The difference in height shows that calcite has been dissolved in contrast to the organic sheaths around the fibres.



MS17-T01

The control of material properties by polyhedral tilting

R. Angel¹, B. Mihailova², R. Pentcheva³

¹Universita di Padova, Geoscienze, Padova, Italy

²Universitaet Hamburg, Geosciences, Hamburg, Germany

³Universitaet Muenchen, Earth and Environmental Sciences, Muenchen, Germany

Designed response of framework structures such as feldspars and perovskites to changes in pressure, temperature and the extra-framework cations can be achieved by understanding the tilting of the strongly-bonded polyhedra. In the perovskites, the complex tilt patterns can be decomposed in to a combination of six fundamental tilts [1] that have been shown to act as the symmetry-breaking order parameters that relate the structural evolution of perovskites to their thermodynamic and elastic properties [2]. Tilts are therefore not only the appropriate fundamental description for the evolution of framework structures, but play a fundamental role as

some of the symmetry-adapted modes in determining electrical, physical and thermodynamic properties of these materials.

When the symmetry-breaking in perovskites is caused by octahedral cation ordering in layers the resulting tilt systems are not simply either ‘in-phase’ or ‘anti-phase’ about each single axis as has been suggested. The correct description of the symmetry-breaking shows that both tilts co-exist, leading to a pattern of octahedral rotations that looks ‘anti-phase’ but is not. The correct description of both tilts and changes in one result in obvious correlations with the change in the electronic structures of thin films of these materials [3].

In feldspars the topology of the framework means that the tilts are not symmetry-breaking, although they control the elastic, chemical and physical properties of the material. Nonetheless, the idea of symmetry-breaking tilts of tetrahedra can be adapted to such a case. The decomposition of the variation of the feldspar structure in to the four fundamental tilts that were previously defined by Megaw [4], and the construction of an exact rigid-body model of the framework can be used to show how the various tilts change the unit-cell parameters, and thus explain the unusual and large elastic anisotropy of the structure.

[1] Glazer (1972)Acta Cryst B28, 3384-3392.

[2] e.g. Carpenter et al. (2005)Phys Rev B72, 024118; Wang & Angel (2011)Acta Cryst B,67, 302.

[3] Blanca-Romero & Pentcheva (2011) Phys. Rev. B 84, 195450

[4] Megaw (1974) in “The Feldspars”, eds Mackenzie & Zussman.

MS17-T02

Structure and properties of the multiferroic BaTiO₃/Fe(001) interface

H.L. Meyerheim¹, F. Klimenta¹, A. Ernst², K. Mohseni¹, S. Ostanin²,

M. Fechner², S. Parihar¹, I.V. Maznichenko³, I. Mertig^{1,3}, J. Kirschner¹

¹MPI f. Mikrostrukturphysik, Experimental Dept. (I), Halle, Germany

²MPI f. Mikrostrukturphysik, Theory Dept., Halle, Germany

³Martin-Luther-Universität Halle-Wittenberg, Institut f. Physik, Halle, Germany

We present a combined surface x-ray diffraction (SXRD) and theoretical study of the multiferroic BaTiO₃/Fe(001) junction [1]. Multiferroic tunnel junctions have become an important theme in solid state research because of their potential for developing new device architectures on the nanometer scale. Theoretical work has established the importance of the interface bonding between the FE barrier and the ferromagnetic (FM) electrode [2-5]. In this context, the BaTiO₃/Fe(001) junction represents an archetype system in which the classical FE film is combined with the FM electrode in an almost perfect lattice match (misfit 1.4 %). Surprisingly, current knowledge is limited to theoretical predictions, while quantitative structure information on growth, film and interface structure is not available so far. Ultrathin BaTiO₃ films were grown on Fe(001) by pulsed laser deposition. The SXRD measurements were carried out by using Co-K α radiation generated by a rotating anode generator. In contrast to common assumptions we find that BaTiO₃ films are characterized by the presence of complete unit cells (m) terminated by a BaO-layer, schematically written as: Fe/(TiO₂-BaO)_m. Onset of polarization is observed at a minimum thickness of two unit cells. Fig. 1(a) and (b) schematically show the m=1 and m=2 structures in side view, respectively. Distances are given in Ångstrom units. The parameter δ represents the height of the cation above ($\delta > 0$) or below ($\delta < 0$) the plane of oxygen atoms. For the m=1 sample, we find $\delta = 0.00$ at the first TiO₂ layer, while $\delta = -0.23$ for the top BaO layer to ensure a flat surface charge profile. Large values for δ (0.46 Å) are found for the m=2 structure at the TiO₂ layers.

Based on the quantitative atomic positions first principles calculations indicate that the BaTiO₃/Fe(001) junction is multiferroic in nature. We find a significant multiferroic effect as a result of the substantial polarizations given by the relative Ti-O

displacements in the 0.4 Å range.

Acknowledgments: We thank F. Weiss for technical support. This work is supported by the DFG through SFB 762

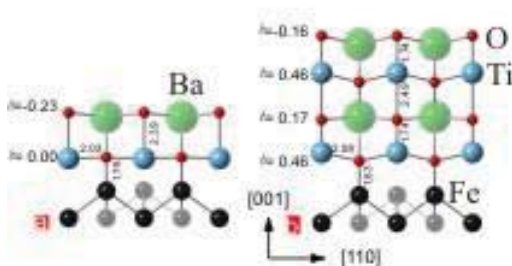
References:

[1] H.L. Meyerheim, F. Klimenta, A. Ernst, K. Mohseni, S. Ostanin, M. Fechner, S.S. Parihar, I.V. Maznichenko, I. Mertig, and J. Kirschner, *Phys. Rev. Lett.* 106, 087203 (2011)
 [2] E. Y. Tsybal and H. Kohlstedt, *Science* 313, 181 (2006).
 [3] C.-G. Duan, S. S. Jaswal, and E. Y. Tsybal, *Phys. Rev. Lett.* 97, 047201 (2006).
 [4] J. P. Velev, C.-G. Duan, K.D. Belashenko, et al., *J. Appl. Phys.* 103, 07A701 (2008)
 [5] M. Fechner, I.V. Maznichenko, S. Ostanin, A. Ernst, J. Henk, P. Bruno, and I. Mertig, *Phys. Rev. B* 78, 212406 (2008)

[1] I. Bloom, M. C. Hash, J. P. Zebrowski, K. M. Myles, M. Krumpelt, *Solid State Ionics* 53-56 (1992) 739.
 [2] S. Zha, J. Cheng, Y. Liu, X. Liu, G. Meng, *Solid State Ionics* 156 (2003) 197.
 [3] J. Schreuer, M. Burianek, M. Mühlberg, B. Winkler, D. J. Wilson, H. Schneider, *J. Phys.: Condensed Matter* 18 (2006) 10977.
 [4] M. Burianek, M. Mühlberg, M. Woll, M. Schmücker, T. M. Gesing, H. Schneider, *Cryst. Res. Technol.* 44 (2009) 1156.

MS17-T04
Structure of disordered Mo-Nb-V-Oxide precursor materials from Pair Distribution Function Analysis

R. Nader¹, T. Kardash², L. Plyasova²
¹Universität Erlangen, Institut für Kristallographie, Erlangen, Germany
²Russian Academy of Sciences, Boreskov Institute of Catalysis, Novosibirsk, Russian Federation



MS17-T03
Structure-property relationships in mullite-type Bi₂M₄O₉ (M = Fe, Ga) and Bi₂Mn₄O₁₀

J. Schreuer¹, T. Krenzel¹, M. Mühlberg², M. Burianek², H. Schneider²
¹Ruhr-Universität Bochum, Institut für Geologie, Mineralogie und Geophysik, Bochum, Germany
²Universität Köln, Institut für Kristallographie, Köln, Germany

Recently mullite-type oxides of the composition (Bi_{1-x}A_x)₂M₄O_{9-x} with A = Sr²⁺, Ca²⁺ and M = Al³⁺, Fe³⁺, Ga³⁺ attracted considerable interest because of their promising thermomechanical and electrical properties [1,2]. For example, the oxygen ion conductivity of Sr-doped Bi₂Al₄O₉ ceramics was described to be superior to that of yttrium stabilized zirconia at 1073 K [2]. Interest in these materials was further stimulated by the catalytic behavior of Bi₂Fe₄O₉ and the magnetic properties of Fe- and Mn- containing crystal species. In order to better understand the structure-property relationships large single crystals of orthorhombic Bi₂Ga₄O₉, Bi₂Fe₄O₉ and Bi₂Mn₄O₁₀ were grown using the top-seeded solution growth (TSSG) technique [3,4] and their thermal expansion behavior and elastic properties were studied in a broad temperature range up to about 1200 K by means of single crystal dilatometry and resonant ultrasound spectroscopy, respectively.

The anisotropy of the elastic and thermoelastic properties of the Bi-compounds is dominated by the characteristic mullite-type chains of edge-sharing octahedra running parallel [001]. The relatively small variations of the elastic anisotropy within the (001) plane is attributed to the specific type of cross-linking of the octahedral chains. The temperature evolution of the individual elastic constants shows no hint on any structural instability or glass-like transition that might be related to the suspected onset of ion conductivity at high temperatures. On the other hand characteristic ultrasound dissipation phenomena, observed in the ultrasonic frequency regime close to room temperature, are interpreted in terms of anelastic relaxation of point defects. The smallest thermal expansion is observed in the (001) plane and not parallel [001], the direction of the stiffest octahedral chains. A model will be discussed to explain the apparent discrepancy in terms of cross-correlations within the three-dimensional framework of edge- and corner-linked coordination polyhedra.

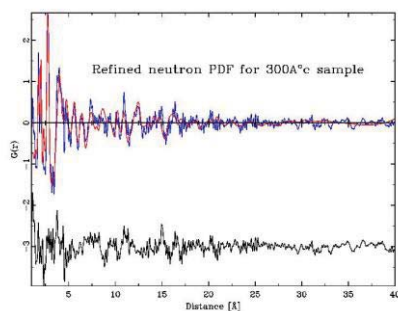
p { margin-bottom: 0.21cm; }

Mixed Mo-Nb-V oxide materials are active catalysts, where the effectiveness of the catalytic activity depends on the Vanadium content and the structural characteristics of the material. The title compound is synthesized from initial precursors by annealing at variable temperatures from 200°C to 600°C. At the highest temperature a well crystallized material forms. This is characterized by a pentagonal bipyramidal coordination of Mo/Nb by oxygen. This unit is surrounded by five edge sharing octahedra and these extended units finally link to each other via corner sharing octahedra. EXAFS data indicate that in the final stages of the synthesis Nb partially migrates from the pentagonal unit to the surrounding octahedral sites.

The material synthesized at approximately 300°C shows the highest catalytic activity. Its powder diffraction pattern consists of very broad peaks except for the 001 reflection. Thus this material consists of nanostructured objects with some 3 nm in diameter. Samples annealed at 400°C indicate predominantly a growth along the c-axis.

To analyze the local structure of these materials X-ray and neutron powder diffraction data were collected at the APS and Los Alamos respectively. Room temperature data were converted to the Pair Distribution Function (PDF). The neutron data for the samples synthesized at lower temperature required special care to correct for a background by incoherent scattering. The experimental PDF's for all samples indicate a fairly complex crystal structure. Within the distance range up to some 1.5 nm the PDF's of all samples are very similar. This shows that the local structure forms early during the synthesis process at low temperatures, followed by a growth in size.

As the PDF's even of the low temperature samples are too complex for an ab initio structure determination, a reverse analysis was chosen. First the structure of the 500°C compound was refined versus both the neutron and X-ray PDF's. This combined refinement was essential, as the materials consists of heavy elements (Mo,Nb) and oxygen, which dominate the X-ray and neutron PDF's respectively. The result of this refinement was taken as the starting structure for the low temperature samples. All three refinements yield a well refined local structure. The 500° sample shows remarkable differences between the local and long range structure. The 300 and 400° samples indicate a local structure consisting of MoO₇ units surrounded by edge sharing octahedra. The main difference between these two sample is the growth along the c-axis.



MS17-T05

Filling vacancies in Ge/Sb/Te materials with lithium

T. Schröder¹, S. Schwarzmüller¹, M.N. Schneider¹, O. Oeckler^{1,2}

¹LMU Munich, Chemistry, Munich, Germany

²University of Leipzig, IMKM, Leipzig, Germany

The structural chemistry of long-periodically ordered compounds $(\text{GeTe})_n(\text{Sb}_2\text{Te}_3)$ is determined by the vacancy concentration ($1/(n+3)$ cation vacancies per anion). Compounds with $n \geq 3$ exhibit disordered rocksalt-type high-temperature phase before melting incongruently; the transition temperature depends on n . Quenching such high-temperature modifications with $n \geq 4.5$ yields metastable pseudocubic phases with intersecting defect layers. Quenching compounds with a higher vacancy concentration, i.e. smaller n , yields rhombohedral phases with parallel van der Waals gaps between rocksalt-type slabs similar to the stable ambient-temperature modifications of all these compounds. The metastable phases are an intriguing class of thermoelectrics with ZT values up to 1.3.^[1,2]

At 450 °C, where the ZT values are maximal, cation (and thus vacancy) diffusion is fast, so that the quenched pseudocubic samples transform to the rhombohedral layered ones within hours. Therefore, the stabilization of the (pseudo-)cubic samples is of great interest. Decreasing the vacancy concentration is one way to efficiently stabilize such compounds. This can be achieved by replacing part of the Ge^{II} with twice the amount of Li^{I} , and thus filling the vacancies with lithium. The resulting series of new compounds $(\text{GeTe})_n(\text{Sb}_2\text{Te}_3)(\text{Li}_2\text{Te}) = (\text{GeTe})_n(\text{Li}_2\text{Sb}_2\text{Te}_4)$ exhibits average rocksalt-type structures for $n = 1, 2, 3$ as shown by Rietveld refinements. Temperature programmed powder X-ray diffraction shows that these are stable with respect to the temperature. For $n = 6$, quenching is required to obtain a homogeneous (pseudo)-cubic phase whereas for $n = 11$ none of the various temperature treatments yields pseudocubic samples. In this case, the average structure at ambient temperature corresponds to a disordered GeTe type and the compound exhibits a reversible trigonal to cubic phase transition comparable to GeTe itself; however, at much lower temperature. This means that the cubic phase of $\text{Li}_2\text{Ge}_{11}\text{Sb}_2\text{Te}_{15}$ is energetically more favorable than that of GeTe. For all samples, layered compounds similar to $(\text{GeTe})_n(\text{Sb}_2\text{Te}_3)$ were not observed as the filled voids are not compatible with the formation of van der Waals gaps. Currently, neutron diffraction experiments are performed in order to reliably locate lithium atoms in the crystal structure.

[1] T. Rosenthal, M. N. Schneider, C. Stiewe, M. Döblinger, O. Oeckler, *Chem. Mater.* **2011**, 23, 4349.

[2] M. N. Schneider, T. Rosenthal, C. Stiewe, O. Oeckler, *Z. Kristallogr.* **2010**, 225, 463.

MS17-T06

In situ X-ray characterization and crystallographic investigation of inorganic catalysts for ammonia decomposition

C. Weidenthaler¹, V. Tagliazucca¹

¹Max-Planck-Institut für Kohlenforschung, Heterogene Katalyse, Mülheim an der Ruhr, Germany

The decomposition of ammonia is one way to produce CO_x -free hydrogen but ammonia can also be used as direct fuel for ammonia-fed solid-oxide fuel cells.[1] As both processes require temperatures above 400°C, highly active catalysts with high temperature stability and long lifetime have to be developed. Supported ruthenium clusters have been shown to be the most active catalysts but high cost and limited availability force the development of alternative active catalysts. At present, transition metal oxides, nitrides and carbides are considered as potential catalysts.

Here we present the preparation of different molybdenum catalysts[2],[3],[4] and their behaviour during ammonia decomposition reaction. The performance of these metal based catalysts depends not only on the surface composition and/or the state of the active species. An important role has also been attributed to the microstructure of the catalysts such as specific surface area, domain size distribution or lattice defects. In order to understand the role of the microstructure properties such as crystalline domain size and the presence of distortion on the catalytic activity, the catalyst powders were ball milled before the reaction. The effect of milling on the ammonia conversion was studied by means of X-ray powder diffraction and electron microscopy studies. From line profile analysis (Whole Powder Pattern Modelling) domain size distributions and dislocation densities of the different samples could be calculated by exploiting the PM2K program based on an implementation of the WPPM algorithm.[5]

Phase transformation processes taking place under reaction conditions, as well as changes of the crystal structure and the microstructure were studied by means of in situ X-ray powder diffraction. Their in situ diffraction experiments were conducted under reaction conditions in a XRK900 reaction chamber (Anton Paar) mounted on an X'Pert Pro diffractometer (PANalytical) in Bragg-Brentano geometry. It was found that for molybdenum oxide catalysts, structural changes at low temperatures are important steps in the formation process of the catalytically active crystalline phases. With the changes of the crystal structure, the microstructure and with this the catalytic activities of the catalyst are positively influenced.

[1] M. Ni, M. K. H. Leung and D. Y. C. Leung, *Int. J. Energy Res.* **33** (2009) 943-959

[2] M. Schwickardi, T. Johann, W. Schmidt, F. Schüth, *Chem. Mater.* **14** (2002) 3913-3919

[3] M. Pechini, U.S. Pat. No. 3 330 697, July 11, 1967

[4] C. Giordano, C. Erpen, W. Yao, and M. Antonietti, *Nano Lett.*, **2008**, 8, 4659-4663

[5] M. Leoni, T. Confente and P. Scardi, *Z. Kristallogr. Suppl.* **23** (2006) 249-254

MS17-T07

Wasserdesinfektion mittels pyroelektrischen mikro- und nanokristallinen LiNbO_3 und LiTaO_3

E. Mehner¹, A. Benke², E. Gutmann^{1,3}, K. Gerth², D.C. Meyer¹

¹Institut für Experimentelle Physik, Fakultät Physik und Chemie, Freiberg, Germany

²Institut für Werkstoffwissenschaft, Fakultät Maschinenwesen, Dresden, Germany

³GMBU, Fachsektion Jena, Jena, Germany

In der Wasseraufbereitung kommen zur Desinfektion häufig Chlor und Chlorverbindungen zum Einsatz. Um dem Gesichtspunkt

Umweltverträglichkeit Rechnung tragen zu können und zur Vermeidung von gesundheitsschädlichen Substanzen, sind in den letzten Jahren alternative Desinfektionsmethoden in den Fokus der Forschung gerückt [1-5]. In die Kategorie der "Advanced Oxidation Processes" ordnet sich die hier untersuchte Desinfektion von *Escherichia coli* mittels mikro- und nanokristallinem Lithiumniobat und Lithiumtantalat ein.

Die Methode nutzt die Ferro- und Pyroelektrizität der Materialien aus. Das heißt, das Vorhandensein einer spontanen elektrischen Polarisierung im Material, welche sich mit der Temperatur ändert und so in wässrigen Medien eine pyroelektrokatalytische Wirkung entfaltet. Es zeigt sich eine klare Abhängigkeit der antimikrobiellen Wirkung von der Partikelgröße, welche anhand von Referenzversuchen mit Fluoreszenzfarbstoffen (DCFH) der Bildung von reaktiven Sauerstoffspezies zugeschrieben wird.

Zum Einsatz kamen sowohl aus kommerziellen Einkristallen, durch Aufmahlung und Siebfraktionierung, hergestellte, als auch eigens zu diesem Zweck solvothermal synthetisierte Lithiumniobat- und Lithiumtantalat-Pulver. Sämtliche Proben wurden hinsichtlich ihrer Morphologie und Struktur per Rasterelektronenmikroskopie (REM) und Röntgendiffraktometrie (XRD) charakterisiert, um den Einfluss von Partikelgrößeneffekten zu untersuchen und die Herstellungsrouten optimieren zu können.

[1] Oppenländer, T. Photochemical Purification of Water and Air; Wiley-VCH: Weinheim, 2003.

[2] Kühn, K.P.; Chaberny, I.F.; Massholder, K.; Stickler, M.; Benz, V.W.; Sonntag, H.-G.; Erdinger, L. *Chemosphere* 2003, 53, 71-77

[3] Chong, M.N.; Jin, B.; Chow, C.W.K.; Saint, C. *Water Res.* 2010, 44, 2997-3027

[4] Chen, C.; Ma, W.; Zhao, J. *Chem. Soc. Rev.* 2010, 39, 4206-4219

[5] Zhang, D.; Li, G.; Yu, J. *C. J. Mater. Chem.* 2010, 20, 4529-4536.

MS18-T01

Experimental Facilities for Macromolecular Crystallography at Diamond Light Source

R. Flaig¹, A. Ashton¹, D. Axford¹, J. Brandao¹, A. Douangamath¹, L. Duke¹, G. Evans¹, D. Hall¹, K. McAuley¹, J. Nicholson¹, R. Owen¹, P. Romano¹, J. Sandy¹, J. Sanchez-Weatherby¹, T. Sorensen¹, M. Williams¹, G. Winter¹
¹*Diamond Light Source, Science, Didcot, United Kingdom*

Diamond Light Source [1] is the UK third generation synchrotron facility located south of Oxford. In the first Phase the structural biology community was served by the macromolecular crystallography (MX) beamlines I02, I03 and I04 starting with the user programme in early 2007. These widely tuneable (5-25 keV) SAD/MAD beamlines were complemented in Phase 2 with a MAD capable microfocus beamline I24 (7-25 keV) and a fixed-wavelength high-throughput station I04-1 (13.53 keV). In Phase 3 the long wavelength beamline I23 (3-12 keV), which is in the planning and construction stage, will complement the MX beamline portfolio [2].

In order to adapt to the future scientific requirements of the structural biology community and to increase efficiency, various areas of the beamlines are being improved and new techniques explored. The automation system is constantly being improved, including a quicker sample exchange with the sample transfer robot and automatic loop finding and centering procedures. All beamlines can now also be fully operated remotely. Three beamlines (I03, I04-1, I24) are now equipped with fast Pilatus detectors and it is planned to provide the other beamlines with fast detector systems as well. This leads to an increase in efficiency and throughput and allows for new methods like faster grid scans for locating hardly visible samples or to find the best area of a larger sample. Data collection strategies and crystal and diffraction image characterization are provided automatically. Very shortly after the data collection has finished the results from our automatic data processing pipeline are available and this extends now to the generation of difference electron density maps if a suitable PDB file is provided.

More recently, an upgrade programme for the experimental end-stations of the Phase 1 MX beamlines (I02, I03, I04) has been initiated and is nearing completion. The completely new design allows for an easier change between experiments at cryo or room temperature or a humidity controlled setup. In-situ screening of crystallization plates is also actively being developed on all beamlines. Beam delivery to the Phase 1 beamlines will be with a refurbished bimorph KB mirror system providing typical beam sizes of 80 µm x 20 µm over the complete energy range. Furthermore, the new end-station is also equipped with two sets of compound refractive lenses (CRL) providing a beam size of 8 x 2 microns, thus enabling microfocus and standard beam size work easily on the same beamline. The implementation of a mini kappa goniometer head is being developed which will allow for more sophisticated data collection strategies. Some new developments and preliminary results will be discussed. Use of the Diamond MX beamlines has resulted in the deposition of 731 structures to the PDB so far and productivity has increased since the start of operation.

[1] <http://www.diamond.ac.uk>

[2] <http://www.diamond.ac.uk/Home/Beamlines/MX.html>

Keywords: Diamond Light Source, macromolecular crystallography, beamlines

MS18-T02

Patterson function solution by δ recycling

J. Rius¹

¹*Institut de Ciència de Materials de Barcelona (CSIC), Dpt. de Cristallografia, Bellaterra, Spain*

Recently, the new direct methods algorithm called "δ recycling" has been introduced (Rius, 2012). This algorithm may be regarded as the direct space counterpart of the origin-free modulus sum function (Rius, 1993) which was entirely defined in reciprocal space. It requires the approximate chemical composition of the compound and the intensity data measured up to atomic resolution. The δ recycling algorithm is based on the properties of the δ syntheses

$$\delta_P(\mathbf{r}) = V^{-1} \sum_{\mathbf{H}} (E_{\mathbf{H}}^2 - \langle E^2 \rangle) \cdot \exp(i\phi_{\mathbf{H}}) \cdot \exp(-i2\pi\mathbf{H}\mathbf{r})$$

which provides an alternative form of calculating the electron density function (Rius, 2012). In this expression P stands for (P)atterson since $E^2 - \langle E^2 \rangle$ are the Fourier coefficients of the origin-free Patterson function. By analogy, the alternative δ_M function can be defined by using the coefficients of the origin-free (M)odulus function, i.e. $E - \langle E \rangle$. For simplicity, the P and M subindices will be omitted hereafter to allow both cases to be treated in a unified way. The standard deviation of the δ synthesis, $\sigma(\delta)$, can be calculated from the experimental data and is phase-independent. This permits the background removal of δ by simply equating to zero those regions below $\Delta = 2.5 \cdot \sigma(\delta)$, thus yielding the modified δ_{Δ} function. Phase refinement begins by assigning randomly generated phase values. New phase estimates are obtained by evaluating the integral

$$\phi_{\mathbf{H}}^{\text{new}} = \sqrt{\int \delta_{\Delta}(\mathbf{r}) \cdot \exp(i2\pi\mathbf{H}\mathbf{r}) dV}$$

This integral is computed by searching for the δ_{Δ} peaks (to a maximum number fixed by the unit cell content) and by the posterior calculation of the corresponding structure factors. The new amplitudes (E) are compared with experimental ones (E_o) through the correlation coefficient (CC)

$$CC^2 = (\sum E_o \cdot E)^2 / (\sum E_o^2) / (\sum E^2)$$

to show the evolution of the phase refinement, and the new phase estimates are used to calculate the next δ synthesis, completing in this way one δ refinement cycle. δ recycling finishes when a preset number of cycles is reached. If the final R value is lower than a preset minimum value, structure solution ends. This algorithm has been implemented in program XLENS@_P2 (www.icmab.es/xlens).

The δ recycling algorithm both for δ_p and δ_M has been successfully applied to a variety of single-crystal diffraction data of inorganic and organic compounds.

References:

- Rius, J. 1993. Derivation of a new tangent formula from Patterson-Function arguments. *Acta Cryst.* A49, 406-409.
 Rius, J. 2012. Direct phasing from Patterson-syntheses by delta recycling. *Acta Cryst.* A68, in press.

MS18-T03

Mapping rocking curves of large crystals with high spatial resolution.

R. Loetzsch^{1,2}, I. Uschmann^{1,2}, E. Förster^{1,2}

¹Helmholtz Institut Jena, Jena, Germany

²Friedrich-Schiller-Universität, Institut für Optik und Quantenelektronik, Jena, Germany

We developed a system to map rocking curves with high spatial resolution on a standard X-ray tube applicable at cryogenic temperatures. A toroidally bent crystal is used to provide a convergent beam with small bandwidth. If this beam impinges on the sample, the angular dependency of the reflectivity in the diffracted beam, i.e. the rocking curve, is converted to a spatially varying intensity. These variations can be recorded with a position sensitive detector, such as a CCD camera. Thus the whole rocking curve could be recorded at once. If the sample is placed behind the focus of the toroidally bent crystal, a whole line on the sample is reflecting, and in the vertical direction the intensity on the detector is directly related to different vertical positions on the sample. Thus it is possible to record simultaneously one-dimensionally resolved rocking curves. Combining this with one lateral movement of the sample, rocking curves can be mapped in two dimensions within short measuring times. The sample is mounted on a helium flow cryostat, allowing to measure rocking curve maps in the temperature range between 300 K and 4 K.

The angular resolution of the setup is determined first by the FWHM of the monochromatic radiation reflected by the bent crystal, which depends on its reflection curve width and the variation of the Bragg angle over its surface and amounts to $7 \cdot 10^{-5}$. Secondly the angular resolution depends on the source size, which is the limiting factor here. For a source size of 40 μm , implemented by a slit in our setup, it amounts to $1 \cdot 10^{-4}$.

The setup is used to investigate the twin domain distribution and the lattice parameter variations associated with the displacive phase transition in SrTiO_3 . By using $\text{Ti-K}\alpha$ (4.5 keV), the probed region is the first micrometer near the surface. We find a very inhomogeneous domain distribution, showing both regions with large monodomains and highly twinned regions, as well as large needle domains. Also the lattice parameters in these different regions vary substantially.

MS18-T04

High-Definition X-ray Polarimetry

B. Marx¹, K.S. Schulze^{1,2}, I. Uschmann^{1,2}, T. Kämpfer^{1,2}, R. Löttsch^{1,2}, O. Wehrhan^{1,2}, W. Wagner³, C. Detlefs⁴, T. Roth⁴, J. Härtwig⁴, E. Förster^{1,2}, T. Stöhlker², G.G. Paulus^{1,2}

¹Friedrich-Schiller-Universität Jena, Institut für Optik und Quantenelektronik / AG Röntgenoptik, Jena, Germany

²Helmholtz-Institut Jena, Jena, Germany

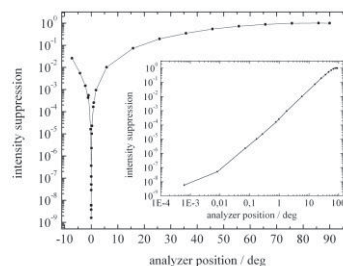
³Helmholtz-Zentrum Dresden-Rossendorf, Dresden, Germany

⁴European Synchrotron Radiation Facility, Grenoble, France

A X-ray polarimeter with extremely high polarization purity is developed at the IOQ in Jena. The motivation for this is a project aiming to observe the vacuum birefringence. By focusing a high-intensity laser pulse in vacuum, the vacuum behaves, induced by the strong electric fields, as a birefringent medium. In interaction with the latter a linearly polarized X-ray pulse will show a small degree of elliptical polarization, in general. With laser intensities of 10^{22}W/cm^2 a X-ray polarimeter with a polarization purity of better than $\delta = 10^{-11}$ is necessary.

To reach this high degree of polarization a polarizer-analyzer setup, based on multiple reflections of synchrotron radiation in channel-cut crystals at Bragg angles near 45° is put into practice. In first experiments at the European Synchrotron Radiation Facility, we have improved the state-of-the-art in X-ray polarimetry by nearly 3 orders of magnitude to the level of $\delta \sim 2.4 \cdot 10^{-10}$.

Fig. 1: Polarization purity measurement for the 400-reflection of a silicon channel-cut polarizer-analyzer set-up. A polarization purity of $1.5 \cdot 10^{-9}$ at 6457 eV was observed.



MS18-T05

High-Brilliance X-ray Sources for Biological Crystallography

J. Graf¹, A. Kleine¹, C. Michaelsen¹, C. Ollinger², J. Lange², M. Biadene², O. Hemberg³

¹Incoatec GmbH, Geesthacht, Germany

²Bruker AXS GmbH, Karlsruhe, Germany

³Excillum AB, Stockholm, Sweden

Modern microfocus X-ray sources define the state-of-the-art for single crystal diffraction on small molecules and proteins, as well as for small-angle scattering. These sources are, usually, combined with a multilayer X-ray mirror as a beam shaping device.

Microfocus rotating anode systems deliver flux densities in the range of 10^{11} photons/ s/mm^2 at power loads of up to $20 \text{ kW}/\text{mm}^2$. However, these sources are very pricey and require regular and, sometimes, time-consuming maintenance.

Low power microfocus sealed tube sources represent an interesting low-maintenance alternative to rotating anode generators [1]. Power loads of several kW/mm^2 in anode spot sizes of $< 50 \mu\text{m}$ deliver a small and brilliant beam. Flux densities of up to 10^{10} photons/ s/mm^2 can be achieved in a focused beam suitable for most protein crystals and weak diffracting small molecule samples.

The brilliance of conventional X-ray sources using a solid metal target is limited by the thermal properties of the anode material and by the heat dissipation mechanism which sets a hard limit for future improvements of X-ray sources based on solid metal targets. However, recent breakthroughs in X-ray source technology push the limits further. Using high-speed liquid metal-jet targets (e.g. a

Gallium alloy) instead of fast spinning solid metal targets, power loads of the order of 500 W/mm² can be provided [2]. This type of source combined with state-of-the-art multilayer mirrors paves the way for home-lab instruments with a brilliance comparable to bending magnet sources. This provides highest flux densities at the sample suitable for X-ray diffraction and scattering investigations on very small samples or with very high spatial resolution.

We will be presenting selected results to demonstrate the impact of modern microfocus X-ray sources on the data quality for applications in small molecule and biological crystallography.

[1] J. Wiesmann, J. Graf, C. Hoffmann, A. Hembd, C. Michaelsen, N. Yang, H. Cordes, B. He, U. Preckwinkel, K. Erlacher, *Particle & Particle Systems Characterization* **2009**, *26*, 112. [2] M. Otendal, T. Tuohimaa, U. Vogt, H. M. Hertz, *Rev. Sci. Instrum.* **2008**, *79*, 016102.

MS18-T06

Yell: program for 3D-PDF diffuse scattering analysis.

A. Simonov¹, T. Weber¹, W. Steurer¹

¹ETH, Materials science, Laboratory of crystallography, Zurich, Switzerland

Over the course of its 100 years history conventional x-ray crystal analysis has become a routine procedure. Nowadays even the solution of complex protein structures can be performed within hours. With the current developments in synchrotron light sources and fast area detectors, not only Bragg intensities but also high quality diffuse scattering is readily available. Thus there is a growing interest in diffuse scattering interpretation. As Bragg scattering describes the average distribution of atoms, diffuse scattering provides information about local interactions of the atoms.

In our group we develop the difference-three dimensional pair distribution function (3D- Δ PDF) method for local order analysis. The 3D- Δ PDF is the Fourier transform of diffuse scattering from a single crystal. It contains the information about interactions of pairs of atoms, ignoring atoms which are perfectly ordered as well as those atom pairs, which are fully uncorrelated. In cases when the average structure of a crystal is known, 3D- Δ PDFs can be easily interpreted qualitatively, and by PDF fitting one can obtain quantitative information about local structure correlations.

We present our program "Yell" for 3D- Δ PDF analysis. It can refine all types of fundamental correlations namely size effects, substitutional correlations and correlations of displacements as well as any combinations of those. The program is also capable of dealing with constraints of any arithmetic complexity. Fast Fourier transform based algorithms allow the program to run reasonably fast on desktop computers. In the current contribution we will show important features of the program and applications to several real-world examples of disorder problems.

MS01-P01

Neue SAXS/WAXS-Anwendungen auf einem Vielzweck-Röntgenpulverdiffraktometer

D. Opper¹, T. Schönbeck¹¹PANalytical GmbH, Sales, Kassel, Germany

Seit einigen Jahren wird in den verschiedenen Disziplinen der Werkstoffwissenschaften intensiv an Nanomaterialien geforscht, wie z.B. an Nanopartikeln, Nanokompositen und nanoporösen Materialien. Für eine genaue Charakterisierung der Nanomaterialien sind Analysen hinsichtlich Teilchengröße, Teilchenform, Partikelgrößen-Verteilung, spezifische Oberfläche und Struktur erforderlich.

Die Kleinwinkel-Röntgenstreuung (SAXS) ist ein seit Jahrzehnten bewährtes Verfahren zur Bestimmung der genannten Parameter. Zusätzlich wird in vielen Laboratorien die Röntgenpulverdiffraktometrie für die Phasenanalyse, Kristallitgrößen-Bestimmung und andere Anwendungen eingesetzt. Daher liegt es nahe, die Fähigkeiten moderner Vielzweck-Diffraktometer zu nutzen und mit Hilfe zusätzlicher Komponenten für die Messung der Kleinwinkelstreuung zu erweitern. Bei dieser Kombination ist es wichtig, dass die volle Leistungsfähigkeit des Pulverdiffraktometers erhalten bleibt, aber trotzdem keine Kompromisse hinsichtlich der SAXS-Anwendungen eingegangen werden müssen. Nur so lassen sich Ergebnisse erzielen, die mit denen spezieller Systeme für die einzelnen Anwendungen vergleichbar sind.

In diesem Beitrag werden Ergebnisse von Streuexperimenten an verschiedenen Materialien gezeigt: (1) Kolloidale Si-Lösungen, (2) Kolloidale Gold-Nanostäbe, (3) Mesoporöses SiO₂, (4) Kollagen, (5) Polyethylen. Im Vordergrund steht die Qualität der Ergebnisse bei Verwendung spezieller Röntgenoptiken (Multilayerspiegel, Hybridmonochromator, semitransparenter Primärstrahlfänger); zusätzlich wird die Handhabung der unterschiedlichen Proben in Kapillaren und in speziellen Festkörperhaltern (für Faserpolymere, Pulver, etc.) vorgestellt. Eine verbesserte SAXS-Auswertesoftware wird präsentiert, die es dem Anwender auch ohne vertiefte Kenntnisse der Kleinwinkelstreuung ermöglicht, die Schlüsselcharakteristika von Nanomaterialien zu ermitteln.

MS01-P02

Olex2 - A Complete Package for Molecular Crystallography

H. Puschmann¹, O. Dolomanov¹, L. Bourhis², R. Gildea³¹Durham University / OlexSys, Chemistry, Durham, United Kingdom²Bruker axs, Paris, France³Berkeley Laboratories, Berkeley, United States

Olex2 [1] has become established in the community of small-molecule crystallographers as an easy-to-use unified package that provides tools needed for day-to-day analyses of small molecule structures. There is a rapidly growing number of installations of the software world-wide and our core paper [2] has attracted more than 200 citations in 2011 alone.

Structure Solution is achieved by our own charge-flipping implementation, **olex2.solve**, based on E². Other commonly used solution programs - ShelXS/D, SIR and SuperFlip - can be used for structure solution from within Olex2.

Structure Refinement can be carried out with **olex2.refine**. The refinement engine is based on the cctbx and provides all the functionality required for a meaningful structure refinement. A general system allows the implementation of *any* constraint, which has been used to provide all ShelXL constraints as well as some new constraints. All ShelX restraints have also been implemented. Of course, ShelXL can be chosen as the refinement engine as an alternative to olex2.refine.

The solution and refinement programs are based on the small-molecule toolbox (**smtbx**), that our group has contributed to the family of tools available in the cctbx[3].

Structure Analysis tools covering most requirements are an integral part - growing, packing, geometric measurements, void, molecular

and solvent accessible volume calculation, π - π analysis and many more.

Structure Publication is made easy. Complete and correct CIFs result automatically, the generation of reports is easy and images - bitmaps or ORTEP-style drawings - can be generated with minimum effort.

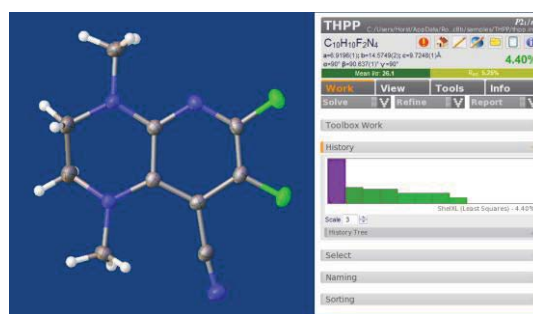
Olex2 is Open Source under the BSD Licence and available free of charge from [1] for academic users for Windows, Linux and MacOSX.

[1] www.olex2.org

[2] Dolomanov, O.V.; Bourhis, L.J.; Gildea, R.J.; Howard, J.A.K.; Puschmann, H., Olex2: A complete structure solution, refinement and analysis program (2009). J. Appl. Cryst., 42, 339-341.

[3] R. W. Grosse-Kunstleve et al, <http://cctbx.sourceforge.net/>

Figure 1



MS01-P03

CHARACTERISATION OF MATTER AND ON SITE QUALIFICATION OF MATERIALS THROUGH X-RAY DIFFRACTION

G. Berti¹¹University of Pisa, Earth Science-Lab.R&D XRD, Pisa, Italy

Since the time when the Family Bragg was going to be awarded by the Nobel prize, in Pisa the young Enrico Fermi was working on x-ray diffraction for his Degree in Physics. Fermi was involved in other theoretical subjects in his life though, his intuition, pushed him to state that finely subdivision of particles were possibly the basic concept for studying the rheology of matter to solicitation in temperature, pressure, mechanic working cycles and so on. This subject is currently still under definition; when using Crystallography and x-ray Diffraction to perform Non Destructive Testing on manufactures in service; several limitations occur.

Since the fifties of last century the continuous filing of crystallographic data and Diffraction patterns are now recognized as basic milestones. In the middle of nineties Bragg Brentano diffractometers for powders were rising in performances when equipped with collimators devices studied by W. Parrish in the application of theory by L. E. Alexander and A.J.C. Wilson [1]. Then Round Robin tests have contributed to rise confidence on either successes and limits; in falling nineties these Round Robin test demonstrated that in spite of highly skilled operators the repeatability and reproducibility of data were limited from a number of different causes. Deviation causes from the expected values were reviewed in standard documents by WG10 of CEN/TC138. [2]

All what aforesaid opens to new challenging objectives and achievements for the second century from the x-ray discovery. The joint application of Crystallography and Diffraction shall provide new concepts, methods, technologies and metrological approach to identify the appropriate set up for early stage diagnoses methods of material components of manufactures.

These challenges start from considering the long standing efforts supported to identify the best procedures and good practices to provide samples and specimens (e. g. certified reference materials)

for the verification of the goniometry optical alignment. These good practices state how and when that specimens shall be manipulated to obtain the best performances of instruments and the best solution methods. These concepts allow to characterize the matter in abstract, independently of the context where the manufacture is in service (or where the nature has put it in place) [3].

In order to qualify the materials (e.g. residual life or consumption) of manufactures, robotics technology, networking (i.e. ICT as the hardware implementation of knowledge), arrangement of neurological networking are becoming the appropriate solutions for the case under investigation wherever they are. To achieve these challenging objectives, one of the key node is the monitoring of the instrument performances and the calibration of measurements in relation to the benchmarks (i.e. nanometer scale and fractions) of the measurements. These benchmarks shall become the origin from where ranking all the unknown cases becoming under investigation.

References:

[1] R. Jenkins, R. L. Snyder (1996), "Introduction to X-ray Powder Diffractometry", Jhon Wiley & Sons ISBN 0-471-51339-3
 [2] EN13925-3 Non destructive testing - X ray diffraction from polycrystalline and amorphous materials - Part 3: Instruments © CEN - AFNOR Paris.
 [3] G. Berti, F. De Marco: "X-Ray Diffraction for Diagnosis at the Nano-Scale". In Proceedings of Symposium of Solving Friction and Wear Problems, Vol 1, Esslingen 2010.

MS01-P05

High-Pressure Cooling of Virus Crystals

A. Burkhardt¹, M. Warmer², A. Wagner³, D. Stuart⁴, R. Reimer², H. Hohenberg², A. Meents¹

¹Deutsches Elektronen-Synchrotron DESY, HASYLAB, Hamburg, Germany

²Heinrich-Pette-Institute for Experimental Virology, Electronmicroscopy, Hamburg, Germany

³Diamond Light Source, Didcot, United Kingdom

⁴University of Oxford, Division of Structural Biology, Oxford, United Kingdom

Most virus structures available to date are obtained from room temperature X-ray diffraction experiments. Virus crystals show comparably weak Bragg reflections and require relatively long exposure times to obtain useful diffraction data. On the other hand, virus crystals are very radiation sensitive. Thus, only few images can be collected per crystal before radiation damage becomes severe.^[1]

Cryocooling extends the lifetime of an irradiated crystal by some orders of magnitude and would allow to use smaller crystals.^[2, 3] Cryogenic data collection from viruses is very complicated and there are only few reports where virus crystals have been successfully frozen.^[4, 5] In general, cryocooling to cryogenic temperatures requires considerable concentrations of cryoprotectants to prevent hexagonal ice formation. Large unit cell systems with weak crystal contacts, such as viruses, are very fragile and will most probably crack due to osmotic shock when soaked in a solution of a different ionic strength. Finding optimal cryoconditions for a specific virus crystal therefore involves extensive testing of solution compositions and soaking protocols. Moreover, cryoprotectants, such as glycerol or ethylene glycol, penetrate the crystal lattice and thereby cause an increase in crystal mosaicity. This results in an overlap of the closely spaced reflections on the detector which limits the data quality. Thus, there is an urgent need for alternative cryocooling technologies in virus crystallography.

A promising approach which allows the formation of amorphous ice without the use of cryoprotectants is high-pressure freezing (HPF). This technique is well established in the field of electron microscopy for cryofixation of cells or tissue^[6] and was recently optimized for macromolecular crystals by our group.^[7] The crystals

are frozen at 210 MPa and 77 K using a Baltec HPM 010 high-pressure freezer. The high cooling rates provided by the HPF device allow vitrification of the solvent inside the crystal and the surrounding solution. Thus, the crystals can be directly frozen in their mother liquor without the need for additional sample manipulation, such as cryoprotection.

The developed HPC protocol was successfully applied to bovine enterovirus (BEV).^[8] For the first time a complete data set was collected from a single, non-cryoprotected virus crystal at 100 K. The BEV crystal showed cubic symmetry and diffracted to an excellent resolution of 2.5 Å.

References:

[1] E. E. Fry et al., Macromolecular crystallography - conventional and high-throughput methods (2007), Oxford University Press, 245.
 [2] E. F. Garman & T. R. Schneider, J. Appl. Cryst. 30 (1997), 211.
 [3] E. F. Garman & R. L. Owen, Acta Cryst. D62 (2006), 32.
 [4] V. S. Reddy et al., Science 329 (2010), 1071.
 [5] K. Tars et al., Virology 310 (2003), 287.
 [6] H. Hohenberg et al., J. Microsc. 175 (1994), 34.
 [7] A. Burkhardt et al., submitted.
 [8] M. Smyth et al., Nat. Struct. Biol. 2 (1995), 224.

MS01-P06

A moment in time: 100 Years of X-Ray Diffraction versus 100 days of PHOTON 100 CMOS detector

H. Ott¹, M. Adam², M. Ruf³

¹Bruker AXS GmbH, Application Laboratories, Karlsruhe, Germany

²Bruker AXS GmbH, Karlsruhe, Germany

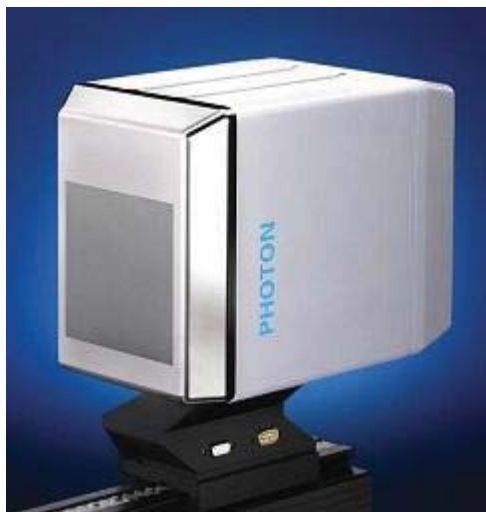
³Bruker AXS Inc., Madison, WI, United States

This year we celebrate the 100th anniversary of the discovery of X-ray diffraction by Laue, Friedrich and Knipping. Ever since the early days, vast improvements in instrumentation were accomplished and single crystal X-ray diffraction became a routine method in natural science. One milestone was the introduction of CCD-based X-ray detectors in 1991, which immediately became the detectors of choice in chemical crystallography. This was mainly due to the good combination of readout speed, sensitivity, dynamic range, and spatial resolution.

Very recently, the first commercial CMOS active pixel sensor for X-ray crystallography, the PHOTON 100, became available. The PHOTON 100 offers a number of features which make it the superior solution:

- Large 100 cm² active area
- High quantum gain, high sensitivity
- Available for Cu, Mo, Ag radiation
- Excellent signal-to-noise
- 3 year Detector Warranty
- Air cooled

The PHOTON 100 is available with the user-friendly D8 QUEST and D8 VENTURE, featuring the latest generation of the ImS (Incoatec Microfocus Source), focusing monochromators (TRIUMPH), and modern rotating anodes (Turbo X-ray Source). After a short historic overview on X-ray detectors with a focus on the technique used in CMOS based detectors, we will present results obtained on the D8 QUEST and D8 VENTURE. The structures presented will include examples of weakly diffracting crystals and crystals exhibiting aperiodicity. Furthermore, high quality data for charge density investigations will be discussed.

**MS01-P07****Revised fine-resolution neutron powder diffractometer E9 at BER II / HZB**D.M. Töbrens¹, M. Tovar², C. Stephan¹, P. Henry³¹Helmholtz-Zentrum Berlin für Materialien und Energie, M-A3 / Kristallographie, Berlin, Germany²Helmholtz-Zentrum Berlin für Materialien und Energie, M-II / Komplexe Magnetische Materialien, Berlin, Germany³European Spallation Source ESS AB, Lund, Sweden

The fine-resolution neutron powder diffractometer E9 at the BER II reactor at the Helmholtz-Zentrum Berlin für Materialien und Energie [1] has undergone major alterations, which improved both the performance and the flexibility of the instrument. The layout between source and sample remained unchanged [2], with the monochromator - reactor core distance of 11 m allowing a large take-off angle, reduced number of epithermal neutrons in the primary beam from a sapphire single crystal filter, and a vertically focussing Ge-monochromator of 300 mm height allowing flexible optimization of the focus of the secondary beam.

The detector, on the other hand, has been completely exchanged and reconstructed. The new detector consists of eight individual 2D detectors with 300 x 300 mm active area, and a radial collimator to reduce background noise. The individual detectors are arranged at an optimized, non-constant distance from the sample. With this novel setup, complete diffraction patterns of the whole diffraction range are now accumulated in only three steps. Position-sensitive data integration results in a strongly reduced asymmetry of the peaks without the need to restrict the detector height. This results for typical sample diameters of 8 mm in a manifold increase of pattern intensity and improved peak shape, without compromising the resolution function. In this mode, the instrument is dedicated to collect diffractograms suited for crystal structure determinations and Rietveld refinements with unit cell volumes up to 1000 Å³. This is equivalent to the original dedication, but with increased data collection speed.

Additionally, four of the individual detectors can be placed at variable distances from the sample. This allows a new high intensity, low resolution conformation of the instrument. This mode is suitable for atomic and magnetic structures with small unit cells and high symmetry. Also, this configuration results in a large angular range being covered by a single detector. This is useful for data collection with fixed detector, which allows for rapid parameterized scans, e.g. temperature or field strength dependency of magnetic structures, cavity fillings or phase compositions. Direct access to the 2D-data is also possible, e.g. to perform texture analysis.

Of course, the upgraded instrument still allows the use of the usual suit of sample environments, covering a wide range of low and high temperatures, pressure, variable magnetic fields, and

controlled gas atmosphere. With BER II back in operation, E9 is now once again open to applications from external users.

References:

[1] Helmholtz-Zentrum Berlin für Materialien und Energie GmbH, <http://www.helmholtz-berlin.de>[2] D. M. Töbrens, N. Stüßer, K. Knorr, H. M. Mayer, G. Lampert: E9: The new high-resolution neutron powder diffractometer at the Berlin Neutron Scattering Center. *Materials Science Forum* **378-381**, 288-293 (2001)**MS01-P08****Modular setup for measurement of pyroelectric coefficients and their temperature dependence**M. Ackermann¹, P. Becker¹, L. Bohatý¹¹Institut für Kristallographie, Universität zu Köln, Köln, Germany

The class of pyroelectrics, including its subgroup of ferroelectrics, are of ongoing interest for many technical applications, such as sensor systems, data memory or energy storage in capacitors. In search of new potentially interesting ferroelectric or non-ferroelectric pyroelectric crystals the availability of a setup for determination of their characteristic pyroelectric and dielectric properties is essential. In this contribution we present a modular experimental setup for the investigation of these two classes of pyroelectrics in the temperature range from liquid nitrogen up to 550 K. Pyroelectric coefficients at constant mechanical stress p_i^σ (unclamped crystals) and their temperature dependence are determined by the method of direct measurement of the pyroelectric current, that arises during a temperature change dT/dt of the crystal. In our setup this method, first introduced with applied constant dT/dt by Byer and Roundy [1] is modified: While applying a constant heating power the temperature change dT/dt is measured continuously and the resulting current between the short-circuited crystal surfaces is registered. By a slight alteration of the setup and the use of a high voltage amplifier the crystals under investigation can also be poled, which offers the opportunity to detect ferroelectric phase transitions and to determine the temperature dependent spontaneous polarization. In addition, a modified Sawyer-Tower circuitry [2, 3] enlarges the capabilities of the setup. Ferroelectric D-E hysteresis loops can be displayed, from which the spontaneous polarization as well as the coercitive field strength are deduced. This applies also to crystals with slight electric conductivity. The capabilities of the setup are demonstrated using the examples of selected well known pyroelectrics and ferroelectrics, e.g. $\text{Li}_2\text{SO}_4 \cdot \text{H}_2\text{O}$, $\text{Ba}(\text{NO}_2)_2 \cdot 2 \text{H}_2\text{O}$, BiB_3O_6 , BaTiO_3 and RbHSO_4 . Additionally, a characterisation of some new pyroelectric crystals is presented.

[1] R. L. Byer, C.B. Roundy, *Ferroelectrics* **3** (1972) 333.[2] C. B. Sawyer, C. H. Tower, *Phys. Rev.* **35** (1930) 269.[3] M. Fukunaga, Y. Noda, *J. Phys. Soc. Jap.* **77** (2008) 064706.**MS01-P09****Novel Microfocus X-ray Sources for High-Pressure Crystallography**T. Samtleben¹, J. Graf¹, B. Hasse¹, F. Fabbiani², M. Probert³, C. Michaelsen¹¹Incoatec, Geesthacht, Germany²Georg-August-University, GZG, Goettingen, Germany³Durham University, Chemistry Department, Durham, United Kingdom

Diamond anvil cells (DAC's) are widely used for examining the crystal structure of materials under high pressure. The area of reciprocal space accessible in a high-pressure X-ray diffraction experiment is primarily restricted by the geometry of the DAC. For a typical high-pressure experiment using Mo radiation, only a small fraction of all reflections can be collected. This can be as low as

30% for triclinic crystal structures. Using radiation with a shorter wavelength, such as Ag-K_α, a larger portion of the reciprocal space is accessible, thus increasing the number of observations and the resolution of the data. However, because of the low intensity of conventional Ag sealed tubes, Ag sources are rarely used for high-pressure studies in the home lab.

Microfocus sealed tube sources have proven to deliver flux densities beyond that of traditional X-ray sources when combined with 2D focusing multilayer mirrors [1, 2]. The sharp beam profile of these sources produces a high flux density at the sample position, thus leading to strong diffracted intensities. Furthermore, the small beam cross-section significantly reduces the background that usually results from scattering at the gasket of the DAC. Therefore, this type of source presents a promising alternative to classical sealed tube sources currently being used in high-pressure crystallography.

We will be reporting on the latest developments on microfocus X-ray sources (Ag and Mo anodes) which enable a clear increase in intensity compared to other sealed tube sources. Selected results on the use of these sources in high-pressure crystallography will be presented.

[1] J. Wiesmann, J. Graf, C. Hoffmann, A. Hembd, C. Michaelsen, N. Yang, H. Cordes, B. He, U. Preckwinkel, K. Erlacher, *Particle & Particle Systems Characterization* 2009, 26, 112.

[2] T. Schulz, K. Meindl, D. Leusser, D. Stern, J. Graf, C. Michaelsen, M. Ruf, G. M. Sheldrick, D. Stalke, *J. Appl. Cryst.* 2009, 42, 885.

MS01-P10

Recent developments of beamline P24 (ChemCryst) at Petra III.14

C. Paulmann¹, A. Berghäuser¹, D. Ropers¹, D. Novikov², U. Bismayer¹, S. Park³, W. Schmahl³, D. Meyer⁴, C. Lehmann⁵, S. van Smaalen⁶, S. Teichert⁷

¹Mineralogisch-Petrographisches Institut, Universität Hamburg, Hamburg, Germany

²Hasylab/DESY, Hamburg, Germany

³Sektion Kristallographie, Dept. für Geo- und Umweltwissenschaften, LMU München, München, Germany

⁴Institut für Experimentelle Physik, TU Freiberg, Freiberg, Germany

⁵MPI für Kohlenforschung, Mülheim, Germany

⁶Laboratory of Crystallography, Universität Bayreuth, Bayreuth, Germany

⁷MPI für biophysikalische Chemie, Göttingen, Germany

The shutdown of DORIS III by the end of 2012 will discontinue a number of successful beamlines which serve techniques not currently implemented at PETRA III. As a result, two additional halls (PETRA III.14) are planned to be build in order to provide competitive beamlines and instrumentation for techniques not requiring brilliance of PETRA III.

One of these beamlines will focus on activities currently being performed at stations like D3, F1 and BW1. The research areas of the user community range from chemical crystallography over materials and earth science till life sciences. Typical applications cover diffuse scattering studies, charge density analysis, phase transitions, also under external fields, disordered and modulated structures all at ambient and non-ambient conditions (low/high temperature, high pressure). As a result of several user workshops, a joint research BMBF project (coordination: University Hamburg) has been granted to build up a new beamline at PETRA III.14 dedicated for a large range of crystallographic research fields.

With the beginning of 2011 the detailed planning gained up in speed. The Chemical Crystallography beamline will be located in the eastern hall with a short undulator (N < 20) as source, delivering photon energies in the range of 8 to 35 keV (25 - 35 keV: 5th harmonic) using a CEMO-type water-cooled DCM (Si111 and Si311). The latter currently induces heat-load restrictions with respect to the source. However, options are designated to upgrade to a standard PetraIII-type undulator in combination with a cryo-cooled monochromator in the future. The preliminary optics layout

will consist of the following parts (downstream): 1. Horizontally focusing CRLs (>25 keV), 2. CEMO-type DCM, 3. Horizontally focusing mirror (< 25 keV), 4. Bendable plane mirror (vertical focusing), 5. (Rotatable) CRLs for final focusing. The optic specifications will be laid out to give a homogenous beam of 0.3 mm² (with collimator). Smaller beam diameters can be achieved by focusing or with slit systems.

Within an experimental hutch of currently 9 m x 4 m size the beamline will offer two independent diffractometers. A completely new Kappa-diffractometer equipped with an motorized xyz-stage will be able to carry sample loads up to 10 kg and provides a sphere of confusion below 25 μm for loads up to 7 kg. Two independent detector circles are designed to take loads of 30 kg. In combination with a modular mounting system, the design will provide easy exchange and combination of different detectors, sample environments (cryostats, heaters), laser systems for pump and probe experiments or high-resolution polarising digital sample microscopes. The public tender for this diffractometer will be placed in the beginning of 2012. In addition, a refurbished eulerian-type diffractometer (D3 or BW1) possibly with an optional horizontal scattering plane will be installed as option for heavier sample loads.

MS01-P11

Investigations on specimen fluorescence using Co radiation with point and line X-ray detection systems

T. Kirsch¹, R. Wenda¹, D. Götz²

¹Georg-Simon-Ohm Hochschule, Institut für Werkstofftechnik, Nürnberg, Germany

²PANalytical B.V., Development, Almelo, Netherlands

In the memory of Prof. Dr. R. Wenda (30.05.1955 - 20.11.2011)

One of the possible sources of an enhanced background in a powder diffractogram is specimen fluorescence. This is characteristic radiation from the sample that is excited by the incident X-ray beam and is accepted by the X-ray detection system. Dependent on the element in the sample, its concentration and the radiation used the background produced by specimen fluorescence can reach the order of the strongest reflections in a powder diagram.

Earlier similar investigations were focused on copper radiation varying the detector's PHD levels or the generator settings [1, 2].

In this investigation the influence of the chosen X-ray optical geometry on the fluorescent background is determined experimentally from diffractograms recorded on a series of 17 samples of row 4 elements ranging from K to Br. The samples were measured with monochromators or K-beta filters in the incident or the diffracted beam using Co radiation. The intensities were measured as well with a point as a line X-ray detection system dependent on the detector's PHD levels and on individual PHD curves. All the data were analyzed using a profile fit algorithm applying a Pseudo-Voigt peak fit function.

For comparison the signal/noise ratio was chosen as figure of merit. This is defined as the net peak intensity divided by the square root of the background. When varying the PHD levels of the detector the ratio signal/noise shows a distinct maximum at the optimum PHD level, whereas the normally used ratio signal/background shows high values even beyond the optimum PHD value that are physically meaningless (Figure 1).

Recommendations are given how to reduce the specimen fluorescence by selecting either the proper lower PHD level for the elements from K to Mn or the upper PHD level for elements from Zn to Br. The results are summarized in Figure 2. For each investigated optical beam path the optimized normalized PHD level values are shown dependent as function of the atomic number of the element in the samples (with the normalization: 6.924 keV = 50% PHD).

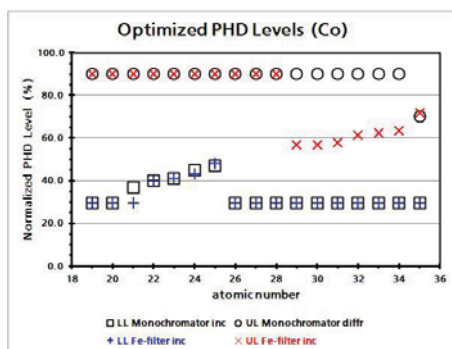
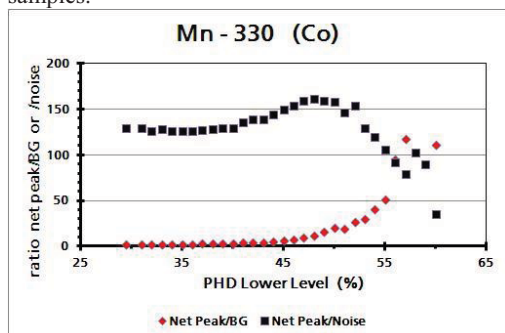
[1] M.J. Fransen: 1- and 2-dimensional detection systems and the problem of sample fluorescence in X-ray diffractometry, *Adv. X-*

ray Anal. 47 (2004) 224-231.

[2] M.J. Fransen: On the influence of generator and detector settings in X-ray powder diffractometry, Adv. X-ray Anal. 48 (2005) 143-149.

Figure 1: Reflection Mn 330: Comparison of figure of merits defined as the ratio of “net peak/background” versus “net peak/noise”.

Figure 2: Optimized normalized PHD levels for Co radiation dependent on atomic number of the element in the investigated samples.



MS01-P12

The improved state of STRESS-SPEC for texture characterization

W. Gan¹, C. Randau², M. Hofmann³, N. Al-hamdany², H.-G. Brokmeier², M. Müller¹, A. chreyer¹

¹Helmholtz-Zentrum Geesthacht, Institute of Materials Research, Garching, Germany

²TU-Clausthal, Institute of Mater. Sci. & Eng., Clausthal-Zellerfeld, Germany

³TU-Munich, FRM II, Garching, Germany

Thermal neutron diffraction is the leading method for non-destructive global texture measurement in metals, alloys, composites, ceramics and rocks up to sample volumes in the cm³ range. Moreover, local or gradient texture analysis along samples' main axis by neutron diffraction takes more advantages over those by normal X-ray and EBSD in desirable detected volume fraction, sample preparation and data processing, etc.

STRESS-SPEC is a high flux neutron diffractometer and offers a flexible instrument setup suitable for fast global and local texture analysis. With a great efficiency increase of the newly installed 2D area detector the pole figure measurement has been speeded up. In-situ strain and FWHM pole figure can also be investigated using the upgraded tensile machine nowadays. In addition, the newly developed robot system will allow the automatic and precise sample changing and positioning for global texture analysis. This greatly improves the efficiency of beam time.

In this contribution, recent examples will be shown to indicate the improved state of STRESS-SPEC for texture characterization. Recent results of texture analysis on deformed coarse grained salts using robot sample changer system; and in-situ pole figure measurement via tensile will be presented.

MS01-P13

The new neutron single crystal diffractometer "BioDiff" for macromolecular crystallography at the FRM II

A. Ostermann¹, T.E. Schrader², M. Monkenbusch³, B. Laatsch⁴, P. Jüttner¹, W. Petry¹, D. Richter^{2,3}

¹Technische Universität München, Forschungs-Neutronenquelle Heinz Maier-Leibnitz, Garching, Germany

²Forschungszentrum Jülich GmbH, Jülich Centre for Neutron Science, Garching, Germany

³Forschungszentrum Jülich GmbH, Institute for Complex Systems, Jülich, Germany

⁴Forschungszentrum Jülich GmbH, Zentralabteilung Technologie, Jülich, Germany

The newly build neutron single crystal diffractometer "BioDiff" is a joint project of the Forschungszentrum Jülich (FZJ/JCNS) and the Forschungs-Neutronenquelle Heinz Maier-Leibnitz (FRM II). "BioDiff" is especially designed to collect data from crystals with large unit cells. The main field of application is the structure analysis of proteins, especially the determination of hydrogen atom positions. For this purpose "BioDiff" provides two independent detector systems. To reduce the data collection time the main detector system covers a large solid angle of approximately 2π and consists of a cylindrical neutron image plate with a radius of 200 mm and a cylinder height of 450 mm (compare fig. 1). The second detector system is a Li/ ZnS scintillator CCD-camera with an active area of 200 mm x 200 mm. The CCD camera can rotate around the sample in a 2θ range between 0° and 113°. By using a highly orientated pyrolytic graphite monochromator (PG002) the diffractometer is able to operate in the wavelength range of 2.4 Å to about 5.6 Å. Contaminations of higher order wavelengths are removed by a neutron velocity selector. "BioDiff" is equipped with a standard Oxford Cryosystem "Cryostream 700 plus" which allows measurements in the temperature regime from 90K up to 500K. The main advantage of this instrument is the possibility to adapt the wavelength to the size of the unit cell of the sample crystal while operating with a clean monochromatic beam that keeps the background level low.

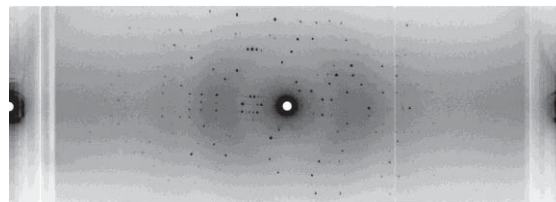


Figure 1: Example of a neutron diffraction pattern collected with the cylindrical neutron image plate detector system.

MS01-P14

PROOFS OF CONCEPT OF ON SITE X-RAY DIFFRACTION USING ROBOTIC TECHNOLOGY

F. De Marco¹, G. Berti^{1,2}, M.E. Del Seppia¹

¹XRD-Tools, R&D, Pisa, Italy

²University of Pisa, Earth Science-Lab. R&D XRD, Pisa, Italy

Since the seventies of last century ideas were born to use x-ray diffraction out of laboratories. These were mostly oriented to investigate the effects on materials of the working cycles and related residual stress. These ideas were and are still based on the back reflection effects of x-rays, where source and detector are placed on the same quarter of the equatorial plane. Instead the Bragg Brentano diffractometers use the normal reflection as the generator line of diffraction cones and Debije rings. The technology DifRob® (i.e. "Diffrattometro Robotizzato") has been designed to cover a wide spectrum of application and types of analyses [1]. These analyses have to be carried out on either blocks or powders by considering that most of the condensed matter is

settled as polycrystalline in aggregation with a wide variety of composition and configuration [2]. Said diffractometer design has a sufficient number of freedom degrees, thus opening to several distinct methods of NDT to converge to an unified approach of investigation; thus improving the knowledge, when passing from the characterization of matter in abstract from the context, where the material is in service, to on site qualification (e.g. quality and integrity) of the material of manufactures. We are going to examine several proofs of concepts where the above mentioned technology can have an impact for NDT monitoring of plants and other civil manufactures or ornamental stones and rocks [3]. The analyses can be carried out without any manipulation or destructive test on the specimen. Civil society is currently and probably will be more and more faced with needs to perform early stage diagnosis, identify minimum compositional changes in order to predict possibly the material residual life and prevent dramatic disasters. In this direction very preliminary stages with still small achievements have been run and mentioned as follows:

Qualification of materials in compliance with XRD standard patterns (e.g. Copper alloys: Bronzes, Golden, Steel, Marble, and others). DifRob[®] prototype shows sensitivity to small amount of material (even less than 1%), capability of detecting materials microstructure, preferred orientation, stacking fault effects, etc.; the prototypes shows sensitivity to detect diffraction lines coming both from the gold thin surface layer and the Copper bulk of the coin. Proofs has been carried out on steel components in order to identify the effects as a consequence of the mechanical assembly of components. The assembly results in effects that can be observed as "peak shift" and variation of the intensity distribution of the diffraction lines and cluster of lines. On site XRD analyses from marble blocks has been approached without any contact with the manufacture or the stone to get at information in relation to composition and deformations induced by loads (e.g. atmospheric, environment, air pollution, etc.) in terms of crystallographic directions and nano-structure.

References:

[1] G. Berti, F. De Marco, S. Aldrighetti (2010), "Advances on NDT methods and technologies for early stage diagnosis of materials", Trans Tech Periodicals, 2011 Vol 681, 461-467 ISBN 978-3-03785-086-2
 [2] EN13925-1 Non-destructive testing - "X-ray diffraction from polycrystalline and amorphous material - Part 1: General principles" © CEN - AFNOR Paris
 [3] G. Berti, F. De Marco (2009), "On site X-ray Diffraction a new technology for diagnosis at the nano-scale". InProceedings of ECOTRIB2009, pp. 247 - 256, ISBN 978-884672426-7.

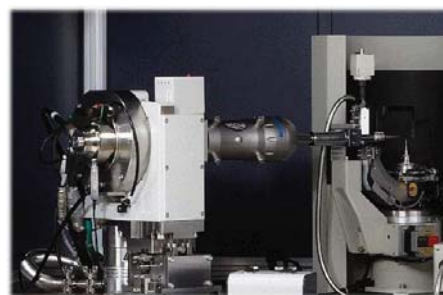
MS01-P15

DW Varimax: one source, two wavelengths, power and flexibility for the ultimate SMX tool

L. Russo¹

¹Rigaku Europe SE, SMX, Berlin, Italy

The drive towards comprehensively equipped analytical facilities is both an economic necessity and a big opportunity for interdisciplinary research; there is a stringent need for manufactures to provide new tools, optimised for this scenario. The DW VariMax is a confocal, high flux, optics system designed to complement Rigaku's high-flux, dual target source. The power and flexibility of such apparatus is an ideal match for the Rapid II image plate detector, capable of exploiting its key capabilities. While the image plate technology suits best a DW setting, its response being non-wavelength dependent, a CCD configuration of the DW VariMax is also proposed, according to customer preferences. A range of selected, advanced studies will be presented, demonstrating the diverse specialist applications for which this machine is designed.



MS01-P16

Rigaku XtaLAB mini™: SMX on a bench

L. Russo¹

¹Rigaku Europe SE, SMX, Berlin, Italy

A carefully thought design and matching software result in an innovative tool for your teaching and training activities, as well as an invaluable support for busy service crystallography environments or wherever open access to SMX facilities is envisaged.

The new XtaLAB mini™ is the ultimate solution for:

- Helping busy service crystallographers to best manage their time and resources, providing a first-instance, open access service
- Training new users, also maximising the impact of any teaching and training activity, with the option to take the instrument on site
- Beginners, who can operate the instrument in auto mode: the ideal entry-point to SMX methods
- Small research groups, as a cost and time-effective alternative to outsourcing their structural work
- Beamline scientist, for sample screening preventing from any waste of precious beamtime



MS01-P17

Molecular excited state-structure determination of Metal Organic Compounds by Time Resolved X-ray Crystallography at Beamline P11 at PETRA III

R. Raghunandan¹, A. Meents¹

¹Deutsches Elektronen-Synchrotron, HASYLAB, Hamburg, Germany

Structural elucidation of short-lived species and rapid dynamic processes has lagged behind conventional structure determination due to the considerable technical difficulties associated with measurements on timescales of microseconds or less. With the advent of increasing brightness and time resolution of new light sources allows the pump and probe experiments to be accomplished and hence the exploration of the excited state structure. ^[1,2]

We plan to determine the excited state structure of different metal-

organic compounds like Iridium, tris(2-phenylpyridine)-Ir(ppy)₃, Tris(dibenzoylmethane) mono(1,10-phenanthroline)europium(III), the promising materials for Organic Light Emitting Diodes (OLEDs) with time resolved micro-crystallography. The ground state structures of these compounds are known, but the transient structures formed after light excitation still remains elusive due to their short-lived nature. So our study plans to capture this process in a "Molecular Movie" with time resolved X-ray crystallographic measurements. Applying X-ray crystallography technique in a time resolved mode should allow to determine the excited state structures of the molecules and to understand the fundamental structural dynamics of organic semiconductor materials under operating conditions (e.g. excitation by light).

Metal organic single crystals were grown by for Ir(ppy)₃ and Eu(dbm)₃phen from dimethyl sulfoxide and acetone solutions simultaneously. The ground state crystal structures of both the compounds were determined by X-ray diffraction at Beamline X13 at EMBL, Hamburg. Ir(ppy)₃ and Eu(dbm)₃phen compounds crystallizes in space group P-3c1 and P-1 simultaneously and both the structures contain the solvent molecule.

References:

- [1] Molecular Excited State Structure by Time-Resolved Pump-Probe X-ray Diffraction. What is New and What are the Prospects for Further Progress? P. Coppens, *J. Phys. Chem. Lett.* 2, 616-621 (2011)
- [2] Chergui, M.; Zewail, A. H. *Electron and X-ray Methods of Ultrafast Structural Dynamics: Advances and Applications.* ChemPhysChem 2009, 10, 28.

MS01-P18

Recent software and hardware developments in the SuperNova dual source micro-focus diffractometer

Z. Gál¹, O. Presly¹, M. Meyer¹
¹Agilent Technologies XRD, Yarnton, United Kingdom

Continued research and development in the core technologies used in the SuperNova dual source micro-focus diffractometer means that key aspects of the instrument have been updated and improved since its initial launch. Here we would like to highlight the overall benefits of these evolutionary changes and refinements in both hardware and software.

The advent of applying micro-focus X-ray lamps coupled to multi-layer focusing optics heralded a new level of capability for data collections in-house. Our co-mounted, software switchable X-ray sources transform a single instrument into a multi-disciplinary facility that can cater to a wide range of research interests ranging from the typical structural chemistry and biology applications to the more specialist fields of physics, materials science and geology. Coupled with the latest generation CrysAlis^{Pro} and AutoChem software, users have access to an unprecedented level of crystallographic expertise that can automatically guide the data collection / integration process in ensuring the best chances for structural elucidation as well as an ever increasing throughput.

Keywords: dual wavelength diffraction, micro-focus sources, CrysAlis^{Pro}, Autochem 2.0

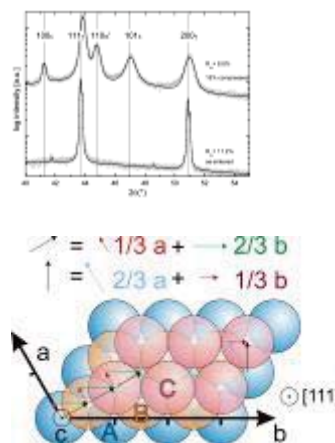
MS02-P01

Crystallographic description of ϵ -martensite via stacking faults in austenitic TRIP-steels

S. Martin¹, D. Rafaja¹
¹TU Bergakademie Freiberg, Institut für Werkstoffwissenschaft, Freiberg, Germany

Plastic deformation of highly alloyed austenitic transformation-induced plasticity (TRIP) steels with low stacking fault energy leads typically to the formation of ϵ -martensite within the austenite.

Despite the commonly opinion, assuming ϵ -martensite as hexagonal close-packed crystal structure, an alternative structure model is presented that describes ϵ -martensite via clustering of stacking faults in austenite. The model was tested on experimental X-ray diffraction data measured on a CrMnNi TRIP steel after 15% compression. Via the DIFFaX routine the faulted austenite and ϵ -martensite were represented by different stacking fault arrangements. The probabilities of the respective stacking fault arrangements were obtained from fitting the simulated X-ray diffraction patterns to the experimental data. The reliability of the model was proven by scanning and transmission electron microscopy. For visualisation of the clusters of stacking faults, the scanning electron microscopy employed electron channelling contrast imaging and electron backscatter diffraction.



MS02-P02

Early Stages of Cement Hydration - An In-Situ Study Utilizing High Resolution SyXRD

M.-C. Schlegel¹, A. Sarfraz¹, U. Mueller¹, U. Panne^{1,2}, F. Emmerling¹
¹BAM Federal Institute for Materials Research and Testing, Structure Analysis, Berlin, Germany
²Humboldt University Berlin, Chemistry, Berlin, Germany

Cement is a complex multi phase system, consisting of different silicate, aluminate, and ferrite phases. After mixing with water and inducing hydration, these systems are colloidal suspensions. Nowadays, these colloidal suspensions are increasingly stabilized by organic additives such as retarding admixtures or superplasticizers [1]. The additives are used to optimize the flow properties of the suspension during construction project or to reduce the water/cement ratio. The result is a higher compressive strength of the hardened hydration product. The formation of the initial hydrate phases changes and leads to a microstructure and phase composition different to non influenced cement [2]. Especially, the phase development at the beginning of the hydration changes and is not well understood [3]. During the first minutes of hydration, one of the most dynamic process is the reaction of C₃A (Ca₃Al₂O₅) with sulphate to form ettringite (Ca₆Al₂(SO₄)₃(OH)₁₂ · 26 H₂O). This reaction is more often influenced by polycarboxylate-ether (PCE), one of the most common superplasticizers [4].

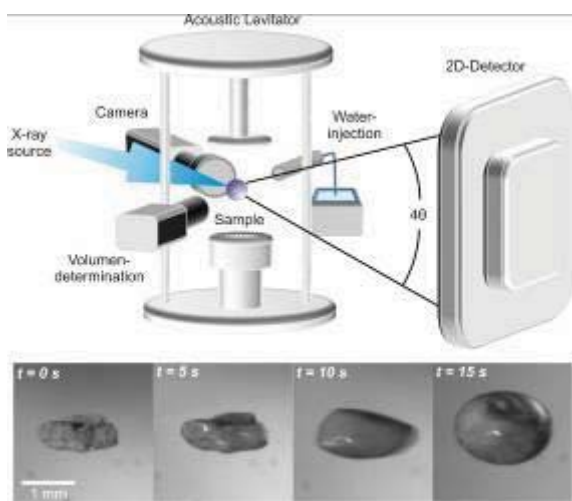
The focus of previous studies was on the change of the rheological behaviour of the suspension and the key factors of the PCE adsorption process [5]. The formation of the hydrate phases is often interpreted by describing the change of fluid behaviours and zeta potentials, and rarely characterized by analyzing the crystallization processes directly [6].

In this study, synchrotron radiation based X-ray diffraction was used to analyze the initial formation of ettringite. The high time resolution of 500 ms provides a detailed view of the hydration processes. The hydration behavior of pure ordinary portland cement is compared with the hydration behavior when the cement hydration is influenced by PCE polymers. Different polymer

backbone charge densities were used. The initial ettringite formation is functionalized as an indicator for the reaction time and intensity of the PCE/C₃A interaction. Providing contact-free analysis, cement pellets were inserted in an acoustic levitator system (Figure 1) and aqueous PCE containing solution was injected with a piezo-electric microdrop dispenser [7, 8]. The time resolved analysis was performed at the beamline ID11 ($\lambda = 0.3444 \text{ \AA}$) at the European Synchrotron Research Facility (ESRF). The high time resolution provides fundamental information about the influence of the organic additive on the formation of ettringite during the first minutes of the cement hydration.

Keywords: in-situ, high resolution, SyXRD, ettringite formation, colloid suspension, hydration process

- [1] R. J. Flatt, I. Schober, E. Raphael, C. Plassard and E. Lesniewska, *Langmuir* 2009, 25, 845-855.
 [2] M. Bishop, S. G. Bott and A. R. Barron, *Chemistry of Materials* 2003, 15, 3074-3088.
 [3] A. N. Christensen, N. V. Y. Scarlett, I. C. Madsen, T. R. Jensen and J. C. Hanson, *Dalton Transactions* 2003, 1529-1536.
 [4] M. Lesti, S. Ng and J. Plank, *Journal of the American Ceramic Society* 2010, 93, 3493-3498.
 [5] L. Ferrari, J. Kaufmann, F. Winnefeld and J. Plank, *Journal of Colloid and Interface Science* 2010, 347, 15-24.
 [6] J. Plank, D. Zhimin, H. Keller, F. Von Hossle and W. Seidl, *Cement and Concrete Research* 2010, 40, 45-57.
 [7] S. E. Wolf, J. Leiterer, M. Kappl, F. Emmerling and W. Tremel, *Journal of the American Chemical Society* 2008, 130, 12342-12347.
 [8] A. Sarfraz, M. C. Schlegel, J. Wright and F. Emmerling, *Chemical Communications* 2011, 47, 9369-9371.



MS02-P03

Does K₂CaSiO₄ exist? - a phase-analytical study in the system K₂O-CaO-SiO₂ with implications for the characterization of residual materials

V. Kahlenberg¹, E. Arroyabe¹, R. Tessadri¹, D.M. Töbrens¹
¹University of Innsbruck, Mineralogy & Petrography, Innsbruck, Austria

The last ten years have seen a constantly growing interest of public authorities, industry and research institutions in sustainable waste management and recycling. This can be directly attributed to the fact that these issues are of vital importance for conserving natural resources, reducing the emission of greenhouse gases and protecting natural ecosystems as well as public health. One of the central aspects towards a more 'ecologically' oriented waste technology is the reuse of residual materials. Since potassium calcium silicates have been encountered in several chemically and mineralogically oriented studies on materials such as ashes from

biomass combustion as well as fertilizers produced from the residues of oil-shale industry or from steelmaking slags, respectively, it is not surprising that the system K₂O-CaO-SiO₂ has been in the focus of research activities. So far, the interpretation of the results concerning the existence, formation and assemblage of certain phases relied exclusively on the only available phase equilibrium study of the corresponding ternary system that was published 80 years ago by Morey et al. [1].

One of the phases that have been frequently described to occur in the above mentioned ashes and slags is K₂CaSiO₄ or K₂O×CaO×SiO₂. Morey et al. [1] reported this so-called '1:1:1' compound to melt congruently at 1630°C. To a certain extent this value is surprising, because all other potassium calcium silicates listed in this early study had melting points that were 500-600°C lower although their amounts of the refractory oxides CaO and/or SiO₂ were equal or even considerably higher than those of the 1:1:1 phase.

Furthermore, contradictory results concerning basic crystallographic and physicochemical data of this compound have been described in the literature [1-3]. In a series of solid state reactions we tried to prepare this material for a more detailed investigation. The temperature regime for the sub-solidus synthesis experiments was selected according to previous studies where the occurrence of this so-called '1:1:1' phase had been reported. The samples were characterized by thermal and X-ray fluorescence analysis as well as X-ray powder diffraction. Our results indicate that 'K₂CaSiO₄' does not exist as a crystalline phase in the ternary system K₂O-CaO-SiO₂ and that the 1:1:1 compound mentioned in earlier studies is actually misinterpreted K₂Ca₂Si₂O₇. The start of melt formation of an oxide mixture with composition K₂O×CaO×SiO₂ has been determined to be 1170°C, which is dramatically lower than the value of 1630°C mentioned in the only available comprehensive phase analytical study on potassium calcium silicates [1].

- [1] G.W. Morey, F.C. Kracek, N.L. Bowen, *J. Soc. Glass Technol.* 1930, 14, 149.
 [2] A.S. Bereznoi, N.V. Lapina, E.V. Lifshits, E.P. Shevyakova, *Neorg. Mater.* 1976, 12, 1653.
 [3] H. Hughes, *Trans. Brit. Ceram. Soc.* 1966, 65, 661.

MS02-P04

Roboter in der Diffraktometrie, keine neue Idee aber sehr effektiv an Stress-Spec

H.-G. Brokmeier¹, M. Hofmann², W. Gan³, C. Randau¹, M. Völler², M. Müller⁴, A. Schreyer⁴, W. Petry²

¹Universität Göttingen, Geowissenschaftliches Zentrum, Göttingen, Germany

²TU München, Forschungsneutronenquelle Heinz Maier-Leibnitz FRM II, Garching, Germany

³Helmholtz-Zentrum Geesthacht, Outstation at FRM II, Garching, Germany

⁴Helmholtz-Zentrum Geesthacht, GEMS, Geesthacht, Germany

Das Materialforschungsdiffraktometer Stress-Spec an der Forschungsneutronenquelle Heinz Mayer-Leibnitz FRM2 ist mit einem Roboter Typ Stäubli RX160 ausgestattet worden. Für die Analyse kristallographischer Texturen und Restspannungen ergänzt der Roboter die Probenbewegungen mittels Eulerwige (Polfigurmessung) oder Rotationseinheit mit x-, y-, z-Linearverschiebung (Spannungsprofil). Die Freiheitsgrade des Roboters, der bis zu 30 kg tragen kann, sind deutlich größer. Dadurch sind sowohl kontinuierliche Probenbewegungen mit simultaner Detektorauslesung als auch bisher nicht realisierbare kombinierte Probescans möglich. Das kontinuierliche Messen führt zu zum Beispiel bei Standardpolfigurmessungen zu einer Zeitersparnis von bis zu 30%. Das führt in der Praxis dazu, dass hochauflösenden Polfigurmessungen in realistischen Zeiten durchgeführt werden können.

Erste Messungen wurden zur Beschreibung von Globaltexturen unterschiedlicher Proben durchgeführt. Es hat sich gezeigt, dass für

diese Experimente der Roboter neben der eigentlichen Messung auch exzellent als Probenwechsler genutzt werden kann. Der Probenwechsler wurde inzwischen konstruiert, installiert und erfolgreich eingesetzt. In einem weiteren Experiment wurde an einer reibgeschweißten Al7020/Stahl 316L Probe sowohl ein Spannungsprofil über beide Phasen als auch der Texturgradient in der Al-Phase ermittelt. Die Abmessungen der Proben sind 20mm Ø und 160mm Länge. Die Untersuchungen von Texturinhomogenitäten an Cu-Rohren zeigen das anisotrope Fließverhalten bei der Rohrherstellung (Strangpressen, Rohrzug). Das besondere bei diesen Untersuchungen neben der Probenpositionierung über den Roboterarm sind die notwendigen Korrekturen bezüglich Volumenkonstanz und anisotroper Absorption während der Probenrotation. Es sollte erwähnt werden, dass diese Messungen und Korrekturen nur möglich sind, wenn die Probengeometrie vorher mittels Laserscanning erfasst worden ist.

References:

- [1] H.-G. Brokmeier, C. Randau, W. Tekouo, M. Hofmann, W. Gan, M. Müller, A. Schreyer, W. Petry: Materials Science Forum Vol. 652, 197-201, 2010.
- [2] H.-G. Brokmeier, W. M. Gan, C. Randau, J. Rebelo-Kornmeier, M. Hofmann: Nuclear Instruments and Methods in Physics A 642 (2011) 87-92.
- [3] M. Hofmann M. Hofmann, J. Robelo-Kornmeier, U. Garbe, R.C. Wimpory, J. Repper, G.A. Seidl, H.-G. Brokmeier, R. Schneider: Neutron News 18, 27-30, 2007.

MS02-P05

Herzenbergite as Absorber Material in Thin-Film Solar-Cells

A. Stadler¹

¹Universität Salzburg, Materialforschung und Physik, Salzburg, Austria

Conventional materials for CIGS solar cells are to replace by price saving, synthetically produced, materials.

Pulsed direct-current (PDC) and radio-frequency (RF) magnetron sputtered herzenbergite absorber thin films were prepared under different geometrical and temporary conditions within a Leybold Optics CLUSTEX 100M sputtering cluster tool. Therefore, sputter-depositions have been examined, referring to positions upon the thin-films, r , target-substrate distances, d_{TarSub} , and sputter durations, t_{sp} . The influences of the equation of state for real gases (gas law) during the sputter process, as well as the influence of typical plasma-parameters on the physical values of the sputtered SnS thin-films have been investigated. Therefore, SnS was sputtered on boron silicate glass (BSG) substrates with different argon pressures, p , and substrate-temperatures, T , within the process-chamber as well as with different frequencies, f , and break times, t_{br} , of the plasma-building electromagnetically fields.

Moreover, thin-film solar cells were produced with Al-doped zincite (ZnO:Al) TCO- and herzenbergite (SnS) absorber-layers. Their I-V characteristics were discussed as well as fill factors, conversion- and quantum efficiencies. The influences of luminance and temperature on the I-V characteristics are shown.

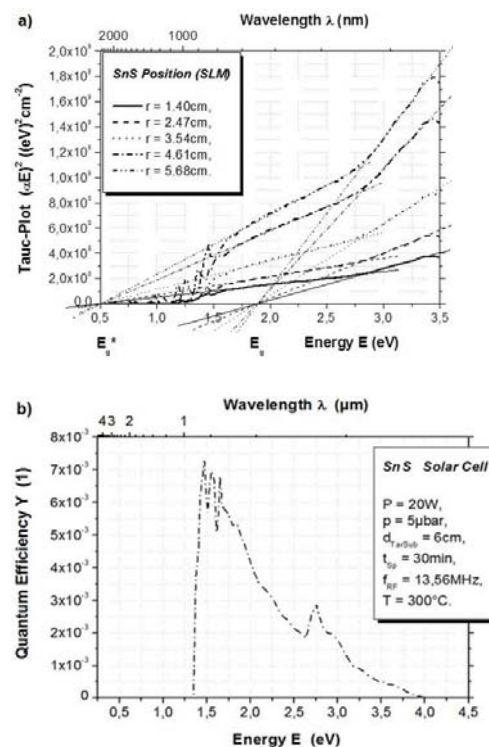
Thin film investigation was done with advanced ultra-violet/visible/near infra-red (UV/Vis/NIR) spectroscopy, applying a Perkin Elmer Lambda 750 spectrometer. This allows exact evaluations of refractive indices, n_L , permittivities, ϵ_L , wave numbers, k_L , absorption coefficients, α_L , conductivities, σ_L , band gaps, E_g , effective doping concentrations, n_e , and lifetimes, μ . Conductivities were also measured with a Lucas Labs Pro4 four-tip measurement system.

For example, a magnetron sputtered herzenbergite thin-film shows typically a gauss-like thickness distribution. So, measurements at different positions, r , upon the substrate provide physical values for layers with different thicknesses, d_L , grown with the same sputter-duration, t_{sp} . Figure a) shows Tauc-Plots calculated from UV/Vis/NIR spectra. Here, the linear interpolations point out, that for herzenbergite thin films two different band gaps exist.

A combination of UV/Vis/NIR measurements on absorber thin

films and I-V measurements on the according thin film solar cells allow the determination of the energy dependent quantum efficiency, see figure b).

Figures.a)Tauc-Plots for band gap determination. Shown are curves for different positions, r , upon the substrate; i.e. for herzenbergite thin-films with different thicknesses.b)Quantum Efficiency, Y , for a solar cell with herzenbergite absorber layer.



MS02-P06

Crystal structures and compaction behaviour of amine salts of acidic drugs

M. Ramirez¹, S. David^{1,2}, C.H. Schwalbe^{1,3}, B.R. Conway^{1,4}, P. Timmins⁵

¹Aston University, School of Life & Health Sciences, Birmingham, United Kingdom

²GlaxoSmithKline, Formulation Process & Analysis, Harlow, United Kingdom

³Cambridge Crystallographic Data Centre, Cambridge, United Kingdom

⁴University of Huddersfield, School of Applied Sciences, Huddersfield, United Kingdom

⁵Bristol-Myers Squibb, Biopharmaceutics R&D, Moreton, United States Minor Outlying Islands

Salt formation is used increasingly to improve the properties of drugs. We report here the mechanical properties of two acidic drugs when the hydrogen bonding functionality of their ⁺H₃NC(CH₃)_{3-n}(CH₂OH)_n amine counterions is systematically varied. Starting with t-butylammonium (tBut), 1 (AMP1), 2 (AMP2) and then all 3 (Tris) methyl groups are changed to hydroxymethyl. The drugs, gemfibrozil (G) and flurbiprofen (F), were chosen because crystal structures could be determined and because their additional heteroatoms (ether O and F respectively) are weaker hydrogen bond acceptors than OCO⁻. These salts of G only formed polycrystalline powders; nevertheless, it was possible to determine their structures from X-ray powder diffraction data [1]. The somewhat larger crystals of F salts were amenable to single crystal analysis but required synchrotron radiation in two cases [2].

Both tBut salts feature ladders composed of R₄³(10) rings, in which ⁺H-N-H...O-C-O⁻ chains with a repeat distance of 6.2 - 6.5 Å constitute the uprights and ⁺N-H...O⁻ interactions by the remaining ammonium H atom form the rungs. Evidently this is a stable motif:

it persists unchanged in FAMP1, where the added OH is disordered. In GAMP1 it is modified by changing the rungs to ⁺N-H...OH...O⁻. The rungs cross-linking the chains in both GAMP2 and FAMP2 are ⁺N-H...OH...OH...O⁻. This second OH is hydrogen bonded to the identical carboxylate group as the ⁺NH₃ of the same AMP2 cation, buttressing the chain with a succession of R₂²(9) rings. In GTris only one ⁺N-H forms a hydrogen bond to carboxylate, and the dominant motif changes from ladders to hydrogen-bonded sheets. FTris gave two polymorphs, one of which has severe disorder. The ordered polymorph (II) exhibits the same ⁺H-N-H...O-C-O⁻ chains with appended R₂²(9) rings as FAMP2, and the extra OH group creates layers from ladders by donating another hydrogen bond to an adjacent carboxylate O atom that previously accepted only one.

The following Young's modulus values (GPa) were measured for rectangular compacts by three-point bending.

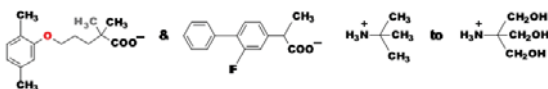
Drug	tBut salt	AMP1 salt	AMP2 salt	Tris salt
Gemfibrozil	2.45	Sticking to die	7.95	18.81
Flurbiprofen	5.95	Laminated	9.97	4.69

The GTris structure with strongly hydrogen bonded layers and a slip plane to facilitate inter-particle adhesion gives the stiffest strongest compacts. The corrugation of layers in FTris II is not helpful.

We thank National Crystallography Service and Diamond synchrotron staff, especially S. Callear, W. Clegg, R. Harrington and L. Russo, for data collection.

[1] E. Y. Cheung et al. (2007) J. Solid State Chem. 180, 1068.

[2] C. H. Schwalbe et al. (2010) ACA Transactions (online).



MS02-P07

Cancrinit-Katoit Kokristallisation beim Recycling von Porenbeton (PB) im System PB-NaOH-NaAlO₂-Na₂CO₃-H₂O

V. Petrov¹, A. Hartmann¹, J.-C. Buhl¹

¹Institut für Mineralogie, Leibniz Universität Hannover, Hannover, Germany

Untersuchungen zum Recycling von Porenbetonabfällen (PB) sind sowohl aus Gründen des Umweltschutzes (Auswaschung von Alkalien bei Deponierung) als auch der Rückgewinnung der wertvollen Inhaltsstoffe (Calciumsilikathydrat „Tobermorit“, Quarz und Aluminium) bedeutsam [1]. Die hydrothermale Umwandlung dieser Bestandteile in technisch nutzbare Vertreter der Zeolithgruppe unter Einsatz von NaAlO₂ als Additiv ist aufgrund der PB-Zusammensetzung sinnvoll und bereits Gegenstand experimenteller Untersuchungen [2, 3].

In der vorliegenden Arbeit wird unter stark alkalischen Bedingungen (16 M NaOH) sowie mit Na₂CO₃ als weiterem Additiv gearbeitet, mit dem Ziel der Synthese möglichst hoher und phasenreiner Mengen an Zeolith CAN (Cancrinit). Die Untersuchung der Kinetik der Phasenbildung erfolgte durch hydrothermale Behandlung von Pulvergemengen aus PB und NaAlO₂ bei 453 K für Reaktionszeiten bis zu 20 h. Es zeigte sich, dass stets Cancrinit und Katoit (Ca₃Al₂SiO₄(OH)₈) kristallisierten, wobei Katoit schon in der Aufheizperiode auf die Reaktionstemperatur ausfällt, dann aber ab 0,5 h Cancrinit hinzu kommt. Beide Phasen erreichen dann schon nach 1 h etwa ein

konstantes Mengenverhältnis, das sich von 5-20 h nur noch wenig zugunsten von Cancrinit erhöht. Die Bildungsreaktion scheint also bereits nach rel. kurzer Zeit abgeschlossen zu sein.

Bei kurzer Syntheszeit liegt im Produkt erwartungsgemäß aber auch noch Quarz-Restanteil vor, der erst zwischen 10 -20 h völlig in Lösung übergeht. Der Cancrinitanteil wächst dadurch aber nicht mehr weiter an. Somit befindet sich noch Silicat in der Lösung, das nicht in den kristallinen Phasen gebunden ist. Eine weitere Nutzung der alkalischen Lösung wurde daher experimentell geprüft und die Reaktion modifiziert: PB wurde zunächst ohne weitere Additive für 20h bei 453 K in 16 M NaOH behandelt und die Lösung vom Feststoff getrennt. Im Gegensatz zur Synthese mit NaAlO₂ und Na₂CO₃ führt die Laugung in NaOH allein zur Bildung von Na-Ca-Silikathydrat/Hydrogenhydrat (PDF 21-1349 und 25-1319 [4]). Zur Lösung wurden wie bisher die Additive gegeben und bei 453 K für 20h synthetisiert. Es entstand nun phasenreiner Carbonat-CAN. Synthese ohne Na₂CO₃ führt zu phasenreinem basischen Cancrinit. Milde Kristallisationsbedingungen ohne Na₂CO₃ (Reduzierung der Alkalinität mit H₂O und Synthese bei 353 K für nur 4 h) ergaben eine intermediäre Phase zwischen Sodalith und Cancrinit (INT) [5]. In zukünftigen Arbeiten wird die Nutzung des Feststoffes Na-Ca-Silikathydrat sowie die Umwandlung von CAN und INT in Zeolith LTA untersucht.

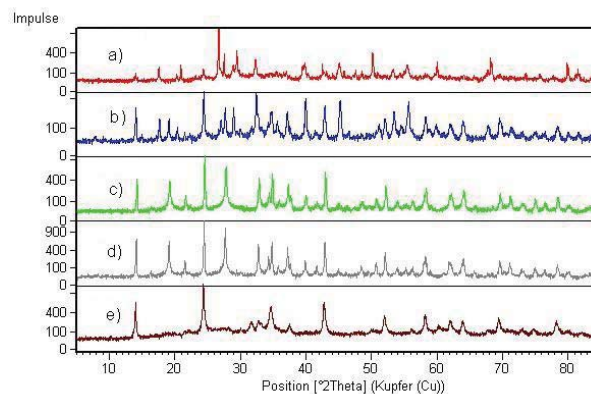


Abb. 1: Röntgen-Pulverdiffraktogramme der Produkte: PB-Restphasen und Katoit nach 0,5 h Synthese (a); Cancrinit und Katoit nach 20h (b); Carbonat-Cancrinit (c); basischer Cancrinit (d) und intermediäre Phase (e); [a] und [b]: Feststoffe der PB-Laugung, c - e): Synthese für 20 h aus alkalischer Lösung der PB-Laugung].

[1] Weber, H., Hullmann, H.: Porenbetonhandbuch, Bauverlag Wiesbaden 2002.

[2] Hartmann, A, Buhl, J.-C.: Z. Krist Supplement Issue No. 28 (2008) 1C 06.

[3] Hartmann, A, Buhl, J.-C, Lutz, W.: Book of abstracts / 23. Deutsche Zeolith-Tagung : 02. bis 04. März 2011 / Friedrich-Alexander-Universität Erlangen-Nürnberg, (2011) 104 - 105.

[4] International Centre for Diffraction Data, 12 Campus Boulevard, Newton Square, Pennsylvania 190073-3272, U.S.A.

[5] Hermeler, G.; Buhl, J.-Ch.; Hoffmann, W.: Catalysis Today, 1991, Vol. 8, 415.

Keywords: crystallization kinetic, zeolites, recyclable fractions, hydrothermal behavior, alkaline leaching

MS02-P08

Kinetics of dissolution/recrystallization of tobermorite, calcite and quartz from autoclaved aerated concrete (AAC) in NaOH and C₆H₈O₇ solutions

G. Pawlas¹, A. Hartmann¹, V. Petrov¹, J.-C. Buhl¹

¹Institut für Mineralogie, Leibniz Universität Hannover, Hannover, Germany

A detailed knowledge of the reactivity of tobermorite-calcite-quartz mixtures from vapour hardened building materials is essential for the development of new recycling routes of autoclaved aerated concrete (AAC) and lime-sandstones. Model reactions like zeolite crystallization from AAC were recently tested [1-2]. In the present study we investigate the alkaline and acid conversion of AAC in 4 M and 16 M NaOH and 0.5 M and 1.0 M citric acid ($C_6H_8O_7$) [3]. The experimental investigation is of interest for future raw materials preserving due to the high content of the valuable potential recyclable AAC components [4].

In the case of alkaline reactions AAC was leached in teflon lined steel autoclaves for times of 0.5 -20 h at 453 K (autogeneous pressure), i.e. the conditions, used for AAC production. Acid reactions were performed at mild conditions of 333 K. After each treatment the weight of the solid residue has been checked before the sample was characterized by XRD and FTIR. Selected samples were further examined by SEM and EDX-analysis.

Fig. 1 includes a summary of the XRD results of the samples obtained under alkaline conditions after 20 h reaction time compared with the pattern of the untreated AAC and the product of leaching in 8 M NaOH from [2]. As to be expected the dissolution of quartz is high already in 4 M NaOH after 5 h. Only the 101 main reflex of quartz can be seen in the pattern, beside very strong tobermorite lines (Fig. 1). Tobermorite is stable under these conditions and from the gravimetric measurement and all other analyses data a slight increase of the total amount of tobermorite has been detected due to the recrystallization of amorphous material. In contrast, a total decomposition of tobermorite and quartz could be stated for the 16 M series. Here already after 0.5 h reaction time a new phase occurred. The reflexes are in agreement with sodium calcium silicate hydrate/ sodium calcium silicate hydrogenhydrate (PDF 21-1349, 22-891 and/or 25-1319) [5].

The results of acid leaching were also found to depend on the acid concentration. The aim of acid reaction, the total dissolution of tobermorite (and its carbonatization product calcite) to separate calcium cations from silicate anions, was reached with a concentration of 1 M citric acid after 1 h. In contrast, an unknown new phase was formed already after 20 minutes when 0.5 M acid was used.

Summarizing the results, alkaline reaction NaOH and acid leaching in citric acid are suitable procedures for AAC recycling process. A combination of both leaching procedures should lead to an effective process of 100% AAC conversion rates into valuable solutions and solids.

[1] Hartmann, A, Buhl, J.-C.: Z. Krist Supplement Issue No. 28 (2008) 1C 06.

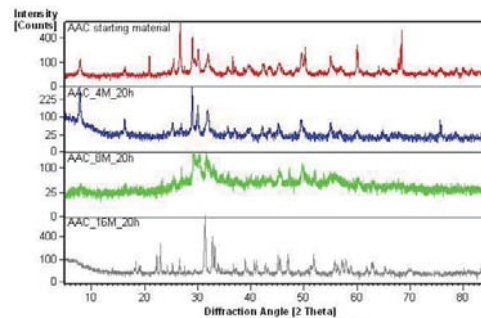
[2] Hartmann, A, Buhl, J.-C, Lutz, W.: Book of abstracts / 23. Deutsche Zeolith-Tagung : 02. bis 04. März 2011 / Friedrich-Alexander-Universität Erlangen-Nürnberg, (2011) 104 - 105.

[3] Pawlas, G.: Bachelorarbeit, Institut für Mineralogie, Leibniz Universität Hannover, 2011.

[4] Weber, H., Hullmann, H.: Porenbetonhandbuch, Bauverlag Wiesbaden 2002.

[5] International Centre for Diffraction Data, 12 Campus Boulevard, Newton Square, Pennsylvania 190073-3272, U.S.A.

Fig. 1: X-ray powder patterns of solid residues of AAC after alkaline leaching process in 4-16 M NaOH solution (the pattern of the untreated AAC and the residue of treatment in 8 M NaOH from [2] is included).



MS02-P09

X-Ray Micro-Diffraction Analysis of Heterogenous Concrete Samples

P. Schaub¹, E. Wieland¹, R. Dähn¹, A. Leemann²

¹Paul Scherrer Institute, Laboratory for Waste Management, Villigen, Switzerland

²Swiss Federal Laboratories for Materials Testing and Research EMPA, Dübendorf, Switzerland

Synchrotron-based x-ray micro-diffraction techniques, with a beam size down to a few micrometres or less, allows a variety of novel diffraction applications with high spatial resolution on fine-structured materials. In addition to investigation on pure crystalline materials only available in very small quantities and sizes, micro-diffraction techniques also allow heterogeneous materials showing chemical and structural zonation on a (sub-)micrometre scale to be probed *e.g.* components in nanotechnology and samples of interest in environmental sciences and engineering, such as structural alterations and reaction products forming at phase contacts.

In the present study, reaction products formed during the alkali-silica-reaction (ASR) in concrete structures have been investigated. The ASR is an important deterioration process in concretes, leading to severe damage in buildings, dams, bridges *etc.* worldwide. The reaction products formed due to the interaction of amorphous or crystalline SiO_2 in aggregates with the alkaline pore solution of concrete produce an expansion pressure which gives rise to damage in the concrete structures. Knowledge of the mechanisms leading to this expansion during the course of ASR is still limited. Analysis and identification of the reaction products formed on a (sub-)micrometre scale is the key to the further understanding of ASR.

Samples taken from an ASR damaged concrete structure showing veins of ASR reaction products were prepared as thin sections with a thickness of about 20 μm . Investigations were performed on the cement-type materials formed within the expansion cracks of aggregates, which have a diameter typically in the range of a few tens of micrometres. X-ray micro-diffraction data were collected at different areas of interest along these veins. These *in-situ* measurements permitted to determine the distribution of the analysed phases within their original environment. Powder diffraction data analysis, and analysis of single crystal diffraction patterns obtained from micrometre or sub-micrometre sized micro-crystalline grains in the ASR zones, were carried out with the aim of identification and structural refinement of the reaction products. Due to the inevitable multi-phase sampling, even with a sub-micrometre beam and the intricate handling and positioning of the samples under the beam, the quality of the diffraction data is less than ideal, thus complicating phase identification and refinement.

MS02-P10

A STATISTICAL METHOD APPLIED TO DEFOCUSING CURVES CALCULATION

J. Palacios Gomez¹, B. Aguilar Sanjuan¹

¹Instituto Politecnico Nacional, Escuela Superior de Fisica y Matematicas, Mexico City, Mexico

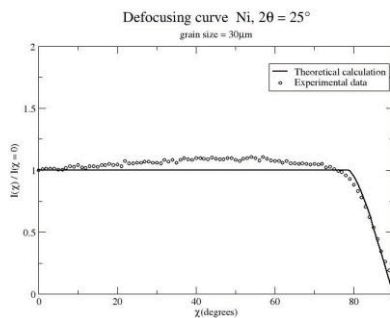
Applying usual parameters and conditions of conventional devices for measurement of pole figures of textured polycrystals by X-ray diffraction, it was found that the numerical integration of integrals proposed by Tenckhoff [1] for the calculation of the defocusing effect, which arises from the rotation, fails to reproduce accurately the defocusing curves, which are necessary for pole figures correction.

According to a more detailed geometrical analysis done on the defocusing curve measurement, a statistical model was made assuming an ensemble of powder samples, showing more explicitly how the diffracted intensity from crystallites orientated randomly depends on the measurement process.

The developed method was applied to low index reflections of fine grained nickel powder samples. Figure below shows results for the defocusing curve of 111 reflection using MoK α radiation.

References:

[1] E. Tenckhoff, (1970), J. Appl. Phys.41(10), pp 3944-3948.



MS02-P11

Texture Inhomogeneity through the Thickness for Copper Tube

N. Alhamdany¹, H.G. Brokmeier²

¹Außenstelle am FRM-II der TUM, IWW-Abt. TEXMAT/ TU Clausthal, Garching, Germany

²TU vlausthal, IWW, Clausthal-Zellerfeld, Germany

Seamless tube are used for many applications, e.g. for plumbing, in heating systems, oil and gas pipes, drinking water system transport of medical and industrial gases, evaporators as well as intermediate products for hydroforming and various mechanical application.

As intermediate production of seamless tube, the first step is the piercing of the billet, for example by extrusion or three-roll-mill process. Because of vibration of the mandrel, tolerance by positioning the die and the billet, and possible temperature inhomogeneities in the billet this step inherently results in variation of thickness around the diameter which cause different flow of material during the production process lead to different texture around the diameter and through the thickness, as well as eccentricity and ovality.

Three samples cut from copper ring at minimum, maximum and middle thickness have been measured by Synchrotron beam at HEMS side station at HASYLAB of energy 87.26keV and wavelength of 0.1421 Å and beam size of 0.5X0.5 mm² was used for local texture measurement.

The quantitative texture shows slightly variation through the thickness for the minimum, maximum and middle thickness. Also there are similarities between the global texture measured by neutron and the global texture from the summation of local texture measured by Synchrotron for every position.

MS02-P12

Influence of mechanical defects on the crystal lattice of silicon

T. Jauß¹, A. Danilewsky¹, J. Wittge¹, A. Cröll¹, J. Garagorri², R. Elizalde², D. Allen³, P. McNally³

¹Universität Freiburg, Institut für Geowissenschaften, Kristallographie, Freiburg, Germany

²University of Navarra, CEIT and Tecnun, San Sebastian, Spain

³Dublin City University, The RINCE Institute, Dublin, Ireland

Micro-cracks, dislocations, and slip bands are generated in originally defect free silicon wafers during wafer handling and heat treatments during device production. Such defects reduce the yield and performance of semiconductor devices. To examine the impact of mechanical defects on the crystal lattice of silicon, controlled damage was applied to silicon wafers with a boron doped epitaxial layer by nanoindentation using a diamond Vickers tip. With increasing loads of 1, 5, and 50 N, the area with micro-cracks and strain around the indents increases. The damage is characterized by high resolution diffractometry using a conventional line focus copper X-ray tube. To increase the damaged crystal volume, a line of seven indents was oriented parallel to the X-ray beam. To raise the contribution of the damage related signal, as much undisturbed sample volume as possible was covered with lead foil. Spatially resolved rocking curves were recorded across the indents and analysed with respect to full width at half maximum. Strain and tilt, which cannot even be distinguished by single rocking curves, are separated in reciprocal space maps of the damaged crystal area. Parallel to the macroscopic increase of damage created by the diamond tip, the range of angular scattering also increases. By analysing the increased scattered intensity in Qx and Qz direction, tilt values from 6.6 to 153.8 arcsec and strain from 3.0 to 65.1 MPa are measured [1]. Synchrotron X-ray diffraction imaging experiments showed that this damage, without additional heat treatment, is insufficient to form dislocations. Further, wafer breakage was only observed for indentation loads of 50 N, and only during heat treatment. It was demonstrated that despite the low count rates of the damage related intensity, this critical damage can be precisely located and characterized with a conventional laboratory high resolution diffractometer.

[1] T. Jauß, A.N. Danilewsky, J.Wittge, A. Cröll, J. Garagorri, R. M. Elizalde, D. Allen, P. McNally, Influence of mechanical damage to the crystal lattice of silicon, Cryst. Res. Tech.(2011) DOI 10.1002/crat.201100488

MS02-P13

X-ray Diffraction Analysis of Epitaxial ZnO/a-Al₂O₃ Thin Film

N. Anouar¹, S. Dieter², F. Hatmut³, B.G. Mohamed Hédi¹

¹Faculté des Sciences de Sfax, Laboratoire de Physique des Matériaux, Sfax, Tunisia

²Fraunhofer-Institut, Material-und strahlentechnologie, Dresden, Germany

³University of Technology, Institute of Materials Sciences, Darmstadt, Germany

ZnO films were grown on R-Al₂O₃ and C- Al₂O₃ substrates using plasma-assisted molecular beam epitaxy (MBE). The films have been epitaxial growth on the substrates. The surface roughness of the films have been analysed by atomic force microscopy. The absolute epitaxial relationships between ZnO films and a-plane sapphire are investigated by X-ray diffraction techniques. An analytical technique to determine residual strain in epitaxial ZnO films by X-ray diffraction (XRD) was studied. Based on piezoelectric constitutive equations and Bragg law, we applied an extended model, in which the elastic, piezoelectric and dielectric constants are introduced, to evaluate the residual stress in these films. The x-ray study is completed by an acoustic investigation utilizing laser ultrasonic equipment. Appropriate dispersion curves relative to Rayleigh waves, for both configurations ZnO/R-Al₂O₃ and ZnO/C-Al₂O₃ have been recorded in the frequency range up to 200MHz.

Keywords: MBE; Epitaxial thin film; X-ray diffraction; Residual Stress; SAW; ZnO.

References:

- [1] Hwang, K., Kang, B., Kim, Y., Hwangbo, S., Kim, J., 2010. Heteroepitaxial ZnO/sapphire (0001) structure prepared by sol-gel process. *Ceramics International*. 36, 2259-2262.
- [2] Eiper, E., Hofmann, A., Gerlach, J. W., Rauschenbach, B., Keckes, J., 2005. Anisotropic intrinsic and extrinsic stresses in epitaxial wurtzitic GaN thin film on γ -LiAlO₂(1 0 0). *J. Cryst. Growth*. 284, 561-566.
- [3] Emanetoglu, N. W., Patounakis, G., Shaohua, C. R., Wittstruck, R., Yicheng, L., 2001. Analysis of SAW properties of epitaxial ZnO films grown on R-Al₂O₃ substrates. *IEEE Trans. Ultrason., Ferroelect., Freq. Contr.* 48, 1389 - 1394.
- [4] El Hakiki, M., Elmazria, O., Assouar, M. B., Mortet, V., 2005. ZnO/AlN/diamond layered structure for SAW devices combining high velocity and high electromechanical coupling coefficient. *Diamond. Relat. Mater.* 14, 1175-1178.

MS02-P14

Thermal stability and quantification of hydrogen release of NaBH₄ enclosed in aluminosilicate gels

L. Schomborg¹, C. Rüscher¹, J.-C. Buhl¹

¹Universität Hannover, Inst. für Mineralogie, Hannover, Germany

A new approach of hydrogen storage could be realised with the enclosure of NaBH₄ in a specially designed aluminosilicate gel [1]. Here the hydrogen storage could be significantly increased compared to the enclosure of the BH₄-anion e.g. in the sodalite cage [2], protecting the NaBH₄ as well against atmospheric moisture and some elevated temperatures. Here some details concerning the thermal stability and absolute content of hydrogen release of this new material will be given.

The synthesis procedure follows [1] using sodium-silicate and sodium-aluminate solutions with the addition of NaBH₄ at room temperature. Gel precipitation was initiated by mixing both solutions. The mixture was dried at 110°C obtaining a solid which is stable under atmospheric conditions for several weeks. Even the addition of distilled water shows no reaction or decomposition. Temperature dependent infrared (TIR) absorption spectra show no significant changes neither for the Gel nor for the BH₄-anion when heated up to 400°C in a KBr pressed pellet (Fig. 1) whereas the NaBH₄ starts to become decomposed above about 300°C. The thermal behavior in both cases is completely different from our observation for BH₄-anion enclosed in the sodalite cage where a thermally controlled release of hydrogen occurs [2]. On the other hand hydrogen release from the NaBH₄ enclosed in the gel could be achieved in a controlled manner by reducing the pH-value, also without the requirement of any catalyst. By dropwise adding diluted acid to the solid NaBH₄-gel obtains a slow gas-release. The gas was analysed with a gas detector showing a CO₂ content below the detection limit (< 1000 ppm). The hydrogen-oxygen-reaction shows the formation of hydrogen. The gas release was quantified by a volumetric determination using different samples. The results indicate the amounts of hydrogen release could be up to 15 wt% of the total sample which corresponds to an enclosure of about 70 wt% NaBH₄ in the gel.

[1] Buhl, J.-Ch.; *Z. Krist. Suppl. Issue No. 31* (2011) 23.

[2] Buhl, J.-Ch., Schomborg, L., Rüscher, C.H.; *Micro. Meso. Mater.* 132 (2010) 210-218.

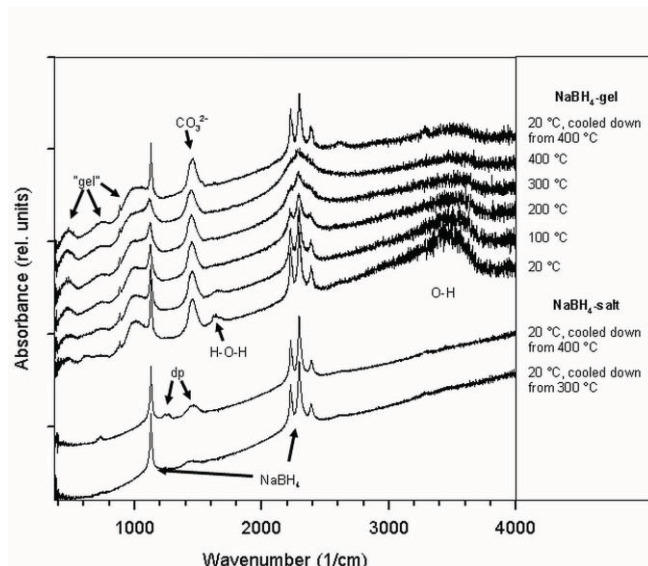


Fig. 1 Infrared absorption spectra (in KBr-pellet): NaBH₄-salt cooled down from 300 and 400 °C and NaBH₄ enclosed in a solid aluminosilicate gel measured up to 400 °C and cooled down to 20°C. Destruction products (dp) could be seen for heating above 300°C for the pure salt.

MS02-P15

Development of a Novel System for Building Artificial Metalloenzymes for Enantioselective Catalysis

M. Genz¹, D. Singer¹, J. Holldorf², E. Hey-Hawkins², R. Hoffmann¹, N. Sträter¹

¹Universität Leipzig, Biotechnologisch-Biomedizinisches Zentrum (BBZ), Leipzig, Georgia

²Universität Leipzig, Anorganische Chemie, Leipzig, Germany

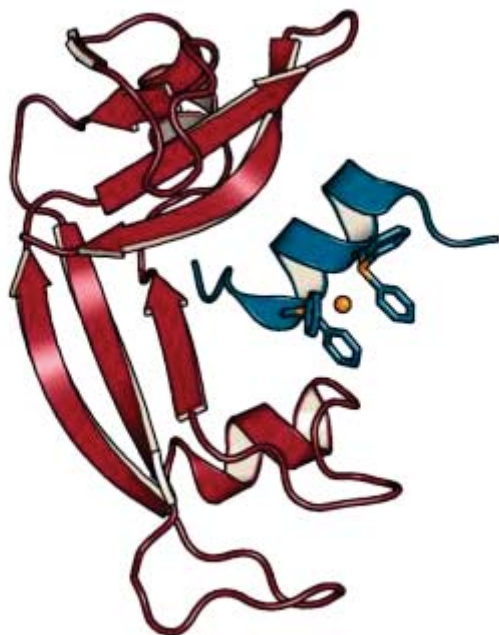
Enzyme catalysis is the most efficient strategy for preparation of enantiopure products by now. Unfortunately, many reactions important for industrial applications are missing from nature's toolbox¹. Most of those reactions (e.g. hydration, hydroformylation) are catalysed by 4d/5d transition-metal ions. Incorporation of transition metals into a protein host via a ligand leads to a novel class of hybrid catalysts, so called artificial metalloenzymes². The resulting hybrid protein comprises the best parts of both worlds. However, creation of synthetic activity from scratch within an existing protein scaffold still remains a challenging task³.

The RNase S system provides an ideal framework for incorporation of non-natural catalytic centres into a protein environment using peptide protein complementation (RNase S = S-protein + S-peptide). The basic catalytic activity is provided by the metal-organic centre whereas the protein environment ensures enantio- and regioselectivity. Based on the structure of RNase S we intend to design a system for creation of various enantioselective catalysts. So far, we produced crystals of an artificial metalloprotein comprising a RNase S variant with cysteines at positions 7 and 11 which is used as metal binding site. The X-ray structure revealed the formation of a stable [Cys2Hg] centre while the protein fold is not altered. The crystal structure guided us for building a model of RNase S with a rhodium ion complexed by two artificial diphenylphosphine amino acids. Currently, we are working on the first RNase S variants for establishing this hybrid catalyst.

Jing et al., *Chem. Eur. J.* 2009, 15, 1370-1376

Wilson & Whitesides, *J. Amer. Chem. Soc.* 1978, 100, 306-307

Creus & Ward, *Org. Biomol. Chem.* 2007, 5, 1835-1844



MS02-P17

Crystal Structure of Hemicarboaluminate Cement Phase

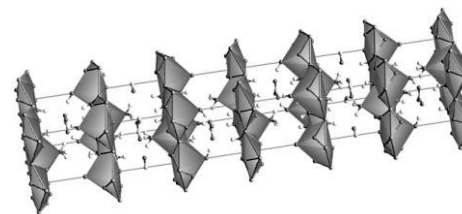
T. Runcevski¹, R. Dinnebier¹, H. Pöllmann²

¹Max-Planck-Institute for Solid State Research, Diffraction Service Group, Stuttgart, Germany

²Institut für Geowissenschaften und Geographie, FG Mineralogie/Geochemie, Halle, Germany

Cement compounds are tetracalcium aluminates belonging to the lamellar double hydroxide family. The crystal structures of cements are composed of positively charged main layers $[\text{Ca}_2\text{Al}(\text{OH})_6]^+$ and negatively charged interlayer $[\text{zX}^-\cdot\text{nH}_2\text{O}]$ where X is either one monovalent anion ($z=1$) or half a divalent anion ($z=1/2$). Different anions can be inserted into the interlayer region. One possibility is the carbonate anion, leading to monocarboaluminate or hemicarboaluminate. Although there are numerous structural studies on cements, very little is known about the hemicarboaluminate phase. In the present work the crystal structure of this phase is solved by using X-ray powder diffraction. In addition, vibrational (Raman and Infrared) spectroscopy and thermal analyses are undertaken to supplement the crystallographic study. Figure 1 shows the crystal structure of the hemicarboaluminate phase with half occupied carbonate sites as interlayer.

Figure 1. Crystal structure of the hemicarboaluminate cement phase



MS02-P16

Synthesis and crystal structure of $\text{CoEu}_2\text{Si}_3\text{O}_{10}$

M. Wierzbicka-Wieczorek¹, G. Giester²

¹University Jena, Mineralogy, Jena, Germany

²University Wien, Mineralogy and Crystallography, Wien, Austria

The title compound was synthesized as part of a detailed study focusing on the incorporation of heavy metals by cation exchange within the crystal structure of mixed-framework silicates. The synthesis of $\text{CoEu}_2\text{Si}_3\text{O}_{10}$ by a high-temperature flux-growth technique (MoO_3 -based flux mixtures in Pt crucibles in air; $T_{\text{max}} = 1200^\circ\text{C}$, cooling rate 3 K/h, $T_{\text{min}} = 900^\circ\text{C}$) yielded small light-violet crystals. The crystal structure was determined from single-crystal X-ray diffraction data. $\text{CoEu}_2\text{Si}_3\text{O}_{10}$ crystallizes in space group $\text{P2}_1/\text{n}$, with $a = 6.5547(13)$, $b = 6.7171(13)$, $c = 16.966(3)$ Å, $\beta = 90.05(3)^\circ$, $V = 747.0(3)$ Å³, $R(\text{F}) = 4.07\%$. Evaluation of measured intensity data gives R_{int} values of 0.035 and 0.531 for monoclinic and orthorhombic symmetry, respectively.

$\text{CoEu}_2\text{Si}_3\text{O}_{10}$ represents a new structure type and is a rare example of a silicate with Si_3O_{10} groups. The structure is built of layers parallel to (010) containing isolated Si_3O_{10} groups, linked via corners to Co_2O_{10} dimers. The dimer is formed from two edge-sharing CoO_6 octahedra. The average Co-O bond distance amounts to 2.17 Å. The Eu(1) cations are located between the layers, whereas the Eu(2) cations are in a position next to Si_3O_{10} units. The six-coordinated Eu^{3+} cations have average bond distances of 2.45 and 2.49 Å, respectively. The Si-Si-Si angle of the Si_3O_{10} units is 115.73° and the Si-O-Si angles are 129.54 and 135.37° .

No close structural relationships between $\text{CoEu}_2\text{Si}_3\text{O}_{10}$ and $\text{BaREE}_2\text{Si}_3\text{O}_{10}$ (REE = Gd, Er, Yb, Sc, Y) (Kolitsch et al., 2006; Wierzbicka-Wieczorek et al., 2010) exist.

We are grateful to Helmar Görls for the single-crystal diffraction measurements in Jena.

References:

- Kolitsch, U., Wierzbicka, M., Tillmanns, E. (2006): $\text{BaY}_2\text{Si}_3\text{O}_{10}$, a new flux-grown trisilicate. *Acta Crystallogr.*, C62, i97-i99.
- Wierzbicka-Wieczorek, M., Kolitsch, U., Tillmanns, E. (2010): Synthesis and structural study of five new trisilicates $\text{BaREE}_2\text{Si}_3\text{O}_{10}$ (REE = Gd, Er, Yb, Sc) and $\text{SrY}_2\text{Si}_3\text{O}_{10}$, including a review on the geometry of the Si_3O_{10} unit. *Eur. J. Mineral.* 22, 245-258.

MS03-P01

Structural, Immunological and Enzymatic Characterization of Phl p 4, a Major Pollen Allergen

D. Zafred¹, A. Nandy², W. Keller¹

¹University of Graz, Institute of Molecular Biosciences, Graz, Austria

²Allergopharma J. Ganzer KG, Reinbek, Germany

Background:

To lower the risk of adverse side effects of the allergen extract administration, new hypoallergenic derivatives could be created that evoke the immune response but do not cause mast cell degranulation, reason for severe side effects. Structural characterization is essential in design of hypoallergens in a rational manner.

Phl p 4 is one of the major pollen allergens from timothy grass (*Phleum pratense*) and thus cause of hay fever and other diseases related to pollen allergy.

Aim:

Structural and immunologic characterization of the allergen to the extent which enables prediction of major epitopes and rational design of hypoallergenic derivatives. Epitope prediction and rational design of the hypoallergenic derivatives.

Enzymatic characterization of the protein.

Methods:

Glycosylated and mutated non-glycosylated recombinant Phl p 4 variants were produced in *Pichia pastoris* and immunologically characterized. Structure was solved by protein crystallization and X-ray diffraction. Putative epitopes were predicted with SPADE, the prediction tool which utilizes structural and immunological data.

Enzymatic activity was monitored by following the DCPIP

conversion at a spectrophotometer.

Results:

All recombinant variants inhibit only partly the binding of patients' sera IgE to natural Phl p 4, showing the importance of plant carbohydrate antigenic determinants in immunogenicity of the allergens. Structure was solved at 1.9 Å, enabling insight into surface characteristic of the FAD containing oxidoreductase. Putative epitopes were predicted. Hypoallergenic derivatives are being designed.

Enzymatic activity was found. The protein is a glucose dehydrogenase with bicovalently bound FAD, thus first enzyme with such activity in this group of proteins. The change from oxidase (other proteins in this family) to dehydrogenase activity can be explained at structural level.

Conclusion:

We solved the first structure of the group 4 grass pollen allergen. We have structurally characterized it and employed the immunological and structural data for epitope prediction and hypoallergenic derivative design. In addition, we have shown the enzymatic activity of the first dehydrogenase with this mode of FAD binding.

MS03-P02

Structural studies of DnaK in complex with proline rich antimicrobial peptides

M. Zahn¹, D. Knappe¹, N. Berthold¹, R. Hoffmann¹, N. Sträter¹

¹Universität Leipzig, Biomedizinisches Biotechnologisches Zentrum, Institut für Bioanalytische Chemie, Leipzig, Germany

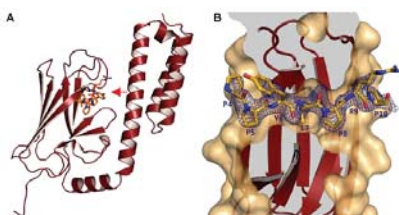
Bacterial infections are a major cause of death worldwide. Due to increasing resistance against the commercially available antibiotics over the past few decades, novel antimicrobial drug classes with new mode of actions are required for future treatments. Small proline rich antimicrobial peptides (PR-AMPs) from mammals and insects were identified to target the E. coli Hsp70 chaperone DnaK after cell penetration. Binding of the peptides to DnaK compromises the activity of the chaperone and thus the viability of the bacterial cells, in particular under conditions of stress. The non-lytic cell penetration of PR-AMPs to Gram-negative bacteria makes them a promising drug candidate against human infections. Therefore, structural information about the interactions between peptide inhibitors and DnaK are necessary for a better understanding of the mode of actions.

After recombinant expression of the substrate binding domain in E. coli and subsequent purification by IMAC and gel filtration, we crystallized the domain with several PR-AMPs. Elucidation of the binding mode of the peptides and characterization of the substrate specificity of DnaK will allow a structure-guided development of peptide inhibitors as antimicrobial agents targeting DnaK.

Figure 1: A) Interaction of the antimicrobial peptide oncocin (orange) with the substrate binding domain of DnaK. B) View along the red arrow in A, Oncocin binds in the forward direction to DnaK, where L7 fits into the central hydrophobic pocket (1).

Reference:

1. D. Knappe, M. Zahn, U. Sauer, G. Schiffer, N. Sträter, R. Hoffmann, *ChemBioChem* 12, (2011), 874-6.



MS03-P03

Pharmaceutical cocrystals as models for the study of drug-receptor interactions

M. Tutughamiarso¹, E. Egerl¹

¹Goethe-Universität Frankfurt, Biochemie, Chemie und Pharmazie, Frankfurt am Main, Germany

In pharmaceutical research cocrystals may be used to optimize the physical properties of drugs or to provide alternative polymorphic forms. Various design strategies, characterizations and applications have been published [1]. We cocrystallized a number of active pharmaceutical ingredients with potential receptors to study drug-receptor interactions. Focusing on complexes held together by N—H···O, N—H···N and N—H···S hydrogen bonds, we also investigated the influence of complementary binding on the conformational and tautomeric equilibria.

Although the antimalaria drug pyrimethamine (I) shows homodimers in most of its structures, it forms a heterodimer with otrotic acid stabilized by three hydrogen bonds [2]. Pyrimethamine, either neutral or protonated, always adopts approximately the same conformation representing the molecular geometry observed in previous studies of drug-enzyme complexes.

The antibiotic nitrofurantoin (II) and its artificial receptor, 2,6-diacetaminopyridine, are also linked by three hydrogen bonds [3]. In this complex nitrofurantoin adopts a conformation, which is not favoured in its (pseudo)polymorphs. However, theoretical calculations showed that this is indeed the lower-energy conformer and explained the unusual preference of the higher-energy conformer in most of the nitrofurantoin structures.

We also cocrystallized the antifungal drug flucytosine (III) with several receptors. In most cases, the drug-receptor interactions resemble the hydrogen-bonding pattern within the Watson-Crick C-G base pair. One cocrystal contains the antiviral drug acyclovir (IV), which (together with flucytosine) may be used for the double-suicide therapy in cancer treatment. In another cocrystal, a receptor has changed its conformation to enable the desired hydrogen-bond interactions.

The pyrimidin-4-one derivative 6-methylisocytosine (V) was cocrystallized to study its various tautomers. In its structures, 6-methylisocytosine shows no tautomeric preference [4], but in the presence of a complementary receptor one tautomer can selectively be crystallized. Again the drug and its receptor are stabilized by interactions similar to the C-G base pair.

Furthermore, we analyzed the cocrystals of the antithyroid drug propylthiouracil (VI) to study the relative strengths of N—H···O and N—H···S bonds [5]. Considering the reduced electronegativity, C=S should be a weaker acceptor group than C=O. Our study, however, revealed that the hydrogen-bonding capability of C=O and C=S groups seems to be comparable.

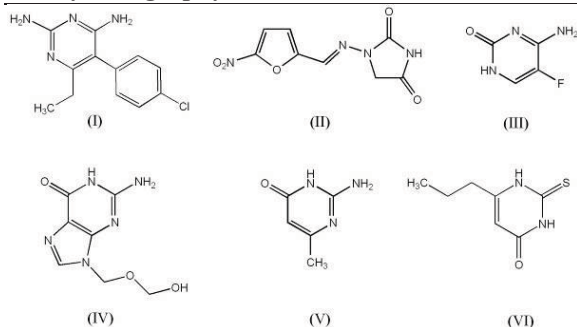
[1] P. Vishweshwar, J. A. McMahon, J. A. Bis & M. J. Zaworotko, *J. Pharm. Sci.* **2006**, *95*, 499-516.

[2] M. Tutughamiarso & M. Bolte, *Acta Cryst.* **2011**, *C67*, o428-o434.

[3] M. Tutughamiarso, M. Bolte, G. Wagner & E. Egerl, *Acta Cryst.* **2011**, *C67*, o18-o25.

[4] V. Gerhardt, M. Tutughamiarso & M. Bolte, *Acta Cryst.* **2011**, *C67*, o179-o187.

[5] M. Tutughamiarso & E. Egerl, *Acta Cryst.* **2011**, *C67*, o439-o445.



MS03-P04

Structure determination complicated by tetragonal pseudosymmetry

S. Barden¹, H. Niemann¹

¹Universität Bielefeld, Fakultät für Chemie / BCIV, Bielefeld, Germany

Here, we report on an α -helical protein which crystallizes reproducible as tetragonal bipyramides. Diffraction images of different crystals show split or smeared spots but symmetry is clearly visible. Indexing works properly using different programs suggesting a primitive tetragonal lattice with $a = b = 66.8 \text{ \AA}$ and $c = 113.2 \text{ \AA}$ and one molecule in the asymmetric unit. Merging statistics and automatic space group assignment in various program packages suggests point group 422 with a $4_{1/3}$ screw axis along the fourfold and also a twofold screw axis (space group $P4_12_12$ or $P4_32_12$). But some strong violations of systematic absences at low resolution along the fourfold and one twofold axis indicate that space group $P4_{1/3}2_12$ may not actually be correct. Despite this, a three-wavelength SeMet-MAD dataset was measured with a resolution of 2.8 \AA and useable anomalous signal to about 3.5 \AA . SHELXD [1] consistently found a solution for the Se-substructure in space group $P4_12_12$ (4 out of 5 Se atoms with CC all of 52.9 and CC weak of 33.6). After solvent flattening with SHELXE [1], the experimental electron density revealed the expected three helical bundle. No improvement was achieved in further attempts of density modification using different programs from the CCP4 program suite [2].

Using the Se positions as anchors for sequence assignment, around 80 amino acids (out of a total of 221) could be built, another 40 could be placed with some uncertainty. The free R-factor stalled at $\sim 46 \%$ with a FOM of $\sim 50 \%$, and little difference density that would have allowed to extend the model. This model was taken for molecular replacement with PHASER [3] into the single datasets of the MAD experiment and other datasets from the native protein. Single solutions were found but with rather low Z-scores of ~ 3.6 (rotation function) and ~ 6 (translation function). We also tried molecular replacement with lower symmetry down to $P4_1$, $P2_12_12$ and $C222_1$ as well as experimental phasing in these space groups. But this did not result in better phases that allowed extending the structure or refining it to lower R-factors.

Apparently, this is a case of severe pseudosymmetry as refinement of an initial model in the suggested high symmetry space group $P4_12_12$ did not work. Pseudo-merohedral twinning in a lower symmetry space group seems possible but analysis with PHENIX Xtriage [4] did not detect any indication for this. Experimental phasing in space groups $P2_1$ or $P1$ did not work due to lower multiplicity of the data. After all, other crystallographic or biochemical approaches may be required to determine the structure of this protein.

[1] G.M. Sheldrick, Acta Cryst. 2008, A64, 112-122.

[2] Collaborative Computational Project, Number 4, Acta Cryst. 1994, D50, 760-763.

[3] A.J. McCoy, R.W. Grosse-Kunstleve, P.D. Adams, M.D. Winn, L.C. Storoni, R.J. Read, J. Appl. Cryst. 2007, 40, 658-674.

[4] P.D. Adams, P.V. Afonine, G. Bunkóczi, V.B. Chen, I.W. Davis, N. Echols, J.J. Headd, L.W. Hung, G.J. Kapral, R.W. Grosse-Kunstleve, A.J. McCoy, N.W. Moriarty, R. Oeffner, R.J.

Read, D.C. Richardson, J.S. Richardson, T.C. Terwilliger and P.H. Zwart. Acta Cryst. 2010, D66, 213-221.

MS03-P05

Unraveling the function of uncharacterized operons in *Pseudomonas aeruginosa*

C. Feiler¹, D.V. Mavrodi², L.S. Thomashow², W. Blankenfeldt¹

¹Universität Bayreuth, Biochemie 2, Bayreuth, Germany

²Washington State University, Department of Plant Pathology, Pullman, WA, USA, United States

Pseudomonas aeruginosa is considered as one of the most problematic opportunistic infectious bacteria, leading to persistent infections that are difficult to treat. This is due to the fact that *P. aeruginosa* produces a large arsenal of virulence factors, embeds itself in biofilm and possesses effective efflux systems that render xenobiotics harmless. In most cases, *P. aeruginosa* strikes hospitalized people and cystic fibrosis patients, where it is the main reason for low life expectancy.

The genome of *P. aeruginosa* contains over 5500 open reading frames in 6.3 million base pairs. Common with other sequenced micro-organisms, a high percentage of over 40% of the identified genes are functionally not annotated. In order to unveil new opportunities for drug discovery, it is important to shed light onto this "white space" of the genome map. We are currently developing a two-tier approach to systematically unveil the function of uncharacterized proteins by making use of the fact that in prokaryotes functionally linked genes are usually clustered in operons that can be predicted by bioinformatics methods. Loss- and gain-of-function mutants of uncharacterized operons are generated and their metabolites are analyzed by UPLC-MS methods. In addition, we are employing x-ray crystallography to gain detailed structural insight and derive functional hypotheses. Combined insight from both techniques will be confirmed with biochemical methods.

Here, we report operon selection and the crystal structures of two targets that are currently being investigated.

MS05-P01

Behind the scenes: An insight into the crystal energy landscapes of two new dimeric toluene-2,4-diisocyanate polymorphs

L. Vella-Zarb¹, R. Dinnebier¹

¹Max Planck Institute for Solid State Research, X-ray services, Stuttgart, Germany

Polymorphism in molecular crystals is a phenomenon that continues to attract the attention of researchers across many scientific disciplines¹, primarily due to the fact that a compound can exhibit significantly different physicochemical properties when its molecules adopt a different arrangement in three-dimensional space. The correlation between crystal structures and their physical properties may go well beyond intermolecular interactions, and insight into the energy landscapes of the different forms may provide a better understanding of the behaviour of such materials.

Toluene diisocyanate (TDI), one of the most widely-used aromatic diisocyanates², is produced as an intermediate in the plastics industry, primarily in the manufacture of adhesives, sprays, foam cushioning for upholstery, elastomers, insulation materials and coatings, with particular use in the formation of high-quality laquers for the car and aviation industries. It exists as two isomers, depending on the positions of the two isocyanate groups. The 2,4 isomer is an asymmetrical molecule whose two isocyanate groups show very different reactivity³, and it dimerises to form a white powder which crystallises in at least two polymorphic forms (Form A and Form B) depending on reaction conditions. At first sight the two forms show very few structural differences. However, in spite of a marked similarity between them, significant discrepancies in

their physical properties exist. Form A is the more flexible material, but it has been found to convert readily to Form B under ambient conditions.

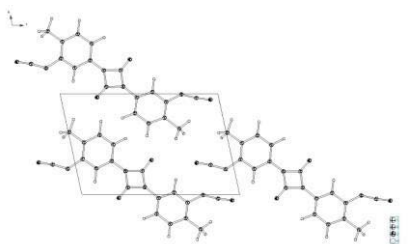
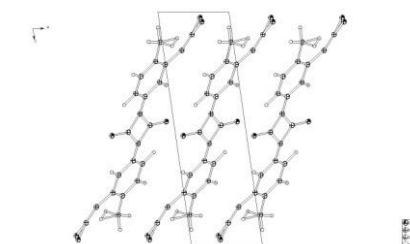
The structures of two polymorphs of dimeric TDI have been successfully solved from high resolution laboratory powder diffraction data. Clear differences between the two thermodynamically similar polymorphs have been observed, and these have been highlighted by analysis of the partitioned energy terms. Dispersion and repulsion contributions in particular have been found to play a very important role in the total energy landscape of these forms. Calculated lattice energies suggest that Form B is slightly more thermodynamically stable than Form A, providing an energetic justification for the preferential conversion of one form into the other.

In this poster we present the crystal structures of the two dimeric TDI polymorphs together with an examination of their packing features by comparison of their total lattice energies and the respective coulombic, polarization, dispersion and repulsion contributions.

1. J. Bernstein, Polymorphism in Molecular Crystals, Oxford University Press, Oxford, 2002.
2. D. Randall and S. Lee, The Polyurethanes Book, Wiley, New York, 2002.
3. UK Health and Safety Executive, Isocyanates: Toxic Hazards and Precautions, Guidance Note EH16, (3rd edition), UK HSE Books, 1984.

Figure 1. Form A - view along the b axis

Figure 2. Form B - view along the b axis



MS05-P02

From x-ray macro- and microstructure characterization substances and materials to sub-nano and electronic levels

B. Kodess^{1,2}, P. Kodess³

¹VNIIMS -ICS&E, Crystals Metrology, Moscow Aurora, Russian Federation

², Russian Federation

³ICS&E, Materials Science, Aurora, United States

The results are considered of development of x-ray characterization methods, which have been realized by the authors during the last 45 years for a wide range of lengths of substances and materials structures.

Our first x-ray works were connected with the Laue pattern analysis for evaluation of phase composition of minerals and precise determination of crystal lattice parameters of steels, alloys after being heavily shocked or after various thermo-mechanical impact [1-2]. Accurate x-ray diffractometry for the same specimens

enabled to ascertain interrelationships between nano-microstructural and functional characteristics - strength, corrosion resistance and survival of products made of them. X-ray methods for measurement of residual stress and immediate and very fast determining of the resource were implemented (for example, in wheels of an airplane's landing gears [3]). The influence both of radiation exposure and the features of behavior of self-organizing processes have been investigated in-situ measurements which were carried out during a very long time (200-1500 hours continuously) for individual groups of reflection and for a full diffraction pattern [4].

X-ray technique we used for the observation of low-temperature phase transition and preceded intensity anomalies (in the range of 4-200 K). The existence of these anomalies have been found first time by us when appear far from the phase transition temperature [5-6].

For better understanding of these phenomena there have been developed methods or high- and higher accurate x-ray measurements at the atomic and electronic levels. New interrelationships were found with Tc [7]. Owing to numerous full Ewald's sphere single crystals experiments we have been reliably informed about important features of valence electron density distribution in key materials of modern technology [8-9]. Charge redistribution was determined by us for substances with different types of chemical bonds (with a dominance of ionic, covalent bonds or metallic part of it). The highest accuracy allowed us to make comparisons with the calculation data from "first" principles, and propose and choose from suggested hypotheses for substances behavior. And moreover, we developed an x-ray research methodology and practice [10] for establishing of parameters of the electron-electronic interactions which today are a basis for modern theories of collective phase transitions (superconductivity, ferroelasticity and magnetism).

In the last decade, based on our groundwork for over the 40 years we have created and certified a system of new reference standard materials (including the use of CCD detectors for digital recording of Laue patterns). This system provides a basis for modern metrological support of the development of measurement techniques, as well as for testing them and validation and pattern approval of x-ray equipment [11-14].

MS05-P03

Static and dynamic charge densities of Lysozyme

J. Netzel¹, S. van Smaalen¹

¹University of Bayreuth, Laboratory of Crystallography, Bayreuth, Germany

Static and dynamic charge densities of hen egg-white lysozyme [1] (HEWL; PDB reference: 2vbl, $d_{\min} = 0.65 \text{ \AA}$) from multipole models and the dynamic density by the Maximum Entropy Method (MEM) are reconstructed. Disorder in main- and side-chain residues and atomic sites can be revealed and described by the MEM without introducing constraints on the parameters to be refined. The electron density at bond critical points, their principal curvatures and their Laplacians are determined according to Bader's Atoms in Molecules Theory [2]. Energy densities at bond critical points are calculated according to Abramov [3]. Geometrical, topological and energetic properties of chemical bonds and non-bonded interactions are characterized to allow a structural study and thus functional study of this enzyme [4]. The effect of thermal motion can be directly studied by comparison of topological properties of the densities by the MEM and the dynamic densities of multipole models.

[1] Wang, J.; Dauter, M.; Alkire, R.; Joachimiak, A.; Dauter, Z., *Acta Cryst. D63*, 1254-1268 (2007).

[2] Bader, R.F.W., *AIM - A Quantum Theory*, Oxford University Press (1994).

[3] Abramov, Y.A., *Acta Cryst. A53*, 264-272 (1997).

[4] Netzel, J.; van Smaalen, S., *Acta Cryst. B65*, 624-638 (2009).

MS05-P04

A new access to extinction corrections

A.K. Hüsecken¹, U. Pietsch²¹Uni Siegen / Delta, Physik, Dortmund, Germany²Universität Siegen, Physik, Siegen, Germany

In x-ray crystal structure analysis a problem, called extinction, occurs due to multiple scattering in crystals. Over the years several extinction correction theorems have been formulated, but the used parameters have never been proved to be valid for a certain crystal under investigation. Perfect crystals scatter according to the dynamical theory ($I \sim |F|$) and imperfect crystals or ideal mosaic crystals due to the kinematical theory ($I \sim |F|^2$). In most cases, the measured intensities of real crystals are in between both cases and an extinction correction is needed to fulfil the kinematic approach.

Present theories dealing with extinction corrections are based on the approach of a mosaic crystal and describe x-ray scattering in terms of the kinematic approach using certain "correction terms" to implement the structure of a real crystal [1, 2, 3]. The whole crystal can also have different shapes, like a sphere, cube or plate. The extinction correction is then only a factor which is multiplied with the theoretical intensity to get the measured intensity. At the moment crystallographers use the extinction correction as a black box. They don't prove whether the extinction model used is valid or invalid because the parameters are typically not verified by the experiment.

The mosaic blocs within a real crystal are misorientated to each other and are affected by lattice strain. In addition both 3D shape and size of the blocs are not known. All these parameters can be determined by high-resolution x-ray diffraction techniques as known from semiconductor research performing ω - and ω -2 θ -scans through certain reciprocal lattice points.

The determined parameters from the FWHMs of these scans can be used to determine extinction.

Our aim for crystallography is to perform ω - and ω -2 θ -scans only for a few reflections, make a short analysis, from which one gets the size of the mosaic blocks, the misorientation and the lattice strain. With these parameters it should then be possible to decide which one is the best extinction correction to use.

Literature:

[1] P.J. Becker and P. Coppens: Acta Cryst. 1974, A30, 129.

[2] P. Suortti: Acta Cryst. 1982, A38, 642.

[3] W.H. Zachariasen: Acta Cryst. 1967, 23, 558

MS05-P05

Direct insight into the effect of protonation and deprotonation of an organic molecule: The case of sulfadiazine

F. Pan¹, R. Wang¹, U. Englert¹¹RWTH Aachen University, Institute of Inorganic Chemistry, Aachen, Germany

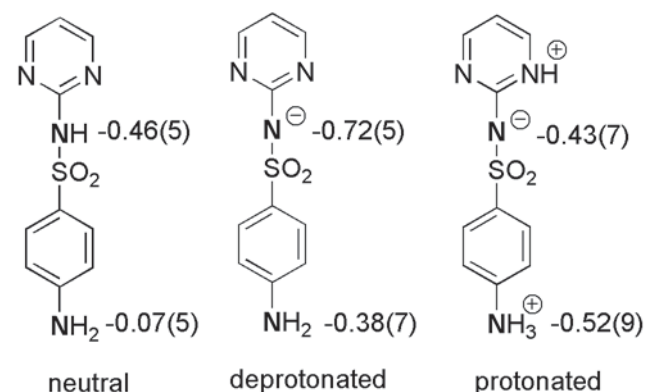
High resolution X-ray diffraction has proven to be a powerful tool to deeply investigate electron density in crystalline materials. Considerable research work on organic compounds has been focused on this field during past decades, and several databases, either with an experimental (ELMAM/ELMAM2) or with a theoretical (Invariom3, UBDB4) background were constructed to facilitate the analysis of electron densities. However, how is coordination to a metal reflected in the electron density of a potential ligand? More comparative studies are required to verify these issues.

In our previous work, we investigated the electron density distribution of a sulfadiazine Zn(II) complex for which the coordination geometry strongly depends on temperature. To further analyze the electron density of the uncoordinated sulfadiazine ligand, we successfully obtained crystals of the neutral, deprotonated and protonated sulfadiazine compounds (see figure 1). The structure was surprising for the protonated ligand (right in the figure 1): In contrast to our expectation, we encountered

protonation at one of the pyrimidine and the aniline N atoms, together with a deprotonated amido-N atom, formally resulting in a negative charge for the amidosulfonato group. The numbers in the figure 1 refer to monopole charges at the N atoms, obtained from a multipole refinement of high resolution X-ray diffraction data for all the three compounds. Multipole refinements according Hansen-Coppens⁵ formalism implemented in XD2006 suite⁶ were employed to obtain the electron density distribution. The results show that there are differences for the monopole charges of N atoms (especially for amido-N and aniline-N) among the three compounds: the negative charges concentrate in the sulfamide groups; however, the N atom with an extra H atom also strives for negative charge. Systematic analyses and comparisons on the electron density distribution will be discussed in detail.

Reference:

- Coppens, P., X-ray Charge Densities and Chemical Bonding; IUCr, Oxford University Press: New York, 1997.
- a) Pichon-Pesme, V., et al. J. Phys. Chem. 1995, 99, 6242; b) Domagała, S. & Jelsch, C. J. Appl. Cryst. 2008, 41, 1140;
- a) Dittrich, B., et al. Angew. Chem. Int. Ed. 2004, 43, 2718; b) Dittrich, B., et al. Acta Cryst. 2006, D62, 1325;
- a) Volkov, A., et al. Phys. Chem. A 2004, 108, 4283; b) Dominiak, P. M., et al. J. Chem. Theory Comput. 2007, 3, 232;
- Hansen, N. K.; Coppens, P. Acta Crystallogr. Sect A, 1978, 34, 909;
- Volkov, A., et al. XD2006, University of New York at Buffalo, USA, 2006.



MS05-T02

The generalized invariom database

B. Dittrich¹, C.B. Hübschle¹, J.J. Holstein¹, K. Pröpper¹, T. Stolper¹¹Georg-August-Universität, Institut für Anorganische Chemie, Göttingen, Germany

The invariom database [1] was further developed and extended with three clear aims in mind: First to enable the refinement of more accurate and more precise geometries and atomic displacement parameters with respect to the independent atom model from good single-crystal x-ray diffraction data of a resolution better than $\sin \theta / \lambda = 0.6 \text{ \AA}^{-1}$ (or $d = 0.83 \text{ \AA}$), mainly for small-molecule structures. Secondly to derive and calculate molecular properties like dipole moments and the electrostatic potential not only for small-molecule structures but also for selected high-quality protein and nucleic acid structures with a resolution not much worse than $d = 1.1 \text{ \AA}$. Thirdly to allow easy application aided by a well-defined scattering factor notation and user-friendly software like molecoolQt [2] to extend the reach of charge-density research. The invariom database and molecoolQt are interfaced to the XD2003 or 2006 suite of programs [3] and are based on the Hansen/ Coppens multipole model [4]. We here report on the extension and the improvement of the invariom database. It currently contains more than 1650 scattering factors derived from over 750 model compounds and covers a wide range of chemical

environments as common in organic chemistry. An extension of the invariom notation [5,6] is introduced. It has been thoroughly tested and allows a generalized application. A future aim is to extend the reach to inorganic compounds.

- [1] Dittrich, B., Hübschle, C. B., Luger, P. & Spackman, M. A. (2006a). *Acta Cryst. D*, 62, 1325-1335.
 [2] Hübschle, C. B. & Dittrich, B. (2011). *J. Appl. Cryst.* 44, 238-240.
 [3] Volkov, A., Macchi, P., Farrugia, L. J., Gatti, C., Mallinson, P., Richter, T. & Koritsánszky, T., (2006). XD2006 - A Computer Program Package for Multipole Refinement, Topological Analysis of Charge Densities and Evaluation of Intermolecular Energies from Experimental or Theoretical Structure Factors.
 [4] Hansen, N. K. & Coppens, P. (1978). *Acta Cryst. A*, 34, 909-921.
 [5] Dittrich, B., Koritsánszky, T. & Luger, P. (2004). *Angew. Chem. Int. Ed.* 43, 2718-2721.
 [6] Dittrich, B., Hübschle, C. B., Messerschmidt, M., Kalinowski, R., Girnt, D. & Luger, P. (2005). *Acta Cryst. A*, 61, 314-320.

MS06-P01

Crystal Structure of *Nicotiana tabacum* malonyltransferase (NtMat1) in complex with its cofactor malonyl-CoA (MLC)

B. Manjassetty¹, X.-H. Yu², S. Panjekar³, M. Chance⁴, G. Taguchi⁵, C.-J. Liu⁶

¹European Molecular Biology Laboratory, BM14, Grenoble, France, France

²Brookhaven National Laboratory, Biology Department, New York, USA, United States

³Australian Synchrotron, Victoria, Australia, Australia

⁴Case Western Reserve University, Case Center for Proteomics & Bioinformatics, Cleveland, USA, United States

⁵Shinshu University, Division of Applied Biology, Tokida, Japan, Japan

⁶Brookhaven National Laboratory, Biology Department, New York, USA, United States

Malonylation is a key reaction in the metabolism of xenobiotic phenolic glucosides and is considered as one of the detoxification system in tobacco plants¹. *Nicotiana tabacum* malonyltransferase 1 (NtMAT1) is an enzyme catalyzing the transfer of a malonyl group onto a range of endogenous flavonoid glucosides and xenobiotic phenolic compounds including naphthol glucosides (NAGs)². In order to gain insights into the molecular basis for the catalytic mechanism and substrate specificity of NtMat1, the recombinant enzyme was produced in *Escherichia coli*, purified, and then crystallized in complex with cofactor malonyl-CoA (MLC) and 2-NAG. Its crystal structure was solved to 3.1Å resolution. The structure shows that the protein is composed of two mixed subdomains typically found in the other BAHD acyltransferases³ and it is structurally most similar (39.7% sequence identity) to anthocyanin malonyltransferase (Dm3Mat3 - PDB ID 2EIT)⁴. The cofactor MLC is modeled based on the partial electron density and refined, whereas the co-crystallized phenolic substrate 2-naphthol glucoside (2NAG) is completely invisible. The partial structure of MLC is bound to NtMat1 and located at the similar region as that of Dm3Mat3 structure; however, the interaction of MLC is quite different. At one end of MLC, which is solvent exposed, the adenosyl ring is not fully visible in the electron density map. At the other end of MLC, the most of the cofactor atoms are highly disorder.

Based on the partial structure of MLC molecule, the full structure of MLC molecule is docked. In the docked MLC molecule the adenosyl ring is flipped to the opposite side to that of MLC molecule when compare to the structure of Dm3Mat3. This might be due to its stacking interactions with adenosyl ring from neighbouring MLC molecule. This clearly hints the basis of tremendous diversity in cofactor binding which in turn might be responsible for substrate specificity differences among BAHD family of enzymes. On the other hand, the basis for disorder nature

and invisibility of malonyl moiety at the other end of MLC might be attributed to the enzyme catalysis, in which the malonylated NAG had been absent from the enzyme active sites. Comparing to the structure of Dm3Mat3, a large structural disparity of NtMat1 was evidenced in the binding site for phenolic acceptor molecules, explaining their functional diversity. The structural data of NtMat1, correlated with the biochemical and biophysical properties of the enzyme, provide the initial clues allowing us to define the substrate specificity, and to understand its catalytic mechanism, particularly how it transfers malonyl group onto the phenolic acceptors.

References:

1. Taguchi G, Ubukata T, Nozue H, Kobayashi Y, Takahi M, Yamamoto, H. & Hayashida N. (2010) Malonylation is a key reaction in the metabolism of xenobiotic phenolic glucosides in *Arabidopsis* and tobacco. *Plant J*, 63(6):1031-1041.
2. Taguchi, G., Shitchi, T., Shirasawa, S., Yamamoto, H. & Hayashida N. (2005) Molecular cloning, characterization, and downregulation of an acyltransferase that catalyzes the malonylation of flavonoid and naphthol glucosides in tobacco cells. *Plant J*, 42(4):481-491.
3. D'Auria, J.C. (2006) Acyltransferases in plants: a good time to be BAHD. *Curr Opin Plant Biology*, 9(3):331-340.
4. Unno, H., Ichimaida, F., Suzuki, H., Takahashi, S., Tanaka, Y., Saito, A., Nishino, T., Kusunoki, M. & Nakayama, T. (2007). Structural and Mutational Studies of Anthocyanin Malonyltransferases Establish the Features of BAHD Enzyme Catalysis. *J Biol Chem*, 282:15812-15822.

MS06-P02

SiiE: insights into a giant 5559 amino acids adhesin of *Salmonella enterica*.

M. Griebel¹, Y.A. Muller¹

¹Lehrstuhl für Biotechnik, Friedrich-Alexander Universität Erlangen-Nürnberg, Erlangen, Germany

Infections of *Salmonella enterica* can cause intestinal inflammation, diarrhoea or even a life-threatening systemic disease. The adhesion and invasion from *Salmonella* into host cells is encoded in two different gene clusters. The *Salmonella* Pathogenicity Island 1 encodes a type III secretion system that injects effector proteins of *Salmonella* into the host cells to enable invasion (Haraga *et al.*, 2008). A second gene cluster referred as *Salmonella* Pathogenicity Island 4 encodes six proteins termed SiiA to SiiF. SiiC, SiiD and SiiF form a type I secretion system that is responsible for the secretion of SiiE (Gerlach *et al.*, 2008, Wagner *et al.*, 2011). SiiE is the adhesin of *Salmonella enterica* and mediates the initial contact between the bacterial cell and the intestinal epithelial cells of the host. SiiE consists of 5559 amino acids and exhibit 53 Ig-like domains. We expressed an engineered deletion variant (miniSiiE, 97 kDa) containing the functional important N- and C-terminus. We used limited proteolysis to reproducibly generate a 30 kDa fragment of miniSiiE. Mass spectrometry experiments revealed that the Ig-like domains 50 to 52 were present in this fragment. We were able to crystallize this protein and solved the structure by SAD-phasing. The structure was solved in space group C2 and refined to a resolution of 1.85 Å.

Gerlach, R. G., Claudio, N., Rohde, M., Jackel, D., Wagner, C. & Hensel, M. (2008). *Cell Microbiol* 10, 2364-2376.

Haraga, A., Ohlson, M. B. & Miller, S. I. (2008). *Nat Rev Microbiol* 6, 53-66.

Wagner, C., Polke, M., Gerlach, R. G., Linke, D., Stierhof, Y. D., Schwarz, H. & Hensel, M. (2011). *Cell Microbiol* 13, 1286-1301.

Figure 1: Crystal structure of Ig-like domains 50 to 52 from the *Salmonella* adhesin SiiE.

**MS06-P03****The *trans*-dienelactone hydrolase from *Cupriavidus necator*: a novel metalloenzyme**C. Roth¹, S. Wegener², M. Schlömann², N. Sträter¹¹University of Leipzig, Center for Biotechnology and Biomedicine, Leipzig, Germany²Technical University "Bergakademie" Freiberg, Environmental Microbiology, Freiberg, Germany

Fluoroaromatic compounds are very persistent exclusively man made environmental pollutants. Their unique properties render them as potent inhibitors for enzymes or as compounds that interfere with membrane transport processes or cell-cell communication. Due to the extraordinary stability of a fluor-carbon bond these compounds are very recalcitrant against degradation. Nevertheless a few bacteria are able to metabolize these compounds and use them as the sole energy and carbon source. *Cupriavidus necator* is able to degrade 4-fluorobenzoate to intermediates of the citric acid cycle. During bacterial growth enzymes of the metabolic pathway of unsubstituted aromatic compounds are induced as well as a dienelactone hydrolase (*tDLH*) and a maleylacetate reductase crucial for complete metabolization. A sequence alignment shows no relationship of *tDLH* to enzymes of the well known dienelactone hydrolase family and *tDLH* does not contain the catalytic triad that is essential for activity of these enzymes. Furthermore, activity of *tDLH* depends on the presence of metal ions with a preference for hard metal ions. However the alignment shows that *tDLH* can be classified in an uncharacterized protein family of putative metal dependent hydrolases and cyclases. In contrast to previously characterized pathways the gene of *tDLH* is not part of a gene cluster inducible in response to available substituted or unsubstituted aromatic compounds. To get insight in the structure and function of this so far uncharacterized enzyme family we expressed and characterized the enzyme for subsequent structural studies.

MS06-P04**Crystal structure of the autochaperone region of the *Shigella flexneri* autotransporter IcsA**K. Kühnel¹, D. Diezmann¹¹MPI for biophysical Chemistry, Dept. of Neurobiology, Göttingen, Germany

The IcsA (intracellular spread gene A) autotransporter is a key virulence factor from *Shigella flexneri* that is essential for the actin based motility of the pathogen inside infected cells. Autotransporters consist of a N-terminal signal sequence, a passenger domain and a C-terminal transmembrane domain. We identified a stable IcsA fragment corresponding to the autochaperone region of the passenger domain. The crystal structure of the autochaperone region (IcsA-AC) comprising residues 591-758 was determined at 2.0 Å resolution. Using far-UV CD measurements we could show that thermal unfolding of the autochaperone region is reversible.

MS06-P05**Structural basis for Furanol formation in strawberry fruits**A. Schiefner¹, Q. Sinz², I. Neumaier¹, W. Schwab², A. Skerra¹¹Technische Universität München, Biologische Chemie, Freising-Weihenstephan, Germany²Technische Universität München, Biotechnologie der Naturstoffe, Freising-Weihenstephan, Germany

Strawberry aroma ranks among the most popular fruit flavors. It is the result of a complex mixture of numerous secondary metabolites, dominated by uncommon furanone compounds. In particular, 4-hydroxy-2,5-dimethyl-3(2H)-furanone (HDMF), known as Furanol, exhibits a fruity, caramel-like odor and has been identified as the key flavor component of strawberry aroma (1). The strawberry (*Fragaria vesca*) genome encodes an enone oxidoreductase (FvEO), which is ripening-induced and negatively regulated by auxin. FvEO catalyzes the reduction of the exo-C=C bond of the highly reactive precursor 4-hydroxy-5-methyl-2-methylene-3(2H)-furanone (HMMF) to HDMF with either NADPH or NADH serving as co-substrate (2). In order to elucidate the structural basis of Furanol formation by FvEO, we expressed FvEO in *Escherichia coli* and determined its X-ray structure both in the apo form, in complex with NADP and with different substrates as well as a substrate analogue. The structure revealed a monomeric two-domain architecture that belongs to the family of zinc-independent medium chain dehydrogenases/reductases (MDR), indicating a preference for NADP(H) as co-substrate. Furthermore, the crystal structures of substrate complexes in conjunction with deuterium labeling experiments revealed the peculiar molecular mechanism of HMMF reduction by FvEO.

(1) Raab, T., López-Ráez, J.A., Klein, D., Caballero, J.L., Moyano, E., Schwab, W., and Muñoz-Blanco, J. (2006) FaQR, required for the biosynthesis of the strawberry flavor compound 4-hydroxy-2,5-dimethyl-3(2H)-furanone, encodes an enone oxidoreductase. *Plant Cell* 18, 1023-1037.

(2) Klein, D., Fink, B., Arold, B., Eisenreich, W., and Schwab, W. (2007) Functional characterization of enone oxidoreductases from strawberry and tomato fruit. *J. Agric. Food Chem.* 55, 6705-6711.

MS06-P06**Structure of a Classical MHC Class I Molecule That Binds****"Non-classical" Ligands**C.S. Hee¹, S. Gao², B. Loll³, M.M. Miller⁴, B. Uchanska-Ziegler¹,O. Daumke², A. Ziegler¹¹Freie Universität Berlin, Institut für Immunogenetik, Charité-Universitätsmedizin Berlin, Campus Benjamin Franklin, Berlin, Germany²Max-Delbrück-Centrum für Molekulare Medizin, Berlin, Germany³Freie Universität Berlin, Strukturbiologie, Berlin, Germany⁴City of Hope, Beckman Research Institute, Duarte, United States

Chicken YF1 genes share a close sequence relationship with classical MHC class I loci, but map outside of the core MHC region. The YF1 heavy chain is closely related to that of classical MHC-B and mammalian MHC class I HC, but not to non-classical CD1 heavy chain. The analysis of MHC-encoded class I molecules of the chicken lags far behind that of mammals, so that many questions, e.g. with regard to the nature of the cellular interaction partners of YF1 and CD1 molecules, are currently unsolved.

To obtain insights into their function, we reconstituted the chicken YF1*7.1/β₂-microglobulin complex in absence of any ligand. The obtained crystals diffracted X-rays to 1.3 Å resolution (1) and the structure could be solved by molecular replacement (2).

The YF1*7.1 complex exhibits the typical architecture of classical MHC class I molecules (3) with binding groove-forming, anti-parallel α1- and α2-helices atop of a β-sheet platform. β₂m and the α3-domain occupy the standard positions below the platform. However, the YF1*7.1 binding cleft is narrower than that of peptide-presenting MHC class I molecules and is lined by many hydrophobic residues (2).

To our surprise we could detect an extended patch of electron density within the hydrophobic binding groove which could be modeled as non-peptidic ligand that prompted us to reconstitute YF1*7.1 also with various self-lipids. An assessment of YF1*7.1 by native isoelectric focusing indicated that the molecules were also able to bind nonself-lipids. The ability of YF1*7.1 to bind to hydrophobic ligands is unprecedented among classical MHC class I proteins and might aid the chicken immune system to recognize a diverse ligand repertoire with a minimal number of MHC class I molecules.

The prerequisites for the latter characteristic are so far met only by the YF1*7.1 molecule which can be regarded as a “hybrid” structure, favouring the interaction with “non-classical” ligands through the combination of a hydrophobic binding groove with a classical scaffold.

The results presented here attest to the unusual versatility of classical MHC class I antigens. Not only do they display peptides or post-translationally modified protein fragments, but they may also bind hydrophobic ligands. Our analyses demonstrate that YF1 molecules deserve to be studied in more detail, because they bridge, at least in structural terms, the traditional gap between peptide-presenting classical and lipid-displaying non-classical class I molecules.

References:

Hee, C.S., Gao, S., Miller, M.M., Goto, R.M., Ziegler, A., Daumke, O., Uchanska-Ziegler, B. Expression, purification and preliminary X-ray crystallographic analysis of the chicken MHC class I molecule YF1*7.1. (2009) *Acta Crystallogr.* F65, 422-425.
 Hee, C.S., Gao, S., Loll, B., Miller, M.M., Uchanska-Ziegler, B., Daumke, O., Ziegler, A. Structure of a classical MHC class I molecule that binds “non-classical” ligands. (2010) *PLoS Biology*,8(12), e1000557.
 Madden D.R. (1995) The 3-Dimensional structure of peptide-MHC complexes. (1995) *Ann. Rev. Immunol.*, 1,587-622.

MS06-P07
The Inhibited Conformation of The Eukaryotic Rrp44 Exonuclease

D.L. Makino¹, M. Baumgärtner¹, F. Bonneau¹, E. Conti¹
¹Max Planck Institute of Biochemistry, Department of Structural Cell Biology, Martinsried, Germany

Many pathways that involve 3'-to-5' RNA degradation in eukaryotic cells require the Exosome complex. The nine core subunits of the Exosome organize into a barrel-like structure, reminiscent of bacterial RNase PH and PNPase. However, the eukaryotic core is catalytically inactive (1,2). The activity of the 10-subunit Exosome stems from the association with the Rrp44 exonuclease. Binding to the Exosome is known to downregulate the activity of Rrp44 (1,2,3), but the mechanisms by which the activity of Rrp44 is modulated are not fully understood.

S. cerevisiae Rrp44 is a 114kDa protein belonging to the RNaseII family of hydrolytic 3'-to-5' exonucleases. In addition, it presents endoribonucleolytic activity at its N-terminal PIN domain (4,5,6). The PIN domain also serves as a tethering element to the Exosome complex, as observed in the X-ray structural analysis of *S.cerevisiae* Rrp44 bound to two Exosome core subunits, Rrp41 and Rrp45 (7). This ternary complex showed that the exonuclease core of Rrp44 is inhibited, unlike the bacterial RNase II structure (8). In the absence of RNA substrate, a beta-hairpin motif approximately 20-residue long folds into the active site. This conformation involves a major movement from that observed in the crystal structure of Rrp44 bound to RNA (3).

In order to assess whether this inhibited conformation is induced upon binding of Rrp44 to the Exosome, we determined the 1.7Å resolution structure of the exonuclease region of *S. pombe* Rrp44 in the RNA unbound form. We find that the *S. pombe* Rrp44 catalytic core is also inhibited in the absence of RNA and Exosome subunits. Furthermore, the preliminary reconstitution and RNase

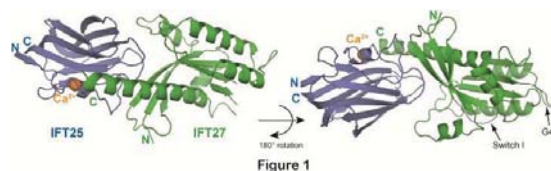
protection results of the 10-subunit *S. pombe* Exosome complex are also presented here.

(1) Dziembowski, A. et al. (2007) A single subunit, Dis3, is essentially responsible for yeast Exosome core activity. *Nat. Struct. Mol. Biol.*, 14, 15-22.
 (2) Liu, Q. et al. (2006) Reconstitution, activities, and structure of the eukaryotic RNA Exosome. *Cell*, 127, 1223-1237.
 (3) Lorentzen, E. et al. (2008) Structure of the active subunit of the yeast Exosome core, Rrp44: Diverse modes of substrate recruitment in the RNase II nuclease family. *Mol. Cell*, 29, 717-728.
 (4) Schneider, C. et al. (2009) The N-terminal PIN domain of the Exosome subunit Rrp44 harbors endonuclease activity and tethers Rrp44 to the yeast core Exosome. *Nuc. Acids. Res.*, 37, 1127-1140.
 (5) Lebreton, A. et al. (2008) Endonucleolytic RNA cleavage by a eukaryotic Exosome. *Nature*, 456, 993-996.
 (6) Schaeffer, D. et al. (2009) The Exosome contains domains with specific endoribonuclease, exoribonuclease and cytoplasmic mRNA decay activities. *Nat. Struct. Mol. Biol.*, 16, 56-62.
 (7) Bonneau, F., Basquin, J. et al. (2009) The Yeast Exosome Functions as a Macromolecular Cage to Channel RNA Substrates for Degradation. *Cell*, 139, 547-559.
 (8) Frazão, C. et al. (2006) Unravelling the dynamics of RNA degradation by ribonuclease II and its RNA-bound complex. *Nature*, 443, 110-114.

MS06-P08
Crystal structure of Intraflagellar Transport Complex 25/27

S. Bhogaraju¹, E. Lorentzen¹
¹MPI of Biochemistry, Structural Cell Biology, Martinsried, Germany

Cilia are microtubule based membrane projections present on the surface of almost every vertebrate cell and serve a wide variety of sensory and mechanistic functions such as vision, olfaction and locomotion. Cilia exist in different shapes and sizes based on the type of cell/organism and on average a single cilium is expected to contain more than 600 different proteins. Intraflagellar transport (IFT) mediates the targeting of these proteins from their site of translation in the cytoplasm to the cilium. The IFT complex (IFTC), consisting of at least 20 proteins, is at the center of this process by transporting cargo proteins back and forth between the cytoplasm and cilium with the help of kinesin-II and dynein motors. The IFT25-IFT27 complex is a part of the core of the IFT complex and is suggested to be involved in the initiation of IFT. We determined the 3D structure of the *Chlamydomonas* IFT25-IFT27 complex at 2.6Å resolution by X-ray crystallography. The structure reveals the typical small GTPase domain of IFT27 and a jellyroll fold adopted by IFT25. It also reveals that the C-terminal helical part of IFT27 interacts with IFT25. Structure-guided point mutations in IFT25 can abolish the interaction with IFT27. Additional biochemical experiments reveal that IFT27 can hydrolyze GTP with extremely low activity (consistent with the lack of a catalytic glutamine) and binds GTP and GDP with micromolar affinities. The low catalytic activity of IFT27 means that it needs a GTPase activating protein (GAP) to enhance its GTPase activity. A BLAST search reveals 7 potential GAPs in the genome of *Chlamydomonas*. We tested two of these proteins so far and found that they don't act as a GAP for IFT27. Additionally, *in vitro* pull-downs and size exclusion chromatography studies reveal that the IFT25/IFT27 complex directly binds to another IFT subcomplex containing IFT81 and IFT74.



MS06-P09

Protein kinase domain of CTR1 from *Arabidopsis thaliana* Promotes Ethylene Receptor Cross-talk

H. Mayerhofer¹, S. Panneerselvam², J. Mueller-Dieckmann¹

¹EMBL Hamburg, DESY, Hamburg, Germany

²DESY, Hamburg, Germany

Ethylene controls many aspects of plant growth and development. Signalling by the gaseous phytohormone is initiated by disulfide linked membrane bound receptors (ETR1, ETR2, ERS1, ERS2 and EIN4) and the formation of heteromeric receptor clusters contributes to the broad range of ethylene responsiveness¹. The binding site for ethylene lies within the conserved hydrophobic N-terminal receptor domain, which is located in the membrane of the endoplasmic reticulum². The C-terminal cytosolic domains resemble classical bacterial two-component systems.

Another fundamental member of the ethylene response pathway is constitutive triple response-1 (CTR1), a cytosolic protein kinase, which bears most resemblance to the RAF family of serine/threonine (S/T) protein kinases³. In *A. thaliana* the TCS-like ethylene receptors interact with CTR1 kinase via C terminal domains. In the absence of the ethylene, the receptors and therefore CTR1 are active. Binding of ethylene inactivates the receptor-CTR1 complex and results in the accumulation of EIN3 and EIN3-like 1 (EIL1) in the nucleus⁴.

CTR1 consists of 821 amino acids and two domains. The N-terminal ~540 amino acids share little sequence homology with the N-terminus of its closest homologue B-RAF. This domain interacts with the histidine kinase domains of ETR1 and ERS1. As with other MAPKKs, deletion of the N-terminal domain of CTR1 leads to a constitutively active kinase. The ~280 amino acid long C-terminal domain contains all sequence motives found in S/T protein kinases. Here, we present the crystallographic structures of the CTR1 kinase domain in its active, three-fold phosphorylated and in its inactive, un-phosphorylated form⁵.

The structures of the active, tri-phosphorylated and the unphosphorylated, inactive kinase domain of CTR1 in complex with staurosporine illustrate the conformational rearrangements that form the basis of activity regulation. Additionally, active kinase domains form back-to-back dimers in analytical ultracentrifugation experiments, while inactive and activation loop variants are remains monomers. Together with a front-to-front activation interface the active protein kinase dimers thereby engage in interactions that promote CTR1 mediated crosstalk between ethylene receptor clusters. This model provides a structural foundation for the suggested higher-order co-operativity among ethylene receptors as a mechanism to explain the high sensitivity of plants to ethylene.

References:

- Schaller, G.E., Ladd, A.N., Lanahan, M.B., Spanbauer, J.M. & Bleecker, A.B. The ethylene response mediator ETR1 from *Arabidopsis* forms a disulfide-linked dimer. *J. Biol. Chem* 270, 12526-12530 (1995).
- Schaller, G.E. & Bleecker, A.B. Ethylene-Binding Sites Generated in Yeast Expressing the *Arabidopsis* ETR1 Gene. *Science* 270, 1809-1811 (1995).
- Huang, Y., Li, H., Hutchison, C.E., Laskey, J. & Kieber, J.J. Biochemical and functional analysis of CTR1, a protein kinase that negatively regulates ethylene signaling in *Arabidopsis*. *Plant J* 33, 221-233 (2003).
- Guo, H. & Ecker, J.R. Plant Responses to Ethylene Gas Are Mediated by SCFEBF1/EBF2-Dependent Proteolysis of EIN3 Transcription Factor. *Cell* 115, 667-677 (2003).
- Mayerhofer, H., Panneerselvam, S. & Dieckmann, J.M. Protein kinase domain of CTR1 from *Arabidopsis Thaliana* promotes Ethylene receptor Cross-Talk. *Journal of Molecular Biology* (In Press)

MS07-P01

Thermal stability of metastable fcc-(Ti,Al)N in nanoscaled TiN/AlN multilayers

U. Ratayski¹, F. Klimaschin^{1,2}, U. Mühle¹, M. Šima³, D. Rafaja¹

¹TU Bergakademie Freiberg, Institute of Materials Science, Freiberg, Germany

²University of Science and Technology MISiS, Institute of New Materials and Nanotechnology, Moscow, Germany

³SHM Ltd., Šumperk, Czech Republic

Titanium aluminum nitride thin films are commonly used for high temperature applications such as machining at high cutting speeds or for dry cutting due to their excellent oxidation resistance. Metastable phases like supersaturated fcc-(Ti,Al)N or fcc-AlN were found to enhance significantly their hardness even after a thermal loading up to 900°C. For this reason, the thermal stability of metastable phases in hard protective coatings is an important issue. In order to be able to quantify the decomposition kinetics, TiN/AlN multilayers with a certain degree of the intermixing of TiN and AlN at their interfaces were investigated both in the as-deposited state and after the annealing up to 850°C.

The nanoscale TiN/AlN multilayer coatings were deposited by cathodic arc evaporation with the individual layer thicknesses of about 2.8 nm and 1.6 nm for the TiN and AlN layers, respectively. The X-ray reflectivity (XRR) measurements were complemented by the glancing angle X-ray diffraction (GAXRD) experiments as well as by transmission electron microscopy (TEM). This combination of the experimental methods allowed the segregation of Ti and Al, the increase of the concentration gradients of the metallic elements and the transformation of fcc-AlN into the wurtzitic AlN to be followed as a function of the annealing temperature.

These phenomena were concluded from the changes in the electron density, from the increase of the individual layer thickness and from the change of the interface morphology. The electron density of the individual layers building up the microstructure model varied between the theoretical electron density of fcc-TiN and fcc-AlN. The increase of the individual layer thickness was related to the transformation of fcc-AlN into w-AlN. The interface roughness changed from a diffuse one in the initial state to the geometrical one in the annealed samples as a consequence of the segregation of Ti and Al.

MS07-P02

How to use Jana2006 to process high-pressure single-crystal data

A. Grzechnik¹, J.M. Posse¹, K. Friese¹, V. Petricek²

¹Univ. Basque Country, Department of Condensed Matter Physics, Bilbao, Spain

²Czech Academy of Sciences, Institute of Physics, Prague, Czech Republic

The use of diamond anvil cells (DAC) in high-pressure diffraction experiments influences the quality of the single-crystal data measured with area-sensitive detectors. The most severe effect is the reduction of the accessible reciprocal space due to a limited opening angle of the DAC. The intensities diffracted by the crystal can be affected when an intense diamond reflection appears on the same frame: part of the primary beam is deflected, decreasing its intensity. This effect is known as diamond dips and, up to now, there is no algorithm to eliminate it.

We developed simple algorithms to alleviate the following effects which lead to wrong single-crystal intensities in an in situ high-pressure diffraction experiment:

- The overlap of the sample and the diamond reflections (including the $\lambda/2$ reflections from the diamonds which are often observed in the data collected using laboratory sources).
- The influence of the gasket can be avoided by using a laboratory microfocus source or a highly focused beam at synchrotron beamlines dedicated to high-pressure research. However, while using standard laboratory diffractometers, the primary beam strikes

the edges of the gasket producing Debye-Scherrer rings with variable intensity. Also, the usage of DACs with Be backing plates gives rise to additional powder rings. The intensities of the sample reflections which partially overlap with these powder rings may be falsified due to a wrong background estimation by the integration software.

3. Sample reflections may be shadowed by the components of the DAC.

In addition, a series of collection runs with different setting angles are usually performed that have to be scaled together using the intensities of the common reflections. Thus, any reflection with a wrong intensity that is used in the scaling process introduces errors in the scale factors and has an influence over a large portion of reflections in the combined dataset.

New functions and interactive graphics interfaces were developed and incorporated into the program Jana2006 (1) as an aid to identify all the outliers. The outliers can be identified in the averaging step on the basis of the deviation of the individual reflection intensities from the averaged intensity in a group of symmetrically equivalent reflections. The values of $|I(i)-I(\text{ave})|/\sigma(I(\text{ave}))$ can alternatively be plotted against the $I(\text{min})$, $I(\text{ave})$, $I(\text{max})$ or the θ values. It is now possible to use the graphics interfaces which plot the values of $|F(\text{obs})-F(\text{calc})|$ from the refinement against $F(\text{obs})$ or the θ values. Finally, $F(\text{obs})/F(\text{calc})$ plots can also be used to identify the outliers.

Our algorithms greatly facilitate the work with the high-pressure single-crystal data. Furthermore, they are also useful for other problematic datasets, not necessarily collected in the DAC.

References

I. V. Petricek, M. Dusek and L. Palatinus, JANA2006 - Crystallographic Computing System, Institute of Physics, Academy of Sciences of the Czech Republic, Praha, 2006.

MS07-P03

Temperatur- und feuchteabhängige Untersuchungen von Kanemit (NaHSi₂O₅ * 3 H₂O)

D. Schmidmair¹, V. Kahlenberg¹, D. Toebbens², J. De Wit³, U. Griesser³

¹University of Innsbruck, Institute of Mineralogy and Petrography, Innsbruck, Austria

²Helmholtz Zentrum Berlin, Abteilung Kristallographie, Berlin, Germany

³University of Innsbruck, Institute of Pharmacy, Innsbruck, Austria

Das Mineral Kanemit wurde erstmals 1972 in einer salinaren Lagerstätte im NO des Tschadsees gefunden und von JOHANN & MAGLIONE beschrieben. Es handelt sich dabei um ein H₂O-haltiges Na-Schichtsilikat der chemischen Formel NaHSi₂O₅ * 3 H₂O. Das synthetische Analogon konnte bereits 1968 von KALT & WEY hergestellt werden. Kanemit findet aufgrund seiner sehr guten Ionenaustauschfähigkeit Anwendung im Bereich der industriellen anorganischen Chemie. Ferner wird Kanemit auch als Katalysator bzw. als Precursor für die Herstellung mesoporöser Silikate verwendet.

Die Kristallstruktur dieser Phase wurde 1999 zeitgleich von VORTMANN et al. bzw. GRAVIE et al. publiziert. Die Verbindung kristallisiert in der Raumgruppe *Pbcn* (a= 4.950 Å; b= 20.519 Å; c= 7.280 Å) und ist aus einer Wechsellagerung von stark gefalteten Schichten aus [SiO₄]-Tetraedern sowie Oktaederschichten aus Na(H₂O)₆-Polyedern aufgebaut, die über Wasserstoffbrückenbindungen miteinander vernetzt sind. Die Lagen werden dabei alternierend parallel zur b-Richtung gestapelt. Die [Si₂O₅]-Schichten sind durch eckenverknüpfte SiO₄-Tetraeder charakterisiert, die in a-Richtung Zweier-Einfachketten bilden. Innerhalb der Oktaederschichten zeigen die Polyeder entlang der a-Richtung eine Verknüpfung über gemeinsame Ecken bzw. entlang der c-Richtung über gemeinsame Kanten. Die Protonen können in der Kanemitstruktur entweder H₂O-Molekülen oder Silanolgruppen zugeordnet werden.

Die im Rahmen dieser Arbeit durchgeführten thermoanalytischen Messungen sowie Feuchtesorptionsuntersuchungen zeigen, dass es

bei einer Erhöhung der Temperatur bzw. einer Erniedrigung der relativen Luftfeuchte unter 15% zu einer stufenweisen Entwässerung kommt.

Bei der Reduktion der Luftfeuchte auf 0% werden etwa 2 Mol H₂O pro Formeleinheit freigesetzt und es bildet sich eine neue Phase, die bei Erhöhung der Luftfeuchtigkeit wieder Wasser aufnehmen kann. Wiederholte De- und Rehydrierung verschlechtert allerdings die Kristallinität des Materials signifikant.

Bei einer Erwärmung von 15°C auf 250°C kann ausgehend vom Kanemit das sukzessive Auftreten von zwei weiteren Phasen festgestellt werden. Es handelt sich dabei um die Verbindungen Na[Si₂O₄(OH)] * H₂O bzw. Na[Si₂O₄(OH)].

Das Monohydrat kristallisiert ebenfalls in der Raumgruppe *Pbcn* (a= 4.887 Å; b= 15.326 Å; c= 7.202 Å). Im Vergleich zur Kanemitstruktur kommt es zu einer signifikanten Verkürzung der b-Gitterkonstante. Die Struktur des Na[Si₂O₄(OH)] kann in der Raumgruppe *P2₁/11* (a= 4.888 Å; b= 6.387 Å; c= 7.294 Å) beschrieben werden. Dabei wird die Elementarzelle in b-Richtung halbiert.

Eine Charakterisierung der beiden Dehydratationsprodukte mittels *simulated annealing* und anschließender Rietveldanalyse zeigt, dass die Silikatschichten nahezu unverändert vorliegen, während es in den Na-haltigen Zwischenschichten zu größeren strukturellen Veränderungen kommt.

Kalt, A., Wey, R. (1968): Composés interfoliaires d'une silice hydratée cristallisée. - Bull. Groupe franc. Argiles, 20, 205-214

Johan, Z., Maglione, G. (1972): La kanemite, nouveau silicate de sodium hydraté de néoformation. - Bull. Soc. fr. Minéral. Cristallogr., 95, 371-382

Vortmann, S., Rius, J., Marler, B., Gies, H. (1999): Structure solution from powder data of the hydrous layer silicate kanemite, a precursor of the industrial ion exchanger SKS-6. - Eur. J. Mineral., 11, 125-134

Gravie, L., Devouard, B., Groy, T., Cámara, F., Buseck, P. (1999): Crystalstructure of kanemite, NaHSi₂O₅*3H₂O, from the Aris phonolite, Namibia. - Am. Mineral., 84, 1170-1175

MS07-P04

Partikelwachstum durch 2D- oder 3D-Rotation und Koaleszenz -- mittels Röntgenpulverbeugung in mesoskaligem NiO aufgedeckt

M. Petrik¹, B. Harbrecht¹

¹Philipps-Universität, FB Chemie, Marburg, Germany

Seit etwa zwei Jahrzehnten ist thermisch induziertes Partikelwachstum durch Rotation und Koaleszenz (PRK) - ein bei Nanopartikeln wichtiger, aber noch nicht hinreichend aufgeklärter Wachstumsmechanismus - Gegenstand sowohl theoretischer, als auch experimenteller Forschung.[1-4] Der entscheidende Schritt ist die Aneinanderlagerung von je zwei kristallinen Nanopartikeln nach kollektiver kristallographischer Ausrichtung, so dass ohne weiteren Massentransport ein neuer größerer Einkristall entsteht.

Aus flüssiger Phase erhaltene Partikelproben werden für gewöhnlich durch direktes Abbilden mittels Transmissionselektronenmikroskopie (TEM) charakterisiert.[1,3,4] In fester Phase hingegen ist man auf indirekte Methoden angewiesen. Hier bietet sich eine eingehende Analyse der Wachstumskinetik an. Dies ist in der Literatur durch numerische Rechnungen dargetan und auch experimentell bestätigt worden, allerdings bislang lediglich für zweidimensionale (2D) Systeme, nämlich aus (hexagonalen) Nanosäulen bestehende Schichten.[2] Wie bei den klassischen Wachstumsmodellen (Ostwald-Reifung oder parabolisches Wachstum nach Burke/Turnbull bzw. Zener) findet man für die Zunahme des Partikeldurchmessers D_p als Funktion der Zeit t (bei konstanter Temperatur T) Isothermen von der allgemeinen Form $D_p = C(T) t^n$, mit der Geschwindigkeitskonstante $C^{1/n}(T)$ und dem charakteristischen Exponenten n .

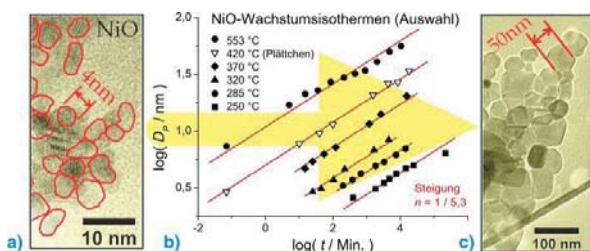
Nun hat sich im Zusammenhang mit strukturellen und

magnetischen Untersuchungen an nanokristallinem NiO das thermisch induzierte Partikelwachstum in agglomerierten NiO-Pulvern präparativ als sehr wertvoll erwiesen (Abb.1 a und c).[5,6] Dabei wurde in isothermen Wachstumsexperimenten die Partikelgröße D_p *ex situ* mittels Röntgenpulverdiffraktometrie als Funktion der Zeit t über die gesamte Mesoskala ($D_p = 2,6\text{-}56$ nm) verfolgt. Aufgrund der großen Anzahl von insgesamt 191 Beugungsexperimenten - durchgeführt an NiO-Pulverproben aus 26 isothermen Wachstumsserien - liegt somit ein statistisch hinreichendes Datenmaterial für das NiO-System vor.

Für den Exponenten n wird aus den 26 Wachstumsserien ein Mittelwert von $1 / 5,3(1,1)$ erhalten (Abb.1 b). Damit liegt n deutlich unter den Werten ($1/3$ bzw. $1/2$), welche man für die oben erwähnten klassischen Mechanismen erwartet, so dass diese auszuschließen sind. Hingegen wird in der Literatur für das 2D-PRK ein n -Wert von $1/4$ bzw. $1/3$ vorausgesagt, je nach dem, ob Oberflächen- oder Volumendiffusion überwiegt.[2] Im vorliegenden Fall folgt aus der Arrhenius-Auflösung der Geschwindigkeitskonstanten $C^{1/n}(T)$ eine Aktivierungsenergie E_A von $175(7)$ kJ/mol, was für die Oberflächendiffusion spricht.[7] Somit ist der hier erhaltene Wert von n (ca. $1/5$) kleiner als für 2D-PRK erwartet ($1/4$). Dies deutet - unseres Wissens zum ersten mal - möglicherweise auf ein 3D-PRK hin, was nunmehr an Hand des neuen experimentellen Materials diskutiert werden soll.

- [1] J. F. Banfield, S. A. Welch, H. Zhang, T. Th. Ebert, R. L. Penn, *Science* **2000**, 289, 751-754. [2] D. Moldovan, V. Yamakov, D. Wolf, S. R. Phillpot, *Phys. Rev. Lett.* **2002**, 89, 206101 (4 pages). [3] C. Frandsen, C. R. H. Bahl, B. Lebeck, K. Lefmann, L. Theil Kuhn, L. Keller, N. H. Andersen, M. v. Zimmermann, E. Johnson, S. N. Klausen, S. Mørup, *Phys. Rev. B* **2005**, 72, 214406 (7 pages). [4] H. Zheng, R. K. Smith, Y.-W. Jun, Ch. Kisielowski, U. Dahmen, A. P. Alivisatos, *Science* **2009**, 324, 1309-1312. [5] M. Petrik, B. Harbrecht, *Z. Kristallogr. Proc.* **2011**, 1, 253-258. [6] M. Petrik, B. Harbrecht, *Solid State Phenomena* **2011**, 170, 244-247. [7] F. H. Stott, *Rep. Prog. Phys.* **1987**, 50, 861-913.

Abb. 1



MS07-P05

Real structure of TSSG grown large Barium hexaferrite single crystals studied by white beam x-ray transmission topography

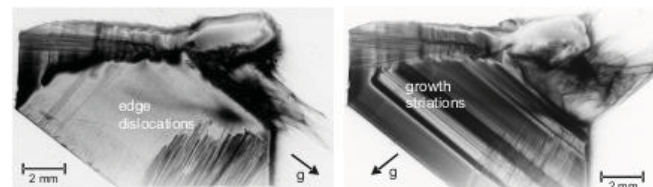
J. Kräußlich¹, C. Dubs², O. Wehrhan¹, P. Görnert²
¹Friedrich-Schiller-Universität Jena, Röntgenoptik / Röntgenphysik, Jena, Germany
²INNOVENT e.V., Jena, Germany

Due to its outstanding magnetic properties, M-type hexagonal ferrites such as Barium hexaferrite single crystals ($\text{BaFe}_{12}\text{O}_{19}$) or with still improved characteristics Scandium substituted Barium hexaferrite ($\text{BaSc}_x\text{Fe}_{12-x}\text{O}_{19}$) are a very suitable basic material for high-frequency filter components used in the 40 to 100 GHz range of modern information and communication technology.

The growth of large Scandium substituted Barium hexaferrite single crystals up to 2 cm edge length had been succeeded using the Top Seeded Solution Growth (TSSG) technique (Fig. 1). Away from the seed, enlarged regions with nearly perfect crystal structure are grown. White beam high resolution X-ray transmission topography (Fig. 1), carried out at the synchrotron facility in

Grenoble (ESRF), has only revealed a few dislocations and growth striations due to stoichiometric fluctuation.

Fig. 1: White beam X-ray transmission topographs of a c-cut Sc substituted Ba hexaferrite single crystal slice. The shown growth sector is almost perfectly, only few dislocations and growth striations are seen. g designates the X-ray diffraction vector. On the left $g_{\perp} (-1-12\ 0)$, right $g_{\perp} (-12-1\ 0)$.



MS07-P06

High (pressure, temperature) phase diagrams of ZnO and AlN from second harmonic generation measurements

L. Bayarjargal¹, B. Winkler¹
¹Institut für Geowissenschaften, Abt. Kristallographie, Frankfurt, Germany

Laser heating experiments in a diamond anvil cell (DAC) are an established tool to study materials under extreme conditions, but in situ measurements to delineate phase boundaries are still challenging. Typical in situ characterization methods for DAC are X-ray diffraction, IXS, XAS, Mössbauer and various optical spectroscopic methods (Raman, IR and UV). In contrast to diffraction and these spectroscopic techniques, second harmonic generation (SHG) has been rather seldom used for high pressure. SHG powder measurements are extremely sensitive to detect the absence of an inversion center in crystalline structures [1] and phase transitions at high temperature [2], but the SHG method has not been used to determine (p, T) phase boundaries. Here, we have performed SHG powder measurements on ZnO and AlN to determine the phase boundaries at high pressure and temperature. Their large SHG coefficients are an important prerequisite for the experiments.

AlN and ZnO are isostructural to wurtzite at ambient conditions, i.e. have the hexagonal, acentric B4 structure type. At high temperature and high pressure, the B4 phase transforms into the rocksalt structure (B1) [3-5].

AlN and ZnO were loaded in a diamond anvil cell. The pressure was determined using the ruby fluorescence method. KCl and Ne were used as a pressure medium for laser heating experiments and KCl was used also to thermally insulate the sample from the diamond. A CO₂ laser was employed for heating the sample. The experimental set-up of the laser heating part and the SHG measurements of quenched samples are described in [3,6]. For the in-situ SHG measurements a Nd:YAG laser system was integrated into the CO₂ laser heating system.

Our results of ZnO are compatible with previous work [4] and extend the phase transition line to significantly higher temperatures. The B4-B1 phase transition of AlN at high pressure and ambient temperature can vary depending on whether a hydrostatic or nonhydrostatic pressure medium is employed. The phase boundary of AlN is significantly shifted to higher pressures with respect to the phase boundary which had been derived using atomistic models [5].

The authors acknowledge financial support from the Deutsche Forschungsgemeinschaft (DFG), Germany, within SPP1236 (project Ba4020).

- [1] S. K. Kurtz and T. T. Perry, *J. Appl. Phys.* 39, 3798 (1968).
 [2] S. Furusawa, O. Chikagawa, S. Tange, T. Ishidate, H. Orihara, Y. Ishibashi, and K. Miwa, *J. Phys. Soc. Jpn.* 60, 2691 (1991).
 [3] L. Bayarjargal, B. Winkler, E. Haussühl, and R. Boehler, *Appl. Phys. Lett.* 95, 061907 (2009).

- [4] F. Decremps, J. Zhang, and R. C. Liebermann, *Europhys. Lett.* 51, 268 (2000).
[5] A. Siegel, K. Parlinski, and U. D. Wdowik, *Phys. Rev. B* 74, 104116 (2006).
[6] L. Bayarjargal, T. G. Shumilova, A. Friedrich, and B. Winkler, *Eur. J. Mineral.* 22, 29 (2010).

MS07-P07

High resolution X-ray diffraction study of single crystals of Lead Zirconate Titanate

S. Gorfman¹, D. Keeble², M. Glazer³, Z.-G. Ye⁴, P. Thomas²

¹University of Siegen, Department of Physics, Siegen, Germany

²University of Warwick, Department of Physics, Coventry, United Kingdom

³University of Oxford, Department of Physics, Oxford, United Kingdom

⁴Simon Fraser University, Department of Chemistry and 4D Labs, Burnaby, Canada

PbZr_{1-x}Ti_xO₃ (PZT) is an archetypical perovskite based material with superior piezoelectric properties. The structural origin of its exceptional piezoelectricity is not yet understood. In particular the symmetry of a single ferroelectric domain of PZT is unresolved, since all the current conclusions regarding PZT structure have been drawn solely from powder diffraction data, where the results are often ambiguous. Single crystals of PZT were unavailable until recently when their successful synthesis for the compositions close to the MPB region has been achieved [1]. The availability of single crystals has initiated renewed studies of the PZT structure and properties, so far involving optical birefringence microscopy [2] and neutron diffraction [3].

The aim of this work was for the first time to perform a detailed X-ray diffraction study of PZT single crystals and to obtain the most precise information about the average symmetry of the material. Single crystals with the compositions $x \approx 0.31$ and $x \approx 0.45$ were investigated. We applied a specialized X-ray diffraction technique [3,4] involving combined use of two different X-ray diffractometers. A CCD-based Oxford Diffraction GeminiR diffractometer was used to define the orientation of a single crystal and investigate large areas of its reciprocal space. A high-resolution Panalytical four circle diffractometer was further used to collect precise reciprocal space maps around selected Bragg reflections from the same crystal. The angular separation of beams diffracted by different ferroelastic domains allowed extraction of the precise information about the symmetry of a single domain.

The results to be presented provide the further proof for the existence of low-symmetry (monoclinic) phases in PZT. Furthermore we have shown that PZT crystals of both compositions are best described by a combination of at least two (rhombohedral and monoclinic) phases.

- [1] X Long, A Bokov, ZG Ye Simon Fraser University (unpublished)
[2] A Bokov, X Long, ZG Ye. *Phys Rev B* 81, 172103, (2010)
[3] D Phelan, X Long, Y Xie, ZG Ye, AM Glazer, H Yokota, PA Thomas, PM Gehring. *Phys Rev Lett* 105, 207601 (2010)
[4] S Gorfman, PA Thomas, *J Appl Cryst* 43, 1409-1414, (2010)
[5] K Datta, S Gorfman, PA Thomas, *APL* 95, 251901-1, (2009)

MS07-P08

X-ray diffraction and spectroscopic study of selected amino acids and their derivatives at extreme conditions - high pressures and low temperatures

B. Zakharov^{1,2}, B. Kolesov^{2,3}, E. Boldyreva^{1,2}

¹Institute of Solid State Chemistry, Siberian Branch Russian Academy of Sciences, Novosibirsk, Russian Federation

²Novosibirsk State University, Novosibirsk, Russian Federation

³Institute of Inorganic Chemistry, Siberian Branch Russian Academy of Sciences, Novosibirsk, Russian Federation

Crystals of amino acids are of special interest for studies at non-ambient conditions. The main reason of this is that the structure-forming units in these crystals are similar to those in the biopolymers and can be used as biomimetics. One of the interesting tasks is a comparison of the properties of individual amino acids and their salts formed with other carboxylic acids.

The main aim of this study was to compare the effect of increasing pressure and decreasing temperature on hydrogen bond network in the individual amino acids L- and DL-serine and some selected salts - bis(DL-serinium) oxalate dihydrate and DL-alaninium semi-oxalate monohydrate. Single-crystal X-ray diffraction at high pressures and low temperatures were combined with polarized Raman spectroscopy measurements.

The crystal structures of amino acids and their salts differ in the structures of the hydrogen-bonded networks; besides, very short O-H...O hydrogen bonds are present in the crystal structures of salts. Hydrogen bonds belong to the most important intermolecular interactions. They determine the structure, properties and phase transitions in molecular crystals; some physical properties of molecular materials (non-linear optic, ferro- and piezoelectric) are also affected by hydrogen bonds.

The properties of several types of O-H...O H-bonds in bis(DL-serinium) oxalate dihydrate and DL-alaninium semi-oxalate monohydrate have been studied on cooling by a combination of variable-temperature single-crystal X-ray diffraction and polarized Raman spectroscopy, and it was possible to correlate donor-acceptor distances with frequencies of OH stretching vibrations. The present study is a rare example when correlations between geometry and energy parameters have been found for selected individual H-bonds in the same crystalline compound at multiple temperatures.

L- and DL-serine, and bis(DL-serinium) oxalate dihydrate were studied at high pressures. The structures of amino acids were refined in the pressure range 0 - 4 GPa for DL- and 0 - 6 GPa for L-serine and compared with polarized Raman spectra recorded at the same conditions. In this case it was possible to find some interesting deviations in hydrogen-bond network and to confirm the formation of bifurcated N-H...O hydrogen bonds on increasing pressure in DL-serine. It is very interesting to note that pressure-induced phase transition related to lowering symmetry and disordering has been detected in the corresponding salt - bis(DL-serinium) oxalate at ~4 GPa.

This work was supported by grants from RFBR (09-03-00451), BRHE (RUX0-008-NO-06), by the Integration Projects No. 13 and 109 of the Siberian Branch of RAS, a FASI Grants P2529 and 16.740.11.0166.

MS07-P09

Thermal expansion of mullite-type $\text{Bi}_2\text{Fe}_4\text{O}_9$

M.M. Murshed¹, H. Krüger², M. Burianek³, G. Nénert⁴, V. Kahlenberg²,

M. Mühlberg³, H. Schneider^{3,5}, R. Fischer⁵, T. Gesing^{1,5}

¹Universität Bremen, Chemische Kristallographie fester Stoffe /FB02, Bremen, Germany

²Universität Innsbruck, Institut für Mineralogie und Petrographie, Innsbruck, Austria

³Universität Köln, Kristallographie, Köln, Germany

⁴Institut Laue Langevin, Grenoble, France

⁵Universität Bremen, Kristallographie, FB Geowissenschaften, Bremen, Germany

Mullite-type $\text{Bi}_2\text{Fe}_4\text{O}_9$ and its isomorphous solid solutions have considerably widened the mullite crystal chemistry [1]. This structure type shows complex magnetic phase transition, semiconductor gas sensing and catalysis activities. We report on temperature dependent structural aspects of $\text{Bi}_2\text{Fe}_4\text{O}_9$ studied by X-ray and neutron diffraction between 173 K and 1200 K. The cell parameters b , c and cell volume did not exhibit deviations between the cooling and heating cycles within the range of estimated error. However, the a cell parameter in the cooling cycle significantly deviated from the heating cycle at the corresponding temperature, thus showing the irreversible alternation of the powder specimen. Whereas the c -axis is the elastically stiffest [2], the lowest thermal expansion occurred along the a -axis. This behavior violates the empirical rule, however, corroborates the common findings in mullites. The highest expansion along the b -axis was explained in terms of the elastic nature of Fe-O bonds of the FeO_6 and FeO_4 polyhedra. The non-linear thermal expansion of the cell parameters were fit using a 4th order polynomial fixing the second coefficient to zero. Such a model provides horizontal tangent and thus zero expansivity at 0 K. Each of the thermal expansion coefficients $\alpha(a)$, $\alpha(b)$, $\alpha(c)$ and $\beta(V)$ showed a nonlinear behavior. The anisotropy factor progressively slowed down with a steep linear increase at about 800 K. Since the lone electron pair of Bi^{3+} cation is stereochemically active, the symmetry of its coordination sphere was monitored in terms of both octahedral quadratic elongation and the absolute value of eccentricity parameter ($|\Phi_i|$). The room temperature bond valence sums (BVS) of Bi^{3+} was found above the formal value (+3 v.u.). The change of $|\Phi_i|$ with increasing temperature is associated with the distribution of the lone electron pair of Bi^{3+} cation. The linear correlation between ($|\Phi_i|$) and BVS validates the Wang-Liebau model [3, 4].

References:

- [1] Fischer, R. X.; Schneider, H.: The mullite-type family of crystal structures. In Mullite, (edited by H. Schneider and S. Komarneni), Wiley-VCH, Weinheim, (2005) p. 1 - 46.
- [2] Krenzler, Th. F., Schreuer, J., Gesing, Th. M., Burianek, M., Mühlberg, M., Schneider, H.: Thermal expansion and elastic properties of mullite-type $\text{Bi}_2\text{Ga}_4\text{O}_9$ and $\text{Bi}_2\text{Fe}_4\text{O}_9$ single crystals. Int. J. Mat. Res. (2012) submitted.
- [3] Wang, X.; Liebau, F.: Influence of lone-pair electrons of cations on bond-valence parameters. Z. Kristallogr. 211 (1996) 437-439.
- [4] Wang, X.; Liebau, F.: Influence of polyhedron distortions on calculated bond-valence sums for cations with one lone electron pair. Acta Crystallogr. B63 (2007) 216-228.

MS07-P10

High pressure behavior of wadeite $\text{K}_2\text{ZrSi}_3\text{O}_9$

N. Niederwieser¹, C. Hejny¹

¹Mineralogy and Petrology, Faculty of Geo- and Atmospheric Sciences, Innsbruck, Austria

Wadeite $\text{K}_2\text{ZrSi}_3\text{O}_9$, naturally occurring in syenites and lamproites, is a cyclosilicate with triple rings of silicon tetrahedra arranged in layers sandwiched between layers composed of Zr octahedral and K in 9-fold coordination [1]. Comparable to other structures with

triple-rings of silicon or germanium tetrahedra, e.g. benitoite $\text{BaTiSi}_3\text{O}_9$ or catapleite $\text{Na}_2\text{ZrSi}_3\text{O}_9 \cdot 2\text{H}_2\text{O}$ to name only a few, wadeite has optical properties of special interest, in particular UV fluorescence, that are well studied for their potential use in LED lights [2]. However, the main focus of this study is on the high-pressure behavior of the ring units of three tetrahedra, because cyclosilicates with triple rings have recently attracted attention due to nonlinear anomalies in the elastic behavior [3].

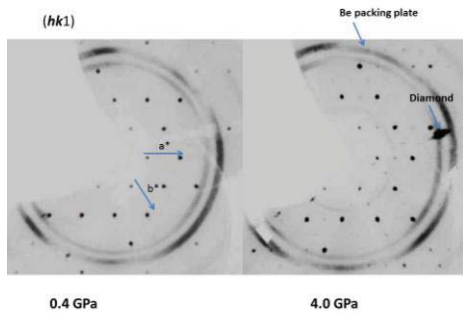
In this study we present the high pressure (HP) behavior of wadeite, performing in-situ high-pressure single-crystal diffraction and Raman spectroscopic investigations in the diamond anvil cell on a naturally grown crystal from Kola peninsula, Russian Federation, up to 7.5 GPa. The analyzed crystal is essentially pure $\text{K}_2\text{ZrSi}_3\text{O}_9$ with minor Ti-contamination of max. 1.3 wt%. Four single-crystal X-ray diffraction datasets of wadeite at ambient conditions, 0.1, 0.4, 1.0 GPa were refined in s.g. $P6_3/m$ with lattice parameters contracting from $a = 6.9334(7)$, $c = 10.2044(2)$ (Å) to $a = 6.8945(9)$, $c = 10.161(2)$ Å (1.0 GPa). Above that pressure additional weak reflections at $(h/2, k/2, l)$ appeared indicating a phase transition (Fig. 1). The HP structure was refined from a dataset at 2.5 GPa with $a' = 2a$, $c' = c$ in s.g. $P6_3$. Lattice parameters of the HP phase contract from $a = 13.617(3)$, $c = 10.161(2)$ at 2.5 GPa to $a = 13.588(2)$, $c = 10.043(2)$ Å at 4.5 GPa. Above this pressure the overall intensity drops prohibiting further high quality data analysis. In the HP $P6_3$ phase of $\text{K}_2\text{ZrSi}_3\text{O}_9$ the octahedral coordination of Zr gets slightly distorted and K changes from initially nine-fold coordination (mean K-O = 3.0666(4) Å) to nine-fold (3.0415(4) Å) and twelve-fold coordination (3.1056(5) Å). In this HP $P6_3$ phase, the two symmetrically independent rings of silicon tetrahedral lose the mirror plane symmetry present in the $P6_3/m$ wadeite form.

Raman spectroscopic data of wadeite show a splitting of the band at 192 cm^{-1} with increasing pressure, which is well in accordance with the diversification of the atom positions at the phase transition from $P6_3/m$ to $P6_3$. Frequencies above 250 cm^{-1} assigned to internal ring modes [4,5] show a blue shift as commonly known for high pressure experiments. However, over the pressure range of 4 - 6 GPa a further slowly evolving splitting of the external modes between 100 and 250 cm^{-1} can be observed. Since this is the pressure range of decreasing Bragg intensities observed in X-ray single-crystal diffraction this might indicate another phase transition.

References:

- [1] Henshaw, D.E. (1955) Min. Mag. 30, p. 585.
- [2] Rainho, JP., Ananias, D., Lin, Z., Ferreira, A. (2004) J. Alloys Comp. 374, p. 185.
- [3] Hejny, C., Miletich R., Jasser A., Layder I., Schouwink P. (2011) Abstractband, CD, Joint Meeting of the German Crystallographic Society, "Crystals, Minerals and Materials", Salzburg, Austria, September 22-24 (P04-P04)
- [4] Mc Keown, D., Nobles, C. (1996) Phys. Rev. B54, p. 291.
- [5] Mc Keown, D.A., Bell M., Kim C.C. (1993) Phys. Rev. B 16, p.357.

Figure caption: Reconstructed (hk1) layer of wadeite $\text{K}_2\text{ZrSi}_3\text{O}_9$ at 0.4 +4.0 GPa. Above 1.0 GPa additional reflections at $(h/2, k/2, l)$ appear.



MS07-P11

The effect of pressure, cooling rate and shear rate on the morphology of isotactic Polypropylene

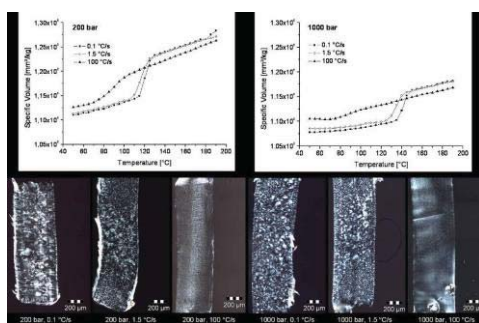
S. Jilg¹, R. Forstner¹

¹Transfercenter für Kunststofftechnik, R&D, Wels, Austria

In this study the crystallisation behaviour of isotactic Homo-Polypropylenes under the combined effect of pressure, cooling rate and shear rate were investigated. The sample preparation was carried out with a novel pvT-Dilatometer, the Pirouette-pvT-Apparatus, to create samples with a defined prehistory nearly under processing conditions as found in injection moulding for example. This novel dilatometer is a combination of a traditional piston die dilatometer and a couette rheometer. Initially it was designed to measure the specific volume polymers as a function of pressure (up to 1000 bar), cooling rates (up to 100°C/s) and shear rates (up to 180 1/s). The Pirouette can be used in several operating modes. Isobaric heating, isobaric cooling and isothermal experiments. In this investigation measurements were performed in the isobaric cooling mode to show the dependency of the transition temperature and the crystallisation kinetic from pressure, cooling rate and shear flow. The gained samples were characterised by optical microscopy, DSC and WAXS.

It can be found that all samples contain mainly monoclinic alpha-form, no hexagonal beta-form and partially orthorhombic gamma-form. Increasing pressure shifts the transition temperature to higher temperatures (see Figure 1). Higher pressures does not change the crystallinity significantly however let increase γ -modification. Increasing cooling rates shifts the transition temperature to lower values and form a more fine grained morphology (see Figure 1). Higher cooling rates reduce the crystallinity significantly and eliminates γ -modification. Nevertheless, the influence of cooling rate on morphology is more pronounced than the influence of pressure for the investigated samples. Higher shear temperatures shift the transition temperature to higher temperatures and higher pressures enhance the effect of shear. The specific volume after cooling to room temperature is mainly depending on cooling rate.

Figure 1. Influence of pressure and cooling rate on the specific volume and morphology of iPP



MS07-P12

Experimental determination of orientation relations between the high- and low-pressure phases of InAs

N. Pukallus¹, H. Sowa¹, H. Klein¹

¹Uni Göttingen, GZG Abteilung Kristallographie, Göttingen, Germany

Indium arsenide InAs is used for photo diodes in infrared detectors. It belongs to the more ionic III-V semi-conductors [1]. At ambient conditions, it crystallizes with a zinc-blende type structure with space group $F\bar{4}3m$. At about 7 GPa a transformation takes place that is accompanied by a change of the coordination numbers from four to six and a volume collapse of about 17% [2]. The high-pressure phase belongs to the NaCl type with space group $Fm\bar{3}m$. The phase transition was studied using synchrotron radiation at beamline BW5 at HASYLAB/DESY with a beam energy of 100 keV. Single crystals of indium arsenide transformed under pressure into a polycrystalline material with a highly preferred orientation. Since information on the transition mechanism may be obtained by investigations of the orientation relations between the unit cells of the phases before and after the phase transition, pole figures of the low and high-pressure phases were measured. The diffracted data were registered using a mar345 area detector.

In order to get an idea of the orientation relations between the high- and low pressure phase, the collected diffractograms were analyzed using the program MAUD [3]. Complete pole figures and orientation density functions (ODFs) were calculated. The observed orientation relations between the zinc-blende and NaCl-type phases of InAs differs from those obtained for other compounds that show similar transitions under pressure like CdTe [4] and AgI [5], leading to the assumption that different transition mechanisms take place.

Portions of this research were carried out at the light source BW5 at DESY, a member of the Helmholtz Association (HGF). This work was supported by the Deutsche Forschungs-gemeinschaft DFG (So276/3-1).

[1] S. Pascarelli, G. Aquilanti, W. A. Crichton, T. Le Bihan, M. Mezouar, S. De Panfilis, J. P. Itié, & A. Polian, *Europhys. Lett.* **61**, 554 (2003).

[2] Y. K. Vohra, S. T. Weir & A. L. Ruoff, *Phys.Rev.* **B31**, 7344 (1985).

[3] L. Lutterotti, S. Matthies, and H.-R. Wenk. *Proceedings of the Twelfth International Conference on Textures of Materials (ICOTOM-12)*, Vol. **1**, 159 (1999)

[4] H. Sowa, *J. Appl. Cryst.* **38**, 537 (2005).

[5] H. Sowa, *Z. Kristallogr.* **222**, 89 (2007).

MS07-P13

Domain redistribution in SrTiO₃ by application of electric fields and mechanical stresses

J. Sidoruk¹, J. Leist¹, H. Gibhardt¹, K. Hradil², B. Pedersen³, M. Meven⁴, G. Eckold¹

¹Georg-August Universität, Institut für Physikalische Chemie, Göttingen, Germany

²TU Wien, Institut für Chemische Technologien und Analytik, Wien, Austria

³Technische Universität München, FRM-II, Garching, Germany

⁴RWTH Aachen and FRM-II, Institut für Kristallographie, Garching, Germany

Strontium titanate (SrTiO₃) is a well-known member of the perovskite family.

It is a widely used in multilayer ferroelectric thin films and as a substrate for high temperature superconductors. Moreover it exhibits an antiferrodistortive phase transition at 105 K leading to a tetragonal phase with three different structural domains. Even at low temperatures a ferroelectric phase like in the isostructural barium titanate (BaTiO₃) is not observed. A polar phase can be induced by the application of electric field [1].

The domain distribution can be changed by applying uniaxial mechanical stresses as well as electric fields, although a direct

coupling between the order parameter and the electric field is forbidden by symmetry [2].

Therefore, we investigated the domain distribution in a single crystal of Strontium Titanate by application of uniaxial stresses and electric fields. In this contribution the intensities of a good number of tetragonal superlattice reflections were studied using the thermal three axis spectrometer PUMA, the hot neutron diffractometer HeiDi and at the crystal diffractometer RESI at the FRM II neutron source over a wide range of temperatures.

Uniaxial stress along [110]-direction leads to a formation of an almost monodomain sample with [001] as the tetragonal axis. The uniaxial stress induced redistribution is temperature-independent and irreversible even after heating to 120 K. The subsequent application of an electric field along [001]-direction leads to an almost complete redistribution of the domains. This effect becomes stronger if the temperature decreases and the induced ferroelectric phase is approached - its reversibility depends on sample-history and temperature. Obviously the application of mechanical stress and electric field lead to competing effects and prevents the formation of a field induced single domain ferroelectric phase. Different directions of stress and field have been used to study the domain redistribution of SrTiO₃ in detail.

MS07-P14

The X-ray study of phase transition in Sc doped TiOCl

J. Zhang¹, A. Wölfel¹, M. Bykov¹, R. Kremer², S. van Smaalen¹

¹University of Bayreuth, Lab of Crystallography, Bayreuth, Germany

²Max planck Institut für Festkörperforschung, Stuttgart, Germany

As one of the low dimensional quantum magnetic systems, the spin-Peierls material TiOCl has attracted huge interest due to its dimerized, spin-Peierls state at low temperatures [1, 2]. TiOCl crystallizes in the FeOCl structure, Ti-O double layers sandwiched by Cl layers, with the orthorhombic space group Pmmn[3]. With the temperature dropping, a phase transition occurs at $T_{c2} = 90\text{K}$ which drive the structure into an incommensurate phase. Below $T_{c1} = 67\text{K}$, a twofold superstructure develops. Accompanying with the incommensurate phase, a temperature-dependent c-axis unique monoclinic distortion of the crystal lattice is observed between T_{c2} and T_{c1} [4]. Detailed temperature-dependent X-ray diffraction measurements on single crystals of Sc-doped TiOCl have been performed in order to study the critical properties of the phase transitions. Here we discuss the results of these experiments and provide a model for the modified transition behavior of doped TiOCl.

Reference:

- [1] A. Seidel, C. A. Marianetti, F. C. Chou, G. Ceder, and P. A. Lee, Phys. Rev. B 67, 020405(R) (2003)
- [2] M. Shaz, S. van Smaalen, L. Palatinus, M. Hoinkis, M. Klemm et al. Phys. Rev. B 71, 100405(R) (2005)
- [3] H. Schäfer, F. Wartenpfehl, and E. Weise, Z. Anorg. Allg. Chem. 295, 268 (1958)
- [4] A. Schönleber, G. Shcheka, and S. van Smaalen, Phys. Rev. B 77, 094117 (2008)

Keywords: X-ray diffraction, phase transitions, spin-Peierls

MS07-P15

Interaction between point defects and higher dimensional defects in SrTiO₃

J. Hanzig¹, B. Abendroth¹, F. Hanzig¹, H. Stöcker¹, D.C. Meyer¹

¹Institut für Experimentelle Physik, TU Bergakademie, Freiberg, Germany

Stoichiometric perovskite-type strontium titanate acts as an insulator because of its big electronic band gap and has therefore great potential as storage material in memory applications. Here, we discuss the volume and surface real structure of single crystals

with intrinsic defects. These include point defects, 1-dimensional defects, stacking faults like Ruddlesden Popper (RP) phases and precipitates (TiO₂, SrO, brownmillerite). To investigate the interactions between defects of different dimension, additional oxygen vacancies were introduced in the crystal by vacuum annealing. The free charge carrier density was determined by infrared (IR) spectroscopy and is correlated with surface and bulk conductivity measurements as well as simulations. Experimental and theoretical findings lead to a discrepancy in the number of free charge carriers, which can be explained by higher dimensional defects. Transmission electron microscopy (TEM) reveals an enrichment of dislocations in the near surface region, which are well known as fast diffusion paths for point defects and can be reduced by temperature treatment. Furthermore we suppose stacking faults, like additional SrO planes at the surface of SrTiO₃ crystals, based on X-ray analysis. Correlations between real structure and functionality will be drawn to demonstrate how defects of all dimensions affect the electronic and optical properties.

MS07-P16

Negative thermal expansion in chalcopyrite type multinary semiconductors

S. Schorr¹, C. Stephan¹

¹Helmholtz Zentrum Berlin für Materialien und Energie, Kristallographie, Berlin, Germany

One of the most intriguing property of tetrahedral coordinated solids is their negative thermal expansion. Conceptually, the occurrence of a negative expansion may be understood in terms of the balance between the Grüneisen parameters of the acoustic shear and compressional modes of the particular crystal structure considered. The first have the tendency towards negative values, whereas the latter are positive.

The thermal expansion behaviour of CuB^{III}X₂ (B^{III}=Ga,In; X=S,Se) compound semiconductors as well as their solid solutions were investigated by low temperature neutron diffraction experiments at the Swiss Spallation Source SINQ (Paul-Scherrer-Institute Villigen) using the high resolution powder diffractometer for thermal neutrons (HRPT, $l=1.1545 \text{ \AA}$, $T=1.5 - 300\text{K}$). These compounds, which crystallize in the chalcopyrite (sg) type structure, belong to the adamantine family, the anions are tetrahedral coordinated by the cations and vice versa.

Using the lattice parameter determined by Rietveld analysis of the neutron diffraction data, the linear thermal expansion was derived in the studied temperature region. The lattice constants and α vary independently with temperature, as expected from the axial symmetry of the crystal. With decreasing temperature the lattice constants decrease but show a flat minimum at a certain temperature, reflecting a change in sign of the linear thermal expansion coefficient. The tetragonal distortion Δ of the chalcopyrite structure ($\Delta = 2-c/a$) decreases nonlinearly with decreasing temperature and has a positive temperature coefficient α_{Δ} in the whole temperature range studied.

The linear thermal expansion coefficients follow the inequality $\alpha_a > \alpha_c$ in the whole temperature range. The linear thermal expansion coefficient α_a and α_c decreases with decreasing temperature anisotropically and becomes negative. This critical temperature, i. e. $T(\alpha=0)$ depends on the chemical composition, which will be discussed in terms of the ionicity of the cation-anion bonds. Because of the negative linear thermal expansion coefficients, negative Grüneisen parameters may be expected in the low-temperature region and as a consequence the existence of low-energy lattice vibrational modes.

Finally the temperature dependent behaviour of the cation-anion bond as well as the bond angles within the coordination tetrahedra will be considered

MS08-P01

Application of a pnCCD in macromolecular crystallography

S. Send¹, A. Abboud¹, W. Leitenberger², M.S. Weiss³, R. Hartmann⁴, L. Strüder^{1,5,6}, U. Pietsch¹¹University of Siegen, Department of Physics, Siegen, Germany²University of Potsdam, Department of Physics, Potsdam, Germany³Helmholtz-Zentrum Berlin, MX group, Berlin, Germany⁴PNsensor GmbH, Munich, Germany⁵MPI Halbleiterlabor, Munich, Germany⁶MPI für extraterrestrische Physik, Garching, Germany

The fast and precise characterization of crystalline materials using the Laue diffraction method requires a simultaneously position- and energy-resolved detection of photons. By means of a back side illuminated pnCCD with frame-store operation [1] the spatial distribution of Laue spots as well as their energies can be measured at the same time. The sensitive volume consists of a fully sideward depleted n-Si layer of 450 μm thickness subdivided into 256x256 pixels of 75 μm x75 μm size with a typical readout frequency of about 120Hz. The system has found applications for soft and hard X-rays [2,3].

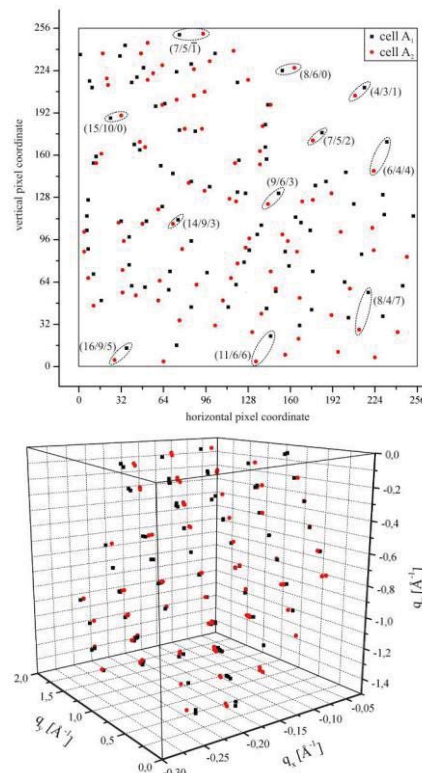
Using white synchrotron radiation the pnCCD delivers a three-dimensional intensity distribution spanned by two pixel directions and an energy direction covering a 3D data volume in reciprocal space which is expanded to 4D in case of dynamic measurements. In this sense the system provides a good possibility to investigate unknown crystal structures in arbitrary orientations in space as well as structural phase transitions at fixed scattering geometry. Previously it was shown that the crystallographic unit cell of a LiAlO₂ crystal can be determined from the three-dimensional pnCCD data sets without any a priori information about the sample [4]. Consequently the energy-dispersive Laue diffraction technique is a powerful tool for single shot structure analyses in macromolecular crystallography. In the subsequent application the potential of the pnCCD is exploited to investigate small organic crystals exhibiting complex structures and weak scattering signals. As a test example the energy-resolved Laue pattern of a tetragonal hen egg white lysozyme polycrystal is considered in transmission geometry and used for lattice determination. Two different unit cells A1 and A2 can be observed generating the Laue pattern shown in Figure 1. After conversion into reciprocal space coordinates the Laue spots occupy the two corresponding reciprocal lattices (Figure 2), each of them belonging to one reciprocal unit cell of lysozyme. Delaunay reduction and basis refinement procedures are applied leading to the real tetragonal unit cells with average lattice constants $a=79.3\text{\AA}$, $c=37.9\text{\AA}$ and a tilt in the order of 1° relative to each other.

References:

- [1] N. Meidinger et al., Nucl. Instr. and Meth. A, 2006, 565, 251-258
 [2] L. Strüder et al., Nucl. Instr. and Meth. A, 2010, 614, 483-496
 [3] W. Leitenberger et al., J. Synchr. Rad., 2008, 15, 449-457
 [4] S. Send et al., J. Appl. Cryst., 2009, 42, 1139-1146

Figure 1: Laue pattern of a lysozyme double crystal measured in a single X-ray shot.

Figure 2: The energy-resolved Laue pattern of Fig.1 after conversion into reciprocal space coordinates.



MS08-P02

X-ray diffraction, magnetization, and ⁵⁷Fe Mössbauer spectroscopic characterization of natural single-crystals of chrysoberylF.J. Litterst¹, S.-U. Weber², W. Lottermoser³, G. Amthauer³¹TU Braunschweig, Institut für Physik der kondensierten Materie, Braunschweig, Germany²TU Braunschweig, Institut für physikalische und Theoretische Chemie, Braunschweig, Germany³Paris-Lodron-Universität Salzburg, Fachbereich für Materialforschung und Physik, Salzburg, Austria

Natural chrysoberyl from Rio das Americas, Minas Gerais, Brazil, was studied by electron microprobe analysis, X-ray single-crystal diffractometry, magnetization and ⁵⁷Fe-Mössbauer spectroscopy. The aim of this study is the structural and magnetic characterisation of the sample.

Microprobe measurements of two chrysoberyl crystals were performed with high grid resolution leading to the average chemical composition Al_{1.96}Fe_{0.03}BeO₄. The crystals seem to be homogenous.

Single-crystal data were collected and refined on a BRUKER Smart Apex 3-circle diffractometer using the ideal chemical composition, Al₂BeO₄, space group Pnma with four formula units per unit cell and the initial fractional coordinates given by [1]. The results of the refinement show, that the untwinned chrysoberyl has a hexagonal closed packed structure of oxygen ions, slightly distorted with Al³⁺ and Be²⁺ occupying the octahedral and tetrahedral sites of chrysoberyl [2], respectively.

Magnetization data taken down to 3 K reveal paramagnetic moment behavior with S=5/2 as expected for high spin Fe³⁺. No indications for magnetically ordered impurities were found.

The ⁵⁷Fe-Mössbauer spectra, collected at different temperatures between 20 K and room temperature, reveal a superposition of several subspectra. Isomer shifts and quadrupole splittings are typical for Fe³⁺ in a comparably weakly distorted six-fold coordination of the M1 and M2 position, the latter with point symmetry m (Al_{II}, 4c-site) in accordance with the EPR measurements of [3]. Remarkable is a strong spectral contribution revealing a magnetic hyperfine splitting, indicative for magnetic order of part of the sample or slow spin relaxation effects. Several

scenarios for the origin of this magnetic contribution will be discussed, e.g., defect sites as reported for alexandrite [4], superparamagnetic iron oxide precipitates, or slow paramagnetic spin relaxation of dilute Fe^{3+} .

- [1] E.F. Farrell, J.H. Fang, and R.E. Newnham, *Am. Min.* 48, 804-810 (1963).
 [2] M.K. Rabadanow and A.P. Dudka, *Inorg. Mater.* 33, 48-51 (1997).
 [3] H. Rager, A. Bakhshandeh-Khiri, and K. Schmetzer, *N. Jb. Miner. Mh.*, 12, 545 - 557 (1998).
 [4] P. P. Phakey, *phys. stat. sol.*, 32, 801 - 814 (1969)

MS08-P03

A Table Top Picosecond pulsed X-ray and Laser induced Fluorescence Spectrometer based on a Streak Camera System using 2D-Photon Counting

N.-P. Pook¹, J.-C. Fruhner¹, T. Franzl², U. Denzer², A. Adam¹

¹*Institut für Anorganische und Analytische Chemie, TU Clausthal, Clausthal-Zellerfeld, Germany*

²*Hamamatsu Photonics Deutschland GmbH, Herrsching, Germany*

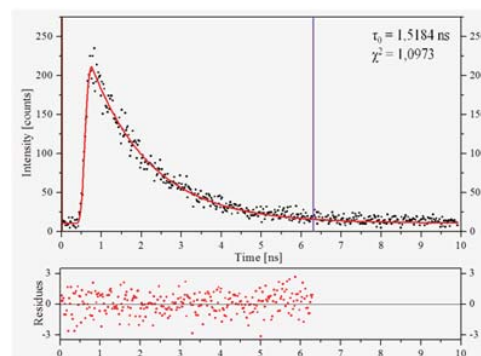
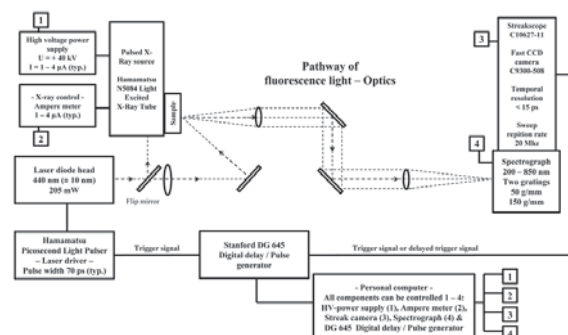
Fluorescence materials offer a great number of applications [1]. Scintillators as fluorescence materials which transfer high energy photons or particles e.g. X- and γ -rays into visible or uv light, are widely used in ionizing radiation detection systems. The field of application includes medical diagnostics, γ -ray imaging in security systems, astro and high energy physics [2]. Regarding the figure-of-merit of scintillation materials decay times as well as the emission wavelengths are important criteria. The classic way of characterization and testing such materials is based on time-correlated single photon counting (TCSPC). The excitation process is induced by radioactive isotopes such as ^{22}Na or ^{137}Cs . An alternative method to excite a scintillator sample is a pulsed X-ray source [3]. Such instrumental set-ups use fast photomultiplier tubes to generate start and stop pulses and band pass filters to select a spectral range of the fluorescence light. So, these methods measure only a single wavelength at a time and it is difficult to create fully spectral-resolved data. Streak camera systems have been a great methodological advance in measuring fluorescence lifetimes [4]. Today, streak system advantages of measuring decay times and emission spectra simultaneously by using two-dimensional photon counting are also available in X-ray excited optical luminescence (XEOL) [5]. Experimental set-up of our system (Fig. 1) is based on a new generation of a pulsed X-ray tube with 40 kV and an optical pathway with a switchable mirror for excitation source selection. This allows using the pulsed laser as an excitation source for optical induced fluorescence and the X-ray tube for high energy excitation of the samples with a mean X-ray energy of approximately 13 - 14 keV. With this table top picosecond pulsed X-ray and laser induced fluorescence spectrometer it is possible to measure scintillation or other fluorescence events in a wavelength range from 200 - 850 nm. Measuring results are full time resolved fluorescence spectra with a temporal resolution up to 20 ps after deconvolution. The instrumental response function (IRF) of the system is around 60 ps for laser excitation and 80 ps for X-ray excitation. For a performance test well known inorganic and organic scintillators as well as rhodamine 6G for laser induced fluorescence are measured and evaluated. Processes of corollance luminescence (CVL) are responsible for fast decay times of some alkali halides [6]. CsF, CsCl and CsBr show very fast scintillation decay times of 2.9 to 0.07 ns. The easily manageable system is able to determine these fast decay times and exhibits satisfying results in agreement with literature values. An example of such a fitting result of CsCl is given in figure 2.

We thank Chemetall GmbH for sponsoring this device and Hamamatsu Photonics GmbH for their professional cooperation.

- [1] B. Valeur *Springer Series on Fluorescence*, Berlin, Heidelberg, 2008.
 [2] C. L. Melcher, *Nucl. Instr. and Meth.* A2005, 537, 6-14.
 [3] a) S. Blankespoor et al., *IEEE Trans. Nucl. Sci.* 1994, 41, 698-702. b) S. E. Derenzo et al., *IEEE Trans. Nucl. Sci.* 2008, 55, 1458-1463.
 [4] M. Watanabe et al., *J. Photochem. Photobiol.* A1994, 80, 429-432.
 [5] a) T. Yanagida et al., *Appl. Phys. Express* 2010, 3, 56202. b) L. Zhao et al., *Photochem. Photobiol. Sci.* 2005, 4, 113. c) H. Odaka et al., *J. Phys. Chem.* C2009, 113, 11969-11974.
 [6] a) P. A. Rodnyi et al., *Phys. Stat. Sol.* (b) 1991, 166, 283-288. b) C. W. van Eijk, *J. Lumin.* 1994, 60-61, 936-941.

Fig. 1 Instrumental set-up.

Fig. 2 Fitting results of CsCl.



MS08-P04

Annealing behaviour of radiation damaged minerals

T. Beirau¹, C. Paulmann¹, B. Mihailova¹, U. Bismayer¹

¹*Universität Hamburg, Mineralogisch-Petrographisches Institut, Hamburg, Germany*

Metamict minerals possess structurally incorporated radioactive impurities and are characterized by a high degree of structural disorder with coexisting defect-rich crystalline and amorphous regions, caused by the radioactive α -decay and β -decay of the embedded actinides. Raman spectroscopy of metamict titanite allows to discriminate radiation-induced defects inside the crystalline areas and crystalline-to-amorphous transformations. The radiation-induced faults in the crystalline substance are related to the disturbance of $\text{SiO}_4\text{-TiO}_6\text{-SiO}_4\text{-TiO}_6$ rings comprising TiO_6 octahedra from different chains. The radiation-induced amorphization is related to the partial change of Ti coordination from octahedral to pyramidal and/or tetrahedral, which in turn violates the Ti-O-Ti intra-chain linkages. [1] During thermal annealing the damaged mineral structure recrystallizes and changes its physical properties. This structural recovery of the metamict minerals allanite and titanite was followed by single-crystal synchrotron X-ray diffraction and Raman spectroscopy. Also the existence of at least two different

mechanisms in the recrystallization process is shown by kinetic analysis. [2,3]

- [1] Beirau et al. (2011) Am. Min. (submitted).
 [2] Beirau et al. (2010) Phase Trans. 83, 694-702.
 [3] Beirau et al. (2011) Min.Mag. 75, 2393-2399.

MS08-P05

Characterisation of Lithium Local Environments in Lithium Cathode Materials by ^6Li and ^7Li MAS NMR Spectroscopy

J. Kovacevic¹, M. Fechtelkord¹, D. Mikhailova², H. Ehrenberg³

¹Ruhr-Universität Bochum, Institute for Geology, Mineralogy and Geophysics, Bochum, Germany

²IFW Dresden, Dresden, Germany

³Karlsruher Institut für Technologie (KIT), Institut für Angewandte Materialien – Energiespeichersysteme (IAM-ESS), Eggenstein-Leopoldshafen, Germany

Lithium cathode materials like lithium manganates with spinel structure or lithium layered materials are interesting compounds to employ in high voltage rechargeable batteries. Knowledge of the local environment is prominent to understand the electronic conductivity process. NMR investigations of lithium ion local order and environments could provide a better understanding here. In this study, ^6Li and variable temperature ^7Li MAS NMR experiments were performed to investigate the lithium local environments in several cathode materials. The samples were additionally characterised by powder X-ray diffraction. High resolution spectra, allowing a number of several local environments to be perceived, could still be acquired although unpaired electrons are present.

We investigated two different types of samples: Spinel type $\text{Li}_x\text{Mn}_{3-x}\text{O}_4$ ($0 \leq x \leq 1.33$) showed two kinds of lithium signals. One broader resonance showed a clear linear correlation to the reciprocal temperature and can be assigned to a Fermi-contact interaction between unpaired electrons of the manganese and the lithium nucleus (Lee et al., 1998). The second signal is narrow and shows no clear temperature dependence. This indicates high lithium mobility and no paramagnetic interaction.

The layered compounds of composition $\text{Li}[\text{Co}_{0.98}(\text{Fe}, \text{Mn})_{0.02}]\text{O}_2$ disclose no paramagnetic interaction (Jakes et al., 2011). However, one of the two lithium resonances is located at higher chemical shifts due to a Knight-Shift possibly caused by delocalized electrons.

References:

Y. J. Lee, F. Wang, and C. P. Grey (1998) ^6Li and ^7Li MAS NMR Studies of Lithium Manganate Cathode Materials. *J. Am. Chem. Soc.*, **120**, 12601-12613.

P. Jakes, E. Erdem, A. Ozarowski, J. van Tol, R. Buckan, D. Mikhailova, H. Ehrenberg, and R.-A. Eichel (2011) Local coordination of Fe^{3+} in $\text{Li}[\text{Co}_{0.98}\text{Fe}_{0.02}]\text{O}_2$ as cathode material for lithium ion batteries—multi-frequency EPR and Monte-Carlo Newman-superposition model analysis. *Phys. Chem. Chem. Phys.*, **13**, 9344-9352

MS08-P06

Investigation of molecular nature of the conjugated polymer films by resonance soft x-ray reflectivity

D. Ksenzov¹, A. Davtyan¹, F. Schäfers¹, U. Pietsch¹, S. Grigorian¹

¹University of Siegen, Physik, Siegen, Germany

The chemically sensitive structural properties of the conjugated polymers were measured in the ranges of Carbon and Sulphur absorption edges. These structural properties are preparation technique dependent and vary with incident angle of the probing x-rays.

Resonant soft x-ray scattering (RSoXR) measurements were

performed at optics beamline PM4 of synchrotron radiation source BESSY II. Thin films with various thicknesses ranging from 40 to 55 nm for spin-coated and around 400 nm for drop cast samples were probed by RSoXR technique under the incidence angles varying from 1 to 3 degree. Near Sulphur L-edge similar features for all poly-3-alkylthiophene polymers were obtained. In the case of Carbon K-edge the behaviour is more complex and RSoXR spectra differ for thin and thick films.

MS08-P07

Optical spectroscopy on MnWO_4

L. Dura¹, H. Gibhardt^{1,2}, J. Leist¹, L. Bohaty³, P. Becker³, G. Eckold¹

¹University of Goettingen, Institute for Physical Chemistry, Goettingen, Germany

²University, Physical Chemistry, Goettingen, Germany

³University, Institute of Crystallography, Cologne, Germany

Multiferroic materials have attracted great interest because of the unique simultaneous appearance of different ferroic properties, such as magnetism, electric polarization and elastic strains. The exceptional coupling mechanisms between these properties are of particular interest. As an interesting representative for this type of materials the tungstate MnWO_4 is investigated in the present contribution. At low temperatures, it exhibits a complex sequence of different phase transitions with three different antiferromagnetically ordered phases. One of these phases (between 12.5 K and 7 K) has a cycloidal spin order with an incommensurate wave vector. In connection with the cycloidal spin order the crystal forms a spontaneous electric polarization and becomes ferroelectric. Optical spectroscopy such as Raman scattering yields interesting information about the dynamics of spins and nuclei or ions and provides evidence for possible coupling mechanisms. While some selected results are already available from literature [1], a full characterization by Raman spectroscopy of this material is still missing. In particular, the influence of external fields on Raman spectra is not investigated yet.

In this work, we present the results of polarized Raman spectroscopic studies of a high quality MnWO_4 single crystal during the phase transitions (investigated temperature range 25 K - 7 K). Special interest was laid on excitations at low wave numbers and their response to an external electric field applied along the polar axis. Clear signatures of the changing dynamics within the multiferroic phase are observed.

[1] Iliev, M.N.; Gospodinov, M.M.; Litvinchuk, A.P.; Phys. Rev. B **80** (2009), 212302

MS08-P08

Structure-property relationships in silicates:

Thermal expansion and elasticity of synthetic emerald

P. Schröer¹, J. Schreuer¹

¹Ruhr-Universität Bochum, Institute of Geology, Mineralogy and Geophysics, Bochum, Germany

The crystal structure of hexagonal beryl, $\text{Be}_3\text{Al}_2\text{Si}_6\text{O}_{18}$, is built up from six-membered rings of SiO_4 tetrahedra parallel (001), which are cross-linked with BeO_4 tetrahedra and AlO_6 octahedra. The three-dimensional framework contains cavities which are linked to form channels parallel [001] and are often occupied by H_2O . H_2O molecules of type I are aligned with their H-H vector parallel to the hexagonal axis. Substitution of framework cations by ones with lower valency requires the incorporation of alkali ions into the channels for charge compensation. Interaction of the alkali ions with the H_2O molecules in the adjacent cavities leads to the formation of type II water [1, 2].

Our work focuses on the influence of water on the physical properties of nominally anhydrous minerals. Elasticity provides an

excellent probe for the study of corresponding structure-property relationships, because it arises exclusively from the interactions between the constituents of a crystal [3]. Therefore, we determined the coefficients of thermal expansion and the elastic constants of synthetic single crystal emerald grown by hydrothermal and flux methods, respectively, between 100 K and 970 K. The emerald crystals were further characterized by electron microprobe analysis, X-ray diffraction techniques and infrared spectroscopy.

The elastic constants at room temperature fit well to those observed on natural beryl [4, 5]. In particular, the empirical rules regarding correlations between mean elastic stiffness and the dominant type of substitution also hold for the synthetic emeralds. Changes in the arrangement of the water molecules at high temperatures do not affect the thermal expansion and elastic properties within experimental error. However, significant differences in the elastic behavior of water-free flux-grown and water-rich hydrothermally grown emeralds are observed.

- [1] R. D. Aines, G. Rossman, *Am. Min.* 69 (1984) 319-327.
 [2] D. L. Wood, K. Nassau, *Am. Min.* 53 (1968) 777-800.
 [3] J. Schreuer, S. Haussühl, *EMU Notes in Mineralogy* 7 (2005) 95-116.
 [4] S. Haussühl, *Z. Kristallogr.* 204 (1993) 67-76.
 [5] H. S. Yoon, R. Newnham, *Acta Crystallogr A* 29 (1973) 507-509.

MS08-P09

Structure-property relationships in silicates:

Thermal expansion and elasticity of natural scapolite

K. Demtröder¹, P. Schröder¹, A. Bürger¹, J. Kovacevic¹, J. Schreuer¹
¹Ruhr-Universität Bochum, Institut für Geologie, Mineralogie und Geophysik, Bochum, Germany

Scapolites are a common group of rock-forming framework silicates. In analogy to the plagioclase series scapolites form a solid solution series of the two tetragonal end members marialite (ma), $\text{Na}_4[\text{Al}_3\text{Si}_9\text{O}_{24}]\text{Cl}$, and meionite (me), $\text{Ca}_4[\text{Al}_6\text{Si}_6\text{O}_{24}]\text{CO}_3$ [1-3]. Until now, only little is known about the physical properties of scapolite single crystals [4]. In order to explore structure-property relationships, we studied the thermal expansion and the elastic properties of scapolite single crystals of gem quality with composition $\text{ma}_{77.5}\text{me}_{22.5}$ by means of dilatometry and resonant ultrasound spectroscopy, respectively. The samples were further characterized using X-ray diffraction methods, electron microprobe analysis and infrared spectroscopy.

Between 100 K and 1270 K the crystals show strong thermal expansion within the (001) plane and slight contraction parallel to the tetragonal axis. The anisotropy of the thermal expansion is closely correlated to specific structural features of scapolite. Furthermore, the direction with minimum thermal expansion coincides with the stiffest direction and vice versa. The deviations from Cauchy relations indicate a dominance of directional bonding within the (001) plane. The temperature evolutions of the shear resistances c_{44} and c_{66} as well as of the longitudinal stiffness c_{33} are quite normal. However, the longitudinal stiffness c_{11} and the transverse interaction coefficients c_{12} , c_{13} show a quite large softening of up to 24% between room temperature and 1270 K. At higher temperatures strong ultrasound dissipation effects develop rapidly.

- [1] D. K. Teertstra, B. L. Sherriff, *Am. Mineral.* 81(1996) 169-180.
 [2] D. K. Teertstra, B. L. Sherriff, *Chem. Geol.* 136(1996) 233-260.
 [3] E. Sokolova, F. C. Hawthorne, *Can. Min.* 46(2008) 1527-1554.
 [4] K. S. Aleksandrov, G. T. Prodaivoda, *Kristallografiya* 38(1993) 214-234.

MS08-P10

Electronic structure of single-crystalline $\text{Sr}(\text{Fe}_{1-x}\text{Co}_x)_2\text{As}_2$ probed by x-ray absorptionspectroscopy: Strong evidence for isovalent substitution of Fe^{2+} by Co^{2+}

M. Merz¹, F. Eilers¹, T. Wolf¹, P. Nagel¹, H. von Löhneysen¹, S. Schuppler¹
¹Karlsruher Institut für Technologie, Institut für Festkörperphysik, Eggenstein-Leopoldshafen, Germany

The doping-dependent valence and spin-state configurations of $\text{Sr}(\text{Fe}_{1-x}\text{Co}_x)_2\text{As}_2$ were investigated with near-edge x-ray absorption fine structure at the $L_{2,3}$ edges of Fe, Co, and As. The present data provide strong evidence for an isovalent substitution of Fe^{2+} by Co^{2+} , which is in obvious contrast to the widely assumed Co-induced electron-doping effect. Moreover, the data reveal that not only does the Fe valency remain completely unaffected across the entire doping range, but so do the Co and the As valency as well. The data underline a prominent role of the hybridization between (Fe,Co) $3d_{xy}$, d_{xz} , d_{yz} orbitals and As $4s/4p$ states for the band structure in $A(\text{Fe}_{1-x}\text{Co}_x)_2\text{As}_2$ (where A denotes Ca, Sr, or Ba) and suggest that the covalency of the (Fe,Co)-As bond is a key parameter for the interplay between magnetism and superconductivity.

MS08-P11

Single crystal dehydration of $\text{NaB}(\text{OH})_4$ -sodalites investigated by Raman depth profiling

A. Schulz¹, C. Rüscher¹, J. Buhl¹

¹Leibniz Universität Hannover, Mineralogie, Hannover, Germany

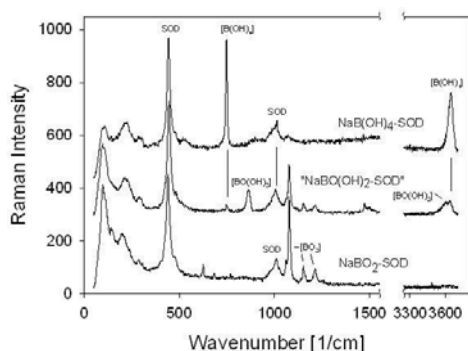
$\text{NaB}(\text{OH})_4$ -sodalite can be synthesized in nano crystalline [1] and micro crystalline [2] powders and even in larger crystals up to about 0.5 mm in size [3]. Characterisation of the nano crystalline and micro crystalline samples have shown two main steps of dehydration for samples heated at 200°C and 400°C, namely $\text{BO}(\text{OH})_2$ - and BO_2 -sodalite respectively [1, 2, 4, 5]. Dehydration seems to occur rather fast, depending only on temperature, which should, however be related to the rather small crystal size. Details of the mechanism of dehydration are presently unknown. Therefore, in this study larger single crystals of $\text{NaB}(\text{OH})_4$ -sodalite were investigated in situ as well as in ex situ heating experiments (20-580 °C) by micro-Raman spectroscopy (Bruker, Senterra, 532 nm, depolarized beam) providing a spatial resolution laterally as well as in depth of about 1 µm.

Typical Raman spectra of the three borate species enclosed in the sodalite cage as could be obtained in "purest form" are shown in Fig. 1. "Purest form" means that the spectra shows either a single phase $\text{NaB}(\text{OH})_4$ -sodalite as provided by the as prepared crystals, and solely NaBO_2 -cage filled forms. Spectra of intermediate form, $\text{NaBO}(\text{OH})$ -sodalite could presently only be obtained still showing some residual amount of $\text{B}(\text{OH})_4$ anions as well as already completely dehydrated BO_2 cage fillings beside a peak assigned to the $\text{BO}(\text{OH})_2$ form. For better understanding it must be noted, that those characteristic spectra were obtained using special heating cooling treatment with temperature up to 560°C for selected crystals of various sizes. Here the development of the spectral characteristic could also be followed in situ focussing the measurement spot on the crystal surface. A more detailed insight could be obtained separating a well shaped crystal of about 400 µm which were heated for about 3 h at 400°C. Raman spectra show mainly $\text{B}(\text{OH})_4$ species and only a relative contribution of intermediate anion species $\text{BO}(\text{OH})_2$ of about 10-20% at the surface. Depth profiling with steps of about 2.5 µm show a gradual increase in $\text{B}(\text{OH})_4$ intensity and a decrease for $\text{BO}(\text{OH})_2$, which could not be detected any more for depth larger than 20 µm. The spectra remain unchanged for depth larger than about 30 µm. A rough estimate of the diffusion coefficient according to $D = z^2/t$ with $z = 15$ µm imply a value of about $1.6 \cdot 10^{-10}$ cm²/s. A more accurate evaluation of the obtained profiles requires further considerations of the emitted intensities, which could be done with

reference to the intensities obtained for the sodalite lattice vibrations and which will be provided.

- [1] A. Schulz, C. H. Rüscher, J.-C. Buhl, Z. Krist. Suppl. 31 (2011) 93.
- [2] H.-H. E. Pietsch, M. Fechtelkord, J.-Chr. Buhl, J. Alloys Comp. 257 (1997) 168-174.
- [3] J.-Ch. Buhl, G. Engelhardt, J. Felsche, Zeolite 9 (1989) 40-44.
- [4] C. H. Rüscher, J.-Chr. Buhl, Z. Krist. Suppl. 15 (1998) 113.
- [5] C. H. Rüscher, Microp. Mesop. Mat. 86 (2005) 58-68.

Fig. 1 Raman spectra (at 20°C) of sodalites showing the enclosure of B(OH)₄, BO(OH)₂ and BO₂ anion species as denoted for some characteristic peaks. The spectra of NaBO(OH)₂-sodalite obviously shows still the presence of B(OH)₄ and BO₂ cage fillings.



MS08-P12

Thermal decomposition of sodium zincophosphate sodalite examined by autocorrelation analysis of temperature dependent FTIR spectra

L. Robben¹, T.M. Gesing¹

¹Universität Bremen, IAPC / Chemische Kristallographie fester Stoffe, Bremen, Germany

Sodium Zincophosphate Sodalite was chosen as a model system for the application of the autocorrelation (AC) method on temperature dependent FTIR spectra. The thermal decomposition of this sodalite was studied by differential thermoanalysis and thermogravimetry (DTA/TG), temperature dependent X-ray powder diffraction (TD-XRD) and temperature dependent infrared spectroscopy (TD-FTIR) from room temperature to 573 K. The TD-FTIR spectra have been analyzed by the AC method as proposed by Salje et al. [1] for the study of systematic changes in the FTIR spectra of minerals with external parameters like temperature or internal ones like the composition in solid solution systems. Peak fitting procedures can be very problematic in FTIR because the number of observable peaks must be known. For the AC analysis no peak fitting is needed. The application of the AC function

$$Corr(a, \omega') = [a(\omega + \omega')a(\omega)]d\omega$$

on the FTIR data does not need any assumptions and gives information about the change of the broadness of the peaks with the external or internal parameter. The broadness of the peaks itself is directly related to the order parameter [1] and is thus able to provide information about the structural development.

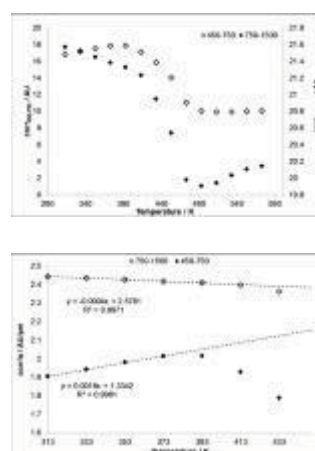
The thermal decomposition and dehydration of sodium zincophosphate sodalite and cobalt substituted zincophosphate sodalites has already been studied by Rajic et al. [2] by means of TG/DTA. Here we present a detailed study of the structural development of this sodalite by Rietveld refinements of TD-XRD data and we show the influence of the structural parameters on the broadness parameter obtained by AC analysis of the FTIR data.

The first linear part of the temperature dependent development of the AC broadness of the 450 to 750 cm⁻¹ spectral range up to 433 K (Fig. 1) is correlated with the thermal expansion of the sodalite, the ratio of broadness to lattice parameter *a* is a strong linear relationship with a slope indicating an almost constant behavior (Fig. 2).

- [1] E. Salje, M. Carpenter, T. Malcherek, T. Boffa Ballaran, Autocorrelation analysis of infrared spectra from minerals, European Journal of Mineralogy. 12 (2000) 503-519.
- [2] N. Rajić, R. Gabrovšek, V. Kaučič, Dehydration behavior of some microporous zincophosphates, Thermochimica Acta. 278 (1996) 157-164.

Figure 1: AC broadness of the spectral ranges 450-750 cm⁻¹ (symmetric T-O-T vibrations) and 750-1500 cm⁻¹ (asymmetric T-O-T vibrations).

Figure 2: Ratio of AC broadness and lattice parameter *a*.



MS09-P01

ELABORATION OF NEW OBJECTS BELONGING TO COORDINATION CHEMISTRY AND MOLECULAR MAGNETISM

M. Amel^{1,2}, B.-C. Nouredine¹, D. Luneau²

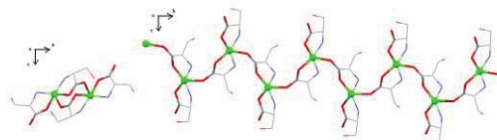
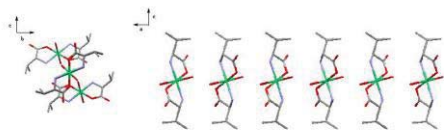
¹centre universitaire de Khenchela, Chimie, Khenchela, Algeria

²université Claude Bernard Lyon 1, Chimie, Lyon, France

Complexes of transition metals and amino acids have been extensively studied as models for the metal-binding sites in proteins. Amino acids are versatile ligands showing flexible coordination modes and they can coordinate to metal ions by their carboxylate and /or amino groups. Amino acid-metal complexes and their derivatives are of great importance because of their biochemical and pharmacological properties.

Valine and serine was an essential amino acids, Valine can chelate to metal ions via its amino N atom and carboxylate O atom. As a part of our studies on structural and properties of metal ion-amino acid complexes, we are reporting here the synthesis, crystal structure of a new Ni(DL-Val)₂(H₂O)₂. The title compound is mononuclear, Ni(II) metal shows an octahedral geometry, it is in trans coordinated to D-bidentate valinate, L- bidentate valinate ions and two water molecules. However serine chelate to metal ions via its amino N atom and carboxylate O atom and O hydroxy; with serine and copper (CuII) we obtain a single magnetic chain. .

Keywords: Complexes; amino acids; single crystals; single-molecule magnets



MS09-P02

The class C Vps tethering complexes HOPS and CORVET

H. Peters¹, U. Heinemann¹

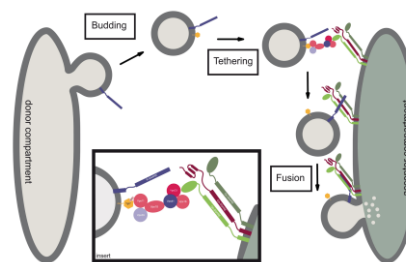
¹MAX-DELBRÜCK-CENTRUM FÜR MOLEKULARE MEDIZIN, Macromolecular Structure and Interaction, Berlin, Germany

Internal transport processes are one of the hallmark developments separating Eukaryotes from Prokaryotes¹ as they are prerequisites for the higher complexity present in eukaryotes. This complexity allows, among other benefits, the spatial separation of specialized processes (e.g. energy production within mitochondria and transcription within the nucleus). However, this development comes with a price: Eukaryotic cells are divided into different internal membrane-enclosed compartments, which need to be connected via specific transport processes. Various proteins and protein complexes have evolved to coordinate the several steps necessary for intracellular transport. The main focus of this study is on protein complexes involved in the tethering step between vesicles and their target membranes, especially on the class C Vps tethering complexes HOPS and CORVET². The reason for our interest is that, contrary to the well-studied fusion process³, little is known of the specific mechanisms of tethering. To date, knowledge is limited to the fact that they have to act as a bridge between the binding partners' GTPases and SNAREs leaving the exact mechanism to be uncovered. This study aims to uncover these structural and functional mechanisms using X-ray diffraction and biochemical assays.

Reference:

- [1] Cavalier-Smith, The phagotrophic origin of eukaryotes and phylogenetic classification of Protozoa. *Int J Syst Evol Microbiol*, 2002.52(Pt 2): p. 297-354.
- [2] Epp, Rethmeier, et al., Membrane dynamics and fusion at late endosomes and vacuoles--Rab regulation, multisubunit tethering complexes and SNAREs. *Eur J Cell Biol*.90(9): p. 779-85.
- [3] Jahn and Scheller, SNAREs--engines for membrane fusion. *Nat Rev Mol Cell Biol*, 2006.7(9): p. 631-43.

Fig. 1: Schematic representation of vesicle transport with focus on the tethering step.



MS09-P03

The Lin28 cold shock domain acts as an RNA chaperone

F. Mayr¹, A. Schuetz¹, U. Heinemann¹

¹MDC Berlin, Macromolecular Crystallography, Berlin, Germany

The highly conserved RNA-binding protein Lin28 regulates the processing of a developmentally important group of microRNAs, the let-7 family. Lin28 blocks the biogenesis of let-7 in embryonic stem cells and thereby prevents differentiation. Although it was shown that both RNA-binding domains (RBDs) of this protein, the cold shock domain (CSD) and the zinc knuckle domain (ZKD), are indispensable for pri- or pre-let-7 binding and blocking its maturation, little is known about the molecular basis of Lin28 binding to its target RNA. Here, we systematically examined the nucleic acid-binding preferences of the Lin28 RBDs and determined the crystal structure of the Lin28 CSD in the absence and presence of nucleic acids. The data show that both RNA-binding domains bind to single-stranded nucleic acids with the ZKD mediating specific binding to a conserved GGAG or GGAG-like motif and the CSD showing a slight preference for pyrimidine-rich sequences. However, only the Lin28 CSD can bind to pre-let-7 alone and thus is able to melt the upper stem region of pre-let-7 including the Dicer cleavage site. This indicates that the Lin28 CSD acts as an RNA chaperone that induces a conformational change in the terminal loop of pre-let-7 and facilitates a subsequent specific binding of the Lin28 ZKD to the conserved GGAG motif. By this means, Lin28 can tightly bind to and block the processing of pri- and pre-let-7.

MS09-P04

Structural basis of allosteric regulation of eukaryotic phosphofructokinases

M. Kloos¹

¹Center for Biotechnology and Biomedicine, Institute of Bioanalytical Chemistry, Leipzig, Germany

The enzyme 6-phosphofructokinase (Pfk) catalyses the formation of fructose 1,6-bisphosphate from fructose 6-phosphate and MgATP and contributes to the control of glycolysis in prokaryotic and eukaryotic cells. The catalytic activity is tightly regulated in a wide variety of organisms by diverse positive (e.g. fructose-2,6-bisphosphate, AMP) and negative (e.g. ATP, citrate) effectors. Eukaryotic Pfk has evolved by a process of tandem gene duplication and fusion to yield a protein with a much more complex structural organization and allosteric regulation. The N-terminal half of a Pfk subunit obviously retained the catalytic function, whereas in the C-terminal half allosteric ligand binding sites have evolved from former catalytic and regulatory sites. *Pichia pastoris* Pfk (PpPfk) is with ~1 MDa the most complex and probably largest eukaryotic Pfk [2]. We have determined the crystal structure of full-length PpPfk to 3.05 Å resolution in the T-state [1]. PpPfk forms an (αβ)₄ dodecamer of D₂ symmetry with dimensions of 161 x 157 x 233 Å mainly via interactions of the α-chains. The N-terminal domains of the α- and β-chains have folds that are distantly related to glyoxalase I, but the active sites are no longer functional. Interestingly, these domains located at the two

distal ends of this protein along the long two-fold axis form a ($\alpha\beta$)₂ dimer as does the core Pfk domains, however, the domains are swapped across the tetramerization interface. InPpPfk, the unique γ -subunit participates in oligomerization of the $\alpha\beta$ -chains. This modulator protein was acquired from an ancient SAM-dependent methyltransferase. The identification of novelATP binding sites, which do not correspond to the bacterial catalytic or effector binding sites, point at marked structural and functional differences between bacterial and eukaryotic Pfk.

[1] Sträter N.et al.; Molecular architecture and structural basis of allosteric regulation of eukaryotic phosphofructokinases;FASEB J.2011;25; 89-98.

[2] Tanneberger K.et al.; A Novel Form of 6-Phosphofructokinase: Identification and functional relevance of a third type of subunit inPichia pastoris;JBC2007;282; 23687-23697

MS11-P01

Layer Disorder in Sodium-Bismuth-Titanate Thin Films grown by Liquid-Delivery Spin MOCVD

M. Schmidbauer¹, J. Schwarzkopf¹, V. Kopp², V. Kaganer², A. Duk¹, F. Waidick¹, A. Kwasniewski¹, T. Remmele¹

¹Leibniz-Institute for Crystal Growth, Physical Characterization, Berlin, Germany

²Paul-Drude-Institute, Berlin, Germany

Sodium-bismuth-titanates are lead-free materials with promising ferro-/piezoelectric properties. Bi₄Ti₃O₁₂ represents an Aurivillius structure consisting of three perovskite units (m = 3) between two (Bi₂O₂)²⁺ intermediate layers. Incorporation of sodium leads to layer-structured compounds with the general formula Bi₄Ti₃O₁₂ + xNa_{0.5}Bi_{0.5}TiO₃. In this study we have deposited various sodium-bismuth-titanate phases with liquid-delivery spin metalorganic chemical vapor deposition. By adjusting the substrate temperature and the Na/Bi ratio during growth thin films of Bi₄Ti₃O₁₂, Na_{0.5}Bi_{8.5}Ti₇O₂₇, Na_{0.5}Bi_{4.5}Ti₄O₁₅ and Na_{0.5}Bi_{0.5}TiO₃ were epitaxially grown on different perovskite substrates. All these films exhibit an Aurivillius structure with integer (m = 3 and 4) and half-integer (m = 3.5) values form or exhibit a pure perovskite structure (m = ∞).

Additionally, in the low Na/Bi ratio region, we have also observed Aurivillius phases with fractional values m between 3 and 3.5. A detailed analysis of the epitaxial films by means of high-resolution x-ray diffraction and high-resolution transmission electron microscopy data proves a strong disorder in the epitaxial films which arises from random stacking of m = 3 and m = 4 perovskite units separated by (Bi₂O₂)²⁺ interlayers. The stacking disorder can be described by probabilities for different sequences of layers. Closed analytical expressions for the diffracted x-ray intensity are obtained when the layers form a stationary Markov chain. The results of the analytical calculations match the experimental data and indicate that the incorporation of sodium in the Bi₄Ti₃O₁₂ phase causes the formation of a fourth perovskite unit. With increasing Na/Bi ratio or substrate temperature structures with four perovskite units are incorporated with higher probability.

MS11-P02

One dimensional liquid-like disorder and phase ordering phase transition in short alkanes/urea inclusion compounds

C. Mariette¹, L. Guérin¹, P. Rabiller¹, B. Toudic¹, M.D. Hollingsworth¹

¹Institut de Physique de Rennes, RENNES, United States

Supramolecular assemblies provide ideal platforms for the systematic studies of phase transitions in aperiodic materials. In particular, channel inclusion compounds of urea with linear alkanes (UICs) have been studied extensively [1,2,3,4]. Short alkanes within urea aperiodic matrix present specific disorder at room temperature related to important translational degrees of freedom.

The shortest possible guest in UICs compounds is heptane. We will show how this compound undergoes a "phase ordering" phase transition from one dimensional liquid-like order to an aperiodic composite. This phase is characterized by the existence of a non-zero offset Δ_g between guest molecules in adjacent channels (see figure), observed for the first time in UICs, and the appearance of phase transition induced host-guest intermodulation [5].

Figure a: the aperiodic host-guest crystal of n-heptane/urea.

Figure b: two dimensional representation of a UIC indicating the definitions of c_{host} , c_{guest} and the offset Δ_g between guest molecules in adjacent channels.

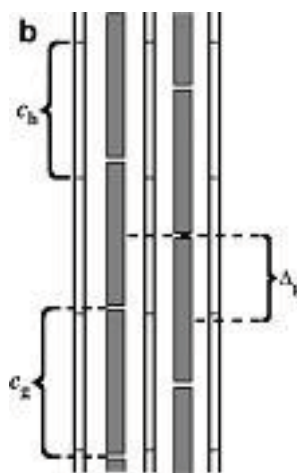
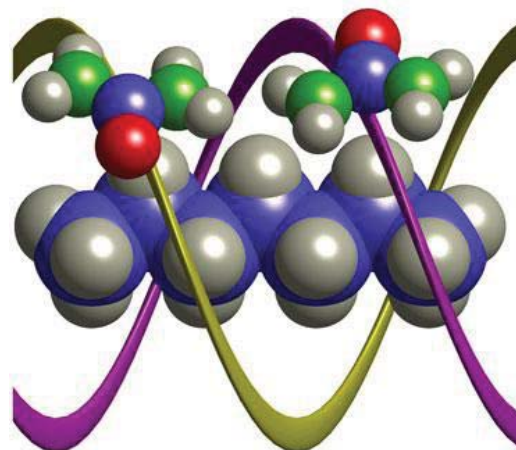
[1] K. D. M. Harris, and M. D. Hollingsworth, Proc. R. Soc. London, Ser. A 431, 245 (1990).

[2] S. van Smaalen, and K. D. M. Harris, Proc. R. Soc. London, Ser. A 452, 677 (1996).

[3] T. Weber, H. Boysen, M. Honal, F. Frey, and R. B. Neder, Z. Kristallogr. 211, 238 (1996).

[4] B. Toudic, P. Rabiller, L. Bourgeois, M. Huard, C. Ecolivet, G. J. McIntyre, P. Bourges, T. Brezowski and T. Janssen, Europhys. Lett. 93, 16003 (2011).

[5] C. Mariette & al., submitted for publication



MS11-P03

The superstructure of trimethyltin hydroxide described in higher-dimensional superspaceS. Dey¹, A. Schönleber¹, S. van Smaalen¹¹University of Bayreuth, Laboratory of Crystallography, Bayreuth, Germany

At room temperature the structure of trimethyltin hydroxide, (CH₃)₃SnOH, crystallizes in a (2a × 8b × 2c) superstructure with monoclinic, b-unique symmetry, space group Pn [1]. The structure itself is built by four independent polymeric chains, each of them containing eight units of (CH₃)₃SnOH [2]. Those units along the chains are linked via Sn-O-Sn bridges. At T = 176 K the compound undergoes a phase transition, at T = 120 K the crystal structure is reported to be twofold disordered in space group P2₁/c [2].

We have performed a temperature-dependent single crystal X-ray diffraction experiment at the synchrotron Hasylab/DESY (Hamburg, Germany) to search for weak superstructure peaks and to explore the crystal structures between room temperature and T = 100 K.

The description of the crystal structure and its change with temperature is presented within the higher-dimensional superspace approach.

[1] N. Kasai, K. Yasuda, R. Okawara, *J. Organomet.Chem.* **3** (1965) 172-173.

[2] K. M. Anderson, S. E. Tallentire, M. R. Probert, A. E. Goeta, B. G. Mendis, J. W. Steed, *Cryst. Growth Des.* **11** (2011) 820-826.

MS11-P04

Comparison of Two Structural Models, “Superstructure” and “Modulated Structure” for Cocrystal of Phenazine Chloroanilic Acid at T=100 KL. Noohinejad¹, S. van Smaalen¹, S. Mondal¹¹University of Bayreuth, Laboratory of Crystallography, Bayreuth, Germany

A glance into the crystallographic literature suggests that aperiodic structures have received considerable attention and the superspace approach is now a well established concept. One example of a modulated molecular compound is phenazine chloranilic acid. This organic cocrystal is formed of two components, phenazine, C₁₂H₈N₂, as a base and chloranilic acid, C₆H₂O₄Cl₂, as an acid. The acid acts as hydrogen-bond donor group and bonds to the base through O—H•••N hydrogen bonds. Phenazine chloranilic acid is a low-molecular-weight organic compound which appears particularly attractive as a ferroelectric material. At room temperature it is paraelectric [1]. But below T_{c1} = 253 K the first ferroelectric phase was reported [1-3]. In the narrow temperature range between T_{c2} = 147 and T_{c3} = 137 K it is assumed that an incommensurate phase is formed [3]. Below T_{c3} the second ferroelectric phase was reported, where a commensurate phase has appeared [3]. Our experiments confirm the formation of the commensurate phase at low temperatures.

The commensurate superstructure of phenazine chloranilic acid is determined based on single-crystal X-ray diffraction data measured at T=100 K. The superlattice reflections are alternatively referred to as satellite reflections. Two different methods have been applied to describe the structure of phenazine chloranilic acid. The first approach based on the superspace approach with a monoclinic basic structure, the modulation vector (1/2, 1/2, 1/2) and the (3+1)-dimensional superspace group P2₁(1/2 β 1/2)0 (standard setting: No. 4.1.6.3, P2₁(1/2 0 γ)0 [4]). The second approach involves the description by a centered fourfold supercell with space group C1 (standard setting: No. 1,P1). In this presentation we would will demonstrate the benefits of using the superspace approach and compare the structural models obtained from two approaches.

[1] Horiuchi, S., Ishii, F., Kumai, R., Okimoto, Y., Tachibana, H., Nagaosa, N., Tokura, Y.: Ferroelectricity near room temperature in co-crystals of nonpolar organic molecules. *Nature Materials*4(2005) 163-166.

[2] Gotoh, K., Asajib, T., Ishida, H.: Hydrogen bonding in two solid phases of phenazine-chloranilic acid (1/1) determined at 170 and 93 K. *Acta Crystallogr.* C63(2007) o17-o20.

[3] Horiuchi, S., Kumaia R., Tokura Y.: Proton-displacive ferroelectricity in neutral cocrystals of chloroanilic acids with phenazine. *J. Mater. Chem.*19(2009) 4421-4434.

[4] Stokes, H. T., Campbell, B. J., van Smaalen, S.: Generation of (3+d)-dimensional superspace groups for describing the symmetry of modulated crystalline structures. *Acta Crystallogr.* A67, 45-55 (2011).

MS11-P05

X-ray diffraction study of TiPO₄ structure at low temperatures.M. Bykov¹, J. Zhang¹, A. Schönleber¹, S. van Smaalen¹, J. Law², R. Kremer², R. Glaum³¹Bayreuth University, Laboratory of Crystallography, Bayreuth, Germany²Max-Planck-Institut für Festkörperforschung, Stuttgart, Germany³Universität Bonn, Institut für Anorganische Chemie, Bonn, Germany

The group of transition metal ortho-phosphates MPO₄ (M = Ti, V, Cr) is a class of low-dimensional quantum chain systems with different number of d-electrons on M. MPO₄ crystallize in the orthorhombic space group Cmc. Their structure can be described in terms of MO₆ octahedra sharing their edges to form MO₄ chains along c-axis. These chains are interconnected by sharing corners with distorted PO₄ tetrahedra [1].

In 1996 Glaum *et. al.* found a commensurate magnetic superstructure in VPO₄ with a propagation vector **k** = (0.5, 0, 0) between 2 and 10 K and incommensurate magnetic ordering between 10 and 25.5 K [2]. No magnetic ordering was detected for TiPO₄. In 2011 Law *et. al.* [3] reported two phase transitions of TiPO₄ at 111 K and 74 K. They described the low-temperature phase as a commensurate spin-Peierls state with Ti-Ti bond alternation within the Ti chains. Model calculations expect very weak superstructure reflections, which couldn't be resolved in an early neutron powder diffraction experiment. It was also proposed that the middle phase is the incommensurate phase which is similar to that found for TiOX [4].

The current work presents low-temperature single-crystal X-ray diffraction of titanium ortho-phosphate using synchrotron radiation (performed at beamline D3 of Hasylab at DESY, Hamburg, Germany). Due to uncertainties about the correct space group and the possibility of the existence of a superstructure in TiPO₄ the structure refinement of this compound is of additional interest. The predicted weak superlattice reflections were observed and can be indexed with the commensurate q-vector (0.5, 0, 0) which is in agreement with recent theoretical calculations.

[1] R. Glaum and R. Gruehn, *Z. Kristallogr.* **198**, 41 (1992).

[2] R. Glaum, M. Reehuis, N. Stüßer, U. Kaiser and F. Reinauer, *J. Solid State Chem.* **126**, 15 (1996).

[3] J.M. Law, C. Hoch, R. Glaum, I. Heinmaa, R. Stern, J. Kang, C. Lee, M.-H. Whangbo, and R.K. Kremer, *Phys. Rev. B* **83**, 180414(R) (2011).

[4] A. Schönleber, G. Shcheka, and S. van Smaalen, *Phys. Rev. B* **77**, 094117 (2008).

MS12-P01

Simulations of Structure, Growth and Equilibrium Form of GdVO₄ Crystals

M. NICOLOV¹

¹Aurel Vlaicu University of Arad, Engineering, Arad, Romania

Question -GdVO₄ crystal

GdVO₄ crystal is a laser host material with laser property. Compact diode pumped crystal laser operating in the infrared and visible spectral regions have applications in the fields of industry, defense, medical uses and scientific research due to its good mechanical, thermal, physical and chemical properties. This crystal has high absorption coefficient and large absorption cross section at 808 nm. Methods - structure analysis of GdVO₄ using Hartman Perdok Theory. In the present study we did the structure analysis of GdVO₄ using Hartman Perdok Theory. We obtained from a PBC analysis of GdVO₄ structure the F faces and the combinations of atoms used in simulations of energies.

Results:

We found from simulations that this crystal at a first analysis have the next F faces: {134}, {1-10}, {100}, {001}, {101} and {211}. The conclusions from the present study is that {101} and {134} are forms which can be obtained together in the same crystal but {211} and {001} can be obtained in another drawn growth form of the crystal. Even we obtained for {1-10} and {100} and from the structure analysis that are F face in the growth form of the crystal these forms don't occur. The growth forms of crystals corrected and uncorrected is different in some situations for volume and surface presented in the present study.

Theoretical growth forms were constructed from the calculated attachment energies E_a which are assumed to be directly proportional with the growth rate of F faces. The F faces calculated here are {100}, {211}, {134}, {001}, {101} and {1-10}. The growth forms were simulated using only Coulomb interactions, van der Waals attractions and Born repulsions.

Conclusions:

In conclusion we can say that in the future we have to decide what case is the best for the real type of crystal: case I or II. This crystal can have 8, 10, 16 or 18 F faces. The final form of this crystal can be solved in the future by using experimental proofs from the experimentally growth crystal.

Acknowledgements: The author want to thanks Professor R. Fornari, Dr. W. Miller, U. Rehse from IKZ Berlin, Germany, for the help to obtained the results from this study in IKZ Berlin.

Selected references:

- Epelbaum B. M., Kiyoshi Shimamura, Katsuhiko Inaba, Satoshi Uda, Kochurikhin V.V., Hiroshi Machida, Yasuko Terada, Tsuguo Fukuda, Edge -Defined film-fed (EFG) growth of rare -earth orthovanadates REVO₄ (RE=Y, Gd): interface morphology effect on crystal shape and materials properties, J. Cryst. Growth, 186(1998), 607-611.
- Matsui M., Molecular dynamics study of the structures and bulk moduli of crystals in the system CaO-MgO-Al₂O₃-SiO₂, Phys. Chem. Minerals, 23(1996) 345-353,
- Milligan W.O., Vernon L.W., Crystal structure of Heavy Metal Orthovanadates, J. Phys. Chem., 56(1952), p.145-148.
- Woensdregt C.F., Computation of Surface Energies in an Electrostatic Point Charge Model: I. Theory, Phys. Chem. Minerals, 19(1992) 52-58.

MS12-P02

Surface energy calculations of fcc-, bcc- and hcp-metals by application of the bond deficiency model.

A. Mutter¹

¹University of Cambridge, Earth Sciences, Cambridge, United Kingdom

The aim of this study is to present an application and methodology which is capable to calculate the surface energies and bond

energies of fcc-, bcc- and hcp-metals. This approach is based on the bond-valence theory which has proven to be a valuable tool to determine the accuracy of experimentally derived crystal structures. Now, we will discuss to which extend the bond-valence theory can as well be applied to predict the surface energy of a crystal face. Here we will correlate bond-length and bond-valence to bond-energy, and thus are able to derive surface energies. Two alternative methods will be presented, which are as well combinable methodologies to derive both the bond-energy as well as the surface energy of fcc-, bcc- and hcp-metals.

This approach is closely related to the well established broken-bond-model of Mackenzie et al. (1962) and the bond-valence deficiency model of Mutter (2007). The presented study is based on the assumptions that i) the bond strength and the atomic coordination in the crystal structure are constant for a given metal and ii) a simple relationship exists between the surface energy, the d- spacings and the standard enthalpy of formation ΔH_f.

In the first part we introduce the correlation factors C_(fcc) and C_(bcc), derived from the bond-deficiency of the crystal surfaces, and we deduce a linear relationship between the lattice spacing and the surface energy of the bulk-termination of fcc- and bcc- metals. This relationship is then linked to the standard enthalpy of formation ΔH_f.

In a second approach we deduce the bond energy from the exponential relationship between the bond-length and the corresponding bond-valence of fcc-, bcc- and hcp-metals. Again this relationship is linked to the standard enthalpy of formation ΔH_f and thus the bonding energy of an atom. Having determined the bond energy for different bond length and by summation of the bond deficiency of a crystal surface the corresponding surface energy of various fcc-, bcc- and hcp-metals can be obtained.

Special attention is given to iron (Fe) and the changes of the surface energy close to the point of phase transition. Fe will change at about 1185.15 K from the α-Fe (bcc) phase to γ-Fe (fcc) phase and again at 1667.15 K to the σ-Fe phase (fcc). In addition Fe will change at 273.15 K and about 13 GPa from the α-Fe (fcc) to the ε-Fe phase (hcp).

References

- (1) J.K. Mackenzie, A.J.W. Moore and J.F. Nicholas (1962) Bonds broken at atomically flat crystal surfaces I: Face-centered and body-centered cubic crystals. J. Phys. Chem. Solids 23 (1962) 185.
- (2) Mutter, A. (2007): The bond-valence deficiency model: A new application to describe mineral surface reactions. URN: urn:nbn:de:hbz: 6-98539587759. (Thesis).

MS12-P03

3D-PDF analysis of disordered single crystals

T. Weber¹, A. Simonov¹

¹ETH Zürich, Dep. für Materialwissenschaft, Zürich, Switzerland

The three-dimensional pair distribution function (3D-PDF) method is an extension of the well-established powder diffraction based 1D-PDF technique for studying crystalline disorder [1]. It allows an easy and direct access to real atomic pair correlations and therefore significantly facilitates our understanding of crystal chemical and physical properties of disordered crystals. The 3D-PDF is obtained by Fourier transformation of the total diffraction pattern from a disordered single crystal or from its diffuse scattering alone ("3D-ΔPDF"). Usage of 3D experimental data does not only provide knowledge about the length of real interatomic vectors, as it is the case in 1D-PDF studies, but also delivers direct information about spatial directions of interatomic correlations. The 3D-PDF method permits modeling techniques that are difficult to be applied when using powder diffraction data, i.e. complexity of disorder problems may heavily be reduced by filtering out information that is already known or not of interest. Elimination of Bragg scattering from the usually well-known average structure, for example, may strongly enhance visibility of disorder information [2]. Furthermore, usage of 3D information

also allows separate modeling of spatially distinct features like intra- and interlayer disorder [3]. In this contribution we will demonstrate several examples of qualitative and quantitative 3D-PDF investigations.

References:

- [1] Th. Weber, A. Simonov, submitted.
- [2] Ph. Schaub, Th. Weber and W. Steurer, *Phil. Mag.* 87, 2781-2787, (2007).
- [3] Ph. Schaub, Th. Weber and W. Steurer, *J. Appl. Crystallogr.* 44, 134-149, (2011).

MS12-P04

CCL - An algorithm for the efficient automatic comparison of clusters

J.C. Schön¹, R. Hundt², M. Jansen¹

¹MPI for Solid State Research, Chemistry III, Stuttgart, Germany

²University Bonn, Chemistry, Bonn, Germany

Clusters of atoms have become an important area of research in materials science, chemistry and physics, both from the experimental and theoretical point of view.[1] In particular, studies of the realm of possible cluster structures in a wide variety of chemical systems ranging from intermetallic over ionic to rare earth based ones are proliferating at an increasing pace. Applying molecular dynamics and Monte Carlo based exploration and global optimization techniques to the study of the energy landscape of a cluster system commonly leads to thousands of cluster structures as potential structure candidates, and sorting them and discarding duplicates is a non-trivial task. Commonly, structures are compared by their symmetries, their energies and/or their pair distribution functions, but these tools become increasingly less useful with increasing clusters size.

Therefore, we have developed an algorithm - CCL -, which allows us to determine, if two given clusters containing the same number of atoms are identical within certain given tolerances. Our approach follows the same general philosophy as the CMPZ-algorithm [2], which we had developed for the comparison of periodic structures, by focussing on the existence of an affine mapping between the two cluster structures. Thus, we do not depend on topological "bond"-based criteria, and the degree of similarity between two structures is defined by the geometric mismatch between the two structures. The algorithm allows us to compare clusters containing different types of atoms of different size, and also to check, whether a smaller cluster can be embedded inside a larger one, or inside a periodic structure.

The algorithm has been implemented in the structure analysis and drawing program KPLOT,[3] and can be employed in an automated command driven fashion when dealing with large numbers of cluster structures.

- [1] R. Ferrando, J. Jellinek, R. L. Johnston, *Chem. Rev.* (2008), 108:845-910
- [2] R. Hundt, J. C. Schön, M. Jansen, *J. Appl. Cryst.* (2006), 39:6-16
- [3] R. Hundt, KPLOT, Version 9.6.12 (2011), Univ. Bonn

MS12-P05

A forcefield simulation study: Properties of amino acids on the magnetite-(111)-surface

A. Bürger¹, U. Magdanz¹, H. Gies¹

¹Ruhr-University, Geology, Mineralogy and Geophysics, Bochum, Germany

Magnetite (Fe₃O₄) is an iron oxide of the spinel group which crystallises in the inverse spinel structure[1]. In nature magnetite is an important biomineral. Birds and magnetotactic bacteria, e.g., use magnetite single-crystals to orientate themselves in the earth magnetic field. The connection between the inorganic magnetite-

(111)-surface and the organic parts of the animals is the magnetosome membrane (MM). The composition of the MM of the magnetotactic bacteria *Magnetospirillum gryphiswaldense* has been analysed[2,3]. The MM is built by different magnetosome membrane proteins (MMPs). Two of these MMPs are the proteins MamJ and MamG. The structure of MamJ is dominated by the amino acids aspartic acid (Asp) and glutamic acid (Glu) whereas MamG is dominated by glycine (Gly) and leucine (Leu). Forcefield simulations of the interaction of the magnetite-(111)-surface and the membrane offer the possibility to investigate if and how the amino acids interact with the surface. Additionally, it is possible to investigate the interactions and the adsorption distances between the surface atoms and the functional groups of the amino acids. We have chosen the COMPASS[4]-forcefield because all bondings and atoms of the surface and of all investigated amino acids are defined in this forcefield. As simulation software we used Forcite which is integrated in the Materials Studio 5.0 software package. In addition to that we use the magnetite-(111)-surface that had already experienced relaxation[5]. Based on the assumption the surface has been defined as a constraint which should not change during simulation.

The amino acids may adsorb in a docking box built by a 47.49 Å x 47.77 Å magnetite-(111)-surface and a 27 Å vacuum slab. For every amino acid 10000 frames has been calculated. The results show that it is energetically favourable for the amino acids to adsorb on the surface. All of them adsorb in Fe-O-distances between 2.6 and 2.7 Å. The involved O-atoms belong to the carboxyl-group (Asp) or to the carboxylate-group (Gly, Glu and Leu). From this it follows that electrostatic interactions dominate. This conclusion can be proven by the results.

During the simulations, according to the frequency of the best results, the global minimum could be attained for all of the amino acids.

Summing up we can show that it is energetically favourable for all of the amino acids to adsorb on the magnetite-(111)-surface and that the electrostatic interaction dominates during adsorption.

- [1] Fleet, M.E., *Acta Crystallographica Section B* 1981, Volume 37, Part 4
- [2] Grünberg, K., Müller, E., Otto, A., Reszka, R., Lindner, D., Kube, M., Reinhardt, R., Schüller, D., *Applied and Environmental Microbiology* 2004, Vol. 70, No. 2, pp 1040-1050
- [3] Schüller, D., *Arch Microbiol* 2004, 181: 1-7
- [4] Rigby, D., Sun, H., Eichinger, B.E., *Polym. Int.* 1998, 44, 311-330
- [5] Ritter, M., Weiss, W., *Surface Science* 1999, 432, 81-94

MS12-P06

Molekularmechanische Simulation von Nitraminen mit dem Kraftfeld COMPASS

P.B. Kempa¹, M. Herrmann¹

¹Fraunhofer ICT, Energetische Materialien, Pfinztal, Germany

Die Erstellung eines geeigneten Strukturmodells für eine RIETVELD-Verfeinerung ist oft schwierig. Daher ist zu diesem Zweck meist eine Kombination verschiedener Methoden notwendig. Auch „Molecular Modeling“ kann dabei helfen ein adäquates Strukturmodell zu entwickeln.

„Molecular Modeling“ kann entweder mit quantenmechanischen ab-initio Methoden oder molekularmechanischen Kraftfeldmethoden durchgeführt werden. Ein Kraftfeld (force field) beschreibt die Hyperfläche der potentiellen Energie auf der sich ein Atom bewegen kann. Da Kraftfelder oftmals auf ganz bestimmte Gruppen von Systemen abgestimmt sind, hängt die Wahl eines Kraftfelds von dem Typ der zu untersuchenden Struktur ab.

Im ersten Schritt wurden die fünf Standardkraftfelder Universal, Dreiding, cvff, peff und COMPASS, die von dem Module Forcite des Simulationsprogramms Materials Studio 5.0 [1] unterstützt werden, auf ihre Brauchbarkeit für die Simulation energetischer Nitramine getestet. Die Molekülstrukturen der energetischen

Nitramine Methylnitramin (MNA), Methylendinitramin (MEDINA), Hexogen (RDX), Octogen (HMX) und Hexanitrohexaazaisowurztan (HNIW) wurden zunächst mit quantenmechanischen DFT-Methoden geometrisch optimiert und deren Bindungsparameter mit denen aus der geometrischen Simulation mit den fünf Standardkraftfeldern verglichen [2, 3]. Dabei zeigte sich das Kraftfeld COMPASS am besten geeignet.

Im zweiten Schritt werden nun Moleküle aus realen, kondensierten Strukturen betrachtet. Ausgewählt wurden die stabilen Modifikationen der energetischen Nitramine HMX und HNIW, β -HMX und e-HNIW. Zur Beurteilung werden nun experimentell bestimmte Bindungsparameter aus Beugungsuntersuchungen mit denen aus der molekularmechanischen Simulation mit dem Kraftfeld COMPASS verglichen. Da der charakteristische Teil der Zielmoleküle die Nitramin-Gruppe N-NO₂ ist, wird insbesondere darauf geachtet, wie COMPASS diese Gruppe behandelt. Diese Daten dienen dann zur Beantwortung der Frage: „Ist das Kraftfeld COMPASS wirklich am besten für die Simulation energetischer Nitramine geeignet.“

[1] Accelrys Software, Materials Studio software environment, Release 5.0 documentation, Accelrys Software Inc., San Diego (2009); www.accelrys.com.

[2] Kempa, P.B., Herrmann, M., Proc. 42th Int. Annual Conf. of ICT, 81.1 - 81.20 (2011).

[3] Kempa, P.B., Herrmann, M., P03-P02, Gemeinsame Jahrestagung DGK, DMG, ÖMG, 20. - 24. 9. 2011, Salzburg, Österreich

MS12-P07

Calculation of thermodynamic parameters of melts from liquidus-curves

B. Simons¹

¹Universität zu Köln, Institut für Kristallographie, Köln, Germany

Keywords: Liquid solution thermodynamics, Enthalpy of melting, Anorthite, Diopside, Bi₂O₃, Bi₄B₂O₉

A phase diagram in principle is nothing but a graphical representation of the thermodynamics of the state function of a chemical system, where the state function is given with $f = f(P, T, V, n_i)$ assuming other variables like the electric, magnetic, gravitational potential and the like constant. On a molar base for pure components n_i (number of moles “n” for the component “i”) is represented by $x_i = n_i/Sn_j$, leading to the familiar T-x diagram. However, for nonideal solution the molfraction “x” has to be substitute by the activity “a”.

Vice versa thermodynamic parameters might be extracted from a phase diagram.

A model for such calculations by a rigorous application of solution thermodynamics has been elaborated and validated for the “simple” and well known system Anorthite-Diopside (Diopside an example of almost ideal solution characteristics of the melt) and the more sophisticated System Bi₂O₃-Bi₄B₂O₉.

The data calculated are internally consistent and yield values of DH_S for Anorthite = 133 kJ/mole, Diopside = 81 kJ/mole, Bi₂O₃ = 19 kJ/mole and Bi₄B₂O₉ = 39 kJ/mole. The activity of Anorthite and Diopside in an anorthitic melt deviates negative from ideality, whereas a diopsidic melt behaves almost ideal. In a “Bi₂O₃” melt the activity of the Bi₂O₃ component is strongly positive, that of Bi₄B₂O₉ is strongly negative. The opposite is observed for the “Bi₄B₂O₉” melt. All calculated liquidus except the Bi₄B₂O₉ liquidus closely match the experimental ones. In contrast to the experimental liquidus the calculated Bi₄B₂O₉ liquidus has an inflection point. The crest of the metastable spinode (solvus) for a “Bi₂O₃” melt is close to the liquidus indicating melt separation at undercooling.

The data are discussed with respect to the melt structures and its consequence for crystal growth.

MS12-P08

Stacking disorder and diffuse scattering in tris(bicyclo[2.1.1]hexeno)benzene evaluated by lattice-energy minimisation

J. Glinnemann¹, M.U. Schmidt¹

¹Goethe-Universität, Anorganische und Analytische Chemie, Frankfurt/Main, Germany

The stacking disorder in the hexagonal polymorph of tris(bicyclo[2.2.1]hexeno)benzene, C₁₈H₁₈, has recently been explored [1] by lattice-energy minimisations using force-field methods.

Fig.1. Molecular structure of tris(bicyclo[2.1.1]hexeno)benzene, C₁₈H₁₈, point group $\bar{6}2m$ (D_{3h})

The molecule with $\bar{6}2m$ (D_{3h}) point-group symmetry forms layers with $p\bar{6}2m$ layer-group symmetry. Each layer can be situated in three positions, the energies of these arrangements vary by 0 to 3 kJ/mole, depending on the positions of nearest and next-nearest layers.

Possible stacking sequences of layers were derived from order-disorder (MO) theory [2, 1] and by a combinatorial approach [1]. The resulting periodic model structures were optimised by lattice-energy minimisations.

The lattice-energy calculations show that eclipsed arrangements of layers are energetically less favourable than non-eclipsed ones. The reason was found in a deviation from $p\bar{6}2m$ symmetry. Molecules in eclipsed layers are almost parallel to the layer plane, whereas molecules in non-eclipsed layers are inclined to it by about 3° leading to a more efficient packing, and with the lattice energy improved by 2 to 3 kJ/mole, depending on the neighbouring layers. The influence of the next-nearest layers was found to be not a direct one, but mediated by the distortion of the layers between them.

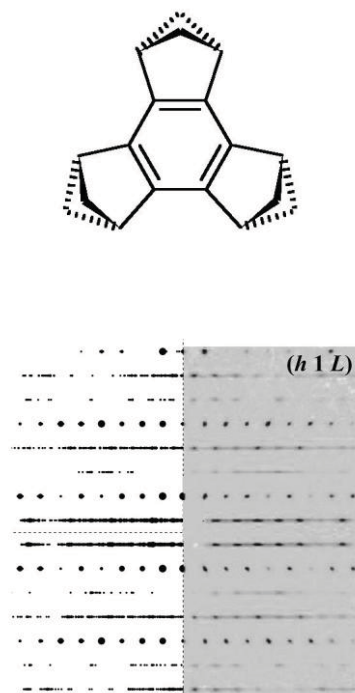
Using Boltzmann statistics, the stacking probabilities for all four-layer sequences were calculated. The results match well with the probabilities derived from the diffuse scattering in [2]. The lattice-energy minimisations allowed to determine the actual local structures in all individual layers including packing effects like rotation of molecules, lateral shifts, and to calculate the stacking layer thickness, depending on the actual layer sequences.

The structures computed with lattice-energy minimisations allow to calculate the diffraction patterns, including the diffuse scattering. As an example the diffraction pattern of a “typical” 54-layer structure is given (Fig. 2). Although this pattern was calculated from one structure only, and without any fit to experimental data, it shows many similar features as the experimental pattern. Thus, the ability of lattice-energy minimisations to simulate experimentally observed diffuse scattering is convincingly demonstrated. This will be highlighted in the presentation.

Fig. 2. Diffraction pattern calculated from a 54-layer structure derived by lattice-energy minimisation (left), compared with the experimental pattern (right; taken from [2]) for the (*h*1*L*) reciprocal-lattice layer.

[1] Schmidt, M. U.; Glinnemann, J.: Explanation for the stacking disorder in tris(bicyclo[2.1.1]hexeno)benzene using lattice-energy minimisations. Z. Kristallogr., submitted.

[2] Bürgi, H.-B.; Hostettler, M.; Birkedal, H.; Schwarzenbach, D.: Stacking disorder: the hexagonal polymorph of tris(bicyclo[2.1.1]hexeno)benzene and related compounds. Z. Kristallogr.220(2005) 1066-1075.



MS12-P09

Application of the Maximum Entropy Method to X-ray powder diffraction data of ionic conductors

O.V. Magdysyuk¹, R.E. Dinnebier¹, M. Jansen¹¹Max Planck Institute for Solid State Research, Stuttgart, Germany

The Maximum Entropy Method (MEM) is in particular well suited to locate missing atoms in incomplete crystal structures and to reconstruct the most probable electron density distribution.

In the present work, the MEM was used for reconstruction of the ionic densities in the superionic conductor α -RbAg₄I₅ and its low temperature phases β - and γ -RbAg₄I₅, that possess a very low ionic conductivity. All three phases of RbAg₄I₅ contained two admixtures with strong overlapping of the peaks of different phases (especially strong for γ -RbAg₄I₅). For comparison, MEM reconstructions of the electron densities of α -, β - and γ -Ag₄Mn₃O₈ were performed. All three phases of Ag₄Mn₃O₈ possess a lower value of ionic conductivity in comparison with α -RbAg₄I₅. The common feature for RbAg₄I₅ and Ag₄Mn₃O₈ is an identical sequence of the group-subgroup relationships during the phase transitions [1, 2].

All MEM calculations were performed based on $F_{\text{obs}}+G$ - constraints and procrystal density. The program BayMEM [3] was used for the MEM calculations. The corresponding structure factors were extracted after the Rietveld refinement using the program Topas 4.1 [4], that allowed to receive the values of structure factors with very high accuracy even in the cases with strong overlapping of peaks of the main phase RbAg₄I₅ and the admixtures.

It was possible to compare the results of the MEM calculations from powder with single crystal data for α -RbAg₄I₅ [5] and α -Ag₄Mn₃O₈ [6].

Fig. 1. MEM reconstructed three-dimensional electron-density maps of α -RbAg₄I₅ (left) and only silver atoms of α -RbAg₄I₅ (right)

1. Ahlert, S.; Dinnebier, R.; Jansen, M. Z. Anorg. Allg. Chem. 2005. 631. 90-98.

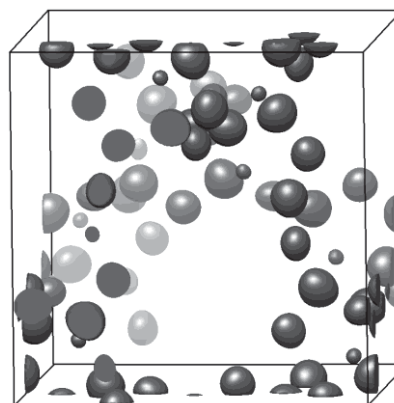
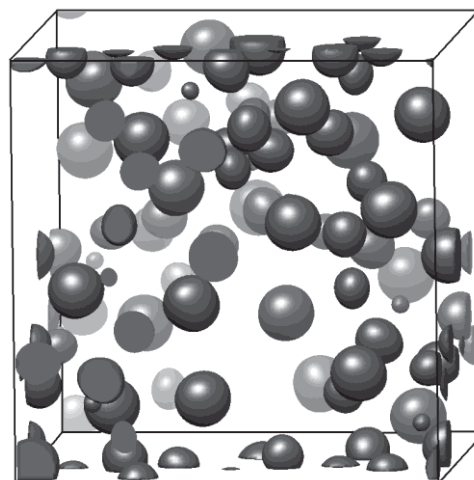
2. Funke, K.; Banhatti, R.D.; Wilmer, D.; Dinnebier, R.; Fitch, A.; Jansen, M. J. Phys. Chem. 2006. 110. 3010-3016.

3. van Smaalen, S.; Palatinus, L.; Schneider, M. Acta Crystallogr. 2003. A59. 459-469.

4. TOPAS version 4.1 (2007), Bruker-AXS, Karlsruhe, Germany.

5. Geller, S. Science. 1967. 157. 310-312.

6. Ahlert, S.; Friese, K.; Jansen, M. Z. Anorg. Allg. Chem. 2002. 628. 1525-1531.



MS12-P10

Structure and IR spectra of Na₈[AlSiO₄]₆(BH₄)₂ sodalite: Comparison between theoretical predictions and experimental dataM. Marcus¹, T. Bredow¹, L. Schomborg², C.H. Rüschler², J.-C. Buhl²¹Universität Bonn, Mulliken Center for Theoretical Chemistry - Institut für Physikalische und Theoretische Chemie, Bonn, Germany²Universität Hannover, Institut für Mineralogie, Hannover, Germany

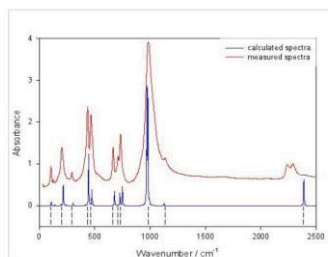
A new material has been developed, namely BH₄-SOD, which encloses and largely protects the BH₄-anion in the sodalite cage both in microcrystalline and in nanocrystalline form [1, 2]. Unlike for the pure salt NaBH₄, BH₄-SOD enables a controlled release of hydrogen from water molecules in consecutive reaction steps for temperatures between 423 and 773 K. The effect of reinsertion of hydrogen within certain reaction steps were reported [3]. For a better understanding of the hosting properties of the sodalite for the BH₄ molecule and its reaction products, quantum-chemical calculations of the BH₄-SOD structure were carried out. Here first results performed with the crystalline orbital package CRYSTAL09 [4] are presented.

Three Hartree-Fock-DFT-Hybrid functionals based on the Perdew-Wang '91 GGA, Perdew-Burke-Ernzerhof GGA, and van-Barth-Hedin LSD functionals were tested with exchange mixings between 0 and 100%. For all three cases best agreement with experimental atom parameters [1] were obtained for about 30-35% mixing. The optimised positions of framework and cagefilling atoms were used to calculate all IR active modes within spacegroup

P-43n. The intensities were calculated by a Barry phase approach [5]. Best agreement between peak positions of measured and calculated spectra was obtained for about 20% of mixing within all three methods. As an example the calculated spectrum with best agreement is compared in Fig.1 with a measured one. The measured spectra consists of a superposition of the two spectra obtained by PE and KBr method for the FIR and MIR range, respectively. For the calculation of the profile Lorentzian function with damping parameter 15cm^{-1} were used. The two IR active stretching and bending vibrations of the tetrahedral BH_4 -anion were theoretically predicted at about $2385\text{-}2418\text{ cm}^{-1}$ and $1122\text{-}1150\text{ cm}^{-1}$, respectively, in very good agreement with experimentally observed peaks assigned to the BH_4 -anion. Here two additional modes can be seen in the spectra in the range between 2200 and 2400cm^{-1} , which are known, however, to correspond to combination modes. Such contributions were not included in the calculations which are based on the harmonic approximation.

- [1] J.-Chr.Buhl, T.M.Gesing, C.H.Rüscher, Microporous Mesoporous Mater. 80(2005) 57-63.
- [2] J.-Chr.Buhl, L.Schomborg, C.H.Rüscher, Microporous Mesoporous Mater. 132(2010) 210-218.
- [3] L.Schomborg, C.H.Rüscher, J.-C.Buhl, Z.Krist.Suppl. (2011). IssueNo. 31(2011) 23.
- [4] R.Dovesi, R.Orlando, B.Civalleri, C.Roetti, V.R.Saunders, C.M.Zicovich-Wilson, Z.Kristallogr. 220(2005) 571.
- [5] A.F.Izmaylov, G.E.Scuseria, Phys.Rev.B77(2008), 165131.

Fig. 1 Measured and calculated infrared absorption spectra of BH_4 -SOD (dashed lines mark the peak positions in the measured spectra).



MS12-P11
Diffraction Anomalous Fine Structure of Ho_2PdSi_3 and $\text{YMn}_2\text{Fe}_5\text{O}_5$

M. Nentwich¹, M. Zschornak¹, C. Richter^{1,2}, D.C. Meyer¹
¹Technische Universität Bergakademie Freiberg, Fakultät für Physik und Chemie, Freiberg, Germany
²DESY/HASYLAB, Hamburg, Germany

Diffraction Anomalous Fine Structure (DAFS) is a site-selective method for studying local electronic structures. As an advantage over X-ray Absorption Fine Structure (XAFS) it is possible to differentiate between atoms of the same kind but different Wyckoff positions which is especially useful for site-ordered mixed valence systems.

Here, this method was applied to study the substitution of Mn atoms with Fe on the octahedral and pyramidal sites in $\text{YMn}_2\text{Fe}_5\text{O}_5$ [2]. Further, the c-ordering of Pd substitutes on Si sites according to a super structure proposal from F. Tang et al. [1] was investigated for the intermetallic compound Ho_2PdSi_3 . Theoretical modelling was performed using the FDMNES code [3]. The measurements of the experimental data have been carried out at beamline E2 of DESY/HASYLAB Hamburg.

- [1] F.Tang et al., Phys. Rev. B 84, 104105 (2011).
- [2] F. Wunderlich et al., Phys. Rev. B 82, 014409 (2010).
- [3] Y. Joly, Phys. Rev. B 63, 125120-125129 (2001).

MS13-P01
Locally resolved determination of anisotropic properties of human dental enamel

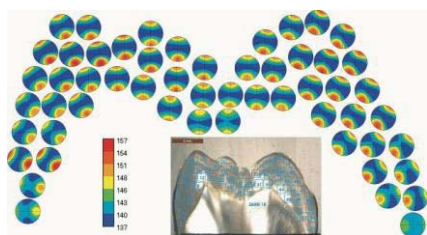
L. Raue¹, H. Klein¹, C. Hartmann¹
¹GZG, Georg-August-University, Dept. Crystallography, Goettingen, Germany

Generally a strong relationship exists between crystallographic textures and the resulting mechanical and functional anisotropy of crystalline materials. Combining the information of texture analysis and single crystal properties, the anisotropy of physical properties can be calculated (Bunge, 1993). Locally resolved texture analysis by means of synchrotron radiation with a small beam cross section allows the calculation of local physical polycrystal properties (Raue & Klein, 2011). The sample material in this study is human dental enamel which is build up of hydroxylapatite (HAP) - $\text{Ca}_5(\text{PO}_4)_3(\text{OH})$ [6/m, $a = 9.418\text{ \AA}$ and $c = 6.875\text{ \AA}$]. The texture of the polycrystalline enamel has been examined in detail with X-Ray diffraction at the synchrotron beam lines BW5 at HASYLAB / Hamburg and PDiff at ANKA / Karlsruhe. Hence HAP shows multiple overlapping reflection peaks in the diffraction pattern, the combined Rietveld texture analysis method with the program MAUD has been used (Lutterotti et al., 1997). The calculation of important anisotropic physical properties (elastic modulus and thermal expansion) has been carried out with the program package Beartex (Wenk et al., 1998). As first results “maps” of locally resolved properties from teeth can be shown.

Figure 1: Scheme of an anisotropic physical properties map of the elastic modulus for a wisdom tooth. The sample can be seen in the middle. The measured data points are marked with blue squares. The stereographic projections show the anisotropy of the elastic modulus depending in the location within the tooth in consistent scaling.

Knowing the local textures and anisotropic properties of dental enamel is of high importance since the anisotropic mechanical properties of materials used to fill cavities differ significant. In the worst case, the filling of a tooth can damage the enamel of the opposite tooth; hence by chewing the interaction of enamel and filling is not equivalent, so that the harder fillings can abrade the softer enamel of the healthy tooth at the opposite side. This could be avoided if the mechanical properties of dental enamel would be known in detail; hence then another filling could be searched or fabricated as an equivalent opponent for the dental enamel with equal properties. To find such a material, one has to characterize the properties of dental enamel first in detail, which is done by this study.

- Bunge, H.-J. (1993). Texture Analysis in Materials Science, 2. ed., Cuvillier Verlag, Göttingen, Germany.
- Lutterotti, L., Matthies, S., Wenk, H.-R., Schultz, A.J. & Richardson, J. (1997). Texture and structure analysis of deformed limestone from neutron diffraction spectra, *J. Appl.Phys.*, **81**, 594-600.
- Raue, L. & Klein, H. (2011). Calculation of anisotropic properties of dental enamel from synchrotron data, *J. Synchr. Rad.*, **18**, 4, 550-556.
- Wenk, H.-R., Matthies, S., Donovan, J. & Chateigner, D. (1998). BEARTEX, a Windows-based program system for quantitative texture analysis, *J. Appl. Cryst.*, **31**, 262-269.



MS13-P02

Rigid structure but mobile unit - crystal engineering as a tool to stabilize the structure. Reducing mobility of a side-chain in cysteine containing crystals

V. Minkov^{1,2}, E. Boldyreva^{1,2}

¹Institute of Solid State Chemistry and Mechanochemistry, Reactivity of Solids, Novosibirsk, Russian Federation

²Novosibirsk State University, REC-008 "Molecular Design and Ecologically Safe Technologies", Novosibirsk, Russian Federation

Cysteine is a very important naturally occurring amino acid. Owing to the presence of thiol group in its side-chain residue, cysteine is prone to formation of S-H...X hydrogen bonds and participates in formation of protein secondary structures. Cysteine also plays a very important role in stabilizing the conformation of protein active site in zinc fingers and iron-sulfur proteins due to high affinity of thiol group for the binding to metal. In addition -SH group can be easily oxidized providing cystine with a covalent disulfide bridge often found in secreted proteins like insulin and trypsin. Besides cysteine and its derivatives are used as drugs.

In crystals cysteine can adopt different conformations since its side chain may easily rotate along C-C bond providing three general types of its orientation which are characterizes by the value of N-C-C-S torsion angle: gauche⁺, gauche⁻ and trans.

Investigations of L- and DL-cysteine on variation of temperature and pressure have revealed many phase transitions. On cooling the orthorhombic L-cysteine its side chain becomes ordered, in monoclinic L-cysteine a subtle phase transition is detected. Increasing pressure leads to series of phase transitions accompanying by changes in intramolecular geometry and hydrogen bonds in both polymorphs. It is remarkable that high-pressure phases are not the same for these two modifications of L-cysteine. DL-cysteine also undergoes phase transitions on cooling and increasing pressure. Even on slow cooling crystals split into several fragments and as recently was shown fragmentation is caused by rupture of weak S-H...S hydrogen bonds between layers in crystal structure. More phase transitions in DL-cysteine are observed on increasing pressure but the first high-pressure phase is similar to the low-temperature phase.

Very recently we have been interested in issues of reducing or removing mobility of the side chain and stabilization of a crystal structure with respect to phase transitions. It was found that the phase transition caused by temperature variation in DL-cysteine is very sensitive to particle size and the preparation techniques. The aim of the present work is to find other chemical methods to reduce mobility of the side chain such as chemical modification of groups capable to form hydrogen bonds (N-acetyl-L-cysteine) and introducing potentially stronger acceptor or donor for hydrogen bonding in the structure (oxalates of DL-cysteine 1:1 and 1:2).

[1] V.S. Minkov, A.S. Krylov, E.V. Boldyreva, S.V. Goryainov, S.N. Bizyaev, A.N. Vtyurin, *J. Phys. Chem. B*, 2008, 112, 8851

[2] V.S. Minkov, S.V. Goryainov, E.V. Boldyreva, C.H. Görbitz, *J. Raman Spectrosc.*, 2010, 41, 1748

[3] B.A. Kolesov, V.S. Minkov, E.V. Boldyreva and T.N. Drebushchak, *J. Phys. Chem. B*, 2008, 112, 12827

[4] V.S. Minkov, N.A. Tumanov, B.A. Kolesov, E.V. Boldyreva, S.N. Bizyaev, *J. Phys. Chem. B*, 2009, 113, 5262

[5] V.S. Minkov, V.A. Drebushchak, A.G. Ogienko, E.V. Boldyreva, *CrystEngComm*, 2011, 13, 4417.

MS13-P03

Structural investigation of isopod cuticle and changes caused by decalcification monitored by sub μ -confocal Raman spectroscopy.

C. Reisecker¹, B. Seidl², A. Ziegler², S. Hild¹

¹Johannes Kepler Universität Linz, Institut für Polymerwissenschaften, Linz, Austria

²Universität Ulm, Institut für Elektronenmikroskopie, Ulm, Germany

The isopod cuticle is known to be arranged in several hierarchical levels and scale.

One of the main components is Calcium carbonate, which occurs in two different modifications known as calcite and amorphous calcium carbonate (ACC). Another component is a fibrous organic matrix, which mainly consists of chitin, as well as other proteins. Phosphate can also be found in some isopods but the content is varying from 9.7 wt% in *Armadillidium vulgare* compared to *Sphaeroma serratum*, where no phosphate can be found.^[1]

Depending on the habitat of the isopods, there are different mechanical requirements concerning the cuticle such as the thickness of the calcite layer, which manifests in a harder and tougher cuticle. Other aspects, which also have to be considered are vital functions for instance as the cuticle performs as a water barrier. Also a good conjunction with muscles has to be ensured, which takes place in the membranous layer and is located in the innermost part of the cuticle.^[2]

As already shown in some recent studies calcite is limited to the most distal part of the cuticle with a little overlap with the following layer where ACC can be detected. Phosphate as well as organic material are organized in a layered structure and can be found in the same part of the cuticle as ACC does. The innermost part of the cuticle just consists of chitin as well as some other proteins and is known as membranous layer.^[2]

Scanning confocal Raman spectroscopy is an excellent method to study the hierarchical arrangement of these minerals and organic compounds.

Due to a strong broad Raman signal caused by the CO stretch swinging band at 1085 cm⁻¹, the phosphate band at 955 cm⁻¹ is difficult to determine.

Selective decalcification therefore should allow a more detailed look at the structure beneath amorphous calcium carbonate. The pH value plays an important part as one just wants to dissolve ACC. On the one hand if the decalcification solvent is too acidic, also calcite would be dissolved but on the other hand if the pH value is too alkaline the proteins and chitin would denaturize. The decalcification therefore is performed with 18.2 mΩ water at pH=7 followed by fixation with methanol.

The samples were measured with area scans over the whole cross section of the cuticle as well as depth scans in order to have a more detailed look at the organic and phosphate components after decalcification.

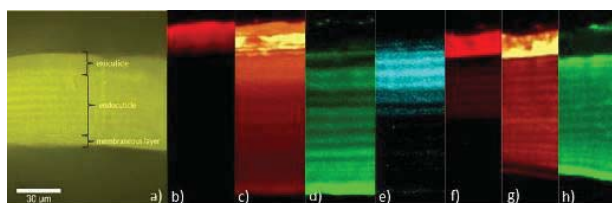
A comparison of the various components measured with confocal Raman spectroscopy before decalcification can be found in figure 1.

References:

[1] Frank Neues; Andreas Ziegler, Matthias Epple: *Cryst. Eng. Comm.*, 9(12), 1245-1251, (2007)

[2] Bastian Seidl; Katja Huemer; Frank Neues; Sabine Hild; Matthias Epple; Andreas Ziegler: *Journal of Structural Biology*, 174(3), 512-526, (2011).

Figure 1: *Armadillidium vulgare* (a-e) and *Sphaeroma serratum* before decalcification (f-h), a) Image showing the three hierarchical levels (50x objective), b) calcite (max. 1500 cts.), c) carbonate (max. 2500 cts.), d) organic material (max. 1600 cts.), e) phosphate (max. 75 cts.), f) calcite (max. 800 cts.), g) carbonate (max. 2400 cts.), h) organic material (max. 1500 cts.).

**MS13-P04**
Eine schwierige Kristallstrukturbestimmung aus Röntgenpulverdaten - Vorzugsorientierung, zwei Chlorid-Ionen auf speziellen Lagen und ein vierfach fehlgeordnetes 2-Butanol

S.M. Hammer¹, J. Brüning¹, N. Nagel², M.U. Schmidt¹

¹Goethe-Universität, Inst. f. Anorg. und Analyt. Chemie, Frankfurt am Main, Germany

²Sanofi-Aventis Deutschland GmbH, Industriepark Höchst, Frankfurt am Main, Germany

Bei der Kristallstrukturbestimmung des Pharmawirkstoffes **I** ($[\text{C}_{25}\text{H}_{27}\text{N}_4\text{O}_4]^+ \text{Cl}^- \cdot 1/2 (\text{C}_4\text{H}_8\text{OH})$) aus Röntgenpulverdaten traten mehrere Probleme auf:

1. großes, flexibles Molekül
2. zwei symmetrieunabhängige Chlorid-Ionen, beide auf 2-zähligen Achsen
3. halbbesetztes, racemisches 2-Butanol, vierfach fehlgeordnet auf einer 2-zähligen Achse
4. ungenügende Auflösung der Synchrotrondigramme (scharfe Reflexe, z. T. nur mit drei Messpunkten beschrieben), dadurch Probleme beim Anpassen der Phasen
5. starke Vorzugsorientierung

Bei der Verbindung **I** handelt es sich um einen pharmazeutischen Wirkstoff zur Hemmung der Blutgerinnung (Inhibierung des Faktor Xa und somit Blockierung der Thrombin-Bildung).

Für die Kristallstrukturbestimmung lagen sowohl Röntgenpulvermessungen mit Cu-K α_1 -Strahlung in Transmission (STOE-Stadi-P-Diffraktometer) sowie auch Synchrotronmessungen ($\lambda = 0,802600$) vor. Für die Verwendung mussten die Synchrotrondaten modifiziert werden.

Die gemessenen Diagramme konnten widerspruchsfrei indiziert werden. Die Indizierung ergab eine monokline Zelle mit Raumgruppe C2, Z = 4 mit einem unabhängigen Molekül in der asymmetrischen Einheit.

Die Struktur wurde mit Realraummethoden mittels Simulated Annealing unter Verwendung des Programms DASH^[1] gelöst. Die Strukturlösung wurde durchgeführt mit einem kraftfeldoptimierten Molekül (Kation) sowie zwei Chlor-Atomen (eines für das Chlorid und eines als Ersatz für das halbbesetzte 2-Butanol). Es waren sowohl die Positionen und die Orientierungen der Moleküle/Ionen als auch die Torsionen freigegeben (23 Parameter). Die Ergebnisse wiesen überzeugende Positionen für das Kation auf, jedoch die Positionen der beiden Chlor-Atome waren fraglich. Bei beiden konnte eine mögliche Positionierung auf speziellen Lagen vermutet werden. Die Positionen der Anionen und des Lösungsmittels konnten erst nach vielen Versuchen während der Rietveld-Verfeinerung bestimmt werden.

Anschließend erfolgte eine, sich in ihrem Verlauf als schwierig erweisende, Rietveld-Verfeinerung mit dem Programm TOPAS^[2]. Es wurden im Wechsel die Röntgenpulverdaten sowie die Synchrotrontrondaten verwendet. Für alle Bindungslängen und -winkel wurden Restraints definiert. Dennoch zeigte die Verfeinerung immer wieder Divergenz. Anschließend wurde die vierfache Fehlordnung des Solvatmoleküles untersucht. Die Verfeinerung konvergiert schließlich mit folgenden R-Werten: für die Synchrotronmessung $R_p = 0,098$, $R_{wp} = 0,195$ und für die Labormessung $R_p = 0,014$, $R_{wp} = 0,018$. Die Kristallstruktur konnte trotz der auftretenden Probleme bestimmt werden.

Referenzen:

- [1] W. I. F. David, K. Shankland, J. van de Streek, E. Pidcock, W.

D. S. Motherwell, J. C. Cole, J. Appl.Cryst. 2006, 39, 910–915.

[2] A. A. Coelho, TOPAS Academic 4.1, 2007, <http://www.topas-academic.net>.

MS14-P01
K₂Ba₅Si₁₂O₃₀ - a member of a homologous series among layered potassium barium silicates

V. Kahlenberg¹

¹University of Innsbruck, Mineralogy & Petrography, Innsbruck, Austria

Single crystals of K₂Ba₅Si₁₂O₃₀ have been grown from the devitrification of a glass with composition K₂O:BaO:SiO₂ = 1:5:15. The crystals of this previously unknown phase exclusively showed an intergrowth of at least two individuals making it impossible to prepare a sample representing a "single crystal". Therefore, the crystal structure has been solved from a diffraction data set of an intergrown sample collected at ambient conditions and refined to a residual of R(F) = 0.0568 for 1390 independent observed reflections. The compound is monoclinic with space group C2/m (a=23.832(2)Å, b=7.7293(7)Å, c=8.2613(9)Å, beta=91.574(8)°, V=1521.2(3)Å³, Z=2) and belongs to the group of single layer silicates. The corrugated tetrahedral layers parallel to (201) can be divided into two different types of alternating bands containing (I) a sequence of four- and eight-membered rings and (II) a two ring wide "zig-zag shaped" unit consisting of exclusively six-membered rings. The stacking of the layers results in a three dimensional structure in which the K- and Ba-atoms reside between the sheets for charge compensation. The distribution of these two different cation species among the four crystallographically independent M-sites (which are coordinated by seven to eight oxygen ligands) has been studied by site occupancy refinements.

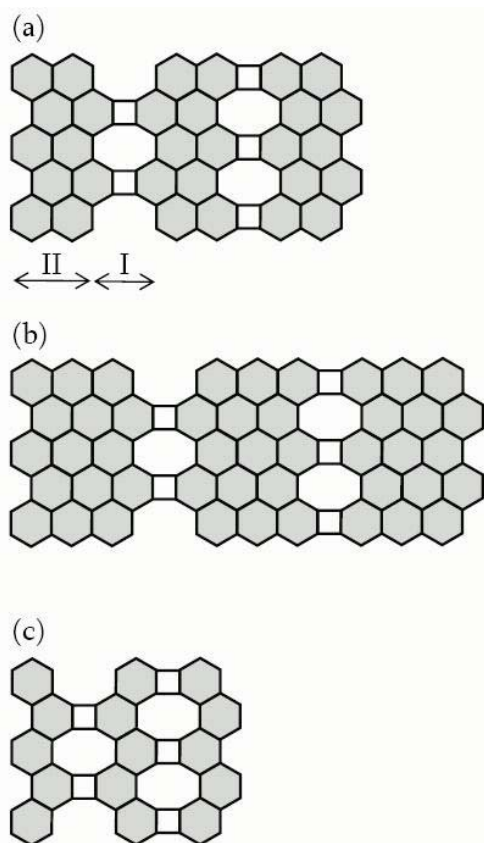
The structure of K₂Ba₅Si₁₂O₃₀ is closely related to that of K₂Ba₇Si₁₆O₄₀ (Cervantes-Lee et al., 1982). First of all, both compounds adopt the same space group type C2/m. Furthermore, the topology and the orientation of the tetrahedral layers as well as the arrangement of the connecting M-cations are almost identical. The main difference is due the number n of six-membered rings defining the width of band type II: n=2 in K₂Ba₅Si₁₂O₃₀ and n=3 in K₂Ba₇Si₁₆O₄₀, respectively (see Fig. 1a and b). This extension of band type II is also reflected in the unit cell metric. Whereas the values for b and c are virtually the same, the a lattice parameter as well as the monoclinic angle increase from 23.832 Å and 91.57° (for n=2) to 31.991 Å and 100.60° (for n=3).

Actually, both materials can be regarded as members of a so called *accretional* homologous series (Makovicky, 1989) in which principal building units (in this specific case: bands) and the rules that specify their correlations are retained but the dimension of the units changes stepwise by the variation the number of constituting fundamental objects (in this case: rings). The general chemical formula of the series can be written as K₂Ba_{2n+1}Si_{2(2n+2)}O_{5(2n+2)}. The member with n=1 corresponding to the chemical composition K₂Ba₃Si₈O₂₀ has not been observed so far. However, from geometrical considerations one can predict the following approximate values for the "variable" lattice constants of the series for n=1: a≈16.3 Å, beta≈76°. The values for b and c would be preserved.

F.J. Cervantes-Lee, L.S. Dent Glasser, F.P. Glasser, R.A. Howie, Acta Cryst. 1982, B38, 2099.

E. Makovicky, N. Jb. Miner. Abh. 1989, 160, 269.

Fig. 1. Idealized representation of the topology of the layers in (a) K₂Ba₅Si₁₂O₃₀, (b) K₂Ba₇Si₁₆O₄₀ and (c) hypothetical K₂Ba₃Si₈O₂₀.



MS14-P02

A new thiooxo-rhenate $(Et_4N)_2[(ReO(S_4))_2(\mu_2-S_2)(\mu_2-S)]$ and the Reinvestigation of the Crystal Structure of $(Et_4N)[ReS_4]$ A.J. Lehner¹, C. Röhr¹¹Universität Freiburg, Institut für Anorganische und Analytische Chemie, Freiburg, Germany

Thioxo-perrhenates were first isolated by Feit [1]. A series of mixed monothioxo-perrhenates $A[ReSO_3]$ ($A = K, Rb, Cs, Tl$) was resynthesized by Müller and coworkers who analyzed the spectroscopic properties of these salts and their solutions. Also, basic studies of the crystal structures were published [2]. As the first compounds of simple thioxo-perrhenate ions with higher sulphur contents, Müller *et al.* described $(Ph_4P)[(ReS_2O_2)Cu]$ and $(Et_4N)_2[(ReS_3O)Cu_3C_{14}]$. The structures contain anions formed by $[ReS_2O_2]^-$ and $[ReS_3O]^-$ ligands coordinating copper halide fragments [3]. The tetrathio-perrhenate $[ReS_4]^-$ displays broad reactivity toward unsaturated organic compounds and its salts have been isolated for several cations (R_4E) ($R =$ organic residue, $E = N, P, As$, e. g. $(nBu_4N)[4]$). Up to now all published structures of $(Et_4N)[ReS_4]$ display disorder of anion and cation (e.g. $(Et_4N)[ReS_4]$, $P6mm$, $a = 814.9(2)$, $c = 653.8(1)$ pm, $V = 376.0$ 10^6 pm³ [5]). In this contribution we present an improved crystal structure model for $(Et_4N)[ReS_4]$ ($P6_3mc$, $a = 814.545(9)$, $c = 1306.406(17)$ pm, $V = 750.652(13)$ 10^6 pm³) resolving the anion's disorder and taking into account the cation's heavy disorder. Moreover we present the (Et_4N) salt of a thiooxo-rhenate, containing the novel anion $[(Re^VO(S_4))_2(\mu_2-S_2)(\mu_2-S)]^{2-}$ (fig.) which is the first example of a binuclear thiooxo-polysulphido complex of rhenium. The title compounds were both synthesized following a simple protocol [5] by adding $(Et_4N)Br$ and $Na[ReO_4]$ to an aqueous ammonium polysulphide solution. After few hours, orange crystal needles of $(Et_4N)_2[(ReO(S_4))_2(\mu_2-S_2)(\mu_2-S)]$ ($Pbcn$, $a = 3106.95(4)$, $b = 1591.99(2)$, $c = 1298.19(2)$ pm, $V = 6421.15(15)$ 10^6 pm³) formed in the violet solution. Upon cooling to 5 °C, a large amount of fine dark red crystals of $(Et_4N)[ReS_4]$ precipitated over night. By recrystallizing this solid from acetonitrile, nice multi-faceted crystals were obtained. Both compounds exhibited

considerable disordering of $(Et_4N)^+$ cations at r. t. Upon cooling $(Et_4N)[ReS_4]$ showed a reversible cell enlargement which could not be clarified. For the salt containing the anion $[(ReO(S_4))_2(\mu_2-S_2)(\mu_2-S)]^{2-}$ the diffraction data recorded at 100 K was used for the structure refinement. In both cases the disorder of non-hydrogen atoms at each alkyl ammonium site could be refined to a set of two interpenetrating $(Et_4N)^+$ tetrahedra. The new anion $[(ReO(S_4))_2(\mu_2-S_2)(\mu_2-S)]^{2-}$ is compared to related polysulphido complexes of rhenium. For example, Müller *et al.* published a $(Ph_4P)^+$ salt containing the anions $[ReS(S_4)_2]$ and $[ReO(S_4)_2]$ in a 70:30 ratio on the same crystallographic positions [6]. The resulting $(Re-O/S)$ bond length was 203.9(4) pm. The new dimeric anion features a $(Re-O)$ bond length of 175.3(8) pm. Its chemical bonding situation is further investigated by vibrational spectroscopy and quantum chemical calculations.

[1] W. Feit, Z. Anorg. Allg. Chem. 199 (1931) 262.

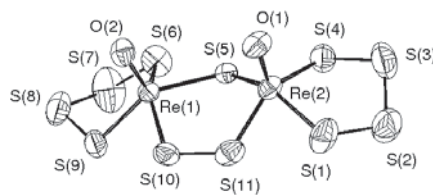
[2] B. Krebs, A. Müller and H. Beyer, Z. Anorg. Allg. Chem. 362 (1968) 44.

[3] A. Müller, A. Hildebrand, E. Krickemeyer, D. Sölter, H. Bögge and A. Armatage, Z. Anorg. Allg. Chem. 614 (1992) 115.

[4] Youngkyu Do, E.D. Simhon and R.H. Holm, Inorganic Chemistry 24 (1985) 4631.

[5] A. Müller, E. Krickemeyer, H. Bögge, Z. Anorg. Allg. Chem. 554 (1987) 61.

[6] A. Müller, E. Krickemeyer, H. Bögge, M. Penk, D. Rehder, Chimia 40 (1986) 50.



MS14-P03

Sillenites: composition, structure, morphology, crystal growth

T. Melnikova¹, G. Kuz'micheva², V. Rybakov³, N. Bolotina⁴, A. Cousson⁵¹Lomonosov State University of Fine Chemical Technology, Solid State Physics and Chemistry, Moscow, Russian Federation²Lomonosov State University of Fine Chemical Technology, Solid State Physics and Chemistry, Moscow, Russian Federation³Lomonosov State University, Moscow, Russian Federation⁴Shubnikov Institute of Crystallography RAS, Moscow, Russian Federation⁵Laboratoire Leon Brillouin, Cea/Saclay, France

The phases $Bi_{24}M_2O_{40}$ or $Bi_{24}(M,M')_2O_{40}$ with sillenite structure (γ - Bi_2O_3 , sp.gr. I23, $z=13$ or $Bi(1)_{24}Bi(2)_2O_{40-d}, z=1$; coordination polyhedra of $Bi(1)$ and $Bi(2)$ are distorted semi-octahedron and tetrahedron, respectively) have physical properties (photoconductivity, piezo- and electrooptical effects and so on) depending on the crystallochemical properties. The aim of this paper is structural characterization (real composition and specific structure peculiarities) of the sillenite phases.

Basic methods for structural characterization of sillenite family with nominal compositions $Bi_{24}M_2O_{40}$ and $Bi_{24}(M,M')_2O_{40}$ were:

Diffraction study:

- X-ray structure analysis of single crystals and ground into fine powder samples;
- neutron study of single crystals;

- synchrotron radiation of ground into fine powder samples;

Spectroscopy study.

- Raman-spectroscopy of single crystals ($\nu=100-1000$ cm^{-1});

- IR-spectroscopy of ground into fine powder samples ($\nu=400-1000$ cm^{-1});

- XANES/EXAFS of ground into fine powder samples.

Electron microscopy with X-ray spectral microanalysis of ground into fine powder samples.

Both defective and defect-free sillenite phases $Bi_{24}M_2O_{40}$ and

$\text{Bi}_{24}(\text{M}, \text{M}')_2\text{O}_{40}$ have been obtained:

- Vacancies in the M site with vacancies in the O(3) site ($M = \text{Zn}^{2+}, \text{Fe}^{3+}, \text{Si}^{4+}, \text{Mn}^{4+}$);
- Vacancies in the Bi(1) site with vacancies in the O(1) and O(2) sites ($M = \text{Zn}^{2+}, \text{Fe}^{3+}, \text{V}^{5+}; M' = \text{V}^{5+}; M'' = \text{Mn}^{4+}$);
- $\text{Bi}^{3+\delta}$ ($\sim 10\div 20\%$) in the M site ($M = \text{Al}^{3+}, \text{Fe}^{3+}, \text{Mn}^{4+}, \text{V}^{5+}; M' = \text{Si}^{4+}, M'' = \text{V}^{5+}$);
- Interstitial atoms Bi^{3+} in the xxx ($x \sim 0.02$) site with vacancies in the M site ($M = \text{Fe}^{3+}, \text{Ga}^{3+}, \text{Mn}^{4+}, \text{P}^{5+}; M' = \text{Fe}^{3+}, \text{Si}^{4+}, \text{Cr}^{4+}, \text{V}^{5+}, M'' = \text{Mn}^{4+}$).

The differences between the crystallochemical properties of the atoms M and M' leads to the two types of phenomena:

1. Dissymmetrization: the transition from sp.gr. I23 to sp.gr. P23 (phase with sp.gr. P23 is formed in the region of phase stability with sp.gr. I23: $M' = \text{Si}^{4+}, M'' = \text{Mn}^{4+}$). This phenomenon is due to both structure peculiarities: a presence of several atoms in M position of structure and preparation conditions simultaneously ($T < 400^\circ\text{C}$).

2. Dissociation: the two isostructural solid solutions with different composition:

- for phase with composition $\text{Bi}_{24}(\text{Bi}_{0.2}(\text{Cr}^{4+}, \text{Mn}^{4+})_{1.8})(\text{O}_{39.9}[\]_{0.1})$ ($\Delta\text{FC} > 0$; this effect was observed by using electron microscopy).
- for phase with composition $\text{Bi}_{24}(\text{Bi}^{3+}_{0.94(4)}\text{Mn}^{4+}_{1.06})(\text{O}_{39.50}[\]_{0.50})$ ($\Delta\text{FC} = 1$; this effect was observed by using synchrotron radiation and electron microscopy).
- for phase with composition $\text{Bi}_{24}(\text{Bi}^{3+\delta}_x\text{P}^{5+}_{1.9-x}[\]_{0.1})(\text{Bi}^{3+}_{\leq 0.1})_2\text{O}_{40}$ ($\Delta\text{FC} = 2$; this effect was observed by X-ray diffraction study).

It was found that some ions of transition elements in the sillenites can have different FC: $M = \text{Mn}^{4+}$ and $\text{Mn}^{5+}, \text{V}^{4+}$ and V^{5+} depending on synthesis condition.

So, the data obtained can provide an exhaustive interpretation of the contradiction of the physical, chemical and crystallochemical properties established earlier for the same phases with sillenite structure.

MS14-P04

$\text{Ca}_x\text{Yb}_{(1-x)}\text{Ga}$: CrB type and related modulated superstructures

B. Bauer¹, C. Röhr¹

¹Albert-Ludwigs-Universität Freiburg, Institut für Anorganische und Analytische Chemie, Freiburg i. Br., Germany

With respect to their radii and charges, the alkaline earth metals calcium and strontium are comparable with the divalent rare earth metals ytterbium and europium. Hence it should be possible to replace them against each other in known intermetallic compounds. Our investigation on rare earth aluminium germanides of europium already led to two new ternary compounds [1], $\text{Eu}_3\text{Al}_2\text{Ge}_2$ and $\text{Eu}_3\text{Al}_2\text{Ge}_4$, which are isotypic with known strontium phases [2,3]. For further investigations we choose the gallides of calcium and ytterbium because of the great variety of the binary border phases: only the phases AGa, AGa_2 and AGa_4 are known in both systems, and only the last two are isotypic. The 1:1 phases crystallize with different structure types: CaGa forms the CrB type [4] and YbGa was identified to form the tetragonal CuAu type [5]. CaGa is the only known trielide $\text{A}^{\text{II}}\text{M}^{\text{III}}$ ($\text{A} =$ alkaline earth/rare earth metal) which crystallizes in the CrB structure type. This type is widespread among the tetrelides of the alkaline earth and rare earth metals. The two-bonded M atoms form planar zig-zag chains, which are surrounded by trigonal prism of A atoms. In all tetrelides (6v.e./M) these prisms are stretched whereas they are compressed in CaGa (5v.e./M). We could show that it is possible to replace calcium in CaGa by ytterbium up to a limit of 70%. The partially ordered incorporation of ytterbium leads to new modulated superstructures of the CrB type with enlarged monoclinic cells. In these structures the b axis is unchanged compared with the CrB type, and the enlarged a - c basis can be described by a general transformation matrix. The zig-zag chains are of undulated form, depending on the occupation of the slightly smaller ytterbium. The gallium chains avoid close distances to larger A sites occupied by more calcium. Similar studies were carried out by Harms et al. [6]

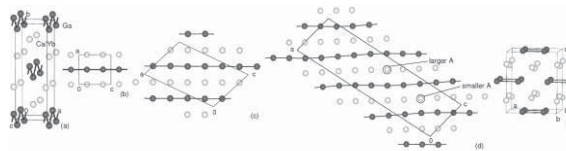
by replacing gallium atoms by the other trielides aluminium and indium.

Furthermore we could identify the binary border phase YbGa in the CaIn structure type [7]. In this structure it is possible to replace ytterbium by calcium up to 10%.

The compounds were synthesized from stoichiometric or A-rich mixtures of the elements at a maximum temperature of 900°C and were characterized by single crystal X-ray diffraction. DFT band structure calculations of the binary border compounds CaGa and YbGa with the crystal structures of CrB, CuAu and CaIn were also realized.

References:

- [1] B. Bauer, C. Röhr, *Z. Naturforsch.*, **2011**, *66b*, 793-812.
- [2] A. Widera, B. Eisenmann, H. Schäfer, K. Turban, *Z. Naturforsch.*, **1977**, *32b*, 1592-1595.
- [3] M. Wendorff, C. Röhr, *Z. Naturforsch.*, **2007**, *62b*, 1071-1082.
- [4] J.-T. Zhao, D.-K. Seo, J. D. Corbett, *J. Alloys Comp.*, **2002**, *334*, 110-117.
- [5] A. Palenzona, S. Cirafici, *J. Less-Common Met.*, **1979**, *63*, 105-109.
- [6] W. Harms, M. Wendorff, C. Röhr, *J. Alloys Comp.*, **2009**, *496*, 89-101.
- [7] M. Wendorff, C. Röhr, *Z. Anorg. All. Chem.*, **2005**, *631*, 338-349.



Crystal structures of CaGa (CrB structure type, (a),(b)), $\text{Ca}_x\text{Yb}_{1-x}\text{Ga}$ (c), $\text{Ca}_x\text{Yb}_{1-x}\text{Ga}$ (d) and YbGa (CaIn structure type, (e))

MS14-P05

Synthesis, crystal structure and ^7Li MAS NMR spectroscopy of the new compound $\text{Li}_3\text{Zn}_6\text{In}_{3.1}$.

V. Mihajlov¹, C. Röhr¹

¹Albert-Ludwigs-Universität, Institut für Anorganische und Analytische Chemie, Freiburg i. Br., Germany

The new compound $\text{Li}_3\text{Zn}_6\text{In}_{3.1}$ ($P6/mmm$, $a = 514.37$, $c = 994.76$ pm, $Z=1$, $R1 = 0.0461$) was synthesized

from stoichiometric melts of the elements in pure phase. The resulting silver, brittle crystals are relative insensitive to air and moisture. The structure was solved and refined using single crystal data and was also investigated by ^7Li -MAS-NMR. The title compound is a substitution variant of the HfFe_6Ge_6 -type [1], a stuffed version of the CoSn-type [2].

Chemical more reasonable is the derivation from the well known CaCu_5 -type (Fig.1(a)) [3]. CaCu_5 consists of Cu-Kagomé-nets (Schläfli-nets 3.6.3.6.) with further Cu atoms above and below the triangles of the nets, forming triangular bipyramids. In $\text{Li}_3\text{Zn}_6\text{In}_{3.1}$ the Kagomé-nets consist of Zn and the caps of the bipyramid are occupied alternately by a mixed site of In/Zn ($\sim 50/50$) and Li leading to the building block $\text{Cu}_5 = \text{Li}(\text{In}/\text{Zn})\text{Zn}_3$ (Fig.1(b)). The Li-'caps' itself form hexagonal 6^3 nets with relativ short Li-Li distances of 297 pm.

The c -axis of unit cell is nearly twice as long as in CaCu_5 , leading to two Kagomé-nets per unit cell.

The Ca positions are occupied by Li and In_2 dumbbells (In-In=286 pm). The latters are connected to the sixmembered rings of the adjacent Kagomé-nets.

The resulting formula is therefore $\text{Li} + \text{In}_2 + (\text{Li}(\text{In}/\text{Zn})\text{Zn}_3) * 2$ resulting in the total formula $\text{Li}_3\text{Zn}_6(\text{Zn}/\text{In})_2\text{In}_2$. Calculations using FP-LAPW-DFT methods revealed a broad pseudo band gap slightly below the Fermi level showing the stability of the compound.

Due to the difficulty to detect Li atoms by x-ray-methods, ^7Li MAS NMR spectroscopy was performed on a SiO_2 -diluted sample (1:5) (Fig.2). The NMR data confirm the structure model, proofing the existence of two different Li sites in a 1:2 proportion. Further investigations on the dynamics of the Li ions are work in progress.

References:

- [1] G. Venturini, *Z. Kristallogr.*, **221** (2006), 511-520.
 [2] O. Nial, *Anorg. Allgem. Chemie*, **238** (1938), 278-296.
 [3] M. Wendorff, C. Röhr, *Z. Naturforsch.*, **62b** (2007), 1549 - 1562.

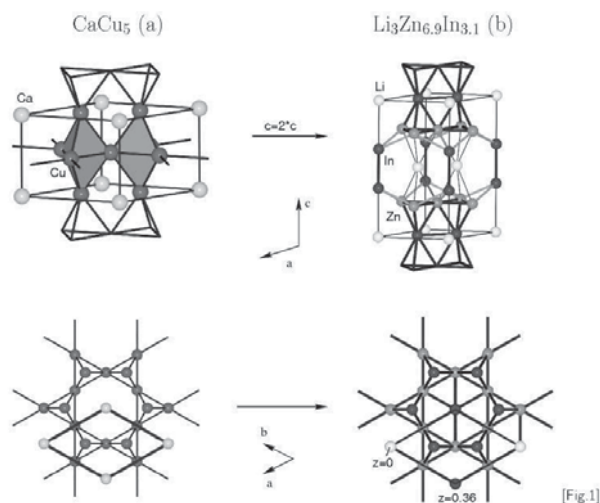


[Fig.1]

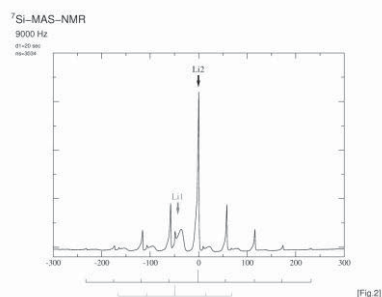


[Fig.2]

MS14-P06

 Metalide Suboxide Hydrides $\text{Ba}_{21}\text{M}_2\text{O}_5\text{H}_x$

M. Jehle¹, H. Kohlmann², H. Scherer¹, C. Röhr¹

¹Institut für Anorganische und Analytische Chemie, Universität Freiburg, Freiburg, Germany

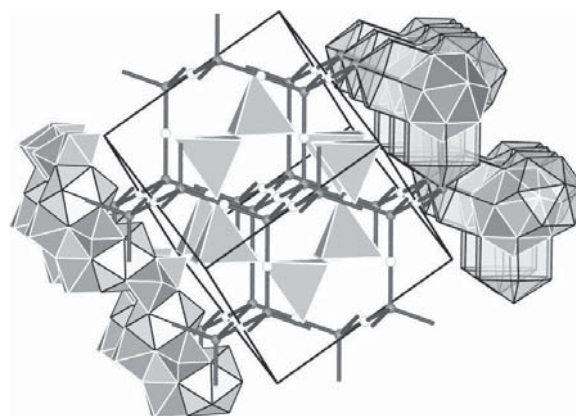
²Anorganische Festkörperchemie, Universität des Saarlandes, Saarbrücken, Germany

The title compounds with a great variety of anions M with both different sizes and formal charges have been synthesized from stoichiometric melts, using BaH_2 as hydrogen source. All phases were characterized by means of single crystal X-ray data (cubic, space group $Fd\bar{3}m$, e.g. $M=\text{Si}$: $a=2033.5$ pm, $R1=0.0451$).

The structure type has first been reported by Fornasini and Merlo as Ba_{10}Ga [1]. Further investigations by us lead to the composition $\text{Ba}_{21}\text{M}_2\text{O}_5$ ($M=\text{Zn}, \text{Cd}, \text{Hg}, \text{Ga}, \text{In}, \text{Tl}, \text{Si}, \text{Ge}$ [2]). The crystal structure exhibits two interpenetrating diamond-like networks: Network A consists of clusters O_5Ba_{18} (PG $-43m$, 8(a)), that resemble the clusters in suboxides, and icosahedra MBa_{12} ($-3m$, 16(c)). Network B contains FK-16 polyhedra $\text{Ba}(4)\text{Ba}_{16}$ ($-43m$, 8(b)) at the nodes and bicapped hexagonal prisms $\text{Ba}(3)\text{Ba}_{14}$ ($-3m$, 16(d)) at the 'bonds'. In 1998, Huang and Corbett [3] proved the hydrogen content of the compounds by means of neutron powder

diffraction and forced the electron precise compositions $\text{Ba}_{21}\text{M}_2\text{O}_5\text{H}_{22}$ ($M=\text{Tr}$) and $\text{Ba}_{21}\text{M}_2\text{O}_5\text{H}_{24}$ ($M=\text{Tt}$), respectively. However, H-H distances smaller than 200 pm, apart from a symmetry reduction from $Fd\bar{3}m$ to $P3_121$, that can not be rationalized by direct group-subgroup relations, makes this structure suggestion and composition less coherent. In best accordance with the present suboxide cluster O_5Ba_{18} , the results of the FP-LAPW bandstructure calculations, the metallic properties and the possible M elements (transition metals and p-elements as well) we conclude that all title compounds are not electron precise metalide oxide hydrides but contain less hydride per f.u. In analogy to $\text{Sr}_{21}\text{Si}_2\text{O}_5\text{C}_6$ [4], where the carbide ions are localized in the twofold capped hexagonal prisms (site 96(g), half occupied), the hydride ions also take this site. The neutron powder diffraction data obtained for the Ba silicide (both H and D compound) and the results of ^1H MAS NMR spectroscopy indicate, that the hydride substructure consists of 6.2(6) hydrogen ions per f. u. for the silicide.

- [1] M. L. Fornasini, F. Merlo, *Rev. Chim. Miner.*, **16**, 458 (1979).
 [2] C. Röhr, *Z. Kristallogr. Suppl.*, **9**, 24 (1994). *Z. Anorg. Allg. Chem.*, **621**, 1496 (1995).
 [3] B. Huang, J. D. Corbett, *Inorg. Chem.*, **37**, 1892 (1998).
 [4] M. Knoth, U. Röbber, B. Eisenmann, *Z. Anorg. Allg. Chem.*, **631**, 1237 (2005).



MS14-P07

 Synthesis and Crystal Structure of the First Yttrium(III) Bromide Oxomolybdate(VI) $\text{YBr}[\text{MoO}_4]$

H. Henning¹, T. Schustereit¹, T. Schleid¹, I. Hartenbach¹

¹University of Stuttgart, Institute for Inorganic Chemistry, Stuttgart, Germany

Although a mixture of bromide anions with molybdenum(VI) oxide represents a redox-active system, it was possible to synthesize $\text{YBr}[\text{MoO}_4]$ by means of a solid-state reaction. For this purpose Y_2O_3 , YBr_3 , and MoO_3 in a molar ratio of 1 : 1 : 3 were annealed at 820 °C in fused silica ampoules for 7 days. Besides elemental bromine and not further investigated reduced molybdenum oxides, coarse transparent colourless single crystals of $\text{YBr}[\text{MoO}_4]$ emerged from this reaction mixture [1]. The title compound crystallizes triclinically ($P\bar{1}$, $a = 685.48(2)$, $b = 717.37(2)$, $c = 1088.81(4)$ pm, $\alpha = 104.917(2)$, $\beta = 107.427(2)$, $\gamma = 93.172(2)^\circ$, $Z = 4$, CSD-423824) with two crystallographically distinguishable Y^{3+} cations, Br⁻ anions and $[\text{MoO}_4]^{2-}$ tetrahedra each. The coordination sphere around $(\text{Y}1)^{3+}$ consists of by three Br⁻ and five O^{2-} anions forming a distorted trigonal dodecahedron. In contrast, $(\text{Y}2)^{3+}$ shows only a coordination number of seven realized as monocapped trigonal prisms with six oxygen atoms building up the prisma and one bromide anion representing the cap. Both sorts of isolated $[\text{MoO}_4]^{2-}$ tetrahedra are surrounded by five Y^{3+} cations. While those bearing $(\text{Mo}2)^{6+}$ are exclusively connected to Y^{3+} centered polyhedra via common vertices, the $[(\text{Mo}1)\text{O}_4]^{2-}$ entities also share one common edge with a

[(Y1)O₅Br₃]¹⁰⁻ unit. The main building blocks within the crystal structure of YBr[MoO₄] are strands consisting of the following units: two [(Y1)O₅Br₃]¹⁰⁻ polyhedra fused together via a common (Br1)⁻⋯(Br1)⁻ bridge and two [(Y2)O₆Br]¹⁰⁻ entities connected by two [(Mo2)O₄]²⁻ tetrahedra, which are finally bonded to one another by common (Br2)⁻ anions and [(Mo1)O₄]²⁻ groups (see Figure). These strands propagate along [102] and join together via oxomolybdate tetrahedra with alike chains forming layers spreading out parallel to the *ac* plane. These layers are stacked along the *b* axis with an offset of one full lattice constant in *c* direction with respect to the previous sheet, linked by shared oxygen vertices of the Y³⁺ centered polyhedra. Thus, the crystal structure of YBr[MoO₄] differs significantly from those of YF[MoO₄] (monoclinic, *P*2₁/*c*) and YCl[MoO₄] (monoclinic, *C*2/*m*) [2].

References:

- [1] T. Schustereit, Exam Thesis, University of Stuttgart, 2010.
[2] Th. Schleid, S. Strobel, P. K. Dorhout, P. Nockemann, K. Binnemans, I. Hartenbach, *Inorg. Chem.* 2008, 47, 3728.



MS14-P08

Derivatives of 2-Aminopyrimidin-4-one: one or two tautomers present in the same crystal

V. Gerhardt¹, E. Egert¹¹Goethe-Universität, Biochemie, Chemie und Pharmazie, Frankfurt am Main, Germany

Pyrimidin-4-ones are of particular interest in pharmacology and molecular biology. Their derivatives include nucleobases and many important pharmaceutical drugs. Pyrimidin-4-ones can occur in three tautomeric forms: a hydroxypyrimidine, a (*I*H)- and a (*3*H)-tautomer (Fig.1). Therefore we crystallized 2,6-diaminopyrimidin-4-one (**I**) and 2-amino-6-methylpyrimidin-4-one (**II**) to study their tautomeric preference.

Crystallization experiments of **I** yielded five structures, namely one anhydrate and four solvates (with dimethylformamide-water, dimethylacetamide or *N*-methyl-2-pyrrolidone). In agreement with results obtained from the Cambridge Structural Database **I** exists only as (*3*H)-tautomer. The molecules form ribbons characterized by R₂²(8) hydrogen-bonding interactions, which are further connected to three-dimensional networks.

For **II** two isostructural solvates (with dimethylacetamide or *N*-methyl-2-pyrrolidone) were obtained. In contrast to **I** both crystals contain a 1:1 mixture of coplanar (*I*H)- and (*3*H)-tautomers together with a solvent molecule, which is hydrogen bonded to the (*3*H)-tautomer. The crystal structures contain discrete R₂²(8) hydrogen-bonded tetramers consisting of symmetry-equivalent dimers, which are linked by three hydrogen bonds similar to the Watson-Crick (C-G) base pair (Fig.2). [1]

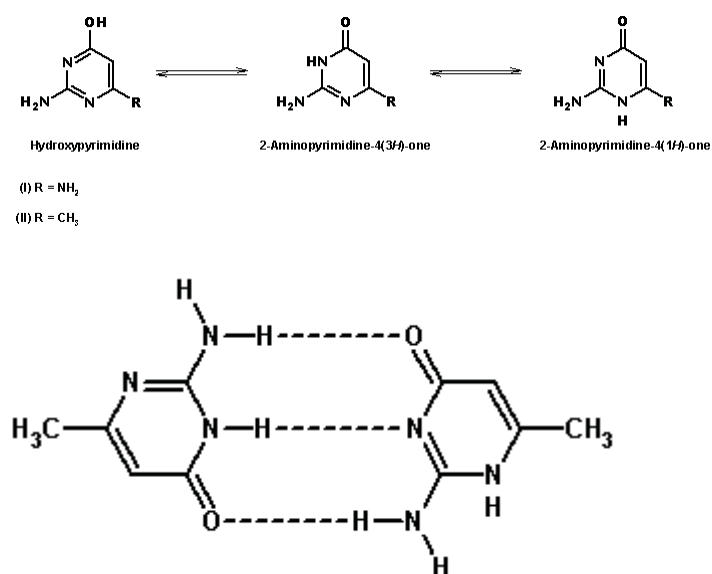
These results suggest that cocrystals of **II** with compounds containing different complementary functional groups may lead to different synthon combinations. [2].

[1] Gerhardt, V., Tutughamiarso, M. & Bolte, M. (2011), *Acta Cryst.*, C67, o179-o187.

[2] Tutughamiarso, M. & Egert, E. (2011). In preparation.

Keywords: pyrimidin-4-one, tautomers, cocrystals

Figure 1) Tautomeric forms of 2-Aminopyrimidinone

Figure 2) Complex between (*3*H)- and (*I*H)-tautomer of **II**

MS14-P09

Synthesis and crystal structure of three new K-thioferrates:

K₉FeS₇, K₃FeS₃ and K_{1,4}FeS₂M. Schwarz¹, C. Röhr¹¹Albert-Ludwigs Universität Freiburg, Institut für Anorganische und Analytische Chemie, Freiburg im Breisgau, Germany

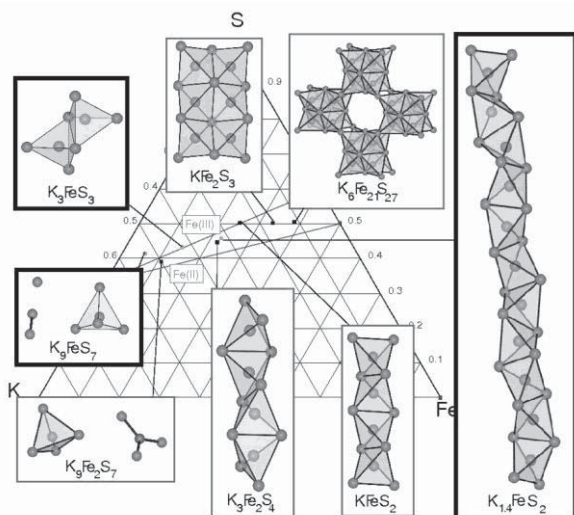
In the series of potassium thioferrates K-Fe-S several structures have been found during the last 143 years. All of them contain FeS₄ tetrahedra as main structural element. These tetrahedra are condensed in a grade depending on the ratio Fe:S. Starting from the highest ratio, K₉Fe₂S₇ [1] is built up of isolated Fe(III)S₄ tetrahedra besides trigonal planar Fe(II)S₃ units. In KFeS₂, first reported by Preis and Schneider in 1869 [2,3] and structurally explored by Boon and MacGillary in 1942 [4], linear chains of edge sharing tetrahedra [Fe(III)S₄]₂ are formed. Similar chains are found in K₃Fe₂S₄ [5] where they form a zig-zag structure. Fe is in a mixed valent state of Fe(II) and Fe(III), statistically distributed over all Fe positions. In the mineral Rasvumite KFe₂S₃ [6] which has lately also been synthesized [7], these chains are even higher condensed so that they form an edge-sharing double chain of tetrahedra also containing both Fe(II) and Fe(III) without a recognized ordering. The highest grade of condensation is realized for the mineral Bartonite with the idealized composition K₆Fe₂₁S₂₇ [8]. Clusters Fe₈S₁₄ of eight edge-sharing tetrahedra are connected via common corners.

Three new compounds in this series were synthesized by melt reactions from the pure elements and structurally explored by single crystal X-ray diffraction:

K₉FeS₇ (*P*21/*n*, *a* = 772.500(1), *b* = 1251.24(2) and *c* = 811.57(1) pm, β = 102.967(1)°, formed at 1100°C) contains isolated FeS₄³⁻ tetrahedra besides S²⁻ and S₂²⁻ anions. The tetrahedra form layers in the *b*-*c*-plane alternating with layers of the simple S-anions S²⁻ and S₂²⁻. The distances within the tetrahedra (d_{Fe-S} = 229.9-230.6 pm) as well as between the S-atoms in S₂²⁻ (d_{S-S} = 213.9 pm) are within the expected range. K₃FeS₃ (*P*21/*c*, *a* = 772.50(1), *b* = 1251.24(2) and *c* = 1002.80(1) pm, β = 127.526(1)°, formed at 1100°C) contains edge-sharing Fe₂S₆ double-tetrahedra known for K-, Rb- and Cs-oxoferrates [9,10,11] and Na- or Cs-thioferrates also [12,13]. Compared to Na₃FeS₃, the tilt of the double tetrahedra against each other is bigger for the K-compound determined by the larger size of the cation. Distances within the tetrahedra (d_{Fe-S} = 224.3-230.5 pm) are comparable to those in the Na- and Cs-compounds, while the Fe-Fe distance (d_{Fe-Fe} = 298.4 pm) is increased. K_{1,4}FeS₂ (*C*2/*c*, *a* = 2790,1(3), *b* = 1153,7(1) and *c* =

720.17(8) pm, $\beta = 102.746(8)^\circ$, formed at 600 °C) exhibits chains of edge-sharing Fe(II/III)S₄ tetrahedra similar to those in K₃Fe₂S₄. Starting from KFeS₂ with linear [FeS_{4/2}]-chains, the tetrahedra in K₃Fe₂S₄ form zig-zag chains. In K_{1,4}FeS₂ these zig-zag chains are undulated, which results in an increase of the axis running along these chains.

- [1] W. Bronger, U. Ruschewitz, *J. Alloys. Compd.* **197**, 83 (1993).
 [2] K. Preis, *J. prakt. Chem.* **107**, 12 (1869).
 [3] R. Schneider, *J. prakt. Chem.* **108**, 16 (1869).
 [4] J. W. Boon, C. H. MacGillary, *Recueil Trav. chim. Pays-Bas* **61**, 910 (1942).
 [5] W. Bronger, U. Ruschewitz, P. Müller, *J. Alloys. Com.* **218**, 22 (1995).
 [6] J. R. Clark, G. E. Brown Jr., *Am. Min.* **65**, 477 (1980).
 [7] R. H. Mitchell, K. C. Ross, E. G. Potter, *J. Sol. St. Chem.* **177**, 1867, (2004)
 [8] H. T. Evans Jr., J. R. Clark, *Am. Min.* **66**, 376 (1981).
 [9] H. Rieck, R. Hoppe, *Z. Anorg. Allg. Chem.* **408**, 151 (1974).
 [10] G. Frisch, C. Röhr, *Z. Naturforsch.* **60b**, 732 (2005).
 [11] G. Frisch, C. Röhr, *Z. Krist.* **220**, 135 (2005).
 [12] P. Müller, W. Bronger, *Z. Naturforsch.* **34b**, 1264 (1979).
 [13] W. Bronger, U. Ruschewitz, P. Müller, *J. Alloys Compd.* **187**, 95 (1992).



MS14-P10

Synthesis and Crystal Structure of the new Cesium Ruthenate Hydrate Cs₂[RuO₃(OH)] · 2 H₂O

C. Hoch¹, C. Lenk¹

¹University of Stuttgart, Institute for Inorganic Chemistry, Stuttgart, Germany

When cesium metal, cesium oxide Cs₂O and iron(III)-oxide Fe₂O₃ are reacted at 150 °C under an argon atmosphere, cesium suboxoferrate, Cs₉[FeO₄] can be obtained [1]. It is a representative of a new class of subvalent compounds that comprise spacial separation of ionic and metallic substructures, and therefore it is an interesting model for studies of materials showing a bonding situation in between metals and salts. As we wish to expand the field of suboxometallates, we have executed a number of equivalent reactions with other metal oxides. In some cases suboxometallates could be isolated, but often "normal", purely ionic cesium oxometallates are the main products [2]. Our first experiments starting from Cs, Cs₂O and RuO₂ have resulted in a plethora of new cesium oxoruthenates, as could be detected from powder X-ray analyses. However, no single crystals could be obtained from the new phases so far and their structure analyses hence are lacking. One of the highly hygroscopic new cesium oxometallate powders was stored several days under paraffin oil

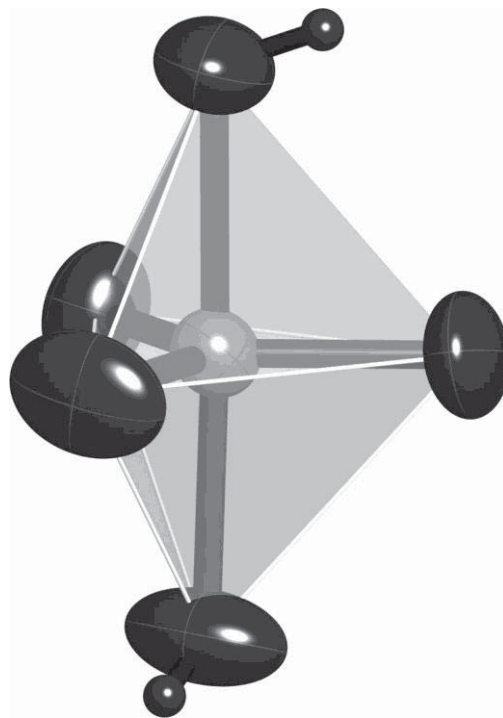
and slowly hydrated by diffusing air moisture, resulting in the formation of red transparent single crystals of excellent quality. Single crystal X-ray studies showed a new dihydrate of dicesium dihydroxotrioxoruthenate(VI), Cs₂[RuO₃(OH)₂] · 2 H₂O. The trigonal planar anion therein has already been described for the crystal structure of the non-hydrated potassium ruthenate K₂[RuO₃(OH)₂] [3]. The tetragonal structure (space group *P4₁2₁2*, $a = 8.2136(3)$ Å, $c = 12.9896(5)$ Å, $Z = 4$, $R_{\text{int}} = 0.0888$, $R1 = 0.0197$, $wR2 = 0.0414$) comprises one crystallographically independent [RuO₃(OH)₂]²⁻ anion with point symmetry 2. The hydrogen atoms could all be located from the difference Fourier map and form a net of hydrogen bonds connecting the OH groups of the complex anion and the water molecules located inbetween them.

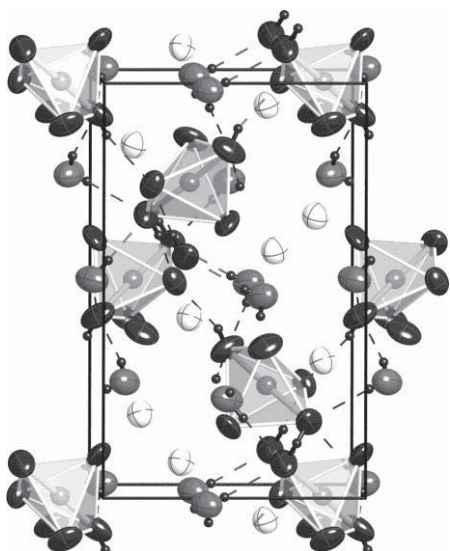
Figure 1: The [RuO₃(OH)₂]²⁻ anion, ellipsoids drawn at a 95 % probability level.

Figure 2: Unit cell of Cs₂[RuO₃(OH)₂] · 2 H₂O with hydrogen bond pattern (thin dashed lines). All ellipsoids are drawn at a 95% probability level.

References:

- [1] C. Hoch, J. Bender, A. Simon, *Angew. Chem.* **2009**, *121*, 2451; *Angew. Chem. Int. Ed.* **2009**, *48*, 2415; C. Hoch, J. Bender, A. Wohlfarth, A. Simon, *Z. Anorg. Allg. Chem.* **2009**, *635*, 1777.
 [2] J. Bender, A. Wohlfarth, C. Hoch, *Z. Naturforsch.* **2010**, *65b*, 1416; C. Hoch, *Z. Naturforsch.* **2012**, submitted.
 [3] M. O. Elout, W. G. Haije, W. J. A. Maaskant, *Inorg. Chem.* **1988**, *27*, 610; D. Fischer, R. Hoppe, *Z. Anorg. Allg. Chem.* **1991**, *601*, 41.



**MS14-P11****Crystal structure and phase transition of anhydrous copper(II) acetate, $\text{Cu}(\text{CH}_3\text{COO})_2$, and its relationship to copper(II) acetate monohydrate**F. Preuschl¹, M. Wildner¹¹Universität Wien, Institut für Mineralogie und Kristallographie, Wien, Austria

Crystals of anhydrous copper(II) acetate, $\text{Cu}(\text{CH}_3\text{COO})_2$, have been synthesized at low-hydrothermal conditions, and the structure was determined at 295K, 120K and 100K from single crystal X-ray diffraction data. α - $\text{Cu}(\text{CH}_3\text{COO})_2$ is triclinic, space group $P-1$, $Z = 2$, $a = 5.154(1)$, $b = 7.591(2)$, $c = 8.271(2)$ Å, $\alpha = 77.86(1)$, $\beta = 76.00(1)$, $\gamma = 84.29(1)^\circ$, $V = 306.6(1)$ Å³ (295K). Around 110K a reversible displacive phase transition to triclinic β - $\text{Cu}(\text{CH}_3\text{COO})_2$ occurs; space group $P-1$, $Z = 4$, $a = 8.154(1)$, $b = 8.702(1)$, $c = 9.494(1)$ Å, $\alpha = 68.61(1)$, $\beta = 72.51(1)$, $\gamma = 87.14(1)^\circ$, $V = 596.9(1)$ Å³ (100K).

Both modifications are built from characteristic dinuclear 'paddle wheel' complexes, *i.e.* two pyramidal CuO_5 polyhedra are linked by four acetate group 'paddles'. The Cu-Cu distance between opposite pyramidal base planes is extremely short with 2.578(1) Å in the α -phase at 295K, and reduced to 2.572(1) Å at 120K and to 2.570(1) Å after the phase transition in the β -phase at 100K. In the 'prototype' structure of such copper acetate complexes, copper(II) acetate monohydrate, this contact is 2.614(2) Å [1], and in a survey of 66 respective copper acetate dimers [2] a distance of 2.575 Å is reported as lower limit and 2.625 Å as average value. Therefore it is quite surprising that the phase transition has no relaxing effect on the short Cu-Cu distance. However, the inversion centre connecting the two Cu positions in the α -phase is lost upon transition to the β -phase, thus leading to a doubling of the cell content. Effective structural changes are, nevertheless, marginal; the most evident one is a slight mutual rotation of the pyramidal base planes (which are nearly congruent in the α -phase) by 6.6°. The detailed character of the phase transition is currently under investigation.

The main structural motif in $\text{Cu}(\text{CH}_3\text{COO})_2$ can be derived from the structure of copper(II) acetate monohydrate, $\text{Cu}(\text{CH}_3\text{COO})_2 \cdot \text{H}_2\text{O}$, by removal of the CuO_5 -pyramids' apical H_2O molecules and consequential direct linkage of neighbouring 'paddle wheel' complexes via common pyramidal edges to infinite chains, where all dimers and hence Cu-Cu vectors are parallel (Fig. 1). In contrast, in the monoclinic monohydrate isolated dimers are mutually tilted by 66.7°.

Like copper acetate monohydrate - which is a relevant component of verdigris, a well-known but rather vaguely defined multi-phase pigment mixture used since ancient times [*e.g.* 3] - anhydrous copper acetate has an intensive bluish-green colour, and single crystals exhibit strong pleochroism from dark blue (perpendicular

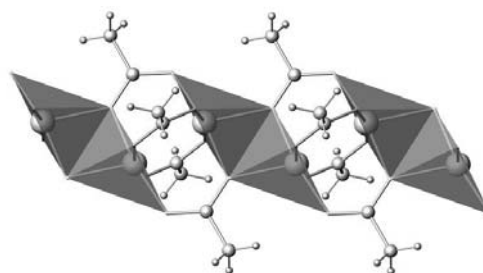
to the dimeric chains) to emerald green (along the chains). Detailed optical and vibrational spectroscopic characterisation is in progress. Anhydrous copper acetate probably occurs as hitherto unidentified component in historic verdigris samples and might be detected in diffraction patterns by its strongest lines at $d(I)_{\text{calc}}$ 7.875(100), 7.412(76), 6.006(31), 3.794(21), and 3.721(17).

[1] G.M. Brown, R. Chidambaram (1973) *Acta Cryst.* B29, 2393-2403.

[2] M.R. Sundberg, R. Uggla, M. Melnik (1996) *Polyhedron* 15, 1157-1163.

[3] G. Chiari, D. Scott (2004) *Periodico di Mineralogia* 73, 227-237.

Figure 1: Chain of dimeric copper(II) acetate 'paddle wheel' complexes in $\text{Cu}(\text{CH}_3\text{COO})_2$.

**MS14-P12****Crystals and Quasicrystals**I. Leban¹¹University of Ljubljana, Faculty of Chemistry and Chem. Technology, Ljubljana, Slovenia

On the occasion 100th anniversary of the first diffraction experiment using X-rays which really enable us to see atoms it is appropriate to comment the general view on the crystalline state. The abstract is also connected with the Nobel Prize in Chemistry for 2011 to Prof. Dan Shechtman for the discovery of quasicrystals. In 1975 Prof. Alan L. Mackay was a plenary lecturer at 10th Yugoslav crystallographic meeting in Kumrovec (now Croatia) with a rather controversial lecture "Generalised Crystallography" in which he strongly attacked the classical crystallography and The International Tables of X-ray Crystallography (A.L.Mackay, *Izv.Jugoslav. Centr. Kristalogr.*, 10, 15-36, 1975) striving to see the crystallography as a general science of structure. He wanted that the "modern crystallography" should explain and control the behaviour of more complicated systems which are not the crystals in the classical sense. Furthermore, A.L. Mackay's special interest was a pentagonal symmetry - for some classical crystallographers "forbidden symmetry" although there are natural crystals in the form of pentagonal dodecahedra like common pyrites (fool's gold). He used the Penrose pattern (Sir R. Penrose, 1931-), which is tiling of two-dimensional and of three dimensional space by identical tiles of two kinds (acute and obtuse rhombi) in 2D and acute and obtuse rhombohedra in 3D. Those patterns were unique and non-periodic. (A.L.Mackay: *De Nive Quinquangula* - On the pentagonal snowflake, *Sov.Phys.Crystallogr.*, 26, 517-522, 1981 and A.L.Mackay: *Crystallography and the Penrose pattern*, *Physica*, 114A, 609-613, 1982). Mackay even produced the optical transform of the Penrose pattern, which exhibited tenfold symmetry, which is very similar to the diffraction pattern of Prof. D. Shechtman obtained under the electron microscope on quasicrystal.

The terms quasi-identity and quasi-equivalence were defined already by A.L. Mackay in 1981 and somehow he forecasted the discovery of the materials with these properties. It so often happens in science that many excellent and hard working scientists are not getting proper rewards for their work. However, they live with the

feeling that they did something good for the humanity. At this point, myself as a chemist, should mention that Dmitrij I. Mendelejev, who established the periodic table of elements (now in general use), who predicted three new elements and their properties and was in favour of the metric system in Russia, never received a Nobel Prize.

MS14-P13

Introducing Disorder into CaF₂-Type Cs₂[B₁₂H₁₂]

C. Hoch¹, L.W. Zimmermann¹, T. Schleid¹

¹University of Stuttgart, Institute for Inorganic Chemistry, Stuttgart, Germany

The synthesis of new subvalent caesium compounds starting from metallic caesium and "normal" ionic metal oxides has led to a number of suboxometalates A₉MO₄ (A = Rb, Cs; M = Al, Ga, In, Sc, Fe) in the recent years [1]. It would therefore be interesting to investigate whether this reaction pathway is limited to oxidic systems only.

As the coordination polyhedra around the *closo*-dodecaborate anions in Cs₂[B₁₂H₁₂] suggest a geometric fitting set of building units in subvalent compounds with metallic caesium atoms in cubic bodycentered environment next to the [B₁₂H₁₂]²⁻ anions coordinated by eight Cs⁺ cations in a cubic arrangement, we conducted a first experiment in which a large excess of metallic caesium was heated together with Cs₂[B₁₂H₁₂] to 250 °C.

However, this did not result in the formation of the desired product Cs_n[B₁₂H₁₂] with n > 2 but in a new modification of Cs₂[B₁₂H₁₂]. The comparison of the two structures of Cs₂[B₁₂H₁₂] shows that the new modification is a disorder variant of its reported CaF₂-type standard modification [2]. The new cubic disorder variant of Cs₂[B₁₂H₁₂] crystallizes in space group *Pm*-3 (no. 200) with a = 563.03(6) pm, which is quite close to half of the lattice constant of the ordered CaF₂-type structure (*Fm*-3, a = 1128.12(7) pm) and indicates the close symmetrical relationship. In both structures, the barycenter of the icosahedral [B₁₂H₁₂]²⁻ anion occupies the position 0,0,0 with point symmetry *m*-3, causing minimal distortions of an icosahedron in a cubic lattice. In the CaF₂-type structure, cubes of caesium atoms filled with *closo*-dodecaborate anions alternate with empty cubes in all three directions (see Figure 2, left). The disordered structure shows *all* cubes filled, but the occupation factors for all boron atoms can be freely refined to result in a half-occupied B₁₂-based anion within the error margins, resembling a CsCl-type arrangement.

Figure 1: Crystallographic data for CsCl-type Cs₂[B₁₂H₁₂].

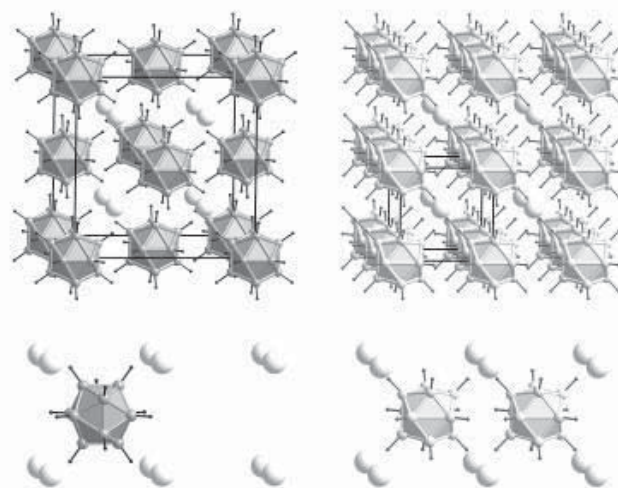
Figure 2: Left: CaF₂-type Cs₂[B₁₂H₁₂] [2]; right: new modification of Cs₂[B₁₂H₁₂] with half-occupied anion positions in a CsCl-type defect structure.

References:

- [1] C. Hoch, J. Bender, A. Simon, *Angew. Chem.* **2009**, *121*, 2451; *Angew. Chem. Int. Ed.* **2009**, *48*, 2415; C. Hoch, J. Bender, A. Wohlfarth, A. Simon, *Z. Anorg. Allg. Chem.* **2009**, *635*, 1777.
 [2] I. Tiritiris, Th. Schleid, K. Müller, W. Preetz, *Z. Anorg. Allg. Chem.* **2000**, *626*, 323.

Figure 1

Sum formula	Cs ₂ [B ₁₂ H ₁₂]			
Space group	<i>Pm</i> -3 (No. 200)			
Lattice parameter a [pm]	563.03(6)			
Z	1			
Reflections all / indep.	637 / 100			
l. s. parameters	10			
R1 / wR2	0.0279 / 0.0636			
R _{int} / R _e	0.0449 / 0.0290			
Atom (Wyckoff-No.)	x/a	y/b	z/c	occup.
Cs (1a)	0	0	0	1
B (12k)	0.5	0.271(5)	0.316(4)	0.49(5)
H (12k)	0.5	0.136	0.175	



MS14-P14

Pb₅TeO₈ - a lead-rich oxotellurate(VI) previously reported as "Pb₃TeO₆"

M. Weil¹

¹TU Wien, CTA, Abteilung Strukturchemie, Wien, Austria

In continuation of recent structure determinations of double perovskites M₂TeO₆ (M = Sr, Ba) which crystallize in complex superstructures [1], the lead analogue Pb₃TeO₆ became interesting. Although preparation, lattice parameters and physical properties were reported for this phase [2], detailed structural information remained unknown until now. Following the procedure for crystal growth of Pb₃TeO₆ given in [2], crystals of the lead-rich phase Pb₅TeO₈ were obtained instead, however with very similar lattice parameters as reported for Pb₃TeO₆.

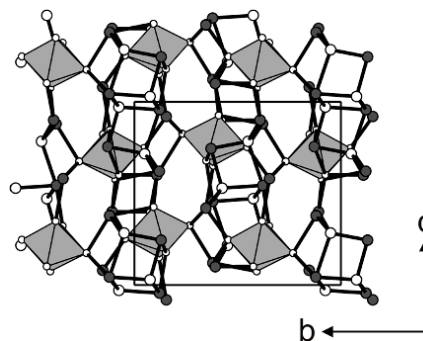
The title compound crystallizes in the space group *P2*₁/*n* with four formula units and lattice parameters of a = 7.4426(2), b = 12.0107(3), c = 10.6567(2) Å, β = 91.040(1)°, V = 952.45(4) Å³, R[F² > 2σ(F²)] = 0.027, wR2(all data) = 0.050, 5910 structure factors, 128 parameters.

The asymmetric unit contains five Pb, one Te, and eight O atoms, all on general positions. In the crystal structure layers parallel to (010) are present that are made up from corner- and edge-sharing PbO_x polyhedra (x = 4,5; d(Pb—O) = 2.198 – 2.809 Å), resembling the arrangement in yellow lead oxide (massicot). These PbO-type layers are connected by TeO₆ octahedra (d(Te—O) = 1.886 – 1.975 Å) along [010] thereby forming voids in which the stereochemically active electron lone pairs of the Pb²⁺ ions protrude.

[1] B. Stöger, M. Weil, E. Zobetz, *Z. Kristallogr.* **225**, 125-138 (2010).

[2] Kosse, L. I., Politova, E. D., Bush, A. A., Stefanovich, S. Yu., Venevtsev, Yu. N., *Sov. Phys. Crystallogr.* **28**, 302-304 (1983).

The crystal structure of Pb₅TeO₈ in projection along [-100



MS14-P15

Crystal structures of proline-derived enamines

D.A. Bock¹, C.W. Lehmann¹, B. List¹¹Max-Planck-Institut für Kohlenforschung, chemistry, Mülheim an der Ruhr, Germany

Within the last ten years, enamine catalysis, the catalytic activation of carbonyl compounds via enamine intermediates, has grown into a powerful approach to organic synthesis [1]. Among the many different primary and secondary amine catalysts that have been developed in this field, the amino acid proline remains a privileged motif and there are literally dozens of reaction types that are catalyzed with this ubiquitously natural product [2]. Proline derived enamines of aldehydes and ketones are key intermediates in the catalytic cycles of these reactions (Scheme 1) [3]. Surprisingly though, such enamines have remained entirely hypothetical and resisted attempts at their structural characterization. Such information however, appears to be highly valuable towards understanding the mechanistic details with which proline catalyzes carbonyl transformations.

Here the isolation and structural characterization of both aldehyde- and ketone derived proline enamines are reported and discussed [4]. Crystal structures of nine proline enamines (Figure 1) provide information on stereochemical aspects, i.e. double bond configuration and syn- vs. anti-positioning of the carboxylate relative to the enamine double bond. The dominant interactions between carbonyl O atoms and the O—H can be seen in the Hirshfeld surface [5] of enamines as the bright red areas marked in Figure 1. Furthermore the obtained crystal structures are compared with the DFT-calculated structures of the ground and transition state and the postulated Seebach-Eschenmoser transition state.

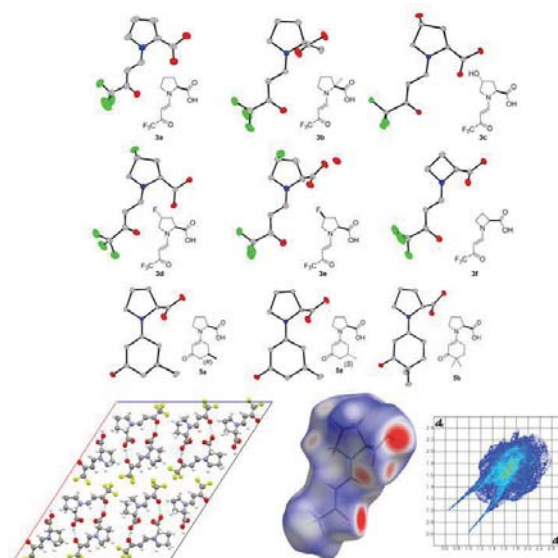
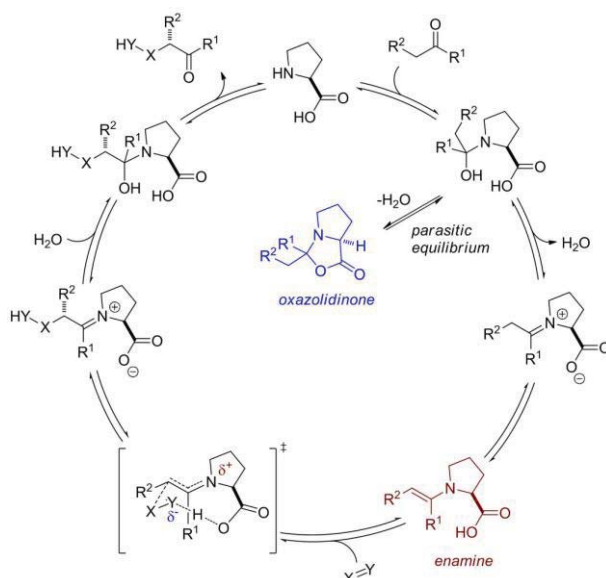
[1] S. Mukherjee, J.W. Yang, S. Hoffmann, B. List, *Chem. Rev.* 107 (2007) 5471-5569.

[2] B. List, *Tetrahedron* 58 (2002) 5573-5590.

[3] B. List, R.A. Lerner, CF Barbas III, *J Am Chem Soc* 122 (2000) 2395-2396.

[4] D.A. Bock, C.W. Lehmann, B. List, *Proc. Natl. Acad. Sci.* 107 (2010) 20636-20641.

[5] M.G. Gorbunova, I.I. Gerus, S.V. Galushko, V.P. Kukhar, *Synthesis* 3 (1991) 207-209.



MS14-P16

Kristallstrukturbestimmung des Bis-Kuppler-Azopigments P.Y. 155 aus Labor-Röntgenpulverdaten

J. Brüning¹, E. Alig¹, S.N. Ivashevskaja², J. van de Streek^{1,3}, M.U. Schmidt¹¹Universität Frankfurt, Institut für Anorganische und Analytische Chemie, Frankfurt am Main, Germany²Karelian Research Centre, Russian Academy of Sciences, Institut für Geologie, Petrozavodsk, Russland, Russian Federation³Avant-garde Material Simulation, Freiburg, Germany

Pigment Yellow 155 (P.Y. 155) ist ein industrielles, organisches, gelbes Bis-Kuppler-Azopigment [1].

Trotz umfassender Kristallisationsexperimente ist es bislang nicht gelungen, ausreichend große Einkristalle der Verbindung, die eine Einkristallstrukturanalyse ermöglichen würden, zu erhalten. Daher wurde die Kristallstruktur aus den Röntgenpulverdaten bestimmt. Die Röntgenpulverdaten wurden auf einem STOE-STADI-P-Pulverdiffraktometer mit Cu-K α_1 -Strahlung (Ge(111)-Monochromator) in Transmission im Bereich zwischen 3 und 74° 2 θ mit einem linearen PSD gemessen. Die Kristallstruktur wurde mithilfe der Programme *DASH* [2] und *TOPAS* [3] bestimmt.

P.Y. 155 kristallisiert in *P*-1, *Z* = 1 mit den Gitterparametern $a = 5.7115(4)$ Å, $b = 9.2894(7)$ Å, $c = 16.673(1)$ Å, $\alpha = 108.472(4)^\circ$, $\beta = 89.906(3)^\circ$ und $\gamma = 95.672(4)^\circ$. Die Moleküle liegen auf Inversionszentren und bilden sechs intramolekulare Wasserstoffbrücken aus, allerdings keine intermolekularen. Die Molekülkonformation ist ungewöhnlich. Im Allgemeinen bilden sich Wasserstoffbrücken zwischen NH-Gruppen und COOCH₃-Fragment aus, wobei die C=O-Gruppe des COOCH₃-Fragments als Akzeptor fungiert. Bei P.Y. 155 ist der Akzeptor jedoch nicht das C=O-Fragment, sondern die OCH₃-Gruppe. Die COOCH₃-Gruppe ist also um 180° gedreht, da sonst ein Loch in der Kristallstruktur entstehen würde, welches nicht ohne weiteres zu füllen wäre. Diese gedrehte Konformation findet man auch in der Kristallstruktur des P.Y. 213 [4].

Die Kristallstruktur von P.Y. 155 wurde mit DFT-D-Rechnungen kontrolliert; dazu wurde das Programm *GRACE* [5] verwendet.

[1] Herbst, W., Hunger, K., *Industrial Organic Pigments*, 3rd ed., Wiley-VCH, Weinheim, 2004.

[2] David, W.I.F., Shankland, K., Van de Streek, J., Pidcock, E., Motherwell, W.D.S., Cole, J.C., *J. Appl. Cryst.*, 2006, **39**, 910-915.

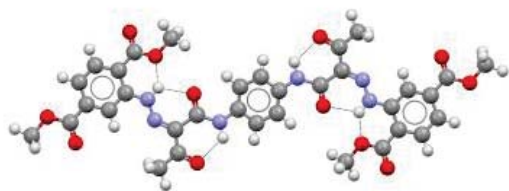
[3] Coelho, A.A., *TOPAS Academic*, version 4.1, 2007.

[4] Schmidt, M.U., Brühne, S., Wolf, A.K., Rech, A., Brüning, J., Alig, E., Fink, L., Buchsbaum, C., Glinemann, J., van de Streek, J., Gozzo, F., Brunelli, M., Stowasser, F., Gorelik, T., Mugnaioli, E., Kolb, U., *Acta Cryst.*, 2009, **B65**, 189-199.

[5] Neumann, M.A., Perrin, M.-A., *J. Phys. Chem.*, 2005, **B109**, 15531-15541.

Keywords: Bis-Kuppler-Azopigment,
Kristallstrukturbestimmung aus Pulverdaten

DFT-D,



MS14-P17

Umweganregung in single crystal neutron diffraction experiments and its impact on the symmetry determination of bismuth metal oxides

J. Birkenstock¹, E. Rossmannith², G. Nénert³, T.M. Gesing⁴, H. Schneider⁵, R.X. Fischer¹

¹Universität Bremen, FB5, Geowissenschaften/ Kristallographie, Bremen, Germany

²Universität Hamburg, Geowissenschaften/ Mineralogie, Hamburg, Germany

³Institut Laue Langevin, Diffraction Group, Grenoble, France

⁴Universität Bremen, FB2, Chemische Kristallographie fester Stoffe, Bremen, Germany

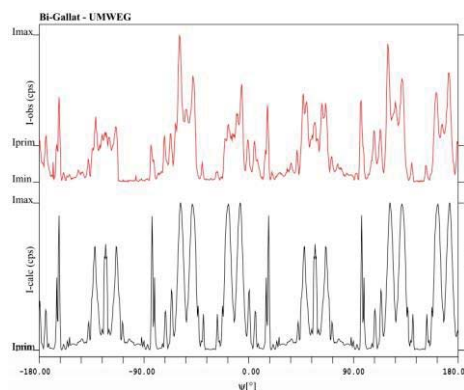
⁵Universität Köln, Institut für Kristallographie, Köln, Germany

Large single crystals of $\text{Bi}_2\text{M}_4\text{O}_9$, as described by Burianek et al. [1], were examined by single crystal neutron diffraction at the Institut Laue Langevin (ILL) in Grenoble. For “M” Fe and Ga with varying ratios were available. A crystal of composition $\text{Bi}_2\text{Ga}_4\text{O}_9$ with cube shape and edges of about 4 mm yielded strong and sharp single crystal reflections. Although the crystal structure could be well refined in the usual space group $Pbma$ this space group had to be questioned as more than 200 observed reflections disagreed with the corresponding reflection conditions. As calculations in possible subgroups of $Pbma$ yielded no improvement it was considered that the “forbidden” reflections might have emerged from multiple diffraction which is also well known as “Umweganregung”.

Psi-Scans were undertaken for selected h,k,l with “forbidden” intensity. In a first attempt a wavelength of 0.837 Å was used at the single crystal diffractometer D9. The corresponding Psi scans could not be interpreted in terms of multiple diffraction since the single reflections were not resolved. In a second attempt, this time on the instrument D10, a wavelength of 2.364 Å was used with which strong maxima were observed on top of a rather flat baseline. Figure 1 shows the measured data (top) of the reflection (0 3 0) compared with a calculation [2] (bottom) of the multiple diffraction intensity expected for the exact settings of the measurement. Observed and calculated data show a reasonable agreement though the psi scans did not include omega scans because of time limitations in the experiment. In detail some of the differences may also arise from limitations in the accuracy of the lattice parameters and/ or wavelength. Despite these it may be concluded that Umweganregung is a strong issue in single crystal neutron diffraction and that it clearly obscured the symmetry determination of the crystals under investigation.

References:

- [1] M. Burianek, M. Mühlberg, M. Woll, M. Schmücker, Th. M. Gesing, H. Schneider (2009), Single crystal growth and characterization of mullite-type orthorhombic $\text{Bi}_2\text{Me}_4\text{O}_9$ (Me= Al^{3+} , Ga^{3+} , Fe^{3+}). Cryst. Res. Technol., 44, 1156-1162.
[2] E. Rossmannith (2003), UMWEG: a program for the calculation and graphical representation of multiple diffraction patterns. J. Appl. Cryst., 36, 1467-1474.



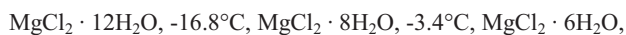
MS14-P18

Crystal structures of Magnesium Chloride Hydrates

H. Schmidt¹, E. Hennings¹, W. Voigt¹

¹TU Bergakademie Freiberg, Institute of Inorganic Chemistry, Freiberg, Germany

In contact with solutions magnesium chloride forms five stable hydrates (van't Hoff & Meyerhoffer, 1898)



$\text{MgCl}_2 \cdot 6\text{H}_2\text{O}$, the mineral bischofite, is stable at room temperature and is formed during evaporation of magnesium-rich waters. The hexahydrate is used as a source for production of magnesium oxide and magnesium metal. Its crystal structure was determined by Andress & Gundermann (1934). $\text{MgCl}_2 \cdot 12\text{H}_2\text{O}$ is the most highly hydrated salt and its crystal structure was determined by Sasvari and Jeffrey (1966) without specifying the hydrogen atom positions. Sugimoto, Dinnebier & Hanson (2007) determined the crystal structures of $\text{MgCl}_2 \cdot 4\text{H}_2\text{O}$ and $\text{MgCl}_2 \cdot 2\text{H}_2\text{O}$ by in situ powder diffraction during dehydration of the hexahydrate.

We present a reinvestigation of the crystal structures of $\text{MgCl}_2 \cdot 12\text{H}_2\text{O}$ and $\text{MgCl}_2 \cdot 4\text{H}_2\text{O}$ and the crystal structure investigation of $\text{MgCl}_2 \cdot 8\text{H}_2\text{O}$ for the first time. The result of Sasvari and Jeffrey (1966) for the crystal structure of $\text{MgCl}_2 \cdot 12\text{H}_2\text{O}$ was confirmed and could be improved with respect to the location of hydrogen atom positions. For $\text{MgCl}_2 \cdot 4\text{H}_2\text{O}$ Sugimoto, Dinnebier & Hanson found a disordered structure where only every second $\text{MgCl}_2(\text{H}_2\text{O})_4$ octahedron is occupied. We report an ordered crystal structure from single crystal data. A scheme for the step-wise structure changes with decreasing water content is developed.

van't Hoff & Meyerhoffer (1898), Z. Phys. Chem. 27, 75.

Andress & Gundermann (1934), Z. Kristallogr. A87, 345.

Sasvari and Jeffrey (1966), Acta Cryst. 20, 875.

Sugimoto, Dinnebier & Hanson (2007), Acta Cryst. B63, 235.

MS14-P19

Low temperature hydrates of sodium salts

E. Hennings¹, H. Schmidt¹, W. Voigt¹

¹TU Bergakademie Freiberg, Institute of Inorganic Chemistry, Freiberg, Germany

New findings of space expeditions reveal large quantities of salt deposits on Mars^[1-3]. Furthermore there are strong hints for the at least temporarily existence of liquids at Martian temperature conditions, down to 190 K^[4]. In-situ analysis at Phoenix Lander provides evidence for presence of perchlorates in appreciable amounts^[5]. These salt-water systems are known to form cryo-brines with such low freezing temperatures. But in most cases the

hydrate at the eutectic point is unknown and structural characterization is missing. The intention of our research is to determine freezing curves of salt-water systems at low temperature and to crystallize the stable salt hydrates at the eutectic point. In this contribution, we discuss similarities and differences in the crystal structures of sodium chloride, bromide and iodide dihydrate known from literature and compare them with the crystal structure of sodium perchlorate dihydrate which was determined by us. Furthermore we discovered that sodium perchlorate dihydrate forms two low-temperature modifications, of which the crystal structures will be presented. The freezing curves of the considered salt-water-systems are discussed in respect to regularities in the curve progressions, ionic radii and hydration shell formation.

- [1] G. W. Brass, ICARUS 1980, 42, 20 - 28.
 [2] B. C. Clark, D. C. van Hart, ICARUS 1981, 45.
 [3] P. Toulmin, A. K. Baird, B. C. Clark, et al., J. Geophys. Res. 1977, 82, 4625-4634.
 [4] N. O. Renno, B. J. Bos, D. Catling, et al., J. Geophys. Res. 2009, 114, E00E03.
 [5] G. M. Marion, D. C. Catling, K. J. Zahnle, et al., ICARUS 2010, 207, 678-685.

MS14-P20

Synthesis and Crystal structure of 1-(3-cyanopropyl)-3-methylpyridin-1-ium hexachloridoantimonate(V)

J. Zahlbach¹, M. Gjikaj¹

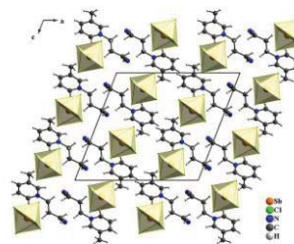
¹Institut für Anorganische und Analytische Chemie, Technische Universität Clausthal, Festkörper- und Koordinationschemie, Clausthal-Zellerfeld, Germany

Antimony pentachloride behaves regularly as a Lewis acidic molecular liquid and it forms with chloride ion donors preferably salts with octahedral [SbCl₆]⁻ units. The hexachloroantimonates(V) with large organic cations as e.g. tetramethylphosphonium, piperidinium and dipropylammonium [1] may be classified into two types: [R]⁺[SbCl₆]⁻ and RSbCl₆ · RCl. Compounds of both types exhibit interesting ferroic (ferroelastic) properties. The mechanism of the relevant phase transitions seems to be complex while both sublattices, cationic and anionic, are involved [2, 3]. Therefore, new [SbCl₆]⁻ compounds and their structural characterization are of interest. Here, we report the synthesis of 1-(3-cyanopropyl)-3-methylpyridin-1-ium hexachloridoantimonate(V), [C₃CNmpy][SbCl₆] (C₃CNmpy = 1-(3-cyanopropyl)-3-methylpyridin-1-ium cation), by single-crystal structure analysis.

The title compound crystallizes in the monoclinic space group P 2₁/c with a = 14.923(2), b = 9.185(1), c = 13.957(2) Å, β = 111.2(1)°, V = 1783.5(3) Å³ and with four formula units in the unit cell. The structure consists of alternating layers of [C₃CNmpy]⁺ cations and octahedral [SbCl₆]⁻ anions (Fig. 1).

[SbCl₆]⁻ shows the expected octahedral O_h arrangement with Sb-Cl bond distances from 2.354 to 2.375 Å, the cis-Cl-Sb-Cl angles range from 89.0 and 90.7°, and trans-Cl-Sb-Cl angles of 178.3 and 179.6°. These values agree very well with those observed in other hexachloridoantimonate(V) salts [4].

- [1] B. Kulicka, R. Jakubas, B. Bednarska-Bolek, G. Bator, Z. Ciunik, J. Mol. Struct. 792 (2006) 151.
 [2] B. Bednarska-Bolek, Z. Ciunik, R. Jakubas, G. Bator, P. Ciapala, J. Phys. Chem. Solids 63(2002) 507.
 [3] B. Bednarska-Bolek, R. Jakubas, G. Bator, J. Baran, J. Mol. Struct. 614(2002) 151.
 [4] T. Xie, W. Brockner and M. Gjikaj, Z. Anorg. Allg. Chem. 635(2009) 1036.



MS14-P21

The Crystal Structure of the Hydrated Acid (H₃O)₂[B₁₂(OH)₁₂] · 3 H₂O Displaying the Dodecahydroxo-*closo*-Dodecaborate Anion

L.W. Zimmermann¹, T. Schleid¹

¹University of Stuttgart, Institute for Inorganic Chemistry, Stuttgart, Germany

Since the first synthesis of the [B₁₂(OH)₁₂]²⁻ anion in 1999 [1] the structure of only a few salts containing this anion have been characterized by X-ray diffraction techniques [2-4]. In 2001 Peymann *et al.* reported several salts of monovalent cations with the dodecahydroxo-*closo*-dodecaborate anion [2]. In this work even the free acid (H₃O)₂[B₁₂(OH)₁₂] was mentioned as stable compound with bad water solubility, but until now the crystal structure remained unknown. We have finally succeeded in the synthesis of single crystals of the free acid as trihydrate and its structural characterization. (H₃O)₂[B₁₂(OH)₁₂] · 3 H₂O was obtained by acidifying a solution of Cs₂[B₁₂(OH)₁₂] · 2 H₂O with hydrochloric acid and a colourless solid precipitated immediately. The reaction mixture was stirred at room temperature for 12 hours and colourless crystals of rectangular shape were then isolated by filtration. The title compound crystallizes in the orthorhombic system with the non-centrosymmetric space group *Iba*2 (*a* = 1503.58(9), *b* = 722.01(4), *c* = 1475.79(8) pm, *Z* = 4). The [B₁₂(OH)₁₂]²⁻ anions (point symmetry: *2m*.) are only slightly distorted from their ideal icosahedral symmetry exhibiting interatomic distances between neighbouring boron atoms in the range of 177 - 182 pm and B-O-distances from 141 to 147 pm. The [B₁₂(OH)₁₂]²⁻ anions and the three crystallographically different water molecules form a plethora of hydrogen bonds. So two pairs of the water molecules build up a zigzag chain, held together by hydrogen bonds between them. These chains are separated by the cluster anions displaying very strong bridging hydrogen bonds (*d*(O...O) = 275 - 282 pm) between the hydroxo substituents and the water molecules of the zigzag chains. Between the anions themselves an additional H₂O molecule is situated (Fig. 1), which separates the highly charged [B₁₂(OH)₁₂]²⁻ anions, so the repulsion between two anions gets reduced. The two protons, which are necessary for the charge balance, can not be localized at two out of five particular water molecules, but build up further hydrogen-bond systems between these water molecules and [B₁₂(OH)₁₂]²⁻ anions (Fig. 2), which stabilize the structure considerably and are one reason for the poor water solubility of the new acid.

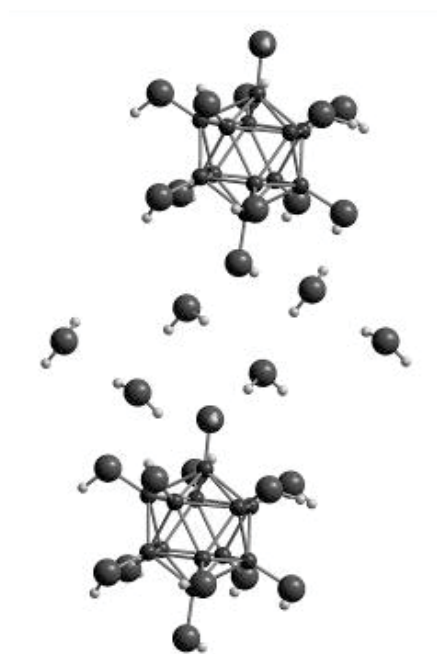
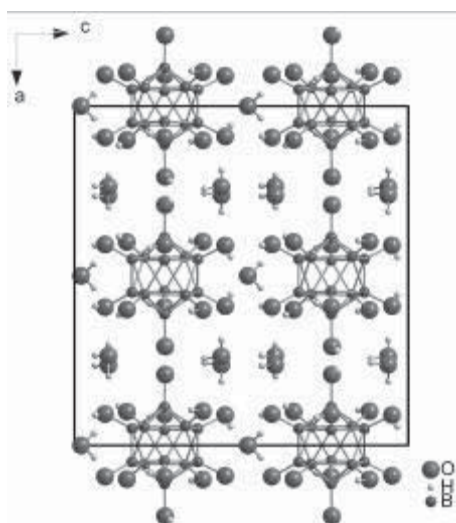
Figure 1: Unit cell of (H₃O)₂[B₁₂(OH)₁₂] · 3 H₂O.

Figure 2: Detail of the zigzag chains of water molecules with coordinating [B₁₂(OH)₁₂]²⁻ anions.

Literature:

- [1] T. Peymann, A. Herzog, C. B. Knobler, M. F. Hawthorne, *Angew. Chem. Int. Ed.* **1999**, 38, 1062.
 [2] T. Peymann, C. B. Knobler, S. I. Kahn, M. F. Hawthorne, *J. Am. Chem. Soc.* **2001**, 123, 2182.
 [3] Th. Schölkopf, Ng.-D. Van, Th. Schleid, *Inorg. Chim. Acta* **2011**, 374, 181.

[4] L. W. Zimmermann, Th. Schleid, *Z. Kristallogr.* **2011**, *Suppl.* *31*, 98.



MS14-P22

Novel Amides and Amines of Gallium: A Brief Discussion on Synthesis and Their Crystal Structures

S. Zhang¹, R. Niewa¹

¹University of Stuttgart, Institute for Inorganic Chemistry, Stuttgart, Germany

Amide (-NH₂) compounds of group IIIA elements are regarded as potential precursors for conversion to group IIIA nitrides. Gallium amides are prone to eliminating ammonia by stepwise thermal deamination and forming GaN. A new gallium amide compound disodium-tetraamido-gallate-amide [Na₂Ga(NH₂)₄]NH₂ was separated and obtained as single crystals from the products after heating Ga and NaNH₂ under temperature of 580 °C and pressure of 1.3 kbar for 48 hours in supercritical ammonia. The crystal structure was refined as an orthorhombic lattice with space group *Pnma* (No. 62). Each Ga atom was in tetrahedral coordination with NH₂⁻ ions. Due to the site disorder of the Na atoms, two 8d sites in the lattice were respectively half occupied by Na(1) and Na(2) (**Figure 1 (a)**). Twin sets of edge-shared tetrahedral chains of Na1 and Na2 coordinated with surrounding NH₂⁻ interlace and form columns running along [010] direction (**Figure 1 (b)**). The bond

lengths of Ga-N in Ga(NH₂)₄⁻ tetrahedron (1.9183(3) Å, 1.9233(3) Å) are close to those in gallium ternary amide compound NaGa(NH₂)₄^[1].

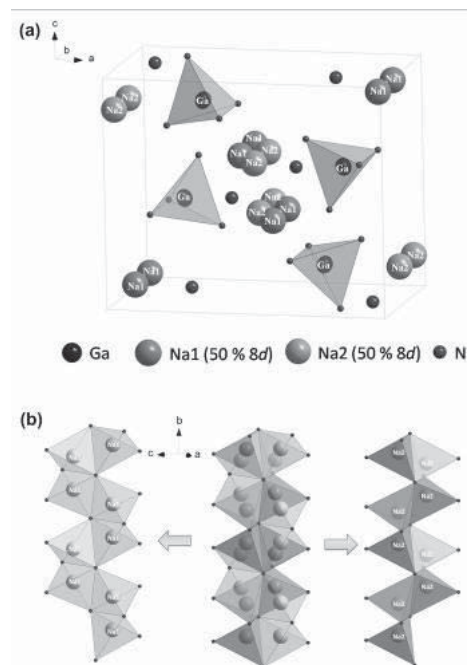
Differed from BX₃ (X = Cl, Br, I) which usually experience ammonolysis in liquid ammonia and give amides^[2, 3], GaX₃ (X = Br, I) tend to be ammoniated and form amines in a wide temperature range (from -76 °C up to R.T.). Colorless crystals of hexamine-gallium-halide-monoamine [Ga(NH₃)₆]X₃·NH₃ (X = Br, I) were obtained from GaX₃ (X = Br, I) in liquid ammonia regardless of the addition of ammonia halides. The single crystal of its aluminum analogue [Al(NH₃)₆]I₃·NH₃ was firstly obtained ammonothermally (120 °C, 90 bar)^[4]. Both crystals exhibit a same structure: cationic [Ga(NH₃)₆]³⁺ forming octahedral coordination geometry in the unit cell; each triangular facet of [Ga(NH₃)₆]³⁺ octahedra is capped by either an iodide/bromide ion (75 %) or N(5) ion (25 %), and thus seven iodide/bromide ions and one N(5) ion forming distorted cube cages corner-shared or edge-shared with each other in the way as shown in **Figure 2**.

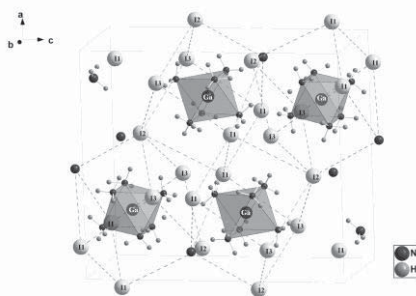
Figure 1: **(a)** The crystal structure of [Na₂Ga(NH₂)₄]NH₂ in a unit cell with indications of Ga(NH₂)₄⁻ tetrahedra and site disorder of Na; **(b)** a column of two sets of edge-shared tetrahedra [Na_n(NH₂)_{2n+2}]⁽²⁺ⁿ⁾⁻.

Figure 2: The crystal structure of [Ga(NH₃)₆]I₃·NH₃ in a unit cell with indication of [Ga(NH₃)₆]³⁺ octahedra and second order coordinations of Ga to I and N forming distorted cubes.

References:

- [1] H. Jacobs, B. Nocker, *Z. Anorg. Allg. Chem.* **1993**, *619*, 381.
- [2] A. Joannis, *Compt. Rend.* **1902**, *135*, 1106.
- [3] W. J. McDowell, C. W. Keenan, *J. Am. Chem. Soc.* **1956**, *78*, 2069.
- [4] D. Peters, J. Bock, H. Jacobs, *J. Less-Common Met.* **1989**, *154*, 243.





MS14-P23

La_{10.25}O_{0.25}N_{0.75}Se₁₄: The First Lanthanum Oxide Nitride Selenide with a Stuffed Pr₁₀OS₁₄-Type Structure and Subtle Interactions of La³⁺ Cations
C.M. Schurz¹, T. Schleid¹¹University of Stuttgart, Institute for Inorganic Chemistry, Stuttgart, Germany

Recently, lanthanide oxide nitride sulfides with the general composition M_{10+x}O_{1-3x}N_{3x}S₁₄ could be obtained as recurrent by-product with a stuffed Pr₁₀OS₁₄-type structure [1]. Here we present the correlated isotopic crystal structure of the first selenide representative La_{10.25}O_{0.25}N_{0.75}Se₁₄ (tetragonal, *I*₄/*acd*, *a* = 1598.56(7), *c* = 2107.62(9) pm, *Z* = 8, further information displayed in Figure 1 and on quoting CSD-423895 at FIZ Karlsruhe: crysdata@fiz-karlsruhe.de). Due to the higher charged light anions (*L*) in the centers of the isolated [(O_{0.25}N_{0.75})(La2)₄]^{9.25+} tetrahedra (see Figure 2, *left*), which are embedded in a lanthanum-selenide matrix, slightly smaller bond (*d*(L-(La2)³⁺) = 242 pm) and edge lengths (*d*((La2)⋯(La2')) = 391 pm, 4×; *d*((La2)⋯(La2')) = 403 pm, 2×) occur in the title compound as compared to the pure lanthanum oxide selenide La₁₀OSe₁₄ (*d*(O-(La2)³⁺) = 245 pm and *d*((La2)⋯(La2)) = 397 pm, 4×; *d*((La2)⋯(La2')) = 408 pm, 2×) [2, 3]. The nitride implementation causes additional cations for electroneutrality resulting in subtle interactions between the three crystallographically independent atoms La3, La4 and La5. Initially, short distances between La3 and La4 (304 pm) necessitate an underoccupation of both atoms following the factors (1-*x*) for La3 situated at the *Wyckoff* position 16*f* and *x* for La4 located at 8*b*. Furthermore, La5 occupies the 16*f* site with the factor *x* as well and exhibits longer separations from La4 (346 pm). This arrangement can be interpreted as a “sidestep” of *x*(La3) to *x*(La5) owing to the occupation of *x*(La4) by the reason of the partial substitution of O²⁻ with N³⁻ anions (Figure 2, *right*). Hence, La3 and La5 bind the same selenide anions (two of each four different Se²⁻ species), but with different bond lengths (*d*(Se-(La3)) = 299 - 323 pm and *d*(Se-(La5)) = 281 - 330 pm). Along with the small bond lengths between Se²⁻ and La³⁺ in La_{0.84}Mo₆Se₈ (289 pm) [4] the value of 281 pm for the shortest bond between Se²⁻ and (La5)³⁺ here represents the smallest that ever has been observed in ionic compounds of this kind.

Figure 1: Fractional Atomic Parameters and *U*_{eq} Values for La_{10.25}O_{0.25}N_{0.75}Se₁₄.

Figure 2: Isolated [(O_{0.25}N_{0.75})(La2)₄]^{9.25+} tetrahedron with all peripheric La³⁺-Se²⁻ bonds (*left*) and view at the square antiprism [(La4)Se₈]¹³⁻ with the subtle interplay between the three La³⁺ species La3, La4 and La5 (*right*).

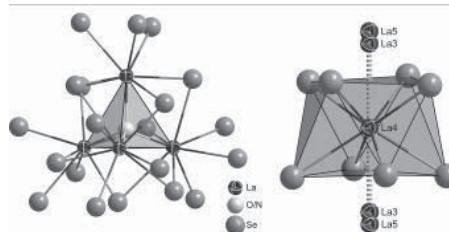
References:

- [1] C. M. Schurz, Doctoral Thesis, University of Stuttgart, **2011**;
M. Meyer, F. Lissner, S. Strobel, P. Talmon-Gros, C. Hoch, Th. Schleid, *Z. Naturforsch.* **2012**, in preparation.
[2] F. A. Weber, Doctoral Thesis, University of Stuttgart, **1999**.
[3] W. Libin, H. Fuqiang, *Z. Kristallogr. - NCS* **2007**, 222, 175.

[4] F. le Berre, O. Peña, C. Perrin, M. Sergent, R. Horyn, A. Wojakowski, *J. Solid State Chem.* **1998**, 136, 151.

atom	Wyckoff site	<i>x/a</i>	<i>y/b</i>	<i>z/c</i>	s.o.f.	<i>U</i> _{eq} ^{a)} /pm ²
La1	32g	0.12946(3)	0.02888(3)	0.04710(2)	1	107(1)
La2	32g	0.37235(3)	0.25687(3)	0.06113(2)	1	124(1)
La3	16 <i>f</i>	0.1346(7)	<i>x/a</i> + 1/4	1/2	0.75(5)	91(10)
La4	8 <i>b</i>	0	1/2	1/2	0.26(5)	101(12)
La5	16 <i>f</i>	0.1540(18)	<i>x/a</i> + 1/4	1/2	0.25(5)	96(22)
O/N	8 <i>a</i>	0	1/2	3/8	1	81(24)
Se1	32g	0.02371(5)	0.38251(5)	0.00420(4)	1	157(2)
Se2	32g	0.34116(5)	0.07371(5)	0.09228(4)	1	135(2)
Se3	32g	0.03702(5)	0.07180(5)	0.17162(4)	1	110(2)
Se4	16 <i>e</i>	0.35178(7)	0	1/2	1	106(2)

^{a)} *U*_{eq} = 1/3(*U*₁₁ + *U*₂₂ + *U*₃₃).



MS14-P24

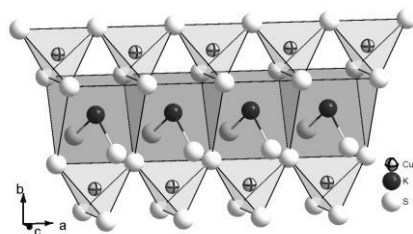
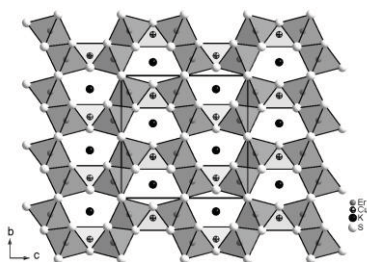
The First Quaternary Potassium Copper Erbium Sulfide: KCuEr₂S₄
M.A. Eberle¹, T. Schleid¹¹University of Stuttgart, Institute for Inorganic Chemistry, Stuttgart, Germany

Three different structure types have been identified in the quaternary systems of potassium, copper, rare-earth metals and sulfur: KCuLn₂S₄ (*Ln* = Gd [1]; *Ln* = Y, Nd, Sm, Tb, Ho [2]), K₂Cu₄Ln₄S₉ (*Ln* = Dy, Ho [2]) and KCuEu₂S₆ [3]. Each one is known just for a few representatives of the rare-earth metals. Despite other alkali-metal copper erbium sulfides already exist with caesium (CsCu₃Er₂S₅ [4]) and rubidium (RbCu₃Er₂S₅ [5]), the combination with potassium and erbium can not be found in the literature up to now. Thus we here report on the structure of the very first compound containing potassium and the lanthanoid erbium: KCuEr₂S₄. Orange coloured, needle shaped single crystals of KCuEr₂S₄ (orthorhombic, *Cmcm*; *a* = 392.47(2), *b* = 1329.75(7), *c* = 1368.81(7) pm; *Z* = 4, further information on quoting CSD-423714 at the FIZ Karlsruhe: crysdata@fiz-karlsruhe.de) could be obtained by the reaction of the elements Cu, Er and S in a molar ratio of 4 : 4 : 9 along with an excess of KCl as fluxing agent and potassium source. This mixture was heated up to 850 °C in an evacuated silica ampoule and kept at this temperature for 8 days. The title compound with six crystallographically different atoms, namely one K, one Cu, one Er and three S, crystallizes isotypically to the KCuLn₂S₄-series members [1, 2], KCuGd₂S₄ in particular [1]. The Er³⁺ cations are surrounded by six S²⁻ anions in the shape of octahedra (*d*(Er³⁺-S²⁻) = 269 - 279 pm). These slightly distorted [ErS₆]⁹⁻ units get connected via *trans*-oriented edges to form chains along [100]. Another linkage by common vertices yields strands of double chains, which are fused to corrugated layers parallel (010) by sharing common edges again. Finally, these layers become condensed to a three-dimensional framework leaving large tunnels parallel to the *a*-axis behind (Figure 1). The Cu⁺ cations fill these channels partly ending up in a tetrahedral surrounding of copper by four S²⁻ anions. The bond lengths of 233.4 pm (2×) and 233.6 pm (2×), respectively, as well as the bond angles of 108.1° - 114.3° are fairly close to an ideal tetrahedron. Since these [CuS₄]⁷⁻ units share common vertices, straight chains occur in the [100] direction (Figure 2), situated within the tunnels of the three-dimensional [Er₂S₄]²⁻ framework. Secondly, the remaining amount of space is filled with K⁺ cations, which are all coordinated by eight sulfide anions in the shape of biccapped trigonal prisms (Figure 2). The K⁺-S²⁻ bond lengths within the prisms are shorter (308 pm (2×) to 321 pm (4×)) as compared to those for the caps (371 pm (2×)).

Figure 1: The three-dimensional $[\text{Er}_2\text{S}_4]^{2-}$ framework in the crystal structure of KCuEr_2S_4 with tunnels filled by K^+ and Cu^+ cations.
 Figure 2: Chains of vertex-shared $[\text{CuS}_4]^{7-}$ tetrahedra along $[100]$ attached to the strands of (bicapped) trigonal prisms surrounding the K^+ cations in the crystal structure of KCuEr_2S_4 .

References:

- [1] P. Stoll, P. Dürichen, C. Näther, W. Bensch, *Z. Anorg. Allg. Chem.* **1998**, 624, 1807.
 [2] J. Yao, B. Deng, D. E. Ellis, J. A. Ibers, *J. Solid State Chem.* **2003**, 176, 5.
 [3] P. Dürichen, W. Bensch, *Chem. Ber.* **1996**, 129, 1489.
 [4] P. Lauxmann, Th. Schleid, *Z. Naturforsch.* **2001**, 56b, 1149.
 [5] F.-Q. Huang, J. A. Ibers, *J. Solid State Chem.* **2001**, 158, 299.



MS14-P25

The anomalous annealing behaviour of Eifel sanidines Status quo and new approach with neutron diffraction

J. Kähn¹, S. Schorr¹

¹Helmholtz-Zentrum Berlin, Kristallographie (M-A3), Berlin, Germany

Sanidines $(\text{K},\text{Na})[\text{AlSi}_3\text{O}_8]$ are alkali feldspars, part of the solid solution series Albite - Orthoclase and their typical composition is in a range between $\text{Al}_{35}\text{Or}_{65}$ and $\text{Al}_{15}\text{Or}_{85}$. The monoclinic tectosilicate occurs at two different modifications, low- and high-sanidine, mainly differing in their Al/Si distribution. Reordering is usually acquired by long-term-annealing (>1000h) at temperatures of 900°C and above, but with sanidine megacrystals from Eifel it's possible to reach much faster Al/Si disordering within short annealing time and starting temperatures around 700°C. Although numerous attempts and studies were carried out, the exact reasons for this anomalous behavior still remains unknown.

We want to outline the current status quo of research about this phenomenon as well as introduce our new approach, where we investigate the structure of Eifel sanidines with neutron diffraction experiments, in particular the Al/Si distribution. We will try to

determine the cause and figure out possible catalysts or catalytic mechanics of this unusual annealing behavior.

MS14-P26

Practical considerations concerning the efficient use of resonant X-ray scattering for distinguishing elements with similar electron count

S. Welzmler¹, P. Urban¹, F. Fahrnbauer², L. Erra³, O. Oeckler^{1,2}

¹IMKM Leipzig, Chemie, Leipzig, Germany

²LMU München, Chemie, München, Germany

³ESRF, Grenoble, France

The X-ray scattering contrast of elements with similar atomic numbers can be enhanced by resonant scattering using synchrotron radiation. As beamtime is costly, efficient strategies are important to obtain many datasets and to ensure that they yield reliable results.

The classical d synthesis, i. e. a difference Fourier map from data collected at the low-energy side of the absorption edge of the element with the lower absorption-edge energy and an additional one far from all edges exhibits some weak points.^[1] It is not applicable to distinguish more than two elements and the anomalous dispersion correction term ($\Delta f'$) were often taken from databases although they depend on the chemical environment and change significantly near the edge energy which may not be known very accurately. However, if wavelengths slightly off the edges are used, the resonance effect is not maximal.

Based on our investigations of Sn-Sb-Te compounds,^[2,3] we measured test samples where the element distribution is obvious. Synchrotron data (ESRF, beamline ID11) were acquired at the Sb, Sn, Te and In absorption edges of CrSbSe_3 , SnSe_2 , PbTe and InSeI , respectively. The refined $\Delta f'$ values were used to confirm the (obvious) element distribution in SnTe and Sb_2Te_3 . In order to assess this “ $\Delta f'$ calibration” method, we chose compounds with a similar chemical bonding situation. In addition, $\Delta f'$ was measured by X-ray fluorescence and $\Delta f'$ was calculated using the Kramers-Kronig transform (CHOOCH^[4]). The refined $\Delta f'$ and those from fluorescence data agree well, but often differ significantly (~2 electrons) from those taken from various databases. Refinements using the $\Delta f'$ -values from different sources show that the $\Delta f'$ from accurate fluorescence spectra yield excellent R values. In the case of noisy spectra the refined values from “calibration crystals” are suitable and also provide a good alternative if a fluorescence detector is not available. The best refinement strategy, also for more complicated compounds like $(\text{Ge},\text{Sn})_2\text{Sb}_2\text{Te}_5$, is a simultaneous refinement on datasets collected at all relevant edges and additionally far from them (JANA2006^[5]). The latter can be laboratory data. Refining both $\Delta f'$ and the site occupancies yields rather large standard deviations due to correlations which can be reduced by sum formula restraints. All approaches suggest that it is best to measure as close to all edges as possible in order to obtain a large resonant effect. This is no problem if neither database values are required nor a δ synthesis is attempted. Absorption corrections did not prove problematic.

[1] R. Wulf, *Acta Crystallogr. A*, **1990**, 46, 681.

[2] O. Oeckler, M. N. Schneider, F. Fahrnbauer, G. Vaughan, *Solid State Sci.* **2011**, 13, 1157.

[3] M. N. Schneider, F. Fahrnbauer, T. Rosenthal, M. Döblinger, C. Stiewe, O. Oeckler, *Chem-Eur. J.* submitted.

[4] G. Evans, R. F. Pettifer, *J. Appl. Crystallogr.* **2001**, 34, 82.

[5] V. Petricek, M. Dusek, L. Palatinus, JANA2006, Prague, **2006**.

MS14-P27

Synthesis and Crystal Chemistry of Manganese Melilites and related Phases

S. Stöber¹, H. Pöhlmann¹¹Martin - Luther - Universität Halle, Institut für Geowissenschaften, Halle, Germany

Melilites with $X_2T''T'O_7$ describe the solid solution series with the end members gehlenite $Ca_2Al_2SiO_7$ and åkermanite $Ca_2MgSi_2O_7$. Principally, gehlenite rich solid solutions are present in SiO_2 containing CAC. But their ability to react with water is not present at ambient temperatures, but these phases start to react at about 40°C [3,4].

The crystal structure of melilites is based on a tetragonal lattice with space group P-42_m, which is built up of twisted T_2O_7 -layers (T = tetrahedral site) with two different tetrahedral sites T' and T'' perpendicular (001). Cations X = Ca link the T_2O_7 -layers [2].

Due to the addition of Manganese rich materials (Mn-ores, secondary raw materials) to the CAC raw meal, Manganese containing melilites crystallize during the sintering process.

In order to investigate properties of Melilite phases, pure phases were synthesised by an optimised glycine combustion sol-gel method [1].

Two different solid solution series $Ca_2Al_{0.6}(Mg_xMn_{0.6-x})Si_{1.7}O_7$ $0.1 \leq x \leq 0.5$ and $Ca_2Al_{1.7-2x}(Mg_{0.7}Mn_{0.3})_xSi_{1.3+x}O_7$ $0 \leq x \leq 1$ were investigated. Due to the synthesis at 1200°C and at least quenching in ice water MnO_2 rich phase assemblages consist of amorphous contents or present purely amorphous material. Furthermore, Mn-rich melilites segregates in two coexisting melilite phases. Structural parameters of pure phases were refined. Both substitution processes influence size, shape and the orientation of T', T'' & CaO_8 polyhedra in the crystal structure.

References:

- [1] Chick, L. A., L. R. Pederson, et al. (1990). "Glycine-nitrate combustion synthesis of oxide ceramic powders." *Materials Letters* 10(1-2): 6-12.
- [2] Röhrlisberger, F. (1989):Zusammenhang Zwischen Chemismus, Stabilität und struktureller Variation der MeliliteDissertation Bayreuth p 178
- [3] Scrivener, K. L. and A. Capmas, A.: Calcium Aluminate Cements. - in P C Hewlett, LEA's Chemistry of Cement and Concrete, 4th Edition, Arnold Publishers, London, pp. 709 - 778, (1998).
- [4] Sorrentino, F. P. & Glasser F. P. (1975): The system $CaO-Al_2O_3 - Fe_2O_3 - SiO_2$ GI. The Pseudoternary Section $Ca_2Fe_2O_5-Ca_2Al_2O_5-SiO_2$ Trans. Br. Ceram. Soc. 74 pp.253-256

MS14-P28

Element distribution and temperature-dependent changes in the crystal structure of $Ge_2Sb_2Te_5$ P. Urban^{1,2}, L. Erra³, F. Fahrnbauer², S. Welzmler^{1,2}, M. Schneider², O. Oeckler^{1,2}¹University of Leipzig, IMKM, Leipzig, Germany²LMU Munich, Department of Chemistry, Munich, Germany³ESRF, Polygone Scientifique Louis Néel, Grenoble, France

$Ge_2Sb_2Te_5$ has received much attention as it is one of the most controversially discussed phase-change materials (PCM) for data storage.[1] The write-erase cycle involves amorphous and metastable crystalline phases; however, the stable phase is an intriguing model system. Its main features have been determined by X-ray powder diffraction.[2] 9P- $Ge_2Sb_2Te_5$ exhibits a trigonal layered structure with 9 alternating cation and anion layers (rocksalt-type block) separated by van der Waals gaps.

Chemical transport reactions now yielded high-quality single crystals of $Ge_2Sb_2Te_5$, which made detailed investigations possible. The element distribution in the structure, which had remained unclear due to the lacking scattering contrast of Sb and Te, was investigated by resonant diffraction with synchrotron radiation

(beamline ID11, ESRF) at the K-absorption edges of Sb and Te. With additional datasets measured far off the absorption edges, a simultaneous refinement on all data (R1 = 0.037) yielded reliable occupancy factors of each element on each position. The dispersion correction terms $\Delta f'$ could be refined and match experimental ones obtained from fluorescence spectra by the Kramers-Kronig transform. Ge prefers the position near the center of the rocksalt-type block ($Ge_{0.60(4)}Sb_{0.36(2)}$), Sb the one near the van der Waals gap ($Ge_{0.33(7)}Sb_{0.66(4)}$). Anti-site disorder is not significant.

During heating up to 471 °C and subsequent cooling, a reversible structural distortion was observed and there was no indication that metastable phases might play a role. A series of datasets was collected at the Sb-K-absorption edge to keep the scattering contrast. The refinements show that with increasing temperature the first anion and cation layers next to the van der Waals gap become slightly detached from the block and resemble a GeTe layer. Thus, the difference between interatomic distances in the 3 + 3 cation coordination sphere becomes more pronounced. Although at ~300 °C cation diffusion is probably easily activated as shown for compounds $(GeTe)_n(Sb_2Te_3)$ with $n \geq 3$, [3] the element distribution did neither change during the experiment nor upon long-time annealing. The cubic high-temperature phase of these compounds, which resembles the metastable one of $Ge_2Sb_2Te_5$, was not observed - probably because of the high vacancy concentration and the resulting low coordination numbers in hypothetical NaCl-type $Ge_2Sb_2Te_5$. All changes in the crystal structure are reversible. Thus, our experiments indicate that the behavior of the single crystals is thermodynamically controlled.

[1] T. Matsunaga, R. Kojima, N. Yamada, K. Kifune, Y. Kubota, Y. Tabata, M. Takata, *Inorg. Chem.* **2006**, *45*, 2235.

[2] T. Matsunaga, N. Yamada, Y. Kubota, *Acta Crystallogr.* **2004**, *B60*, 685.

[3] M. N. Schneider, X. Biquard, C. Stiewe, T. Schröder, P. Urban, O. Oeckler, *Chem. Commun.* **2012**, in print.

MS14-P29

Crystal Structures of Ammonium Halogenidobismuthates(III)

S. Schlöts¹, A.Q. Sachawars¹, W. Poll¹, S. Jörgens¹, W. Frank¹¹Heinrich-Heine-Universität Düsseldorf, Institut für Anorganische Chemie und Strukturchemie II, Düsseldorf, Germany

The only known crystal structures of compounds of the System $NH_4Cl-BiCl_3$ are those of ammonium hexachloridobismuthate(III), $(NH_4)_3BiCl_6$ ^[1], and pentammonium undecachloridobismuthate(III), $(NH_4)_5Bi_2Cl_{11}$ ^[2], which were prepared from stoichiometric amounts of the halides in hydrochloric acid solution. Here we report on the syntheses and the crystal structures of $NH_4Bi_3Cl_{10}$ (**1**) and $(NH_4)_5Bi_4Cl_{17}$ (**2**) as well as $(NH_4)_3Bi_2Br_9$ (**3**) and $(NH_4)_3BiBr_6$ (**4**). Single crystals of **1-4** suitable for X-ray structure analysis were obtained by heating stoichiometric quantities of NH_4X and BiX_3 (X=Cl, Br) to 500 °C in evacuated glass ampoules and adjacent cooling (5 °C/h) to room temperature. Crystallographic data of **1-4** can be found in the table below. The solid of **1** contains three crystallographically independent Bi atoms and can be described as $[Bi_2Cl_7]^- \cdot BiCl_3$ due to substantially varying distances Bi-Cl. In the anionic partial structure of **2** two crystallographically independent $BiCl_6$ units, each slightly distorted octahedral, form layers perpendicular to the crystallographic *c*-axis by sharing corners. Both crystallographically independent Bi atoms of **3** are nearly regular octahedrally coordinated by six Br atoms. The structure can be rationalized as an arrangement of rings of six corner-shared polyhedra, which form waved layers perpendicular to the crystallographic *a*-axis. **4** crystallizes isotypically to the above-mentioned $(NH_4)_3BiCl_6$ ^[1]. The anionic partial structure is composed of two independent and isolated $BiBr_6^{3-}$ octahedra. A yet unexplained significant high residual electron density in a gap of the structure has to be reviewed. According to the shortest $N \cdots X$ distances weak $N-H \cdots X$ hydrogen-bonds in some of the presented crystal structures can be assumed.

Empirical formula	NH ₄ Bi ₃ Cl ₁₀	(NH ₄) ₅ Bi ₄ Cl ₁₇	(NH ₄) ₃ Bi ₂ Br ₉	(NH ₄) ₃ BiBr ₆
Crystal system	Orthorhombic	Monoclinic	Monoclinic	Orthorhombic
Space group;Z	P2 ₁ 2 ₁ 2 ₁ ; 4	C2/c; 4	P2 ₁ /c; 4	Pnma; 8
Unit cell dimensions	a=7.153(1)Å	a=23.895(5)Å	a=19.308(2)Å	a=13.110(2)Å
	b=8.891(2)Å	b=7.323(1)Å	b=7.914(1)Å	b=26.266(6)Å
	c=25.102(5)Å	c=19.211(3)Å	c=13.526(1)Å	c=8.651(1)Å
		β=106.61(2)°	β=90.64(1)°	
R ₁	0.0467	0.0610	0.0593	0.0442
wR ₂	0.1065	0.1301	0.1320	0.0960

[1] I. Belkhal, R. Mokhlisse, B. Tanouti, K.F. Hesse, W. Depmeier, *Eur. J. Solid State Inorg. Chem.* **34**, 1085-1091 (1997).

[2] I. Belkhal, R. Mokhlisse, B. Tanouti, W. Depmeier, *Eur. J. Solid State Inorg. Chem.* **34**, 239-240 (1997).

MS14-P30

Ordered superstructures of Cu_xTa_{1+y}S₂ at low temperatures

S.I. Ali¹, S. van Smaalen¹, B. Harbrecht², S. Zöhrb²

¹University of Bayreuth, Laboratory of Crystallography, Bayreuth, Germany

²Phillipps University, Marburg, Department of Chemistry, Marburg, Germany

Superstructures of transition metal dichalcogenides (MX₂, M=transition metal and X=chalcogen) which occur in several polytypes are of considerable interest in solid state physics and chemistry. The transition metal has trigonal prismatic or octahedral coordination sphere by six chalcogen atoms. These coordination sphere is further connected to neighbouring coordination spheres to form a layered structure. Interaction between atoms within a slab are mainly covalent. Slab to slab interaction are weak, and in general van der Waals types of interaction. Due to this weak interlayer interaction several different slab stacking sequences (crystal polytype) are possible. Intercalation compounds of transition metal dichalcogenides can be formed with a wide range of guest atoms or molecules including alkali metals and transition metals. The intercalated guest atom may be incorporated on octahedral or tetrahedral sites surrounded by chalcogen atoms in the van der Waals gaps. Intercalation of Cu atom in 6R-Cu_xM_{1+y}S₂ shows six sandwiches per unit cell stacked in rhombohedral symmetry [1]. Intercalated Cu atoms and additional M atoms are incorporated on octahedral and tetrahedral sites in the Van der Waals gaps between MS₂ layers. Here we present the evolution of the complex superstructures of selected intercalated compounds at different temperatures between 14K and 400K using single-crystal X-ray diffraction data. The interest in these compounds are structural changes which are associated with phase transitions related to ordering of vacancies on the sites of the intercalated atoms.

[1] Harbrecht B., Kreiner G., *Z. anorg. allg. Chem.*, 572(1989) 47-54

MS14-P31

Structural characterization and discussion of new tetramethylgermane phases from powder data

Y. Krysiak¹, L. Fink¹, E. Alig¹, J. Glinnemann¹, M. Schmidt¹
¹Inorg. Analyt. Chemistry, FB14, Frankfurt, Germany

Until now, no crystal structure of tetramethylgermane, Ge(CH₃)₄ (TMGe, m.p. 185 K, b.p. 317 K), is known but some phases of TMGe have been predicted [1] by lattice energy minimization. In this work we can corroborate the predicted first and second ranked structures and one orthorhombic distorted cubic phase, too (see table 1).

The powder diffraction of TMGe was performed with Cu Kα₁ radiation (λ = 1.54056 Å) using a Stoe Stadi-P diffractometer in transmission mode. The samples, placed in glass or kapton capillaries, were measured over a temperature range from 100 K to 135 K and rotated during the measurements. By variation of the cooling rate or the capillary diameter different phases of TMGe could be crystallized on the diffractometer.

The crystal structures were determined with Direct Methods and Patterson Methods using EXPO [2] or with Simulated Annealing using DASH [3]. The Rietveld Refinement was performed with TOPAS [4].

The crystal structure of the cubic phase (Pa-3, Z = 8) of TMGe is isotopic to the known cubic phases of homologous tetramethylcarbon compounds [5], [6], [7], [8]. The orthorhombic phase (Pbca, Z = 8) of TMGe can be described as a pseudo cubic phase, see figure 1.

In addition, the crystal structure of a second orthorhombic phase (Pnma, Z = 4) was solved, which is isotopic to that of tetramethylsilane [1].

Table 1: Experimental and predicted [1] crystallographic data of TMGe. (* capillary diameter)

Figure 1: Unit cells of TMGe phases, view along [001] (left: Pa-3, right: Pbca, down: Pnma).

[1] Wolf, A. K., Glinnemann, J., Fink, L., Bolte, M. & Schmidt, M. U., *Acta Cryst. Sec. B* **66** (2010), 229-236.

[2] Altomare, A., Camalli, M., Cuocci, C., Giacovazzo, C., Moliterni, C. & Rizzi, R., *J. Appl. Cryst.* **32** (1999), 339-340.

[3] David, W. I. F., Shankland, K., van de Streek, J., Pidcock, E., Motherwell, W. D. S. & Cole, J. C., *J. Appl. Cryst.* **39** (2006), 910-915.

[4] A. A. Coelho: TOPAS-AcademicVersion 4.1, Coelho Software, Brisbane, Australien.

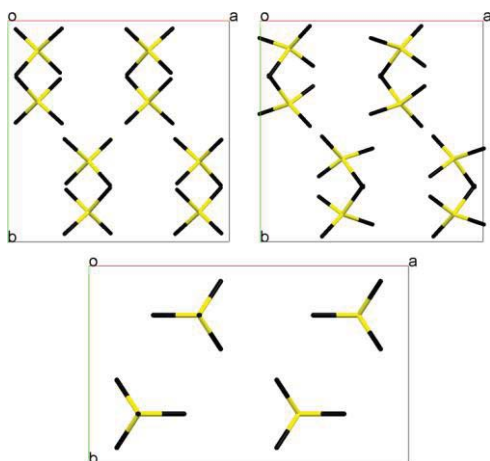
[5] Mones, A. H. & Post, B., *J. Chem. Phys.* **20** (1952), 755-756.

[6] Krebs, B., Henkel G. & Dartmann, M., *Acta Cryst. C* **45** (1989), 1010-1012.

[7] Fleischer, H., Parsons, S. & Pulham, C. R., *Acta Cryst. E* **95** (2003), 86-93.

[8] Gajda, R. & Katrusiak, A., *Cryst. Growth Des.* **8** (2008), 211-214.

	Pa-3, Z = 8		Pbca, Z = 8		Pnma, Z = 4	
	exp.	calc.	exp.	calc.	exp.	calc.
a [Å]	11.0313(6)	11.132	11.1179(2)	11.663	13.273(2)	13.198
b [Å]	-	-	11.0610(2)	11.241	8.202(2)	8.412
c [Å]	-	-	11.0192(2)	10.736	6.3620(9)	6.346
V [Å ³]	1342.4(3)	1379.49	1355.1(4)	1407.53	692.6(4)	704.54
T [K]	103	-	103	-	133	-
d* [mm]	0.8	-	1.0	-	0.7	-


MS14-P32
Structure determination from low-resolution powder diffraction data: Crystal structure of the hydrous silicate RUB-52.

 B. Marler¹, R. Wandolowski¹, Z. Li¹, H. Gies¹
¹*RU Bochum, Inst. für Geologie, Mineralogie und Geophysik, Bochum, Germany*
Introduction:

Hydrous layer silicates, HLS, are an important class of natural minerals as diagenetic and weathering products, but also of industrial interest as adsorbents and precursor materials. We present the crystal structure of a new, synthetic HLS, RUB-52, which was solved from powder diffraction data of limited resolution.

Methods:

RUB-52, $C_6H_{16}N_2[H_2Si_{10}O_{22}]$, was obtained from hydrothermal synthesis as metastable intermediate at 150° C/ 7days from aqueous silicate solution in the presence of dimethyl-diethylammonium (DEDMA) cation as template. Powder X-ray diffraction data were obtained from a capillary-loaded sample at RT with Cu $K\alpha_1$ -radiation in the range from 4 - 60° 2 θ in quasi-Debye-Scherrer mode on a Siemens D5000 Diffractometer. The structure was analysed using DicVol for indexing, TOPAS for structure solution, and FullProf for Rietveld analysis.

Results:

The powder pattern was indexed in triclinic symmetry. Because of the limitation of the diffraction information, direct space structure determination has been carried out using the program TOPAS. The confirmation of the structure model was performed with the FullProf Suite of programs. A summary of the results is given in the table. In the figure a projection of the crystal structure is presented.

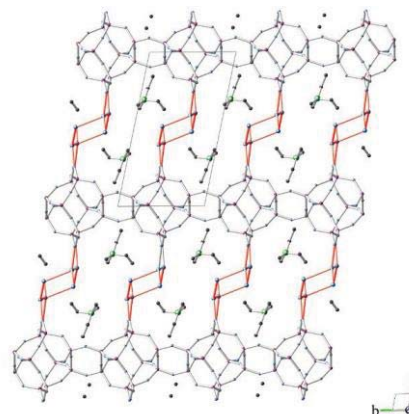
Sample	RUB-52
Number of data points	7174
Number of reflections	620
Lattice parameters in SG P-1 [Å]	$a = 16.095(1), b = 9.496(1), c = 7.284(1)$
	$\alpha = 115.7(1)^\circ, \beta = 104.5(1)^\circ, \gamma = 94.2(1)^\circ$
Peak profile	Thompson-Cox-Hastings pseudo-Voigt * Axial divergence asymmetry
Distance restraints, [Å]	78, ($d(\text{Si-Si}) = 3.08(3), d(\text{Si-O}) = 1.62(1), d(\text{O-O}) = 2.61(4)$)
Number of parameters for refinement	78 structural, 8 profile
Conventional Rietveld R-factors	Rwp = 6.9, Rexp = 3.7, $\chi^2 = 3.5, R_{\text{Bragg}} = 2.3$

Discussion:

The silicate layer is built from the $[4^25^4]$ -subunit already known from the heulandite layer, however in a different connectivity. Hydrogen-bonded water molecules connect neighboring layer and provide residual space for the DEDMA-template. The full pattern Rietveld refinement yields bond distances and angles within the expected range.

The example nicely shows that low resolution X-ray powder data still provide enough information for structure solution and complete structure refinements.

Fig.: Projection of the crystal structure of RUB-52 showing the silicate layer connected via hydrate water. The voids are filled by dimethyl-diethylammonium cation for charge compensation.


MS14-P33
Anhydrous Sodium Trifluoroacetate - A 3D coordination polymer with 15 molecules in the asymmetric unit of the crystal structure

 G. Genchev¹, W. Frank¹
¹*Heinrich-Heine-Universität, Institut für Anorganische Chemie und Strukturchemie Lehrstuhl II, Düsseldorf, Germany*

The knowledge concerning the alkali metal salts of the trifluoroacetic acid (TFA) is limited especially with respect to structural aspects. 1965 Golic and Speakman reported on the acid salts $MH(\text{CF}_3\text{CO}_2)_2$ ($M = \text{K}, \text{Rb}, \text{or Cs}$) [1]. 2009 an 2:1 adduct of TFA with sodium trifluoroacetate was described by Pietsching and co-workers [2]. So far, no method for the preparation of well-crystallized unsolvated sodium trifluoroacetate was described. Here we report on the single-crystal preparation and structure determination of $\{\text{Na}(\mu\text{-O}_2\text{CCF}_3)\}_x$ (1).

Single-crystals of the colourless 1 were prepared by recrystallization of "Na(O₂CCF₃)" powder in acetonitrile in the presence of the highly water attracting Lewis-acid aluminium trifluoroacetate. 1 crystallizes in the triclinic space group P-1 ($a = 12.803(3) \text{ \AA}, b = 13.961(3) \text{ \AA}, c = 20.005(4) \text{ \AA}, \alpha = 81.19(3)^\circ, \beta = 72.25(3)^\circ, \gamma = 81.34(3)^\circ; T = 173 \text{ K}; Z = 30; R_1 = 0.063, wR_2 = 0.112, 11592 \text{ reflexes}, 1081 \text{ parameters}$). The asymmetric unit contains 15 molecular fragments forming a 3D network with complicated topology that does not contain any kind of oligomeric quasi-molecular cages. 1 seems to be the first structure with a true $Z' = 15$ value. The CF_3CO_2^- ligands within the network coordinate to the sodium cations quite different in μ^3 to μ^6 bridging modes (Na-O distances from 2.1998(5) to 2.9481(8) Å) with most of the individual oxygen atoms two- (μ^2) and the rest three-coordinate (μ^3) [3]. Taking into account the Na-F contacts (2.4297(9) - 2.9240(7) Å), the resulting coordination numbers for sodium vary from 4 to 7.

[1] L. Golic, J. C. Speakman, J. Chem. Soc. 1965, 2530-2542.

[2] S. Spirk, F. Belaj, J. Kahr, R. Pietsching, J. Fluorine Chem. 2009, 130, 365-367.

[3] G. B. Deacon, R. J. Phillips, *Coord. Chem. Rev.*, 1980, 33, 227-250.

MS14-P34

Average structure of a new hydrous layered TMA-silicate, RUB-55, with silicate layers representing a section of the sodalite as well as octadecasil framework.

B. Marler¹, A. Grünwald-Lüke¹, S. Grabowski¹, H. Gies¹

¹Ruhr University Bochum, Geology, Mineralogy and Geophysics, Bochum, Germany

Hydrous Layer Silicates (HLSs) have some important applications and, in addition, represent structurally interesting materials since many of them are constructed from layers of the same topology as the layer-like building units of framework silicates. It is, therefore, instructive to compare structures and synthesis conditions of these related materials.

RUB-55 was synthesized at 160°C as very thin, colorless, intergrown plates from a simple reaction mixture of SiO₂ / TMAOH / H₂O. X-ray powder diffraction data of the sample were collected at 295 K using a Siemens D5000 diffractometer with CuKα1 radiation. The material was further characterized by SEM, TG-DTA, solid state NMR and FTIR spectroscopy.

The XRD powder pattern of as-made RUB-55 was indexed in tetragonal symmetry with unit cell parameters $a_0 = 8.79 \text{ \AA}$ and $c_0 = 14.65 \text{ \AA}$. The average structure was solved by model building based on the results of the general characterization. Rietveld refinement in space group P-42₁m converged to residual values $R_{\text{Bragg}} = 0.038$ and $R_F = 0.036$ confirming the structure model. The profile fit is less good ($\chi^2 = 7.9$) due to anisotropic peak broadening and a very slight deviation of the atomic arrangement from the average structure described here. The anisotropic broadening of the reflexions indicates a slight disorder of the structure. A deviation from a strictly regular layer stacking along [001] is typical for HLSs with weak interactions between neighboring layers. A careful analysis of the powder pattern revealed a few very weak reflections which indicated the existence of a superstructure with $c_0 = 29.3 \text{ \AA}$.

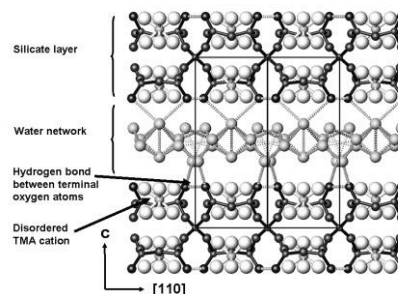
The silicate layers of RUB-55 are made up of 4- and 6-rings forming a sheet of interconnected cup-shaped voids which point alternatively up and down. The cups can be described as cut-open [4⁶6⁸]-cages of the sodalite type or as halved [4⁶6¹²]-cages forming the octadecasil framework. Consequently, the layers represent a section of either the framework structure of sodalite or octadecasil [1]. The structure of RUB-55 is completed by tetramethylammonium cations (TMA) which occupy the half-cages and by a sheet of hydrogen-bonded water molecules intercalated between neighboring silicate layers (Fig.1).

The ¹H, ¹³C and ²⁹Si NMR spectra confirm the results of the X-ray structure analysis. The ¹H spectrum displays a strong signal at 3.5 ppm attributed to the protons of the TMA cation and of the water molecules, and a weak broad signal centered at 15.5 ppm corresponding to strong hydrogen bonds with an O...O distance of about 2.5 Å. The structure of RUB-55 with unit cell content [Si₁₀O₁₈(OH)₆]₂ * 2 C₄H₁₂N * 16 H₂O is related to the structures of HUS-1 [2] and helix-layered silicate [3].

References:

- [1] P. Cautlet, J.L. Guth, J. Hazm, J.M. Lamblin, H. Gies, *European J. Solid State and Inorganic Chemistry* 28, 345-361, 1991.
 [2] T. Ikeda, Y. Oumi, K. Honda, T. Sano, K. Momma, F. Izumi, *Inorg. Chem.* 50, 2294-2301, 2011.
 [3] T. Ikeda, Y. Akiyama, F. Izumi, Y. Kiyozumi, F. Mizukami, T. Kodaira, *Chem. Mater.* 13, 1286-1295, 2001.

Fig. 1: (110)-Projection of the structure of RUB-55. Hydrogen bonds are displayed as dashed lines.



MS14-P35

Synthesis and Crystal Structure of AgErS₂ and AgTmS₂

S. Strobel¹, B. Spohn¹, T. Schleid¹

¹University of Stuttgart, Institute for Inorganic Chemistry, Stuttgart, Germany

Single crystals of AgErS₂ and AgTmS₂ are obtained by the oxidation of the corresponding metals (silver and erbium or thulium) with elemental sulfur (molar ratios: 1:1:2) in the presence of NaBr as fluxing agent after several days at 900 °C in evacuated fused silica ampoules. They crystallize as orange- or yellow-coloured cubes or square platelets in the tetragonal space group *I4₁md* (no. 109) with $a = 538.94(3) \text{ pm}$, $c = 1190.15(8) \text{ pm}$, $c/a = 2.208$ for AgErS₂ and $a = 536.41(3) \text{ pm}$, $c = 1184.06(8) \text{ pm}$, $c/a = 2.207$ for AgTmS₂ ($Z = 4$, further information in Figure 1 and on quoting CSD-423921 for AgErS₂ and CSD-423922 for AgTmS₂ for AgTmS₂ at FIZ Karlsruhe: crysdata@fiz-karlsruhe.de). Their crystal structure can be best described as a stuffed anatase-type arrangement, in which [LnS₆]⁹⁻ octahedra ($d(\text{Ln-S}) = 261 - 278 \text{ pm}$, Figure 2) share common edges (4×) and corners (6×) within the cubic close S²⁻-anion packing. Thus, half of the octahedral interstices get filled with Ln³⁺ cations and the other half could be stuffed with Ag⁺ cations according to the α-LiFeO₂-type structure [1] (Figure 2) in the centrosymmetric tetragonal space group *I4₁amd* (no. 141). However, the demand of Ag⁺ for a lower coordination number (CN = 5 instead of 6) is better satisfied in the non-centrosymmetric space group *I4₁md*, hence providing square pyramids ($d(\text{Ag-S}) = 269 - 283 \text{ pm}$, Figure 2) as suitable coordination polyhedra, while the sixth S²⁻ ligand that completes this sphere to an octahedron shows up more than 365 pm apart. The same description of the crystal structure has been given for AgYbS₂ ($a = 535.6 \text{ pm}$, $c = 1180.3 \text{ pm}$, $c/a = 2.204$) before [2], whereas the analogous copper compounds CuLnS₂ ($\text{Ln} = \text{Er, Tm and Yb}$) [3] crystallize with the CuYS₂-type structure (orthorhombic, *Pnma*) [4] offering a tetrahedral coordination of sulfur for the Cu⁺ cations ($d(\text{Cu-S}) = 228 - 251 \text{ pm}$) within the ramsdellite-type arrangement of edge- and corner-connected [LnS₆]⁹⁻ octahedra ($d(\text{Ln-S}) = 263 - 277 \text{ pm}$). As already mentioned in [2], all three tetragonal AgLnS₂ phases with $\text{Ln} = \text{Er, Tm and Yb}$ should be addressed as low-temperature modifications revealing cubic high-temperature forms with the aristotypic rock-salt structure of NaCl (*halite: Fm3m*) [5].

Figure 1: Fractional Atomic Parameters and U_{ij} Values^{a)} (in pm²) for AgErS₂ and AgTmS₂.

Figure 2: Square pyramids [AgS₅]⁹⁻ (left) and [LnS₆]⁹⁻ octahedra (right) in the α-LiFeO₂-related crystal structure of AgLnS₂ ($\text{Ln} = \text{Er, Tm and Yb}$) (bottom).

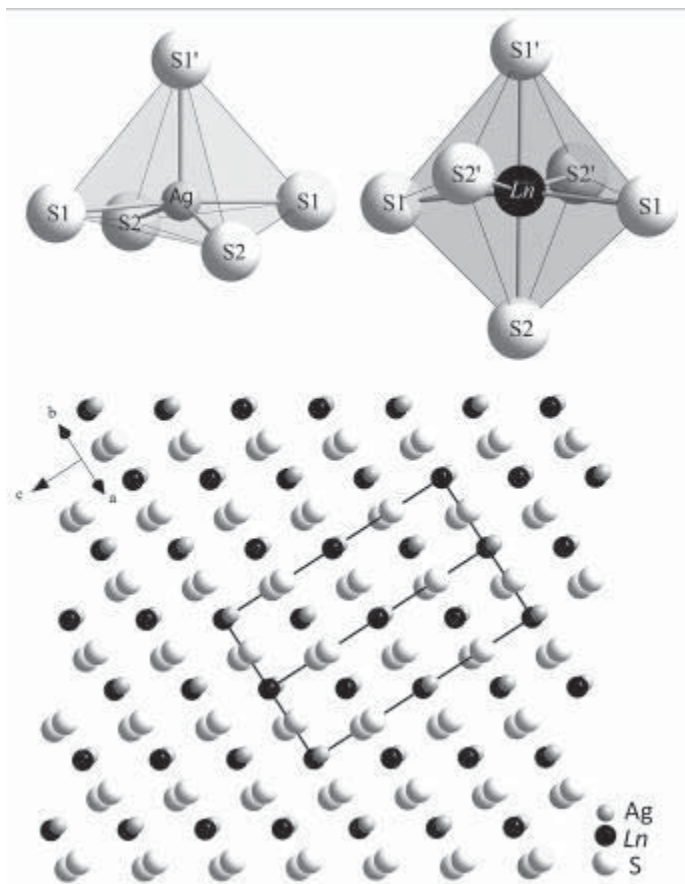
References:

- [1] F. F. Barblan, *Schweizer. Mineral. Petrogr. Mitt.* 1943, 23, 295.
 [2] R. Ballestracci, *Compt. Rend. Hebd. Seanc. Acad. Sci.* 1966, C 262, 1253.
 [3] S. Strobel, Th. Schleid, *Z. Naturforsch.* 2007, 62 b, 15.
 [4] P. Lauxmann, Th. Schleid, *Z. Anorg. Allg. Chem.* 2000, 626, 1608.

[5] A. van der Lee, R. van de Belt, G. A. Wiegers, *J. Alloys Compds.* **1992**, 178, 57.

atom	Wyckoff site	x/a	y/b	z/c	U_{11}	U_{22}	U_{33}
AgErS₂							
Ag	4a	0	0	0.46951(16)	543(11)	355(10)	471(12)
Er	4a	0	0	0.00000(8)	101(4)	158(5)	179(4)
S1	4a	0	0	0.2318(9)	206(3)	121(2)	148(3)
S2	4a	0	0	0.7773(9)	192(3)	346(5)	182(4)
AgTmS₂							
Ag	4a	0	0	0.46982(14)	505(11)	364(10)	473(12)
Tm	4a	0	0	0.00000(7)	106(4)	198(5)	143(3)
S1	4a	0	0	0.2353(8)	189(3)	117(2)	156(3)
S2	4a	0	0	0.7794(8)	204(3)	352(5)	210(4)

^{a)} $U_{12} = U_{13} = U_{23} = 0$ for all atoms.



MS14-P36

Tm₂TeO₆: A Dimorphic Thulium(III) Oxotellurate(VI)

P. Höss^{1,2}, S. Zitzer², T. Schleid²

¹Karlsruhe Institute of Technology (KIT), Institute for Nuclear Waste Disposal (INE), Eegenstein-Leopoldshafen, Germany

²Universität Stuttgart, Institut für Anorganische Chemie, Stuttgart, Germany

Based on single-crystal data, two structure types are known for rare-earth metal(III) oxotellurates(VI) with the composition M₂TeO₆: the orthorhombic *A*-type (M = Y, La, Pr, Nd, Sm - Tb, Ho) [1-5] isotypic with Nd₂WO₆ [6] and the trigonal *B*-type (M = Sc, Yb, Lu) [1, 5, 7, 8] adopting the Na₂SiF₆-type structure [9]. Tm₂TeO₆ is the first representative, where single-crystals could be obtained in both structure types: *A*-Tm₂TeO₆ (orthorhombic, *P*2₁2₁1; *a* = 520,24(5), *b* = 898,78(8), *c* = 988,02(9) pm, *Z* = 4) and *B*-Tm₂TeO₆ (trigonal, *P*321; *a* = 896,37(5), *c* = 513,16(4) pm, *Z* = 3). Pale green single-crystals of both structure types were synthesized in evacuated, fused silica ampoules by the reaction of Tm₂O₃ and TeO₃ in a 1:1 molar ratio at 800 °C for 8 d using CsCl as fluxing agent. In both structure types the Te⁶⁺ cations exhibit sixfold oxygen coordination spheres (*A*-Tm₂TeO₆: d(Te–O) = 191 -

195 pm, *B*-Tm₂TeO₆: d(Te–O) = 197 - 198 pm) in form of isolated [TeO₆]⁶⁻ octahedra. Whereas in *A*-Tm₂TeO₆ the rare-earth metal(III) cations are surrounded sevenfold by oxygen (d(Tm–O) = 219 - 255 pm), the coordination number in *B*-Tm₂TeO₆ is reduced to six oxygen atoms (d(Tm–O) = 211 - 237 pm), which provides an octahedral coordination around the Tm³⁺ cations as observed for the Te⁶⁺ cations. This allows for the *B*-type the formation of a slightly distorted hexagonal close packing of O²⁻ anions with cations in half the octahedral interstices (¹/₃ M³⁺ and ¹/₆ Te⁶⁺) according to a stuffed β-WCl₆ type structure [10], while in the *A*-type structure two interpenetrating tetragonal rod packings according to [Tm₂O₆]⁶⁻ are formed by edge shared [(Tm1)O_{3/1}O_{4/2}]⁷⁻ and vertex shared [(Tm2)O_{5/1}O_{2/2}]⁹⁻ chains, whose channels along [100] accommodate the Te⁶⁺ cations.

[1] M. Trömel, F. W. Hützler, H.-G. Burckhardt, C. Platte, E. Münch, *Z. Anorg. Allg. Chem.* **1987**, 551, 95.

[2] S. F. Meier, Th. Schleid, *J. Solid State Chem.* **2003**, 171, 408.

[3] S. F. Meier, Th. Schleid, *Z. Kristallogr. - NCS* **2004**, 219, 359.

[4] P. Höss, Th. Schleid, *Acta Crystallogr.* **2007**, E 63, i133.

[5] P. Höss, *Dissertation*, Univ. Stuttgart, **2009**.

[6] V. A. Efremov, A. V. Tyulin, V. K. Trunov, *Kristallografiya* **1984**, 29, 673.

[7] P. Höss, K. Kojer, Th. Schleid, *Z. Kristallogr.* **2007**, Suppl. 25, id203.

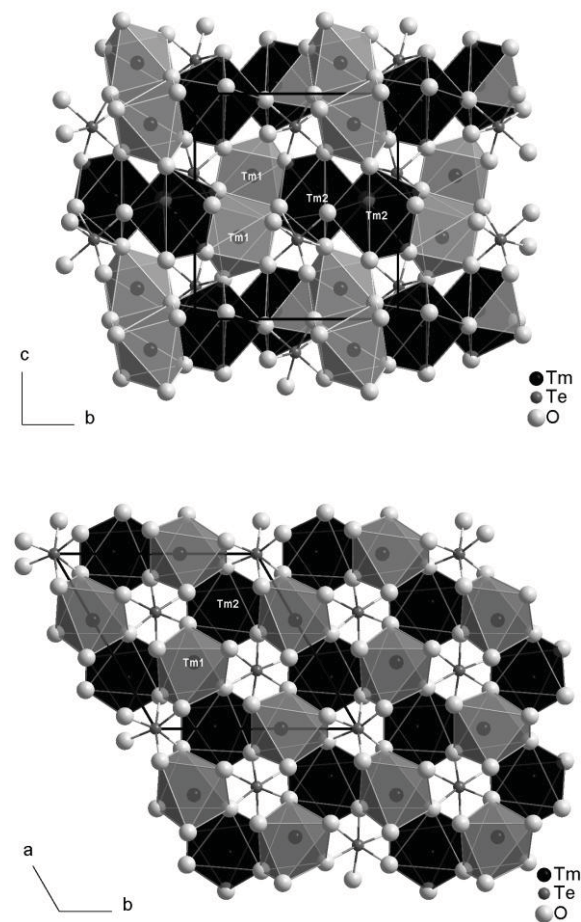
[8] P. Höss, Th. Schleid, *Z. Anorg. Allg. Chem.* **2007**, 633, 1391.

[9] A. Zalkin, J. D. Forrester, D. H. Templeton, *Acta Crystallogr.* **1964**, 17, 1408.

[10] J. C. Taylor, P. W. Wilson, *Acta Crystallogr.* **1974**, B 30, 1216.

Fig. 1: Crystal structure of orthorhombic *A*-Tm₂TeO₆.

Fig. 2: Crystal structure of trigonal *B*-Tm₂TeO₆.



MS14-P37

Isomorphous gallium substitution in mullite-type $\text{Al}_4\text{B}_2\text{O}_9$ K. Hoffmann¹, M.M. Murshed¹, R.X. Fischer², T.M. Gesing¹¹Chemische Kristallographie fester Stoffe, IAPC, Universität Bremen, Bremen, Germany²Kristallographie, FB Geowissenschaften, Universität Bremen, Bremen, Germany

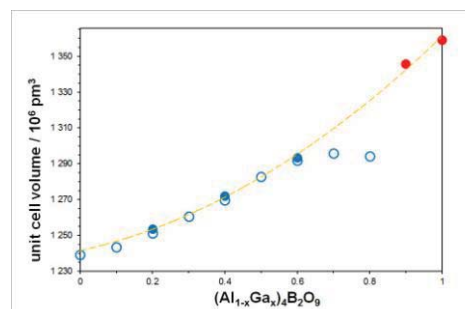
Aluminum borates of the type $\text{Al}_4\text{B}_2\text{O}_9$ (A_2B) belong to the family of mullite-type materials; they are also termed as “boron-mullites” [1]. The crystal chemical properties of A_2B are of considerable research interests, for example as whiskers for the use in oxidation-resistant reinforced composites or chemical and heat-insulating materials [2]. For A_2B two different modifications are reported; one described in the orthorhombic space group Pbam with a pseudo-tetragonal metric [3] and one in the monoclinic space group C2/m in an enlarged unit cell with all lattice parameters doubled with respect to the Pbam structure [4]. The corresponding gallium containing mullite-type compound $\text{Ga}_4\text{B}_2\text{O}_9$ (G_2B) is described in the monoclinic symmetry C2/m as well [5] but the structure differs significantly from those of A_2B . Ga_2B is reported to be stable up to 923K.

Here we report on the synthesis and characterization of a series of $(\text{Al}_{1-x}\text{Ga}_x)_4\text{B}_2\text{O}_9$ compounds. The samples were synthesized following the nitrate decomposition method (details in [6]) from the stoichiometric ratios of aluminum nitrate nona-hydrate and gallium nitrate hepta-hydrate and an excess of boric acid finally heated at 1223K in a closed crucible. To synthesize the gallium-rich compounds the synthesis has to be modified according to Cong et al. [5]. The crystalline powder samples were studied by means of X-ray diffraction data refinements, using the Rietveld method, in combination with SEM/EDX analysis to control the Al/Ga ratios which were found close to the initial composition.

As shown in Figure 1, successive volume expansions can be observed with increasing ratio of gallium in the synthesis. This can be seen in all three lattice parameters and indicates an incorporation of gallium in the A_2B structure. Above about 60 % gallium incorporation into the A_2B structure the lattice parameter increase stops and Ga_2O_3 was found in the samples. Therefore the incorporation limit of gallium in the A_2B structure can be supposed to be between 60 - 70 % gallium. Nevertheless, the volume of the gallium substituted A_2B structure and the doubled volume of the aluminum substituted G_2B structure could be described with one non-linear volume curve, thus resulting in a phase change at the gallium rich part of the series.

Fig. 1: Variations of unit cell volume vs. the initial chemical composition; blue: A_2B structure with incorporated gallium (dots and circles refer to different synthesis series); red: Doubled volume of the G_2B structure with incorporated aluminum.

[1] Werding, G., Schreyer, W. (1984): Geochi. Cosmochim. Acta, 48, 1331-1344. [2] Zhang, J., Lin, J., Song, H.S., Elssfah, E.M., Liu, S.J., Luo, J.J., Ding, X.X., Tang, C., Qi, S.R. (2006): Mater. Lett., 60, 3292-3295. [3] Mazza, D., Vallino, M., Busca, G. (1992): J. Am. Ceram. Soc. 75, 1929. [4] Fischer, R. X., Kahlenberg, V., Voll, D., MacKenzie, K. J. D., Smith, M. E., Schnetger, B., Brumsack, H. J., Schneider, H. (2008): Am. Mineral. 93, 118. [5] Cong, R., Yang, T., Li, K., Li, H., You, L., Liao, F., Wang, Y., Lin, J. (2010): Acta Crystallogr., B66, 141-150. [6] Gesing, Th. M., Fischer, R. X., Burianek, M., Mühlberg, M., Debnath, T., Rüscher, C. H., Ottinger, J., Buhl, J.-Ch., Schneider, H. (2011) J. Eur. Ceram. Soc. 31, 3055-3062.



MS14-P38

Crystal Structures of Short-Chain Alkali Metal Alkanesulfonates: Anhydrous Potassium Methanesulfonate, Rubidium Methanesulfonate Hemihydrate and an Unusual 13:2 Addition Compound of Potassium Ethanesulfonate and Potassium Bicarbonate.

J. Volk¹, W. Frank¹¹Heinrich-Heine-Universität Düsseldorf, Institut für Anorganische Chemie und Strukturchemie II, Düsseldorf, Germany

In view of crystal engineering, alkanesulfonates are adequate building blocks to generate layered inorganic-organic hybrid materials.^[1] In the course of our studies on the solid state structures of short-chain alkanesulfonates we succeeded in structure determinations of potassium ethanesulfonate—water (5/4)^[2] and the three methane- and ethanesulfonates mentioned below.

In all cases crystals have been grown in aqueous solutions of alkali metal carbonate and alkanesulfonic acid by slow evaporation of the solvent at room temperature.

Potassium methanesulfonate, KCH_3SO_3 , (**1**) crystallizes as colourless needles in the tetragonal space group $I4/m$ and crystals usually suffer from twinning by merohedry ($a = 21.820(3) \text{ \AA}$, $b = 21.820(3) \text{ \AA}$, $c = 6.055(1) \text{ \AA}$, $T = 173 \text{ K}$, $Z = 24$, $R_1 = 0.0529$, $wR_2 = 0.1144$, 1393 refl. and 116 param.).

Rubidium methanesulfonate hemihydrate, $\text{Rb}_2(\text{CH}_3\text{SO}_3)_2(\text{H}_2\text{O})$, (**2**) crystallizes as colourless rod shaped crystals in the monoclinic space group $P2_1/c$ ($a = 6.141(2) \text{ \AA}$, $b = 19.862(7) \text{ \AA}$, $c = 8.930(3) \text{ \AA}$, $\beta = 89.243(3)^\circ$, $T = 293 \text{ K}$, $Z = 4$, $R_1 = 0.0390$, $wR_2 = 0.0834$, 1916 refl. and 126 param.).

Potassium ethanesulfonate—potassium hydrogen carbonate—water (13/2/2), $\text{K}_{13}(\text{C}_2\text{H}_5\text{SO}_3)_{13}(\text{H}_2\text{O})_2\text{K}_2(\text{HCO}_3)_2$, (**3**) crystallizes as colourless rods in the monoclinic space group Cc ($a = 17.530(4) \text{ \AA}$, $b = 19.583(4) \text{ \AA}$, $c = 24.096(5) \text{ \AA}$, $\beta = 100.29(3)^\circ$, $T = 173 \text{ K}$, $Z = 4$, $R_1 = 0.0435$, $wR_2 = 0.1014$, 11342 refl. and 880 param.).

The solids of **1-3** can be described as 3D networks with clearly separated regions of inorganic and organic structural fragments dominated by Coulomb interactions (including hydrogen bonding) and van der Waals forces, respectively. According to the distribution of these different types of regions, **1** and **2** exhibit channel structure type arrangements, whereas **3** is best described as a layered structure with some additional connections between its layers.

Three crystallographic independent potassium ions arranged in special positions (m) establish the cationic partial structure of the solid **1**. Connecting these cations the sulfonate anions are arranged with their methyl groups pointing to the centre of the unit cell and the centres of the its side surfaces, respectively, establishing two types of small hydrophobic channels along the tetragonal axis.

In the solid of **2** the ions also form a channel-like structure. In contrast to **1** the cross section of the channels of **2** is ellipsoidal. The water of hydration is directly coordinated to one of the rubidium atoms.

In the solid of **3** all 15 potassium ions and 12 ethanesulfonate ions are arranged to layers perpendicular to the c axis of the unit cell. Connecting elements between these layers are one sulfonate ion, a bicarbonate ion dimer and the two water molecules. Strong hydrogen bonds within the bicarbonate dimer and hydrogen bonding of the water molecules give significant additional

contributions to the electrostatic potassium-oxygen interlayer bonding forces.

[1] W. Frank, S. Wallus, *Z. Anorg. Allg. Chem.* **2006**, 632, 2154.

[2] S. Wallus, W. Frank, *Z. Kristallogr. Suppl.* **2006**, 24, 105.

MS14-P39

Pseudo-symmetry and unusual Cu^{2+}O_5 coordination figures in $\text{Na}_{18}\text{Cu}_3(\text{PO}_4)_8 \cdot 2\text{H}_2\text{O}$ and $\text{Na}_{18}\text{Cu}_3(\text{PO}_4)_8 \cdot 2\text{H}_2\text{O}$.

H. Effenberger¹

¹Universität Wien, Institut für Mineralogie und Kristallographie, Wien, Austria

Single crystals of $\text{Na}_{18}\text{Cu}_3(\text{PO}_4)_8 \cdot 2\text{H}_2\text{O}$ [1] and $\text{Na}_{18}\text{Cu}_3(\text{PO}_4)_8 \cdot 2\text{H}_2\text{O}$ [2] were synthesized under hydrothermal conditions. The unit cell of [1] is unusually large for an inorganic compound: $a = 21.620(4)$, $b = 14.157(3)$, $c = 20.448(4)$ Å, $\beta = 92.50(3)^\circ$, $V = 6252.7$ Å³, space group $C2/c$. As indicated by the cell metrics, the atomic arrangement features a pseudo-tetragonal symmetry in the [010] direction. The Cu atoms are located at $[\frac{1}{4}y0]$ and $[0y\frac{1}{4}]$; the former exhibit $\text{Cu}_2(\text{PO}_4)_6$ groups: CuO_4 squares are corner-linked by PO_4 tetrahedra; further PO_4 tetrahedra are branched.

CuO_4 squares located on $[0y\frac{1}{4}]$ are arranged parallel to each other and corner-linked by PO_4 tetrahedra to dimers. With four additional phosphate tetrahedra, $\text{Cu}_2(\text{PO}_4)_6$ groups are formed again. These units form continuous $-\text{Cu}-(\text{PO}_4)_2-\text{Cu}-(\text{PO}_4)_2-$ rows with formula $[\text{Cu}(\text{PO}_4)_2(\text{H}_2\text{O})]$. However, some coordination figures around the Cu atoms are worthy to note. Besides four ligands belonging to the phosphate tetrahedra, each of these two Cu atoms has two sites of half occupied water molecules in their surroundings. Notwithstanding the accurate location of the Ow atom, the five ligands and the vacancy form an only slightly distorted octahedron. The bond length distribution is $\text{Cu}-\text{O}_p = 1.91$ and 2.13 Å, each $2\times$, $\text{Cu}-\text{O}_w = 2.05$ Å. Moreover, the two longer Cu—O bonds are in a *cis*-arrangement. Such five-fold coordination figures are not compatible with the expectations for the surrounding of Cu^{2+} ions because of the distortion in an octahedral field. The existence of a dynamically disordered Jahn-Teller effect is discussed. Extensive dislocations are indicated by the anisotropic displacement parameters.

Further linkage is verified by the Na^+ ions. The crystal structure exhibits some disorder with respect to one Na-atom position, the water molecules and at least one phosphate group. During crystal-structure refinement different models were considered including spitted atom positions as well as symmetry reductions.

As in [1], also in [2] one of five Cu atoms exhibits an unusual coordination which disagrees with the expectations: $\text{Cu}-\text{O} = 1.957(2)$, $2.086(8)$, $2.102(13)$, $2.189(14)$ and $2.391(8)$ Å; the coordination figure is an extremely distorted tetragonal pyramid. Extensive dislocation phenomena are observed. The average space-group symmetry is $P2_1/m$, $a = 9.653(2)$, $b = 9.702(2)$, $c = 9.744(2)$ Å, $\beta = 101.25(2)^\circ$.

[2] exhibits besides two crystallographically distinct phosphate tetrahedra a diprotonated phosphate group $[\text{PO}_2(\text{OH})_2]$ with the average site symmetry m . One O-atom corner not protonated; a second corner is protonated. The two remaining O-atom corners are formally symmetrically equivalent by average mirror symmetry. These O atoms are coordinated by half occupied Cu atom positions. Depending on the accurate coordination by a vacancy or this Cu atom, a protonated or not protonated corner of the phosphate group is formed.

MS14-P40

Dimorphism of Bismuth(II) trifluoroacetate

W. Frank¹, V. Verheyen¹

¹Heinrich-Heine-Universität Düsseldorf, Institut für Anorganische Chemie und Strukturchemie II, Düsseldorf, Germany

Bismuth(II) trifluoroacetate, $\text{Bi}_2(\text{O}_2\text{CCF}_3)_4$, (**1**) is a unique example of a main group element compound exhibiting the „paddle wheel structure“, that is well known from transition metal chemistry.^[1, 2, 3]

Usually, this carboxylate is prepared as orange to red crystals by reduction of bismuth(III) trifluoroacetate with bismuth powder. Depending on the conditions of synthesis we also observed a yellow phase of the compound. From thermal analyses there is evidence that yellow **1** is stable at $T < 55^\circ\text{C}$ only and therefore might be considered to be a low temperature modification. The yellow form of the compound crystallizes in the triclinic space group $P-1$ with the following parameters: $a = 8.3161(5)$ Å, $b = 14.9809(9)$ Å, $c = 22.2370(15)$ Å, $\alpha = 89.876(8)^\circ$, $\beta = 81.390(8)^\circ$, $\gamma = 89.837(8)^\circ$, $Z = 6$, $V = 2739.1(6)$ Å³, $T = 223$ K. The other modification - the red one - crystallizes in the monoclinic space group $P2_1/n$ with lattice parameters $a = 8.3650(13)$ Å, $b = 15.057(2)$ Å, $c = 22.656(4)$ Å, $\beta = 99.06(3)^\circ$ and $Z = 6$, $V = 2818.0(8)$ Å³, $T = 333$ K. In the solid of both forms the molecules are arranged to trimeric units *via* weak $\text{Bi}\cdots\text{F}$ as well as $\text{Bi}\cdots\text{O}$ non-covalent bonding. Due to the high amplitudes of libration of the CF_3 groups in the solid, it is extremely difficult to detect significant structural differences of the red and yellow solid by X-ray diffraction experiments. However, a detailed investigation of the vibration spectra shows striking differences in the regions of CO_2 group and the CF_3 group vibration bands. Therefore we have to assume that the phases differ mainly by the ordering of CF_3 groups and subtle differences in the secondary $\text{Bi}\cdots\text{O}$ bonding between neighbouring molecules. Further evidence for this is given by the detection of a very limited number of superstructure reflections for the anorthic phase. Unfortunately, due to the low intensity, we did not succeed in the detection of the mode of ordering that is associated to these reflections, until now.

[1] W. Frank, V. Reiland, G. Reiß, *Angew. Chem.* **1998**, 110, 3153; *Angew. Chem. Int. Ed.* **1998**, 37, 2983.

[2] B. Kugel, W. Frank, GDCh-Jahrestagung Chemie **2001**, *Kurzreferate*, p. 47; ISBN 3- 936028-00-1; B. Kugel, *Thesis*, Heinrich-Heine-Universität Düsseldorf **2004**.

[3] E. Dikarev, B. Li, *Inorg. Chem.* **2004**, 43, 3461.

MS14-P41

Crystal Structures of Two Alkaline Earth Methanesulfonate Hydrates

T. Trella¹, V. Verheyen¹, W. Frank¹

¹Heinrich-Heine-Universität Düsseldorf, Institut für Anorganische Chemie und Strukturchemie II, Düsseldorf, Germany

Regarding catalysis and crystal engineering, the properties of methanesulfonates as eco-friendly Lewis acids^[1] and as components of layered inorganic-organic hybrid materials^[2] have been increasingly investigated during the last decade. The structures of strontium and barium methanesulfonate hydrates that are obtained from aqueous solutions at room temperature shall be presented here to give further information concerning the crystal chemistry of alkaline earth methanesulfonates.

While in the case of magnesium (dodecahydrate)^[3] and calcium (anhydrate)^[4] the structures of the compounds that crystallize from aqueous solutions at room temperature have already been determined, the literature gives partially contradictive information for the grade of hydration of the respective strontium and barium compounds.^[5, 6, 7] By means of crystal structure and thermogravimetric analyses, we could clearly identify them as strontium methanesulfonate monohydrate, $\text{Sr}(\text{CH}_3\text{SO}_3)_2 \cdot \text{H}_2\text{O}$ (**1**), and barium methanesulfonate one and a half hydrate, $\text{Ba}(\text{CH}_3\text{SO}_3)_2 \cdot 1,5 \text{H}_2\text{O}$ (**2**).

Colourless needles of **1** were grown from aqueous solutions of methanesulfonic acid and strontium carbonate by slow evaporation of the solvent at room temperature. This compound crystallises in the monoclinic space group $P2_1$ with the following parameters: $a = 8.6204(17)$ Å, $b = 6.0665(12)$ Å, $c = 9.0885(18)$ Å, $\beta = 113.10(3)^\circ$, $V = 437.18(15)$ Å³, $Z = 2$, $R_1 = 4.58$, $wR_2 = 12.32$,

3885 reflections and 145 parameters.

2 crystallises as thin, colourless platelets in the monoclinic space group $P2_1/c$ with $a = 22.6619(5)$ Å, $b = 12.0413(3)$ Å, $c = 15.0111(3)$ Å, $\beta = 108.828(2)^\circ$, $V = 3877.03(15)$ Å³, $Z = 4$, $R_1 = 4.57$, $wR_2 = 11.81$, 6764 reflections and 505 parameters. Instead of a carbonate the respective hydroxid was used for synthesis.

The strontium methanesulfonate hydrate **1** consists of two different kinds of layer-like regions: one hydrophobic area with methyl groups being geared into each other, one hydrophilic part containing eightfold coordinated strontium ions. From a molecular point of view, the solid is built up by cage-like fragments consisting of two monohydrated strontium atoms which are bridged by four sulfonate groups in a $\kappa O:\kappa O'$ mode. These cages are further connected to chains along the b axis of the unit cell via Sr-O contacts. In c direction these chains are connected to layers by O-H...O hydrogen bonding between the water ligands.

A very similar structure is found for the barium methanesulfonate hydrate **2**, but in this case the sevenfold coordinated barium ions are bridged by one water molecule, respectively. The remaining water molecule coordinates one barium ion while connecting the hydrophobic and hydrophilic layers via hydrogen bonding.

[1] M. Wang, G. F. Tian, Z. G. Song, H. Jiang, *Chin. Chem. Lett.* **2009**, *20*, 1034.

[2] S. Wallus, W. Frank, *Z. Anorg. Allg. Chem.* **2006**, *632*, 2154.

[3] F. E. G. Guner, M. Lutz, T. Sakurai, A. L. Spek, T. Hondoh, *Cryst. Growth & Des.* **2010**, *A*.

[4] F. Charbonnier, R. Faure, H. Loiseleur, *J. Appl. Cryst.* **1977**, *B33*, 1478.

[5] A. Collmann, *Liebigs Ann. Chem.* **1868**, *146*, 101.

[6] Y. Garaud, F. Charbonnier, R. Faure, *J. Appl. Cryst.* **1980**, *13*, 190.

[7] M. Wang, Z. G. Song, H. Jiang, H. Gong, *J. Therm. Anal. Calorim.* **2009**, *98*, 801.

MS14-P42

Complex structures of first uranyl borophosphates, borate phosphate and aluminoborate

S. Wu¹, S. Wang², J. Divu², O. Beermann¹, W. Depmeier¹, A. Holzheid¹, T. Malcherek³, E. Alekseev⁴, T. Albrecht-Schmitt²

¹Kiel University, Institute of Geosciences, Kiel, Germany

²University of Notre Dame, Department of Civil Engineering and Geological Sciences and Department of Chemistry and Biochemistry, Notre Dame, United States

³Universität Hamburg, Mineralogisch-Petrographisches Institut, Hamburg, Germany

⁴Forschungszentrum Jülich GmbH, Institute for Energy and Climate Research (IEK-6), Jülich, Germany

Borosilicate and borophosphate glasses (containing up to 19.8 wt. % of Al₂O₃) are widely used as waste form for the disposal of nuclear waste.^{1, 2} During the long time of storage, different crystalline products are expected to form³. Recently, much progress in actinide borate chemistry has been achieved⁴. However, the knowledge of actinide borates mixed with other oxo-anions (e.g., PO₄, AlO_x and SiO₄) is scarce. In order to predict the potential crystalline phases in vitrified nuclear waste, we synthesized several uranyl borates mixed with phosphate or aluminate, including Ba₃[(UO₂)(PO₄)₃(B₅O₉)]·nH₂O (BaUBP-1), M₂(UO₂)₁₂(BO₄)(PO₄)₁₂(H₂O)₄ (M=K, Na: KUBP-1 and NaUBP-1) and UO₂(BO₃)₃Al₄O₂OH(UBAIO-1).

The structure of BaUBP-1 is based on complex nanotubular fragments with an external diameter of ~2 x 2 nm (Fig. 1a). Oxo-borate nanotubes and [UO₂(PO₄)₃] moieties are linked together via shared BO₃ triangles to form entities with a cross-section resembling a Celtic cross. H₂O is located at the center of the borate tube channels, whereas Ba atoms are between [UO₂(PO₄)₃] groups and the tube walls.

The frameworks of isostructural KUBP-1 and NaUBP-1 are built up by two main fragments, [(UO₂)₈(PO₄)₈]_{1∞} nanotubes and

[(UO₂)₄(BO₄)(PO₄)₄] clusters (Fig. 1b). The nanotube is based on an uranophane related anion-topology⁵ with replacement of SiO₄ by PO₄. K or Na atoms are located at the center of the nanotubes. The [(UO₂)₄(BO₄)(PO₄)₄] cluster looks like a concentric circle with a BO₄ tetrahedron residing at the center which is surrounded by four PO₄ tetrahedra and four UO₇ pentagonal bipyramids. Finally, each UO₇ pentagonal bipyramid in the cluster shares an oxygen atom with a PO₄ tetrahedron from the nanotube to form a complex framework.

UBAIO-1 possesses an aluminoborate framework that incorporates dioxo uranyl groups (Fig. 1c). AlO₆ square bipyramids connect to each other via edge sharing to form [AlO₆]_∞ chains. AlO₆ chains are linked by BO₃ triangles by corner-sharing with a 90° rotation. AlO₅ tetragonal pyramids are connected with the [AlO₆]_∞ chains by corner-sharing and edge-sharing. Finally, the uranyl hexagonal bipyramids surrounded by BO₃ reside in the space between AlO₅ groups and AlO₆ chains.

Besides P and Al, other elements forming oxo-anions, such as Cr, Zr, Si, Mo, Mn may also exist within nuclear glasses. Therefore, uranyl borates containing other oxo-anions can also be anticipated.

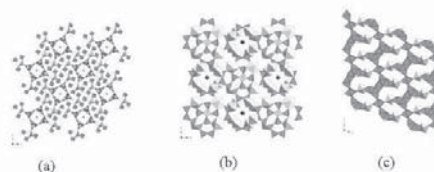
Figure 1: General views of the structure of BaUBP-1 (a), K/NaUBP-1 (b) and UBAIO-1 (c).

Acknowledgement:

Financial support by the Deutsche Forschungsgemeinschaft under contract number DE 412/43-1 is gratefully acknowledged.

References:

1. Commission on Geosciences, Environment and Resources, Glass as a Waste Form and Vitrification Technology: Summary of an International Workshop, National Academy of Science, 1996, Washington.
2. International Atomic Energy Agency, Spent Fuel and High Level Waste: Chemical Durability and Performance under Simulated Repository Conditions, 2007, Vienna.
3. T. F. Meaker, Neptunium Immobilization and Recovery Using Phase Separated Glasses, 1996, Department of Energy.
4. S. Wang, E. V. Alekseev, W. Depmeier, T. E. Albrecht-Schmitt., *Chem. Commun.*, 2011, *47*, 10874-10885.
5. F. V. Stohl, D. K. jr. Smith, *Am. Mineral.*, 1981, *66*, 610-625.



MS14-P43

Morphology and crystal structure of fully hydrated Zeolite Na-A

R.X. Fischer¹, M. Šehović¹, W.H. Baur², C. Paulmann³, T.M. Gesing⁴

¹Universität Bremen, Fachbereich Geowissenschaften, Bremen, Germany

²University, Western Springs, United States

³Universität Hamburg, Mineralogisch-Petrographisches Institut, Hamburg, Germany

⁴Universität Bremen, FB2, Chemische Kristallographie fester Stoffe, Bremen, Germany

Zeolite Na-A with idealized composition usually stated as Na₁₂Al₁₂Si₁₂O₄₈·27 H₂O, is one of the most prominent zeolites due to its outstanding ion-exchange properties mainly used for the softening of water by exchanging Ca and Mg ions by Na. The

annual production of zeolite A just for household detergents exceeds one million metric tons. Its crystal structure was solved in 1956 by Reed and Breck [1] in space group $Pm\bar{3}m$ with $a = 12.3 \text{ \AA}$, but later on it has been shown by Gramlich and Meier [2] that the compound is better described in space group $Fm\bar{3}c$ with $a = 24.6 \text{ \AA}$. The face-centered unit cell permits the ordering of Si and Al atoms which would allow a ratio of 1 : 1, but usually zeolite A is reported to have a slight excess of Si.

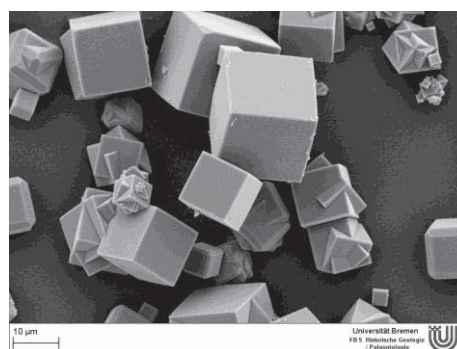
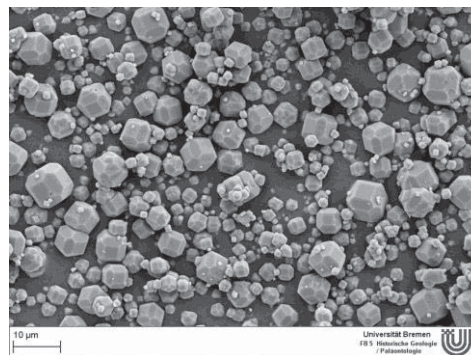
All in-house syntheses of growing single crystals of zeolite A have been performed using a modified procedure after Charnell [3]. A crystal from the original synthesis [3] with dimensions of $0.08 \times 0.08 \times 0.08 \text{ mm}^3$ was used for the synchrotron experiments performed at the F1 beamline at DESY, Hamburg, using a MarCCD165 detector. In-house samples were investigated by SEM, EDX, simultaneous thermal analysis (STA), and X-ray powder diffraction methods.

Zeolite Na-A was synthesized with various amounts of triethanolamine (TEA) between 0.25 and 2.5 mole/l, and constant amounts of sodium, silicon, aluminum, and water. The maximum crystal size increased from $9 \mu\text{m}$ to $28 \mu\text{m}$ with decreasing lattice parameters upon increasing amounts of TEA in the initial gel. The mean composition resulting from 37 EDX analyses is $11.5 \pm 0.7 \text{ Al}$ and $12.5 \pm 0.5 \text{ Si}$ corresponding to a Si/Al ratio of 1.09 ± 0.11 . Crystals synthesized with low amounts of TEA exhibit both $\{100\}$ and $\{110\}$ crystal forms while the bigger crystals made with high amounts of TEA are cubes with $\{100\}$ faces only.

Figure 1 shows SEM images of zeolite A synthesized with low amounts of TEA (0.25 mole TEA / l, Fig. 1a) yielding small crystals with equally occurring cube and rhomb-dodecahedral faces which vanish completely upon higher amounts of TEA in the initial gel (1.75 mole TEA / l, Fig. 1b) exhibiting predominantly the cube faces. The crystal structure of fully hydrated zeolite A, $\text{Na}_{94}\text{Al}_{94}\text{Si}_{198}\text{O}_{384} \cdot n \text{ H}_2\text{O}$ (unit-cell composition, n refined to 243 compared with about 225 expected), was investigated by single-crystal synchrotron methods (space group $Fm\bar{3}c$, $a = 24.550(3) \text{ \AA}$, room temperature, $R1 = 0.071$) yielding a very regular framework geometry with Si-O distances between $1.599(1) \text{ \AA}$ and $1.611(1) \text{ \AA}$, and Al-O distances between $1.719(1) \text{ \AA}$ and $1.737(1) \text{ \AA}$. Water molecules form a sodalite-cage-like cluster in the big grc units (α -cages) and are statistically distributed over octahedral positions in the *toc* units (sodalite cages) with Na atoms close to the centers of the 6-rings and 8-rings.

Figure 1: SEM photograph of zeolite Na-A synthesized with 0.25 mole TEA / l

Figure 2: SEM photograph of zeolite Na-A synthesized with 1.75 mole TEA / l



**MS15-P01
EMBL MX1 BEAMLINE FOR MACROMOLECULAR
CRYSTALLOGRAPHY AT PETRA III @ DESY,
HAMBURG, GERMANY**

*M. Cianci¹, G. Bourenkov¹, S. Fiedler¹, M. Roessle¹, T. Schneider¹
¹EMBL, Hamburg, Hamburg, Germany*

In the recent years new trends and challenges have appeared in biocrystallography. With an increasing number of mammalian proteins directly purified from natural sources, heavy atom derivatization for phasing is having a second golden age and, for most of these projects, only low resolution phasing will be the option.

Combination of softer X-rays and heavy atom derivatization would allow harnessing very strong anomalous signals. For instance a single uranyl derivative at 5 keV will have a f'' of 24 e⁻; on the other hand a Tantalum cluster like $\text{Ta}_6\text{Br}_{12}$ will generate a combined f'' of 66 e⁻ at low resolution.

EMBL macromolecular crystallography MX1 beam line is part of

Acknowledgements:

We thank Karl Seff (Hawaii) for providing the single crystal for this study, Petra Witte (Bremen) for the SEM images and EDX analyses, and Johannes Birkenstock (Bremen) for his comments on the XRD analyses.

References:

- [1] Reed, T.B., Breck, D.W.: J. Amer. Chem. Soc. 78 (1956) 5972.
- [2] Gramlich, V., Meier, W.M.: Z. Kristallogr. 133 (1971) 134.
- [3] Charnell, J.F.: Journal of Crystal Growth 8 (1971) 291.

the European Molecular Biology Laboratory integrated infrastructure for life science applications at PETRA III, the new 3rd generation synchrotron at DESY in Hamburg.

MX1 double crystal monochromator will be tunable over the energy range from 5(4) to 17 keV to allow crystallographic data acquisition on a broad range of elemental absorption edges for experimental phase determination.

This beam line will also provide a very collimated beam (0.2 mrad (H) x 0.15 mrad (V)) with variable focus size (20 to 100 microns) to harness anomalous data from relatively small samples or large unit cells. Most likely data sets will need to be completed with multiple crystal data collections given radiation damage diffraction decay or diffraction anisotropy for instance. These type of problems will be tackled with a EMBL- MAATEL MD2 with 1 µm sphere of confusion, in-house developed robotic sample changer with 150 sample capacity, mini Kappa goniometer, detector translation with 2theta-arm, Si-drift fluorescence detector to cite a few.

As part of the Petra III facilities the DLab currently offer more than hundred heavy atom compounds and the Sample Preparation and Crystallization facilities allows for rapid screening of samples, which is offered to users as additional service.

These capabilities will be applied to push the limits of phasing with weak anomalous signal for challenging crystal systems.

Finally softer X-rays can be applied for studying the fine details macromolecular structure with identification of anions and cations [1]. Given MX1 capability to produce beam up to 5(4) keV is possible to plan data collections to map the position of single ions. We will present the current status of MX1 beam line and future plans.

References:

[1] Cianci et al., J. Am. Chem. Soc.132, 7:2293-2300 (2010)

MS15-P02

STARTUP OF MACROMOLECULAR CRYSTALLOGRAPHY BEAMLINE P14/MX2@PETRAIII

G. Bourenkov¹, M. Cianci¹, S. Fiedler¹, T. Schneider¹

¹EMBL-Hamburg, PETRAIII, Hamburg, Germany

The macromolecular crystallography beamline P14/MX2 at PETRAIII, the new 3rd generation synchrotron at DESY, Hamburg, is a part of the integrated structural biology facility being constructed by EMBL-Hamburg. In 2011 the beamline has been brought into initial operation phase and started providing beam time to friendly users. We will present the current beamline setup along with the results of the beamline commissioning experiments and first applications.

The beamline currently operates with the collimated unfocused beam and cryogenically cooled double-crystal monochromator (DCM) as the only optical element. Owing to the outstanding properties of the radiation source, unfocused beam provides very good conditions for many applications. The flux density is over 5×10^{12} photon/sec/mm² and the energy range 6 to 11 keV, with no significant higher harmonic contamination. The flux translates into radiation damage-limited maximum data collection time of approximately two hours per sample. The energy range is currently restricted by a combination of factors related to spectral purity and the DCM thermal stability. Most applications are carried out at 11 keV, using the fundamental undulator harmonic at low deflection. The beam divergence is negligible and permits precise definition of the beam shape and homogeneous intensity distribution across the sample. Both the beam position and the intensity are essentially stable on relevant time scales. Thus, current beam conditions are fairly unique for MX field and are best suited for large unit cells and moderate crystals sizes, 100-200 µm, although successful application examples involved crystals smaller than 20 µm in three dimensions. Overall, commissioning experiments had proven that excellent data quality can be achieved stably; e.g. successful sulfur

SAD phasing on test systems with anomalous signals $\leq 1\%$ is performed routinely.

The beamline is equipped with high-precision vertical Kappa goniometer, HPGonioV (Cipriani et al., 2010). The device parameters, e.g. Omega cylinder of confusion ≤ 300 nm, are targeting future micro-crystallography applications at P14. We used mosaic CCD RAYONIX-225HE and PILATUS2M detectors; commissioning experiments involved, in particular, their side-by-side comparisons.

As next steps, early in 2012 the micro-focusing mirror system and end-station will be installed and commissioned. The aim is to achieve the smallest focal spot size of 1×4 µm. Furthermore, we plan to achieve state-of-the-art energy tunability (6 to 30 keV range) and provide the users with competitive conditions for the most demanding experimental phasing applications.

MS15-P03

EMBL@PETRA3: THE NEW BioSAXS BEAMLINE P12

M. Roessle¹, S. Fiedler¹, G. Bourenkov¹, M. Cianci¹, V. Haramus²,

R. Willumeit², D. Svergun¹, T. Schneider¹, M. Wilmanns¹

¹EMBL Hamburg, Hamburg, Germany

²Helmholtz Zentrum Geesthacht, Geesthacht, Germany

SAXS is a versatile tool for investigation of biological particles such as protein and large macro-molecular complexes in solution. It is a unique method for studying structures at low resolution and of structural transitions between individual states.

The projected BioSAXS beamline at the upgraded PETRA-III storage ring will allow challenging experiments, which are currently being carried out at the limit of existing SAXS stations in terms of sensitivity and sample consumption. The beamline combines a high brilliance X-ray beam with low scattering background and energy tunability (4keV to 20keV) for anomalous SAXS experiments on metals such as Calcium up to Molybdenum. The beamline is positioned in sector 8 of the PETRA-III on a straight section of a 2m canted undulator. The focal point is at 87 m (focus on the detector) and the optical layout permits beamsizes of 200×60 mm² and a beam divergence of 40×10 mrad². The standard mode operates a Si 111 double crystal monochromator and a pair of bimorph mirrors in Kirkpatrick Baez geometry. Further options such as high flux multilayer monochromator and a white beam option are under planning.

A 5 m detector stage is operated in collaboration with the Helmholtz research center Geesthacht. This stage allows recording of different scattering angular regimes by changing the sample to detector distance. The device is automated and widens the BioSAXS applications towards biological soft condensed matter such as lipid membranes, fibres and biological nanoparticles.

A liquid handling robot facilitates fast and reliable automated sample changing as standard operation for solution scattering experiment. First friendly users collected data on several biological systems with promising results. Recent experiments on nanoparticle and protein solutions at very low volumes showed SAXS data of good quality and high performance could be expected when the beamline reaches its final specifications.

For future SAXS experiments in ultra-small sample volumes (< 1 nano liter) microfluidic sample environments are under development. Cutting-edge experiments, such as kinetic experiments on an ultra-short time scale and pilot experiments for future X-FEL applications biological samples will be possible.

MS15-P04

Facilities for Macromolecular Crystallography at BESSY II - Berlin

M. Weiss¹, M. Bommer¹, R. Förster¹, M. Hellmig¹, M. Krug¹,
K.S. Paithankar¹, M. Steffien¹, M. Ühlein¹, U. Mueller¹

¹Helmholtz-Zentrum Berlin, Macromolekular Crystallography, Berlin, Germany

The Macromolecular Crystallography (MX) group at the Helmholtz-Zentrum Berlin (HZB) has been in operation since 2003. Since then, three state-of-the-art synchrotron beam lines (BL14.1-3) for MX have been built up on a 7T-wavelength shifter source [1,2]. Currently, the three beam lines represent the most productive MX-stations in Germany, with more than 500 PDB depositions. BLs14.1 and 14.2 are energy tunable in the range 5.5-15.5 keV, while BL14.3 is a fixed-energy side station (13.8 keV). All three beam lines are equipped with CCD-detectors. Beam lines BL14.1 and BL14.2 are in regular user operation providing about 200 beam days per year and about 600 user shifts to approximately 50 research groups across Europe. BL14.3 has been equipped with a HC1 crystal dehydration device and has been set back to user operation as a screening and test beam line in 2010. BL14.1 has recently been upgraded with an MD2-microdiffractometer including a kappa-geometry option and an automated sample changer. Additional user facilities include office space adjacent to the beam lines, a sample preparation laboratory, a biology laboratory (safety level 1) and high-end computing resources. On the poster, a summary on the experimental possibilities of the beam lines and the provided ancillary equipment for the user community will be given.

[1] Heinemann U., Büsow K., Mueller, U. & Umbach, P. (2003). *Acc. Chem. Res.* 36, 157-163.

[2] Mueller et al., submitted for publication

MS17-P01

Structural and electrochemical studies of the Li-Zn alloys

I. Chumak¹, V. Pavlyuk², H. Ehrenberg¹

¹Karlsruhe Institute of Technology, Institute for Applied Materials - Energy Storage Systems, Eggenstein-Leopoldshafen, Germany

²Ivan Franko Lviv National University, Department of Inorganic Chemistry, Lviv, Ukraine

The crystal structures of both low- and high-temperature modifications of binary Li_2Zn_3 were determined by single-crystal X-ray diffraction. The low-temperature (LT) modification is a strongly disordered variant of the Li_5Sn_2 structure type (trigonal crystal system, space group $R\bar{3}m$ (No. 166), $a = 4.386$ (4) Å, $c = 18.738$ (18) Å, $R(F^2) = 0.029$, $wR(F^2) = 0.082$). The high-temperature (HT) modification crystallizes as an anti-type to the Li_5Ga_4 structure (trigonal, $P\bar{3}m1$ (No. 164), $a = 4.3528$ (14) Å, $c = 8.003$ (3) Å, $R(F^2) = 0.058$, $wR(F^2) = 0.142$). The rhombic dodecahedra coordination polyhedra for all atoms in both polymorphs are typical. The two polymorphs can be described as derivative structures from the CdI_2 and Cd_2Ce types. The phase transition temperature was determined by DSC and is equal to 165 °C.

The performance of the LiZn electrode was tested in half-cells against metallic lithium as the counter electrode with 1M LiPF₆ in a 1:1 mixture of ethylencarbonate and dimethylcarbonate as the electrolyte. The structural changes in LiZn electrode during electrochemical lithium extraction-insertion were studied by ex situ and in situ XRD using a STOE STADI/P powder diffractometer (Mo-K α_1 radiation).

MS17-P02

Characterisation of nanocrystalline $\gamma\text{-Fe}_2\text{O}_3$ with synchrotron radiation techniques

M. Hagelstein¹, S. Doyle¹, T. Liu¹, R. Steininger¹, D. Szabo², S. Schlabach²,
C. Ferrero³, A. Fitch³, M. Scavini⁴

¹KIT, ISS, Eggenstein-Leopoldshafen, Germany

²KIT, Eggenstein-Leopoldshafen, Germany

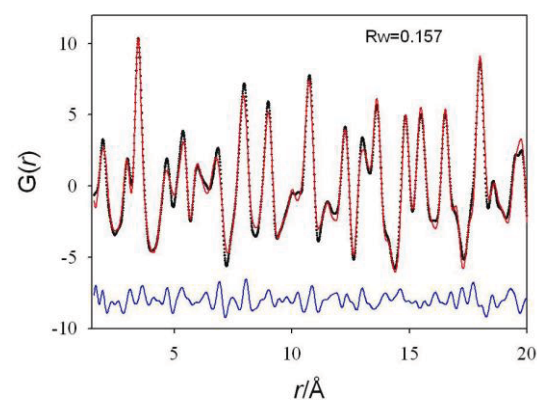
³European Synchrotron Radiation Facility, Grenoble, France

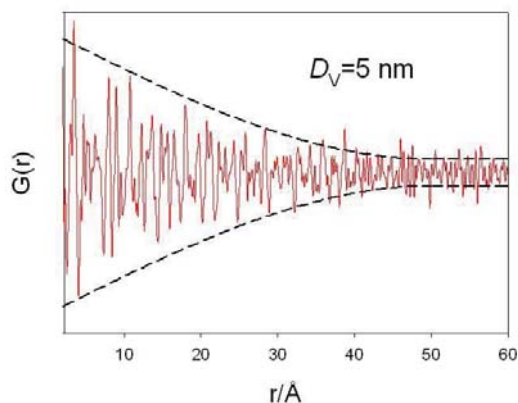
⁴University of Milan, Milano, Italy

Synchrotron radiation X-ray scattering and X-ray absorption spectroscopy techniques have been used to characterise the size distribution, crystallographic structure and the local atomic environment of nanocrystalline Fe_2O_3 particles in order to correlate structure with magnetic properties. The material has been prepared using the microwave plasma technique and $\text{Fe}(\text{CO})_5$ as a precursor. The synthesis parameters have been varied to obtain particles with a narrow particle size distribution and a typical weighted mean diameter of 5 nm. A subset of samples has in addition been coated with methylacrylic acid in order to prevent particle growth. The particles crystallise in the cubic maghemite ($\gamma\text{-Fe}_2\text{O}_3$) structure with iron occupying tetrahedral and octahedral sites in the inverse spinel lattice. Due to vacancies on octahedral sites, competing magnetic interactions of disordered crystal sublattices as well as surface effects, the spin lattices experience frustration and disorder. An accurate determination of the local geometrical structure and possible structural disorder should provide the basis for detailed modelling of the magnetic structure. In addition to the determination of local structure using EXAFS, the radial distribution function $G(r)$ of the $\gamma\text{-Fe}_2\text{O}_3$ reference (figure 1) as well as of a nanocrystalline sample (figure 2) has been derived using high quality data from the ESRF beamline ID 31 and a scattering range up to $q=2.6 \text{ nm}^{-1}$. The magnetic blocking temperature as well as AC susceptibility of the ultra-fine particles have been determined and related to particle structure and particle size.

Figure 1: $G(r)$ of a maghemite reference sample (experimental data - black dots, fit using maghemite as structural model - red line, difference - blue line)

Figure 2: $G(r)$ experimental data of nanocrystalline maghemite (red line) and envelope function (black dashed line) derived for a spherical particle size distribution with average size of 5 nm. A noticeable decrease of the $G(r)$ peak amplitude is apparent as a consequence of the finite size of the particles. The noise at high r values is due to the limited effective sample volume.




MS17-P03
GTECS3D: A new Program for Graphtheoretical Evaluation of extended Network Structures

K. Lamberts¹, C. Merckens¹, R. Wang¹, U. Englert¹, D. Hons², S. Grüter², Y. Guo², S. Porsche³, A. Hamacher³, D. Bündgens³, T. Kühlen³

¹RWTH Aachen University, Institute of Inorganic Chemistry, Aachen, Germany

²RWTH Aachen University, Institute for Mathematics, Aachen, Germany

³RWTH Aachen University, Virtual Reality Center, Aachen, Germany

As the interest in the characterization of extended, periodic network-structures grew continuously in the last decades [1], the need for powerful visualization and algorithmic determination of the underlying nets increased likewise. Today, programs and databases like TOPOS [2] or RCSR [3] support precise and comprehensible description and comparison of complex frameworks. By drawing on graph-theory and high-end visualization we present the new, straightforward program GTECS3D for this purpose, which is being created in an interdisciplinary project of chemists, mathematicians and computer scientists (cf. our list of coauthors). By using the established ViSTA toolkit [4] it is possible to run GTECS3D on standard PCs as well as on powerful 3D systems. It's development is focussed on the implementation of automated, easy-to-use functions based on standard CIF input files, assuring best compatibility with the whole diversity of network structures (especially with the tremendous variety of bridging ligands).

Basic functions of our first release version will be presented by taking the example of new Al-Ag networks, showing many different network types. The simplification process, as well as the topological investigation of the resulting network will be displayed to show the implementation of the plain approach towards fast and easy structure evaluation.

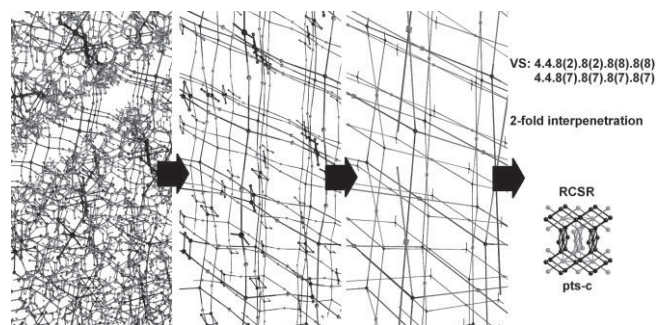
[1] See for example: The pervasive chemistry of metal-organic frameworks, Chem. Soc. Rev., 5, 2009

[2] V. A. Blatov, IUCr CompComm Newsletter, 7, 2006, 4-38

[3] M. O'Keeffe, M. A. Peskov, S. J. Ramsden, O. M. Yaghi, *Acc. Chem. Res.*, 41, 2008, 1782-1789

[4] I. Assenmacher, T. Kühlen (2008), The ViSTA Virtual Reality Toolkit, The SEARIS Workshop on IEEE VR 2008, Reno

Acknowledgement: This work was supported by a Seed Fund grant of the RWTH Aachen University


MS17-P04
Bimetallic Coordination Networks based on Al(acacCN)₃: A Building Block between Inertness and Lability

C. Merckens¹, N. Becker¹, K. Lamberts¹, U. Englert¹

¹RWTH Aachen University, Institute of Inorganic Chemistry, Aachen, Germany

Coordination polymers represent an area of very active studies and provide an attractive meeting ground for basic research and applied materials science. The synthesis of coordination networks incorporating two different cations is associated with additional synthetic challenges. [1, 2]

Ditopic ligands in which an acetylacetonate moiety and a nitrogen donor site are combined have been used for the construction of well-ordered bimetallic networks: Our earlier work relied on the inert Cr(acacCN)₃ tecton [3] and the work of Burrows et. al. refers to Cu(II), Fe(III) and Al(III) compounds. [4] For the Al(acacCN)₃ building block only the transmetalation [Ag(acacCN)]_∞ has been reported.

We present the organic ligand 3-cyano-2,4-pentanedione (HacacCN) [5] as linker for the construction of Al(III)-Ag(I) networks. The networks are synthesized in a stepwise approach in which the Al(acacCN)₃ complex serves as building block for further cross-linking with silver(I). The result of cross-linking reaction showed a strong dependence on the solvents as well as on the silver-salts. Three different kinds of networks have been encountered by combining different silver salts and solvent mixtures: a) Networks containing the building block in an almost unchanged geometry; the building block serves as inert tecton. b) Networks which show that the Al(III) building block ranges between inertness and lability: the networks contain a rearranged coordination sphere where one of the ligands is exchanged by bridging methoxy groups between two aluminum centers. c) The transmetalation product without Al(III): it reflects the potential lability of the building block.

[1] U. Mueller, M. Schubert, F. Teich, H. Puetter, K. Schierle-Arndt, J. Pastre, *J. Mater. Chem.* 2006, 16, 626-636.

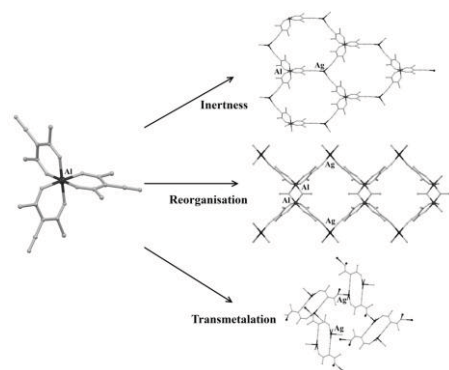
[2] K.A. Williams, A.J. Boydston, C.W. Bielawski, *Chem. Soc. Rev.* 2007, 36, 729-744.

[3] M. Kondracka, U. Englert, *Inorg. Chem.* 2008, 47, 10246-10257.

[4] A.P. Burrows, K. Cassar, M.F. Mahon, J.E. Warren, *Dalton Trans.* 2007, 24, 2499-2509.

[5] C.M. Silvernail, G. Yab, R. Sommer, A.L. Rheingold, V.W. Day, J.A. Belot, *Polyhedron* 2001, 20, 3313-3117.

This work was financially supported by DFG (International Research Training Group "SeleCa - Selectivity in Chemo- and Biocatalysis" at RWTH Aachen University)


MS17-P05
Phase-matched spontaneous parametric down-conversion in optically biaxial crystals, example BiB₃O₆

 P. Becker¹, A. Halevy², E. Megidish², L. Dovrat², H.S. Eisenberg², L. Bohatý¹
¹Universität zu Köln, Institut für Kristallographie, Köln, Germany

²Hebrew University, Racah Institute of Physics, Jerusalem, Israel

By the second order nonlinear optical process of parametric down conversion (PDC) a photon from a pump laser beam may be split into a pair of photons amid conservation of energy and momentum. The generated two photons are strongly correlated in time, wavelength, polarisation state and in momentum [1]. Using special geometries and realisation of phase matching for the PDC process, about 15 years ago a first demonstration of an efficient polarization entangled photon source was reported [2]. Ever since, the most common nonlinear optical crystal for this purpose is optically uniaxial β -BaB₂O₄ (BBO) due to its rather high nonlinear coefficients and broad range of phase matching possibility (see, e.g. [3]). In a recent publication we demonstrated the suitability of monoclinic, optically biaxial crystals of BiB₃O₆ (BiBO) as a source of polarization entangled photons with an efficiency of ca. 2.5 times that of BBO, using non-collinear type-II phase matching of the PDC process [4]. However, the biaxiality of low-symmetric crystals such as BiBO results in enhanced complexity of the underlying crystal optics, compared to BBO.

In the present contribution we describe a rigorous treatment of the background for the choice of crystal parameters, such as direction of wave normal and polarisation of the pump beam and the down-converted photons, spatial walk-off effects and effective second order nonlinearity χ_{eff} (as an approximate measure of χ_{eff} we use the effective coefficient of second harmonic generation, d_{eff}^{SHG}). The calculation strategy for suitable geometries and polarisations for non-collinear type II phase matched PDC basically follows that given in [5], relating the calculations to a Cartesian reference system $\{e_i\}$, with $e_3 \parallel a_3$, $e_2 \parallel a_2^*$ and $e_1 = e_2 \times e_3$ ($a_3 =$ axis of the crystallographic system, $a_2^* =$ axis of the reciprocal system). This simplifies the treatment of wavelength dispersion of the optical indicatrix orientation. The same (wavelength-independent) reference system $\{e_i\}$ is also used for the calculation of d_{eff}^{SHG} of low-symmetric crystals, that proceeds basically by tensorial transformation of the SHG tensor. In addition, an analytical treatment of spatial walk-off angles, i.e. the angles between the wave normals and the corresponding Poynting vectors of the down-converted photons is demonstrated on the example of BiB₃O₆.

 [1] R. Ghosh and L. Mandel, Phys. Rev. Lett. **59** (1987) 1903.

 [2] P.G. Kwiat, K. Mattle, H. Weinfurter, A. Zeilinger, Phys. Rev. Lett. **75** (1995) 4337.

[3] D.N. Nikogosyan, Nonlinear Optical Crystals: A Complete Survey. Springer (New York) 2005.

 [4] A. Halevy, E. Megidish, L. Dovrat, H.S. Eisenberg, P. Becker, and L. Bohatý, Opt. Express **19** (2011) 20420.

 [5] N. Boeuf, D. Branning, I. Chaperot, E. Dauler, S. Guérin, G. Jaeger, A. Muller, A. Migdall, Opt. Eng. **39** (2000) 1016.

MS17-P06
 $\chi^{(3)}$ -nonlinear optical interactions in aragonite

 A.A. Kaminskii¹, P. Becker², H. Rhee³, O. Lux³, H.J. Eichler³, V.V. Koltashev⁴, R. Kleinschrodt⁵, L. Bohatý²
¹Russian Academy of Sciences, Institute of Crystallography, Moscow, Russian Federation

²Universität zu Köln, Institut für Kristallographie, Köln, Germany

³Technische Universität Berlin, Institut für Optik und Atomare Physik, Berlin, Germany

⁴Russian Academy of Sciences, Fiber Optics Research Center, Moscow, Russian Federation

⁵Universität zu Köln, Institut für Geologie und Mineralogie, Köln, Germany

With stimulated Raman scattering (SRS), a $\chi^{(3)}$ -nonlinear optical inelastic process, laser radiation of a fundamental wavelength can be converted into laser emission at Stokes and anti-Stokes wavelengths, accompanied by the excitation, respectively deexcitation, of an internal SRS-promoting vibration mode of the material. While the well-known $\chi^{(2)}$ nonlinear optical processes (such as second harmonic generation, SHG) require non-centrosymmetry of the material, Raman induced $\chi^{(3)}$ -lasing is possible in media of any symmetry. In a recent publication, for calcite, the trigonal modification of CaCO₃, new cascaded multi-wavelength $\chi^{(3)}$ lasing processes were observed. In particular, based on its SRS-promoting vibration mode A_{1g} (the breathing mode of the [CO₃]²⁻ groups) one of the broadest Stokes and anti-Stokes frequency lasing combs known so far can be generated in calcite crystals via SRS and Raman induced four wave mixing (RFWM) [1]. Broadband lasing frequency combs offer an attractive possibility for the realization of ultrashort laser pulses. In spontaneous Raman spectra of aragonite the A_{1g} breathing mode of the [CO₃]²⁻ groups also appears as the dominant Raman band (see, e.g. [2]), however, in the orthorhombic modification of CaCO₃ with space group *Pmcn* (see e.g. [3]) the carbonate groups are arranged in a manner different to that in calcite. This stimulated our interest in SRS and RFWM properties of aragonite crystals.

For our investigations natural untwinned crystals of high optical quality from the locality Čičov hill (Czech Republic) were used. The crystals possess a transparency range from $\sim 0.27 \mu\text{m}$ to $\sim 2.25 \mu\text{m}$. SRS experiments were performed with single-wavelength picosecond laser excitation in the near IR ($\lambda_{f1} = 1.06415 \mu\text{m}$), in the visible spectral range ($\lambda_{f2} = 0.53207 \mu\text{m}$) and in the UV ($\lambda_{f3} = 0.3547 \mu\text{m}$) as well as with collinear dual-wavelength excitation using the wavelengths λ_{f1} and λ_{f2} simultaneously. SRS in aragonite arises from the dominant SRS-promoting vibration mode with $\omega_{SRS1} \approx 1087 \text{ cm}^{-1}$, but also from two further vibration modes with $\omega_{SRS2} \approx 152 \text{ cm}^{-1}$ and $\omega_{SRS3} \approx 205 \text{ cm}^{-1}$. With single-wavelength pumping the generation of a multi-component lasing frequency comb of almost two octaves bandwidth is observed. With the same pumping conditions also the (non-phase matched) third harmonic of λ_{f1} is generated. With dual-wavelength pumping cascaded up-conversion $\chi^{(3)} \leftrightarrow \chi^{(3)}$ nonlinear lasing effects are observed. In addition, the occurrence of "combined" frequency combs with a spectral extension of more than two octaves (from $0.3415 \mu\text{m}$ to $1.5845 \mu\text{m}$), consisting of Stokes and anti-Stokes components of the two pumping wavelengths and including also components of their interactions in the UV range [4], is shown.

 [1] A.A. Kaminskii, L. Bohatý, P. Becker, H.J. Eichler, and H. Rhee, Laser Phys. Lett. **7** (2010) 142.

 [2] T. Sato and J. Suda, J. Phys. Soc. Japan **65** (1996) 482.

 [3] E.N. Caspi, B. Pokroy, P.L. Li, J.P. Quintana, and E. Zolotoyabko, Acta Cryst. B **61** (2005) 129.

[4] A.A. Kaminskii, H. Rhee, O. Lux, H.J. Eichler, V.V. Koltashev, R. Kleinschrodt, L. Bohatý, and P. Becker, Laser Phys. Lett. (2011), accepted.

MS17-P07

Synthesis and characterisation of new compositions with mullite type structure: $\text{Bi}_2\text{Cr}_x\text{M}_{4-x}\text{O}_9$ (M= Al, Ga) and $\text{Bi}_{2-x}\text{Sb}_x\text{Al}_4\text{O}_9$ T. Debnath¹, A. Hussain¹, L. Schomborg², C. Rüscher²¹University Dhaka, Chemistry, Dhaka, Bangladesh²Leibniz Universität Hannover, Mineralogie, Hannover, Germany

New series of compositions $\text{Bi}_2\text{Cr}_x\text{M}_{4-x}\text{O}_9$ (M = Al, Ga) and $\text{Bi}_{2-x}\text{Sb}_x\text{Al}_4\text{O}_9$ with mullite type structure could be synthesized within limited x following a route also used for the preparation of complete series of $\text{Bi}_2(\text{M}_x\text{M}'_{1-x})_4\text{O}_9$ with M/M' = Fe/Al, Fe/Ga, and Ga/Al [1]. In particular, the synthesis succeeded by mixing in glycerine appropriate proportions of hydrated nitrates of Bi, Al, Cr, Ga, and antimony oxide as ingredients. The stepwise conversions were gelation, foam formation at 120°C, calcination at about 300°C for the removal of volatile materials and finally annealing at 800°C in air for 24 hours.

Analysis of XRD data of $\text{Bi}_2\text{Cr}_x\text{M}_{4-x}\text{O}_9$ (M = Al, Ga) shows the mullite type pure phase exists for $x \leq 1.2$. The lattice parameters (a, b and c) of $\text{Bi}_2\text{Cr}_x\text{Al}_{4-x}\text{O}_9$ series increases with increasing Cr content up to $x = 1.2$ and remains constant for further increase in x indicating a limiting value for Cr doping. A more complicated behaviour were obtained within $\text{Bi}_2\text{Cr}_x\text{Ga}_{4-x}\text{O}_9$ series. The lattice parameter a remains constant, b decreases, and c increases up to $x \approx 1.0$ and then all remains constant. The effect of changing Cr/M contents was observed in infrared and Raman spectra, too. In particular, the absence of any significant shifting or splitting of the high energy IR absorption peak as assigned to the M-O_c vibration (O_c = common oxygen within the tetrahedral dimer, M₂O₇) shows that Cr occupies only the octahedrally coordinated sites.

XRD patterns for $\text{Bi}_{2-x}\text{Sb}_x\text{Al}_4\text{O}_9$ series reveal up to $x \approx 0.7$ mullite type single phase, possessing however, no significant change in lattice parameters. For $x > 0.7$ mullite type phase could not be detected. A systematic shift of the M-O_c related IR absorption peak which could be seen up to $x = 0.3$ could be related to the Sb doping. SEM/EDX analysis additionally show the presence of Sb for samples with x up to 0.7.

[1] T. Debnath, C.H. Rüscher, P. Fielitz, S. Ohmann, G. Borchardt, J. Solid State Chem. 183 (2010) 2582-2588.

MS17-P08

Structural study of hydrous neodymium acetatesP. Held¹, P. Becker¹, L. Bohatý¹¹Institute for Crystallography, University of Cologne, Koeln, Germany

While the crystal structures of the anhydrous lanthanide acetates $\text{Ln}(\text{CH}_3\text{COO})_3$ are comprehensively documented in literature [1-3], structural information about the aquo adducts $\text{Ln}(\text{CH}_3\text{COO})_3 \times x \text{H}_2\text{O}$ ($x = 1, 1.5, 3$ and 4) is far from being complete. All known crystal structures of the hydrates are reported to be centrosymmetric (space group P-1 or P2₁/c). In particular, for the tetrahydrates $\text{Ln}(\text{CH}_3\text{COO})_3 \times 4 \text{H}_2\text{O}$ that are structurally known the space group P-1 is given [4-6]. However, in three earlier papers [7-9] positive tests of piezoelectricity of the tetrahydrates are reported, which signal non-centrosymmetry (i.e. space group P1 instead of P-1).

In the present contribution we focused our study on the neodymium acetates. Large single crystals of the tetrahydrate (dimensions > 1cm³) were grown from aqueous solution by slow evaporation of the solvent at ca. 20°C. Using differently oriented plate-shaped samples which were cut from a large single crystal the occurrence of the longitudinal piezoelectric effect was tested. However, no hints for any piezoelectricity were found. In addition, a powdered sample of $\text{Nd}(\text{CH}_3\text{COO})_3 \times 4 \text{H}_2\text{O}$ was tested by the SHG powder test [10], which confirmed the result from our piezoelectric test by showing no significant SHG effect. Therefore, the centrosymmetric space group (P-1) is most probably the correct one. High-quality

small single crystals for structural investigations were obtained from aqueous solution of glycine and neodymium acetate. The crystal structure determination of $\text{Nd}(\text{CH}_3\text{COO})_3 \times 4 \text{H}_2\text{O}$ resulted in space group P-1 and cell parameters $a_1 = 9.0230(4) \text{ \AA}$, $a_2 = 9.4156(4) \text{ \AA}$, $a_3 = 10.5855(9) \text{ \AA}$, $\alpha_1 = 65.467(8)^\circ$, $\alpha_2 = 66.184(6)^\circ$, $\alpha_3 = 61.290(6)^\circ$ (R1 = 1.90%, wR2 = 5.0%). In addition, single crystals of two further neodymium acetate hydrate compounds, $\text{Nd}(\text{CH}_3\text{COO})_3 \times 1.5 \text{H}_2\text{O}$ and $\text{Nd}(\text{CH}_3\text{COO})_3 \times \text{H}_2\text{O}$, were obtained from aqueous solutions of glycine and Nd-acetate at 50°C. From the determination of their crystal structures we found for $\text{Nd}(\text{CH}_3\text{COO})_3 \times 1.5 \text{H}_2\text{O}$: Space group P-1, $a_1 = 8.4097(9) \text{ \AA}$, $a_2 = 10.0879(9) \text{ \AA}$, $a_3 = 13.3760(8) \text{ \AA}$, $\alpha_1 = 86.999(8)^\circ$, $\alpha_2 = 76.093(8)^\circ$, $\alpha_3 = 75.682(8)^\circ$ (R1 = 3.99%, wR2 = 11.14%) and for $\text{Nd}(\text{CH}_3\text{COO})_3 \times \text{H}_2\text{O}$: Space group P2₁/c, $a_1 = 8.4196(12) \text{ \AA}$, $a_2 = 7.9312(5) \text{ \AA}$, $a_3 = 15.0023(12) \text{ \AA}$, $\alpha_2 = 93.91(1)^\circ$ (R1 = 2.27%, wR2 = 6.32%). While the main structural features of the tetrahydrate are dimers $[\text{Nd}_2\text{O}_{16}]$, in the monohydrate chains of edge-sharing $[\text{NdO}_9]$ polyhedra are present, similar to chains of $[\text{PrO}_9]$ polyhedra described for $\text{Pr}(\text{CH}_3\text{COO})_3 \times \text{H}_2\text{O}$ [11]. Analogous chains are found in the sesquihydrate, however, here, the chains are linked by dimers of ten-fold coordinated neodymium to form layers perpendicular to the a_2 axis, as it was also found earlier for the corresponding praseodymium compound [12].

References:

- [1] G. Meyer and D. Gieseke-Vollmer, Z. Anorg. Allg. Chemie **619** (1993) 1603.
- [2] A. Lossin and G. Meyer, Z. Anorg. Allg. Chemie **619** (1993) 1609.
- [3] S. Gomez Torres and G. Meyer, Z. Anorg. Allg. Chemie **634** (2008) 231.
- [4] J.W. Bats, R. Kahlus, and H. Fuess, Acta Cryst. **B35** (1979) 1225.
- [5] M.C. Favas, D.L. Kepert, B.W. Skelton, and A.H. White, J. Chem. Soc. Dalton Trans. (1980), 454.
- [6] F. Ribot, P. Toledano, and C. Sanchez, Inorg. Chim. Acta **185** (1991) 239.
- [7] G.V. Nadezhdina, V.I. Ivanov, V. Shubina, and V.E. Plyushchev, Zh. Obshch. Khim. **36** (1966) 1560.
- [8] R. Vadura and J. Kvapil, Mat. Res. Bull. **6** (1971) 865.
- [9] R. Vadura and J. Kvapil, Mat. Res. Bull. **8** (1973) 813.
- [10] S.K. Kurtz and T.T. Perry, J. Appl. Phys. **39** (1968) 3798.
- [11] S. Ganapathy, V.P. Chacko, R.G. Bryant, and N.C. Etter, J. Am. Chem. Soc. **108** (1986) 3159.
- [12] A. Lossin and G. Meyer, Z. Naturforschung **47b** (1992) 1602.

MS17-P09

High-Pressure Investigations of spinel-type LiTM_2O_4 (TM = transition metal) cathode materialsC. Braun^{1,2}, N. Kiziltas Yavuz², E. Reitz², K. Nikolowski^{3,4}, J.M. Gallardo-Amores⁵, M.E. Arroyo-de Dompablo⁵, H. Ehrenberg^{2,3}¹TU Dresden, IFWW, Dresden, Germany²KIT, Institut für Anorganische Chemie, Karlsruhe, Germany³KIT Karlsruhe, Institut für Angewandte Materialien, Eggenstein-Leopoldshafen, Germany⁴IFW Dresden, Institut für Komplexe Materialien, Dresden, Germany⁵Facultad de Ciencias Químicas, Universidad Complutense de Madrid, Madrid, Spain

New synthesis strategies are needed to prepare novel electrode materials for lithium-ion batteries. High pressure / high temperature routes are widely used within other fields of Solid State Chemistry to induce structural transformations of materials, conducting to novel polymorphs possessing structures not accessible at ambient pressure. The high pressure treatment changes both the crystal structure as well as the electronic characteristics of the material. High pressure driven transformations of several electrode materials have been studied and reported, for example Li_xFePO_4 ,^[1,2] V_2O_5 ,^[3] Li_2MSiO_4 (M = Mn, Co).^[4,5] It is proven that after exposure to high pressure/high

temperature conditions, the electrochemical properties varied compared to the ambient pressure materials.

For LiMn_2O_4 various studies report structural examinations at high pressure of these spinel phase^[6-9]. But, only little is known about the electrochemical behaviour of these phases, when they are used as intercalation compound for an electrode in a lithium ion battery.^[10] In this communication we investigate the pressure driven structural and electrochemical modifications of spinel LiTM_2O_4 (TM = transition metal) cathode materials.

- [1] M. E. Arroyo de Dompablo, N. Biskup, J.M. Gallardo-Amores, E. Morán, H. Ehrenberg, U. Amador, *Chem. Mater.* 2010,22, 994.
- [2] M. E. Arroyo-de Dompablo, J.M. Gallardo-Amores, U. Amador, *Electrochem. Solid St.*2005,8, A564-A569.
- [3] M. E. Arroyo de Dompablo, J. M. Gallardo-Amores, U. Amador, E. Morán, *Electrochem. Commun.* 2007,9, 1305-1310.
- [4] M. E. Arroyo y de Dompablo, U. Amador, J.M. Gallardo-Amores, E. Morán, H. Ehrenberg, L. Dupont, R. Dominko, *J. Power Sources*2009,189, 638.
- [5] M. E. Arroyo-de Dompablo, R. Dominko, J.M. Gallardo-Amores, L. Dupont, G. Mali, H. Ehrenberg, J. Jamnik, E. Moran, *Chem Mater*2008,20, 5574-5584.
- [6] P. Piszora, W. Nowicki, J. Darul, B. Bojanowski, S. Carlson, Y. Cerenius, *Radiat. Phys. Chem.*2009,78, S89-S92.
- [7] J. Darul, W. Nowicki, C. Lathe, P. Piszora, *Radiat. Phys. Chem.*2011,80, 1014-1018.
- [8] A. Paolone, A. Sacchetti, P. Postorino, R. Cantelli, A. Congeduti, G. Rousse, C. Masquelier, *Solid State Ionics*2005,176, 635-639.
- [9] K. Tokiwa, K. Matsukura, S. Kasahara, S. Tsuda, S. Mikusu, K. Takeuchi, A. Iyo, Y. Tanaka, J. Akimoto, J. Awaka, N. Kijima, Y. Takahashi, T. Watanabe, *J. Phys.: Conf. Ser.*2009,150, 042210.
- [10] K. Yamaura, Q. Huang, L. Zhang, K. Takada, Y. Baba, T. Nagai, Y. Matsui, K. Kosuda, E. Takayama-Muromachi, *J. Am. Chem. Soc.*2006,128, 9448-9456.

MS17-P10

Analysis of photochromic nanoparticles in silica monolith: A total scattering study

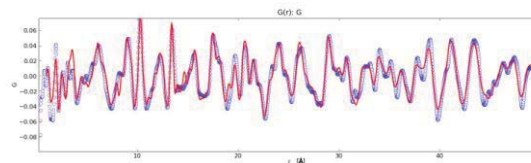
K.-Y. Hsieh¹, D. Schaniel¹, E.-E. Bendeif¹

¹Nancy Université, Laboratoire de Cristallographie, Résonance, Magnétique et Modélisations (CRM2, UMR UHP-CNRS 7036), Vandoeuvre les Nancy, France

Nanoparticles and isolated molecules of the photosensitive compound $\text{Na}_2[\text{Fe}(\text{CN})_5\text{NO}]$ (SNP) have been embedded in silica monoliths. These SNP compounds form linkage isomers of the NO group upon light irradiation, which renders them interesting for optical applications[1].

In order to study in detail the local structure of this $\text{SNP}@\text{SiO}_2$ guest-host system, we performed total scattering X-ray measurements, that were analysed using Pair distribution function (PDF) methods[2] and Debye Function (DF) analysis[3]. The study of PDF on different length scales allows for obtaining information about the nano-scale or disorder structures. Meaningful results of PDF analysis on a range of samples with different particle size have been obtained by measurements on a standard laboratory X-ray powder diffractometer, equipped with a Mo source ($Q_{\text{max}} \sim 17 \text{ \AA}^{-1}$). Fig. 1 shows the PDF of crystalline SNP that serves as a reference for the structure analysis of the host-guest systems. It allows for a thorough calibration of all correction parameters necessary for the detailed analysis of the local molecular structure. Figure 1 PDF of crystalline SNP measured on a laboratory X-ray diffractometer. Experimental data in blue, calculated PDF in red. Peaks in PDF ($G(r)$ in [Å]) present all the atom pair contributions in the solid.

- [1]D. Schaniel et al.,*Adv.Mater.*19, 723 (2007)
- [2]S. J. L Billinge, I. Levin,*Science*316, 561 (2007)
- [3]A. Cervellino et al.,*Appl.Crystallography*43(2010)



MS17-P11

Ternary and quaternary mixed valence compounds with interesting electrical properties

K. Xhaxhiu¹, K. Bente², M. Lorenz³

¹University of Tirana, Faculty of Natural Sciences, Tirana, Albania

²University of Leipzig, Institute of Mineralogy, Crystallography and Material Science, Leipzig, Germany

³University of Leipzig, Department of Physics II, Leipzig, Germany

The ternary mixed valence compounds $\text{In}_5\text{Ch}_5\text{X}$ ($\text{Ch} = \text{S}, \text{Se}; \text{X} = \text{Cl}, \text{Br}$), consisting of needle-shaped crystals show very interesting electrical properties measured on individual crystals and/or bulk samples. $\text{In}_5\text{Se}_5\text{Br}$ which crystallize in the orthorhombic crystal system ($Pmn2_1$), reveals regular structures and show tremendously high Seebeck coefficient $10^5 \mu\text{V/K}$ (measured on bulk). Substitution of one selenium position with sulfur decreases this value approx. 10 times, meanwhile, a full sulfur substitution, leads to low negative Seebeck coefficients ($-16.7 \mu\text{V/K}$), shifting the character of this semiconductor from n - to p -type. The resistivity of bulk $\text{In}_5\text{Se}_5\text{Br}$ (as grown sample) oscillated between $3.4 \times 10^7 - 4.3 \times 10^8 \Omega$, while its individual needles showed values ranging from $1.2 \times 10^{11} - 8.4 \times 10^{12} \Omega$ respectively. The sulfur substitution of three selenium positions in the structure caused a decrease of the resistivity of individual needles to $3.8 \times 10^8 \Omega$. A further decrease of the resistivity couldn't be reached by fully sulfur substitution. Instead, slightly higher values compared to $\text{In}_5\text{Se}_5\text{Br}$ were observed. Partial substitution of In^{3+} with Tl^{3+} in $\text{In}_5\text{Se}_5\text{Br}$ did not improve a lot the resistivity of the needles, while similar substitutions followed by mutual halogen substitution of bromine with chlorine displayed lower resistivities up to $2.8 \times 10^6 \Omega$. In this course of investigations, our latter I-U measurements on the individual needle-shaped crystals of the compounds $\text{In}_5\text{Ch}_5\text{Cl}$, crystallizing in the monoclinic crystal system ($P2_1/m$), and revealing several structural problems [1], showed significant light sensitivities. Current jumps up of two orders of magnitudes ($10 \text{ pA} - 0.1 \text{ nA}$) for voltages changing from 0 to 10 V were observed for on-off-switching between dark and maximal light intensity corresponding to resistivities between ca. 6.3×10^{12} and $6.3 \times 10^{11} \Omega$. An intensification of this phenomenon was observed by partial substitution of one selenium position with sulfur in the structure.

Keywords: mixed valence compounds, Seebeck coefficient, resistivity, light sensitivity

- [1] Deiseroth, H. J., Reiner, C., Xhaxhiu, K., Schlosser, M., Kienle, L. (2004) *Z. Allg. Anorg. Chem.*, 630 (13-14), 2319-2328.

MS19-P01

The intermediate phase between sodalite and cancrinite: stability investigations of nanocrystals by TIR, STA and hydrothermal leaching

C. Grader¹, J.-C. Buhl¹

¹Institut of Mineralogy, Leibniz University, Hanover, Germany

The behaviour of zeolites at elevated temperature as well as in water can attain high importance for special technical applications in sorption, ion exchange or catalysis [1-2]. Whereas thermal and

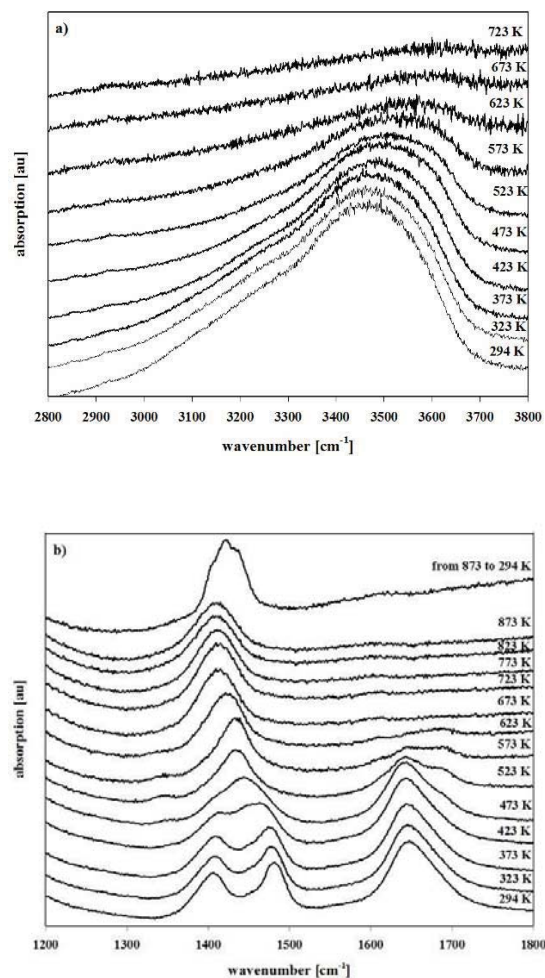
hydrothermal framework decomposition was investigated for many zeolites of well ordered structure types of exact topology there is only minor knowledge on the behaviour of phases with disordered intermediate framework structures between different types, like those of sodalite (SOD) and cancrinite (CAN) [3]. We investigate here an intermediate nanocrystalline carbonate enclathrated zeolite phase of this type. Our sample was observed from gels under addition of high amounts of NaOH and Na₂CO₃ at low temperature (333 K) and short time (3h) reaction conditions, as recently described in [4-5] and analyzed by X-ray powder diffraction (XRD) and scanning electron microscopy (SEM).

In the present study thermal behavior was investigated by temperature dependent Fourier transform infrared spectroscopy (TIR) and simultaneous thermal analysis (STA). Because the intermediate phase can be regarded as a disordered CAN, its properties were compared with microcrystalline carbonate CAN obtained by common alkaline hydrothermal transformation of kaolinite at 473 K for 48 h. A remarkable high thermal stability of the nanocrystalline INT-framework was found according to exothermic framework destruction at 1133 K (microcrystalline CAN: endothermic decomposition at 1113 K).

In addition to thermal behaviour the hydrothermal stability of the intermediate phase was examined at 353 K for periods between 4 h to 48 h by water treatment at a solid:liquid mass ratio of 1:150. The kinetics of decomposition was followed by the loss in weight, the change of the pH-value of the hydrothermal solution as well as the loss of crystallinity of the sample according to X-ray powder diffraction an FTIR spectroscopy in comparison with the behaviour of the microcrystalline CAN of common synthesis.

Analysis data of hydrothermal behavior clearly reveal a much higher decomposition rate of the intermediate phase compared to microcrystalline CAN. Whereas the entrance of water molecules is blocked by the cations in the ϵ -cages and the carbonate anions inside the CAN-channel, the random AB (CAN) and ABC (SOD) stacking of aluminosilicate sheets in hexagonal c-direction of the INT structure gives rise to formation of cages of various sizes with large "windows", mainly filled with water. Instead of the clathralite-like behaviour of CAN typical zeolite properties can be assumed for INT-phases [6].

Fig. 1: TIR-spectra of INT in the region of enclathrated guests: a) H₂O stretching mode (δ); b) stretching modes of CO₂₃⁻ (ν_{as}) and bending mode of H₂O (δ).



MS19-P02

Hydrothermal synthesis of eulytite (Bi₄(SiO₄)₃) crystals.

E. Marina¹, A. Marin¹, T. Bublikova¹, V. Balitsky¹

¹Institute of Experimental Mineralogy RAS, LSMM, Chernogolovka, Moscow Distr., Russian Federation

Eulytite (Bi₄(SiO₄)₃) is one of the rarest minerals in a nature. It occurs in the albitized pegmatites in the tetrahedral crystals form and crust around tantalum grain in the Caucasus, find out together with quartz and native bismuth in the Schneeberg and Johanngeorgenstadt (Germany), in the Dognecea (Rumania), single finding - in the Czech Republic, England, USA, Canada, China and Australia. [1-3].

Crystals of eulytite are uses for scintillator in the high-energy physics, computer tomography, dosimetry [4-6]. Since eulytite difficult to grow from the melt due to high viscosity, it is better to obtain ceramics based on it. It is known that the ceramics of optical quality are produced by pressing small natural or synthetic crystals [7]. We believe that the ceramics obtained from crystals of bismuth orthosilicate that we grow, will have better scintillation characteristics than the ones obtained by direct sintering of the initial oxide components.

Hydrothermal synthesis of eulytite was produced at temperature 260°C and pressure about 500 bar. Starting material was stoichiometric mix of Bi₂O₃ и SiO₂. Solvents were aqueous solutions of hydrogen peroxide (H₂O₂) with concentrations from 1 to 5 wt %, alkaline (NaOH) (from 5 to 20 wt %) and fluoride (NH₄F) (from 1 to 3 wt %). The fine crystalline eulytite got in experiments with duration from 7 to 12 days. Use of contact Teflon fettle was feature of the technique applied by us, allowing to exclude ingress of the elements containing in a steel of autoclaves

[1] Breck, D. W.: Zeolite Molecular Sieves, Wiley & Sons, London 1974.

[2] Buhl, J.-C., Gerstmann, M., Lutz, W., Ritzmann, A.: Z. Anorg. Allg. Chem. 630 (2004) 604.

[3] Hermeler, G.; Buhl, J.-Ch.; Hoffmann, W.: Catalysis Today, 1991, Vol. 8, 415.

[4] Grader, C. diploma thesis, 2009, Institut für Mineralogie, Universität Hannover. Hannover 2009.

[5] Grader, C., Robben, L., Buhl, J.-Ch.: Abstracts of the 26th European Crystallographic Meeting, ECM 26, Darmstadt 2010, Acta Cryst. (2010). A66, 230.

[6] Liebau, F.: Structural Chemistry of Silicates. Springer Berlin, Heidelberg, New York, Tokyo, 1985.

in a solution.

We had been received powders of eulytite with the sizes of crystals from first microns to the tenth shares of millimeter (fig.1). X-ray patterns show the presence of eulytine eumorphic crystals virtually without admixtures of other minerals.

Previously eulytite was synthesized in NaOH [8], but subsequent researches in this field don't carried out. Eulytite crystals in ammonium fluoride and hydrogen peroxide we grown in a first time in the world. The analysis of the results of our researches has shown that hydrogen peroxide is the most perspective solvent for eulytite synthesis. Since the system is missing elements that are not included in the composition of eulytine, this automatically settles the problem of solvent's impurities in the obtained crystals. It is of great importance for the growth of small crystals, because technologically it is as very complicated process of nano- or micro-particles segregation from the source solvent and from the foreign solid phases, created in the process of growth; therefore, it is desirable, that all the components of the solution are involved in the crystallization.

References:

- [1] F.V.Chuhrov, at al. Minerals. Moscow, Nedra,(1972), 883 (in Russian)
- [2] J. Sejkora, J. Cejka, J. Hloulek, at al., Can. Mineral. (2004) 42, 963.
- [3] E. E. Foord, Mineral. Mag. (1996) 6, 387.
- [4] Phillips, W.R. and D.T. Griffen (1981) Optical mineralogy, 412.
- [5] Rehwald W., Widmer R. (1973) J.Phys.Chem.Solids. 34, 12, 2269-2272
- [6] Kaminsky A. at al. Jour. of Theor. Phys. (1976) 2, 4, 156-161(in Russian).
- [7] Basiev T. at al. Proc. of the Russian Acad. of Sci. (2008). 5, 863-873. (in Russian)
- [8] Litvin B. at al. Crystallography (1968) 13, 6, 1106. (in Russian)

This study was supported by a grant (09-02-00647) from the Russian Basic Research Foundation.

MS19-P03

Synthesis of Large Single Crystal of Sugilite

S. Park¹, J. Heimhilger¹

¹Crystallography / LMU, Geo- & Environmental Sciences, LMU, Germany

The double cyclosilicates sogdianite and sugilite are of interest due to Li- and Na cationic conductivity [1, 2]. A direct current conductivity value of $\sim 1 \times 10^{-3} \text{ S cm}^{-1}$ at $T = 1093 \text{ K}$ was estimated with impedance spectra of sugilite, the best cationic conductor among this type materials, reported so far. However, for industrial application sugilite-type materials are to be modified to show superionic conductivity. On the other hand, to study direction-dependent conductivity measurement it is necessary to obtain large single crystals of this type of compounds occurring seldom as well-formed minerals. For this purpose a series of hydrothermal synthesis has been performed at 300-400°C under autogenously induced pressure up to 400 bar. Synthesis results will be presented at DGK 2012 along with structural reports.

MS19-P04

Neue Einblicke in mehr als 150 Jahre alte anorganisch - organische Hybridmaterialien auf Basis des Elementes Zinn: Synthese und strukturelle Charakterisierung von [Et₂Sn(OH)NO₃]

M. Reichelt¹, H. Reuter¹

¹Universität Osnabrück, Institut für Chemie, Osnabrück, Germany

Anorganisch - organische Hybridmaterialien auf Basis des Elementes Zinn wurden erstmals von A. Cahours [1] im Jahre 1860 eingeführt, um Organozinnverbindungen, die kurz vorher erstmals hergestellt worden waren [2], über die Bildung von Derivaten besser charakterisieren zu können. Im Fall der Diethylzinnverbindungen umfasste diese Vorgehensweise die Herstellung des Oxids, welches dann mit Mineralsäuren (z.B. HNO₃) oder Carbonsäuren (z.B. AcOH) umgesetzt und die neuen Verbindungen im Hinblick auf ihre chemische Zusammensetzung, Farbe, Löslichkeit und Kristallform untersucht wurden.

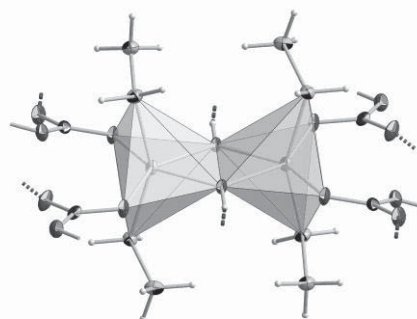
So erhielt er bei der Umsetzung von Diethylzinnoxid mit verdünnter Salpetersäure Prismen. Dem gegenüber bildeten sich bei unserem Versuch zur Reproduktion farblose nadelförmige Kristalle.

C₄H₁₁NO₄Sn: $M_m = 255.83 \text{ g/mol}$, monoclinic, $P2_1/c$ (no. 14), $a = 7.4015(4) \text{ \AA}$, $b = 13.1003(6) \text{ \AA}$, $c = 8.4847(5) \text{ \AA}$, $\beta = 106.9280(10)^\circ$, $V = 787.05(7) \text{ \AA}^3$, $Z = 4$, $d_{\text{cal}} = 2.159 \text{ g/cm}^3$, $T = 100(2) \text{ K}$, $F_{000} = 496$, $2\theta_{\text{max}} = 28.00^\circ$, $R_{\text{collected}} = 46509$, $R_{\text{unique}} = 1888$, $R_{\text{int}} = 0.0338$, multiscan absorption correction, $T_{\text{min}} = 0.5677$, $T_{\text{max}} = 0.8905$, completeness = 99.3%, $\text{Par}_{\text{ref}} = 98$, $R_1[\text{I} > 2\sigma(\text{I})] = 0.0136$, $R_1[\text{all data}] = 0.0176$, $wR_2[\text{I} > 2\sigma(\text{I})] = 0.0286$, $wR_2[\text{all data}] = 0.0297$, $\Delta e_{\text{max/min}} = 0.358 / -0.412 \text{ e\AA}^{-3}$.

Die asymmetrische Einheit besteht aus einer Formeleinheit der Titelverbindung. Sie besteht aus stark verzerrten $\{\text{Et}_2\text{Sn}(\text{OH})_{2/2}(\text{NO}_3)_{2/2}\}$ - Oktaedern, die über eine gemeinsame Kante aus Hydroxylgruppen ($\mu_2\text{-OH}$) zu zentrosymmetrischen Dimeren verknüpft sind, während die trigonal-planaren Nitratgruppen über zwei verschiedene Sauerstoffatome jeweils zwei Dimere miteinander verbinden ($\mu_2\text{-NO}_3$), wobei leicht gewellte Schichten entstehen, bei denen die Ethylgruppen oberhalb und unterhalb abstehen.

Schlüsselwörter: Zinnverbindungen, anorganisch-organische Hybridmaterialien, Nitrate

- [1] A. Cahours, Ann. Chem., 114 (1860) 354 - 382.
- [2] E. Frankland, Ann. Chem., 85 (1853) 329 - 373.



MS19-P05

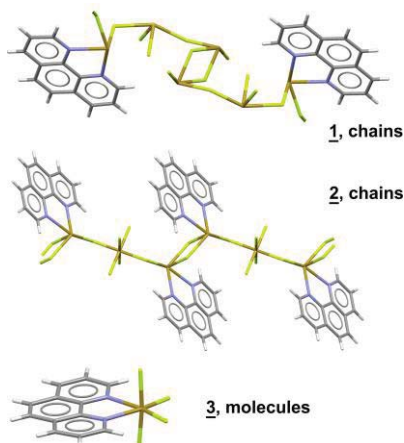
From tin(II) to tin(IV): one pot synthesis of three coordination compounds with tin in three different oxidation states (II-II/IV-IV) in the presence of fluorine ions and 1,10-phenanthroline.

H. Reuter¹, S. Schröder¹, N. Röwekamp-Krugley¹, M. Imwalle¹

¹Universität Osnabrück, Institut für Chemie, Osnabrück, Germany

Coordination compounds of tin(II) halides are counted to be sufficiently studied. Looking into more detail, however, reveals that there are many blank spots in this area, especially with respect to precise X-ray diffraction data. For instance, from the 1,10-phenanthroline (Phen) adducts with SnHal₂ only the 1:1 compound of the chloride (Hal = Cl) is listed in the Cambridge Crystallographic Database (FEDIW [1]). Therefore, we have started a project to prepare the Phen adducts of all tin(II)-halides in order to examine the influence of the halide atom on the coordination behavior of tin in these coordination compounds. In the case of Hal = F, we were able to isolate from a dimethylsulfoxide (DMSO) solution of SnF₂ and Phen in the course of three days single crystals of the following compounds: thick, bright yellow blocs of 2SnF₂ · SnF₂(phen), **1**, small, colorless prism of 2SnF₂(phen) · SnF₄, **2**, and thick, red-brown to colorless columns of SnF₄(phen), **3**, the last two ones as a result of slow oxidation of tin(II) to tin(IV). In these compounds (Fig. 1) tin adopts its typical oxidation states +II (**1**) and +IV (**3**), whereas **2** represents a new mixed valent tin compound with tin in both oxidation states.

1. S.J. Archer, K.R. Koch and S. Schmidt: *Nitrogen Donor Chelates of Bivalent Tin Chloride. Part II. The Crystal Structures of SnCl₂ · (2,2'-bipyridyl) and SnCl₂ · (1,10-phenanthroline)*, Inorg. Chim. Acta **126** (1987) 209-218.



MS19-P06

Single crystal growth and characterization of the intermetallic compound InPd

M. Hahne¹, P. Gille¹

¹Ludwig-Maximilians-Universität München, Department of Earth and Environmental Sciences, Crystallography Section, München, Germany

To generate hydrogen for fuel cells, methanol steam reforming is one of the possibilities. For this chemical reaction a catalyst with high activity, selectivity and thermal stability is needed and the intermetallic compound InPd could be a promising material for this. Although large specific surfaces are wanted to achieve effective catalysis, for a number of studies single crystalline and crystallographically oriented bulk samples with a certain size are necessary to understand the mechanisms of catalysis.

The structure of InPd is quite simple as it has a CsCl type of structure. Using the Czochralski technique crystal growth is done from In-rich solutions because the vapour pressure of indium is a

limiting factor at very high temperatures. Compared to Czochralski growth from stoichiometric melts some important differences have to be considered. In order to avoid inclusions of the solution in the growing crystal the pulling speed has to be very low. Further to stabilize the diameter of the crystal an appropriate temperature program is necessary to take into account the liquidus temperature which is changing with the amount of material already crystallized. At lower temperatures, according to the binary phase diagram [1], the stability region of InPd is shrinking. So this retrograde solubility theoretically enables the formation of precipitates of the neighbouring phase In₃Pd₂ while the grown crystal is cooling down.

Our experimental setup, the growth parameters and the seeding strategy to get the first crystal of InPd will be explained in detail. We will show the results of the characterization and will discuss the quality of the grown crystals.

[1] H. Okamoto, J. Phase Equilib. 24 (2003), 481.

MS19-P07

Characterization of thin films of Sn_{1-x}Pb_xS mixed crystals (0.0 < x < 0.5)

S. Lobe¹, G. Wagner¹, R. Kaden¹, V. Gremenok², V. Lazenka², K. Bente¹

¹Universität Leipzig, Institut für Mineralogie, Kristallographie und Materialwissenschaft, Leipzig, Germany

²Scientific Research Center of the NAS of Belarus, Minsk, Belarus

Mixed crystals within the orthorhombic series of Sn_{1-x}Pb_xS are promising materials for low cost thin film solar cells and thermoelectrical devices. Depending on the composition the direct band gap is found to be between 1.1(SnS) [1] - 1.65 eV (PbSn₂) [2].

Highly interesting Sn_{1-x}Pb_xS thin films with x = 0.0 and 0.5 were prepared by a hot wall beam technique. SnS and PbS as initial compounds were evaporated using independently heated tubes and reacted to thin films next to the substrate, usually silica glass. By the selected evaporation of starting binary compounds the composition of the resulting mixed crystal materials is controlled. The products were investigated by X-ray diffraction and transmission electron microscopy.

The polycrystalline thin films show crystallite sizes depending on evaporation and substrate temperatures. The intergrown grains, containing small pinholes, show predominant orientations ((hk0) or (00l)) parallel to the substrate surface depending on the film thickness. Exceeding a critical film thickness these orientations are lost.

[1] Albers et al., J. Phys. Chem. Solids 15, 306-310, 1960

[2] Unuchak et al. Phys. Status Solidi C 6 (5), 1191-1194 (2009)

MS19-P08

Crystalline Rare Earth Complex Synthesis by Solvent-drop Assisted Grinding

U. Baisch¹

¹Newcastle University, School of Chemistry, Newcastle-upon-Tyne, United Kingdom

Rare earth crystal engineering is a challenging field in chemistry, which is due to the high number of parameters to be considered when developing a synthetic bottom-up approach wherein crystallographic and chemical knowledge in rare earth chemistry is required to design and construct inorganic tectons. These tectons may then be used to prepare new materials in a controlled manner with specific optical or magnetic properties.^[1,2]

This approach allowed us to engineer and study crystals in which protonated melamine is involved in metal-organic coordination salts, co-crystals, and solvates (see e.g. Fig. 1). The compounds were conveniently synthesised by simple solvent drop assisted grinding of the reagents with a catalytic amount of water. Because of the low solubility of both the lanthanide anion and melaminium

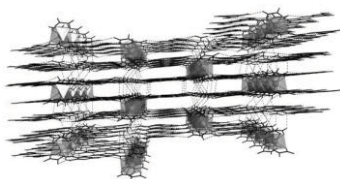
nitrate, crystallisation of the products proved problematic. Single-crystals suitable for the determination of the structures were obtained from the mother liquor by refluxing the aqueous reaction mixture for several days.^[2] Two of the four crystal structures presented were measured at the DIAMOND synchrotron facility in Oxfordshire.

Crystal structures of melaminium salts (melamine = 2,4,6-triamino-1,3,5-triazine) were analysed towards their different patterns of intermolecular interactions. The relationships between the different degrees of protonation of the melamine salts and their ability to form layered or zig-zag arrangements of molecules was examined.

Figure 1 Crystal structure of hexamelaminium tetraoxalato-ytterbium(III) 3.5 hydrate. View along cell axis a.

[1] G. R. Desiraju, *Angew. Chem., Int. Ed.*, (2008), 46, 8342-8356.

[2] U. Baisch, D. Braga, *CrystEngComm*, (2009), 11, 40-42.



Index

Abbound, A.	78	Brandao, J.	47	Eichler, H.J.	118
Abendroth, B.	77	Braun, C.	119	Eilers, F.	81
Abrikosov, I.	35	Bredow, T.	89	Eisenberg, H.S.	118
Ackermann, M.	52	Brokmeier, H.-G.	54, 57, 61	El-Sayed, K.	11
Adam, A.	79	Browning, F.	39	Emmerling, F.	40, 56
Adam, M.	41, 51	Brüning, J.	92, 100	Enax, J.	42
Aguilar Sanjuan, B.	61	Bublikova, T.	81, 121	Englert, U.	67, 117
Albrecht-Schmitt, T.	113	Buhl, J.-C.	10, 59, 62, 82, 89, 120	Epple, M.	42
Alekseev, E.	37, 113	Bündgens, D.	117	Ernst, A.	44
Alexa, P.	43	Bürger, A.	81, 87	Erra, L.	105, 106
Alhamdany, N.	61	Burgert, I.	36, 37	Evans, G.	47
Ali, S.I.	107	Burghammer, M.	9, 26	Fabbiani, F.	18, 52
Alig, E.	100, 107	Burkhardt, A.	51	Fabritius, H.-O.	37
Allen, D.	9, 61	Bykov, M.	77, 85	Fabrizio, P.	21
Amel, M.	82	Bykova, E.	22, 23	Fahrnbauer, F.	105, 106
Amthauer, G.	25, 78	Campbell, B.J.	31, 34	Falkenberg, G.	26
Angel, R.	8, 44	Chan, G.	20	Fechner, M.	44
Angelkort, J.	29	Chance, M.	68	Fechtelkord, M.	24, 80
Anouar, N.	61	Chatterjee, H.	19	Feiler, C.	65
Aroyo, M.I.	35	Chumak, I.	116	Fernandez-Alonso, F.	38
Arroyo-de Dompablo, M.E.	119	Cianci, M.	40, 114, 115	Ferrero, C.	116
Ashton, A.	47	Ciniawsky, S.	19	Fiedler, S.	40, 114, 115
Authier, A.	3	Conti, E.	20, 70	Fillenber, S.	28
Axford, D.	47	Cousson, A.	93	Finger, L.	8
Baisch, U.	123	Dahms, S.	13, 41	Fink, L.	107
Baker, E.N.	4	Dähn, R.	60	Fischer, R.X.	38, 75, 101, 111, 113
Balitsky, V.	121	Danilewsky, A.	9, 61	Fitch, A.	116
Barden, S.	65	Daoud-Aladine, A.	12	Flaig, R.	47
Bauer, B.	94	Datta, K.	19	Förster, E.	48
Baumbach, T.	9	Daumke, O.	69	Förster, R.	116
Baumgärtner, M.	70	Davtyan, A.	80	Forstner, R.	76
Baur, W.H.	113	de la Flor, G.	35	Fortes, D.	39
Bayarjargal, L.	22, 73	De Marco, F.	54	Frank, W.	106, 108, 111, 112, 113
Becker, K.-D.	25, 29	De Wit, J.	72	Franzl, T.	79
Becker, N.	117	Debnath, T.	119	Fratzl, P.	37
Becker, P.	52, 80, 118, 119	Del Seppia, M.E.	54	Friedrich, A.	7
Beermann, O.	113	Demtröder, K.	81	Friese, K.	32, 71
Behrendt, K.	33	Denzer, U.	79	Frost, D.	9, 22
Beirau, T.	79	Depmeier, W.	37, 113	Fruhner, J.-C.	79
Bendeif, E.	120	Detlefs, C.	48	Fuess, H.	11
Benke, A.	46	Dey, S.	85	Gallardo-Amores, J. M.	119
Bente, K.	120, 123	Diehl, A.	27	Gan, W.	54, 57
Berghäuser, A.	53	Diestel, U.	20	Ganschow, S.	29
Bergmann, C.	16	Diezmann, D.	69	Gao, S.	69
Berthold, C.	8	Dinnebier, R.E.	34, 63, 65, 89	Genchev, G.	108
Berthold, N.	64	Dittrich, B.	18, 67	Genz, M.	62
Berti, G.	50, 54	Diwu, J.	113	Gerhardt, V.	96
Betzler, S.	43	Doert, T.	32	Gerth, K.	46
Bhogaraju, S.	70	Dolomanov, O.	50	Gesing, T.M.	25, 75, 82, 101, 111, 113
Biadene, M.	41, 48	Dosch, H.	3	Gibhardt, H.	33, 76, 80
Biertümpfel, C.	29	Douangamath, A.	47	Gierlotka, S.	41
Birkenstock, J.	101	Dovrat, L.	118	Gies, H.	87, 108, 109
Bismayer, U.	31, 41, 53, 79	Doyle, S.	116	Gildea, R.	50
Blankenfeldt, W.	13, 65	Dubrovinskaia, N.	18, 22, 23	Gille, P.	123
Bock, D.A.	100	Dubrovinsky, L.	18, 22, 23	Gjikaj, M.	102
Boffa-Ballaran, T.	9, 22, 23	Dubs, C.	73	Glaum, R.	85
Bohaty, L.	52, 80, 118, 119	Duk, A.	84	Glazer, M.	30, 74
Boldyreva, E.	74, 91	Duke, L.	47	Glazyrin, K.	23
Bolotina, N.	93	Dura, L.	80	Glinnemann, J.	88, 107
Bommer, M.	116	Dybkov, O.	21	Gnutzmann, T.	40
Bonneau, F.	70	Eberle, M.A.	104	Gorfman, S.	30, 74
Bono, F.	28	Eckert, M.	3	Görnert, P.	73
Borisova, D.	10	Eckold, G.	33, 76, 80	Gospodinov, M.	31
Bourenkov, G.	40, 114, 115	Eder, M.	36	Götz, A.J.	26
Bourhis, L.	50	Effenberger, H.	112	Götz, D.	53
Bracher, A.	19	Egert, E.	64, 96	Grabowski, S.	109
Braden, M.	5	Ehrenberg, H.	30, 80, 116, 119	Grader, C.	120

Index

Graf, J.	48, 49, 52, 53	Hoppe, R.	26, 27, 97	Kothai, V.	12
Greenberg, E.	23	Höss, P.	110	Kovacevic, J.	80, 81
Gregory, M.	29	Hradil, K.	76	Kramer, K.	21
Gremenok, V.	123	Hsieh, K.-Y.	120	Krauss, M.	20
Griesser, U.	72	Huber, R.	4	Kräußlich, J.	73
Griesshaber, E.	42, 43	Hübschle, C.B.	18, 67	Krbetschek, C.	10
Grießl, M.	68	Hundt, R.	87	Kremer, R.	77, 85
Grigorian, S.	80	Hüsecken, A.K.	67	Krenzel, T.	45
Grodzicki, M.	25	Hussain, A.	119	Kriegel, T.	14
Gröschel, A.	16	Imwalle, M.	123	Krug, M.	41, 116
Grünewald-Lüke, A.	109	Isaeva, A.	32	Krug, U.	20
Grünwald, M.	28	Ivashevskaja, S.N.	100	Krüger, H.	75
Grüter, S.	117	Janneck, E.	26	Krysiak, Y.	107
Grzechnik, A.	32, 71	Jansen, M.	5, 87, 89	Ksenzov, D.	80
Guerin, L.	33	Jauß, T.	61	Kucera, N.	14
Guo, Y.	117	Jayachandran, U.	20	Kuester, M.	13, 41
Gutmann, E.	46	Jehle, M.	95	Kuhlen, T.	117
Gutmann, M.	38	Jeyaprakash, A.A.	20	Kühnel, K.	69
Hagelstein, M.	116	Jilg, S.	76	Kungl, H.	11, 30
Hahne, M.	123	Jo, W.	11	Kurnosov, A.	9, 22
Halevy, A.	118	Jordan, G.	43	Kuzmicheva, G.	92
Hall, D.	47	Jörgens, S.	106	Küttner, B.	14
Hamacher, A.	117	Jura, M.	38	Kwasniewski, A.	84
Hammer, S.M.	92	Jüttner, P.	54	Laatsch, B.	54
Hanaoka, F.	29	Kaden, R.	123	Lamberts, K.	117
Hanfland, M.	22, 23	Kadletz, P.M.	26	Lange, J.	48
Hanna, J.V.	38	Kaganer, V.	84	Langner, R.	24
Hanzig, F.	77	Kahlenberg, V.	57, 72, 75, 92	Law, J.	85
Hanzig, J.	77	Kähn, J.	105	Lazenka, V.	123
Haramus, V.	115	Kalawy-Fansa, E.	13	Lazzaretti, D.	28
Harbrecht, B.	72, 73, 107	Kamdem, N.	27	Leban, I.	98
Hartenbach, I.	95, 96	Kaminskii, A.A.	118	Lecomte, C.	17
Hartl, U.	19	Kämpfer, T.	48	Lee, J.Y.	29
Hartmann, A.	10, 59	Kardash, T.	45	Leemann, A.	60
Hartmann, C.	10, 90	Keeble, D.	74	Lehmann, A.R.	29
Hartmann, R.	78	Keller, W.	63	Lehmann, C.	53
Härtwig, J.	48	Kelm, K.	42	Leist, J.	33, 76, 80
Hasse, B.	52	Kemmerzehl, S.	13	Leitenberger, W.	78
Hayer-Hartl, M.	19	Kempa, P.B.	87	Lenk, C.	97
Hee, C.S.	69	Kettner, K.	14	Li, Z.	108
Heimhilger, J.	122	Keuper, M.	8	List, B.	100
Heinemann, U.	27, 41, 83	Khakhutov, M.	10	Litterst, F.J.	78
Hejny, C.	75	King, S.	38	Liu, T.	116
Held, P.	119	Kipry, J.	26	Lobe, S.	123
Hellmig, M.	116	Kirfel, A.	25	Loetzsch, R.	48
Hemberg, O.	48	Kirsch, T.	53	Loll, B.	69
Hennig, Si.	37	Kirschner, J.	44, 45	Lorentzen, E.	70
Hennig, Sv.	14	Kiziltas Yavuz, N.	119	Lorenz, M.	120
Henning, H.	95	Kledi, X.	119	Lottemoser, W.	25, 78
Hennings, E.	101	Klein, H.	10, 76, 90	Löttsch, R.	48
Henry, P.	52	Kleine, A.	48	Lufaso, M.	25
Herrmann, M.	87	Kleinschrodt, R.	118	Luger, P.	17, 68
Hild, S.	37, 91	Klemm, V.	10	Lührmann, R.	21, 22
Hinterstein, M.	11, 30	Klimakow, M.	40	Lührs, H.	38
Hoch, C.	85, 97, 99, 104	Klimaschin, F.	71	Luneau, D.	18, 82
Hoelzel, M.	11, 30	Klimenta, F.	44, 45	Luo, H.	31
Hoffmann, K.	111	Klocke, A.	41	Lux, O.	118
Hoffmann, Ral.	61, 63	Kloos, M.	83	Magdans, U.	87
Hoffmann, Ram.	43	Knapp, M.	30	Magdysyuk, O.V.	89
Hoffmann, R.	43, 62, 64	Knappe, D.	64	Magerl, A.	16
Hofmann, M.	54, 57, 58	Kodess, B.	66	Maier, B.	31
Hohenberg, H.	51	Kodess, P.	66	Makino, D.L.	70
Hollingsworth, M.D.	84	Kohlmann, H.	95	Malcherek, T.	82, 113
Holzheid, A.	113	Kolesov, B.	74	Manjasetty, B.	68
Hönig, S.	26, 27	Koltashev, V.V.	118	Marcus, M.	89
Hons, D.	117	Kondo, Y.	29	Mariette, C.	33, 84
Hopfner, K.-P.	6	Kopp, V.	84	Marin, A.	121

Index

Marina, E.	121	Nigg, E.A.	20	Ramón-Maiques, S.	29
Marler, B.	108, 109	Nikolowski, K.	119	Randau, C.	54, 57
Martin, S.	56	Nitsche, F.	32	Ranjan, R.	12
Marx, B.	48	Noguchi, Y.	30	Rasche, N.	21
Masutani, C.	29	Nolze, G.	14	Ratayski, U.	71
Matic, S.	43	Noohinejad, L.	85	Raue, L.	10, 90
Mavrodi, D.V.	65	Noureddine, B.-C.	82	Refson, K.	38
Mayerhofer, H.	71	Novikov, D.	53	Reichelt, M.	122
Mayr, F.	83	Oeckler, O.	15, 46, 105, 106	Reimer, R.	51
Maznichenko, I.V.	44, 45	Ollinger, C.	48	Reisecker, C.	91
McAuley, K.	47	Opper, D.	50	Reitz, E.	119
McNally, P.	9, 61	Oschkinat, H.	27	Remmele, T.	84
Meents, A.	51, 55	Ostanin, S.	44	Reuter, H.	122, 123
Megidish, E.	118	Ostermann, A.	54	Rhee, H.	118
Mehner, E.	46	Ott, H.	51	Richter, C.	90
Meijers, R.	40	Otte, K.	26, 35	Richter, D.	54
Meldrum, F.	6	Owen, R.	47	Rius, J.	47
Melnikova, T.	93	Paikaray, S.	26	Robben, L.	82
Merkens, C.	117	Paithankar, K.S.	116	Roeser, D.	13
Merlini, M.	22, 23	Palosz, B.	41	Roessle, M.	40, 114, 115
Mertig, I.	44	Pan, F.	67	Röhr, C.	93, 94, 96
Merz, M.	81	Pandey, C.S.	29	Romano, P.	47
Metzger, H.	37	Panjikar, S.	68	Ropers, D.	53
Metzger, S.J.	39	Panneerselvam, S.	71	Rosenthal, T.	15
Meven, M.	76	Parakhonskiy, G.	18, 22	Roske, Y.	27
Meyer, D.C.	46, 77, 90	Parihar, S.	44	Rossmann, E.	101
Meyerheim, H.L.	44	Park, S.	53, 122	Roth, C.	69
Michaelson, C.	48, 52	Park, S.H.	26	Roth, T.	48
Mihailova, B.	31, 44, 79	Patommel, J.	26	Rouquette, J.	30
Mihajlov, V.	94	Paulmann, C.	53, 79, 113	Röwekamp-Krugley, N.	123
Mikhailova, D.	80	Paulus, G.G.	48	Rueggeberg, M.	37
Müller, M.M.	69	Pavlyuk, V.	116	Ruf, M.	51, 53
Minkov, V.	91	Pawlas, G.	59	Rüggeberg, M.	36
Mittl, P.	12	Pecher, O.	24	Runcevski, T.	63
Mohammed, M.B.	11	Pedersen, B.	29, 76	Rüscher, C.	62, 81, 89, 119
Mohseni, K.	44	Peiffer, S.	26	Russo, L.	55
Mondal, S.	18, 85	Pena, V.	21	Rybakov, V.	93
Monkenbusch, M.	54	Pentcheva, R.	24, 26, 35, 44	Sachawars, A.Q.	106
Morgenroth, W.	32	Perez-Mato, J. M.	35	Samtleben, T.	52
Mueller, U.	41, 56, 116	Peters, H.	83	Sanchez-Weatherby, J.	47
Mueller-Cajar, O.	19	Petricek, V.	71	Sandy, J.	47
Mueller-Dieckmann, J.	71	Petrik, M.	72	Santamaria, A.	20
Mühlberg, M.	75, 101	Petrov, V.	59	Santos, K.	21
Mühle, U.	71	Petry, W.	54, 57, 58	Saupe, J.	27
Müller, A.	43	Pietsch, U.	67, 78, 80	Saxe, F.	36
Müller, M.	8, 34, 54, 57	Plyasova, L.	45	Scavini, M.	116
Müller, Ma.	53, 56	Poll, W.	106	Schäfers, F.	80
Müller, Mar.	8	Pöllmann, H.	63, 106	Schaniel, D.	120
Müller, Me.	34	Pook, N.-P.	79	Schaub, P.	31, 60
Muller, Y.	28	Porsche, S.	117	Scherer, H.	95
Murshed, M.M.	75, 111	Posse, J. M.	71	Scheu, C.	43
Mutter, A.	86	Poulsen, H. F.	3	Schiefner, A.	69
Nagel, N.	92	Prakapenka, V.	22, 23	Schlabach, S.	116
Nagel, P.	81	Presser, V.	8	Schlegel, M.-C.	56
Nandy, A.	63	Preuschl, F.	98	Schleid, T.	39, 95, 99, 102, 104
Neder, R.	19, 45	Probert, M.	52		109, 110
Nénert, G.	75, 101	Prymak, O.	42	Schlichting, I.	6
Nentwich, M.	90	Pukallus, N.	76	Schlömann, M.	26, 69
Netzel, J.	66	Puschmann, H.	50	Schloots, S.	106
Neudert, L.	15	Quiroga, C.	24	Schmahl, W.W.	24, 26, 35, 42, 43, 53
Neumaier, I.	69	Raabe, D.	42	Schmalen, I.	14
Nicholson, J.	47	Rabiller, P.	33, 84	Schmidbauer, M.	84
Nicolov, M.	86	Rademann, J.	27	Schmidmair, D.	72
Nickel, K.G.	8	Rademann, K.	40	Schmidt, H.	101
Niederwieser, N.	75	Rafaja, D.	10, 56, 71	Schmidt, M.U.	88, 92, 100, 107
Niemann, H.	12, 65	Raghunandan, R.	55	Schmitzova, J.	21
Niewa, R.	103	Ram, F.	15	Schneider, H.	25, 38, 45, 75, 101

Index

Schneider, M.	46, 106	Svergun, D.	115	Wilmanns, M.	40, 115
Schneider, T.	40, 114, 115	Szabo, D.	116	Winkelmann, A.	14
Schöder, S.	26	Tagliazucca, V.	46	Winkler, B.	22, 73
Schomborg, L.	62, 89, 119	Taguchi, G.	68	Winter, G.	47
Schön, J.C.	87	Tasci, E.S.	35	Wittge, J.	9, 61
Schön, C. C.	86	Techert, S.	53	Wochnik, A.	43
Schönbeck, T.	50	Tessadri, R.	57	Wolf, E.	14
Schönitzer, V.	28	Than, M.	13	Wolf, T.	81
Schönleber, A.	29, 32, 85	Thomas, N.	34	Wölfel, A.	77
Schorr, S.	77, 105	Thomas, P.	30, 74	Wood, I.	39
Schrader, T.E.	54	Thomashow, L.	65	Wu, S.	37, 113
Schreiber, G.	10	Timmins, P.	58	Xhaxhiu, K.	120
Schreiner, M.	12	Tkachev, S.	22	Yang, W.	29
Schreuer, J.	29, 45, 80, 81	Többens, D.M.	52, 57	Ye, Z.-G.	74
Schreyer, A.	57	Toudic, B.	33, 84	Young, J.	43
Schröder, S.	123	Tovar, M.	52	Yu, S.	13
Schröder, T.	46	Trella, T.	112	Yu, X.-H.	68
Schroer, C.	26	Trots, D.	9, 22	Zaefferer, S.	15
Schröer, P.	80, 81	Tutughamiarso, M.	64	Zafred, D.	63
Schropp, A.	26	Ubhi, H.S.	42	Zahlbach, J.	102
Schuetz, A.	83	Uchanska-Ziegler, B.	69	Zahn, M.	64
Schulz, A.	81	Ühlein, M.	116	Zakharov, B.	74
Schulz, H.	43	Urban, P.	105, 106	Zebisch, M.	20
Schulze, K.S.	48	Urlaub, H.	21	Zhang, J.	29, 77, 85
Schuppler, S.	81	Uschmann, I.	48	Zhang, S.	103
Schurz, C.M.	104	van de Streek, J.	100	Zhao, Y.	29
Schustereit, T.	95	van Smaalen, S.	18, 29, 31, 32	Zhuravlev, K.	22
Schwab, W.	69		53, 66, 77, 85, 107	Ziegler, A.	26, 37, 69, 91
Schwalbe, C.H.	58	Vella-Zarb, L.	65	Zimmermann, L.W.	99, 102
Schwarz, M.	96	Verheyen, V.	112	Zitzer, S.	110
Schwarzenbach, D.	3	Vit, A.	13	Zörb, S.	107
Schwarzkopf, J.	84	Voigt, W.	101	Zschornak, M.	90
Schwarz Müller, S.	46	Volk, J.	111		
Send, S.	78	von Löhneysen, H.	81		
Senyshyn, A.	12, 29	von Zimmermann, M.	38		
Sheldrick, G.M.	18	Wagner, A.	38, 51		
Shi, J.	29, 41	Wagner, F.E.	26		
Sidoruk, J.	76	Wagner, G.	64, 123		
Simonov, A.	49, 86	Wagner, W.	48		
Simons, B.	88	Waidick, F.	84		
Sinz, Q.	69	Wandolski, R.	108		
Skerra, A.	69	Wang, R.	67, 117		
Smith, V.	41	Wang, S.	113		
Sommerdijk, N.	15, 36	Warmer, M.	51		
Sorensen, T.	47	Weber, G.	27		
Sowa, H.	76	Weber, M.	17		
Spohn, B.	109	Weber, S.-U.	25, 78		
Stadler, A.	58	Weber, T.	31, 49, 86		
Steffien, M.	116	Weckert, E.	5		
Steilmann, T.	31	Wegener, S.	69		
Steininger, R.	116	Wehrhan, O.	48, 73		
Stephan, C.	52, 77	Weidenthaler, C.	46		
Stephan, S.	26	Weil, M.	99		
Steurer, W.	31, 49	Weiss, I.	28		
Stokes, H. T.	31	Weiss, M.	28, 41, 78, 116		
Stöber, S.	106	Wellenreuther, G.	26		
Stöcker, H.	77	Welzmilller, S.	15, 105, 106		
Stöger, B.	34	Wenda, R.	53		
Stöhlker, T.	48	Wendler, P.	19		
Stolze, K.	32	Wiacek, C.	26		
Stopford, J.	9	Wieczorek, C.	14		
Stotz, M.	19	Wiehl, L.	22		
Sträter, N.	14, 20, 62, 64, 69	Wierzbicka-Wieczorek, M.	63		
Strauss, H.M.	14	Wildner, M.	98		
Strobel, S.	109	Will, J.	16		
Strüder, L.	78	Williams, M.	47		
Stuart, D.	51	Willumeit, R.	115		

Supplement Issue No. 32
Zeitschrift für Kristallographie